



THE UNIVERSITY *of* EDINBURGH

This thesis has been submitted in fulfilment of the requirements for a postgraduate degree (e.g. PhD, MPhil, DClinPsychol) at the University of Edinburgh. Please note the following terms and conditions of use:

This work is protected by copyright and other intellectual property rights, which are retained by the thesis author, unless otherwise stated.

A copy can be downloaded for personal non-commercial research or study, without prior permission or charge.

This thesis cannot be reproduced or quoted extensively from without first obtaining permission in writing from the author.

The content must not be changed in any way or sold commercially in any format or medium without the formal permission of the author.

When referring to this work, full bibliographic details including the author, title, awarding institution and date of the thesis must be given.



THE UNIVERSITY
of EDINBURGH

**Establishing an anatomically and clinically
relevant tissue engineered tendon-bone model
of the flexor digitorum profundus insertion**

Jeremy William Mortimer

Ph.D. Thesis

The University of Edinburgh

2021

Declaration

I declare that this thesis is my own composition, from work completed between 3rd October 2016 and 7th January 2021, and has not been submitted for any other degree or professional qualification.

Jeremy William Mortimer

7th January 2021

Acknowledgements

My deepest thanks and appreciation are bestowed upon my supervisor, *Dr Jennifer Paxton*, for helping me set sail on this voyage of discovery, and for unflinching support, guidance, patience and positivity throughout all facets of the PhD and my continued career. This really would not have been possible without you.

Sincere thanks to my clinical supervisor, *Miss Philippa Rust*, for supporting me through conferences, continued funding and providing regular input to steer the work. As thesis chair, thank you to *Prof Tom Gillingwater* for experienced advice and challenging me as 'devil's advocate', with contribution from *Prof Norah Spears*.

I am indebted to the selfless gift of the *body donors* who made this work possible, and very grateful to *Orthopaedic Research UK* for providing project funding.

Our laboratory group has been a constant source of assistance, joy and sanity. Eternal gratitude to my good friend, the master, *Dr Hamad Alsaykhan*; from settling me in on day 1, to teaching me all I know by day 1555 – shukran jazeelan. *Christina Loukopoulou* has helped me successfully round the last lap, thank you for your encouragement in both work and beyond. Thank you to *Subashan Vadibeler* and *Nika Vonk* for significant contributions as 2nd observers for morphometric measurements; *Miriam Graute* for early fish shape and lattice mold ideas; and *Jan Spende*, *Mario Macía* and *Vicky Fassoula* for keeping my cells alive.

Office 228 was home for 3½ years, and I couldn't have asked for better resident humans to share knowledge, dilemmas, stories, laughter, tea and cake. Much love to *Alison Thomson*, *Natalie Courtney*, *Rachel Kline*, *Roxanna Munir*, *Vicky Zimmer*, *Nithya Nair*, *Laura Comley*, and extra special thanks to *Alannah Mole* for lovingly hauling me over the line. Not forgetting the office radiator for making long solo evenings and weekends bearable. Life outside the office was rare, but friendships forged in the Hugh Robson corridors were hugely important for motivation and a sense of humanity; so thank you to *Anna Motyl*, *Dinja Van Der Hoorn*, *Ewout Groen*, *Hannah*

Shorrocks, Helena Chaytow, Ines Boehm, Kiterie Faller, Leire Ledahawsky, Nikky Huang, Penelope Boyd, Hamish Runciman and Brenda Murage.

My gratitude and appreciation extend to many for their technical and specialist expertise. Special thanks to the Anatomy@Edinburgh support staff, managed by the inimitable *Iain Campbell*, including (past and present) *Laura Sheils, Susan Bond, Fraser Bisset* and *Karen Scott*, who have always been accommodating and conversant with the practicalities of my anatomy research. Thank you to *Viv Allison* and *Louise Dunn* for histology training, *Dr Flora Gröning* and *Rebecca Quinn* from the University of Aberdeen for decalcification and staining guidance, *Keith Erskine* at Roslin for slide scanner training, and *Yousef Almajed* and *Abdulaziz Alomiery* for helpful discussions on entheses staining and analysis. Particular thanks to *Dr Michael Crichton* at Heriot-Watt University for use of the OCT scanner, with help from *Chloe Newlands*. *Dr Crispin Jordan* provided statistical guidance throughout, stimulating a much deeper personal grasp of experimental design and analysis. Thank you to *Richard Collins* and *Gosia Walton* at Edinburgh College of Art for 3D printing the mold designs. For troubleshooting and running a tight ship in the lab and research building, I thank *Deb Allen, Mike Molinek, Krisztina Vinko, Derek Thomson, Andrew Dinse-Harrower, James Griffiths* and *Carol Wollaston*.

I would also like to acknowledge the companionship and encouragement of particular friends who have shepherded me through this life chapter, most already 'PhD positive': *Will Ferguson, Richard McLauchlan, Sam Wilkinson* and *Jim Ferguson*. Top of this very list is a great man of shared consciousness and vision, *Ross Jones*. We describe our musical collections as friends who are always there for us, and for sustenance through the many long hours of image quantification I am especially grateful to *Kraftwerk, Erra, Tool, Isis, Architects, Nine Inch Nails, David Bowie, Phoebe Bridgers, Ben Howard* and *Ludovico Einaudi*. And as a friend who inspired me to gaze towards the academic light, your memory will remain with me, so thank you *Sophie Miller*.

The constant support of my family has always laid the foundation for any personal achievement, and here I can record my eternal gratitude. Thank you to my brother, *Justin*, and sister, *Julia*, for inspiration, kindness, wisdom and playing host on many occasions. *I would like to dedicate this work to my mother and father, for providing opportunities and supporting me in every aspect; thank you for always being there.*

Abstract

Avulsion of the flexor digitorum profundus (FDP) tendon from the distal phalanx (DP) in the finger is a common and distinct clinical injury of the hand ('jersey finger') with considerable functional morbidity. Multiple surgical techniques are employed to reattach the tendon to the bone, but no single technique has emerged as the optimal treatment method. Issues such as reduced range of movement, infection, nail deformity and cost complicate the requirement for strong fixation and prevention of re-rupture.

Crucially, repair of avulsion injuries does not regenerate the enthesis, the region of graded multiphasic microanatomy at the tendon-bone insertion. The enthesis allows uniform muscle force transmission between the mechanically distinct tendon and bone through specialised adaptations to dissipate stress foci. Avulsion repair is scar-mediated and of low mechanical strength, prone to re-rupture at the tendon-bone interface. Interfacial tissue engineering provides the opportunity to create an *in vitro* tendon-bone model with potential to re-establish the enthesis through co-culture of tendon and bone cells, which could be used to evaluate repair techniques or as a composite tissue graft for clinical use.

The aim of this project was to establish an *in vitro* model system that was anatomically representative and clinically applicable to the investigation and treatment of FDP avulsion injury. The 2 main objectives were to thoroughly evaluate the native anatomy of the human FDP insertion, and to design and develop a relevant 3-dimensional (3D) *in vitro* tendon-bone co-culture model.

Human cadaveric tissue was dissected and photographed for image analysis to determine gross shape and dimension morphometrics of the FDP-DP tendon-bone interface, FDP tendon and DP bone. Finger and gender differences were found to significantly influence measurement values, with data groupings informing design guidelines for 'small', 'medium' and 'large' model sizes. Cadaveric tissue was also histologically processed to qualitatively describe the fibrocartilaginous FDP enthesis for the first time. Quantitative analysis of tendon fibres revealed a mean angle of

insertion across the soft-hard tissue interface of 30°, providing a guide to the angled attachment of the tendon and bone model components.

Development of the *in vitro* model enhanced an existing multi-tissue fibrin scaffold soft tissue-bone anchor design into an FDP tendon analogue-DP bone anchor single species co-culture construct. Rat fibroblast and osteoblast cultures were established and characterised in standard growth medium, mineralising medium and a 50:50 media mix. Formation and maturation of the fibroblast-seeded fibrin tendon analogue was analysed histologically in single and multi-strand cultures for morphological development and collagen deposition. Long term tendon analogues were cultured with different anchor sizes, fibrin constituent volumes, cell numbers and growth media for width comparison with cadaveric tendon data, and assessment of 3D morphology with optical coherence tomography. Investigation of the bone anchor component focused on brushite, a phosphate mineral-based bone scaffold material, including assessment of attachment and proliferation of seeded osteoblasts.

Model assembly required development of a novel 3D printed mold and silicone impression system for guided tendon analogue culture and angled bone anchor attachment. Optimal design elements and *in vitro* culture materials ultimately combined to produce a fibroblast-seeded tendon analogue and osteoblast-seeded bone anchor 3D model, co-cultured in 3 anatomical sizes clinically relevant to FDP tendon avulsion. These models can be used as the basis to study entheses formation and further optimised towards a clinical product for use in FDP avulsion repair.

Lay Summary

The flexor digitorum profundus (FDP) is a hand tendon that bends the finger and allows gripping and pinching. A problematic injury that reduces hand use is the FDP tendon pulling away from its attachment to the furthest bone of the finger, the distal phalanx (DP). Many surgical reattachment methods exist but issues such as poor finger movement and infection are common, and no method restores the original tendon-bone attachment strength, so the tendon is more likely to detach again.

Tendons attach to bones through a millimetre sized connecting region, consisting of specialised cells in an environment distinct from the tendon and bone, called the 'enthesis'. During tendon contraction for bone movement, the enthesis helps prevent potentially excessive and harmful forces at the join between the soft tendon and hard bone. However, after injury, the enthesis is damaged and not regenerated after tendon-bone reattachment, so the attachment is weaker and detachment more likely to reoccur. In the laboratory, cells can be grown inside 3-dimensional (3D) materials resembling tendon and bone, and controlled to try to form the enthesis ('tissue engineering'). Such a tendon-bone laboratory model could be implanted into patients by surgeons to improve treatment of these injuries.

This project aimed to make a tendon-bone model, using cells in the laboratory, that would be the correct size and shape to potentially use in patients with FDP tendon attachment injury. This first involved detailed study of the human FDP attachment, then design and production of the laboratory model using this information.

Observations and measurements were made of the FDP tendon, DP bone and their connecting region using human material donated to the university after death. Measurement results were variable between the different fingers and genders, leading to a model design of 3 particular sizes. The FDP tendon enthesis was also examined microscopically in the human material, providing the first specific description in this particular tendon. The tendon was found to attach to the bone at an overall angle of 30°, which was an important part of the laboratory model design.

The laboratory model required a number of parts, including cells, supporting materials in which the cells grow, and nutritional substances ('media'). These parts were tested to find the most suitable of each to use in the model. Tendon and bone cells were obtained from rats and, since they would be grown together in the same model, their behaviour in different media mixtures was observed. The soft tendon portion of the model, containing the tendon cells, was examined microscopically and with a 3D scanner for formation and shape, and its width was specifically compared to human tendon measurements when grown using different media, volume of supporting material and number of tendon cells. A promising bone-like ceramic material was investigated for the hard bone portion, assessing how well it allowed attachment and growth of bone cells.

Based on the human observations, specialised molds were produced so that the tendon and bone parts of the model could attach together correctly in a defined shape and size, whilst the cells in the materials were grown. A 3D tendon-bone laboratory model was ultimately achieved, in 3 sizes appropriate for a broad range of patients with FDP tendon attachment injury. With the specific structure in place, the model can be used to focus on laboratory development of the enthesis and improvement of strength between the tendon and bone parts, nearing eventual use as a patient treatment.

Contents

<i>Declaration</i>	<i>ii</i>
<i>Acknowledgements</i>	<i>iii</i>
<i>Abstract</i>	<i>v</i>
<i>Lay Summary</i>	<i>vii</i>
<i>Contents</i>	<i>ix</i>
<i>Figures</i>	<i>xx</i>
<i>Tables</i>	<i>xxiii</i>
<i>Abbreviations</i>	<i>xxv</i>

Chapter 1:

General Introduction	1
1.1 Chapter Overview	2
1.2 The Flexor Digitorum Profundus	2
1.2.1 Overview	2
1.2.2 Muscle	4
1.2.3 Tendon	4
1.2.3.1 Gross Anatomy.....	4
1.2.3.2 Architecture	5
1.2.3.3 Flexor Sheath	6
1.2.3.4 Nutrition	7
1.2.3.5 Biomechanics	8
1.2.3.6 Insertion	9
1.2.4 Distal Phalanx Bone	10
1.2.5 Distal Interphalangeal Joint	11
1.2.6 Summary	12
1.3 Flexor Digitorum Profundus Insertion Injury	12
1.3.1 Overview	12
1.3.2 Epidemiology	13
1.3.3 Aetiology and Pathophysiology	14
1.3.4 Presentation	15
1.3.5 Classification	16

1.3.6	Surgical Management.....	18
1.3.6.1	Tendon-Bone Fixation	18
1.3.6.1.1	Techniques	18
1.3.6.1.2	Drawbacks	21
1.3.6.1.3	Optimal Approach	22
1.3.6.1.4	Outcomes.....	24
1.3.6.2	Tendon-Tendon Fixation.....	24
1.3.7	Summary	25
1.4	The Enthesis.....	26
1.4.1	Overview	26
1.4.2	General Structure and Function Principles.....	26
1.4.3	Classification	28
1.4.4	The Fibrocartilaginous Enthesis.....	28
1.4.4.1	Dense Fibrous Connective Tissue	31
1.4.4.2	Fibrocartilage.....	31
1.4.4.2.1	Uncalcified Fibrocartilage	32
1.4.4.2.2	Calcified Fibrocartilage	33
1.4.4.2.3	Tidemark.....	34
1.4.4.3	Bone.....	35
1.4.5	The Fibrous Enthesis.....	36
1.4.6	Vascularity and Innervation	37
1.4.7	Development	38
1.4.7.1	Overview	38
1.4.7.2	Biological Factors	39
1.4.7.3	Mechanical Factors	40
1.4.8	Injury and Repair	41
1.4.8.1	Surgical Treatment	42
1.4.8.2	Healing	42
1.4.8.2.1	Augmentation.....	43
1.4.9	Summary.....	44
1.5	Interfacial Tissue Engineering	45
1.5.1	Overview	45
1.5.2	2-Dimensional versus 3-Dimensional.....	46
1.5.3	Design Components	46
1.5.3.1	Scaffolds.....	46
1.5.3.1.1	Materials	48

1.5.3.1.2	Fabrication Methods	48
1.5.3.2	Cells	49
1.5.3.2.1	Co-Culture.....	51
1.5.3.2.2	Stem Cell Culture	51
1.5.3.3	Stimulators	52
1.5.3.3.1	Growth Factors	52
1.5.3.3.2	Mechanical Loading	53
1.5.3.4	Bioreactors	54
1.5.4	3-Dimensional Multi-Tissue Strategies.....	55
1.5.4.1	Stratified	55
1.5.4.2	Gradient	56
1.5.5	Future Developments	57
1.5.5.1	Anatomy in Tissue Engineering	58
1.5.6	Summary	59
1.6	Project Rationale.....	59
1.7	Aims	60

Chapter 2:

	Morphology of the Flexor Digitorum Profundus Insertion	61
2.1	Chapter Overview.....	62
2.2	Introduction	62
2.3	Aim and Objectives	64
2.4	Materials and Methods.....	64
2.4.1	Cadaveric Specimens.....	64
2.4.2	General Dissection	65
2.4.3	Tendon-Bone Interface	66
2.4.3.1	Footprint Generation.....	66
2.4.3.2	Image Acquisition	67
2.4.3.3	Image Analysis	68
2.4.4	Tendon Width	70
2.4.4.1	Sample Preparation.....	70
2.4.4.2	Image Acquisition	70
2.4.4.3	Image Analysis	71
2.4.5	Bone Depth	72
2.4.5.1	Sample Preparation.....	72
2.4.5.2	Measurements.....	72

2.4.6	Inter-Observer Reliability	73
2.4.7	Data Analysis	73
2.5	Results	75
2.5.1	Tendon-Bone Interface	75
2.5.1.1	Footprint Morphometrics	76
2.5.1.2	Positioning on Distal Phalanx	82
2.5.1.3	Inter-Observer Reliability	85
2.5.2	Tendon Width	87
2.5.2.1	Morphometrics	87
2.5.2.2	Inter-Observer Reliability	91
2.5.3	Bone Depth	91
2.5.4	Effect of Side	94
2.5.5	Combined Data Groupings	95
2.6	Discussion	97
2.6.1	Tendon-Bone Interface	98
2.6.1.1	Methodology Rationale	98
2.6.1.2	Tendon-Bone Interface Model Design	98
2.6.1.2.1	Shape	98
2.6.1.2.2	Dimensions	100
2.6.1.3	Surgical Positioning	102
2.6.1.4	Validity and Reliability	105
2.6.2	Tendon Width	107
2.6.2.1	Methodology Rationale	107
2.6.2.2	Tendon Analogue Model Design	108
2.6.2.3	Validity and Reliability	110
2.6.3	Bone Depth	110
2.6.3.1	Methodology Rationale	110
2.6.3.2	Bone Anchor Model Design	111
2.6.3.3	Surgical Bone Anchor Fixation	113
2.6.3.4	Validity and Reliability	116
2.6.4	Overall Model Design	117
2.6.5	General Limitations	120
2.6.5.1	Sample	120
2.6.5.2	Dissection Methodology	122
2.6.5.3	Measurement Methodology	123

2.7	Summary of Findings.....	124
------------	---------------------------------	------------

Chapter 3:

	Histology of the Flexor Digitorum Profundus Insertion	125
3.1	Chapter Overview.....	126
3.2	Introduction	126
3.3	Aim and Objectives	128
3.4	Materials and Methods.....	128
3.4.1	Cadaveric Specimens.....	128
3.4.2	Sample Preparation.....	128
3.4.3	Decalcification	129
3.4.3.1	Endpoint Testing.....	130
3.4.4	Paraffin Wax Processing	130
3.4.5	Sectioning.....	130
3.4.6	Staining	131
3.4.6.1	Hematoxylin and Eosin.....	132
3.4.6.2	Toluidine Blue.....	132
3.4.6.3	Van Gieson's.....	132
3.4.6.4	Masson's Trichrome	132
3.4.7	Tendon Fibre Angle Measurements.....	133
3.4.7.1	Inter-Observer Reliability	135
3.4.8	Data Analysis	135
3.5	Results.....	138
3.5.1	Qualitative Analysis	138
3.5.1.1	Enthesis Classification.....	138
3.5.1.2	General Findings	138
3.5.1.3	Regional Variation	142
3.5.1.4	Histopathology.....	142
3.5.2	Tendon Fibre Angle Measurements.....	145
3.5.2.1	Tidemark Intersection Fibres	145
3.5.2.1.1	Effect of Enthesis Distance	151
3.5.2.2	Approaching Fibres	151
3.5.2.3	Angle Change.....	154
3.5.2.4	Effect of Side	156
3.5.2.5	Inter-Observer Reliability	157

3.6	Discussion.....	160
3.6.1	The FDP Enthesis	160
3.6.2	Tendon Fibre Insertion Angle.....	162
3.6.2.1	Methodology Rationale.....	162
3.6.2.2	Tidemark Intersection Fibres	166
3.6.2.3	Approaching Fibres	169
3.6.2.4	Angle Change.....	170
3.6.2.5	Validity and Reliability.....	171
3.6.3	Tendon-Bone Interface Model Design	173
3.6.4	General Limitations.....	174
3.6.4.1	Sample	174
3.6.4.2	Sample Preparation.....	175
3.6.4.3	Tissue Analysis.....	177
3.7	Summary of Findings.....	177

Chapter 4:

Assessment of Tendon and Bone Components for In Vitro Model

	Development	179
4.1	Chapter Overview.....	180
4.2	Introduction	180
4.3	Aim and Objectives.....	182
4.4	Materials and Methods.....	183
4.4.1	Cell and Tissue Culture	183
4.4.1.1	Sterility	183
4.4.1.2	Phosphate Buffered Saline.....	183
4.4.1.3	Culture Media	183
4.4.1.3.1	S-DMEM	183
4.4.1.3.2	RODM	183
4.4.1.3.3	50:50 Medium	184
4.4.1.3.4	Ascorbic Acid and Proline.....	184
4.4.1.3.5	Media Changes.....	184
4.4.1.4	Culture Methods	184
4.4.1.4.1	General	184
4.4.1.4.2	Sub-Culture.....	184
4.4.1.4.3	Cell Counting	185
4.4.1.5	Cell Storage.....	185

4.4.1.6	Cell Thawing.....	185
4.4.1.7	Imaging and Photography.....	186
4.4.2	Cells.....	186
4.4.2.1	Procurement, Isolation and Expansion	186
4.4.2.1.1	General Rat Dissection.....	186
4.4.2.1.2	Rat Tendon Fibroblasts.....	186
4.4.2.1.3	Rat Bone Marrow-Derived Mesenchymal Stem Cells	187
4.4.2.1.4	Rat Osteoblasts	188
4.4.2.1.5	Differentiated Rat Osteoblasts.....	188
4.4.2.1.6	Chick Tendon Fibroblasts	189
4.4.2.2	Mineralisation Testing.....	189
4.4.2.2.1	S-DMEM	189
4.4.2.2.2	RODM	190
4.4.2.2.3	50:50 Medium	190
4.4.2.2.4	Alizarin Red Staining.....	190
4.4.3	Tendon Analogue	190
4.4.3.1	Fibrin Hydrogel Reagents.....	190
4.4.3.1.1	Thrombin.....	191
4.4.3.1.2	Aminohexanoic Acid	191
4.4.3.1.3	Aprotinin.....	191
4.4.3.1.4	Fibrinogen.....	191
4.4.3.2	Basic Suture-Suture Constructs.....	192
4.4.3.2.1	General Method	192
4.4.3.2.2	Investigations	193
4.4.3.3	Multi-Strand Suture-Suture Constructs	193
4.4.3.4	Histology.....	194
4.4.3.4.1	Paraffin Wax Embedding and Sectioning	194
4.4.3.4.2	Staining	194
4.4.3.5	Suture Manipulation Experiments	194
4.4.3.5.1	Vertical/Vertical	195
4.4.3.5.2	Vertical/Horizontal.....	195
4.4.3.5.3	Suture Gel Contraction	196
4.4.3.6	Anatomical Suture Experiments.....	198
4.4.3.6.1	Standard Volume Gel.....	198
4.4.3.6.2	Double Volume Gel.....	199
4.4.3.6.3	Hypotheses	199
4.4.3.6.4	Optical Coherence Tomography.....	200
4.4.4	Bone Anchor.....	201

4.4.4.1	Brushite	201
4.4.4.1.1	β-Tricalcium Phosphate	201
4.4.4.1.2	Cement Formation	201
4.4.4.1.3	Cement Casting	201
4.4.4.1.4	Sterilisation	202
4.4.4.2	Reprobone.....	202
4.4.4.3	Basic Tendon-Bone Constructs	202
4.4.4.4	Brushite Acid Washout Trials.....	203
4.4.4.5	Osteoblast Seeding Trial	204
4.4.4.5.1	Preparations.....	204
4.4.4.5.2	Acid Washouts	204
4.4.4.5.3	Cell Seeding.....	205
4.4.4.5.4	Cell Collection and Freezing.....	205
4.4.4.5.5	Assaying	206
4.4.4.5.6	Standard Curves	207
4.4.5	Data Analysis	208
4.5	Results.....	209
4.5.1	Cells	209
4.5.1.1	Isolation and Phenotype	209
4.5.1.1.1	Rat Tendon Fibroblasts.....	209
4.5.1.1.2	Rat Bone Marrow-Derived Mesenchymal Stem Cells	209
4.5.1.1.3	Rat Osteoblasts	209
4.5.1.1.4	Differentiated Rat Osteoblasts.....	210
4.5.1.1.5	Chick Tendon Fibroblasts	210
4.5.1.2	Mineralisation Testing.....	212
4.5.1.2.1	S-DMEM	212
4.5.1.2.2	RODM	213
4.5.1.2.3	50:50 Medium	213
4.5.2	Tendon Analogue	217
4.5.2.1	Basic Suture-Suture Constructs.....	217
4.5.2.2	Multi-Strand Suture-Suture Constructs	221
4.5.2.3	Suture Manipulation Experiments	223
4.5.2.3.1	Vertical/Vertical	223
4.5.2.3.2	Vertical/Horizontal.....	228
4.5.2.3.3	Suture Gel Contraction	232
4.5.2.4	Anatomical Suture Experiments.....	233
4.5.2.4.1	Standard Volume Gel.....	233

4.5.2.4.2	Double Volume Gel.....	235
4.5.2.4.3	Summary of Effect of Culture Variables.....	239
4.5.3	Bone Anchor.....	250
4.5.3.1	Basic Tendon-Bone Constructs	250
4.5.3.2	Brushite Acid Washout Trials.....	251
4.5.3.3	Osteoblast Seeding Trial	253
4.5.3.3.1	Seeding Efficiency	253
4.5.3.3.2	Proliferation.....	253
4.6	Discussion.....	254
4.6.1	Cells	254
4.6.1.1	Mineralising Ability and Effect of Culture Medium	254
4.6.1.1.1	Rat Tendon Fibroblasts.....	255
4.6.1.1.2	Rat Bone Marrow-Derived Mesenchymal Stem Cells	255
4.6.1.1.3	Rat Osteoblasts	256
4.6.1.1.4	Differentiated Rat Osteoblasts.....	257
4.6.1.2	Selection for Co-Culture	258
4.6.1.3	Limitations	259
4.6.1.3.1	Isolations and Cell Type.....	259
4.6.1.3.2	Applicability and Validity	261
4.6.2	Tendon Analogue	262
4.6.2.1	Formation and Maturation.....	262
4.6.2.1.1	Single-Strand	262
4.6.2.1.2	Multi-Strand.....	264
4.6.2.2	Suture Anchor Manipulation.....	266
4.6.2.3	Effect of Culture Variables	267
4.6.2.3.1	Culture Medium.....	268
4.6.2.3.2	Additional Anchor Points.....	270
4.6.2.3.3	Fibrin Gel Volume	270
4.6.2.3.4	Cell Number	271
4.6.2.4	Optimum Set Up for Co-Culture Construct.....	271
4.6.2.5	Limitations	273
4.6.3	Bone Anchor.....	275
4.6.3.1	Tendon Analogue Attachment	275
4.6.3.2	Brushite Acid Washout	276
4.6.3.3	Osteoblast Seeding	277
4.6.3.3.1	Methodology Rationale	277
4.6.3.3.2	Seeding.....	279

4.6.3.3.3	Proliferation.....	282
4.6.3.3.4	Integration into Co-Culture Construct	283
4.6.3.3.5	Limitations.....	283
4.7	Summary of Findings.....	284

Chapter 5:

	Integrated Anatomical Model Design and Tendon-Bone Cultures	287
5.1	Chapter Overview.....	288
5.2	Introduction	288
5.3	Aim and Objectives	289
5.4	Materials and Methods.....	290
5.4.1	Model Design and Production.....	290
5.4.1.1	Bone Anchor.....	290
5.4.1.2	Culture Zone.....	290
5.4.1.2.1	'Fish Shape' Mold	290
5.4.1.2.2	Lattice Frame Mold	290
5.4.1.2.3	Preparation and Set Up	294
5.4.2	Construct Cultures.....	296
5.4.2.1	Culture Methods	296
5.4.2.2	Monoculture Constructs.....	296
5.4.2.2.1	Without Brushite Acid Washout	296
5.4.2.2.2	With Brushite Acid Washout	297
5.4.2.3	Co-Culture Constructs	298
5.4.2.3.1	Osteoblast Bone Anchor Seeding.....	298
5.4.2.3.2	Co-Culture Integration.....	299
5.5	Results.....	299
5.5.1	Culture Zone.....	299
5.5.2	Construct Cultures.....	301
5.5.2.1	Monoculture Constructs.....	301
5.5.2.1.1	Without Brushite Acid Washout	301
5.5.2.1.2	With Brushite Acid Washout	305
5.5.2.2	Co-Culture Constructs	308
5.6	Discussion.....	314
5.6.1	Culture Zone.....	314
5.6.1.1	Anatomical Design.....	314
5.6.1.2	3D Printing and Molding	315

5.6.2	Construct Cultures.....	316
5.6.2.1	Brushite Acid Leaching.....	316
5.6.2.2	Contraction and Morphology.....	317
5.6.2.2.1	General Contraction.....	318
5.6.2.2.2	Gel Volume and Cell Number.....	319
5.6.2.2.3	Culture Media.....	320
5.6.2.3	Tendon-Bone Interface Attachment.....	320
5.6.2.4	Co-Cultures.....	322
5.6.2.5	Limitations.....	324
5.7	Summary of Findings.....	324

Chapter 6:

	General Discussion.....	327
6.1	Chapter Overview.....	328
6.2	Review of Results.....	328
6.3	Implications, Applications and Future Work.....	330
6.3.1	Tendon Analogue.....	331
6.3.2	Bone Anchor.....	332
6.3.3	Tendon-Bone Interface.....	334
6.3.4	Cells.....	335
6.4	Conclusion.....	336
	Bibliography.....	337
	Appendices.....	362

Figures

1.1	Flexor Digitorum Profundus Anatomy	3
1.2	Hierarchical Tendon Structure	5
1.3	The Digital Fibrous Flexor Sheath	7
1.4	Flexor Tendon Vincula	8
1.5	FDP Insertion Vasculature	10
1.6	Comparison of Insertional Angle Change at Epiphyseal and Diaphyseal Tendon Insertions	29
1.7	The Fibrocartilaginous Enthesis	30
1.8	Optimum Interfacial Tissue Engineering Gradient Approach	58
2.1	General Dissection Methodology	66
2.2	FDP Footprint Generation	67
2.3	FDP Footprint Measurements	69
2.4	Distal Phalanx Measurements	70
2.5	FDP Tendon Width Measurements	71
2.6	Distal Phalanx Bone Depth Measurements	72
2.7	Complete Specimen Set of FDP Footprints	75
2.8	Surface Area of FDP Footprint	77
2.9	Height of FDP Footprint	78
2.10	Base Width of FDP Footprint	79
2.11	Apex Width of FDP Footprint	80
2.12	Side Comparison of FDP Footprint Trapezoid Internal Angles	81
2.13	Gender Breakdown of FDP Tendon Width	89
2.14	Individual Finger Breakdown of FDP Tendon Width	90
2.15	Gender Breakdown of Distal Phalanx Bone Depth at FDP Insertion	93
2.16	Individual Finger Breakdown of Distal Phalanx Bone Depth at FDP Insertion	94
2.17	Size Category Groupings for FDP Footprint, Tendon Width and Bone Depth	96
2.18	Representative FDP Footprints from Equivalent Study	104
2.19	Combination FDP Fixation Technique for Optimal Footprint Recreation	116
3.1	Dissection of Tendon-Bone Histological Sample	129

3.2	Tendon Fibre Angle Measurement Methodology	134
3.3	Histology of the FDP Enthesis (1)	140
3.4	Histology of the FDP Enthesis (2)	141
3.5	Comparison of Proximal, Middle and Distal Regions of the FDP Enthesis.....	143
3.6	FDP Enthesis Histopathology.....	144
3.7	Angle of Tidemark Fibres at 20% Enthesis Distance	148
3.8	Angle of Tidemark Fibres at 40% Enthesis Distance	148
3.9	Angle of Tidemark Fibres at 50% Enthesis Distance	149
3.10	Angle of Tidemark Fibres at 60% Enthesis Distance	149
3.11	Angle of Tidemark Fibres at 80% Enthesis Distance	150
3.12	Angle of Tidemark Fibres Averaged Across All Enthesis Distances.....	150
3.13	Angle Change between Approaching and Tidemark Fibres.....	155
4.1	Established Fibroblast-Seeded Fibrin Gel Soft Tissue Constructs.....	182
4.2	Method of Tendon Analogue Formation in Basic Suture-Suture Constructs.....	193
4.3	Set Up and Measurement Methodology for Suture Manipulation Experiments	197
4.4	Primary Rat Cell Isolation Cultures and Proliferation	211
4.5	Differentiated Rat Osteoblasts in Early Culture.....	212
4.6	Mineralisation Testing of RTF, BMSC, ROb and dROb Cultures in S- DMEM.....	214
4.7	Mineralisation Testing of RTF, BMSC, ROb and dROb Cultures in RODM.....	215
4.8	Mineralisation Testing of RTF and dROb Cultures in 50:50 Medium	216
4.9	Tendon Analogue Formation in the Basic Suture-Suture Construct.....	218
4.10	Histology of the Basic Single-Strand Tendon Analogue (1)	219
4.11	Histology of the Basic Single-Strand Tendon Analogue (2)	220
4.12	Multi-Strand Tendon Analogue Constructs	222
4.13	Histology of the Double Multi-Strand Tendon Analogue	223
4.14	Formation of Vertical/Vertical Suture Tendon Analogue Constructs	226
4.15	Gel Width in the Formation of Vertical/Vertical Suture Tendon Analogue Constructs.....	227
4.16	Formation of Vertical/Horizontal Suture Tendon Analogue Constructs	230
4.17	Gel Width in the Formation of Vertical/Horizontal Suture Tendon Analogue Constructs.....	231
4.18	Width Comparison of Gel at Suture and Suture Itself	232

4.19	Maturation of Standard Volume Gel Anatomical Suture-Suture Constructs.....	241
4.20	Maturation of Double Volume Gel Anatomical Suture-Suture Constructs ..	242
4.21	Gel Width at 0% Distance in Anatomical Suture-Suture Constructs.....	243
4.22	Gel Width at 25% Distance in Anatomical Suture-Suture Constructs.....	244
4.23	Gel Width at 50% Distance in Anatomical Suture-Suture Constructs.....	245
4.24	Gel Width at 75% Distance in Anatomical Suture-Suture Constructs.....	246
4.25	Gel Width at 100% Distance in Anatomical Suture-Suture Constructs.....	247
4.26	OCT Images at 50% Distance through Anatomical Suture Constructs	248
4.27	OCT Images through a 'Double Gel/Double Cells/+AA+P' Anatomical Suture Construct.....	249
4.28	Basic Tendon-Bone Construct Formation.....	250
4.29	Attachment of Basic Tendon-Bone Construct at 12 Weeks	250
4.30	Brushite Acid Washout Trials	252
4.31	Osteoblast Seeding Efficiency on Brushite Scaffold	253
4.32	Osteoblast Proliferation on Brushite Scaffold and Plastic	254
5.1	Bone Anchor Production	291
5.2	'Fish Shape' Culture Zone Mold Design	292
5.3	Lattice Mold Design.....	293
5.4	Culture Zone Production and Set Up.....	295
5.5	Tendon-Bone Monocultures without Acid Washout in S-DMEM	302
5.6	Tendon-Bone Monocultures without Acid Washout in S-DMEM with AA and P	304
5.7	Tendon-Bone Monocultures with Acid Washout in S-DMEM	306
5.8	Tendon-Bone Monocultures with Acid Washout in S-DMEM with AA and P (1)	307
5.9	Tendon-Bone Monocultures with Acid Washout in S-DMEM with AA and P (2)	308
5.10	Tendon-Bone Co-Cultures in S-DMEM with AA and P (1)	310
5.11	Tendon-Bone Co-Cultures in S-DMEM with AA and P (2)	311
5.12	Tendon-Bone Co-Cultures in 50:50 Medium (1)	312
5.13	Tendon-Bone Co-Cultures in 50:50 Medium (2)	313
5.14	Isolated Tendon-Bone Co-Culture Constructs	313

Tables

1.1	Classification of FDP Avulsion Injuries	17
1.2	FDP Avulsion Repair: Techniques, Complications and Limitations	20
2.1	Demographics and Utilisation of Specimens	65
2.2	Build and Application of Linear Mixed Effects Model Series	74
2.3	Surface Area of FDP Footprint	77
2.4	Height of FDP Footprint.....	78
2.5	Base Width of FDP Footprint.....	79
2.6	Apex Width of FDP Footprint.....	80
2.7	Internal Angles of FDP Footprint Trapezoid.....	81
2.8	General Dimensions of Flexor View of Distal Phalanx	82
2.9	Ratio of FDP Footprint Measurements to Related Distal Phalanx Measurements	83
2.10	Distance of FDP Footprint Base and Centroid from DIPJ	84
2.11	Inter-Observer Reliability of FDP Footprint and Distal Phalanx Measurements	86
2.12	FDP Tendon Width Measurements	88
2.13	Inter-Observer Reliability of Tendon Width Measurements.....	91
2.14	Distal Phalanx Bone Depth Measurements at FDP Insertion.....	92
2.15	Influence of Side on FDP, Distal Phalanx, Tendon Width and Bone Depth Measurements	95
2.16	Size Category Values for FDP Footprint, Tendon Width and Bone Depth ...	97
2.17	Component Design Guide for Tissue Engineered Model	120
3.1a	Build and Application of Linear Mixed Effects Model Series (1)	136
3.1b	Build and Application of Linear Mixed Effects Model Series (2)	137
3.2	Tidemark Intersection Angle Measurements	147
3.3	Tidemark Intersection Fibres Enthesis Distance Comparison.....	151
3.4	Approaching Angle Measurements.....	153
3.5	Angle Change between Approaching and Tidemark Fibres.....	155
3.6	Influence of Side on Tendon Fibre Angle Measurements	156
3.7	Inter-Observer Reliability of Collective Tendon Fibre Angle Measurements	158

3.8	Inter-Observer Reliability of Individual Tendon Fibre Angle Measurements	159
4.1	Width Difference between Gel at Suture and Suture Itself	233
5.1	Bone Anchor Scaling for Osteoblast Seeding	298

Abbreviations

#	Fracture
1°	Primary
2°	Secondary
3°	Tertiary
2D	2-Dimensional / 2-Dimensions
3D	3-Dimensional / 3-Dimensions
AA	Ascorbic Acid
ABAM	Antibiotic-Antimycotic
ABS	Acrylonitrile Butadiene Styrene
AC	Articular Cartilage
ACL	Anterior Cruciate Ligament
AL	Apex Left angle
ALP	Alkaline Phosphatase
ANOVA	Analysis of Variance
AR	Apex Right angle
ASC(s)	Adipose-derived mesenchymal Stem Cell(s)
AW	Apex Width
bFGF	Basic Fibroblast Growth Factor
BL	Base Left angle
BM	Bone Marrow
BMI	Body Mass Index
BMP(s)	Bone Morphogenetic Protein(s)
BMSC(s)	Bone Marrow-derived Mesenchymal Stem Cell(s)
BR	Base Right angle
BW	Base Width
C	Control
CAD	Computer-Aided Design
CB	Cortical Bone
CC	Camper's Chiasm
CF	Calcified Fibrocartilage
CRISPR	Clustered Regularly Interspaced Short Palindromic Repeats

CT	Computed Tomography
CTF(s)	Chicken Tendon Fibroblast(s)
d	Depth
D	Day
DIPJ(s)	Distal Interphalangeal Joint(s)
DMEM	Dulbecco's Modified Eagles Medium
DMSO	Dimethyl Sulfoxide
DNA	Deoxyribonucleic Acid
DP	Distal Phalanx
DPX	Dibutylphthalate Polystyrene Xylene
dROb(s)	Differentiated Rat Osteoblast(s)
ECM	Extracellular Matrix
EM	Estimated Marginal
FBS	Fetal Bovine Serum
FDP	Flexor Digitorum Profundus
FDS	Flexor Digitorum Superficialis
FPL	Flexor Pollicis Longus
GAGs	Glycosaminoglycans
GDF(s)	Growth Differentiation Factor(s)
GF	Growth Factor
GP	Glycerophosphate
H	Height
HA	Hydroxyapatite
H+E	Hematoxylin and Eosin
HEPES	4-(2-hydroxyethyl)-1-piperazineethanesulfonic acid
ICC	Intraclass Correlation Coefficient
IF	Index Finger
IGF	Insulin-like Growth Factor
Ihh	Indian Hedgehog
IMS	Industrial Methylated Spirit
iPSC(s)	Induced Pluripotent Stem Cell(s)
ITE	Interfacial Tissue Engineering
K-wire	Kirschner Wire
L	Large
LIL(s)	Lateral Interosseous Ligament(s)

LF	Little Finger
M	Medium
MCL	Medial Collateral Ligament
MCPJ	Metacarpophalangeal Joint
MF	Middle Finger
MMP	Matrix Metalloproteinase
MP	Middle Phalanx
MRI	Magnetic Resonance Imaging
MSC(s)	Mesenchymal Stem Cell(s)
MTT	3-(4,5-dimethylthiazol-2-yl)-2,5-diphenyltetrazolium bromide
n/a	Not Applicable
ns	Non-Significant
OCT	Optical Coherence Tomography
ORIF	Open Reduction Internal Fixation
P	Proline
P _{number}	Passage _{number}
PBS	Phosphate Buffered Saline
PCL	Polycaprolactone
PDGF	Platelet-Derived Growth Factor
PEGDA	Polyethylene Glycol Diacrylate
PGA	Polyglycolic Acid
PIPJ	Proximal Interphalangeal Joint
PLA	Polylactic Acid
PLGA	Polylactic-co-glycolic Acid
PLM	Polarised Light Microscopy
PP	Proximal Phalanx
PTHrP	Parathyroid Hormone-related Protein
qPCR	Quantitative Polymerase Chain Reaction
RCL	Radial Collateral Ligament
RF	Ring Finger
RNA	Ribonucleic Acid
ROb(s)	Rat Osteoblast(s)
RODM	Rat Osteoblast Differentiation Medium
ROM	Range of Movement
rpm	Revolutions Per Minute

RTF(s)	Rat Tendon Fibroblast(s)
S	Small
Scx	Scleraxis
S-DMEM	Supplemented Dulbecco's Modified Eagles Medium
SEM	Standard Error of the Mean
Sig	Significant Difference
Sox9	Sex-determining region Y-box 9
SPSS	Statistical Package for the Social Sciences
T	Tendon
TB	Trabecular Bone
TCP	Tricalcium Phosphate
TDSC(s)	Tendon-Derived Mesenchymal Stem Cell(s)
TGF	Transforming Growth Factor
TM	Tidemark
UCL	Ulnar Collateral Ligament
UF	Uncalcified Fibrocartilage
US	Ungual Spine
UT	Ungual Tuberosity
UV	Ultraviolet
VBP	Vinculum Brevis Profundus
VBS	Vinculum Brevis Superficialis
VLP	Vinculum Longus Profundus
VLS	Vinculum Longus Superficialis
VP	Volar Plate
vs	Versus
w/v	Weight by Volume

Note: SI units and prefixes are not listed

CHAPTER 1

GENERAL INTRODUCTION

1.1 Chapter Overview

This introduction reviews the 4 key topics pertinent to the project – the flexor digitorum profundus, flexor digitorum profundus tendon-bone insertion injury, the enthesis, and interfacial tissue engineering. Each section ends with key summary points that outline the context of the project. The chapter concludes by condensing the summary points into the rationale for the project, and setting out the global aim and objectives for the proceeding data chapters.

1.2 The Flexor Digitorum Profundus

1.2.1 Overview

The human flexor digitorum profundus (FDP) (**Figure 1.1**) is a muscle in the flexor (anterior or palmar/volar, in respective additional anatomical or clinical description) compartment of the forearm. Along with its superficial counterpart, the flexor digitorum superficialis (FDS), it provides the long flexor tendons to the index, middle, ring and little fingers that give strength to finger flexion for grip. The 4 FDP tendons attach to the distal phalanx (DP) of each finger, with muscle contraction causing concomitant flexion of each DP. As the only musculotendinous unit to cross the flexor surface of the distal interphalangeal joint (DIPJ), purposeful DP flexion in the fingers is provided solely by the FDP. Additionally the FDP contributes to flexion of more proximal joints crossed by each tendon – the proximal interphalangeal joint (PIPJ), metacarpophalangeal joint (MCPJ) and wrist joint. The anatomical and biomechanical organisation of the FDP and other long digital flexors in the upper limb add a high degree of strength to the precise digital positioning provided by the intrinsic muscles, giving the human hand its distinguishing motor characteristics.

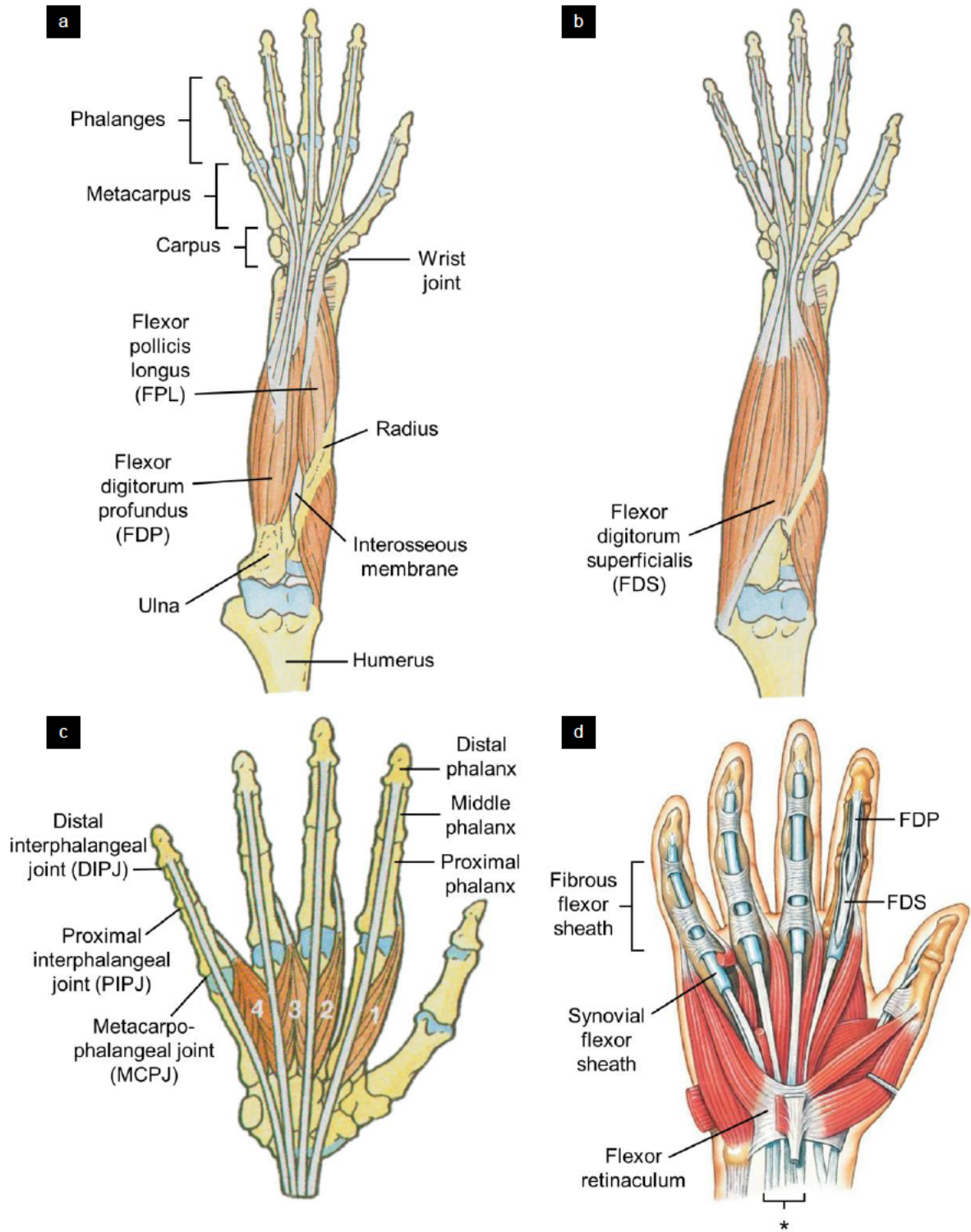


Figure 1.1 | Flexor Digitorum Profundus Anatomy

Flexor/anterior views. **a)** Deep layer of forearm flexor musculature. The *flexor digitorum profundus* (FDP) muscle arises mainly from the *ulna*, giving long flexor tendons to the 4 fingers. Note the segregation in the forearm of the tendon to the index. **b)** Intermediate layer of forearm flexor musculature. The *flexor digitorum superficialis* (FDS) muscle, also providing long flexor tendons to the 4 fingers, lies superficial to the FDP. **c)** The 4 lumbrical muscles (numbered) deep within the hand, arising from the FDP tendons. Note lumbricals 1 and 2 are unicipital, 3 and 4 are bicipital. **d)** Flexor tendon attachments and sheaths. * denotes the 4 FDS and 4 underlying FDP tendons entering the carpal tunnel beneath the *flexor retinaculum* (common synovial sheath not shown). In each finger, the FDS and FDP tendon are surrounded by both a *synovial sheath* and *fibrous sheath*. The opened sheaths of the index finger show the FDS splitting around the FDP to attach to the middle phalanx, and the FDP attaching to the distal phalanx (see also **Figures 1.3** and **1.4**). (a), (b) and (c) adapted from Moore and Agur (2002); (d) adapted from Martini, Timmons and Tallitsch (2015).

1.2.2 Muscle

The FDP muscle (**Figure 1.1a**) is the most powerful and bulky of the forearm musculature (Sinnatamby, 2011). Lying beneath the FDS muscle (**Figure 1.1b**), the FDP arises from the upper three-quarters of the anterior and medial surfaces of the ulna, including aponeurotic origin from the posterior border, and the anterior surface of the interosseous membrane. Fibres longitudinally descend the forearm and contribute with medial-lateral (ulnar-radial) regional distinction to form the 4 deep flexor tendons in the distal half of the forearm. The tendon of the index finger typically detaches from the other tendons in the forearm and remains separate in its course (Sinnatamby, 2011). The middle, ring and little finger tendons are united by areolar tissue and tendinous slips until the palm (Warwick and Williams, 1973; Malerich *et al*, 1987).

The nerve supply of the FDP muscle is compartmental, with the medial half (the muscle bellies for the little and ring finger tendons) innervated by the ulnar nerve and the lateral half (bellies for the middle and index) by the anterior interosseous branch of the median nerve (C8, T1 root values). This 'standard' 2:2 muscle belly innervation pattern occurs in 60% of individuals, with 1:3 or 3:1 distributions found equally in the remaining 40% (Sinnatamby, 2011). The blood supply to all muscle belly divisions is from the anterior interosseous artery, a branch of the ulnar artery, running on the interosseous membrane.

1.2.3 Tendon

1.2.3.1 Gross Anatomy

The 4 FDP tendons traverse the carpal tunnel invested within a common synovial sheath shared with the 4 more superficially lying FDS tendons. Distal to the carpal tunnel the tendons run in deep and superficial pairs towards the fingers. Where the tendons are then free of synovial sheath in the mid palm, small lumbrical muscles arise from the sides of each FDP tendon (**Figure 1.1c**), travelling on the lateral sides of their tendons and sharing a common innervation with their parent muscle belly. The lateral 2 lumbricals are unicipital in tendon origin, whereas the medial 2 are bicipital from adjacent tendons (Sinnatamby, 2011), forming a further point of unification of the middle, ring and little finger FDP tendons.

At the level of the metacarpal heads the tendon pairs enter the digital fibrous flexor sheaths ('flexor sheaths') of the fingers (**Figure 1.1d**). Just proximal to the flexor sheaths the tendon pairs of the index, middle and ring fingers are reinvested in a synovial sheath, continuing to their insertion; the little finger usually maintains a continuous synovial sheath through the palm from the carpal tunnel (Moore and Agur, 2002). Within the flexor sheath the FDS tendon splits near the level of the PIPJ into radial and ulnar slips which spiral around the FDP and re-join in a gutter-shaped bed on the flexor surface of the middle phalanx (MP) (Camper's chiasm). The majority of the FDS slips attach to the sides of the MP, where their principle function is to flex the PIPJ. The FDP tendon continues through the partial decussation of the FDS and inserts onto the base of the flexor surface of the DP.

1.2.3.2 Architecture

The FDP tendon, like any tendon, is predominantly composed of collagen by dry weight. A hierarchical tendon structure is assembled from mainly parallel collagen fibrils, fibres, and fascicles to form the tendon proper (**Figure 1.2**). The connective tissue providing route for vessels and nerves condenses as endotenon, ensheathing bundles of fibres associated with more than one tendon cell - subfascicles and fascicles, and as epitenon, investing the whole tendon. The connective tissue remains loose as it surrounds the tendon as paratenon, a false tendon sheath allowing unrestricted movement from surrounding tissues, only developing into a true discrete sheath in areas of increased friction such as the flexor sheath (Kannus, 2000) (see *Section 1.2.3.3*).

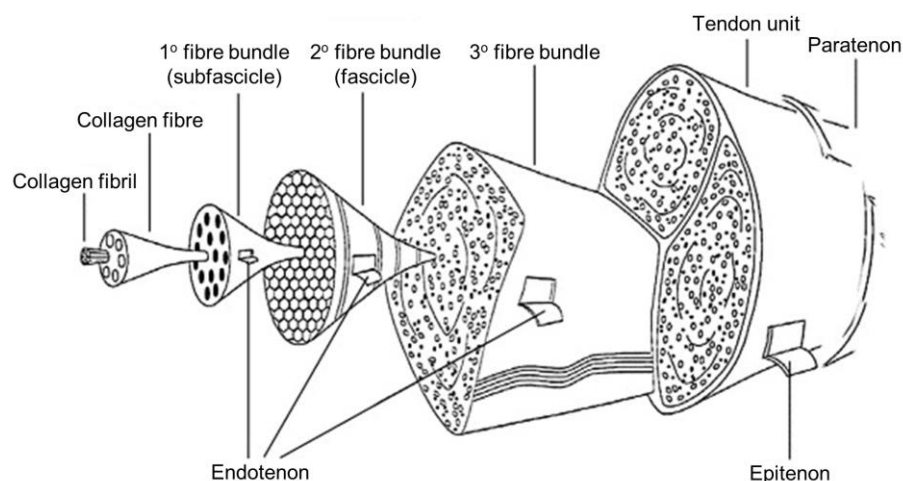


Figure 1.2 | Hierarchical Tendon Structure

Illustration of tendon microarchitecture, adapted from Kannus (2000) and Fedorczyk (2006). Collagen *fibrils* are formed of microfibrils aggregated from insoluble collagen molecules. *Fibrils* (visible on low power electron microscopy) are gathered together as a *fibre* (visible on light microscopy), bound in primary (1°), secondary (2°) and tertiary (3°) bundles by *endotenon*. The *epitenon* and *paratenon* together form the peritenon.

The FDP tendons are long and flexible, but densely fibrous and practically inelastic (Warwick and Williams, 1973; Kannus, 2000; Thorpe and Screen, 2016). The vascular network, primarily fed by descending vessels from the muscle (Sinnatamby, 2011), is sparse, exposing the white appearance of the tendon. Large fascicles may also add striation to the gross structure. In cross section the tendons are typically oval, but distally they develop a biconcave bean-shape form due to the longitudinal rearrangement of coarse fasciculi (Warwick and Williams, 1973). A median groove, more conspicuous on the flexor than dorsal side, is usually grossly perceptible by the MCPJ, becoming clearly apparent distal to the FDS decussation where the tendon appears almost cleaved apart (Wilkinson, 1953). The presence of a parallel fissure in the tendon may permit the tendon to modify its form within the flexor sheath pulley system during muscle contraction (Benjamin and Ralphs, 1998).

1.2.3.3 Flexor Sheath

The digital fibrous flexor sheath is an osseo-fibrous tunnel from the metacarpal head to the DP base. The fibrous component consists of a particular arrangement of transverse (annular) and cruciate fibre condensations (ligaments, or 'pulleys'), that facilitate flexion and overall function of the sheath (**Figure 1.3**). The flexor sheath provides protection and, by binding the tendons down to the phalanges, prevents bowstringing and improves the biomechanical advantage of tendon excursion on joint flexion (see *Section 1.2.3.5*).

The synovial sheath, within the osseo-fibrous tunnel, develops from the peripheral discrete layer of the tendon (epitenon) and its surrounding loose connective tissue (paratenon) (see *Section 1.2.3.2*). It comprises a visceral layer, surrounding the tendon, and a parietal layer, on the internal aspect of the fibrous sheath, with a closed synovial space between (Kannus, 2000). The visceral layer is covered by synoviocytes which secrete synovial fluid into the space, bathing and lubricating the tendon. The fluid allows smooth tendon glide within an enclosed area of potential friction, and diffusion of nutrients.

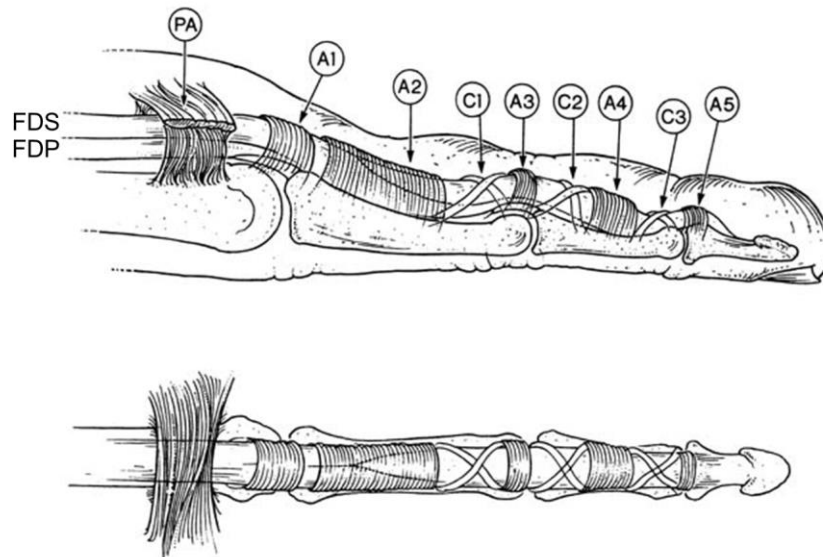


Figure 1.3 | The Digital Fibrous Flexor Sheath

Illustration of lateral view (*above*) and flexor view (*below*) of the flexor sheath of the finger, from Strickland (2000). The fibrous sheath is organised into annular (A) and cruciate (C) pulleys, labelled numerically from proximal (*left*) to distal (*right*). A1, A3 and A5 pulleys overlie the MCPJ, PIPJ and DIPJ, respectively, whilst the larger and denser A2 and A4 pulleys overlie the shafts of the proximal and middle phalanx. The cruciate pulleys, less substantial and collapsible in finger flexion, lie in the intervening space between all annular pulleys except A1 and A2. The palmar aponeurosis pulley (PA), formed by the transverse fascicular fibres and paratendinous bands of the palmar aponeurosis, provides a functional proximal extension to the sheath (Manske and Lesker, 1983). FDP – flexor digitorum profundus; FDS – flexor digitorum superficialis.

1.2.3.4 Nutrition

Nutrition of both FDP and FDS tendons within the synovial sheath is provided by 2 routes: vascular perfusion and synovial diffusion (Seiler, 2017; Shapiro and Kamal 2020). Their maintenance or disruption in injury and restoration in repair are essential to pathophysiology, healing and operative technique. The primary vascular supply is through well-developed long and short vincula, from segmental branches of the ulnar and radial (palmar) digital arteries (**Figure 1.4**). A vinculum is a mesentery (mesotendon) formed by a double layer of synovial membrane, connecting parietal and visceral layers, which transmits blood to (or from) the dorsal (deep) aspect of the tendon from these digital vessels. The flexor (superficial) aspect of the tendons within the flexor sheath are subsequently relatively avascular, obtaining nutrition through passive diffusion of solutes and gases (Boyer, 2005). Diffusion is achieved through the synovial fluid by the process of imbibition, whereby tendon flexion and extension

pumps synovial fluid into its fascicular interstices through conduits on the tendon surface (Manske and Lesker, 1985; Strickland, 2000).

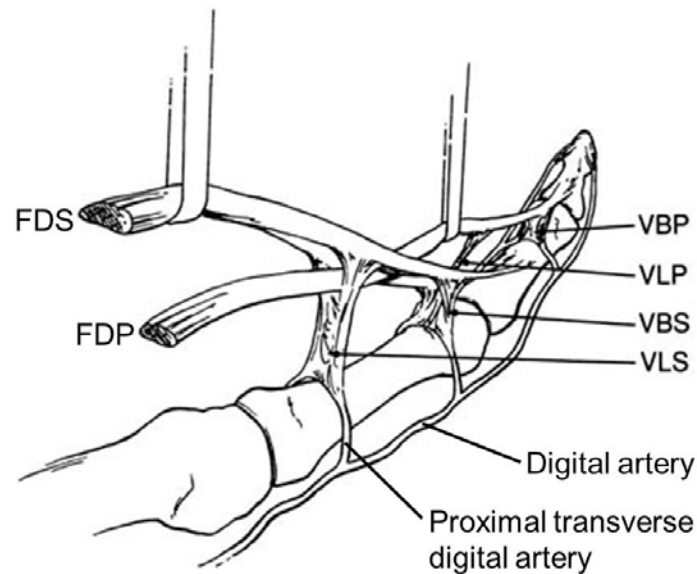


Figure 1.4 | Flexor Tendon Vincula

Illustration of the vincular blood supply within the flexor sheath to the *FDS* and *FDP* tendons, cut over the metacarpal (*left, proximal*), adapted from Strickland (2000). 2 vincula, 1 long (*longum*) and 1 short (*brevis*), distribute to each deep (*FDP*) and superficial (*FDS*) flexor tendon. The vinculum brevis profundus (*VBP*) and vinculum brevis superficialis (*VBS*) are triangular bands attaching to the deep surface of the *FDP* and *FDS* tendons, respectively, near the tendon insertions. The vinculum longus profundus (*VLP*) to the *FDP*, and the vinculum longus superficialis (*VLS*), often double to the *FDS*, are thread-like slips. The *VLP* arises in conjunction with the *VBS* in the distal region of the proximal phalanx, then passes between the *FDS* slips to reach the *FDP* at the level of the PIPJ. The *VLS* arises at the base of the proximal phalanx, passing either side of the *FDP* to reach the *FDS*. The arterial vessels within the vincula originate from *proximal, intermediate and distal transverse (segmental) branches* of the longitudinal digital arteries.

1.2.3.5 Biomechanics

The long flexor tendons of the *FDP* and *FDS* are cables that allow the power generated by a large area of contracting muscle in the forearm to be conveyed into the rotary force of flexion in the fingers (Goodman and Choueka, 2005). Muscle contraction causes tendon excursion, producing joint rotation. Following mechanical principles, the relationship of tendon excursion to joint rotation is determined by the shortest perpendicular distance of the tendon, producing linear force across the joint, from the axis of rotation (moment arm) (Zajac, 1992). The shorter the moment arm, the greater the joint rotation for the same tendon excursion (Strickland, 2000). Average moments arms for the *FDP* tendons across the DIPJ have been calculated to range from 7.00mm (ring finger) to 8.69mm (little finger) (Franko *et al*, 2011). These values would be substantially greater but for the flexor sheath pulleys, particularly A2

and A4, which considerably increase the efficiency of the biomechanical system by holding the tendons adjacent to the joints. The greatest power in flexion can then be achieved when the tendons are maximally lengthened, and are thus able to undergo maximum excursion, achieved through extension of the wrist (power grip).

The FDP tendon has a resting tension of 1N (Bright and Urbaniak, 1977). Unresisted passive and active flexion are generally reported to generate an FDP tendon force of 1-4N (Bright and Urbaniak, 1977; Kursa *et al*, 2006), with active flexion against mild and moderate resistance resulting in 10N and 17N, respectively (Strickland, 2000). A tendon force of around 20N may however be required to produce active flexion without any resistance (Schuind *et al*, 1992). During strong composite grasp the FDP tendon force is 63N, roughly doubling to 118N when performing fingertip pinch (Schuind *et al*, 1992). Ex vivo, the limit of force through the FDP before failure (bony avulsion or intratendinous rupture close to the insertion) in cadavers ranges from 263-548N, with an average of 400N (Felder *et al*, 2013).

1.2.3.6 Insertion

The FDP tendon inserts onto the flexor surface of the lower third (base) of the DP. The insertion area represents the proximal metaphyseal region of the bone (Al-Qattan, 2016a; Bachoura, Ferikes and Lubahn, 2017) with the volar plate attaching just proximally onto the epiphysis (see *Section 1.2.5*). The approaching tendon fibre bundles, after crossing the DIPJ, diverge such that the more superficial flexor fibres attach laterally at the base of the insertion, while the deeper dorsal fibres attach more distally and centrally (Wilkinson, 1953). The insertion footprint is always widest at its base and tapers distally, occupying an average surface area of 20% of the flexor surface of the DP (Chepla, Goitz and Fowler, 2015).

Leversedge *et al* (2002) delineated the vascular anatomy at the FDP insertion, dispelling previous notions suggesting that the bone provided little if any vascular contribution (Warwick and Williams, 1973; Mankse and Lesker, 1982) (**Figure 1.5**). Clinically this matches with the haematoma usually noted at the insertion site after true acute tendon-from-bone avulsion. Both a dorsal and volar vascular supply are described at the insertion, in contrast to the vincula within the flexor sheath, whose supply solely penetrates from the dorsal tendon surface (see *Section 1.2.3.4*).

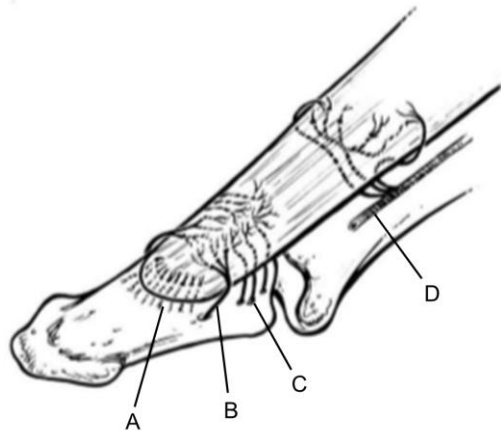


Figure 1.5 | FDP Insertion Vasculature

Illustration of perfusion of the distal FDP tendon, as reported by Leversedge *et al* (2002). Osseous vessels (A, B, C) supply the tendon insertion and the vinculum brevis profundus (D) supplies the distal tendon proximal to the insertion, with an area of hypovascularity between the 2 sources. A = intraosseous vessels directly penetrating tendon insertion; B = bilateral vessel leashes from bony ostia densely covering flexor surface; C = extraosseous vascular leashes supplying the dorsal surface. Adapted from Ruchelsman *et al*, 2011.

1.2.4 Distal Phalanx Bone

The distal phalanx (DP) is the terminal bone of the digits in the hand and foot. In the hand, the index, middle, ring and little fingers, receiving the FDP tendon, exhibit a similar morphology. The DP of the thumb, flexing at its articulating interphalangeal joint through action of the flexor pollicis longus (FPL), and the DPs of the foot digits, are of similar but distinct form in comparison.

The base of the DP in the fingers is wide for attachment of the respective FDP and extensor tendons on the flexor and dorsal surfaces. The base conforms to receive the articulating pulley-shaped head of the MP; lateral tubercles provide base width on each side and the bone protrudes and extends proximally at the DIPJ more on the dorsal than flexor surface. The base tapers into a slender rounded shaft covered by periosteum (Al-Qattan, 2016a), with the distal end (the unguis fossa) representing the narrowest portion of the bone (Darowish, Brenneman and Bigger, 2015). From the unguis fossa the bone expands distally into the head as a bulbous unguis tuberosity ('tuft', clinically), obliquely set from anterior-proximal to posterior-distal. The unguis tuberosity is thus more pronounced on the flexor surface, with bilateral unguis spines projecting proximally, lending the whole tuberosity an inverted horse-shoe shape. Between identical medial and lateral borders the bone is convex dorsally, but more

flattened on the flexor side. Along its longitudinal axis there is typically a gentle concavity. Anterior and distal to the unguis tuberosity is the finger pulp, consisting of fat loculated by fibrous septa running from bone to dermis, which roughen the corresponding surfaces of the tuberosity. The dorsal surface of the tuberosity is comparatively smooth, upon which lies the delicate nail bed tissue, with germinal nail matrix more proximally over the shaft. Between the lateral tubercles on the base of the bone to the unguis spines at the head stretch the bilateral lateral interosseous ligaments, protecting distal neurovascular structures passing from the flexor surface dorsally to the nailbed (Wilkinson, 1953). These neurovascular structures pass to the nail bed and nail matrix through bilateral spaces (*rima unguis*) between the lateral interosseous ligaments and the bone (Kakinoki, 2012).

1.2.5 Distal Interphalangeal Joint

The distal interphalangeal joint (DIPJ) of the fingers is a uni-axial synovial hinge joint between the base of the DP and the head of the MP. The active joint movements are flexion and extension; although minor asymmetry of the condyles on the MP head causes slight supination of the DP in flexion, allowing the finger pulps to more fully face the thumb pulp (Warwick and Williams, 1973; Merrell and Hastings, 2017). Minimal accessory movements of rotation, abduction, and anterior-posterior glide can also passively occur, permitting gripping fingers to adapt to the shape of a held object (Warwick and Williams, 1973). The normal range of motion (ROM) at the DIPJ is 0-85° (Bachoura, Ferikes and Lubahn, 2017), however the average flexion posture for functional tasks is 39° (Hume *et al*, 1990), approximately at the point of mid-flexion.

The stability of the joint is provided principally by the ligamentous condensations reinforcing the flexor and lateral surfaces of the fibrous joint capsule. Adhering to the thin flexor surface of the true capsule is a 2-3mm thick plate of fibrocartilage ['volar plate' (VP)], providing the main resistance to joint hyperextension. The VP arises proximally from the subcondylar fossa of the MP and attaches distally to the base of the DP approximately 1mm proximal to the FDP insertion (Al-Qattan, 2016a). The lateral margins of the VP are suspended by the collateral ligaments; at its distal insertion onto the DP, the VP is only densely attached peripherally where it is confluent with these collateral attachments (Merrell and Hastings, 2017). The stout collateral ligaments, on the ulnar and radial sides of the capsule, are the primary

stabilisers against lateral deviation of the joint. They consist of proper and accessory divisions, both arising dorsally on the lateral aspect of each MP condyle, passing obliquely to insert either onto the anterolateral base of the DP (proper) or into the VP (accessory) (Rozmaryn, 2017). The joint has substantial stability, particularly in extension, due to the opposing insertions and short lever arms of the FDP and terminal extensor, and tight arrangement of the soft tissue envelope, in addition to these main capsular ligaments (Merrell and Hastings, 2017).

1.2.6 Summary

Key points:

- *The FDP is a forearm muscle providing a tendon to each of the 4 fingers;*
- *Digital flexor sheaths afford tendon protection and biomechanical advantage;*
- *The tendons flare out to a defined attachment on the DP flexor surface base;*
- *The FDP primarily flexes the DIPJs, providing fingertip pinch and power grip;*
- *FDP contraction generates large forces at its tendon-DP attachments.*

1.3 Flexor Digitorum Profundus Insertion Injury

1.3.1 Overview

FDP insertion injury is technically and clinically defined as within flexor zone I: flexor tendon injury distal to the FDS insertion (Verdan, 1960 and 1972). This includes both true FDP avulsion from the distal phalanx (with or without a bone fragment) and distal FDP tendon substance injury or rupture (with a variable tendon stump remaining attached to the bone). The typical zone I injury mechanism is closed (no skin wound) bony avulsion or laceration, although open (skin wound) avulsion and crush injury also occur (Murphy and Mass, 2005), and subsequently the patient is unable to flex their DP causing difficulty with everyday manual tasks. In addition to avulsions, distal zone I FDP tendon ruptures may not leave an attached tendon stump of sufficient length or health to perform primary tendon-tendon repair. The focus of surgical treatment at or adjacent to the distal phalanx insertion is therefore effective restoration of the tendon-bone attachment. Achieving a strong tendon-bone repair at the original

anatomical attachment without re-rupture or complications is however challenging and suboptimal with current surgical methods.

1.3.2 Epidemiology

Trauma at the FDP insertion is the most frequent type of closed flexor tendon injury (Boyes, Wilson and Smith, 1960; Imbriglia and Goldstein, 1987; Freilich, 2015) and 10.7% of flexor tendon injuries lie in zone I (de Jong *et al*, 2014). However data on incidence and frequency of FDP insertion injury is scarce as no specific large scale clinical series or investigations are reported. Nonetheless, reviews describe the injury as common (Tuttle, Olvey and Stern, 2006; Ruchelsman *et al*, 2011; Abrego and Shamrock, 2019) and it is a distinct clinical entity in both younger and older populations entailing continued review and discussion of optimum management.

Injury to tendons in the hand in general is frequent. 33.2 injuries per 100,000 person-years occurred in the United States between 2001-2010, with highest incidence in males and those aged 20-29 (de Jong *et al*, 2014). Indeed, 20-30% of accident and emergency department presentations are hand and wrist injuries (Angermann and Lohmann, 1993; Dias and Garcia-Elias, 2006; de Putter *et al*, 2012; Polinder *et al*, 2013), and fingers are the most common region of upper limb injury presentation, accounting for 38.4% (Ootes, Lambers and Ring, 2012). FDP tendons are more frequently injured than FDS tendons, most commonly in the index finger, followed by the little, ring, and lastly middle finger (de Jong *et al*, 2014). These studies also show that finger injuries occur most often at home (51.9%), with 11.3% in places of recreation (Ootes, Lambers and Ring, 2012), however tendon damage specifically is most frequently work-related (24.9%) (de Jong *et al*, 2014).

Our reliance on effective manual function for work and daily living means that hand injuries have a very extensive and wide-ranging impact, both economically and socially, on the individual and society (Rosberg, Carlsson and Dahlin, 2005; Dias and Garcia-Elias, 2006). Injuries to the hand and wrist have the most significant economic repercussions of any body region, with hand and finger fractures being the most expensive, due to both direct health care costs and loss of productivity costs from absenteeism (de Putter *et al*, 2012). Work absence due to hand injuries in fact accounts for over 1.5 million days lost per year in the United States (Kelsey *et al*,

1997). More recently, a meta-analysis of 21 studies on acute hand and wrist injuries shows that loss of productivity represents the greatest fraction of total costs incurred from injury, with a median net cost estimate per injury of \$6,951 (Robinson *et al*, 2016).

1.3.3 Aetiology and Pathophysiology

Avulsion of the FDP tendon from its bony insertion is caused by forced passive hyperextension of the distal phalanx at the DIPJ during active FDP flexion. Typically this is during clenching of the fist, when the FDP muscle belly is at maximum contraction (Abrego and Shamrock, 2019). Excess mechanical force accrues around the tendon-bone interface, leading to failure and disinsertion. Early experimental work by McMaster (1933) showed that the tissue transition from tendon to bone represents the weakest point in the muscle-tendon-bone unit, and, clinically, the majority of flexor tendon ruptures seen are FDP insertion avulsions (Boyes, Wilson and Smith, 1960; Bois, Johnston and Classen, 2007).

FDP avulsion injury is known as 'jersey finger', which portrays the classic causative history and injury mechanism. The injury is commonly sports related, often seen in football, American football and rugby, when a player grabs or has a finger trapped in an opponent's jersey (Leddy and Packer, 1977; Reef, 1977; Lunn and Lamb, 1984; Bachoura, Ferikes and Lubahn, 2017; Shapiro and Kamal, 2020). The flexing finger is forced into sudden hyperextension by the evading player as they abruptly pull away. The position of flexed fingers with hyperextended DIPJs is also noted in other athletes, such as rock-climbers employing the 'crimp grip' and baseball pitchers (Marco *et al*, 1998; Vigouroux *et al*, 2006; Shapiro and Kamal, 2020), who also represent at-risk groups. Avulsion injury has been reported in all ages, and although sporting injury is the most common presentation, further at-risk groups of tendon rupture are those with systemic inflammatory diseases, such as rheumatoid arthritis (Ruchelsman *et al*, 2011).

The extreme location and function of the distal phalanx place it at particular risk of injury (Bachoura, Ferikes and Lubahn, 2017). The fingertips are exposed and substantial torque can be conveyed through the FDP insertion (Tuttle, Olvey and Stern, 2006), with the FDP on average 50% stronger than the FDS (Bois, Johnston and Classen, 2007). Experimental studies investigating power grip vary in describing

the stress load on the FDP as either equal to or greater than the FDS (Imbriglia and Goldstein, 1987; Goislard de Monsabert *et al*, 2012). Interestingly however, Vigouroux *et al* (2006) compared FDP and FDS tendon tensions during grip with either a hyperextended or flexed DIPJ, with all other finger joints flexed, and found a nearly 2:1 FDP:FDS tension ratio during DIPJ hyperextension compared to approximately 1:1 when flexed. This suggests the considerable transfer of load to the FDP when finger position changes from a grip of flexion in all joints to DIPJ hyperextension, risking rupture of the FDP insertion.

The ring finger is considered the most commonly affected in FDP avulsion, although the injury has been reported in all fingers and thumb (FPL) (Murphy and Mass, 2005; Tuttle, Olvey and Stern, 2006). Leddy and Packer's classic early series of 36 cases and review of the injury (1977) recounted that 75% of cases concerned the ring finger. The reason for particular ring finger involvement is not entirely certain, but postulated on grounds of anatomical restraint, vulnerability and distinct insertion weakness. Lack of independent movement of the ring finger is suggested as the common anatomical theme (Eglseder and Russell, 1990): it is uniquely tethered on both radial and ulnar sides by bipennate lumbricals (Lunn and Lamb, 1984; Bachoura, Ferikes and Lubahn, 2017) (see **Figure 1.1c**); the juncturae tendinae limit its independent metacarpophalangeal joint movement (Leddy and Packer, 1977); and its muscle fibres are wedged between that of the little and middle fingers in a common muscle belly (Gunter, 1960) (see **Figure 1.1a**). Experimentally, Bynum and Gilbert (1988) found that the ring finger was 5mm more prominent than others during grip, and absorbed the most pull away force, whilst Manske and Lesker (1978) reported that the load to failure of the FDP insertion in cadaveric testing was weaker in the ring compared to middle finger.

1.3.4 Presentation

The pathognomonic sign of FDP insertion injury is the inability to actively flex the DIPJ in the injured finger. DIPJ flexion may however be somewhat present due to the influence of the volar plate and distal vinculum (Sasaki and Nomura, 1987; Stewart *et al*, 2007), so assessment against resistance is essential. The normal cascade is altered as the affected finger adopts a more extended resting position (Ruchelsman *et al*, 2011). Functionally, reduced DIPJ motion leads to decreased dexterity, pinch

strength and grasp capability (Bachoura, Ferikes and Lubahn, 2017) which affects the whole range of daily manual tasks.

Acutely there is usually tenderness, swelling and ecchymosis particularly on flexor aspect of the finger, and localised pain on palpation with a subcutaneous mass may represent the position of the retracted tendon end in the finger or palm. Delayed presentation with less apparent clinical findings is however also a relative feature, particularly in athletes not appreciating the injury or dismissing it as minor (Tuttle, Olvey and Stern, 2006; Bachoura, Ferikes and Lubahn, 2017), which may impact on treatment options.

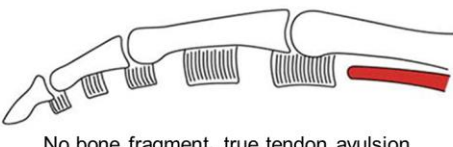
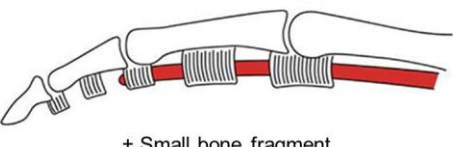
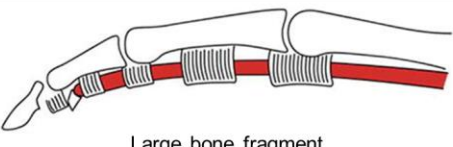
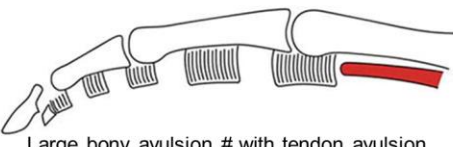
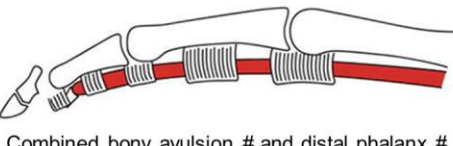
1.3.5 Classification

FDP avulsion injury classification is described and summarised in **Table 1.1**. Leddy and Packer (1977) first defined the original Type I-III classification as a staging system to guide treatment. The key feature is the level of retraction of the proximal tendon end, influencing vascular tendon nutrition from the vincula and thus treatment and prognosis. The Type IV injury pattern was originally described by Robins and Dobyns (1974) and later proposed as an addition to the classification system by Smith (1981). Type V was suggested by Al-Qattan (2001), where the presence or absence of intra-articular fracture necessitated varied treatments and directed a Va and Vb subtype. More recently, further fracture patterns have been described with potential additional or redeveloped classifications (Cheriyana, Neuhaus and Mudgal, 2013; Azeem *et al*, 2017; Narang *et al*, 2019), which may further improve treatment guidance.

Type I injuries are the most severe, due to vascular compromise and need for early treatment, and may develop from Type II with continued activity (Stamos and Leddy, 2000). Type II injuries are the most frequent (Leddy and Packer, 1977; Shapiro and Kamal, 2020), followed by Type III, then Type I, with IV and V less common (Tuttle, Olvey and Stern, 2006; Ruchelsman *et al*, 2011). Approximately 50% of avulsions are reported to involve a bony fracture fragment (Eglseder and Russell, 1990; Ruchelsman *et al*, 2011).

Table 1.1 | Classification of FDP Avulsion Injuries

Overview of FDP avulsion patterns, vascular sequelae and suggested treatments. Retraction level is principally determined by bone fragment size, with consequential vincular injury and vascular disruption. Treatment is informed by timing (*acute* ≤ 10 days from injury; *chronic* > 10 days from injury) and associated tendon vascularity, and fracture pattern. Note Type V can be sub-classified into Type Va (extra-articular fracture comminution) and Type Vb (intra-articular fracture comminution). Illustrations taken from Huq, George and Boyce (2013), showing typical bony finger in sagittal section from metacarpal (*right*) to DP (*left*) with underlying annular pulleys from A1 (*right, metacarpophalangeal joint*) to A5 (*left, DIPJ*). The FDP tendon is highlighted in red and the FDS is removed for clarity. Details on vincular disruption and treatment taken from Ruchelsman *et al* (2011) and Tuttle *et al* (2006), respectively. # = fracture; 1° = primary; *DIPJ* = distal interphalangeal joint; *FDS* = flexor digitorum superficialis; *ORIF* = open reduction internal fixation; *PIPJ* = proximal interphalangeal joint; *ROM* = range of movement; *VBP* = vinculum brevis profundus; *VLP* = vinculum longus profundus.

FDP Avulsion Injuries			
	Retraction Level (Obstruction)	Vincular Disruption	Treatment (Acute/Chronic)
Type I			
 <p>No bone fragment, true tendon avulsion</p>	Palm (Lumbrical)	VLP + VBP	1° tendon-bone repair ROM exercises
Type II			
 <p>± Small bone fragment</p>	PIPJ (A3 pulley/ FDS chiasm/ VLP)	VBP only	1° tendon-bone repair Consider delayed 1° tendon-bone repair
Type III			
 <p>Large bone fragment</p>	Middle phalanx (A4 pulley)	None	ORIF fragment ORIF fragment
Type IV			
 <p>Large bony avulsion # with tendon avulsion</p>	Bone fragment: DIPJ/Middle phalanx (A5/A4 pulley) Tendon: Palm or finger (Variable)	Variable	ORIF fragment + 1° tendon-bone repair Consider ORIF or fragment excision + delayed 1° tendon- bone repair
Type V			
 <p>Combined bony avulsion # and distal phalanx #</p>	Finger (Variable)	Variable	ORIF fragment Consider arthrodesis

1.3.6 Surgical Management

Table 1.1 suggests surgical treatment options for each class of avulsion injury. These exist where the tendon can be delivered beneath the pulleys and does not require significant advancement. Unfavourable conditions, increasing with time from injury, require greater consideration of more extreme measures such as DIPJ fusion, tendon grafting as a single-stage or 2 stage reconstruction, or no surgical treatment (Ruchelsman *et al*, 2011). This section focuses on the optimum surgical option where significant fracture is not present - direct tendon-bone repair, which aims to restore the anatomical tendon-bone interface.

In avulsions or distal zone I FDP injuries, up to 1cm of tendon advancement is deemed acceptable to perform tendon-bone reattachment. Any remaining distal tendon stump of <1cm can be debrided away to prepare the reattachment site. Further tendon advancement results in appreciable loss of extension in the repaired finger and the 'quadriga' phenomenon (Wagner, 1958; Malerich *et al*, 1987). 'Quadriga' refers to flexion lag in the fingers adjacent to the repaired tendon with increased tension, due to the common FDP muscle belly, particularly of the middle, ring and little finger (see *Section 1.2.2*).

1.3.6.1 Tendon-Bone Fixation

1.3.6.1.1 Techniques

A multitude of avulsion repair techniques exist, many illustrated in **Table 1.2**. These techniques are based on 2 principal methodologies: the traditional pull-out suture with dorsal button (Bunnell, 1948), or all-inside (internal) fixation, primarily represented by the bone anchor (also known as suture anchor). The pull-out button suture consists of sutures placed in the proximal avulsed tendon end, with the free suture strands passed obliquely through holes drilled in the distal phalanx, exiting the nail plate and tied over a button dressing (see **Table 1.2**). Sutures are then typically removed at 6 weeks. Bone anchors are expandable or threaded fixation devices of varying size with attached sutures, inserted into the bone through pilot drill holes. The tendon end is subsequently affixed using the sutures on the anchor. The standard bone anchor for FDP reattachment is the Mitek 'micro' anchor (see **Table 1.2**), or slightly larger 'mini' anchor (DePuy Mitek, Raynham, MA, USA), expandable anchor types that deploy flanges to hold in the bone.

More recently new or combination techniques have been devised and performed. Al-Qattan (2016a and 2016b) describes the use of end-to-end attachment of the proximal FDP tendon end to the entire DIPJ volar plate, released at its middle phalanx insertion and used as a distally based flap, in zone I injuries 1-3mm from insertion. The entire *in situ* volar plate can also be incorporated into a more standard avulsion repair from below to increase biomechanical strength (Al-Qattan *et al*, 2010; Brar *et al*, 2014). Authors are also more commonly augmenting bone anchors with additional internal or external fixation, for example with miniscrews (Nho *et al*, 2018), tension banded suture reinforcement (Halát *et al*, 2018), buried dorsal tie-over (Polfer, Sabino and Katz, 2019), or pull-out dorsal tie-over (Lee *et al*, 2011; Ruchelsman *et al*, 2011).

Table 1.2 | FDP Avulsion Repair: Techniques, Complications and Limitations

Overview of *external* and *internal fixation* techniques for tendon-bone surgical repair of FDP avulsions without significant fracture. The foremost techniques are the pull-out dorsal button suture and the Mitek ‘micro’ bone anchor. Real and potential complications are drawn from case series described by the authors using each technique. *General* complications refer to all techniques in the fixation category. Illustrations show sagittal section of finger from middle phalanx (*right*) with underlying A4 annular pulley, to DP (*left*); FDS is removed. Illustrations and review of complications adapted from Huq, George and Boyce (2013). *DIPJ* = distal interphalangeal joint; *K-wire* = Kirschner wire.

FDP Avulsion Repair Techniques			
	Technique: Author	Complications and Limitations	
		Specific	General
External Fixation			
	<p>Pull-out suture + dorsal nail plate button tie-over: <i>Bunnell 1940</i> (Bunnell, 1948)</p> <p>Pull-out suture + finger tip button tie-over: <i>Mantero 1973</i> (Guinard <i>et al</i>, 1999)</p> <p>Trans-osseous pull-out wire K-wire-button complex tie-over: <i>Grant 2002</i> (Grant, 2002)</p> <p>Steel wire pull-out secured with tendon suture + K-wire tie-over: <i>Zhang 2012</i> (Zhang <i>et al</i>, 2014)</p>	<ul style="list-style-type: none"> Abnormal nailplate growth <ul style="list-style-type: none"> Nailplate deformity Nailbed pain Nailfold necrosis Pulp dystrophy Requires good tendon stump Bulky/Cumbersome Germinal matrix injury Bulky/Cumbersome Germinal matrix injury 	<ul style="list-style-type: none"> Infection Wound irritation Prolonged hypersensitivity Construct catching on clothing Snagging/rupture Difficult hand hygiene Obstruction to mobilisation therapy Construct removal before full healing Construct/dressing adjustments Suture retention Non-locking sutures (weaker than locking) Gapping (long suture/wire length between insertion and external fixation) Repair/suture failure
Internal Fixation – Sutures/Wires			
	<p>Internal trans-osseous fixation (dorsal skin incision): <i>Shultz, 1999</i> (Schultz <i>et al</i>, 1999)</p> <p>Transverse intra-osseous loop suture: <i>Tripathi 2009</i> (Tripathi <i>et al</i>, 2009)</p> <p>Oblique trans-osseous repair + volar tie-over: <i>Teo 2009</i> (Teo <i>et al</i>, 2009)</p> <p>Loop suture + tendon tunnelling (dorsal skin incision): <i>Kapickis 2009</i> (Kapickis, 2009)</p> <p>Transverse trans-osseous suture (fishmouth pulp incision): <i>Sood 1999</i> (Sood and Elliot, 1996)</p>	<ul style="list-style-type: none"> Germinal matrix injury Wound infection/irritation Prolonged hypersensitivity Subcutaneous knot irritation / / Germinal matrix injury Wound infection/irritation Prolonged hypersensitivity Extensor insertion transection Wound infection/irritation Prolonged hypersensitivity Gapping 	<ul style="list-style-type: none"> Technical challenge in limited space Repair/suture failure
Internal Fixation - Anchors			
	<p>Acuflex bone anchor + locking suture: <i>Skoff 1995</i> (Skoff <i>et al</i>, 1995)</p> <p>1-2 Mitek ‘micro’ bone anchor(s): <i>McCallister 2006</i> (McCallister <i>et al</i>, 2006)</p> <p>1-2 Mitek ‘micro’ bone anchor(s) + pullout suture: <i>Lee 2011</i> (Lee <i>et al</i>, 2011)</p>	<ul style="list-style-type: none"> / / As per pullout button issues: <ul style="list-style-type: none"> Nailplate/bed/fold Infection/wound Dressing 	<ul style="list-style-type: none"> Cost Dorsal cortex penetration DIPJ penetration Osteolysis Osteomyelitis Anchor extrusion Repair/suture failure

1.3.6.1.2 Drawbacks

Flexor tendon surgery in general has inherent difficulties. Strickland (2000) opens his 25 year review of flexor tendon surgery saying that “*regaining satisfactory digital function after flexor tendon laceration and repair has long been one of the most difficult problems in hand surgery*”. Reparative surgery itself contributes to adhesion formation between the tendon and surrounding structures during healing. The multi-tissue pathology and more complex surgical handling techniques associated with tendon-bone injury and repair may contribute to greater adhesions than pure tendon injury alone. Adhesions can affect tendon excursion, and in addition to tendon advancement can lead to flexion (joint) contracture. Indeed, flexion contracture stands as the main general adverse post-operative outcome for tendon-bone repair.

The array of complications and limitations for avulsion repair techniques are listed in **Table 1.2**. The chief drawback of external fixation techniques, such as the pull-out button suture, is infection risk due to the externalised suture or wire, which may also be partially retained on attempted removal (Kang, Marsh and Dewar, 2008; Lee *et al*, 2011). Kang, Marsh and Dewar’s case series (2008) of pull-out button suture repair in 23 patients in fact reported a 22% infection rate, as well as 35% abnormal nail growth. Consequently, there has been an inclination towards internal fixation (Huq, George and Boyce, 2013), in particular the simplicity of bone anchors. Bone anchors are also appealing as they can allow incorporation of more modern multi-strand (e.g. 4 strand) locking sutures to the repair (Seiler, 2017). These are more resistant to failure than the non-locking 2 strand repairs used for external fixation techniques (Brustein *et al*, 2001), and furthermore they do not require removal.

The primary disadvantage of bone anchors is cost, with a single Mitek ‘micro’ anchor costing around £180 (Huq, George and Boyce, 2013), whereas other techniques usually only require sutures at substantially less price. Many authors also advocate and employ multiple anchors (Brustein *et al*, 2001; McCallister *et al*, 2006; Lee *et al*, 2011; Ruchelsman *et al*, 2011; Chepla, Goitz and Fowler, 2015). Bone anchors can fail from anchor site pull-out or suture material failure (Brustein *et al*, 2001; Latendresse *et al*, 2005; Halát *et al*, 2014), and are also not without complications of foreign body reaction, infection and extrusion (Vadodaria *et al*, 2007; Giannikas *et al*, 2009; Tiong and O’Sullivan, 2011), although these are rare. There is also a real risk of DP dorsal cortex and DIPJ penetration through pre-drilling and anchor placement,

with inherent inflammatory reaction, particularly in the little finger (Rehak *et al*, 1994; Jain *et al*, 2011; Samson and Gupta, 2018; Bond, Rust and Boland, 2019). Bone anchors may not be suitable with concomitant DP fractures or osteoporotic bone (Matsuzaki *et al*, 2008). Furthermore, bone mineral density has been shown experimentally to reduce by up to 41% after tendon-bone repair, which may particularly lead to failure in techniques requiring robust bone for anchorage (Ditsios *et al*, 2003a).

1.3.6.1.3 Optimal Approach

The ideal repair should achieve anatomical reunion of the tendon-bone insertion with the strength to withstand the loading stresses of early post-operative mobilisation with no surgical complications. A number of studies have compared the strength, functional outcomes and complication rates of varying techniques, in both laboratory and clinical studies, but no one technique is generally regarded as superior overall. In the only clinical outcome study to compare pull-out button suture and micro bone anchor, McCallister *et al* (2006) found no difference in sensibility, active ROM, flexion contracture or grip strength between techniques. Both pull-out button suture and bone anchor repairs are strong enough to endure the forces of passive rehabilitation regimes, but the tendency for reduced tendon-bone gap formation and increased stiffness with bone anchors may be preferential for active post-operative rehabilitation (Huq, George and Boyce, 2013; Putnam and Adamany, 2019). Yet this comes at a cost, particularly where additional strength is provided by 2 anchors (Brustein *et al*, 2001). The alternative method of internal fixation with all-inside sutures/wires avoids the infection risk of an external device and the cost of anchors. However they are technically demanding, and the method shows no difference in tensile stiffness, load to failure or ultimate load when compared to the pull-out button suture or bone anchor (Chu *et al*, 2013). Choice of repair technique is therefore often personal, with different surgeons preferring different techniques.

Whichever technique is employed, the key features of optimal avulsion repair are close apposition of tendon to bone, and return of the tendon to the same footprint position on the bone. Maximal secure tendon-bone contact area will encourage healing processes to directly adhere tendon to bone. In view of this principle, and to guide an anatomically-positioned repair, Leddy and Packer (1977) originally utilised a bone 'trough' in the distal phalanx to seat the FDP. A more distinct 'bone tunnel' is

common in anterior cruciate ligament (ACL) tendon-bone reattachment in the knee (Lu *et al*, 2019), however a flattened tunnel has been shown to have improved early stage healing (Zhao *et al*, 2019). Moreover, for FDP repair, maturation of tendon-bone healing is inferior in a bone tunnel compared to surface repair, potentially due to increased tendon inflammation from deformation around the bone tunnel edge, or restricted availability of DP trabecular bone for tendon-bone contact (Silva *et al*, 2006). Evidence therefore suggests that clinical FDP avulsion repair should maximise cortical bone contact in a surface repair, and no gapping between the tendon and bone should exist.

Accurate reduction of the tendon to its original DP attachment area ('anatomical reduction/repair') is crucial to reinstate the balance of biomechanical forces across the traversed joints, especially the DIPJ. In addition to re-establishing optimal muscle and joint function, restoring correct flexor moment arms across finger joints is important to match rehabilitation protocols developed from normal anatomy (Franko *et al*, 1990). Too distal a reinsertion effectively shortens the FDP tendon, causing flexion contracture and potentially decreased grip strength and quadriga (see *Section 1.3.6*). Although Malerich *et al* (1987) proposed that up to 1cm of advancement (shortening) is permissible before adverse clinical signs are apparent, Gillig *et al* (2015) later reported that the force required to make a fist increases linearly with tendon shortening up to 2.5cm. This implies that any avulsed FDP tendon repositioned too distally could precipitate reduced functionality. Too proximal a reinsertion slackens the FDP tendon, decreasing the mechanical advantage of the muscle. Flexion is ultimately weaker, which will diminish the range of active DIPJ motion. This is demonstrated in the distally-based volar plate flap repair technique (see *Section 1.3.6.1.1*), where the author cites a reduction in active DIPJ flexion as a consequence of the FDP connection to bone, via the volar plate, being more proximal than the anatomical tendon insertion (Al-Qattan, 2016a). Finally, any unintended rotary (pronation/supination in flexion) forces should be prevented by accurate tendon orientation at the interface and avoidance of a lateralised reinsertion position. Such forces may reduce flexion and grip strength, and place chronic abnormal stresses on the DIPJ, potentially leading to laxity and arthritis.

1.3.6.1.4 Outcomes

The diversity and non-standardisation of outcome criteria contributes to the difficulty in acknowledging if a particular technique is superior to others. Randomised studies are lacking and case series are generally small, involving a variety of injury classifications, and occasionally with no reference criteria for outcomes. In general, current techniques of primary avulsion repair do not deliver a satisfactory outcome, and patients should be aware of potentially losing over half of their arc of DIPJ motion, with inherent lack of full extension (Tuttle, Olvey and Stern, 2006). Less than half of DIPJ ROM was observed in two-thirds of cases by Moiemmen and Elliot (2000), and in a significant proportion of surgical follow-ups in further reports (Zhang, Shao and Zhang, 2014; Al-Dubaiban *et al*, 2014; Al-Qattan, 2016a), although a mean of up to two-thirds of normal DIPJ ROM is described in some series (McCallister *et al* 2006; Teo *et al* 2009; Tripathi *et al* 2009). Extension deficit, where documented, amounts to around 10-15° (Leddy and Packer, 1977; Halát *et al*, 2017). As an overall classification of functionality, Tempelaere *et al* (2017) describe a poor outcome in 40% of 19 post-operative repair follow-ups.

1.3.6.2 Tendon-Tendon Fixation

Although tendon-bone repair is the principal concern with insertion injuries, tendon-tendon repair (tenorrhaphy) also warrants consideration. In flexor zone I, end-to-end tenorrhaphy is the favoured technique for FDP injuries more than 1 cm from the bony insertion, to avoid the aforementioned complications of over advancement in attempted tendon-bone repair (see *Section 1.3.6*). It is also relevant for inseting tendon grafts, which may be applicable to insertion injury. End-to-end tenorrhaphy can be used at either end of a graft, although for free flexor tendon grafts a weaving technique is usually preferred proximally. Furthermore, the principles of tenorrhaphy guide the surgical technique in tendon-bone repair when securing the tendon end.

Tenorrhaphy aims to provide robust and accurate tendon apposition to establish optimal healing whilst limiting external adhesions and friction to allow smooth tendon glide, particularly in the area of the flexor sheath (zone II). Strength is primarily provided by sutures across the core of the tendon, with an approximately proportional increase in strength with the number of core sutures employed (Shaieb and Singer, 1997; Choueka, Heminger and Mass, 2000; Strickland, 2000; Boyer *et al*, 2001; Seiler, 2017). An abundance of core suture techniques exist, and increasing placement of

sutures for strength is balanced against excessive tissue handling, needle damage, technical difficulty, time and space limitations (Rawson, Cartmell and Wong, 2013). The principle extends to tendon-bone repair, where repair strength is improved with increased core strands, whether using a pull-out button or suture anchor technique (Silva *et al*, 1998).

The use of peripheral circumferential (epitendinous) sutures is also particularly important in tenorrhaphy. The initial advocacy for epitendinous sutures was to attain smoother approximation of the tendon ends at the circumference (Mason and Shearon, 1932; Rawson, Cartmell and Wong, 2013; Seiler, 2017) and certainly reducing friction improves glide, especially in the tendon sheath. As with tendon-bone repair, maximum contact between the apposed tissues is paramount, since gap formation prevents the normal accumulation of strength and stiffness in healing (Gelberman *et al*, 1999). Gapping may also bring about adhesions, further affecting rehabilitation and limiting tendon excursion (Strickland, 2000). Epitendinous sutures significantly reduce gapping at the repair site and increase overall strength (Wade, Wetherell and Amis, 1989; Silfverskiöld and Andersson, 1993; Kubota *et al*, 1996; Strickland, 2000), therefore as well as improving apposition of the tendon ends and maximising intrinsic healing, they contribute to inherent repair stability.

1.3.7 Summary

Key points:

- *FDP tendon avulsion from the DP is a common and challenging injury;*
- *Reduced manual function has extensive impact on the individual and society;*
- *A variety of surgical techniques exist to reattach the FDP tendon to bone;*
- *All surgical repair techniques have drawbacks, with no single optimal method;*
- *Surgical repairs generally have poor outcomes.*

1.4 The Enthesis

1.4.1 Overview

The enthesis is the region of tendon, ligament or joint capsule attachment to bone. More broadly it may be known as an attachment/insertion site, or more specifically as the osteotendinous/osteoligamentous junction. The enthesis lies at interfacial areas between soft and hard tissue in the musculoskeletal system, allowing the functions of musculotendinous movement and ligamentous/capsular stability of the skeleton. It must facilitate the transmission of force in both directions between the tissues, including ground reaction and impact forces back to the soft tissue (Shaw and Benjamin, 2007), whilst maintaining the integrity of the interface. The influence of mechanical factors dictates the principle of 'form follows function' underpinning Wolff's Law (Benjamin *et al*, 2006; Milz, Benjamin and Putz, 2005), where, akin to bone and other major musculoskeletal tissues, the enthesis displays a number of structural and compositional features that optimise function. Despite adaptations, the enthesis is liable to damage and deterioration from overuse, frank acute avulsion injuries and spondyloarthropathies (Benjamin and McGonagle, 2009), and it is thus of particular clinical interest. Furthermore, the microanatomical characteristics of the enthesis are not regenerated after injury or repair, and, since the complex developmental mechanisms that originally create the enthesis are not fully elucidated, the region is also a spotlight for basic science research. The focus of clinical and research interest in this thesis is specifically the tendon-bone enthesis, although its pertinent features are similar to all soft tissue entheses.

1.4.2 General Structure and Function Principles

In the transfer of muscular force to move a bone, the tendon enthesis has 2 major functions: 1) anchorage, and 2) dissipation of stress. The macroscopic structure of tendon attachments addresses both purposes. Tendons flare out at their bony insertion, providing a greater contact surface area for attachment and dispersal of interfacial stress forces, and resistance to the effects of insertional angle change during joint movement (Benjamin *et al*, 2006; Schlect, 2012). Flaring also allows wider interconnections and overlap with other entheses and fasciae for extra stability;

examples include the tendons of sartorius, gracilis and semitendinosus at the pes anserinus on the tibia (Shaw and Benjamin, 2007), vastus lateralis, vastus intermedius, adductor magnus and adductor brevis along the lateral lip of the linea aspera (Schlect, 2012) and the continuation of quadriceps tendon fibres anteriorly over the patella to the patellar ligament (Toumi *et al*, 2006). Additionally, flaring resists stretch, which limits the propensity for tendon narrowing and consequent vulnerability to rupture (Knese and Biermann 1958; Schlect, 2012). Where tendons do require narrow attachments for more precise movement control, other gross adaptations exist to reduce rupture and avulsion risk, such as spreading the force generated by a single muscle belly over multiple tendon attachment sites (e.g. the FDP) (Shaw and Benjamin, 2007).

Anchorage of tendon to bone provides resistance to static and dynamic loads otherwise acting to disconnect the interface. At the true anatomical tendon-bone junction, the bone is highly irregular (Milz *et al*, 2002), affording maximum surface area contact between the tendon and bone. The 'jigsaw'-like interdigitations are also multidirectional, interlocking the tissues and resisting failure in any one direction (shear) (Shaw and Benjamin, 2007). This design is analogous to a tree root system, where minimal material is devoted to anchorage and the majority allotted for primary functions requiring compliance and flexibility (Benjamin *et al*, 2006; Schlect, 2012). For tendon, these functions are the transfer of contracting muscle force to bone and storage of strain energy (Benjamin and Ralphs, 1998).

Tendon and bone are biomechanically distinct structures of essentially dissimilar physical properties, although notably of comparable ultimate tensile strengths (Hems and Tillman, 2000). Tendon is a compliant material, with a Young's modulus (elastic/tensile modulus) of 200MPa in the direction of contracting muscle force, but buckles on compression; bone is stiff and brittle, with a Young's modulus of 20GPa in both tension and compression (Thomopoulos, Genin and Galatz, 2010). In engineering terms, the junction between these materials is a mechanical impedance mismatch, vulnerable to failure as a focal point of stress concentrations. As well as the macroscopic features to dissipate stress over a large surface area and to surrounding structures, the enthesis possesses microscopic structural and compositional qualities to traverse the material mismatch. In particular, an intervening layer of fibrocartilage provides a transitional zone of increasing stiffness from soft to

hard tissue through a gradation of tissue properties (Doschak and Zernicke, 2005). Not all entheses contain this fibrocartilaginous transition zone; it is present in those many tendon attachments that are precisely localised for a specific function (Benjamin *et al*, 2006), which are less able to dissipate stress over a large interfacial area.

1.4.3 Classification

Entheses are conventionally classified as 'fibrocartilaginous' or 'fibrous', referring to their tissue structure at the tendon-bone interface (Benjamin and Ralphs, 1995; Benjamin *et al*, 2002; Apostolakos *et al*, 2014). The classification has developed from previous terminologies which were less universal or clear. The original German histological descriptions differentiated 'chondral-apophyseal' and 'diaphyseal-periosteal' attachments (Biermann, 1957; Knese and Biermann, 1958), respectively representative of fibrocartilaginous and fibrous entheses, but with application to long bones only. Woo *et al* (1988) distinguished 'direct' (fibrocartilaginous) and 'indirect' (fibrous) entheses, which, although understandably describing an indirect tendon attachment through periosteum to the bone (fibrous), confuses an equally indirect tendon attachment through fibrocartilage to the bone (fibrocartilaginous), despite highlighting the absence of periosteum.

1.4.4 The Fibrocartilaginous Enthesis

The fibrocartilaginous entheses is structured as a sequence of 4 tissue zones: 1) dense fibrous connective tissue (tendon), 2) uncalcified fibrocartilage, 3) calcified fibrocartilage, and 4) bone (Dolgo-Saburoff, 1929; Cooper and Misol, 1970; Benjamin and Ralphs, 1998). A tidemark demarcates the boundary of soft and hard tissue, lying between the uncalcified fibrocartilage and calcified fibrocartilage, with the true anatomical boundary and site of union of the tendon and bone at the junction of the calcified fibrocartilage and bone (Benjamin *et al*, 2002). The fibrocartilage zones are often not present along the complete length of the entheses, where the absence of fibrocartilage represents a focal region of fibrous attachment, however the existence of any fibrocartilage classifies the entire entheses as fibrocartilaginous (Benjamin *et al*, 2002).

Fibrocartilaginous entheses are present at soft tissue attachments to bony epiphyses and apophyses (Benjamin, Evans and Copp, 1986; Apostolakos *et al*, 2014) and, as the majority of tendons and ligaments attach around joints, most entheses are fibrocartilaginous (Benjamin and Ralphs, 1998). There is no periosteum at the insertion site, and the subchondral cortical bone is typically thin (Benjamin *et al*, 2002). Examples of the most clinically relevant muscles and ligaments attaching through fibrocartilaginous entheses are the rotator cuff muscles, the ACL, and the Achilles tendon (Benjamin and McGonagle, 2001; Lu and Thomopoulos, 2013). Such entheses are clinically relevant as they are prone to injury through overuse and rupture. Tendons attaching to epiphyses typically undergo a large change in angle between the long axis of the tendon and their attached bone in fulfilling their function, such as the supraspinatus abducting the humerus, with resultant stress and abrasion at the insertion site (Benjamin and Ralphs, 1998) (**Figure 1.6**). In comparison, the mid-diaphyseal attachment of the deltoid, a fibrous enthesis insertion, endures a much more minimal change in angle (see *Section 1.4.5*). The fibrocartilage layer within fibrocartilaginous entheses is an adaptation to diminish damaging stress concentrations enhanced by the compression and shear forces generated through large functional angle changes at the insertion.

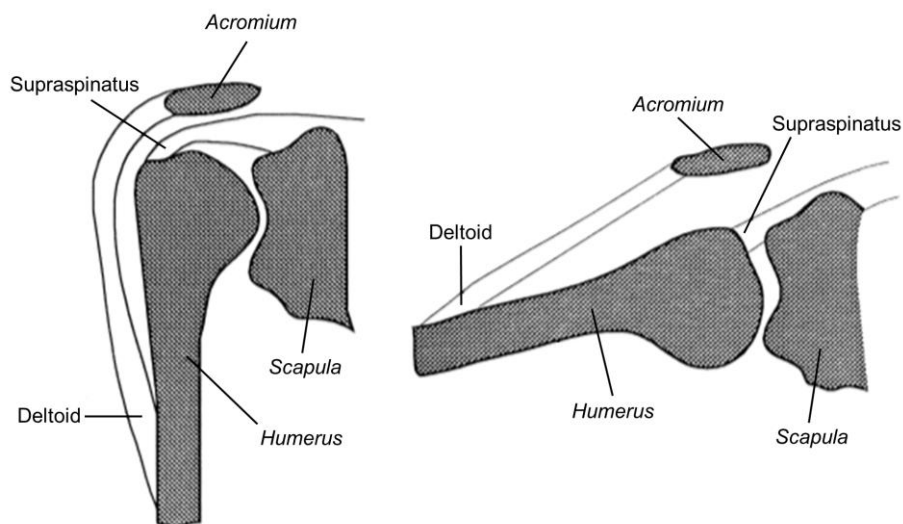


Figure 1.6 | Comparison of Insertional Angle Change at Epiphyseal and Diaphyseal Tendon Insertions Anterior view of the shoulder joint in resting adduction (*left*) and abduction (*right*), showing the epiphyseal insertion of *supraspinatus* and diaphyseal insertion of *deltoid* on the *humerus*. As the *humerus* is abducted, the inserting tendon fibres of *supraspinatus* undergo a large change in angle, whereas those of *deltoid* remain relatively unchanged. The variable loading with changing angles of the fibres causes compression and shear forces, countered by the presence of fibrocartilage at the *supraspinatus* insertion. Illustration adapted from Benjamin and Ralphs (1998).

The fibrocartilagenous enthesis provides smooth and efficient transmission of force through a specialised compositional and architectural microstructure. In the short distance of the enthesis between the mechanically distinct tendon and bone, typically 100µm-1mm (Lu and Thomopoulos, 2013), there is a wide variation in tissue properties across the 4 zones: cell morphology, extracellular matrix (ECM) composition, collagen structure, geometry and viscoelastic biomechanical properties (Thomopoulos *et al*, 2003). This allows a micromechanical optimal distribution of stress with limited expenditure of material (Thomopoulos, Genin and Galatz, 2010). The 4 zones are continuous but compositionally distinct (Lu and Thomopoulos, 2013), although studies suggest a gradation in microstructure without abrupt boundaries between the zones, with a decrease in collagen orientation and increase in mineralisation from tendon to bone (Wopenka *et al*, 2008; Genin *et al*, 2009; Thomopoulos, Genin and Galatz, 2010; Schwartz *et al*, 2012). As well as smooth stress distribution, interfacial gradients eliminate stress singularities, decrease stress concentration, improve bonding strength and reduce the risk of failure (Suresh, 2001; Benjamin *et al*, 2006). Indeed the biomechanical efficiency of the fibrocartilagenous enthesis is appreciated in the frequent occurrence of avulsions fracturing through the adjacent subchondral bone as well as at the true anatomical tendon-bone interface (Lam, Shrive and Frank, 1995; Gao *et al*, 1996a; Schlect, 2012). The following sections describe the composition, structure and function of each of the 4 zones that contribute to the fibrocartilagenous enthesis as a whole, summarised in **Figure 1.7**.

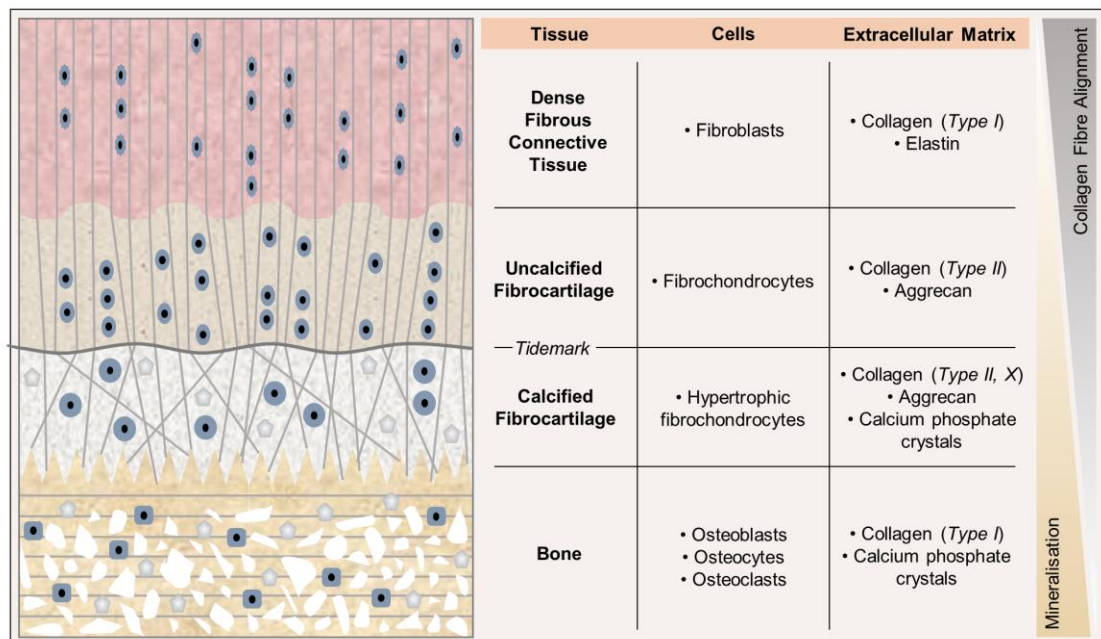


Figure 1.7 | The Fibrocartilagenous Enthsis

Diagram and summary of the composition and structure of the fibrocartilagenous enthesis. The key cellular and extracellular matrix constituents are listed, further elaborated in the main text. Note the increase in mineralisation and decrease in collagen fibre alignment from *dense fibrous connective tissue* to *bone*, as well as a decrease in the longitudinal arrangement of cells.

1.4.4.1 Dense Fibrous Connective Tissue

Dense fibrous connective tissue is composed of fibroblast cells within an ECM of predominantly collagen fibres. Tendon is a typical regular dense fibrous connective tissue, very similar to ligament, where collagen fibres are arranged in a highly compact and aligned hierarchical structure (**Figure 1.2**). Tendon fibroblasts (tenoblasts, the active precursor of mature tenocytes) are spindle-shaped and elongated, arranged in longitudinal rows parallel to the length of the tendon, lying freely between the collagen fibres (Kannus, 2000; Kuntz *et al*, 2018). They communicate via gap junctions between cytoplasmic processes both along and amongst the rows (McNeilly *et al*, 1996). Collagen is the strongest fibrous protein (Schlect, 2012) and its dense, organised assembly provides tendon with an ultimate tensile strength superior to most soft tissues (Gelberman *et al*, 1988). The most abundant collagen in tendon is type I (Kannus, 2000; Apostolakos *et al*, 2014; Calejo, Costa-Almeida and Gomes, 2019), with other minor types including III, V and IX (Calejo, Costa-Almeida and Gomes, 2019). Collagen also affords some tendon elasticity, with potential for stretch and recoil of 6% without damage (Benjamin *et al*, 2006), due to initial straightening of relaxed wavy fibres preceding shearing between the stiffened parallel fibres (Schlect, 2012). Elastin is also present, but at <3% overall dry weight, compared to 10-15% in ligament (Yang and Temenoff, 2009). The other main constituent of the ECM is the proteoglycan group in the ground substance, binding extracellular fluid and forming a gelled matrix (Schlect, 2012), containing primarily decorin and biglycan (Thomopoulos *et al*, 2003; Killian *et al*, 2012; Rothrauff and Tuan, 2014), with fibromodulin, lumican and versican (Yang and Temenoff, 2009).

1.4.4.2 Fibrocartilage

Fibrocartilage is a type of cartilage with abundant collagen fibres in the ECM. It resembles dense fibrous connective tissue as the orientated layers of collagen fibres from the tendon continue within it, but with intervening bands of hyaline cartilage matrix. The most prevalent collagen is type II (Waggett *et al*, 1998; Milz *et al*, 2005; Galatz *et al*, 2007), almost fully replacing type I from the tendon, with type III and other minor types also reported (Benjamin *et al*, 2006; Apostolakos *et al*, 2014; Calejo, Costa-Almeida and Gomes, 2019). The cartilaginous ground substance provides a solid yet flexible tissue consistency, bridging the properties of tendon and bone, due to the predominance of glycosaminoglycans (GAGs), existing as proteoglycans or hyaluronic acid (Young, O'Dowd and Woodford, 2014). The most typical proteoglycan

in fibrocartilage is aggrecan (Waggett *et al*, 1998; Benjamin and McGonagle, 2001; Smith *et al*, 2012), in contrast to tendon and bone. Other proteoglycans present are similar to those found in tendon, excluding versican, important for the regulation of collagen fibril formation (Benjamin and Ralphs, 1998; Shaw and Benjamin, 2007). GAGs, and particularly those associated with aggrecan, are potently hydrophilic, imbibing water and providing a tissue incompressibility to stiffen the ECM (Benjamin *et al*, 2002; Yoon and Halper, 2005; Young, O'Dowd and Woodford, 2014). It is this ECM property of fibrocartilage that provides the protection against compression forces, and, as such, enthesis fibrocartilage is thicket in the deepest part of the tendon where it is compressed by the superficial part against the bone (Benjamin and Ralphs, 1998; Benjamin *et al*, 2006).

Cells in the fibrocartilaginous layer of the enthesis resemble cartilage cells more than tendon cells, in morphology and biomarker expression, but are not as fully chondrocyte-differentiated as cartilage cells (Rossetti *et al*, 2017; Kuntz *et al*, 2018). Such fibrochondrocyte cells are usually aligned in rows between the layers of dense collagen fibres, maintaining the same arrangement as the fibroblasts from which they derived by metaplasia (Gao *et al*, 1996b; Benjamin *et al*, 2006) (see *Section 1.4.7*), but with larger, oval/round morphology. The fibrocartilage cells are often packed with intermediate filaments, which may be vital for load transduction across the enthesis (Ralphs, Benjamin and Thornett, 1991; Benjamin and Ralphs, 1998). Secretion of cartilage matrix by active fibrochondroblasts completely isolates mature fibrochondrocytes and, since these cells do not express connexins and do not form gap junctions, intercellular communication is indirect via cell-matrix interactions or soluble factors (Benjamin and Ralphs, 1998; Benjamin and McGonagle, 2009). In addition to the avascular and aneural properties of enthesis fibrocartilage (see *Section 1.4.6*), this likely contributes to the poor healing response at the insertion site (Font Tellado, Balmayor and Van Griensven, 2015) (see *Section 1.4.8.2*).

1.4.4.2.1 Uncalcified Fibrocartilage

The boundary between the dense fibrous connective tissue of the tendon and the uncalcified fibrocartilage is not readily distinct. Uncalcified fibrocartilage is signified by the first presence of fibrochondrocytes and a pericellular metachromatic matrix, representing proteoglycans granules at ultrastructure level (Rufai, Ralphs and Benjamin, 1996; Benjamin *et al*, 2002). As the uncalcified fibrocartilage zone blends

with the tendon, longitudinal rows of fibrochondrocytes are particularly pronounced. The cells are generally more ovoid than rounded, maintaining a phenotype closer to fibroblasts. As the tissue properties gradually change from tendon to bone, the collagen fibres also become less parallel than in tendon, isolating some cells from their longitudinal arrangement (Benjamin *et al*, 2002). In addition to type II collagen and aggrecan, there are also high levels of pericellular collagen type III, with small amounts of type I, IX and X collagen and further proteoglycans associated with chondroitin sulfate GAGs (Thomopoulos, Genin and Galatz, 2010; Font Tellado, Balmayor and Van Griensven, 2015; Calejo, Costa-Almeida and Gomes, 2019).

Uncalcified fibrocartilage in particular is most prominent where there is a large degree of movement between the tendon fibres and bone during joint movement (Evans, Benjamin and Pemberton, 1990; Benjamin *et al*, 1991; Benjamin and Ralphs, 1995; 1998) (see **Figure 1.6**). Across the enthesis, collagen fibres are flexible in the tendon but fixed in stiff mineral in the calcified fibrocartilage as they insert into bone. Where there is a considerable change in angle between flexible approaching fibres and stiff inserting fibres, the solid but pliable uncalcified cartilage matrix promotes the gradual bending of fibres to the insertion point just like a rubber grommet guiding a wire into a plug (Schneider, 1956; Benjamin and Ralphs, 1998; Benjamin *et al*, 2002). The gradual fibre bending, occurring nearly entirely in the uncalcified fibrocartilage region (Benjamin, Evans and Copp, 1986), rather than a sudden angle change, diminishes cumulative damage and abrasion, as a particular feature of adapting to compression and shear forces. The heterogeneity of uncalcified fibrocartilage thickness across the same enthesis suggests varying degrees of angle change in the inserting fibres, with corresponding compression and shear forces (Toumi *et al*, 2012; 2014; 2016; Beaulieu *et al*, 2016), most notably present in the deepest part of the tendon closest to the rotating joint (Frowen and Benjamin, 1996).

1.4.4.2.2 Calcified Fibrocartilage

The zone of calcified fibrocartilage is small and typically less cellular, likely due to cell death from reduced nutrient diffusion through the mineralised ECM (Benjamin and Ralphs, 1998; Benjamin *et al*, 2006). Fibrochondrocytes are hypertrophic, displaying a rounded and larger morphology more similar to chondrocytes (Rothrauff and Tuan, 2014; Font Tellado, Balmayor and Van Griensven, 2015). As well as the typical cartilage markers of type II collagen and aggrecan, type X collagen is notably

expressed in the ECM of the calcified fibrocartilage layer (Fukuta *et al*, 1998; Galatz *et al*, 2007; Font Tellado, Balmayor and Van Griensven, 2015). Type X collagen is characteristic of hypertrophic chondrocytes (Thomopoulos, Genin and Galatz, 2010) and has a role in controlling excess mineralisation into the tendon (Benjamin and Ralphs, 1998). Inorganic ECM mineral is in the form of calcium phosphate crystals, increasing the Young's modulus in comparison to the uncalcified fibrocartilage zone (Moffat *et al*, 2008) and holding the increasingly dispersed collagen fibres stiff as they attach to bone.

The thickness and extent of the calcified fibrocartilage region (i.e. area) appears to be related to the physiological strength and loading of the tendon on the bone, particularly of maximum transmitted force (Evans, Benjamin and Pemberton, 1991; Benjamin *et al*, 1991; Gao and Messner, 1996; Benjamin and Ralphs, 1998). Regional variations in thickness or amount of calcified fibrocartilage exist within the same enthesis as per uncalcified fibrocartilage, suggesting non uniformity of load along the interface (Sasaki *et al*, 2012; Toumi *et al*, 2012; 2014; 2016; Beaulieu *et al*, 2016). The shear stresses potentially generated on tendon loading are protected against by the stiff anchorage of the calcified fibrocartilage as the Young's modulus increases towards bone.

1.4.4.2.3 Tidemark

The tidemark provides a readily visible border between the uncalcified and calcified fibrocartilage zones. It is traditionally described as a calcification front where material has accumulated (Benjamin *et al*, 2002; Shaw and Benjamin, 2007), often being intensely basophilic from the dense granulation (Rufai, Ralphs and Benjamin, 1996; Benjamin and Ralphs, 1998). The more intense metachromasia around the deepest uncalcified fibrocartilage fibrochondrocytes is thought to be representative of a calcium 'sink' as they function to constrain mineral deposition just ahead of the tidemark (Benjamin *et al*, 2002).

The tidemark is the level at which macerated soft tissues separate from bone in the preparation of a dry skeleton, leaving a smooth surface, similar to articular cartilage but in contrast to fibrous enthesis attachments, representative of the smooth (straight or wavy) tidemark line (Benjamin, Evans and Copp, 1986). Collagen fibres traverse the tidemark, possibly functioning as a shear-reducing anchorage point (Redler *et al*,

1975), on their way to insert into bone. As the tendon moves on the calcified tissue, the likelihood of fibre damage and abrasion is reduced by the smooth form of the tidemark (Benjamin *et al*, 2002; Apostolakos *et al*, 2014). The tidemark is thus designated as the mechanical boundary between soft and hard tissues (Benjamin *et al*, 2002; Shaw and Benjamin, 2007; Apostolakos *et al*, 2014). However, the illumination of an increasing gradation in mineral content from tendon to bone across the fibrocartilaginous enthesis (Wopenka *et al*, 2008; Genin *et al*, 2009; Schwartz *et al*, 2012) suggests that the notion of a soft-hard tissue border may not be so well-defined.

1.4.4.3 Bone

Bone primarily consists of osteoblasts, osteocytes and osteoclasts in a mineralised ECM of principally type I collagen. Mature lamellar bone is composed of parallel sheets of collagen, mineralised and structured for lightweight strength and rigidity, as well as providing elasticity and resistance to deformation. Lamellar bone is organised as densely compact cortical bone in the walls of long bones, or as a network of trabecular bone in the medullary cavity, approximately 80% porous (Yang and Temenoff, 2009) but surrounded by marrow tissue. Compact bone consist of 30% organic matrix (90% collagen, with a small proportion of GAGs, mainly as chondroitin sulfate-containing proteoglycans and hyaluronic acid) and 70% inorganic mineral salts (primarily calcium and phosphate as hydroxyapatite crystals) by weight (Young, O'Dowd and Woodford, 2014). Active osteoblasts ($\leq 6\%$ of resident bone cell population) are cuboidal cells found on bone surfaces, and through the activity of alkaline phosphatase secrete the bone matrix-related proteins, including osteocalcin, osteopontin, osterix and bone sialoprotein, in addition to the type I collagen (Calejo, Costa-Almeida and Gomes, 2019). With deposition and mineralisation of the ECM they become encased in lacunae and mature into dendritic shaped osteocytes (up to 95% of bone cells), communicating across gap junctions between long cytoplasmic processes extended through canaliculi, and continue a role in bone formation (Calejo, Costa-Almeida and Gomes, 2019). Other cells of osteoblastic lineage are bone-lining cells: mature, inactivated osteoblasts that have avoided encasement in lacunae; and pre-osteoblasts: proliferative osteoprogenitor cells with osteogenic capability (Gartland *et al*, 2012). Bone resorption is chiefly performed by the phagocytic osteoclasts, of distinct lineage to the osteoblastic cells.

A cement line signifies the true anatomical tissue boundary at the tendon insertion site onto bone, at the calcified fibrocartilage-bone junction. The irregular 'jigsaw' arrangement at this interface as an important feature of secure anchorage has been described in *Section 1.4.2*. Even at the largest fibrocartilaginous entheses, the anchoring cortical bone is extremely thin, appearing as if a continuous shell of the trabecular network (Benjamin *et al*, 2007). This feature may contribute to stress dissipation by permitting slight deformation of the bony shell under the tendon load (Benjamin *et al*, 2002; Benjamin *et al*, 2007). The trabecular bone itself may also contribute to mechanical function, since the trabecular architecture at the enthesis, as in other bone regions, is closely aligned with the direction of principle strain force (Biewener *et al*, 1996; Inoue *et al*, 1998). Indeed the trabeculae in the calcaneus orientate in a parallel anisotropic alignment between the Achilles tendon and plantar fascia insertions, seemingly relaying the transfer of force from the tendon to the fascia (Milz *et al*, 2002).

1.4.5 The Fibrous Enthesis

Fibrous entheses are composed of dense fibrous connective tissue at the tendon-bone interface, with no intervening fibrocartilage. They are further subdivided as 'bony' or 'periosteal' depending on their particular point of attachment: uninterrupted to cortical bone or via periosteum, respectively (Hems and Tillmann, 2000). Periosteal fibrous entheses are weaker, but they are able to retain their relative position on a developing bone during appositional bone growth, migrating with the interstitial growth of the periosteum, with potential to become bony on skeletal maturity (Matyas *et al*, 1990; Shaw and Benjamin, 2007). In anchoring to bone directly through tendon, ligament or periosteum, Sharpey's mineralised perforating fibres characterise the fibrous enthesis insertion (François, Braun and Khan, 2001; Benjamin *et al*, 2002; Lu and Thomopoulos, 2013). Compositionally, fibroblasts are present in the dense fibrous connective tissue without any fibrocartilage cells, and although collagen type I and III are associated with Sharpey's fibres, specific molecular knowledge of the fibrous enthesis is sparse (Benjamin *et al*, 2002).

Muscles attaching via a fibrous tendon enthesis include the deltoid and pronator teres to the humerus, adductor magnus to the linea aspera, and pectoralis minor to the ribs (Benjamin, Evans and Copp, 1986). Ligamentous fibrous entheses include the tibial

insertion of the medial collateral ligament of the knee (Woo *et al*, 1988). They attach to the metaphysis and, more commonly, the diaphysis of long bones and are generally associated with thick cortical bone in the appendicular skeleton (Benjamin *et al*, 2002). Their tendons are typically short but with expansive attachment sites, helping to spread the stress focus over a wide area of interface and limiting stretch and splay (Shaw and Benjamin, 2007; Lu and Thomopoulos, 2013). During muscle action of a fibrous tendon enthesis on a bone, such as the deltoid abducting the humerus, the change in angle between the long axis of the tendon and bone is minimal, reducing the likelihood of enthesis damage from overuse (Benjamin and Ralphs, 1998; Apostolakos *et al*, 2014) (see **Figure 1.6**). These structural and mechanical features allow the fibrous enthesis to suitably function without the need for a specialised fibrocartilaginous tissue transition.

Fibrous entheses are less common than fibrocartilaginous entheses and are less frequently injured in acute avulsions or chronic enthesopathies (Shaw and Benjamin, 2007; Apostolakos *et al*, 2014). They are thus the subject of comparatively little investigation or literature coverage, in basic science or translational applications such as tissue engineering. Similarly, the remainder of this chapter and future chapters will focus on the fibrocartilaginous enthesis, with 'enthesis' assumed as a fibrocartilaginous enthesis unless specifically stated as fibrous.

1.4.6 Vascularity and Innervation

The enthesis derives a blood supply from the adjacent peritenon and bone marrow vessels (McGonagle and Benjamin, 2015). Enthsis fibrocartilage is however avascular (Dörfl, 1969a; Benjamin, Evans and Copp, 1986), in accordance with (fibro)cartilage elsewhere in the body (Benjamin and Ralphs, 2004), and representative of the compressive mechanical environment which would occlude any potential vessels (Benjamin and McGonagle, 2001). Intratendinous and bone marrow vessels may however anastomose across the tendon-bone junction in the fibrous enthesis (Dörfl, 1969b), and since nearly all fibrocartilaginous entheses exhibit a discontinuous fibrocartilage layer, interfacial vessel communication may potentially occur at the 'fibrocartilaginous' enthesis (Benjamin and McGonagle, 2001). Absence of the whole subchondral plate of cortical bone and calcified fibrocartilage is also apparent in many histological observations of the enthesis and, whether this is

pathological or nutritional, can result in bone marrow vessels contacting the uncalcified fibrocartilage layer (Benjamin and McGonagle, 2001; Benjamin *et al*, 2007).

Although previously considered richly innervated (Palesy, 1997), the healthy enthesis is aneural (Shaw *et al*, 2007; McGonagle and Benjamin, 2015). This is again appropriate for a tissue region, like articular cartilage, that sustains heavy compression, where continued mechanical nerve stimulation would be detrimental, and thus nerves are limited to the periphery of the insertion site (Benjamin *et al*, 2004a). Nociceptive and mechanoreceptive nerve fibres are found in adjacent fat pads (Shaw *et al*, 2007) and the epitenon (Benjamin *et al*, 2004a), which, in addition to purely tendon and bone nerve fibres, are likely to be the sensory origins of enthesis pain and proprioception. Such surrounding structures, including fat pads, bursae, and sesamoid and periosteal fibrocartilages, contribute to the concept of an 'enthesis organ': adjacent tissue specialisations that are functionally related to dissipate stress, influencing enthesis physiology and pathology (Benjamin and McGonagle, 2001).

1.4.7 Development

1.4.7.1 Overview

The precise mechanisms of enthesis development are not fully understood. Animal studies have captured the essential presence and interplay of biological and mechanical factors, and associated formation with that of the growth plate, but a process unifying all elements of molecular control to tissue formation has not been delineated specifically for the enthesis. Enthesis development requires a spatial gradation of tendon, fibrocartilage and bone. Tendon and bone precursors arise in foetal life at a similar stage, but the critical events forming the intervening fibrocartilaginous transition are post-natal (Bland and Ashhurst, 1997; Thomopoulos, Genin and Galatz, 2010). However, at 7 days after birth in a murine model, the 4 zones of the fibrocartilaginous enthesis are distinguishable (Galatz *et al*, 2007) and a mineral gradient is already detectable at the leading edge of the hard-soft tissue interface (Schwartz *et al*, 2012).

Gao *et al* (1996b) studied fibrocartilaginous enthesis formation in the rat, relating the process to the endochondral ossification of the attached bone precursor. At first the

tendon attaches to a bone precursor of hyaline cartilage. As the cartilage is ossified proximally towards the tendon, with a plug of hyaline cartilage not yet ossified on the 'bone' side of the enthesis, fibrocartilage develops on the tendon side by metaplasia of tendon cells. As the hyaline cartilage on the 'bone' side is completely ossified, the enthesis fibrocartilage advances further into the tendon. The enthesis therefore acts as a growth plate, with cartilage resorption and formation balanced on the 'bone' and tendon side of the interface (Benjamin and Ralphs, 1998).

Enthesis fibrocartilage forms entirely from within the tendon, in a process fully separate to that of bone morphogenesis (Zelzer *et al*, 2014; Calejo, Costa-Almeida and Gomes, 2019). Cells initially differentiating as fibroblasts and arranged in rows in the tendon undergo phenotypic change to fibrocartilage cells, remaining likewise arranged in rows and separated by parallel type I collagen fibres coursing across the tidemark to the bone junction (Benjamin and Ralphs, 1998; Benjamin and McGonagle, 2009). Calcification in the deepest fibrocartilage zone occurs only when fibrocartilage formation slows (Benjamin and Ralphs, 1998), following which remodelling of collagen fibres and mineral creates the well organised tendon-bone transition (Lu and Thomopoulos, 2013).

1.4.7.2 Biological Factors

Several important molecular signals have been recognised in enthesis development. The principle biological molecules involved appear to be sclexaris (Scx) and sex-determining region Y-box 9 (Sox9) for tenogenesis and chondrogenesis, respectively; transforming growth factor(TGF)- β and bone morphogenetic protein (BMP) for initiation of growth; and Indian hedgehog (Ihh) and parathyroid hormone-related protein (PTHrP) for mineralisation and maturation. The coordinated spatiotemporal expression pattern of these signalling molecules allows the development of the specialised tissue gradation of cellular phenotype and ECM composition from tendon to bone (Lu and Thomopoulos, 2013; Rothrauff and Tuan, 2014; Zelzer *et al*, 2014).

Scx, essential for tenogenesis, is expressed in all tendon tissues and Sox9, essential for chondrogenesis, is expressed in proliferative chondrocytes (Font Tellado, Balmayor and Van Griensven, 2015). Sugimoto *et al* (2013) and Blitz *et al* (2013) proposed that the tendon-bone insertion is formed by differentiation of a multipotent pool of Scx⁺/Sox9⁺ progenitor cells. An interface is established through increasing Scx

expression (formation of tenocytes) or Sox9 expression (formation of enthesal chondrocytes), in a region between tenoprogenitors (Scx⁺/Sox9⁻) and chondroprogenitors (Scx⁻/Sox9⁺) (Sugimoto *et al*, 2013). TGF- β appears crucial to directing tendon or cartilage differentiation (Galatz *et al*, 2007; Rothrauff and Tuan, 2014) and BMP-4 is necessary to mediate formation of the enthesal bone ridge (Blitz *et al*, 2009; Blitz *et al*, 2013; Calejo, Costa-Almeida and Gomes, 2019).

The Ihh/PTHrP feedback loop is important in control of growth plate chondrocyte proliferation/differentiation and mineralisation, and the expression of these signalling molecules in the enthesis (Chen *et al*, 2007; Liu *et al*, 2013) suggests that they also influence the mineral gradient at the tendon-bone attachment (Lu and Thomopoulos, 2013; Zelzer *et al*, 2014). In the longitudinal columns of chondrocytes in the growth plate, the deepest cells extending towards the metaphysis become hypertrophic and loaded with calcium, mineralising the surrounding matrix (Thomopoulos, Genin and Galatz, 2010). Ihh is expressed by hypertrophic chondrocytes and, by negative feedback and induction of PTHrP, prevents inappropriate chondrocyte hypertrophy and mineralisation, possibly analogous to the control of the unmineralised-mineralised transition in the enthesis (Thomopoulos, Genin and Galatz, 2010; Font Tellado, Balmayor and Van Griensven, 2015; Calejo, Costa-Almeida and Gomes, 2019).

1.4.7.3 Mechanical Factors

Mechanobiology is evidently an important mechanism in enthesis development. All enthesis cell types are mechanoresponsive (Lu and Thomopoulos, 2013) and the appearance of enthesis fibrocartilage is a post-natal phenomenon (Galatz *et al*, 2007). The initiation of enthesis formation does not require muscle loading, appearing to be fully biologically controlled, but mechanical cues sustain enthesis growth and maturation after birth (Blitz *et al*, 2009; Lu and Thomopoulos, 2013). Studies on the developing enthesis of the paralysed rat supraspinatus from birth show that although no difference exists compared to controls up to day 14, continued reduced muscle load impairs fibrocartilage formation and mineral deposition (Thomopoulos *et al*, 2007), and collagen fibre organisation, maximum strength and Young's modulus (Schwartz *et al*, 2013). Compression and shear forces at the tendon insertion are also the probable signals for metaplasia of fibroblasts to enthesal fibrocartilage cells (Benjamin and McGonagle, 2009). Although Ihh and PTHrP are associated with the mechanoresponse (Chen *et al*, 2007; Schwartz *et al*, 2015), knowledge of the

mechanically evoked molecular cascades determining development remain unclear (Font Tellado, Balmayor and Van Griensven, 2015).

1.4.8 Injury and Repair

Damage to the enthesis can occur through mechanical injury or distinct rheumatological conditions. Mechanical injury may be in the form of acute rupture, or chronic degeneration from overuse or subclinical injury, leading to inflammation. Common sites of mechanical enthesis pathology include the ACL, medial collateral ligament (MCL) and meniscal root in the knee; the rotator cuff attachment to the humerus; the Achilles tendon on the calcaneus; the common origin of the forearm/wrist flexors on the medial epicondyle of the humerus ('tennis elbow'); and the quadriceps tendon and patellar ligament attachment on the patella ('jumper's knee') (Derwin *et al*, 2018).

Enthesis injuries around the large joints are particularly common. In the United States, 2/1000 people per year suffer knee ligament injury, 90% involving the ACL and MCL (Rothrauff and Tuan, 2014), and rotator cuff tears are present in more than 40% of the population over 60 (Ricchetti *et al*, 2012). Locally in Edinburgh, the incidence/100,000 adults of soft tissue injuries has been reported as 8.06 (ACL), 5.21 (MCL), 3.73 (rotator cuff tear), and more commonly 23.76 (meniscal tear) and 11.33 (Achilles tendon rupture) (Clayton and Court-Brown, 2008). The majority of injuries occur in the young, active population (Clayton and Court-Brown, 2008) where the economic and societal impact from missed work days for treatment is greatest. Injuries frequently require surgical repair, with conservative treatment often failing and leaving a chronic disability that can predispose the adjacent joint to osteoarthritis. Such surgical repairs are costly, estimated at \$17,000-\$25,000 for ACL reconstruction and rehabilitation (Hewett *et al*, 2010).

Idiopathic rheumatological inflammatory conditions affecting the enthesis are the seronegative spondyloarthropathies, including ankylosing spondylitis, reactive arthritis and psoriatic arthritis (Benjamin and McGonagle, 2001). The mainstay of treatment is immune modulation medications, however surgical replacement may be indicated for local advanced disease.

1.4.8.1 Surgical Treatment

The basic premise of surgical repair of a ruptured or damaged enthesis is to provide secure reattachment of the soft tissue to bone with sutures or bone anchors. The ruptured soft tissue end and bony insertion are first debrided to healthy tissue, destroying any remaining fibrocartilage (Rothrauff and Tuan, 2014). Reattachment does not then reconstitute the complex fibrocartilaginous insertion with its graded mechanical properties, relying on a capacity for sustained and functional soft tissue-bone integration. The inability to re-establish the enthesis compromises successful long term outcomes, as the exposed mechanical mismatch and stress focus at the interface predisposes to gapping and frank rupture (Derwin *et al*, 2018). Re-rupture necessitates further surgery, increased costs and longer rehabilitation. Surgical grafting, for reconstruction or transfer of an already intact enthesis, additionally introduces the potential for increased surgical complications and side-effects.

The unsatisfactory nature of surgical treatment is illustrated by 2 of the most common structural repairs. Rotator cuff repairs are performed by direct apposition of the debrided tendon(s) against the humeral head. 275,000 are performed annually in the United States (Jain *et al*, 2014), with failure rates from 20% with partial tears (Harryman *et al*, 1991) to 94% for large and massive tears (Galatz *et al*, 2004). Similarly, 130,000 ACL repairs are performed (Buller *et al*, 2014), with 56% experiencing knee pain at 1 year follow-up (Corry *et al*, 1999). ACL surgery is an example of a repair usually demanding reconstruction with a graft, bringing associated morbidity and cost. Autograft repairs typically utilise hamstring tendon or bone-tendon-bone patellotibial grafts, fixed into tibial and femoral bone tunnels, creating harvest site morbidity such as further wounds, muscle weakness and chronic joint pain (Corry *et al*, 1999). Allografts require availability, tissue sizing and sterilisation procedures, and risk tissue rejection, reduced biological and mechanical integrity from processing, and donor pathogen transmission (Smith *et al*, 2012). Synthetic grafts generally perform poorly, with complications including mechanical breakdown, pain, sterile effusion, synovitis and osteoarthritis (Paxton, Baar and Grover, 2012).

1.4.8.2 Healing

Surgical debridement and reattachment produces a fibrovascular scar at the enthesis site rather than the fibrocartilaginous transition zone (Rodeo *et al*, 1993; Liu *et al*, 1997; Galatz *et al*, 2006; Silva *et al*, 2006), eventually maturing to resemble a fibrous

entheses (Newsham-West *et al*, 2007; Paxton, Baar and Grover, 2012). The repaired interface is biomechanically inferior (Rodeo *et al*, 1993; Thomopoulos, Williams and Soslowky, 2003; Galatz *et al*, 2006), and does not recreate the gradation in collagen fibre orientation and mineral (Rodeo *et al*, 1993; Silva *et al*, 2006; Derwin *et al*, 2018). A new layer of woven bone forms on the pre-existing lamellar bone, however there is significant underlying bone loss, potentially contributing to repair weakness (Ditsios *et al*, 2003a; Galatz *et al*, 2005; Silva *et al*, 2006). Overall the repaired entheses are of reduced structural integrity and mechanical functionality.

The early features of a fibrovascular scar are a hypercellular environment with a disorganised ECM of increased type III collagen (Thomopoulos, Williams and Soslowky, 2003; Galatz *et al*, 2006). Healing is thought to progress through the stages of 1) inflammation (0-7 days), 2) repair (5-14 days), and 3) remodelling (>14 days); associated particularly with TGF- β -mediated scar formation and matrix metalloproteinase (MMP)-mediated remodelling to establish aligned type I collagen fibres (Angeline and Rodeo, 2012; Apostolakos *et al*, 2014). This acute inflammatory healing process is however in contrast to the chronic overuse injury model. Chronic injury represents a continuum of tendinopathy through 1) reactive tendinopathy (non-inflammatory proliferation), 2) tendon disrepair (ECM disorganisation and collagen separation), and 3) degenerative tendinopathy (increased acellularity with poor capacity to remodel the disorganised ECM) (Cook and Purdam, 2009). Whether acute or chronic, it is likely that the avascularity and relative hypocellularity of the entheses contribute to a poor healing response (Rothrauff and Tuan, 2014). Understanding of the specific mechanisms of entheses healing is however limited. This knowledge gap, along with an incomplete picture of the interrelated mechanisms of entheses development (see *Section 1.4.7*), are the principle reasons for the lack of satisfactory treatments for entheses injury.

1.4.8.2.1 Augmentation

There is limited evidence that fibrocartilage can reform after considerable time from surgical entheses repair (Gerber *et al*, 1999; Uthoff *et al*, 2002). This suggests that a regenerative capacity does exist, requiring a natural transdifferentiation of fibroblasts or osteoblasts into fibrochondrocytes, or chondrogenesis from endogenous progenitor cells (Rothrauff and Tuan, 2014). Researchers have attempted to augment this capacity *in vivo* in animal models through a number of strategies, focusing on direct

fibrocartilage formation or enhancement of healing. Cellular therapy at the repair site has employed a variety of mesenchymal stem cells (MSCs), mature chondrocytes and periosteal progenitor cells, generally promoting fibrocartilage formation and enhancing associated mechanical properties (Rothrauff and Tuan, 2014). Addition of growth factors has aimed to replicate the healing response, with notable success in fibrocartilage formation and mechanical strength using BMPs, although with limited success using TGF- β (Paxton, Baar and Grover, 2012). Likewise, dampening the effects of certain factors can improve healing, in particular with inhibition of MMP (Demirag *et al*, 2005; Bedi *et al*, 2010). Bone cements, such as calcium phosphate, brushite and magnesium-based cements, provide an osteoconductive material to induce bone ingrowth and increase ultimate failure strength, or act as a carrier for growth factors (Paxton, Baar and Grover, 2012). Both hypoxia (Zhao *et al*, 2011) and delayed loading (Thomopoulos, Williams and Soslowsky, 2003) also appear beneficial to fibrocartilaginous healing, as broad modifications to the general environment. These promising developments in animal models have currently had limited exploration in human trials. However, exogenous biochemical modulation and maturation are key strategies in interfacial tissue engineering, where an original, uninjured enthesis may potentially be fully formed *in vitro*.

1.4.9 Summary

Key points:

- *Tendon/ligament and bone are biomechanically distinct structures;*
- *The enthesis is the specialised transition between tendon/ligament and bone;*
- *A gradation of cell phenotype and ECM facilitates smooth force transmission;*
- *Enthesis development is complex and remains incompletely understood;*
- *The enthesis is not regenerated after injury or surgical repair;*
- *Repair is of inferior strength and tissue organisation, risking re-rupture.*

1.5 Interfacial Tissue Engineering

1.5.1 Overview

Tissue engineering is a discipline that “*applies the principles of engineering and the life sciences toward the development of biological substitutes that restore, maintain, or improve tissue function*” (Langer and Vacanti, 1993). Tissue damage from trauma or disease may be beyond effective pharmaceutical or surgical treatment, and suitable organ transplantations are notoriously lacking and risk immune rejection, leaving tissue engineering as an increasingly promising therapeutic option. The musculoskeletal system is particularly befitting to the application of tissue engineering due to relatively well characterised structure and function, and limited functional treatment options (Rothrauff and Tuan, 2014). Furthermore, musculoskeletal conditions are one of the major causes of worldwide disability (Brooks, 2006), only increasing with an aging population.

Interfacial tissue engineering (ITE) aims to regenerate the connecting interface between distinct tissue types. Many musculoskeletal interfaces exist, including the tendon/ligament-bone enthesis, with furthest ITE progress at the osteochondral and periodontal junctions (Boys *et al*, 2017). Engineering homogenous musculoskeletal tissues is well established, such as bone (Amini, Laurencin and Nukavarapu, 2012), tendon (Butler *et al*, 2008) and ligament (Yilgor, Yilgor Huri and Huri, 2012), however their interfacial regions often contain separate biochemical and mechanical properties. The challenge of ITE is to replicate a highly heterogenous, complex structure of small size that provides native mechanical functionality. By generating a replica interface between 2 tissues *ex vivo*, *in vivo* integration can then occur more reliably between homogenous native and engineered tissues at either end of the ITE model.

A biological interface can be studied in 2-dimensional (2D) or 3-dimensional (3D) culture, however a 3D setting provides a more simulated *in vivo* environment, and is necessary to form an implantable replica model. A model is designed and cultured through the interactions of the 3 pillars of tissue engineering: scaffolds, cells and stimulators. These elements may be employed in compartmentalised, stratified

designs or continuous, gradient designs, which are then matured to create the interface between tissues. The optimal design is not yet established, and research continues to ascertain a practical synergy between the most advantageous scaffold and cell properties and stimulation and maturation techniques.

1.5.2 2-Dimensional versus 3-Dimensional

2D tissue engineering studies involve a cellular monolayer anchored to a favourable attachment surface, typically treated cell culture plastic. Such studies are cheap, maintain continuous contact with culture medium for similar nutrition to an evenly distributed cell population, and provide easy access to the culture environment for manipulation (Bicho *et al*, 2018). They may particularly provide the basis for cell characterisation studies or co-culture interactions (Wang *et al*, 2007). However, cell behaviour differs in 2D compared to 3D culture. As an example, in screening for cancer chemotherapeutics, drugs are much less effective against 3D *in vitro* tumour models compared to 2D models, reproducing the chemoresistance found *in vivo* that results from 3D cellular function (Longati *et al*, 2013).

3D tissue culture represents a more physiological and relevant *in vivo* environment. Cells demonstrate more natural morphology, cell-cell and cell-environment interactions, enhancing their viability, proliferation, differentiation, migration and response to stimuli (Antoni *et al*, 2015). Overall cellular function is thus enhanced, and gene expression and protein synthesis is more realistic. Such 3D models usually involve a cellular scaffold, which can then be scalable to an anatomical model of appropriate size to integrate into the *in vivo* tissue. Furthermore, although difficulty in equal diffusion of nutrients through scaffolds may be viewed as a disadvantage, this also mimics the *in vivo* diffusion environment (Kinney *et al*, 2013). 3D models are therefore much more appropriate to study cellular interactions and tissue regeneration, and provide closer possibilities for clinical translation.

1.5.3 Design Components

1.5.3.1 Scaffolds

A scaffold acts as an artificial ECM. Scaffold function is thus that of the ECM: to give structural integrity and support 3D tissue formation by providing the medium through

which cells, soluble proteins and mechanical cues are hosted and delivered to the tissue (Armitage and Oyen, 2015). Additionally, a scaffold intended for implantation to replace or enhance repair of the enthesis requires the capability to integrate *in vivo*. 3D models may also be scaffold-less, particularly effective as *in vitro* tools for characterisation of cultures or drug screening, but which can also form structurally viable units for implantation once cells secrete and mature their own ECM (Alsaykhan, 2019).

The essential considerations for a scaffold are its structural and biological properties (Font Tellado, Balmayor and Van Griensven, 2015). Structural properties are the architectural design, such as pore size, and mechanical attributes. Pore size affects cell proliferation and function, nutrient diffusion and mechanical properties. Fibroblasts and chondrocytes prefer smaller pores (in the order of 10 μ m) whilst bone cells favour larger pores (of 100 μ m order magnitude) (Armitage and Oyen, 2015), with *in vivo* trabecular bone notably averaging a pore size on the order of 1mm (Keaveny *et al*, 2001). Pore size can be highly controlled in many materials, and size gradients are possible with techniques such as freeze casting and salt leaching (Font Tellado *et al*, 2017). Mechanical attributes may be inherent to the pore size, such as an upper size limit for providing structural integrity. However microwall or individual fibre stiffness also particularly influence cell phenotype expression, with stiffer materials promoting osteogenic differentiation (Engler *et al*, 2006; Armitage and Oyen, 2015).

Biological properties include cell-material interactions, biodegradation and biocompatibility. Cells must anchor to a scaffold to function appropriately and sense the mechanical microenvironment, binding better to some scaffolds than others. Cell-scaffold adhesion is promoted through ligands, molecules present in proteins naturally found in the ECM (e.g. collagen, proteoglycans) that bind to integrins on cell membranes, and therefore synthetic protein-lacking materials may first need to be functionalised with ligands for improved cell adhesion (Paxton *et al*, 2009; Armitage and Oyen, 2015). Biodegradation, through hydrolysis or enzymes, must balance *in vivo* integration and infiltration by host tissue with any requirement for retained structural support. The presence and degradation of a scaffold *in vivo* should also be biocompatible and elicit a minimal immune response, since any additional scar-mediated healing undermines the aim of enthesis regeneration.

1.5.3.1.1 Materials

Since the elastic moduli of enthesis tissues vary widely, there are a diverse range of ITE material options, each with their own advantages and disadvantages. They must fulfil scaffold function in structural and biological properties, either peculiar to a specific enthesis tissue region, or to host graded modulations over the entire enthesis.

Stiff materials commonly used for tissue engineering bone include calcium phosphate ceramics, such as hydroxyapatite (HA) and β -tricalcium phosphate (TCP), which show high osteointegration and biocompatibility, but are brittle and slow to degrade (Font Tellado, Balmayor and Van Griensven, 2015). Bioactive glasses, silicate- or borate-based glass-ceramics, have a similar mineral content to bone and can be controlled to degrade faster than HA and β -TCP, but are of lower strength (Fu *et al*, 2011). Polymers, natural and synthetic, can be used for both bone and for more compliant soft tissue engineering. Natural polymers include collagen, fibrin, agarose and alginate, with high biocompatibility and biodegradability but low tensile strength, and silk, which offers higher tensile strength and the ability to form micro/nanofibres, but requires pre-treatment to avoid immune rejection (Font Tellado, Balmayor and Van Griensven, 2015). Synthetic polymers, including polycaprolactone (PCL), polylactic acid (PLA), polyglycolic acid (PGA), polylactic-co-glycolic acid (PLGA) and polyethylene glycol diacrylate (PEGDA), are cheaper and can be fabricated into many shapes, sizes and fibres. Decellularised bone, tendon and ligament matrices preserve the material structure, mechanical properties and biochemical components of separate tissues (Boys *et al*, 2017), but are a predetermined shape and risk immune rejection on implantation from residual allograft or xenograft cells (Font Tellado, Balmayor and Van Griensven, 2015).

1.5.3.1.2 Fabrication Methods

The surface topography of the scaffold is important for cell-scaffold interaction, such as sensing mechanical environment and phenotype expression. Scaffold materials may be processed into a number of different formats to influence and optimise this interaction, such as hydrogels, films, sponges, porous scaffolds (e.g. foams), meshes and micro/nanofibers.

Hydrogel materials are a particularly important approach, with simple manufacture and cell addition processes, and allowing flexible manipulation. They are a hydrophilic

polymer network (natural or synthetic) with opportunities for gradients of multiple polymers (Armitage and Oyen, 2015). In their liquid or gel form they can be encapsulated with a homogenous spread of cells and molded into any shape on curing. As a bioink they are also compatible with the emerging technique of 3D bioprinting, allowing fine control of the size and shape of the cellular scaffold (O'Connell, Garcia and Amir, 2017) with the potential to print a multi-tissue interface (Latenser *et al*, 2018). Hydrogels however have poor mechanical properties, less suitable for engineering load-bearing tissues (Chan and Leong, 2008).

The nanofibrous scaffold is a further important configuration. The scaffold provides nanoscale cell-material interactions where cells are predisposed to adhere, proliferate, differentiate and function, whilst increasing porosity and surface area to volume ratio (Font Tellado, Balmayor and Van Griensven, 2015). The scaffold is typically produced by electrospinning a polymer solution into a meshwork of fibres, where fibre diameter, alignment and pore size can be controlled and graded (Armitage and Oyen, 2015). Multiple polymers can be integrated together, and ceramics or glass-ceramics incorporated to add a mineral gradient, distributing the most appropriate material properties along the scaffold to promote each enthesis tissue region. The optimal contemporary scaffold is likely to be a combination of different materials organised at nanoscale level with opposing gradients in fibre alignment and mineral content.

1.5.3.2 Cells

Cells are the natural engineers that develop the enthesis *in vivo*, and are similarly harnessed in tissue engineering to guide enthesis regeneration. They may be incorporated into a scaffold as a true 3D environment, such as encapsulation within a hydrogel, or seeded onto a scaffold, where they may migrate into the material or remain on surfaces as strictly 2D attachments. They mature scaffolds pre-implantation and integrate scaffolds post-implantation, responding to material and cell-cell interactions, substrate stiffness, mechanical conditioning and biochemical signalling (Boys *et al*, 2017).

The heterogenous cell population of the enthesis (see *Section 1.4.4*) dictates 2 main cell culture strategies: co-culture of differentiated cells, or variable differentiation of MSCs, with a combination of strategies possible. Active cells for ITE cell culture are

usually therefore differentiated tendon/ligament cells (fibroblasts) and bone cells (osteoblasts), or MSCs, from primary cells or immortalised cell lines. Since a central aim of enthesis generation is chondrogenesis, differentiated cartilage cells (chondrocytes) may also be employed. Terminally differentiated cells are already tissue specific, but inherently have less regenerative capacity (Font Tellado, Balmayor and Van Griensven, 2015). Bone cells in particular are often modelled through immortalised cell lines, where their fundamental biology may not be fully comparable to their *in vivo* counterparts (Calejo, Costa-Almeida and Gomes, 2019). MSCs are multipotent cells with the potential to differentiate into the range of musculoskeletal cells that contribute to the enthesis. They secrete bioactive molecules that provide a regenerative microenvironment (Rothrauff and Tuan, 2014) and, compared to fibroblasts, possess an increased proliferation rate and collagen deposition rate (Ge, Goh and Lee, 2005). Since an enthesis culture model based on MSCs requires only one cell source, compared to multiple for differentiated cells, MSCs may be the most appropriate cell choice for clinical application.

The majority of MSCs are sourced as bone marrow-derived mesenchymal stem cells (BMSCs), although adipose-derived mesenchymal stem cells (ASCs), tendon-derived mesenchymal stem cells (TDSCs) and ACL-derived MSCs may also be used. BMSCs respond to their biochemical and mechanical environment in a predictable manner (Smith *et al*, 2012), but ASCs can offer many advantages. Harvest of ASCs via lipoaspiration provides higher cell yield and lower associated pain than BMSCs (Liao and Chen, 2014), and at surgery adipose tissue is readily accessible and considered discard tissue. In culture, ASCs also have a higher proliferation capacity and lower senescence rate than BMSCs, with improved maintenance of phenotype (Zhu *et al*, 2008). Use of ASCs in enthesis tissue engineering is however currently at an early stage and requires further investigation, as although of multipotent character, ASCs can be less effective at cartilage and bone differentiation than BMSCs (Im, Shin and Lee, 2005). TDSCs and ACL-derived MSCs are minor region-specific multipotent cell populations of more recent discovery, as yet of limited ITE application due to a lack of reliable and practical isolation protocols (Rothrauff and Tuan, 2014; Calejo, Costa-Almeida and Gomes, 2019).

1.5.3.2.1 Co-Culture

Co-culture of different cell types allows heterogenous cell-cell contact and communication to provide closer *in vivo* models of multicellular tissues (Goers, Freemont and Polizzi, 2014). It exploits paracrine signalling as a method of tissue engineering, and since heterotypic cellular interaction is implicated in enthesis development (see *Section 1.4.7*), co-culture is a prominent ITE technique.

Cellular cross talk influences cell response, function and gene expression (Bicho *et al*, 2018), and can modify characteristics and ultimately the phenotype of either cell population. Co-culture of osteoblasts and chondrocytes lowers osteoblast-mediated mineralisation and chondrocyte-mediated GAGs deposition (Jiang, Nicoll and Lu, 2005). Similarly, co-culture of osteoblasts and fibroblasts dampens osteoblast mineralisation whilst inducing fibroblast-mediated mineralisation (Wang *et al*, 2007). Moreover, the same study demonstrated expression of fibrocartilage markers in cells at the osteoblast-fibroblast interface, showing the potential for co-culture cellular transdifferentiation and eventual fibrocartilage tissue formation.

Co-cultures demand particular attention to culture methodology and design. The technique may be achieved through multiple means, such as monolayers, scaffolds, transwell plates or scaffold-less methods, but different cell types ideally require different culture environments. A particular cell type's optimum growth medium, oxygen tension, material stiffness or fibre alignment may lead to undesirable phenotypic drift in the other cell type(s), not present in the primary cell line (Bicho *et al*, 2018). Such co-cultures can be difficult to control, and may be best suited to the regulated and potentially compartmentalised environment of a bioreactor (see *Section 1.5.3.4*).

1.5.3.2.2 Stem Cell Culture

MSCs are directed towards a specific lineage by biochemical and mechanical cues. Biological growth factors (see *Section 1.5.3.3.1*) and mechanical load (see *Section 1.5.3.3.2*) are important exogenous differentiation factors. Cell-material interactions inherent to the scaffold environment also affect cell phenotype. MSCs cultured on scaffolds of aligned fibres elongate and develop a fibrogenic phenotype, whereas cells in scaffold-less pellets remain rounded with a chondrogenic phenotype (Baker

et al, 2010), whilst stiff scaffolds promote osteogenic differentiation (Engler *et al*, 2006).

MSCs may be differentiated separately and co-cultured together, or variably differentiated by a gradient of biochemical or material factors. They may also be cultured with terminally differentiated cells, and undergo differentiation by intercellular signals and paracrine factors. MSCs cultured between fibroblasts and osteoblasts can induce differentiation to a fibrocartilage lineage, including a gradual mineral transition (Nayak *et al*, 2010; He *et al*, 2012).

Modelling the enthesis accurately via MSCs depends on reliable differentiation and confirmation of component enthesis cells, posing challenges to method and theory. Osteogenic and chondrogenic inductive media and protocols are well established, however attempting tenogenesis can be more diverse as an ideal medium formulation is not available (Calejo, Costa-Almeida and Gomes, 2019). Knowledge of the character of specific cells at the enthesis interface has also been lacking, limiting confirmation of successful interface generation, however recent proteomics (Rossetti *et al*, 2017) and transcriptomics (Kuntz *et al*, 2018) have elucidated 10 enthesis biomarkers as a benchmark for interface differentiation.

1.5.3.3 Stimulators

1.5.3.3.1 Growth Factors

Growth factors are proteins secreted by cells that act as signalling molecules to other cells, helping to develop, repair and maintain homeostasis of the enthesis tissues (Boys *et al*, 2017). They may be exogenously added to ITE models via culture media supplementation or incorporation into or onto scaffolds, differentiating stem cells, encouraging a particular cell phenotype, and depositing and maturing ECM. Growth factor selection therefore depends on the tissue phase of the enthesis, cell behaviour to induce and stage of cell differentiation. Local delivery and control of concentration are important to match the multi-tissue enthesis environment, ideally with compartmentalised culture (such as with a bioreactor, see *Section 1.5.3.4*), stratified scaffolds or in gradient design. A synergistic effect may also be achieved through multiple combinations of growth factors employed simultaneously or in sequence (Font Tellado, Balmayor and Van Griensven, 2015). The ideal enthesis model

therefore utilises spatiotemporal regulation of growth factor delivery, most likely influencing a single pool of multipotent cells, although the optimum constituents and distributions have not yet been established due to the complexity of the enthesis (Armitage and Oyen, 2015).

Use of particular growth factors *in vitro* is based on knowledge of enthesis development and separate tendon/ligament, cartilage and bone tissue engineering, as well as success in *in vivo* enthesis repair augmentation strategies (see *Section 1.4.8.2.1*). Promotion of cartilage generation presents a principal objective. Insulin-like growth factor(IGF)-1 and TGF- β both increase GAGs and collagen production in tissue engineered cartilage constructs, as well as increasing chondrogenic differentiation of MSCs on scaffolds (Park *et al*, 2010; Sundararaj *et al*, 2015; Boys *et al*, 2017). BMP-2 can also influence chondrogenic differentiation of MSCs at low doses, and at high doses promotes hypertrophic chondrocyte development with expression of collagen type X, ALP and osteocalcin (Demoor *et al*, 2014). The BMP family are however primarily the growth factors most important for bone formation and healing (Bessa, Casal and Reis, 2008) and are commonly employed for bone engineering as they induce mineralisation and stimulate osteoblast proliferation on scaffolds (Boys *et al*, 2017). Common tendon/ligament engineering growth factors include basic fibroblast growth factor (bFGF), platelet-derived growth factor (PDGF) and growth differentiation factors (GDFs) (Font Tellado, Balmayor and Van Griensven, 2015), with GDFs promoting tenogenesis of MSCs seeded on a 3D scaffold (James *et al*, 2011).

1.5.3.3.2 Mechanical Loading

Mechanical signals are fundamental to enthesis maturation (see *Section 1.4.7.3*). The association of compression with the presence of fibrocartilage in the native enthesis has already been highlighted in *Section 1.4.4*. This also translates to *in vitro*, where compression is associated with chondrogenesis, high uniaxial tensile stress with tenogenesis, and low tensile stress with osteogenesis, directing both MSCs and the behaviour of differentiated cells (Font Tellado, Balmayor and Van Griensven, 2015). For example, in MSCs, compressive force upregulates Sox9, type II collagen and aggrecan (Takahashi *et al*, 1998), cyclic tension of 10% strain upregulates fibroblastic markers such as Scx and type I collagen (Qiu *et al*, 2016) whilst cyclic 2.5% tensile strain upregulates osteogenic markers including osteocalcin and BMP-2 (Kearney *et*

al, 2010). Of particular note, Thomopoulos *et al* (2011) showed that cartilage markers could only be upregulated in MSCs when compression was combined with TGF- β , emphasising the synergistic effect of biochemical and mechanical factors. The fundamental mechanisms of how cells respond to mechanical forces is not clear, but a combination of growth factor and mechanical stimulation is likely to provide the best *in vitro* strategy for enthesis generation.

1.5.3.4 Bioreactors

Bioreactors provide an advanced design environment for *in vitro* 3D models that aims to better reproduce *in vivo* physiological conditions. They allow dynamic cell culture through control of microenvironmental parameters (e.g. temperature, pH, oxygen tension), aseptic parameters (e.g. feeding, waste removal, sampling) and automated processing (Salehi-Nik *et al*, 2013). Furthermore, bioreactors can be designed to apply mechanical load, exploited to mature tendon, ligament and cartilage constructs, although this has not yet been applied to enthesis ITE where simultaneous tension and compression on the distinct tissue components would be the ideal (Boys *et al*, 2017). Advanced dual- or multi-chamber bioreactors with separate compartments are however employed for other culture conditions, especially the delivery of tissue specific media or additive solutions, used particularly in osteochondral models (Malafaya and Reis, 2009; Bicho *et al*, 2018). Microfluidic techniques can also be applied to not only enable the distribution of separate solutions but also control precise physical factors such as shear stress via the perfusion rate, additionally influencing the micromechanical environment (Goldman *et al*, 2016).

Fine control of culture parameters dictates that bioreactors, and in particular microfluidic systems, are difficult to design and expensive. Nevertheless, production of large-scale, anatomically-matched, functional 3D engineered enthesis tissues are likely to require bioreactor designs. Multi-tissue constructs ideally demand specific culture conditions for each tissue element. In addition, without a vascular system, cells rely on diffusion for nutrition and waste removal, which may only be equally distributed throughout the tissues in larger dimensions through the use of bioreactors (Salehi-Nik *et al*, 2013).

1.5.4 3-Dimensional Multi-Tissue Strategies

To create replacement or representative *in vitro* models of the enthesis, tissue engineers use a combination of scaffolds, cells and stimulators to build multi-tissue 3D structures with a focus on the interfacial tissue transition. The ultimate aim is a tissue system of a spatially and phenotypically varied cell population with a graded mechanical structure (Smith *et al*, 2012). The 2 design paradigms to achieve this are stratified constructs or gradient constructs. Stratified constructs are more representative of the classical description of a sharp boundary between soft and hard tissues at the interface. However, more recent descriptions of a gradual mineral transition (see *Section 1.4.4.2.3*) are better matched to gradient designs, which can also address the gradient in ECM fibre alignment and mechanical properties. Yet stratified constructs may also develop a natural physiologically relevant composition gradient *in vivo* after host degradation (Patel *et al*, 2018). The following sections highlight a selection of the most relevant stratified and gradient ITE designs.

1.5.4.1 Stratified

Stratified designs use separate biomaterial strata usually with a variety of cell populations. Creation of an enthesis interface relies on cell-mediated metaplasia between distinct cell populations, or the interposition of a discrete interface-like layer. Commonly, homogenous scaffolds may be separately formed and joined together, however this does not mediate the transition between dissimilar materials, and inhibits cellular infiltration, nutrient transport and cell-cell signalling (Armitage and Oyen, 2015). The primary risk with such designs is delamination from interfacial stress concentrations. This has been countered in the tri-phasic scaffold design described by Mosher, Spalazzi and Lu (2015), based on regions with different forms of PLGA-based material sintered together, providing material similarity and structural continuity. Spalazzi *et al* (2006) originally employed this design to investigate enthesis formation by seeding fibroblasts on the soft tissue region (knitted sheets), osteoblasts on the bone region (microspheres with bioactive glass), with an intervening interface region of microspheres. Although matrix heterogeneity and cell migration across the interface occurred, it was only on the addition of chondrocytes to the interface region (Spalazzi *et al*, 2008) that a fibrocartilaginous region formed between soft tissue and bone regions. The effect of the neo-fibrocartilage on mechanical properties *in vivo* was not however clear.

For ligament, the ideal construct includes 2 interfacial regions as a bone-ligament-bone whole multi-tissue construct. With the interfacial regions engineered *in vitro*, the focus of implantation is the less challenging issue of osteointegration. Paxton *et al* (2009) created a bone-ligament-bone construct using fibroblasts seeded in fibrin hydrogel, representing ligament, stretched between 2 PEGDA anchors incorporated with HA, representing bone. The attachment longevity of the ligament-bone interface was later optimised by replacing the bone element with brushite anchors (Paxton, Grover and Baar, 2010). The greatest progress with enthesis formation in a whole multi-tissue construct has been made by Ma *et al* (2009 and 2012), fashioning separate scaffold-less ligament and bone cultures from differentiated BMSCs and co-culturing them as bone-ligament-bone constructs. The constructs remodelled *in vivo* and did not fail under physiological tensile loading, as a replacement rat MCL and sheep ACL. Furthermore, a fibrocartilaginous transition with aligned cells was attained (Ma *et al*, 2012). Such constructs are complex and time-consuming to manufacture, however Mahalingam *et al* (2015) have demonstrated that they remain viable after frozen storage and thawing, showing their versatility and substantial clinical potential.

1.5.4.2 Gradient

Gradient designs generally employ a single population of multipotent cells, influenced by biochemical and mechanical stimuli to promote local cell differentiation. Gradients are typically achieved by materials processing, or creating mineral and growth factor gradients. Microstructure gradients can be created by directional freezing and salt leaching to cause fibre orientation and pore size gradients, respectively, in silk fibroin, affecting ASC differentiation and proliferation (Font Tellado *et al*, 2017). Hybrid materials such as co-polymers are particularly useful for mineral gradient design, especially exploiting polymer-ceramic/bioglass composites. Liu *et al* (2014) used a gradient mineral coating on a PLGA-based nanofiber scaffold to induce graded osteogenesis of ASCs, and similarly Samavedi *et al* (2012) manufactured a HA particle gradient on a co-polymer electrospun scaffold to produce graded osteogenesis of BMSCs. Phillips *et al* (2008) created a concentration gradient of osteogenic transcription factors on collagen scaffolds, causing osteoblastic transdifferentiation of fibroblasts and a gradient of mineralised matrix which was maintained *in vivo*. Although a fibrocartilaginous region was not formed, graded mechanical properties were achieved with a single cell type. In added complexity, a reverse gradient of increasing BMP-2 and decreasing IGF-I was engineered by Wang

et al (2009) using microspheres on silk porous scaffolds. The contrasting growth factor gradients directed BMSCs to generate a gradient increase in mineral, GAGs and collagen types II and X, resembling the uncalcified to calcified fibrocartilage transition. Although potentially the most representative enthesis constructs, translating microscale and nanoscale gradients to relevant *in vivo* scales presents a significant challenge.

1.5.5 Future Developments

ITE is challenging, due to the critical interrelationships between structure, function and biomechanics. The enthesis is a complex transitional design, and a complete understanding of how tissue boundaries and gradients in cell phenotype and ECM are developed and maintained has not been fully realised. Furthermore, although studies on single component tissues or cartilage development, such as growth plate function, are insightful, it is likely that the cell type at the enthesis interface is phenotypically distinct from tendon/ligament, cartilage, and bone cells (Lu and Thomopoulos, 2013). Until specific molecular and cellular biophysical mechanisms in response to endogenous and exogenous factors at the enthesis are entirely known, ITE strategies remain experimental.

The breadth of ITE strategies to model the enthesis demonstrates that the optimal design has not yet been achieved. However much progress has been made, particularly in the development of materials processing and establishing gradient properties. A combination of leading cell, scaffold, growth factor and mechanical stimuli techniques is likely to represent the ideal current theoretical design (**Figure 1.8**). Incorporating nanoscale and high resolution 3D bioprinting techniques for precision control of scaffold structure and gradient would provide an optimum cell environment. Next generation 'smart biomaterials' are emerging with tuneable chemical, physical and biological properties, which may allow spatially or temporally regulated biochemical delivery (Font Tellado, Balmayor and Van Griensven, 2015). Advanced biological techniques such as gene therapy, including clustered regularly interspaced short palindromic repeats (CRISPR) gene editing, and induced pluripotent stem cells (iPSCs) could also facilitate spatially guided local cell differentiation for phenotype gradients (Boys *et al*, 2017). A bioreactor would provide optimal delivery of biochemical and mechanical cues, and with optimal engineering

parameters experimental time could be reduced, and construct functionality enhanced. Such technologies are expensive, and contrasting strategies exploit the body as a bioreactor to mature the construct for augmentation of healing, as 'facilitated endogenous repair' (Rothrauff and Tuan, 2014). This approach aims to develop optimal implantable and degradable scaffolds, with a recent example 3D bioprinted scaffold sleeves seeded with MSCs that provide a fibrocartilage transition for *in vivo* enthesis healing (Park *et al*, 2018).

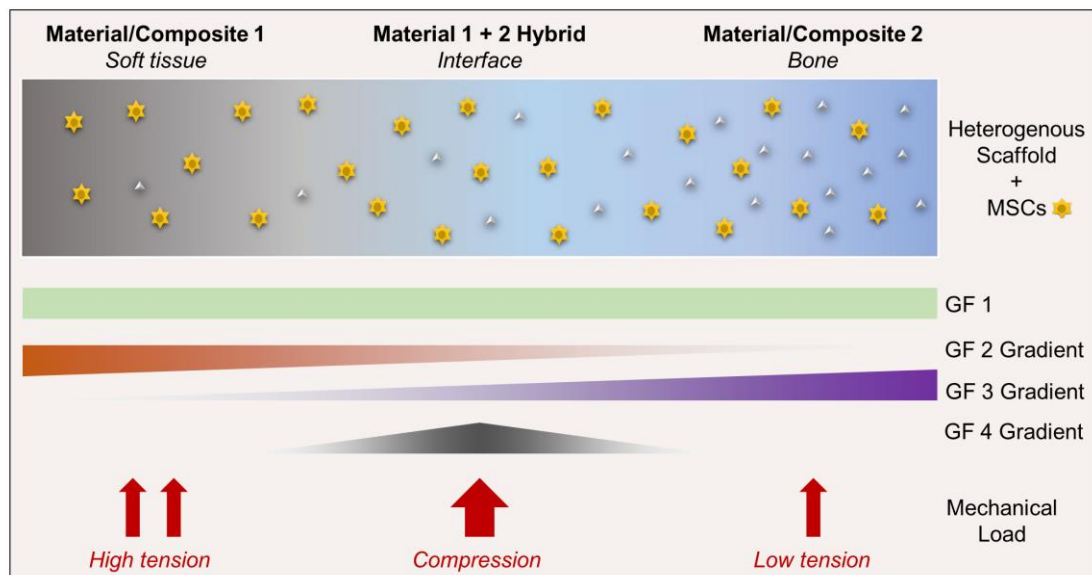


Figure 1.8 | Optimum Interfacial Tissue Engineering Gradient Approach

Illustration of theoretical combined approach to generate an interfacial tissue engineered model of *soft tissue*, *interface* and *bone*, with gradient properties. A continuous nanoscale scaffold of hybrid materials with mineral gradient is seeded with multipotent *mesenchymal stem cells* (MSCs). A gradient of differentiated cell phenotype and matured matrix is achieved through *cell-scaffold interactions*, and spatiotemporal *growth factor* (GF) and *mechanical stimuli* in a bioreactor system. Adapted from Font Tellado, Balmayor and Van Griensven, (2015).

1.5.5.1 Anatomy in Tissue Engineering

The complexity of ITE encourages a multidisciplinary approach. Success will likely be achieved through collaboration of a broad range of specialists, including biomedical scientists, mechanical engineers, material scientists and clinicians. A further important, but less well recognised, collaborator is the anatomist. Anatomists relate structure to function, inherent to the foundations of tissue engineering, which aims to develop new biological structures for the restoration of function. Indeed, tissue engineering has been described as a new phase of anatomical research (Mironov and Markwald, 2001). Researchers need to consider the design of not only an imitating system, but the native size and shape of a model to function as the body originally

created. Macroscopic structure-function relationships are generally overlooked when considering scaling up models for clinical relevance. Furthermore, regional anatomical knowledge is crucial to successful *in vivo* integration and interaction with surrounding structures. ITE models are inherently connections, and do not function in isolation *in vivo*. Anatomists can add an appreciation of musculoskeletal system-wide relationships that may close the translational gap between *in vitro* studies and clinical adoption.

1.5.6 Summary

Key points:

- *ITE aims to recreate the interface between 2 distinct tissues;*
- *3D ITE models can be implanted to replace or augment healing of entheses;*
- *Key constituents of ITE models are scaffolds, cells and stimulators;*
- *Co-culture is an important ITE methodology;*
- *Multi-tissue model design uses a stratified or gradient approach;*
- *Anatomy is a crucial, but often neglected, discipline in tissue engineering.*

1.6 Project Rationale

FDP tendon avulsion is a common injury with considerable patient morbidity. Current repair techniques are suboptimal due to surgical complications and low healing strength from lack of enthesis regeneration. ITE provides an opportunity to develop a specific FDP tendon-DP bone *in vitro* model system that may be employed to study this particular enthesis, used as a replica model to practise, improve or discover novel repair techniques, or eventually be implanted to replace or augment healing of the damaged interface. Such a model can also bring cost, availability and ethical benefits over the use of human and animal tissue. Crucially, to be relevant and translatable to clinical practice, the model must be anatomically matched to the native tendon-bone insertion.

1.7 Aims

The overall aim was to establish a tendon-bone *in vitro* tissue engineered model system that replicated the FDP-DP insertion, forming the basis for a clinically applicable product for the treatment of FDP avulsion injury.

The objectives were to:

- 1) Examine and evaluate the native anatomy of the FDP-DP enthesis,
 - a) morphologically (macroscopically),
 - b) histologically (microscopically);

- 2) Develop and characterise a relevant, anatomically matched, 3D *in vitro* model,
 - a) based on a multi-tissue stratified approach,
 - b) integrating novel design and co-culture methods.

CHAPTER 2

MORPHOLOGY OF THE FLEXOR DIGITORUM PROFUNDUS INSERTION

2.1 Chapter Overview

This chapter investigates the gross morphology of the human flexor digitorum profundus (FDP) insertion through dissection and measurement analysis of cadaveric tissue. The key components of the insertional anatomy – the tendon-bone interface, tendon, and bone – are sequentially examined with a particular focus on the size influence of different genders and fingers. The results are assimilated to produce a design guide for recreating the component elements in an *in vitro* tissue engineered model that is relevant to surgical repair of FDP avulsion injury.

2.2 Introduction

The fundamental concept of this project was ‘human tissue engineered anatomy’ as the basis for clinically-significant advancement (Mironov and Markwald, 2001). The principle initial phase of this design approach was a thorough understanding of the morphology of the native tissues, before the development of the matching tissue engineered components. The observation and investigation of real human tissue was therefore an essential and substantial component of the work, standing as a distinguishing feature in the cellular and materials focused discipline of tissue engineering. The human body demonstrates the principle of form following function, hence to achieve a functional (‘clinical’) tissue engineered model, the form of the human FDP insertion was closely studied. Incorporating the analysis of human tissue into the engineering design consequently aimed to expedite the translational clinical potential of the model.

The prototype of a scaffold-based *in vitro* model of the soft-hard tissue interface for this project was already previously established by Paxton, Grover and Baar (2010). The model is based on fibroblast-seeded fibrin hydrogel contracting between anchor points (see *Chapter 4, Figure 4.2*), with size dimensions of 4x4x3mm for the 3D trapezoidal bony anchor component and <2mm width for the formed soft tissue analogue (Paxton *et al*, 2012a) (see *Chapter 4, Figure 4.1b*). These basic hard and soft tissue components required modification to a model replicating the gross anatomy of the FDP tendon-distal phalanx (DP) bone insertion. As well as size dimensions, an appreciation of 3D shape was essential. Although tendon dimensions are commonly

clinically explored by imaging such as computed tomography (CT), magnetic resonance imaging (MRI) and ultrasound (Hayes *et al*, 2019), single live images are limited to snapshot 2D information. Furthermore, validation of imaging techniques for dimensional measurements is made in comparison to 'control' measurements made on the tendon itself *in vivo* (intra-operative) (Yasumoto *et al*, 2006; Chang, Seong and Kim, 2009; Galanis *et al*, 2016) or *ex vivo* (cadaveric) (Noguchi *et al*, 2002; Alghamdi *et al*, 2019). The opportunity to explore human tissue by dissection therefore provided an optimum method to both acquire a variety of morphological measurements and observe 3D structural relationships.

Literature on the detailed anatomy of the FDP insertion is sparse. Observational studies of in-depth regional anatomy are rarely the contemporary focus of leading anatomical journals. More historic papers such as Wilkinson's '*The insertions of the flexores pollicis longus et digitorum profundus*' (1953) provide perceptive descriptions connecting the gross form and function of particular structural elements that are often absent in general anatomical texts. Specialist surgical texts provide a high level of regional anatomy detail, but naturally focus on clinical relationships over comprehensive anatomical description. Insights into certain structures related to the FDP insertion can be gleaned from *in vivo* and *ex vivo* studies of surgical technique, such as the close relationship of the distal interphalangeal joint (DIPJ) volar plate (Al-Qattan, 2016a) or the shape and dimensions of the DP bone at insertion (Jain *et al*, 2011; Samson and Gupta, 2018; Bond, Rust and Boland, 2019). Recent studies on the specific insertional anatomy of the FDP tendon are however limited to 2 papers: vascular anatomy (Leversedge *et al*, 2002) and clinical anatomy (Chepla, Goitz and Fowler, 2015). The approach to the morphological investigations of the FDP insertion by Chepla, Goitz and Fowler (2015) proved the stimulus to the first stage of this project.

This chapter is primarily a collection of exploratory studies on the tendon-bone interface, tendon and bone components of the human FDP-DP insertion. In any single person there are 8 FDP tendon insertions to consider. A single tissue engineered replica, although an acceptable general or pilot design, is unlikely to be of use in a clinical setting, for example in selecting an appropriately-sized composite graft to aid in tendon-bone repair. 8 specific tissue engineered models, although seemingly of optimal relevance, are not a pragmatic use of resources for an anatomical region of limited size range, and do not take into account the natural variation of finger sizes in

a population. Certain factors may have a greater influence on size dimensions than others, potentially targeting where size modifications may be necessary. Those factors pre-selected as most important to explore were gender, finger and side, based on expectations of influence on size variables. This formed hypotheses-driven investigations and analysis regarding whether a particular (1) gender, (2) finger, or (3) side had a significant effect on size dimensions. The most influential features could then direct the most practical, resourceful and relevant designs.

2.3 Aim and Objectives

The aim of the chapter was to obtain gross morphological information on the FDP tendon-DP bone insertion, relevant to the size and shape design of a clinically-applicable *in vitro* tendon-bone tissue engineered model.

The objectives were to measure and analyse:

- 1) The FDP-DP tendon-bone interface dimensions;
- 2) The position of the tendon insertion on the bone;
- 3) The approaching FDP tendon dimensions;
- 4) The receiving DP bone dimensions.

2.4 Materials and Methods

2.4.1 Cadaveric Specimens

Human cadaveric tissue was obtained from The University of Edinburgh Medical School body donation programme, regulated by The Anatomy Act (1984) and The Human Tissue (Scotland) Act (2006). All donors had consented to photography before death. 12 body donation specimens were used in the project, detailed in **Table 2.1**. Due to availability restrictions, a sample of convenience was necessary; however, effort was made to balance genders and maximise samples for each investigation. Previous operative details, comorbid conditions not contributing to death, and hand dominance were unknown. No specimens displayed gross external or internal pathology warranting sample exclusion. Fresh frozen cadaveric fingers were

detached by technical staff in a transverse plane through the mid proximal phalanx (PP) and thawed overnight at 4°C before dissection.

Table 2.1 | Demographics and Utilisation of Specimens

All investigations are described in this chapter except for Histology (*Chapter 3*).

Human Cadaveric Tissue Details							
Specimen	Demographics			Investigations			
	Age	Gender	Occupation	Tendon-Bone Interface	Tendon Width	Bone Depth	Histology
1	93	Female	Unknown	✓		✓	
2	95	Male	General Practitioner	✓		✓	
3	86	Female	Secretary	✓	✓	✓	
4	65	Female	Physiotherapist	✓	✓	✓	
5	66	Male	Airline Pilot	✓	✓	✓	
6	88	Male	Company Director	✓	✓	✓	
7	91	Female	School Teacher			✓	✓
8	73	Female	Book Keeper			✓	✓
9	76	Female	Secretary		✓	✓	✓
10	90	Male	Secretary		✓	✓	✓
11	73	Male	School Teacher		✓	✓	✓
12	73	Male	Company Director		✓	✓	✓

2.4.2 General Dissection

All cadaveric tissue investigations began with the same finger dissection methodology to expose the DP and attached FDP. Dissections were performed with standard dissection tools (Fine Science Tools, Cambridge, UK) with number 15 carbon steel blades (Swann-Morton, Sheffield, UK), under x3 loupe magnification (UKloupes, Bristol, UK), at room temperature, using 0.9% saline (Baxter Healthcare Ltd, Norfolk, UK) for tissue moistening throughout. The common dissection steps are described in **Figure 2.1**.

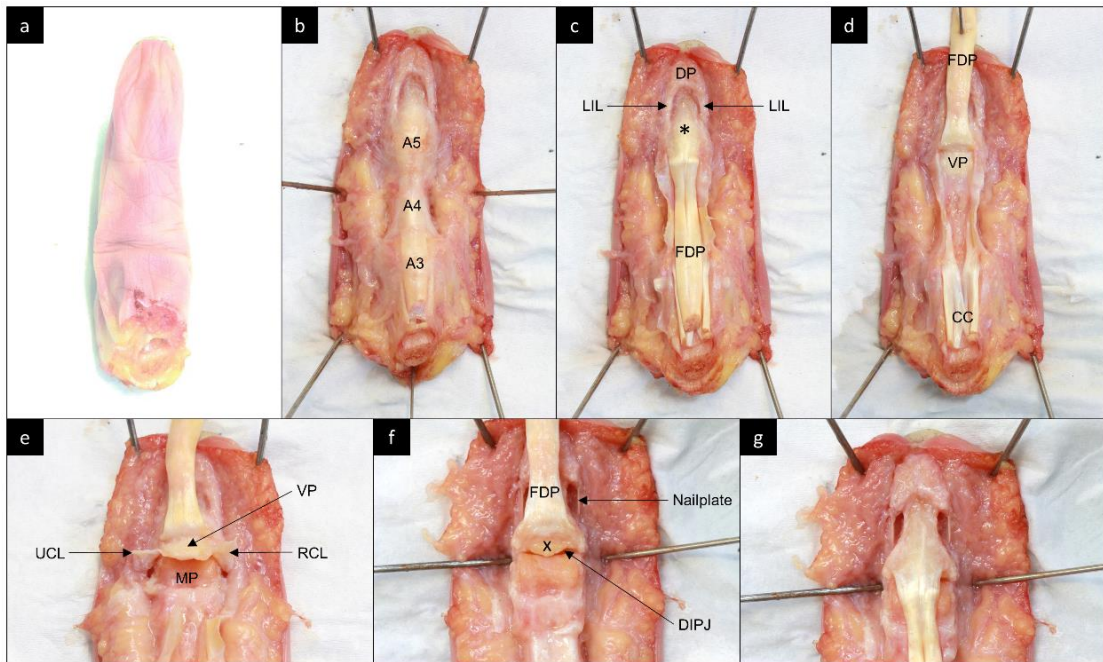


Figure 2.1 | General Dissection Methodology

a) Defrosted fresh frozen cadaveric finger, flexor view. **b)** Exposure of the fibrous flexor sheath after midline flexor incision, dissecting in plane between the subcutaneous tissue and flexor sheath. The A3 and A5 annular pulleys overlie the proximal interphalangeal joint (PIPJ) and distal interphalangeal joint (DIPJ), respectively, while A4 overlies the middle phalanx (MP). **c)** Midline opening of the fibrous flexor sheath exposing the FDP tendon. * indicates the area of FDP insertion on the distal phalanx (DP). Note a lateral interosseous ligament (LIL) on each side of the DP. **d)** The FDP is dissected from its 2 vincula and carefully flipped over about its insertion point, exposing the DIPJ volar plate (VP) and Camper's Chiasm (CC) of the flexor digitorum superficialis. Blunt dissection is employed when separating the FDP from the VP to avoid disruption of the FDP insertion. **e)** Opening of the DIPJ by dissecting the VP, ulnar collateral ligament (UCL) and radial collateral ligament (RCL) initially from their proximal attachments on the MP. **f)** Complete excision of the VP, UCL and RCL exposing the DIPJ. x indicates the excised distal attachment of the VP, with particular care to avoid sharp dissection into the FDP insertion. The LILs on the DP have also been excised, exposing the nailplate. **g)** With its insertion now exposed, the FDP is replaced in preparation for further specific investigation techniques. Female right ring finger.

2.4.3 Tendon-Bone Interface

48 fingers from 6 cadavers (3 male, 3 female; mean age 82.2, range 65-95) (**Table 2.1**) were prepared to investigate the FDP-DP tendon-bone interface morphology (shape, size, position).

2.4.3.1 Footprint Generation

An inking methodology adapted from Chepla, Goitz and Fowler (2015) was employed to visualise the FDP insertion as a footprint, from which accurate digital measurements could then be taken. After the initial dissection steps (**Figure 2.1**), the entire DP with attached FDP tendon was isolated from surrounding tissues and

excised. The tendon-bone sample was next immersed in methylene blue 1% w/v aqueous solution (Scientific Laboratory Supplies Ltd, Coatbridge, UK) for 10 seconds, with excess ink being briefly blotted away as the sample was removed. The FDP was then directly dissected away at the tendon-bone interface with a fresh number 15 blade, revealing the FDP footprint (**Figure 2.2**).

Initial samples trialed a varying length of methylene blue immersion times to establish optimal footprint clarity. 5 minutes (n=6), 45 minutes (n=3) and 90 minutes (n=1) were tested before adopting the standardised 10 second methodology. The 90 minute immersion noticeably overstained and reduced the footprint and was excluded from sample analysis. Samples immersed for 5 and 45 minutes however produced footprints without gross discernible difference to the 10 second immersion, and were included. Sample size for tendon-bone interface analysis therefore totalled 47 FDP footprints and DPs.

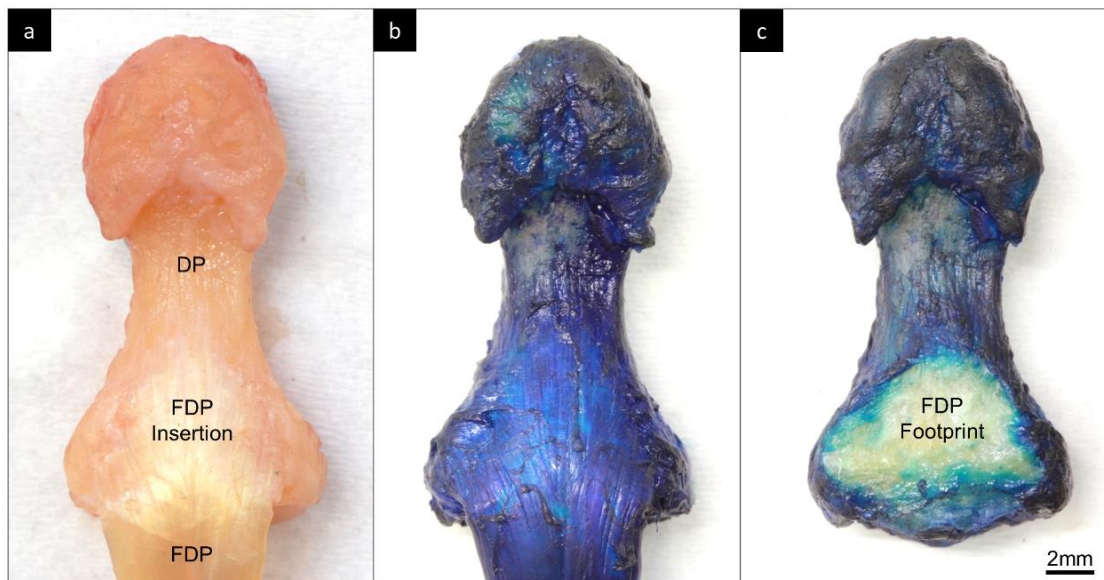


Figure 2.2 | FDP Footprint Generation

a) Excised distal phalanx (*DP*) bone with attached *FDP* tendon (flexor surface) from **Figure 2.1**, after disarticulation at the DIPJ, and detachment from surrounding extensor tendon, nailplate, and remaining soft tissues. **b)** Tendon-bone sample after 10 second methylene blue immersion. **c)** DP after excision of the FDP at the tendon-bone interface, leaving the *FDP footprint*. This final flexor view image is used for digital software processing and measurement. Scale bar 2mm throughout; female right ring finger.

2.4.3.2 Image Acquisition

After approximately 1 hour to dry the ink at room temperature, a digital photograph of the flexor surface of the entire stained DP with unstained FDP footprint was taken

using a macro lens on a mounted Canon EOS 60D camera (Tokyo, Japan). The FDP footprint surface was presented parallel to the camera lens, with camera settings remaining the same for all samples to achieve maximum light and focus on the FDP footprint region.

2.4.3.3 Image Analysis

2D measurements were obtained from the digital photographs using ImageJ software (National Institutes of Health, Bethesda, USA). Firstly, the FDP footprint perimeter was manually outlined at the demarcation of peripheral colour change, at the point where variation from the standard dark blue of the methylene blue was first perceived. A software-generated bounding box was then applied to the perimeter, allowing creation of a binary black 'mask' FDP footprint shape and perimeter box on a white background, from which measurements could be clearly made. Surface area, height, widths, internal angles and distances of the shape from the base of the distal phalanx (DIPJ) were assessed, described in **Figure 2.3**. A similar approach and comparable measurements of surface area, height and width were also taken for the DP itself (**Figure 2.4**).

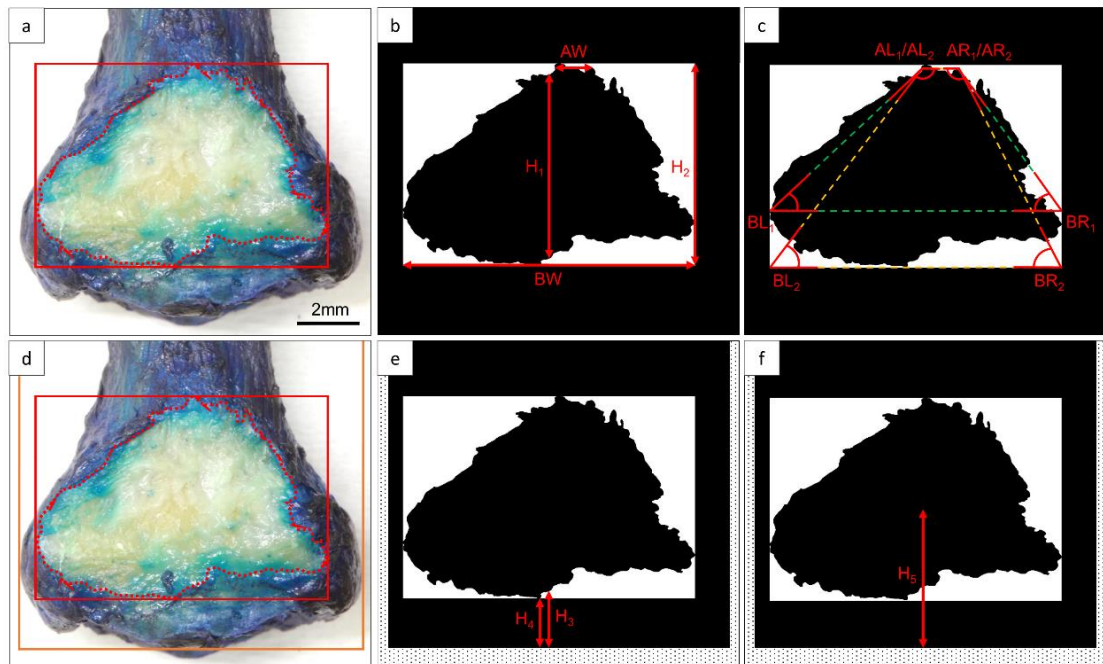


Figure 2.3 | FDP Footprint Measurements

a) Mapped FDP footprint perimeter (*dotted red line*) with FDP footprint bounding box (*full red line*), creating binary mask image of the trapezoidal FDP footprint shape within perimeter box [(b) and (c)]. Surface area is quantified from the area inside the footprint perimeter. **b)** General FDP footprint measurements. Base width (BW) is taken as the widest measurement (i.e. width of perimeter box), and apex width (AW) as the highest point at which the sides turn horizontally towards the midline. Height is calculated from a mean of height at mid-width of the perimeter box (H_1) and maximum height (H_2 , i.e. height of perimeter box). **c)** 4 internal angles (apex left, AL ; apex right, AR ; base left, BL ; base right BR) are calculated as a mean of 2 trapezoids (subscripts 1 and 2). The base of the trapezoids are defined by the perpendicular at the highest point of left or right perimeter box intersection (subscript 1, *broken green line*) or at the lowest point of the footprint (subscript 2, *broken gold line*). Apices are positioned the same for both trapezoids. **d)** DP bounding box (*full orange line*) generated after mapping the entire DP perimeter (not shown, see **Figure 2.4**), allowing subtraction of the external area [*dotted pattern*, (e) and (f)] and clear delineation of the lowest point of the DP base (i.e. DIPJ line). **e)** FDP base to DIPJ measurement, calculated as a mean of the height between the DIPJ line (DP perimeter box at lowest point of DP) and the FDP base at the mid-width of the FDP footprint perimeter box (H_3) and lowest point of FDP base (H_4 , i.e. FDP footprint perimeter box). **f)** Centroid to DIPJ measurement (H_5). The centroid is the geometric centre of the FDP footprint bounding box as determined by the ImageJ software. Where the lowest point of the DP (DIPJ line) does not coincide with the mid-width of the FDP footprint perimeter box, all measurements in (e) and (f) are repeated to the DP base (DIPJ line) at the FDP footprint perimeter box mid-width using an underlying original photo, and a mean of the 2 measurements taken. Scale bar 2mm throughout; female right ring finger.

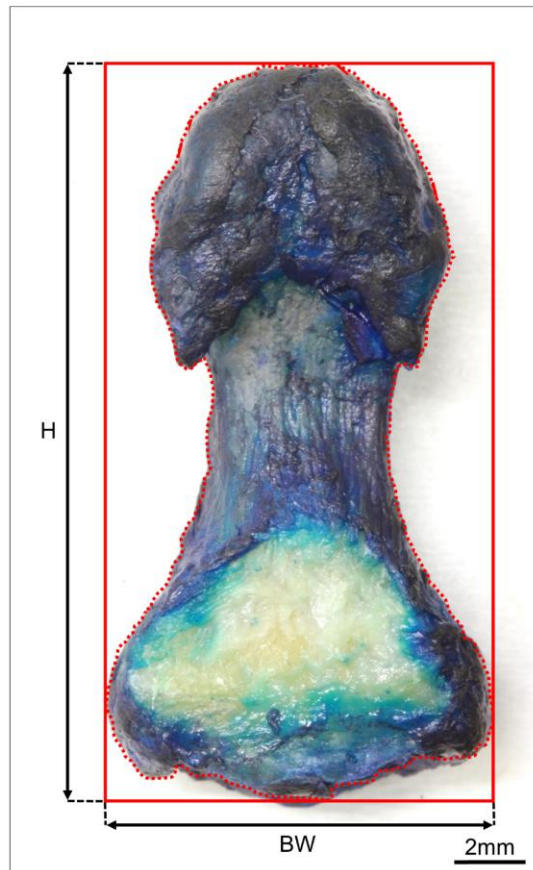


Figure 2.4 | Distal Phalanx Measurements

Flexor surface view of the entire DP. Surface area is quantified from outlining the DP perimeter (*dotted red line*). Base width (*BW*) and height (*H*) are determined by the dimensions of the bounding box (*full red line*). Female right ring finger.

2.4.4 Tendon Width

The width of the approaching FDP tendon to its DP insertion was evaluated in 64 fingers from 8 cadavers (5 male, 3 female; mean age 77.1, range 65-90) (**Table 2.1**).

2.4.4.1 Sample Preparation

Cadaveric specimens underwent the general dissection methodology (*Section 2.4.2*) to the point of first full exposure of the FDP tendon (**Figure 2.1c**).

2.4.4.2 Image Acquisition

A digital photograph was taken of the undisturbed distal tendon and its DP attachment, with a pin placed to indicate the base of the FDP insertion. Tendons were

photographed through a macro lens on a mounted Canon EOS 60D camera, using the same approach and camera settings throughout as adopted in *Section 2.4.3.2*.

2.4.4.3 Image Analysis

ImageJ software was employed to measure the 2D width of the FDP tendon from the digital photographs. Width measurements were made perpendicular to the median longitudinal sulcus in the tendon at 3mm intervals from the FDP insertion base (**Figure 2.5**). Measurements were performed up to and including 12mm proximal from the insertion base. 12mm represented the standard distance between the 2 points anchoring the soft tissue analogue in the prototype *in vitro* tissue engineered model (Paxton *et al*, 2012a), and assessment of intervening width variation was deemed important for both native tendon morphological description and future tendon engineering experiments (see *Chapter 4, Section 4.4.3.6*).

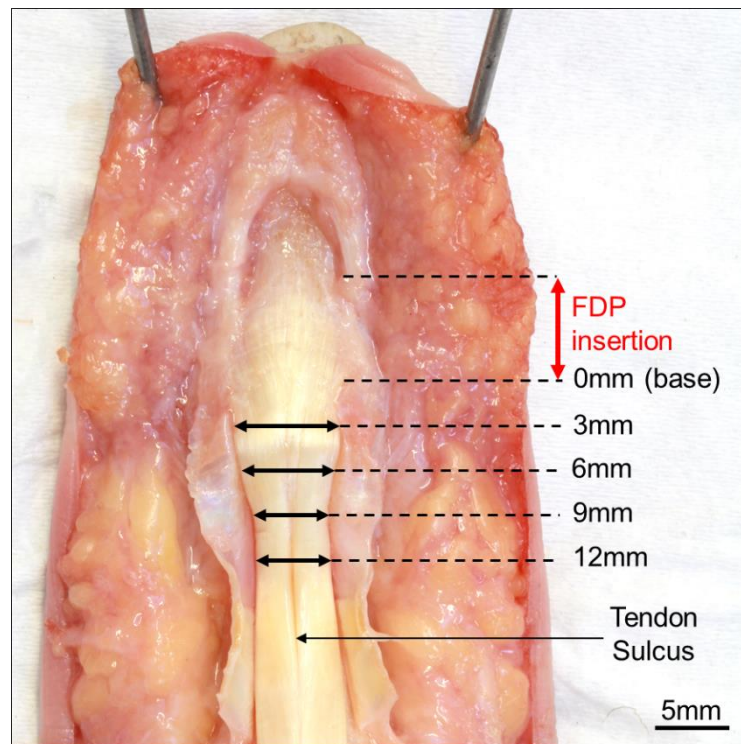


Figure 2.5 | FDP Tendon Width Measurements

Flexor surface view of the FDP attachment to the DP, after opening of the flexor sheath (**Figure 2.1c**). 4 measurements are made, at 3mm, 6mm, 9mm and 12mm proximal to the FDP insertion base, perpendicular to the median longitudinal tendon sulcus. Female right ring finger.

2.4.5 Bone Depth

The depth of the DP bone at the FDP insertion was investigated in 96 fingers from 12 cadavers (6 male, 6 female; mean age 80.8, range 65-90) (**Table 2.1**).

2.4.5.1 Sample Preparation

The entire DP and attached FDP tendon was excised from the cadaveric specimen (**Figure 2.2a**) after completing the general dissection methodology (*Section 2.4.2*) (**Figure 2.1**). Measurements were taken immediately before the sample was inked for FDP insertion footprint generation (*Section 2.4.3.1*) or before preparation for histology (*Chapter 3*).

2.4.5.2 Measurements

The anterior-posterior depth of the DP bone was measured at the proximal and distal insertion points of the FDP (**Figure 2.6**), primarily to inform depth design of the future bone anchor. A digital Vernier caliper (Draper Tools, Eastleigh, UK), with an accuracy of 0.01mm, was selected to gauge the measurements as there was concern that a true lateral photographic image for ImageJ application could not be reliably achieved. The caliper was gently clamped astride the bone perpendicular to the desired insertion point, viewed under x3 loupe magnification (UKloupes), and the reading recorded.

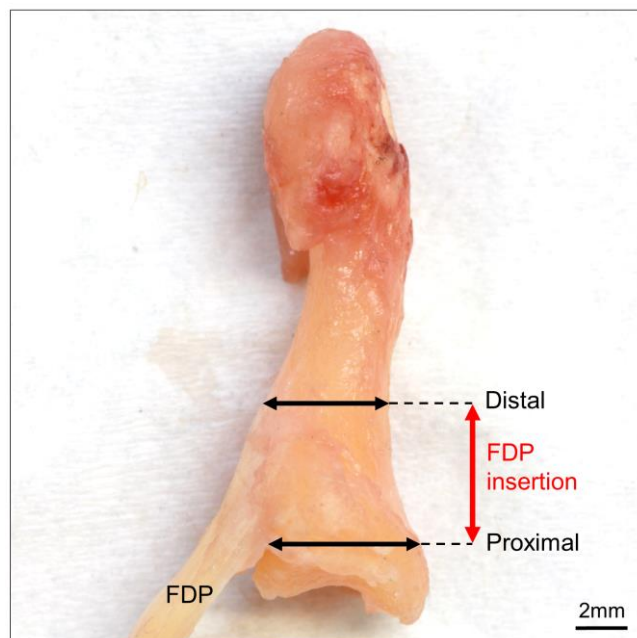


Figure 2.6 | Distal Phalanx Bone Depth Measurements
Lateral view of isolated DP bone with attached FDP tendon. Depth measurements are taken perpendicular to the proximal and distal points of FDP insertion. Female right ring finger.

2.4.6 Inter-Observer Reliability

Measurement analyses of the tendon-bone interface (FDP footprint and DP measurements) and tendon width were repeated once by a new observer (different observers for each investigation set) to assess the reliability of the measurement methodologies. 2nd observers were trained in the methodology by the 1st observer, then undertook the same full set of measurements on the original unprocessed and unannotated digital photographs using the same software on different workstations. Agreement and reliability between the 1st and 2nd observers was determined by the intraclass correlation coefficient (ICC) of single measures of absolute agreement, and by Cronbach's alpha, using SPSS version 24 (IBM, Armonk, USA) statistical package.

2.4.7 Data Analysis

Measurement data was collected and tabulated in Excel 2016 (Microsoft, Redmond, USA) and graphed in GraphPad Prism version 8 (GraphPad Software Inc, San Diego, USA). Linear mixed effects models were employed in SPSS version 24 (IBM) to account for the non-independence of fingers sampled and measured from the same cadaveric specimen, generating estimated marginal means (**Table 2.2**). Models were explorative, and, for specific hypothesis testing of the effects of factor levels for fingers, genders, sides and sizing categories, multiple pairwise comparisons were performed with an alpha level of 0.05, and a Bonferroni post-hoc correction applied. Output from models was accepted without further correction for running multiple models. Unless otherwise stated, data in the chapter is presented as estimated marginal (EM) means \pm standard error of the mean (\pm SEM), with graphical error bars also indicating \pm SEM, and the level of any statistical significance highlighted as * $p < 0.05$, ** $p < 0.01$, *** $p < 0.001$.

Table 2.2 | Build and Application of Linear Mixed Effects Model Series

Multiple explorative SPSS linear mixed effects models were utilised to adjust for the non-independence relationship of individual fingers measured from the same specimen. *Specimen* (identifier) was therefore always a random effect in the model series. Fixed factors included *gender*, *finger*, *individual finger* (gender specified) and *size category* (gender and finger specified). *Side* was excluded as a fixed factor to simplify models, except where the effect of side was specifically investigated (*models 3, 4 and 5*). Statistical output generated estimated marginal (*EM*) means and standard error of estimated marginal means (*SEM*), used as the reported means and for multiple pairwise comparisons in figures and tables throughout the chapter. Factors are tested as main effects, and a type III sum of squares model is applied to fixed effects. Models assume normal data distributions, checked graphically as Q-Q normal probability plots of observed versus expected residual values from each model.

Linear Mixed Effects Models					
Factor Analysis	Effect of Factor		Application		
	Fixed	Random	EM Means; SEM	Tables	Figures
Model 1					
Genders (Combined Fingers)	Gender	Specimen	All (Collective)	2.3	
			Male (All)	2.4	
Fingers (Combined Genders)	Finger	Specimen	Female (All)	2.5	
			Index (All)	2.6	2.8a,b
			Middle (All)	2.7	2.9a,b
			Ring (All)	2.8	2.10a,b
			Little (All)	2.9	2.11a,b
			Universal	2.10	
				2.12	
	2.14				
	2.17				
Model 2					
Individual Fingers	Individual Finger	Specimen	Male Index	2.3	
			Male Middle	2.4	2.8c
			Male Ring	2.5	2.9c
			Male Little	2.6	2.10c
			Female Index	2.7	2.11c
			Female Middle	2.8	2.13
			Female Ring	2.9	2.14
			Female Little	2.10	2.15
				2.12	2.16
				2.14	
Model 3a					
FDP Footprint Base Angle Side (Individual Fingers)	Individual Finger Base Angle Side	Specimen	Base Angle Left Base Angle Right	/	2.12
Model 3b					
FDP Footprint Apex Angle Side (Individual Fingers)	Individual Finger Apex Angle Side	Specimen	Apex Angle Left Apex Angle Right	/	2.12
Model 4a					
Male Side (Combined Fingers)	Finger Side	Specimen	Male Left Male Right	2.15	/
Model 4b					
Female Side (Combined Fingers)	Finger Side	Specimen	Female Left Female Right	2.15	/
Model 5a					
Index Side (Combined Genders)	Gender Side	Specimen	Index Left Index Right	2.15	/
Model 5b					
Middle Side (Combined Genders)	Gender Side	Specimen	Middle Left Middle Right	2.15	/
Model 5c					
Ring Side (Combined Genders)	Gender Side	Specimen	Ring Left Ring Right	2.15	/
Model 5d					
Little Side (Combined Genders)	Gender Side	Specimen	Little Left Little Right	2.15	/
Model 6					
Size Categories	Size Category	Specimen	Large Medium Small	2.16 2.17	2.17

2.5 Results

2.5.1 Tendon-Bone Interface

The FDP insertion footprints were roughly trapezoidal in shape, and almost triangular. A flat, wide base narrowed distally to a more variable flat or rounded apex (**Figure 2.7**). This primary finding determined the range of measurement dimensions, treating the shape as a trapezoid and thence including assessment of the shape's apex and internal angles.

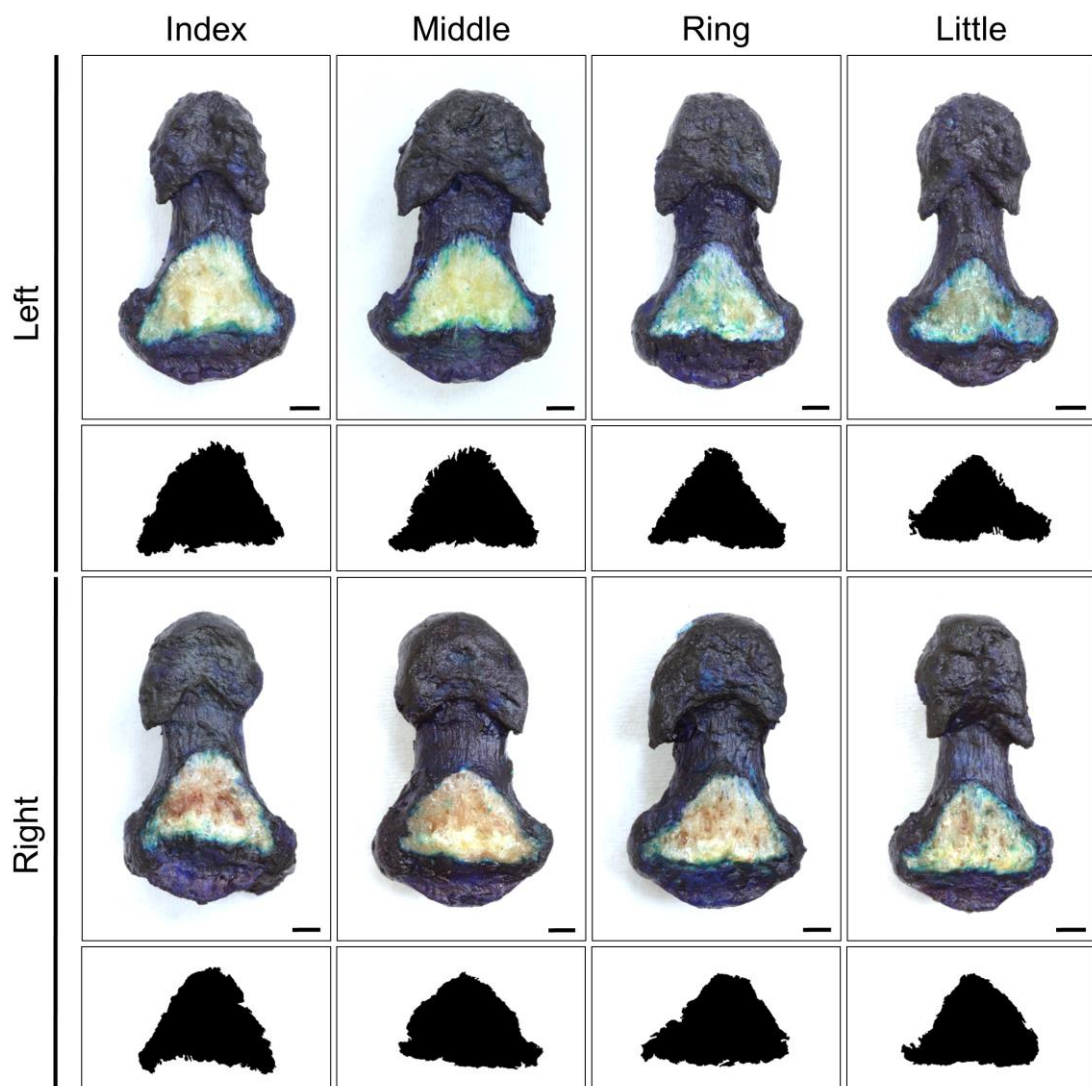


Figure 2.7 | Complete Specimen Set of FDP Footprints

Flexor surface view of stained DPs with unstained FDP footprints from 1 male cadaveric specimen. The binary 'mask' image of the footprint from which measurements were analysed is shown below each DP. Note the trapezoidal, near triangular shape. Scale bars 2mm.

2.5.1.1 Footprint Morphometrics

Tabulated and graphical summaries of the general FDP footprint shape measurements are shown in **Table 2.3** and **Figure 2.8** (surface area), **Table 2.4** and **Figure 2.9** (height), **Table 2.5** and **Figure 2.10** (base width) and **Table 2.6** and **Figure 2.11** (apex width).

The mean surface area of the FDP footprint from fingers of both genders was $29.29 \pm 2.35\text{mm}^2$, with a mean of $34.72 \pm 3.32\text{mm}^2$ for males and $23.86 \pm 3.31\text{mm}^2$ for females (**Table 2.3**). The little finger (combined genders) was significantly smaller than all other fingers ($p < 0.01$ overall) (**Figure 2.8b**). This significance pattern was echoed in male fingers to various levels, and in females the little finger was also the smallest (**Figure 2.8c**). The largest mean surface area was the male middle finger ($39.11 \pm 3.56\text{mm}^2$), with the smallest being the female little ($19.50 \pm 3.56\text{mm}^2$).

Height of the FDP footprint was significantly different between males ($6.14 \pm 0.30\text{mm}$) and females ($4.75 \pm 0.29\text{mm}$) ($p < 0.05$) (**Table 2.4** and **Figure 2.9a**). The little finger (combined genders) was significantly shorter than all other fingers ($p < 0.001$) (**Figure 2.9b**), also seen to various significance levels within males (**Figure 2.9c**). The female little finger was the shortest of either gender finger ($4.23 \pm 0.34\text{mm}$), and was also significantly shorter than the tallest of all fingers, the male middle finger ($6.59 \pm 0.34\text{mm}$) ($p < 0.05$) (**Table 2.4** and **Figure 2.9b**).

Base width averaged $8.58 \pm 0.37\text{mm}$, with a mean of $9.18 \pm 0.52\text{mm}$ in males and $7.99 \pm 0.52\text{mm}$ in females (**Table 2.5**). The little finger (combined genders) again demonstrated the smallest dimension, significantly smaller than the middle ($p < 0.001$) and ring ($p < 0.05$) (**Figure 2.10b**). Both genders once more revealed middle fingers as having the largest dimension (male $9.77 \pm 0.56\text{mm}$, female $8.62 \pm 0.56\text{mm}$), and the little fingers the smallest (male $8.46 \pm 0.56\text{mm}$, female $7.46 \pm 0.56\text{mm}$), ranging from the male middle to the female little finger (**Table 2.5**).

Apex width exhibited no discernible pattern. No significant differences were demonstrated between genders or fingers, and standard errors were proportionally the greatest of all general footprint dimensions (**Figure 2.11**). Male and female means were similar at $1.57 \pm 0.16\text{mm}$ and $1.63 \pm 0.15\text{mm}$, respectively, whilst the middle finger (combined genders) ($1.77 \pm 0.20\text{mm}$) was slightly wider than all other fingers

(Table 2.6). Females had both the widest (middle, $2.11 \pm 0.27\text{mm}$) and narrowest (ring, $1.33 \pm 0.27\text{mm}$) apices (Table 2.6 and Figure 2.11c).

The internal angles of the FDP footprint trapezoid shape are given in Table 2.7. The overall mean base angles were $53.54 \pm 1.53^\circ$ (left) and $54.92 \pm 0.85^\circ$ (right), and mean apex angles were $126.47 \pm 1.53^\circ$ (left) and $125.10 \pm 0.86^\circ$ (right). Left and right angles were not significantly different, implying the shape was approximately symmetrical (Figure 2.12).

Table 2.3 | Surface Area of FDP Footprint

Table of collated measurements. 'All' represents mean of combined genders, fingers, or both. EM mean (\pm SEM). See Figure 2.8.

Surface Area (mm ²)			
	Male	Female	All
Index	35.90 (3.56)	23.65 (3.56)	29.77 (2.51)
Middle	39.11 (3.56)	27.21 (3.56)	33.16 (2.51)
Ring	36.00 (3.62)	25.08 (3.56)	30.53 (2.53)
Little	27.88 (3.56)	19.50 (3.56)	23.69 (2.51)
All	34.72 (3.32)	23.86 (3.31)	29.29 (2.35)

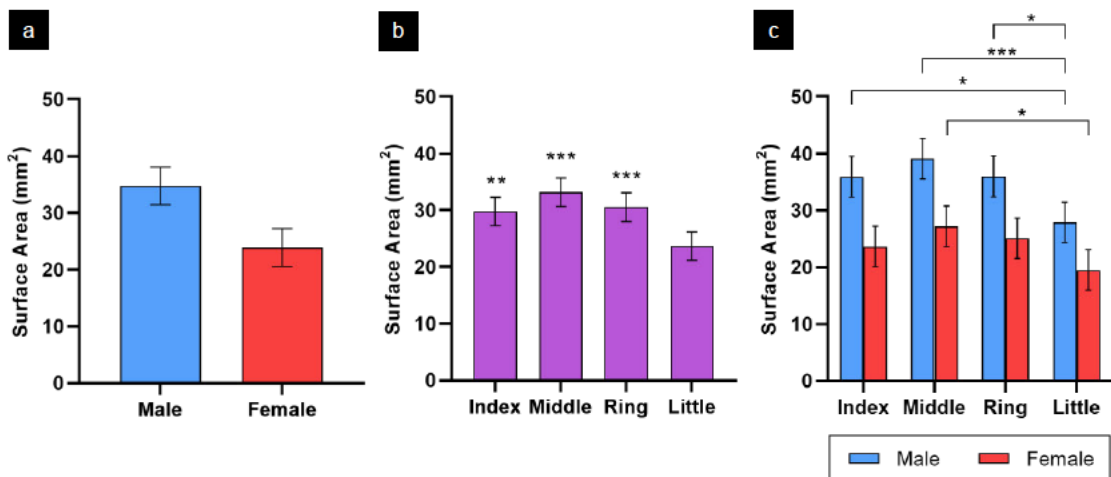


Figure 2.8 | Surface Area of FDP Footprint

a) Male versus female comparison, all fingers combined. Non-significant ($p=0.081$). **b)** Finger comparison, genders combined. Stars represent significant differences as compared to little finger (no other pairwise comparison significant differences present). **c)** Separated finger and gender comparison. Multiple significant differences are apparent. EM mean \pm SEM. * $p<0.05$, ** $p<0.01$, *** $p<0.001$. See Table 2.3.

Table 2.4 | Height of FDP Footprint

Table of collated measurements. 'All' represents mean of combined genders, fingers, or both. EM mean (\pm SEM). See Figure 2.9.

Height (mm)			
	Male	Female	All
Index	6.51 (0.34)	4.95 (0.34)	5.73 (0.24)
Middle	6.59 (0.34)	4.86 (0.34)	5.73 (0.24)
Ring	6.24 (0.36)	4.97 (0.34)	5.61 (0.25)
Little	5.20 (0.34)	4.23 (0.34)	4.72 (0.24)
All	6.14 (0.30)	4.75 (0.29)	5.45 (0.21)

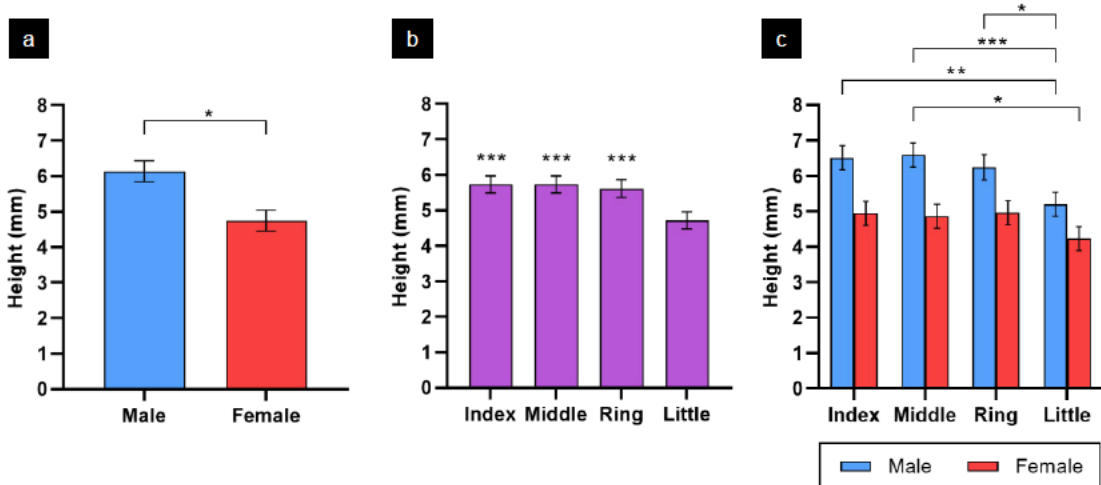


Figure 2.9 | Height of FDP Footprint

a) Male versus female comparison, all fingers combined. Height difference is significant ($p=0.029$). **b)** Finger comparison, genders combined. Stars show significant differences as compared to little finger. **c)** Separated finger and gender comparison. Multiple significant differences are apparent. EM mean \pm SEM. * $p<0.05$, ** $p<0.01$, *** $p<0.001$. See Table 2.4.

Table 2.5 | Base Width of FDP Footprint

Table of collated measurements. 'All' represents mean of combined genders, fingers, or both EM mean (\pm SEM). See **Figure 2.10**.

Base Width (mm)			
	Male	Female	All
Index	9.04 (0.56)	7.79 (0.56)	8.41 (0.40)
Middle	9.77 (0.56)	8.62 (0.56)	9.20 (0.40)
Ring	9.44 (0.58)	8.11 (0.56)	8.77 (0.40)
Little	8.46 (0.56)	7.46 (0.56)	7.96 (0.40)
All	9.18 (0.52)	7.99 (0.52)	8.58 (0.37)

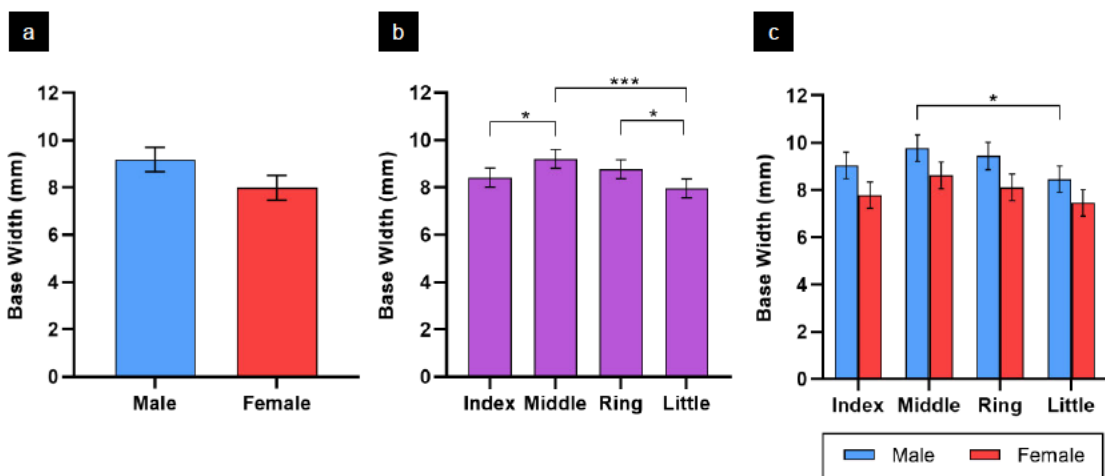


Figure 2.10 | Base Width of FDP Footprint

a) Male versus female comparison, all fingers combined. Non-significant ($p=0.182$). **b)** Finger comparison, genders combined. Multiple significant differences exist, greatest between middle and little fingers. **c)** Separated finger and gender comparison. The only significant difference lies between the male middle and little fingers ($p=0.026$). EM mean \pm SEM. * $p<0.05$, *** $p<0.001$. See **Table 2.5**.

Table 2.6 | Apex Width of FDP Footprint

Table of collated measurements. 'All' represents mean of combined genders, fingers, or both. EM mean (\pm SEM). See **Figure 2.11**.

Apex Width (mm)			
	Male	Female	All
Index	1.72 (0.27)	1.44 (0.27)	1.58 (0.20)
Middle	1.42 (0.27)	2.11 (0.27)	1.77 (0.20)
Ring	1.83 (0.29)	1.33 (0.27)	1.56 (0.20)
Little	1.37 (0.27)	1.66 (0.27)	1.52 (0.20)
All	1.57 (0.16)	1.63 (0.15)	1.60 (0.11)

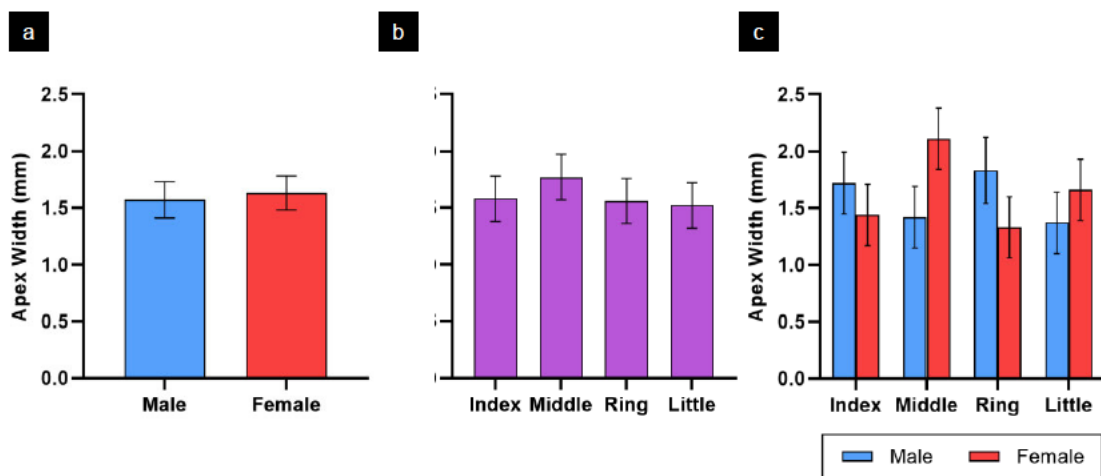


Figure 2.11 | Apex Width of FDP Footprint

Values are generally similar between genders **(a)**, and between fingers with genders combined **(b)**. No clear trends or significant differences are apparent when separating fingers and gender **(c)**. EM mean \pm SEM. See **Table 2.6**.

Table 2.7 | Internal Angles of FDP Footprint Trapezoid

Table of internal angle measurements for individual fingers and gender total means. 'All' refers to combined finger means within gender or collective individual finger means. Differences between individual fingers or gender totals within base or apex groups on either side are all non-significant. EM mean (\pm SEM).

Internal Angle (°)				
	Base		Apex	
	Left	Right	Left	Right
Male				
Index	57.88 (3.02)	60.02 (2.09)	122.14 (3.02)	119.91 (2.09)
Middle	56.50 (3.02)	53.86 (2.09)	123.49 (3.02)	126.14 (2.09)
Ring	54.50 (3.22)	55.02 (2.28)	125.51 (3.23)	124.96 (2.28)
Little	52.48 (3.02)	52.65 (2.09)	127.55 (3.02)	127.50 (2.09)
All	55.36 (2.17)	55.43 (1.22)	124.65 (2.17)	124.58 (1.22)
Female				
Index	54.60 (3.02)	55.32 (2.09)	125.38 (3.02)	124.70 (2.09)
Middle	50.18 (3.02)	52.95 (2.09)	129.83 (3.02)	127.08 (2.09)
Ring	51.69 (3.02)	55.79 (2.09)	128.29 (3.02)	124.17 (2.09)
Little	50.41 (3.02)	53.56 (2.09)	129.62 (3.02)	126.53 (2.09)
All	51.72 (2.15)	54.41 (1.20)	128.28 (2.15)	125.62 (1.21)
Collective				
All	53.54 (1.53)	54.92 (0.85)	126.47 (1.53)	125.10 (0.86)

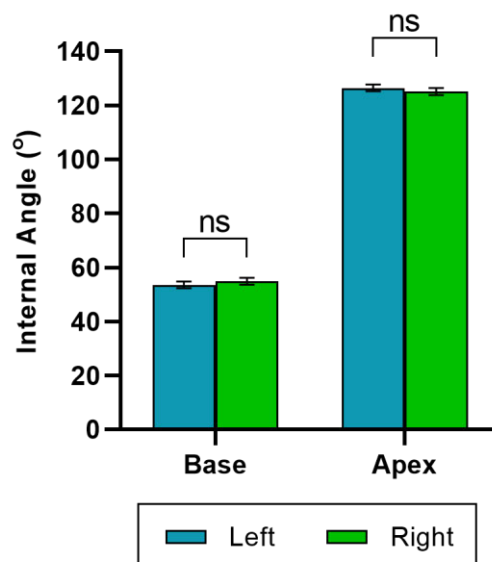


Figure 2.12 | Side Comparison of FDP Footprint Trapezoid Internal Angles

Pairwise comparison of left and right sided angles of all individual fingers. Base angle side or apex angle side is analysed as an added fixed factor to the linear mixed effects model (SEM 1.26° throughout) (see **Table 2.2 – Models 3a and 3b**). Left and right comparisons are non-significant (*ns*), suggesting a symmetrical FDP footprint trapezoid across the vertical axis. EM mean \pm SEM.

2.5.1.2 Positioning on Distal Phalanx

Dimensions of the flexor view of the DP are summarised in **Table 2.8**. These general measurements allowed calculation of FDP:DP measurement ratios (**Table 2.9**), which, along with the distances of the FDP footprint from the DIPJ (**Table 2.10**), provided a guide to the FDP insertion position on the DP.

Table 2.8 | General Dimensions of Flexor View of Distal Phalanx

Individual finger breakdown and gender total means for surface area, height and base width. Male middle finger has the largest dimensions throughout; female little finger has the smallest dimensions except for height (female index). Multiple significant differences exist between fingers within separate genders (not highlighted). 'All' refers to combined finger means within gender or collective individual finger means. EM mean (\pm SEM).

Distal Phalanx Dimensions			
	Surface Area (mm ²)	Height (mm)	Base Width (mm)
Male			
Index	147.90 (12.02)	20.03 (0.81)	11.68 (0.66)
Middle	177.54 (12.02)	21.49 (0.81)	12.74 (0.66)
Ring	171.41 (12.09)	21.35 (0.82)	12.41 (0.66)
Little	118.27 (12.02)	18.74 (0.81)	10.68 (0.66)
All	153.62 (11.81)	20.41 (0.79)	11.87 (0.64)
Female			
Index	106.04 (12.02)	16.38 (0.81)	10.57 (0.66)
Middle	127.64 (12.02)	18.36 (0.81)	10.81 (0.66)
Ring	122.60 (12.02)	18.59 (0.81)	10.19 (0.66)
Little	88.05 (12.02)	16.60 (0.81)	8.97 (0.66)
All	111.08 (11.81)	17.48 (0.79)	10.13 (0.64)
Collective			
All	132.35 (8.35)	18.94 (0.56)	11.00 (0.45)

The mean ratio of FDP to DP surface area was $22.26 \pm 1.11\%$ collectively, ranging between $20.51 \pm 1.86\%$ (female ring) and $24.13 \pm 1.86\%$ (male index) (**Table 2.9**). All fingers showed similar ratios, and no significant differences existed between individual fingers, gender means or combined gender finger means.

The FDP:DP height ratio (**Table 2.9**) is interpreted as the height of the centre of the FDP footprint distally along the DP. The overall mean was $27.05 \pm 0.73\%$ along the DP, ranging from $23.53 \pm 1.32\%$ (female little) to $31.22 \pm 1.32\%$ (male middle). Male

mean was $29.10 \pm 1.04\%$ (finger range 26.75% - 31.22%), which was significantly greater than females (mean $25.00 \pm 1.03\%$, finger range 23.53% - 26.73%) ($p=0.048$). When finger means from combined genders were compared, the middle ($28.97 \pm 0.93\%$) was significantly greater than the little ($25.14 \pm 0.93\%$) ($p<0.01$), however there was no significance when the individual fingers were split across genders.

The mean FDP:DP base width ratio (**Table 2.9**) was $78.34 \pm 1.59\%$ collectively, ranging from $74.69 \pm 3.08\%$ (female index) to $83.40 \pm 3.08\%$ (female little), with no significant differences between individual finger, gender, or combined gender finger means.

Table 2.9 | Ratio of FDP Footprint Measurements to Related Distal Phalanx Measurements

Individual finger breakdown and gender total means for 3 measurement ratios as a guide to the position of the FDP insertion on the DP. The only significant difference (*) between individual fingers or gender total data sets within each ratio occurs between male and female means for FDP centroid height related to DP height ($p=0.048$). 'Surface Area' = surface area of FDP footprint to surface area of flexor view of DP; 'Height' = height of FDP footprint centroid from DIPJ compared to total height of DP; 'Base Width' = greatest width of FDP footprint trapezoid base to greatest width of DP base. 'All' refers to combined finger means within gender or collective individual finger means. EM mean (\pm SEM).

Ratio FDP:DP (%)			
	Surface Area	Height	Base Width
Male			
Index	24.13 (1.86)	30.01 (1.32)	77.48 (3.08)
Middle	21.86 (1.86)	31.22 (1.32)	76.53 (3.08)
Ring	20.89 (1.93)	28.37 (1.40)	75.88 (3.28)
Little	23.56 (1.86)	26.75 (1.32)	78.82 (3.08)
All	22.62 (1.58)	29.10* (1.04)	77.21 (2.26)
Female			
Index	22.77 (1.86)	25.04 (1.32)	74.69 (3.08)
Middle	21.95 (1.86)	26.73 (1.32)	80.22 (3.08)
Ring	20.51 (1.86)	24.70 (1.32)	79.55 (3.08)
Little	22.37 (1.86)	23.53 (1.32)	83.40 (3.08)
All	21.90 (1.57)	25.00* (1.03)	79.46 (2.24)
Collective			
All	22.26 (1.11)	27.05 (0.73)	78.34 (1.59)

Table 2.10 summarises the distances between the DIPJ (i.e. the base, or most proximal point, of the DP) and the FDP footprint base and centroid, and delineates significant differences between genders and combined gender fingers.

The overall mean distance between the DIPJ and the FDP (**Table 2.10**) was 2.55 ± 0.10 mm. The male middle showed the greatest distance of all fingers (3.56 ± 0.24 mm), significantly greater than the male little (2.45 ± 0.24 mm) ($p < 0.05$), and all female fingers except the middle [index, 1.74 ± 0.24 mm ($p < 0.001$); ring, 2.15 ± 0.24 mm ($p < 0.05$); little, 1.92 ± 0.24 mm ($p < 0.01$)]. The female index showed the least distance of all fingers (1.74 ± 0.24 mm), significantly smaller than all male fingers except for the little finger [index, 3.07 ± 0.24 mm ($p < 0.05$); middle, 3.56 ± 0.24 mm ($p < 0.001$); ring, 3.00 mm ± 0.24 ($p < 0.05$)].

The overall mean distance between the DIPJ and FDP centroid (**Table 2.10**) was 5.16 ± 0.20 mm, ranging significantly between 3.87 ± 0.33 mm (female little) and 6.71 ± 0.33 mm (male middle) ($p < 0.05$). Within genders, the male little finger (5.02 ± 0.33 mm) was significantly smaller than all other fingers [index, 6.03 ± 0.33 mm ($p < 0.05$); middle, 6.71 ± 0.33 mm ($p < 0.001$); ring, 6.06 ± 0.34 mm ($p < 0.05$)] but the female little finger (3.87 ± 0.33 mm) was only significantly smaller than the middle (4.93 ± 0.33 mm) ($p < 0.05$).

Table 2.10 | Distance of FDP Footprint Base and Centroid from DIPJ

Collated measurement means for individual fingers, gender totals and finger totals. Comparative analysis within gender totals and finger totals reveal multiple significant differences (not highlighted): male vs female for both FDP base ($p < 0.01$) and FDP centroid ($p < 0.05$); for combined gender fingers - for FDP base, middle vs little ($p < 0.01$) and vs index ($p < 0.05$), and for FDP centroid - little vs ring, vs middle (both $p < 0.001$), and vs index ($p < 0.05$), and middle vs index ($p < 0.01$). 'All' represents mean of combined genders, fingers, or both. EM mean (\pm SEM).

Distance from DIPJ (mm)						
	FDP Base			FDP Centroid		
	Male	Female	All	Male	Female	All
Index	3.07 (0.24)	1.74 (0.24)	2.40 (0.17)	6.03 (0.33)	4.09 (0.33)	5.06 (0.24)
Middle	3.56 (0.24)	2.51 (0.24)	3.04 (0.17)	6.71 (0.33)	4.93 (0.33)	5.82 (0.24)
Ring	3.00 (0.26)	2.15 (0.24)	2.58 (0.18)	6.06 (0.34)	4.58 (0.33)	5.33 (0.24)
Little	2.45 (0.24)	1.92 (0.24)	2.19 (0.17)	5.02 (0.33)	3.87 (0.33)	4.45 (0.24)
All	3.02 (0.15)	2.08 (0.14)	2.55 (0.10)	5.96 (0.29)	4.37 (0.29)	5.16 (0.20)

2.5.1.3 Inter-Observer Reliability

Reliability statistics and interpretation scales comparing the agreement of 2 observers measuring the FDP footprint and DP dimensions are provided in **Table 2.11**. From all measurements taken, the collective reliability was extremely high, with an intraclass correlation coefficient (ICC) of 0.997 and Cronbach's alpha of 0.998.

The most reliable FDP footprint measurements were internal angles (ICC 0.992) and surface area (ICC 0.971), with 'good' reliability also between base width (ICC 0.846) and height (ICC 0.807) measurements. Isolated apex width measurements were however of 'poor' reliability (ICC 0.398).

DP measurements showed either 'excellent' reliability [surface area (ICC 0.933) and height (0.929)] or a high 'moderate' reliability (base width, ICC 0.728). Measurements of the FDP footprint from the DIPJ were 'excellent' (FDP centroid, ICC 0.977) or near-excellent (FDP base, ICC 0.877).

Table 2.11 | Inter-Observer Reliability of FDP Footprint and Distal Phalanx Measurements

SPSS reliability statistics (95% confidence intervals) comparing 2 observers. *Raw measurements* are the total number of measurements taken for the variable. *Measurement sets per variable* represents the number of different procedural groups measured to achieve the stated variable (e.g. to obtain an average). A 2-way mixed effects model for the *Intraclass correlation coefficient* (ICC) is employed: observers are not randomly selected and each observer measures each variable. The ICC stated is for absolute agreement (comparing exact measurements) of single measures [reliability of a single observer's reported measurements (i.e. the 1st observer's measurements)]. *Cronbach's alpha* approximates the ICC of average measures (reliability of both observers' measurements averaged together). ICC interpretation (Koo and Li, 2016): <0.5 poor; 0.5-0.75 moderate; 0.75-0.9 good; >0.9 excellent reliability. Cronbach's alpha interpretation (Portney and Watkins, 2000): ≥0.70 acceptable. Full SPSS statistical output is provided in *Appendix 1.1*.

Reliability Statistics											
	All	FDP Footprint				Distal Phalanx				Distance from DIPJ	
		Surface Area	Height	Base Width	Apex Width	Internal Angles	Surface Area	Height	Base Width	FDP Base	FDP Centroid
<i>Raw Measurements</i>	1081	47	94	47	47	376	47	94	47	188	94
<i>Measurement Sets per Variable</i>	23	1	2	1	1	8	1	2	1	4	2
<i>Intraclass Correlation Coefficient</i>	0.997 (0.996-0.997)	0.971 (0.947-0.984)	0.807 (0.722-0.868)	0.846 (0.733-0.913)	0.398 (0.042-0.645)	0.992 (0.990-0.993)	0.933 (0.879-0.963)	0.929 (0.895-0.952)	0.728 (0.561-0.838)	0.877 (0.834-0.909)	0.977 (0.966-0.985)
<i>Cronbach's Alpha</i>	0.998	0.986	0.887	0.923	0.671	0.996	0.968	0.963	0.843	0.938	0.989

2.5.2 Tendon Width

The gross morphology of the FDP tendon altered along its course towards insertion onto the DP. At the point of finger detachment from the cadaveric specimen, around the distal A2 pulley, the cross section of the tendon was oval shaped. Progressing distally, a developing median longitudinal sulcus gradually furrowed the tendon's flexor surface. Beneath the A4 pulley the sulcus became much more evident, which coincided with a marked flattening of the tendon, giving the tendon a kidney-shaped or biconcave cross section. Between the A4 and A5 pulleys (C3 region) the sulcus flattened as the tendon then fanned out to its insertion on the DP (see **Figure 2.1b,c**). The more superficial fibres on the flexor surface, either side of the median sulcus, fanned out to attach more laterally and proximally at the insertion, whereas the deeper dorsal fibres, beneath the median sulcus, emerged to attach more centrally and distally (see **Figure 2.5**).

2.5.2.1 Morphometrics

The breakdown of all FDP tendon width measurements across gender and fingers is shown in **Table 2.12**. The fanning out of the tendon towards its DP attachment was described by the increasing overall width measurements from 12mm proximal to the FDP insertion base ($4.69 \pm 0.20\text{mm}$), to 9mm ($5.08 \pm 0.26\text{mm}$), 6mm ($6.05 \pm 0.25\text{mm}$), 3mm ($7.16 \pm 0.23\text{mm}$), and finally the insertion base itself ($8.58 \pm 0.37\text{mm}$) (see **Table 2.5**). This pattern was seen in either gender and any finger, except for the female little finger, where the width at 12mm ($3.75 \pm 0.36\text{mm}$) was greater than that at 9mm ($3.61 \pm 0.47\text{mm}$).

Figure 2.13 depicts and describes the finger pattern of tendon widths for each gender. **Figure 2.14** similarly graphs the tendon widths for individual fingers, and summarises the significant differences between them, at each distance proximal to the insertion base.

Table 2.12 | FDP Tendon Width Measurements

Collated measurement means of the FDP tendon width at points 3mm, 6mm, 9mm and 12mm proximal from the FDP insertion base. 'Average' is the calculated mean from measurements made at the 4 proximal distances. 'All' represents mean of combined genders, fingers, or both. EM mean (\pm SEM). Values are plotted in Figure 2.13 and Figure 2.14.

	Tendon Width at Proximal Distances from FDP Insertion Base (mm)														
	3mm			6mm			9mm			12mm			Average		
	Male	Female	All	Male	Female	All	Male	Female	All	Male	Female	All	Male	Female	All
Index	8.12 (0.33)	6.94 (0.42)	7.54 (0.26)	7.16 (0.36)	5.88 (0.46)	6.53 (0.29)	5.93 (0.36)	4.78 (0.47)	5.35 (0.29)	5.21 (0.28)	4.62 (0.36)	4.89 (0.22)	6.61 (0.32)	5.56 (0.41)	6.08 (0.26)
Middle	8.51 (0.33)	7.42 (0.42)	7.96 (0.26)	7.61 (0.36)	6.22 (0.46)	6.93 (0.29)	6.51 (0.36)	5.15 (0.47)	5.85 (0.29)	5.64 (0.28)	4.59 (0.36)	5.15 (0.22)	7.07 (0.32)	5.84 (0.41)	6.47 (0.26)
Ring	7.84 (0.33)	6.57 (0.42)	7.22 (0.26)	6.64 (0.36)	5.44 (0.46)	6.03 (0.29)	5.66 (0.36)	4.45 (0.47)	5.06 (0.29)	5.15 (0.28)	4.20 (0.36)	4.69 (0.22)	6.32 (0.32)	5.16 (0.41)	5.75 (0.26)
Little	6.46 (0.33)	5.45 (0.42)	5.94 (0.26)	5.31 (0.36)	4.18 (0.46)	4.73 (0.29)	4.57 (0.36)	3.61 (0.47)	4.07 (0.29)	4.33 (0.28)	3.75 (0.36)	4.02 (0.22)	5.17 (0.32)	4.25 (0.41)	4.69 (0.26)
All	7.73 (0.28)	6.59 (0.36)	7.16 (0.23)	6.68 (0.31)	5.43 (0.40)	6.05 (0.25)	5.67 (0.32)	4.50 (0.42)	5.08 (0.26)	5.08 (0.25)	4.29 (0.32)	4.69 (0.20)	6.29 (0.29)	5.20 (0.37)	5.75 (0.23)

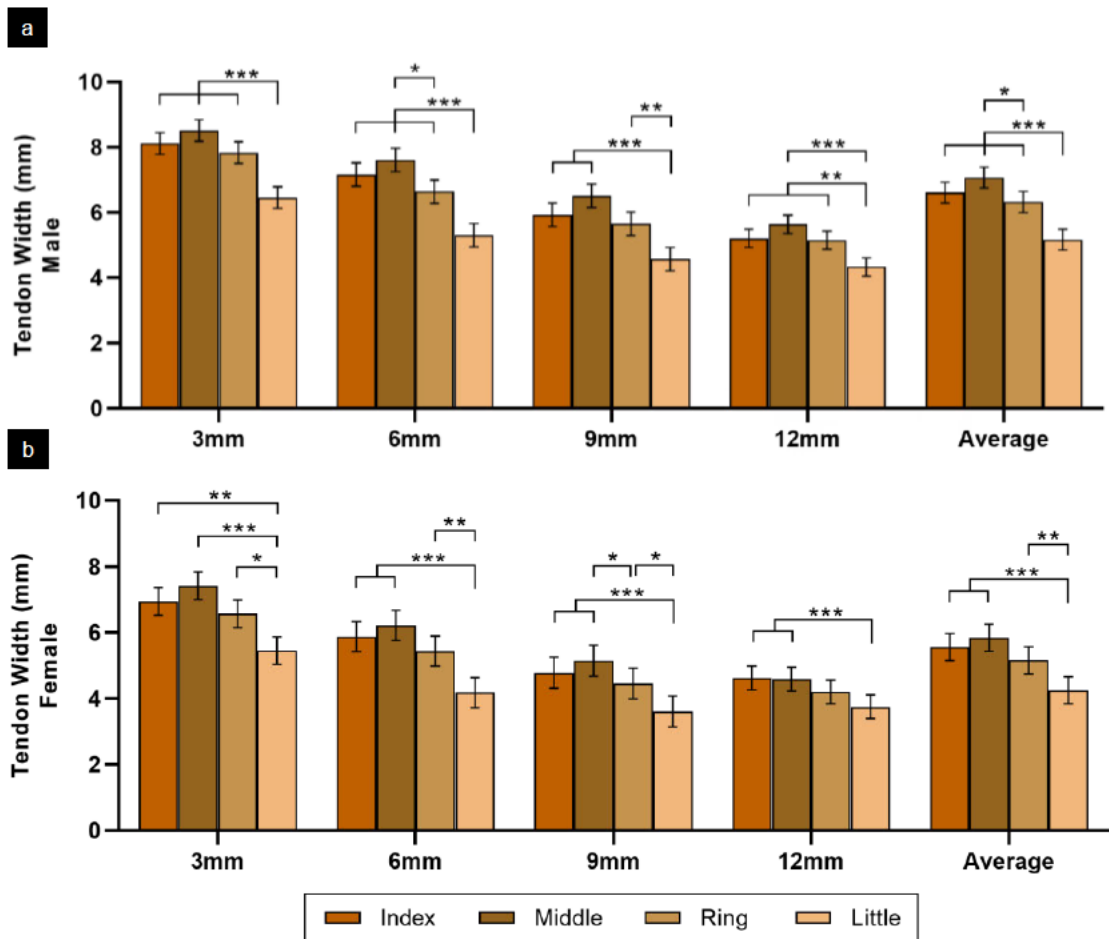


Figure 2.13 | Gender Breakdown of FDP Tendon Width

Graphical distribution of male (a) and female (b) FDP tendon widths for all finger clusters at points 3mm, 6mm, 9mm and 12mm proximal from the FDP insertion base. The same arrangement of widths (middle>index>ring>little) is seen at all distances for both genders except for a greater width at index over middle finger at 12mm in females. Each finger follows a downward trend of tendon width as the distance from the FDP insertion increases, in both males and females, except a slight increase in width in the female little finger from 9mm to 12mm. Little finger tendon widths are always significantly smaller than every other finger, except the female ring finger at 12mm. Comparison of male and female combined finger mean at each distance shows a significant difference at 3mm and 6mm only ($p < 0.05$) (not highlighted on graph). 'Average' refers to calculated mean from measurements made at 3mm, 6mm, 9mm and 12mm. EM mean \pm SEM. * $p < 0.05$, ** $p < 0.01$, *** $p < 0.001$.

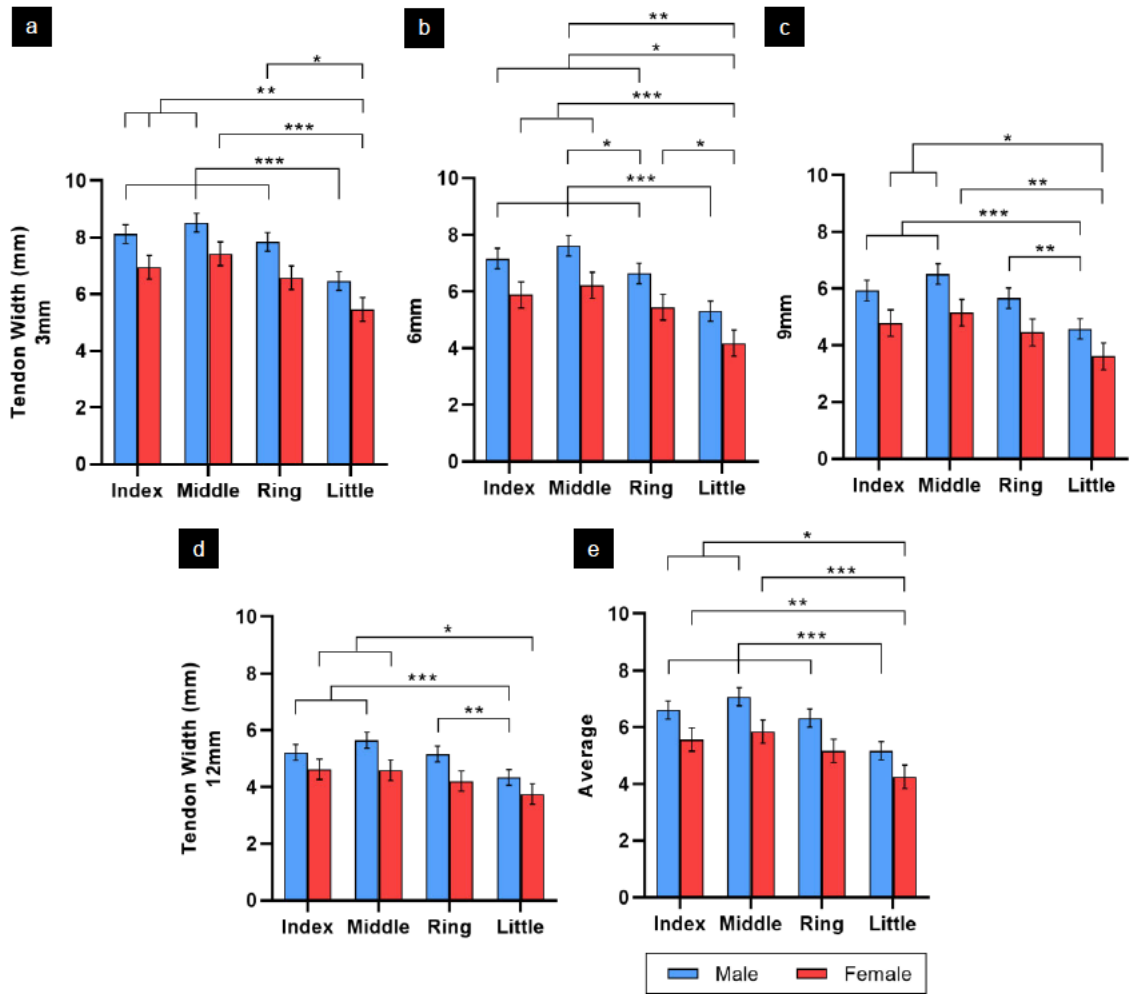


Figure 2.14 | Individual Finger Breakdown of FDP Tendon Width

Graphical distribution of individual finger tendon widths from measurements made at 3mm (a), 6mm (b), 9mm (c), and 12mm (d) proximal from the FDP insertion base, and calculated mean from the 4 measurement points (e). Noteworthy amongst significant differences in the multiple comparisons is that male little is always smaller than all the other male fingers; similarly the female little is always smaller than the female index and middle fingers, but only also including ring at 6mm; female little is smaller than all or some of male index, middle and ring at all distances except 12mm; and the only female finger smaller than all male fingers is the female little. 'Average' refers to calculated mean from measurements made at 3mm, 6mm, 9mm and 12mm. EM mean \pm SEM. *p<0.05, **p<0.01, ***p<0.001.

2.5.2.2 Inter-Observer Reliability

Reliability statistics of the agreement of 2 observers measuring the same tendon width images are presented in **Table 2.13**. Overall reliability was ‘excellent’ with an intraclass correlation coefficient (ICC) of 0.938 and Cronbach’s alpha of 0.970. All separate measurements at different distances from the FDP insertion base were either ‘excellent’ [3mm (ICC 0.910), 6mm (ICC 0.916), 9mm (0.919)] or ‘good’ (12mm, ICC 0.849).

Table 2.13 | Inter-Observer Reliability of Tendon Width Measurements

SPSS reliability statistics (95% confidence intervals) comparing 2 observers. See **Table 2.11** for details and interpretation. Full SPSS statistical output is provided in *Appendix 1.2*.

Reliability Statistics					
	All	Distance from FDP Insertion Base			
		3mm	6mm	9mm	12mm
<i>Raw Measurements</i>	256	64	64	64	64
<i>Measurement Sets per Variable</i>	4	1	1	1	1
Intraclass Correlation Coefficient	0.938 (0.917-0.953)	0.910 (0.852-0.945)	0.916 (0.863-0.948)	0.919 (0.868-0.950)	0.849 (0.760-0.906)
Cronbach's Alpha	0.970	0.955	0.958	0.959	0.922

2.5.3 Bone Depth

Grossly, the FDP tendon attached to the DP over a relatively flat vertical plane, where the anterior commencement of the DP bone depth (anterior-posterior) measurements lay on the same coronal plane for both proximal and distal insertion points (see **Figure 2.6**). The proximal third of the DP flared out in both medial-lateral (see **Figure 2.7**) and posterior directions (see **Figure 2.6**) to provide a larger articular surface for the head of the middle phalanx at the DIPJ. Accordingly, the measurements at the proximal point of FDP insertion were always deeper than at the distal point, for any finger in either gender, as shown by the full measurement sets in **Table 2.14**. The overall mean depth at the proximal insertion point was $6.20 \pm 0.17\text{mm}$ [ranging from $5.23 \pm 0.27\text{mm}$ (female little finger) to $7.05 \pm 0.27\text{mm}$ (male middle)] compared to $4.20 \pm 0.06\text{mm}$ at the distal insertion point [similarly ranging from $3.48 \pm 0.11\text{mm}$ (female little) to $4.86 \pm 0.11\text{mm}$ (male middle)] ($p < 0.001$).

Figure 2.15 graphs and summarises the pattern of finger values for each gender, and **Figure 2.16** likewise describes patterns and comparisons between individual fingers at each measurement point.

An ‘average’ data set was also calculated and plotted from the mean of the measurements made at the 2 insertion points. Note that this did not necessarily indicate the bone depth at the mid-point of proximal-distal distance (height) of insertion, since the flaring in the proximal third of the bone was not an oblique straight line, but curved.

Table 2.14 | Distal Phalanx Bone Depth Measurements at FDP Insertion

Collated measurements of DP anterior-posterior bone depth. ‘Proximal’ and ‘Distal’ refer to measurements made from the extreme points of FDP insertion, at the base and apex, respectively. ‘Average’ is the calculated mean from the 2 measurements. ‘All’ represents mean of combined genders, fingers, or both. EM mean (\pm SEM). Values are plotted in **Figure 2.15** and **Figure 2.16**.

Bone Depth at FDP Insertion (mm)									
	Proximal			Distal			Average		
	Male	Female	All	Male	Female	All	Male	Female	All
Index	6.43 (0.27)	6.08 (0.27)	6.25 (0.19)	4.53 (0.11)	4.16 (0.11)	4.34 (0.08)	5.48 (0.16)	5.12 (0.16)	5.30 (0.11)
Middle	7.05 (0.27)	6.62 (0.27)	6.84 (0.19)	4.86 (0.11)	4.35 (0.11)	4.61 (0.08)	5.96 (0.16)	5.49 (0.16)	5.72 (0.11)
Ring	6.51 (0.27)	5.82 (0.27)	6.16 (0.19)	4.40 (0.11)	3.95 (0.11)	4.18 (0.08)	5.46 (0.16)	4.89 (0.16)	5.17 (0.11)
Little	5.88 (0.27)	5.23 (0.27)	5.56 (0.19)	3.89 (0.11)	3.48 (0.11)	3.69 (0.08)	4.89 (0.16)	4.36 (0.16)	4.62 (0.11)
All	6.47 (0.24)	5.94 (0.24)	6.20 (0.17)	4.42 (0.08)	3.99 (0.08)	4.20 (0.06)	5.45 (0.14)	4.96 (0.14)	5.20 (0.10)

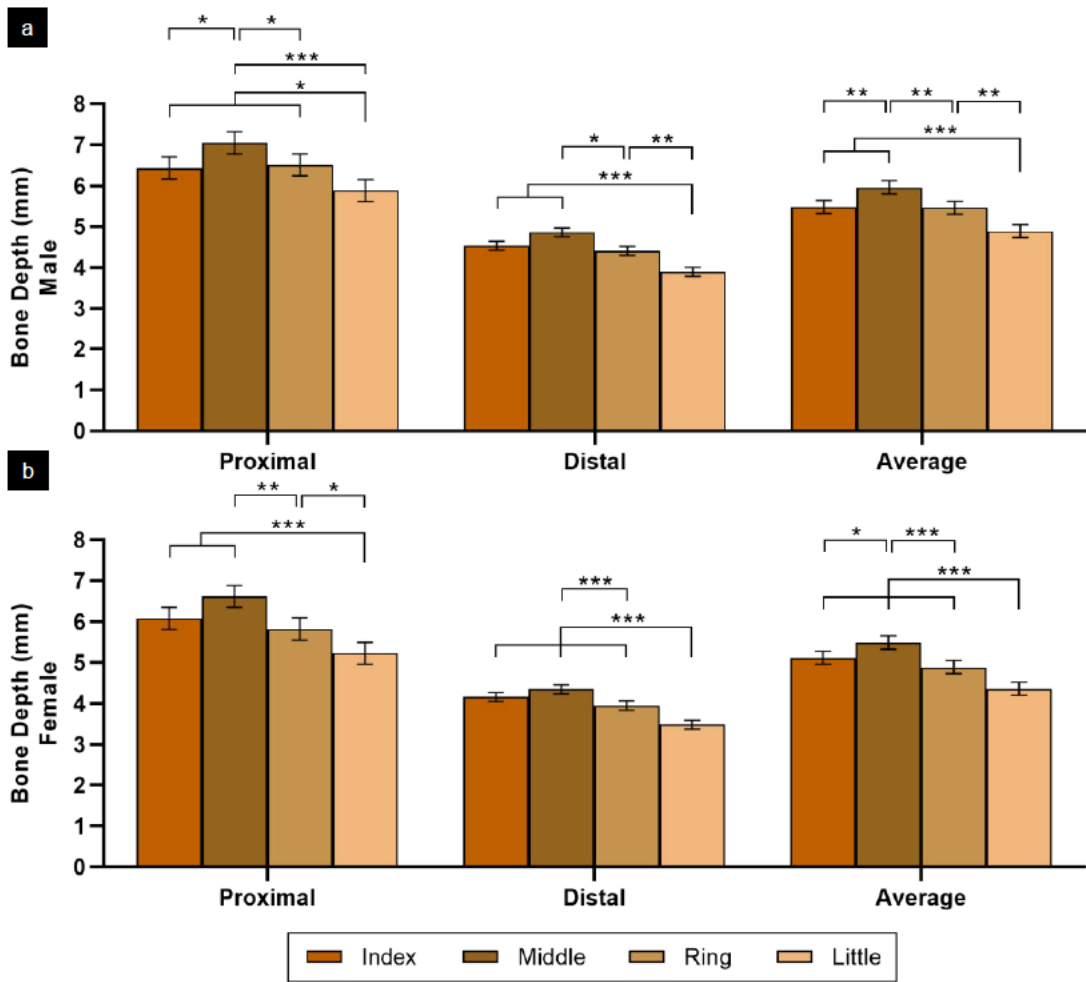


Figure 2.15 | Gender Breakdown of Distal Phalanx Bone Depth at FDP Insertion

Graphical distribution of male (**a**) and female (**b**) DP anterior-posterior bone depth at proximal and distal points of FDP insertion for all finger clusters. Similar analysis is apparent as for gender breakdown of tendon width (**Figure 2.13**). The pattern of bone depth magnitude in finger clusters (middle>index>ring>little) is seen at both points for both genders except for greater depth in ring over index finger proximally in males. The depth of each finger is smaller distally than proximally, and no distal depth is greater than any proximal depth when comparing all fingers. Little finger depth is also significantly smaller than all other fingers, and ring depth is significantly smaller than middle depth. Comparison of male and female combined finger mean shows a significant difference distally ($p<0.01$) and as the average calculated measure ($p<0.05$), but not proximally (not highlighted on graph). 'Average' refers to calculated mean from measurements made at proximal and distal FDP insertion points. EM mean \pm SEM. * $p<0.05$, ** $p<0.01$, *** $p<0.001$.

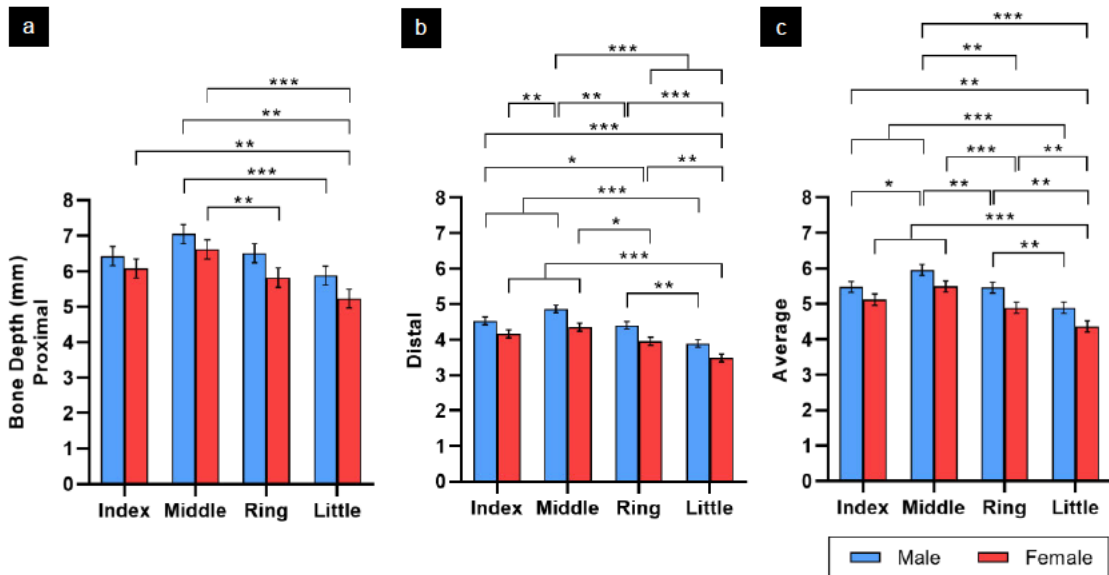


Figure 2.16 | Individual Finger Breakdown of Distal Phalanx Bone Depth at FDP Insertion

Graphical distribution of individual finger DP anterior-posterior bone depth at the proximal (a) and distal (b) point of FDP insertion, and the average calculated from both points (c). A large number of significant differences are apparent, particularly distally (and for the calculated average). At this distal point, within each gender, the little finger is always significantly smaller than all other fingers, and the ring is always significantly smaller than the middle. Multiple significant differences also exist across genders. EM mean \pm SEM. *p<0.05, **p<0.01, ***p<0.001.

2.5.4 Effect of Side

For all variables defined in each data set (FDP footprint, FDP:DP ratios, distance from DIPJ, tendon width, bone depth), samples were split into left and right side categories and means compared to investigate if side exerted a significant effect. **Table 2.15** summarises the results. The overall influence of a particular side on mean results for all data collected was low, although some significant differences did exist in certain variables.

Table 2.15 | Influence of Side on FDP, Distal Phalanx, Tendon Width and Bone Depth Measurements
 Statistical results from left versus right comparisons of all variables within gender (combined fingers) and finger (combined genders) using a series of linear mixed effects models (see **Table 2.2 – Models 4a, 4b, 5a, 5b, 5c, 5d**). <13% of total comparisons are significant; excluding bone depth measurements <6% are significant. Where significant differences are present, parentheses indicate mean difference of left and right means. All mean differences are <0.5mm or <5% ratio, except for FDP footprint base in males (0.73mm). Overall, side influence is low; however particular differences are noted in males and middle fingers for bone depth measurements. For comparison of FDP footprint internal angles see **Table 2.7** and **Figure 2.12**. ‘Sig’ = significant difference; ‘ns’ = non-significant. *p<0.05, **p<0.01, ***p<0.001.

Left vs Right Comparison						
	Gender		Finger			
	Male	Female	Index	Middle	Ring	Little
FDP Footprint						
Surface Area	ns	ns	ns	ns	ns	ns
Height	ns	ns	ns	ns	ns	ns
Base Width	Sig* (0.73mm)	ns	ns	ns	ns	ns
Apex Width	ns	ns	ns	ns	ns	ns
Ratio FDP:DP						
Surface Area	ns	ns	ns	ns	ns	ns
Height	ns	ns	ns	ns	ns	ns
Base Width	Sig* (4.97%)	ns	ns	ns	ns	ns
Distance from DIPJ						
FDP Base	ns	ns	ns	ns	ns	ns
FDP Centroid	ns	ns	ns	ns	ns	ns
Tendon Width proximal from FDP insertion base						
3mm	ns	ns	ns	Sig* (0.47mm)	ns	ns
6mm	ns	ns	ns	ns	ns	ns
9mm	ns	ns	ns	ns	ns	Sig* (0.40mm)
12mm	ns	Sig* (0.26mm)	ns	ns	ns	ns
Average	ns	ns	ns	ns	ns	ns
Bone Depth at FDP insertion						
Proximal	Sig*** (0.44mm)	ns	ns	Sig* (0.37mm)	Sig* (0.34mm)	ns
Distal	Sig** (0.27mm)	ns	Sig* (0.20mm)	Sig* (0.28mm)	ns	ns
Average	Sig*** (0.35mm)	ns	ns	Sig** (0.33mm)	ns	ns

2.5.5 Combined Data Groupings

In order to distil the large collection of data into a small set of appreciably different values, data from FDP footprint, tendon width and bone depth measurements was rearranged and replotted into 3 distinct size categories – ‘large’, ‘medium’ and ‘small’ (see *Section 2.6.4*). ‘Large’ was comprised of male index, middle and ring finger data; ‘medium’ was comprised of male little and female index, middle and ring finger data; and ‘small’ was female little finger data alone. **Figure 2.17** portrays the graphical data and well defined size differences, with all the values given in **Table 2.16**.

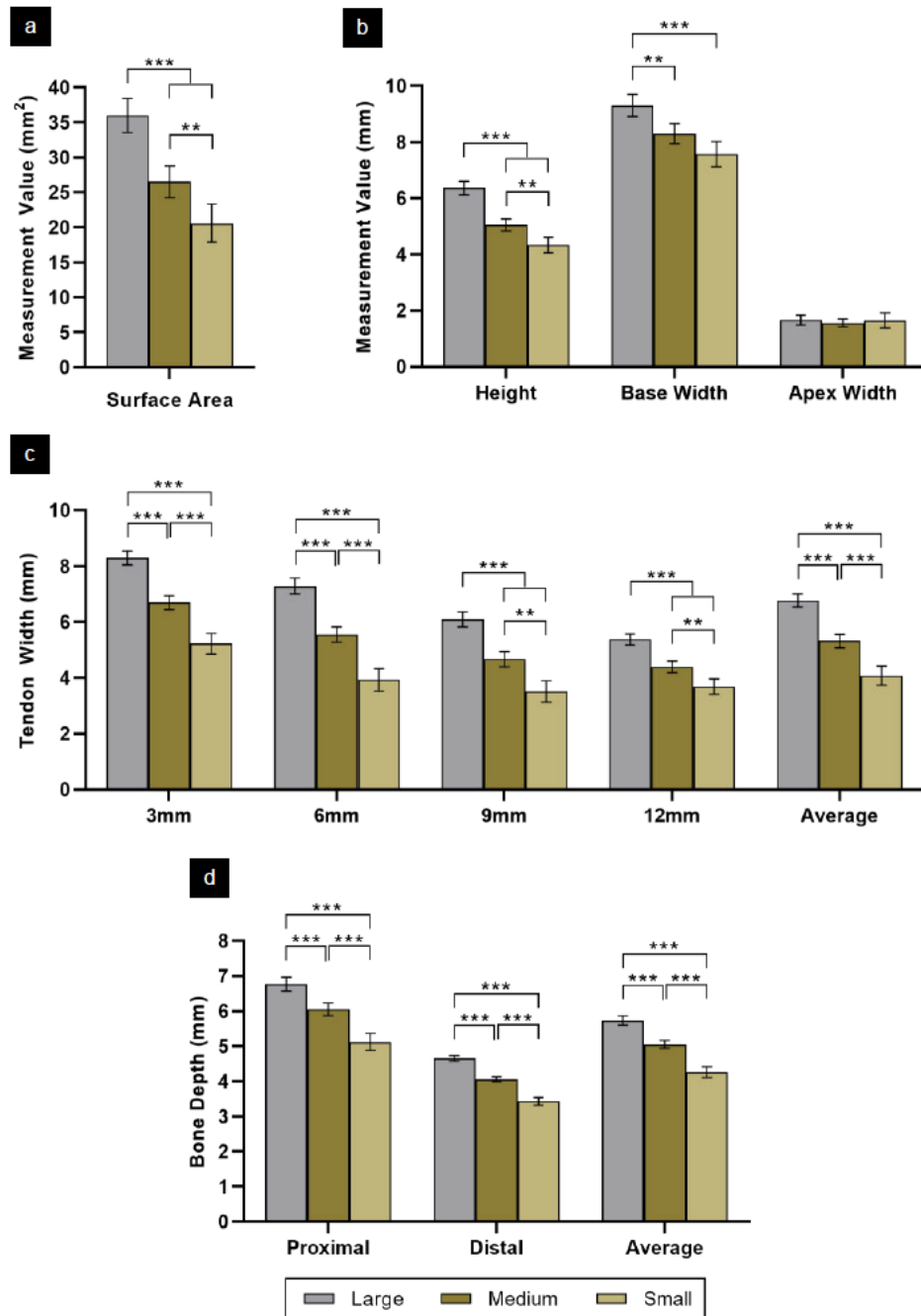


Figure 2.17 | Size Category Groupings for FDP Footprint, Tendon Width and Bone Depth
 Graphical representation of individual finger data re-arranged into 3 distinct size category groupings – ‘large’, ‘medium’, ‘small’ – for FDP footprint surface area (a), FDP footprint trapezoid dimensions (b), FDP tendon widths at points proximal to the FDP insertion base (c), and DP bone depth at the FDP insertion (d). ‘Large’ – male index, middle, ring; ‘medium’ – male little, female index, middle, ring; ‘small’ – female little finger. Grouping data into these 3 size categories provides a reliable stepped gradient in values. Differences between groups are maximised, and size comparisons are highly significant (majority $***p < 0.001$). Values for FDP footprint apex width however remain similar across the 3 size categories and are not significantly different. EM mean \pm SEM. $**p < 0.01$, $***p < 0.001$.

Table 2.16 | Size Category Values for FDP Footprint, Tendon Width and Bone Depth

Measurements of individual finger data for the FDP footprint, tendon width and DP bone depth re-arranged into 3 distinct size category groupings. EM mean (\pm SEM). See **Figure 2.17** for details, plots and significant difference levels between size categories.

Size Category Values			
	Large	Medium	Small
FDP Footprint			
Surface Area (mm ²)	35.97 (2.43)	26.50 (2.28)	20.59 (2.72)
Height (mm)	6.36 (0.24)	5.05 (0.21)	4.33 (0.28)
Base Width (mm)	9.30 (0.39)	8.30 (0.36)	7.57 (0.45)
Apex Width (mm)	1.66 (0.17)	1.56 (0.14)	1.65 (0.27)
Tendon Width proximal from FDP insertion base (mm)			
3mm	8.29 (0.25)	6.69 (0.25)	5.22 (0.37)
6mm	7.29 (0.28)	5.55 (0.27)	3.93 (0.40)
9mm	6.09 (0.27)	4.67 (0.27)	3.51 (0.38)
12mm	5.38 (0.20)	4.39 (0.20)	3.68 (0.28)
Average	6.77 (0.24)	5.32 (0.24)	4.08 (0.34)
Bone Depth at FDP insertion (mm)			
Proximal	6.77 (0.20)	6.05 (0.18)	5.12 (0.24)
Distal	4.65 (0.08)	4.06 (0.07)	3.43 (0.11)
Average	5.73 (0.13)	5.05 (0.11)	4.26 (0.15)

2.6 Discussion

Work in this chapter has collected morphological measurement data on the human FDP insertion in 3 major study groups: the FDP-DP tendon-bone interface, FDP tendon width and DP bone depth. Each set of measurements within each major study group is now reviewed for implications on design of a clinically-relevant tissue engineered model and surgical repair of FDP avulsion, focusing on how factors such as gender and finger, and reliability of the methodologies, affect model size and repair position.

2.6.1 Tendon-Bone Interface

2.6.1.1 Methodology Rationale

Achieving an accurate morphological representation of the native FDP insertion was the principle concern in designing a tissue engineered tendon-bone interface. The methodology employed by Chepla, Goitz and Fowler (2015) utilised a number of techniques that were perceived to increase the accuracy of morphometric data acquisition beyond standard gross measurements made by ruler or caliper. Furthermore, by creating a negative impression of the footprint in ink, analysis of an entire footprint shape was possible. Software-based image analysis added the ability for close magnification and potential for more objective measurements, including calculation of the 'centroid' (centre point) of an area. Their published investigative method related to the exact region of interest as for this project, and the necessary equipment was readily available, in contrast to other considered techniques such as image-based scanning or serial histological sectioning.

The present study therefore followed the principles of the Chepla, Goitz and Fowler (2015) methods, but with standardised or enhanced processes in order to try to further increase accuracy and objectivity. Timings of the steps to generate the footprint required optimisation as they did not describe the length of time that the FDP-DP sample was exposed to methylene blue, or the drying time that elapsed between excising the tendon and photographing the bone. Imaging software was used to take all measurements of the FDP insertion and tendon, extending their use of the modality from footprint surface area and centroid only. A more representative insight into the causal effect of finger, gender type and side on all measurements in the chapter was also explored through statistical models accounting for the non-independence of fingers from the same cadaver, improving on the inappropriate tests in their study that ignored pseudo-replication.

2.6.1.2 Tendon-Bone Interface Model Design

2.6.1.2.1 Shape

The inking methodology generated a yellow-beige insertion footprint of unstained thin cortical bone, contrasting against the surrounding dark methylene blue stain (**Figure 2.7**). An initial endeavour to objectively analyse the lighter insertion shape was attempted in ImageJ software by thresholding light/dark pixels through a validated

algorithm to generate a binary computerised shape, such as devised by Jones *et al* (2016). Despite the emphasis on maintaining the same camera settings, thresholding recognised lighting reflections on the varied surface topography on the DP as light pixels, even in the stained areas, so the technique could not be standardised across images and was abandoned. The next best approach was to manually trace around the lighter insertion area, producing the binary 'mask' shape (**Figure 2.7**). This established a clear image from which the shape could be analysed and measurements taken.

The FDP insertion footprint was, roughly but reliably, a trapezoid shape. Initial dissections, inkings and mask images revealed an insertion shape with a relatively flat, horizontal base, tapering distally through roughly symmetrical sloping sides. The roof of the insertion shape formed an apex, which was either flat or more rounded. It was therefore decided to consistently approach the shape as a trapezoid, standardising dimension measurements to an averaged trapezoid shape. The maximum width measurement was taken as the base width, since although it may not have always encompassed the most proximal (lowest) edge of the footprint, the maximum width was of most morphological interest and always lay in the base region. The horizontal apex width was measured between the points where the tapering oblique sides of the trapezoid made a final discrete horizontal turn towards the midline at the distal (highest) region of the shape. Height was averaged from maximum height of the entire shape and at the midpoint of the shape, to account for any discrepancy in the maximum (base) width not lying at the most proximal point of the shape, and the apex measurement not encompassing the most distal tip. Similarly, to register the internal angles of the ideal average trapezoid, the internal angles of 2 trapezoids were measured and averaged: a 'maximum' trapezoid from apex measurement to lowest point of the shape, and a 'minimum' trapezoid to the highest possible point considered a base (where the widest point of the shape intersected the perimeter box). Through these means, the most average representation of a trapezoidal footprint shape could be constructed.

Establishing a consistent shape as the tendon-bone interface was an important design step for the tissue engineered model. The interface represents the attachment area of a tendon analogue to a bone anchor in the model, and as such reflects the shape of the bone anchor itself. Although footprint surface area was an important

measurement helping to dictate size of the overall interface and model (see *Section 2.6.4*), obtaining standardised exterior measurements to scale the dimensions of a fixed shape was more comparable between footprints and practical for design. Initially, unsuccessful attempts were made to merge all of the binary mask images into one single average image with analysis software to dictate the interface shape. This shape would have had highly irregular borders and would still have required manipulation to achieve a practical design, most likely still best matched geometrically to a trapezoid. Although a triangle was considered, with the shape tapering to a single point, a trapezoid was judged as the most representative shape due to a discrete roof at the highest point of the shape in the majority of cases. In repair of an avulsed tendon, the shape of the FDP attachment may even be more critical than its position, due to differential loading across the DIPJ (Chepla, Goitz and Fowler, 2015). Re-creating a trapezoidal insertion shape in tendon-bone fixation is therefore also an important surgical consideration (see *Section 2.6.3.3*).

2.6.1.2.2 Dimensions

Morphometric measurements set out to provide accurate mean values of the dimensions of the FDP insertion trapezoid shape to guide the size of the tendon-bone interface for the model. The effect of gender, finger and side was tested to identify any important differences in levels of these factors that might inform diversity in the model design. These factors were deemed the most clinically relevant from the available data provided with the cadaveric specimens, for example in matching a specific model size to a particular injured finger. Side had a negligible effect on all dimensions (**Table 2.15**), however gender and finger did influence mean values.

Surface area measurements (**Table 2.3, Figure 2.8**) provided a useful overall gauge of size patterns, but were not directive of the trapezoid model design dimensions. They anticipated and amplified the size patterns and relationships between gender and finger types subsequently shown more subtly in the directive dimensional measurements. The little finger was the smallest finger and was significantly smaller than other fingers, whilst the middle finger was the largest. Index and ring fingers had similar measurements, which were closer in value to middle fingers than little fingers. Overall female fingers were smaller than male fingers, which for surface area was by approximately one-third of male size. All significant differences in surface area found through multiple comparisons of individuals fingers involved the little finger,

suggesting that of any data category (level of any factor) the little finger may be the most important influence on size differentiation. These findings were not unexpected, with measurement discrepancies corresponding to gross observation of the size or length of fingers in an average hand.

Height measurements (**Table 2.4, Figure 2.9**) showed a very similar arrangement of values and significant differences as surface area. The exception was that the female middle finger was not the largest female finger, although only by an insubstantial 0.09mm from the most sizeable finger (ring), and still within its own SEM. Mean values for index, middle and ring fingers for either gender all in fact occurred within the boundaries of each other's SEM, suggesting they are indistinguishable. The significantly smaller comparative height of the little finger to other fingers in each gender meant that the male little finger was similar in height to the female index, middle and ring, while the female little finger appeared relatively isolated from all other finger heights.

Base width measurements (**Table 2.5, Figure 2.10**) showed the same pattern of mean measurement values as surface area. Mean values between fingers and genders were however closer, leading to a reduced number of significant difference comparisons, although when present the majority involved the little finger as expected. Changes in base width size between fingers and genders may therefore have less of an influence on overall insertion surface area than height.

Apex width measurements (**Table 2.6, Figure 2.11**) did not follow the usual pattern or comparative relationships. Indeed, no clear pattern was evident. For combined genders, middle fingers had the widest apices, although this was principally due to the magnitude of the female middle finger (0.69mm greater than the male counterpart, non-significant). Error bars were the widest of any of the FDP footprint measurements, showing that apex width mean values were the least precise. However, an average width of 1.60mm distinguished the insertion shape as trapezoidal rather than triangular. Unlike the surface area, height, and base width measurements, apex width of the insertion trapezoid did not appear related to the general gross size of a finger, and showed no appreciable differences between genders or fingers.

The apex measurement also allowed the investigation of the internal angles of the trapezoid (**Table 2.7, Figure 2.12**). As per the surface area measurements these were not directive of the trapezoid model design dimensions, but they helped define the trapezoid shape. Left and right sided angles at the base and apex of the trapezoid were very similar and within a narrow range of values, confirming that a simple symmetrical shape design about a vertical axis was appropriate and representative.

Height and base width of the FDP footprint were also measured by Chepla, Goitz and Fowler (2015), with a greater height of 0.7mm and narrower base width of 0.7mm for overall combined finger and gender means. Their range of values for both dimensions for individual fingers across genders were all approximately within 1mm of the values recorded in this study, and in surgical scale terms these are of limited disparity. Small discrepancies between the studies may have been due to their use of calipers to record measurements rather than image analysis software, and non-standardisation of the timings involved in the generation of their footprints. Their study primarily used morphometric footprint measurements to infer the position of the FDP insertion relative to the DP for reattachment surgery, and so further discussion of this study follows in *Section 2.6.1.3*.

In summary, the FDP footprint measurements described a symmetrical trapezoidal tendon-bone interface shape whose overall surface area, height and base width were influenced by gender or different fingers. To translate these findings into the bone anchor design of a clinically relevant model, both tendon width data (*Section 2.6.2*) and bone depth data (*Section 2.6.3*) required similar analysis before an overall design guide for the model components could be devised (*Section 2.6.4*).

2.6.1.3 Surgical Positioning

The FDP tendon insertion position on the DP is an important anatomical feature that influences the biomechanics of the muscle-tendon-bone unit across the DIPJ (see *Sections 1.2.3.5 and 1.3.6.1.3*). After avulsion injury, surgical restoration of the insertion to its original native position avoids flexion contracture and quadriga (too distal a reinsertion) and reduced flexion power and active arc of motion (too proximal). As well as primary tendon-bone repair, this also applies to inseting a graft, either as autografted tendon or potentially as a tissue engineered tendon-bone interface graft. Although an *in vitro* tendon-bone model includes a 'bone' component, it is still

essential to know where to affix the model 'bone' in relation to the native DP bone in order to re-establish the original location of the tendon-bone interface and moment arm across the DIPJ.

The DP dimensions of surface area, height and base width were measured by image analysis (**Table 2.8**) after thorough removal of soft tissue from the DP by sharp dissection, inking, FDP excision and photography. These dimensions were used to calculate the position of the FDP insertion in relation to the DP, as a ratio of each dimension (**Table 2.9**). This followed an initiative by Chepla, Goitz and Fowler (2015) (for surface area and height) to control for the varying dimensions of the DP, attempting to establish an overall surgical guide for re-insertion positioning in any finger. The same study's concept was followed to investigate specific fingers and genders in their distances from the DIPJ (base, or most proximal point, of the DP) to the FDP footprint base or footprint centre point ('centroid') (**Table 2.10**). Combining and distilling data from these different perspectives aimed to provide surgeons with the most relevant and practical information to correctly reposition the insertion, working in measurement units applicable to surgical practice.

From the present results, the general surgical aim is to create an FDP insertion surface area of 20-25% of the total surface area of the flexor surface of the DP. The design of the tendon-bone interface surface area for a clinically-applicable model should also lie within these limits. The height of the centre of the insertion should be 25-30% distally along the DP, closer to 25% for males and 30% for females. The base width of the insertion should occupy 75-80% of the maximum base width of the DP, which also pertains to the pre-determined base width of the tendon-bone interface in a clinically-applicable model.

The measurement results of the distance of the FDP insertion from the DIPJ suggested more specific aims that seem best outlined by gender. For males, the distance from insertion base to the DIPJ should be approximately 3mm, and from the insertion centre approximately 6mm. For females, the approximate equivalent distances should be 2mm and 4-5mm. Different fingers also evidently had an influence on distances from the DIPJ, highlighted by a number of significant differences between them. In practical terms it may be appropriate to more simply consider the approximate values for male and female distances as the average over

a range from larger middle finger distances to smaller little finger distances. The finding that these distances from the DIPJ were roughly 1mm less for females is in line with data suggesting that the insertion trapezoid height was roughly 6mm for male and 5mm for females (**Table 2.4**), and the base width roughly 9mm for males and 8mm for females (**Table 2.5**). Thus the most clinically relevant distances when re-inserting the FDP tendon, that of insertion size and particularly position on the DP, have a useful general distinction of 1mm difference in magnitude between males and females.

These results showed both conformity and inconsistencies with those of Chepla, Goitz and Fowler (2015), who used the same general methods and organisation of data. Surface area % of the footprint on the DP was in general agreement at 20%. Their lower mean range of values (17-22%, compared to 20.51-24.13%) was potentially due to the lack of complete soft tissue clearance on their DPs, particularly the lateral interosseous ligaments (**Figure 2.18**). Excess soft tissue increases the flexor surface area of the 'DP' and therefore decreases the relative ratio % of the FDP footprint. They also did not report the timings of their inking and drying stages before photography. Extended time periods may have allowed bleeding of the ink into the footprint before photography, reducing its perceived surface area.

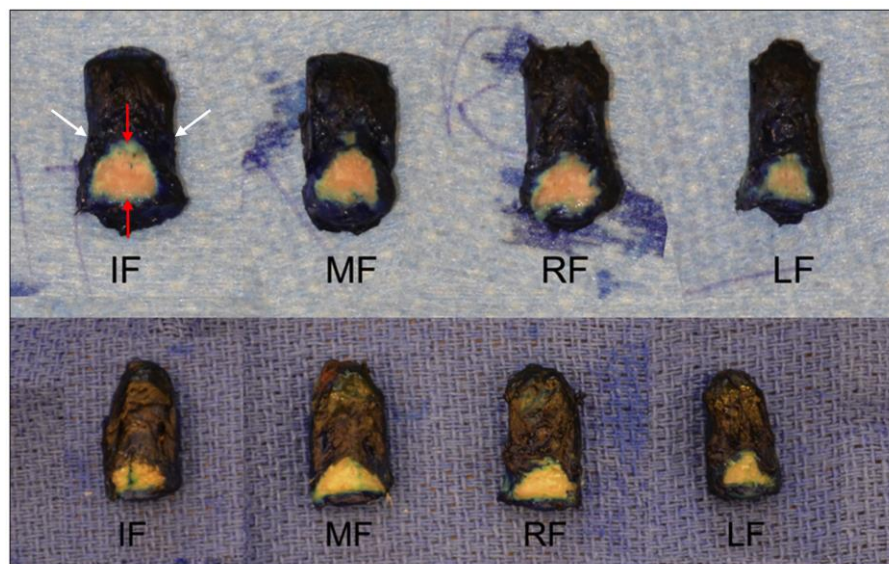


Figure 2.18 | Representative FDP Footprints from Equivalent Study

Figure as previously published by Chepla, Goitz and Fowler (2015), with additional arrow annotations, showing flexor view of full set of DPs from a single human cadaveric specimen. Unstained FDP footprints were achieved through the same inking methodology as this project. Compare with **Figure 2.7**. Not all soft tissue has been removed, especially in the region of the lateral interosseous ligaments (*white arrows*). Mild green-coloured bleeding of ink into the unstained footprint is seemingly evident (*red arrows*). Note the small but variable distance between the base of the FDP footprint and the proximal point (base) of the DP. *IF* = index finger; *MF* = middle finger; *RF* = ring finger; *LF* = little finger.

Chepla, Goitz and Fowler's (2015) concluding surgical guidelines proposed positioning the centre of the FDP insertion 4mm from the DIPJ in males and 3mm in females, equivalent to roughly 20% distally along the DP. Corresponding guidelines in this project were up to 2mm greater and 5-10% more distal. A similar discrepancy was found in measurements of FDP insertion base from the DIPJ, reporting approximately half the size in distance compared to this project, at a difference of 1-1.5mm in the majority of mean individual finger sizes. As there was relative agreement in the morphometrics of the footprint itself (*Section 2.6.1.2*), these comparative differences in footprint position imply that the main discrepancy was the distance between the DIPJ (base of the DP) and FDP insertion base, which also then impacted upon the distance to the centre point. Comparison of **Figure 2.7** and **Figure 2.18** indicates a generally larger bony length over the DIPJ-FDP insertion base distance in the current study. This may be explained by the older age of the cadaveric specimens used in this project (mean age 82.2, range 65-95; compared to a mean of 54, range 43-64), possibly presenting with a variable lip of DP osteophytic growth over the flexor surface of the DIPJ from mild degenerative osteoarthritis. The DIPJ articular cartilage in these specimens was however noted to be grossly intact. For guidelines on positioning of the FDP insertion it is therefore perhaps prudent to appreciate that position relative to the proximal point of the DP, labelled in both studies as the 'DIPJ' for ease of description, may elongate in an older population. The insertion should however remain the same distance from the axis of rotation of the DIPJ (moment arm unchanged). During surgery the proximal point of the DP is not visible in health, being covered by the volar plate on the flexor surface and the collateral ligaments of the joint capsule laterally. The joint line may nevertheless be palpated and so guidelines regarding distances from the DIPJ may still be of practical value for both primary re-insertion and placement of a tendon-bone interface graft.

2.6.1.4 Validity and Reliability

General limitations of the collected studies in this chapter, concerning the sample, dissection methods and 2D measurements, are discussed in *Section 2.6.5*.

The inking technique of Chepla, Goitz and Fowler (2015) was regarded as an effective method to observe the FDP insertion shape. It was considered a truer representation of the insertion than drawing or point marking on the bone around the tendon, and more applicable to developing a scanning and analysis method. However it

necessitate destruction of the interface to reveal the footprint, and the technique required optimisation to improve the perceived validity of the generated negative footprint in representing the actual insertion area, as timings of the inking steps were not reported in the referenced study. The length of time that the tendon-bone sample was immersed in the methylene blue ink impacted on the size of the footprint, since the trial of a 90 minute immersion noticeably reduced the unstained area on gross examination after excising the tendon. Presumably the ink had 'bled' through the bony foramina and trabecular spaces and between tendon fascicles to stain the bone surface of the interface beneath the tendon in this time period. This sample was excluded from analysis, however other early trial samples immersed for 5 and 45 minutes (n=9) were included with those of the later standardised timing of 10 seconds (n=38). Although there was concern that the ink in these longer stained samples may have bled into the negative footprint, gross observation of their footprints found them to be similar to the 10 second immersion samples and justified their inclusion. The decrease in study power by reducing samples to 38 from 47 was felt to be more severe than including samples with a confounding factor of immersion time leading to a possible, but grossly imperceptible, alteration in footprint size. Furthermore, early 'bleeding' of the ink into the footprint appeared to manifest as a green colour on the bone surface. These areas were included in the assessment of the footprint surface area since the area was manually outlined at the first perceptible colour change from the dark blue ink (see **Figure 2.3**).

Assessment of the trapezoidal footprint shape and position on the FDP demanded a large number of subjective image analysis measurements. This measurement methodology was therefore checked for reliability in comparison with a 2nd observer, through the intraclass correlation coefficient (ICC) of absolute agreement, as most strict assessment of identical recorded values (**Table 2.11**). Overall reliability of all measurements taken, as a guide to the general methodology, was extremely high. For measurement of each separate dimension, nearly all had excellent or good reliability, however a poor result was achieved for apex width.

The apex width measurement was included to attempt to define the horizontal roof of the trapezoid footprint shape. The point where the obliquely narrowing sides of the footprint discretely turned to form a roof was clearly subjective, attempting a collective description of the variably more rounded or pointed distal tapering. The subjectivity

may have been an influence on the finding of similar apex widths across fingers and genders, and no discernible comparative pattern, in contrast to all other FDP footprint measurements. However it is a dimension that would have been difficult to predict, for example by gross observation of an average set of fingers, and significant differences would have been unexpected. The apex width is a small measurement between 1-2mm and has a limited impact on discernible scale for surgery or relevant model design. If the 2nd observer's measurements were used to calculate the definitive model design guide at the end of the chapter (**Table 2.17**, *Section 2.6.4*) the apex widths for each size would still be within two-thirds of a millimetre. Since the apex width dimension was important to include in order to define the trapezoid shape and bone anchor design, although having a limited effect on size scale, no readjustments or reassessments were made on this particular measurement despite its unreliability.

2.6.2 Tendon Width

2.6.2.1 Methodology Rationale

Cadaveric finger dissection to expose the FDP insertion allowed an appreciation of the tendon morphology along the distal two-thirds of the flexor sheath. Cross sectional morphology varied from oval at the distal A2 pulley, flattening to a kidney/biconcave shape around the A4 pulley, finally fanning out to a trapezoidal insertion area on the DP. The structural rearrangement of the gross distal tendon fasciculi into 2 discrete, almost fully separated, halves by a midline longitudinal sulcus agreed with the detailed description of Wilkinson (1953) (see *Section 1.2.3.2*). In establishing their attachment footprint, the 2 halves of the segregated fasciculi on the flexor surface formed the left and right halves of the proximal region of the footprint trapezoid and base, whilst those fasciculi deep to the sulcus provided the distal region and apex.

The changing morphology of the FDP tendon as it approached insertion demonstrated a need to quantify dimensions of a length of tendon proximal to its insertion. Since the length of the soft tissue analogue in the undeveloped soft tissue-bone model was 12mm (Paxton *et al*, 2012a), the 12mm length of the most distal tendon was investigated. This was divided into 4 equal increments to maximise the assessment of change in morphology as the tendon fanned out at its insertion. The 12mm length was found to be the part of the tendon that lay beneath the A5 and C3 pulleys. The

point at 12mm proximal to the insertion base roughly coincided with the middle and deepest point of the grossly-observable median longitudinal sulcus (see **Figure 2.5**).

Since a 12mm length of tendon was selected for model design, the point at 12mm proximal to the insertion base was the crucial measurement for clinical relevance. At this point a potentially implantable tissue engineered tendon-bone graft requires integration with the native tendon. Although the proximal end of a tendon graft is usually weaved into the native tendon, a 12mm length of engineered tendon lying in the distal flexor sheath would require direct end-to-end tenorrhaphy with the native tendon in the C3 pulley region. The engineered tendon would thus require morphological matching with the native tendon to give a smooth transition across the native-engineered tendon ends in the tenorrhaphy, allowing unobstructed glide in the flexor sheath and reduction of adhesions. Tendon width was selected as the most relevant and measurable dimension to guide native and engineered tendon morphology matching. The method of photography and image analysis, as per assessment of the FDP insertion dimensions, was thus again employed to gain the most accurate measurement of width.

2.6.2.2 Tendon Analogue Model Design

As per the tendon-bone interface morphometrics, tendon width measurements aimed to provide a model design guide, and to explore the effect of finger, gender and side differences. Left or right side did not have a substantial influence on mean measurements (**Table 2.15**). Finger and gender differences were significant, with a generally reliable descriptive pattern.

The fanning out of tendon fibres to their insertion is not only portrayed by a shorter tendon width at 12mm proximal to the insertion than at 3mm (or at the insertion base width itself, **Table 2.5**) in all fingers and gender breakdowns, but also by an increasing width between each progressively distal increment measured (i.e. for overall means: 0.39mm (12-9mm proximal from insertion), 0.97mm (9-6mm proximal), 1.11mm (6-3mm proximal) and 1.42mm (3mm proximal-insertion base width)). As a minimum therefore, the tissue engineered model would require a proximal anchorage point for the tendon analogue of smaller width than the bone block base at the tendon-bone interface. Furthermore, the ideal tendon replica should aim to increasingly fan out to the insertion base. An abrupt change of width (i.e. a step) at either end or within the

length of the tendon analogue could present obstruction to smooth glide in the flexor sheath. Unless the tendon analogue naturally assumes the desired fanning out shape, it may require manipulation at some or all of the 3mm incremental points towards its bony insertion to match the native morphology.

Finger and gender clearly influenced the magnitude of tendon width, as shown by the large number of significant multiple comparisons (**Figures 2.13** and **Figure 2.14**), and should be acknowledged in designing a model relevant for different male and female fingers. The most helpful approach to evaluating finger and gender effects was to initially consider the graphical data patterns, then the importance of the differences within these patterns could be assessed through the presence or level of significant differences.

The pattern of tendon width magnitude for fingers is reliably middle>index>ring>little. This varies slightly compared to FDP insertion morphometrics, where mean values for index and ring are extremely similar. Although this pattern of tendon widths might be partially expected by simple correlation with grossly observed average widths of entire fingers on a typical hand, the index and ring appear grossly similar. To explain the discrepancy in tendon width, it may be that the index finger tendon has undergone slight hypertrophy due to its comparative freedom compared to the ring finger, which is anatomically restrained by bipennate lumbricals on both sides (Lunn and Lamb, 1984; Bachoura, Ferikes and Lubahn, 2017), by juncturae tendinae, particularly limiting MCPJ movement (Leddy and Packer, 1977) and also by being lodged between the middle and little finger muscles in a shared muscle belly (Gunter, 1960). The extensor indicis also provides the index with greater power and range of movement which may demand more service of the index FDP over the ring (and other fingers') FDP. Despite a consistent difference in mean values however, there were no actual significant differences between index and ring finger tendon widths in gender or finger breakdowns. Similarly, the middle finger was consistently the widest tendon, but it very rarely showed any significant difference to the index or ring fingers. The most isolated finger in the finger patterns was the little finger, which was significantly different from all other fingers at all points of measurement in both genders (bar one: 12mm proximal to the insertion in females, compared to the ring finger, but it was still the smallest width) (**Figure 2.13**). The importance of the significantly narrower width of the little finger was underlined in the comparison of individual fingers amongst both

genders (**Figure 2.14**). The female little finger was the only female finger significantly smaller than male fingers. However, it was never significantly smaller than the male little finger, although it was always of a smaller mean value. The little finger may therefore require particular consideration in the sizing of a clinically-relevant tissue engineered model.

2.6.2.3 Validity and Reliability

Tendon width was perceived as the most valid and useful dimension readily measurable to describe the changing morphology of the tendon close to its insertion. As a design guide for a 3D model, 3D measurements would likely have provided more descriptive information, particularly as the cross sectional shape was observed to undergo changes along the distal tendon. However, a well-defined 2D measurement such as width was considered to give a more powerful and comparable native tendon data set than attempting to establish a 3D scanning method. Despite the subjectivity involved in taking measurements, reliability of the tendon width method was consistently excellent between 2 observers, over all measurements in total or at each incremental point individually (**Table 2.13**). Accurate incremental measurement points near the insertion were vital to describe the changing tendon morphology, which may have been difficult to achieve with some scanning methods (e.g. ultrasound). Furthermore, 2D assessment of the undeveloped soft tissue-bone model for this project is a viable method to evaluate the maturation and morphology of the engineered tendon/ligament (Paxton *et al*, 2012a). Tendon width measurements can thus be optimally employed as both a design guide and assessment tool to directly compare the native and engineered tendon (see *Chapter 4*). Nevertheless it is acknowledged that tendon width is not a true representation of the 3D morphology.

2.6.3 Bone Depth

2.6.3.1 Methodology Rationale

Dimensions of the DP bone have previously been studied as they are relevant to the placement of bone anchors for FDP insertion repair (Jain *et al*, 2011; Samson and Gupta, 2018; Bond, Rust and Boland, 2019) and headless compression screws for DIPJ arthrodesis (Wyrsh *et al*, 1996; Song *et al*, 2012; Mintalucci *et al*, 2014; Braun, Bogle and Wiesler, 2015; Darrowish, Breneman and Bigger, 2015). The majority of studies measured radiographs, but 3 studies used cadaveric tissue dissection and

digital caliper measurement (Wyrsh *et al*, 1996 Jain *et al*, 2011; Bond, Rust and Boland, 2019). Since human tissue was available in this project, this was deemed preferable to radiographs, allowing live manipulation of the DP for the most accurate plane of measurement. Additionally, in the development of a model design guide, there would be greater association with the FDP insertion and tendon width values, as data collected for bone depth would be from a sample inclusive of the DPs that generated these other morphometric data sets (see **Table 2.1**). Initially, the measurement method of photography and image analysis was trialed as per the previous morphometric data sets; however, as further discussed in *Section 2.6.5.3*, digital caliper measurement was found to be the optimal available method.

Due to the variable width profile of the DP, multiple depth measurements were considered most appropriate to describe bone depth at the FDP insertion. Depths at the proximal and distal insertion points were selected as they were easily discernible by the still attached FDP tendon. Initial samples also suggested that these were an approximation of the deepest dimension (proximal) and narrowest dimension (distal) beneath the tendon insertion (see **Figure 2.6**), providing an effective guide to the range of bone depth and extreme values. A measurement of depth at the mid-height of the FDP insertion was also originally attempted, however this was not deemed sufficiently accurate to judge with calipers, or by calculation as the average depth from combined measurements at the DP base and mid-height DP, as employed by Jain *et al* (2011). The 'average' depth in the present study, calculated here using the values from the proximal and distal insertion depths, was helpful to substantiate the general overall effects of finger and gender, but was not based on a measured data point.

2.6.3.2 Bone Anchor Model Design

Native DP bone depth was assessed to direct the depth design of the tissue engineered bone anchor component. To be surgically relevant as a graft, the bone component needs to integrate with the native bone, unless it is designed as the entire DP itself. Additionally, the bone anchor component needs to provide the interface for fixation to the native bone, perhaps either mechanically by a screw, or chemically by an adhesive compound. These are more advanced engineering considerations. The primary design concern was to be confident of a depth of bone anchor that was shallow enough to sit within the native DP and not sit proud of the native dorsal cortex,

but also deep enough to provide a robust anchorage point for the tendon interface *in vitro* and to allow potential fixation techniques to the native bone *in vivo*.

The effect of gender, finger and side on bone depth were explored as per the previous morphometric data sets to consider how they might affect the model design. The larger data pool here (twice the size of that for tendon-bone interface morphometrics) brought more study power and confidence in mean values, and so a large number of significant differences became apparent. As such, the effect of side was more evident for bone depth (**Table 2.15**). Right and left differences were significant at all 3 depths assessed in males, but not in females. Although an unusual finding, this could perhaps be explained by slight bony hypertrophy from greater lifetime manual activity in males, focused then on their dominant hand. The middle finger may also present this significant effect of side as, being the largest DP overall (see **Table 2.8**), it may undergo the largest dimension changes as a result of hypertrophy. This is however very speculative and cannot be matched to data on cadaveric donor hand dominance (unavailable), or indeed to occupation, which does not allude to a manual bias in either gender (see **Table 2.1**). Where side difference was significant, the difference was only of less than 0.5mm, which may be too small for practical or clinical relevance.

Gender and finger type also significantly influenced depth and, as with tendon width data, ascertaining the consistent patterns was most insightful. Females were smaller than males at the consistently smaller distal measurement point, and also according to the average measurement (see **Figure 2.15**). The lack of significant difference at the proximal point may be due to females being at greater risk of osteoarthritis and presenting with bony osteophytes near the DIPJ, potentially increasing some or all proximal depth measurements (see *Section 2.6.3.4*). The overall finger pattern of middle>index>ring>little was as seen for tendon width measurements, and similarly the little finger was the most influential in significant comparisons. From the average and distal measurements, the female little finger was significantly smaller than all other fingers across either gender, except for the male little. The male little finger was significantly smaller than all other male fingers, but not significantly smaller than any female fingers.

An engineered bone anchor component of roughly 50% of the depth of the native bone was deemed a reasonable initial estimate to balance the requirements of leaving

enough native bone for potential graft fixation and maintaining a sturdy 'platform' for the tendon interface. Yet with a suitable depth of bone anchor platform established, this could potentially then be applied to any individual finger of any gender, affecting the depth of the remaining native bone only. Since side may also have a very slight effect on depth, a standard bone anchor depth for all fingers would also prevent the impractical doubling of models specific to right and left sides. The smallest bone depth dimensions therefore provided the key directing measurements. Female fingers at the distal point of the FDP insertion had the narrowest dimensions, averaging 3.99mm over all fingers (**Table 2.14**). 50% of this distance is roughly 2mm, which was regarded as a convenient depth of bone anchor, large enough to provide a solid platform for the interface of a model relevant to any individual finger. Since the female little finger had the smallest depth (3.48mm, distally), and was the only dimension substantially smaller than the average dimension of 3.99mm, it was considered whether an approximate 1.5mm was enough remaining native dorsal bone in this particular finger. Although small, this would however be a minimum value at only the distal FDP insertion edge, as the posterior flaring of the bone beneath the insertion provides an ever-increasing bone depth moving proximally, with 3.23mm of native bone remaining in this female little finger by the proximal point of insertion (at 5.23mm depth, see **Table 2.14**). Across the whole length of the insertion this was therefore regarded as enough surrounding native dorsal bone for stability and potential fixation, and the standard bone anchor depth for the model of 2mm was thus decided.

2.6.3.3 Surgical Bone Anchor Fixation

The amount of available native DP bone is surgically significant for the correct anatomical repositioning of an avulsed FDP tendon. Many surgeons prefer the simple bone anchor for repair, over the more complex all inside suture/wire internal fixation techniques or the infection risk of the pull-out button suture (see *Section 1.3.6.1*). Ideally the bone anchor is placed at a 45° retrograde angle for the greatest resistance to anchor pull-out (Schreuder *et al*, 2006), based on the 'deadman theory' of stabilisation first applied to rotator cuff anchorage (Burkhart, 1995). This also reduces the risk of dorsal bone cortex penetration from an anchor placed perpendicularly to the insertion surface. Indeed, the greatest depth of bone beneath the FDP insertion to accommodate an anchor was found to be at the proximal point of the insertion, retrograde to the centre of insertion, in the current project. However, the DP remains a small bony compartment into which to place a bone anchor originally designed for

large soft tissue avulsions such as the rotator cuff. Too long a bone anchor risks dorsal cortex penetration with perpendicular insertion but also DIPJ penetration with retrograde insertion. To account for this a surgeon may place a perpendicular bone anchor too proximally, or a retrograde anchor too distally (Chepla, Goitz and Fowler, 2015), upsetting the original biomechanics across the DIPJ and causing reduced flexion power or flexion contracture, respectively. These surgical concerns highlight the importance of the FDP insertion position, also applicable to relevant tissue engineering design and implantation as an interface graft.

Surgical interest in DP dimensions allows comparison of the bone depth measurements recorded here to other published studies using cadaveric dissection and caliper measurements, as a gauge of reliability. Jain *et al* (2011) measured bone depth (unknown sample age) at the mid-height of the FDP insertion, calculated by the average of the depth at the base of the DP and at the mid-height of the DP. Although not the exact same measurement points used to calculate the 'average depth' in this project, they are similar approximations and mean values of each finger for combined genders are within 0.25mm between the studies. Bond, Rust and Boland (2019) measured bone depth (mean age 88) at the 'widest (deepest), most proximal point', which is a similar, but more proximal, measurement point to the depth at proximal point of FDP insertion in this project. Due to the observation of the DP flaring out proximally, their study's results for finger means for combined genders are all expectedly larger than the proximal insertion depth in this project, but are all within 0.55mm. Both these studies relate DP bone depth to insertion of perpendicular bone anchors: the Mitek 'micro' (length 3.7mm) and 'mini' (length 5.4mm), which both require pre-drilling with a 5mm long drill bit. In the current study, the 5mm drill bit would penetrate the calculated average depth of little fingers (agreeing with both studies) and the female ring (additionally agreeing with Jain *et al*, 2011) (all <5mm), and the only perpendicular depth that would not seat the micro anchor without dorsal cortex penetration would be the female little finger (<3.7mm, although specifically at the distal point of FDP insertion) (agreeing with both studies) (see **Table 2.14**). Overall therefore, these studies provide a similar descriptive picture of DP bone depth to that presented here.

In radiological comparison, Samson and Gupta (2018) measured lateral radiographs (patient ages unknown) to find the deepest DP measurement beneath the FDP

insertion, based on the position of the radiolucent FDP insertion as reported by Chepla, Goitz and Fowler (2015). The deepest measurement beneath the FDP insertion for the current study was the proximal measurement point, which measured up to 0.75mm greater for each combined gender finger mean compared to their study. Although well within a millimetre, the greater measurement discrepancy with this study could be due to greater age and potential osteophytic growth, enlarging the proximal measurements, in the current study (discussed further in *Section 2.6.3.4*), and the use of radiographs and software measurement compared to cadaveric material and calipers.

Many authors recommend the use of 2 side-by-side bone anchors (McCallister *et al*, 2006; Lee *et al*, 2011; Ruchelsman *et al*, 2011) due to the extra strength in fixation over a single anchor (Brustein *et al*, 2001). Moreover, Chepla, Goitz and Fowler (2015) recommend 2 anchors in order to recreate the anatomical width of the FDP insertion footprint. Such recreation of the footprint base requires anchor insertion at the proximal point of the FDP insertion. At this insertion point, the results in the current study recommend micro anchors, as the longer mini anchors placed perpendicularly would penetrate the dorsal cortex in female little fingers (<5.4mm) and risk DIPJ penetration in retrograde placement. The 1.3mm diameter of the micro anchor (Jain *et al*, 2011) suggests that 2 side-by-side anchors are well within the base width dimensions of the DP [smallest width 8.97mm (female little finger), see **Table 2.8**], even when the flanges are deployed. For optimal recreation of the trapezoidal footprint shape of the FDP insertion, a further single point of midline fixation could then be employed distal to the bone anchors, such as a pull-out button (**Figure 2.19**).

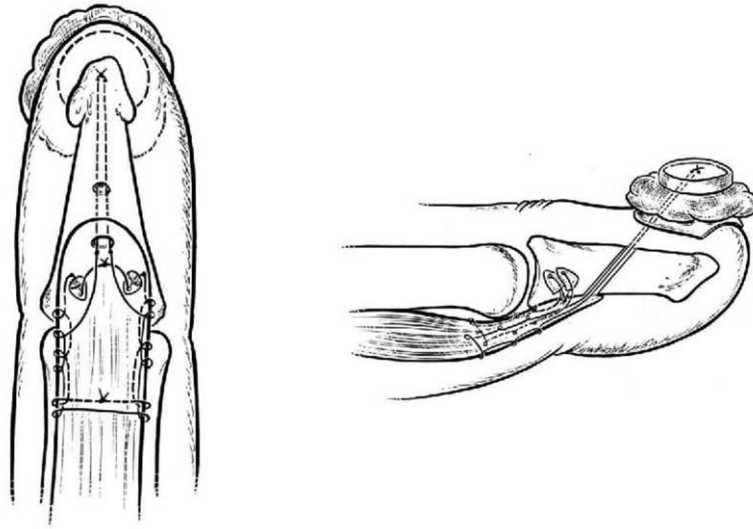


Figure 2.19 | Combination FDP Fixation Technique for Optimal Footprint Recreation

Figure from Ruchelsman *et al* (2011) depicting 2 side-by-side retrograde micro bone anchors with a distal dorsal pull-out button suture in flexor view (*left*) and lateral view (*right*). As well as providing a reinforced repair with protection against gapping at the tendon-bone interface, data from this chapter suggests that this may be the optimal technique to recreate the original trapezoidal shape of the FDP insertion. The 2 bone anchors provide the width of the FDP insertion base, whilst the pull-out button draws the insertion up to an apex, creating an overall trapezoid shape. The 3 points of fixation also correspond to the 3 discrete groupings of tendon fibres that form the insertion footprint; 2 forming the left and right halves of the insertion base and the 3rd forming the midline apex, as described in *Section 2.6.2.1*.

2.6.3.4 Validity and Reliability

No inter-observer comparison was performed to test the reliability of bone depth measurements. It was judged that the larger data pool for bone depth assessment, compared to the previous morphometric measurement data sets that did test inter-observer reliability, may help to reduce any inaccuracy of measurements through the resulting mean values. The presence of observer bias however cannot be checked. The limitation of measuring a 3D surface through 2D means, particularly relevant here to bone depth measurements, is discussed with the general limitations of this chapter in *Section 2.6.5.3*.

Bone depth measured at the proximal point of the FDP insertion was close to the DIPJ. As such, osteophytic growth from mild degenerative joint disease may have existed, as noted on the flexor surface in a potential increase in distance between DIPJ and FDP insertion base (see *Section 2.6.1.3*). This may have also increased the distance of the proximal bone depth measurement, particularly by excess bone posteriorly. This may also account for why proximal measurements are less consistent

than distal measurements (greater SEMs). Proximal depth measurements are therefore most valid to the age range of the sample (65-90). However, the proximal measurement point is always the deepest dimension of bone at the FDP insertion, and both the model design guide and surgical bone anchor fixation are concerned with how narrow the bone may be. The narrower measurement at the distal point of insertion is more consistent and unlikely to have substantially changed with age and therefore the model design and surgical guidelines presented here, based on this distal measurement, should be valid across all skeletally mature age ranges.

2.6.4 Overall Model Design

The aim of this chapter was to analyse the morphology of the native human FDP insertion and translate this into the design of an anatomically and clinically relevant tissue engineered model. Pertinent gross structural components and arrangements were analysed – the FDP-DP interface, FDP tendon, and DP bone – to inform the construction of a multi-tissue 3D model that could potentially be implanted as a composite surgical graft, or used as a standalone morphological replica for investigating and improving repair techniques. A wealth of data was collected and the particular effects of finger, gender and side, as pre-selected factors of interest, were explored to investigate whether levels of these factors were important to inform different model categories. The data now required assimilation into a practical and representative guide for the next stage of the project.

Finger and gender type had significant influences on the mean morphometric values of all data sets, whilst the effect of side was small overall. The design of 8 models for index, middle, ring and little fingers in both male and female varieties would not however be pragmatic or cost effective. Furthermore, the various dimensions for these models based on mean values would differ in most cases by fractions of millimetres beyond practical relevance to even magnified hand surgery. Yet a single design, although useful as a basic average model, most relevant for investigating and improving FDP avulsion repair techniques, would limit its surgical application as a potential graft by providing a poor size match to the larger or smaller finger and gender groups revealed in the data. The data was therefore reviewed to identify the main patterns signifying the presence of potential major size groupings and discrepancies, in order to find a balance of practicality and relevance for the model design.

For FDP footprint morphometrics, the surface area of the footprint provides an insightful guide to overall size as it contains the largest values and spread of data. Visual appraisal of graphical data of individual fingers separated by finger and gender (**Figure 2.8c**) suggests a cluster of mean values in 3 groupings: male index, middle and ring fingers; male little and female index, middle and ring fingers; and female little finger. This is reinforced by the little finger being the only finger to show significant difference to other fingers within each gender. The pattern is similar for FDP footprint height (**Figure 2.9c**) and base width (**Figure 2.10c**). Furthermore the pattern is repeated for tendon width values at all points proximal to the FDP insertion (**Figure 2.14a-e**). Analysis of the many significant differences present in the FDP footprint data and tendon width data pinpointed the little finger as the most significantly different in multiple comparisons to other fingers, which supports its position in a lower size grouping to the other fingers (see *Section 2.6.1.2.2* and *Section 2.6.2.2*, respectively). Although the middle finger was the largest in all dimensions (except for female tendon width at 12mm proximal to the FDP insertion) it was very rarely significantly larger than any other finger besides the little finger, supporting its grouping with index and ring fingers within the same gender. Bone depth data showed a tendency to a similar pattern, although it was not as clear (**Figure 2.16a-c**).

After recognition of these data cluster observations, the data was then categorised and separated into the 3 group levels to generate amalgamated mean values and new differential comparisons (**Figure 2.17** and **Table 2.16**). Although apex width of the FDP footprint did not follow the pattern of 3 cluster groupings, it was included in the data re-arrangement for consistency with the other dimensions. Highly significant differences were apparent between all 3 groupings, with a wide spread of mean values. Differences in size dimensions were around 1mm, which was considered of surgical and tissue engineering design significance, in comparison to fractions of millimetres. These groupings therefore satisfied a division of the data that was most disparate but remained both practical and relevant to potential clinical use. The groups were thus labelled 'large' (male index, middle and ring finger), 'medium' (male little and female index, middle and ring finger), and 'small' (female little finger) as different size categories for design of the model.

Although pre-selected factors, particularly finger and gender, were tested to analyse their specific influence on mean measurement variables as the basis for describing

and differentiating the data set, an alternative approach could have been to explore the total data variation. A greater focus on the spread of data for each measurement variable may have better determined the need for multiple model sizes rather than categorisation based on finger and gender groupings alone. This may have been particularly worthwhile with a larger data set, but, for the current sample, testing of specific factors thought most influential to size was chosen as the analysis approach.

The majority of data within this chapter concerned the design of the bone anchor. The FDP-DP interface was trapezoidal, and this should represent the area of attachment of the engineered tendon analogue onto the bone anchor. A bone anchor design larger than the tendon attachment area was considered, however it was predicted that it would be easier to engineer a tendon analogue to attach to an entire area, rather than partial area, of bone anchor. Thus the dimensions determining the trapezoidal interface shape (height, base width and apex width) provide the 2D attachment surface dimensions of the bone anchor. Bone anchor depth was established at 2mm for all model sizes, as described in *Section 2.6.3.2*. In addition, the pattern of 3 mean value clusters within data separated by finger and gender was not as well defined for bone depth as for FDP footprint and tendon width data, and since side appeared to have some effect on bone depth, a single value was most appropriate.

An ultimate design guide based on the 3 size categories could now be prepared for the tissue engineering stage (**Table 2.17**). This would allow set up of the 2 anchor points between which the tendon analogue would form. At one point is the bone anchor with a 3D shape representative of the FDP insertion area and applicable to the depth of the native bone, with the proximal anchorage point (such as the length of suture employed by Paxton *et al*, 2012a) at a 12mm distance, aiming to establish a tendon analogue width matching the native tendon.

Table 2.17 | Component Design Guide for Tissue Engineered Model

Dimensions for construction of 3D trapezoidal bone anchor and tendon analogue width (anchor) at 12mm from bone anchor. 3 main size categories are most clinically relevant: 'large', 'medium', and 'small'. *Universal* size is the overall mean of all fingers and genders combined, as a guide to a single basic model. See **Table 2.16** and **Figure 2.17** for selected data. EM mean. As with all data in this chapter, mean values are calculated through statistical modelling (see **Table 2.2**), with slight adjustment but close proximity to raw means (see *Appendix 2*).

Model Design Guide (mm)					
	Bone Anchor				Tendon Width at 12mm
	Height	Base Width	Apex Width	Depth	
Large	6.36	9.30	1.66	2.00	5.38
Medium	5.05	8.30	1.56	2.00	4.39
Small	4.33	7.57	1.65	2.00	3.68
<i>Universal</i>	5.45	8.58	1.60	2.00	4.69

2.6.5 General Limitations

This chapter attempted to obtain living population morphometric values from a sample of cadaveric material, to represent the native FDP-DP tendon-bone insertion and infer the effects of finger, gender and side on size differences. A number of limitations were therefore inherent in the sample, and general dissection and measurement methodologies, which must be considered when interpreting the results.

2.6.5.1 Sample

The analysis of human tissue was integral to the clinical-relevance of a tissue engineered model. The most appropriate source of precious human tissue for research purposes was cadaveric tissue from the university anatomy department. The sample was therefore necessarily one of convenience from the available donated and research-appropriate material. A formal power calculation for each morphological study was not performed, however a number of factors were considered in the experimental design to maximise the power of the studies. Reasonable sample size was determined through review of similar morphological cadaveric studies with significant inferential statistics on the FDP insertion or DP dimensions. Sample number used in these studies was 40 (Chepla, Goitz and Fowler, 2015), 36 (Leversedge et al, 2002) and 32 (Bond, Rust and Boland, 2019). The sample number in each of the present morphological studies was 48 (FDP insertion), 64 (tendon width) and 96 (bone depth), with greater sample numbers helping to account for the

loss of power factored into the statistical mixed effects models that adjusted for the non-independence of samples. However, since the mixed effects models allowed non-independent samples, all fingers from one cadaver could be used to maximise samples, rather than limiting to one finger from one cadaver. Attempts to limit random variation were also made in standardising experimental techniques (e.g. inking methodology timings for FDP footprint) and material (e.g. aiming to match sample number from each gender). Despite this, a greater number of samples would have likely improved the reliability of population traits inferred from the data.

The sample was taken from a Scottish population, and therefore may be more applicable regionally than internationally. Differences in the world-wide population from factors such as race genetics or lifetime levels of manual or physical work may have a slim effect on the morphometrics studied here. Perhaps most importantly, the age range of the cadavers (65-90) is focused in later life. Although FDP avulsion injury is found in older populations, this age range is most likely older than the average age of an injured patient. The size and shape of the FDP insertion and tendon itself seems unlikely to grossly change over time in healthy individuals and this data should translate to younger populations. However some bony change around the DIPJ may be apparent, such as discussed in *Section 2.6.1.3* and *Section 2.6.3.4*. Since bone depth measurements were investigated as a rough guide to depth of the bony model component, rather than a definitive dimension such as at the interface, measurements should still be approximately relevant to a human population. Repetition of the studies on a younger sample population, free of any potential degenerative change, would inform how important a factor age is regarding the morphometrics of the FDP insertion. Moving forward, it should be remembered and acknowledged that the results and design guide produced in this chapter are based on a regional, older population.

Data provided with the cadaveric specimens was limited (see **Table 2.1**). The sample of specimens may have contained levels of other variables that may have inferred stronger correlations or have affected the associations of gender, finger and side described in this chapter. For example, body mass index (BMI) may have a greater influence on morphometrics than gender. Hand dominance may have been associated with side differences. A relevant past surgical history may have led to reduced use of a particular finger or hand with potential atrophy. However, prospective

body donors with extreme BMIs were not suitable for original donation (a local policy of accepting BMIs of 18-25 only) and specimens with obvious external deformities were not selected for the sample, protecting against data skewing from outlying values or confounding factors. A greater sample number would further limit any effect from more subtle confounding factors.

2.6.5.2 Dissection Methodology

The human tissue analysed was cadaveric, and not living, tissue. The material was however fresh frozen, so it was unlikely to have undergone perceptible decomposition or degeneration to distort the gross FDP insertion morphometrics found in life, from either the initial point of freezing soon after death or through the freeze-thaw process. Dissection provided an appreciation of 3D structure, not only of the component tissues for the model but of surrounding topographical relationships and tissue planes, only otherwise possible in surgery. Dissection inherently disturbs the tissue envelope as structures are approached, which may affect some positional relationships such as the natural lie of the FDP tendon. It should not however have affected the measurement variables of insertion position, tendon width or bone depth. The FDP tendon was photographed for width analysis immediately on opening its own tissue envelope, the fibrous flexor sheath. Excision of the DIPJ ligaments and volar plate to free the DP did require some manipulation of the FDP tendon (see **Figure 2.1d-f**), with minor traction potentially avulsing a few insertional tendon fibres at the microscopic level, however tissue handling was always gentle.

Techniques to assess interface component structures without disturbing the surrounding soft tissues were considered, such as ultrasound or MRI for tendon and insertion analyses, and radiographic or CT images to assess bony dimensions. Such techniques or specific image databases were not readily available for living anatomy, and cadaveric tissue necessitated staying on licensed premises. Use of scanners may have been able to generate *in vivo* objective computational morphometric analyses, but these would first have to be validated, for example due to signal noise (Hayes *et al*, 2019), and are unlikely to have allowed the range of measurements achieved through dissection. The ability to maintain a 360° view of the dissected cadaveric tissue was in fact crucial to appreciate the most important measurement dimensions around the interface.

2.6.5.3 Measurement Methodology

The approach to taking morphometric measurements in all of the studies in this chapter was to approximate linear measurements to describe imperfectly straight or even curving surfaces. The rationale and limitations associated with defining the shape and dimensions of the tendon-bone interface using this approach is described in *Section 2.6.1.2*. The macroscopic interface was a relatively 2D surface due to the flexor surface of the DP base being generally flat, however tendon width and bone depth measurements reported 2D measurements of curved 3D structures. 2D measurements can only provide a guide to a structure's dimensions viewed from a single plane. Such analyses have here provided useful clinical measurements and tissue engineering design guides, but bias the focus of attention to the chosen plane rather than characterising the 3D configuration. Although working with cadaveric tissue allowed an appreciation of 3D structure and selection of the most pertinent 2D measurements, the human body is 3D and therefore requires design of 3D tissue engineered models. Where scanning techniques are available, they may provide useful additional 3D information to 2D measurements to enhance model design, particularly in describing shape and cross-sectional area. This is most relevant to the native tendon and engineered tendon in this project, discussed further with the use of optical coherence tomography in *Chapter 4*.

When taking the 2D measurements, subjectivity was required to judge what orientation of the sample was indeed the defined anatomical plane. Although image analysis allowed a greater degree of accuracy in measuring an image (tendon-bone interface and tendon width studies), an important pre-determining factor of representative accuracy of the sample was the camera angle in obtaining a parallel 'flexor surface view'. Indeed the difficulty in determining a reliable lateral view of the curved surface of the DP for bone depth measurements led to the use of calipers over the image analysis method. Although more subjective and limited in analytic scope, calipers allowed interaction with the bone itself rather than with the camera to determine the plane of measurement. Once the correct viewing plane was established, reliable repetition of the plane for each repeat sample was required to obtain the most precise measurement mean. Human judgement error here was unlikely to have had a substantial effect due to a minimal measurement change for a small discrepancy in sample orientation and averaging of repeats. The subjectivity of judging the measurement itself from the image analyses once the plane of view was

set was a potentially more pertinent source of error, addressed in *Section 2.6.1.4* and *Section 2.6.2.3*.

2.7 Summary of Findings

Morphometric assessment of the human FDP insertion revealed a trapezoidal, near triangular, footprint attachment shape between the FDP and DP, of 20-25% surface area and 75-80% base width of the DP flexor surface, positioned 25-30% distally along the DP. This will inform the distinctive trapezoidal shape at the interface of engineered bone anchor and tendon analogue, and ideal surgical positioning of the interface. The distal FDP tendon was composed of 2 major fibre bundles, flaring out over its distal 12mm, with mean widths of 7.16mm, 6.05mm, 5.08mm and 4.69mm, at 3mm, 6mm, 9mm and 12mm, respectively, from the FDP insertion base, as a guide to ideal engineered tendon analogue widths. Bone depth was on average 2mm narrower at the distal point of the FDP insertion compared to the proximal point, averaging 4.20mm distally and 6.20mm proximally, most narrow in female little fingers. The mean depth of the smallest gender (females) at the smallest measurement point (distal insertion) was 3.99mm, suggesting a reasonable future engineered bone anchor depth of 2mm, equating to at least 50% remaining native bone depth even when accounting for these smallest average dimension factors. Gender and finger type highly influenced mean values of insertion footprint dimensions, tendon width and bone depth, whilst side influence was minimal. Morphometric mean values from individual fingers, distinguished by both gender and finger, clustered into 3 distinct data groupings as the basis for 3 clinically relevant size categories in a design guide for the tissue engineered FDP-DP model.

CHAPTER 3

HISTOLOGY OF THE FLEXOR DIGITORUM PROFUNDUS INSERTION

3.1 Chapter Overview

This chapter examines the microscopic anatomy of the flexor digitorum profundus (FDP) insertion onto the distal phalanx (DP) through histology of human cadaveric tissue. A qualitative appraisal of the overall histological features is reported and the angle of inserting tendon fibres across the enthesis is quantified. The results are integrated into the design guide devised in *Chapter 2* to enhance the anatomical reproduction of an *in vitro* tissue engineered FDP-DP tendon-bone model.

3.2 Introduction

The macroscopic exploration of native human FDP insertion anatomy in *Chapter 2* is continued and complemented in this chapter with a microscopic evaluation. The specialised enthesis tissue zones are a particularly fine and detailed example of the form following function principle of the human body, and since the majority of these design features are revealed microscopically, considerable project work was invested into histological study. After reviewing the existing descriptive enthesis literature, both a qualitative and quantitative investigative approach were designed, with histological assessment providing a resourceful and effective method to obtain a data set large enough for inferential statistics as well as novel insights.

A detailed description focusing on the human FDP enthesis is not found in the known literature. The majority of published FDP histology is incidental to a canine FDP model of tendon-bone avulsion, an easy-access site used for studying surgical techniques, tissue changes and repair processes (Ditsios *et al*, 2003a; 2003b; Silva *et al*, 2002, 2006; Boyer *et al*, 2003; Thomopoulos *et al*, 2009), with little description in health. Morphological studies of the human FDP insertion are limited and dissection based, macroscopically (Chepla, Goitz and Fowler, 2015) or microscopically (Leversedge *et al*, 2002). Where human FDP enthesis histology is mentioned, it is part of a broad survey of numerous enthesis sites in the body, assessing specific features. Benjamin *et al* (2004a) noted the presence of fat at the insertional angle of the FDP enthesis, and furthermore suggested that it forms an 'enthesis organ' as the tendon fuses with the volar plate (Benjamin *et al*, 2004b). Benjamin and McGonagle (2007) also perceived that it creates a synovial-enthelial complex, lying adjacent to the distal

interphalangeal joint (DIPJ), in reference to synovial disease. The only remark that the FDP enthesis is fibrocartilaginous is mentioned by Benjamin *et al* (2007), observing that it can be a site of histopathological changes. In the current project, it was therefore worthwhile to provide an overall description of the FDP enthesis based on qualitative histological observations, as the first in depth account of this anatomical region and a reference for the design pinnacle of a tissue engineered replica.

In addition to a general description, it was important to undertake a quantitative investigation with direct relevance to the design of the *in vitro* model. In anticipation of finding a fibrocartilaginous enthesis, measuring the thickness of the uncalcified or calcified fibrocartilage layers was considered. Uncalcified fibrocartilage is associated with a large degree of movement of the inserting tendon fibres (Evans, Benjamin and Pemberton, 1990; Benjamin *et al*, 1991; Benjamin and Ralphs, 1995; 1998), and calcified fibrocartilage thickness appears related to tendon loading on the bone (Evans, Benjamin and Pemberton, 1991; Benjamin *et al*, 1991; Gao and Messner, 1996; Benjamin and Ralphs, 1998). Both layers are often quantified concurrently for insights into the functionality of particular entheses (Benjamin *et al*, 1991; Kumai *et al*, 2002; Toumi *et al*, 2012; 2014; 2016; Shinohara *et al*, 2014; Beaulieu *et al*, 2015; 2016). Although these could have provided interesting insights into the FDP enthesis, tissue engineering any fibrocartilage at the enthesis is an immense challenge, let alone a desired thickness, so effort was focused towards a simpler *in vitro* design feature. The studies of Beaulieu *et al* (2015; 2016) investigated the gross angle of insertion of anterior cruciate ligament (ACL) fibres at the knee, and adapting their methods to the FDP enthesis was thought both reproducible to guide the tendon-bone insertion angle in the model, and also valuable descriptive information to enhance the qualitative observations.

As per *Chapter 2*, the investigations in this chapter are exploratory of FDP enthesis anatomy with reference to the design of a relevant *in vitro* model. A similar approach to the quantitative data analysis was implemented, testing hypotheses of whether a particular gender, finger or side had a significant effect on the angle of tendon fibre insertion onto the bone, using explorative mixed effects models. Furthermore, the size category data groupings developed in the *Chapter 2* design guide were also compared to establish whether significantly different tendon-bone insertion angles were demanded of their *in vitro* designs.

3.3 Aim and Objectives

The aim of the chapter was to investigate the microscopic structure of the human FDP enthesis through histology, to augment the design guide established in *Chapter 2* for an anatomically relevant *in vitro* tendon-bone tissue engineered model.

The objectives were to provide:

- 1) A qualitative descriptive overview of the magnified FDP enthesis;
- 2) A quantitative assessment of the angle of FDP tendon fibres at insertion.

3.4 Materials and Methods

3.4.1 Cadaveric Specimens

Human cadaveric tissue was obtained as detailed in *Chapter 2, Section 2.4.1*. As for the FDP morphology investigations, the sample was one of convenience, however effort was made to balance genders and maximise sample use with all fingers. 48 fingers from 6 cadavers (Specimens 7-12 in *Chapter 2, Table 2.1*) (3 male, 3 female; mean age 79.3, range 73-91) were prepared for histological analyses. 8 thumb samples of the flexor pollicis longus (FPL) insertion from 4 of the 6 cadavers were also prepared for initial optimisation trials of decalcification timings, but not used for analysis.

3.4.2 Sample Preparation

The aim of sample preparation was to excise an en-bloc tissue composite of the FDP tendon and attached distal phalanx (DP) bone, large enough to encompass the entire tendon insertion undisturbed, but small enough for routine histological processing and minimal decalcification treatment. The preliminary dissection steps to expose the FDP and DP are described in *Chapter 2: Section 2.4.2* and **Figure 2.1**. The ensuing method to isolate the FDP-DP tendon-bone sample is described in **Figure 3.1**. As soon as the sample was obtained it was submerged and fixed in 10% neutral buffered formalin (Sigma-Aldrich, Merck Life Science, Gillingham, UK) at 4°C for 48 hours.

FPL-DP tendon-bone samples for initial optimisation trials were isolated in the same manner.

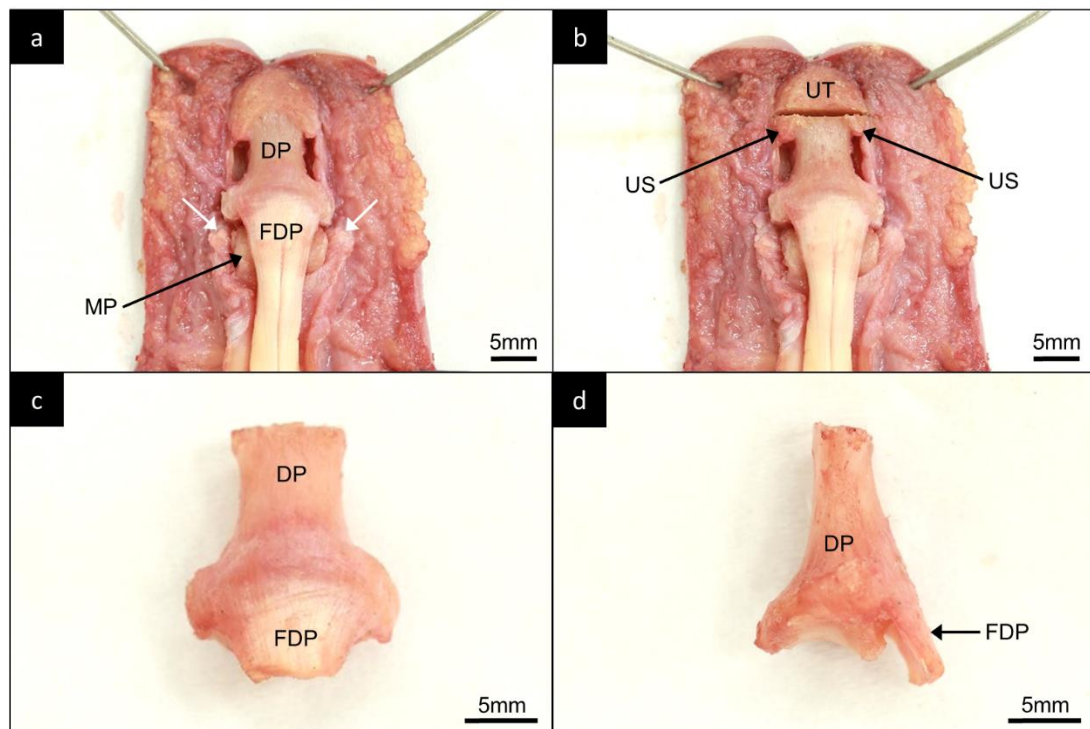


Figure 3.1 | Dissection of Tendon-Bone Histological Sample

a) Exposure of the *FDP* tendon attachment to the *DP*. The skin, subcutaneous tissue envelope and fibrous flexor sheath have been opened in the midline of the flexor surface and retracted. The collateral ligaments (*white arrows*) of the distal interphalangeal joint have been dissected off the *DP*, and the volar plate has been carefully excised, freeing the *DP* from the head of the middle phalanx (*MP*). Superfluous soft tissue surrounding the *DP* has also been dissected away. Flexor view. **b)** The unguis tuberosity (*UT*) of the *DP* is cut horizontally with an electric rotary saw (Dremel, Uxbridge) at the point where the tuberosity meets the shaft at the unguis fossa in the midline. The remaining unguis spines (*US*) are then removed with bone cutting forceps. Flexor view. **c)** Flexor view, and lateral view (**d**), of the excised *FDP-DP* tendon-bone sample after detachment from any residual soft tissues, ready to be fixed for histological processing. The unguis tuberosity is entirely removed and the tendon cut at 5-10mm from the base of its bony insertion, to minimise excess calcified tissue and sample bulk. Male right middle finger.

3.4.3 Decalcification

Decalcification of samples was required for smooth microtome sectioning of the bone and tendon-bone junction, balanced against the risk of over decalcification and loss of tissue detail on staining. Initial methodology investigations with FPL-DP samples trialled 48, 60, 72 and 96 hour decalcifications, with 72 hours providing the optimal timing for both satisfactory sectioning and staining. Samples were decalcified in Decalcifying Solution-Lite (Sigma-Aldrich), an aqueous solution of hydrochloric acid and proprietary compounds, at room temperature.

After formalin fixation, each sample was washed thoroughly with tap water and submerged in 30-40ml of decalcifying solution in a 50ml centrifuge tube. The tube was set on a gyro-rocker (VWR, Lutterworth, UK) at low speed to enhance even penetration of the solution and reduce decalcifying time, with fresh solution exchanged every 24 hours. At 48 and 72 hours end point testing was performed to check decalcification progress (see *Section 3.4.3.1*). At 72 hours decalcification was deemed complete and the samples were removed from solution, washed thoroughly in tap water and returned to 10% neutral buffered formalin at 4°C until paraffin wax processing.

3.4.3.1 Endpoint Testing

Samples were tested both chemically and physically. Chemical testing entailed adding 5ml of 5% ammonium oxalate (Fisher Scientific, Loughborough, UK), followed by 5ml of 5% ammonium hydroxide (Sigma-Aldrich), to a 5ml aliquot of decalcifying solution from the sample tube. Decalcification was complete when no precipitate formed. Physical testing required careful slicing into the bone portion of the sample away from the enthesis with a number 11 carbon steel blade (Swann-Morton, Sheffield, UK), assessing for mineral resistance or grating. A suitably decalcified sample was compressible with no gritty resistance to the blade.

3.4.4 Paraffin Wax Processing

Samples were removed from formalin and held in tissue cassettes immersed in 70% ethanol (industrial methylated spirits) (Fisher Scientific) before processing in a VIP E300 Tissue-Tek processor (Sakura, Alphen aan den Rijn, Netherlands). During the 17.5 hour programme, samples were dehydrated through an ethanol series from 70% to 100%, followed by 100% xylene, then submerged in 60°C paraffin wax and placed under vacuum for paraffin infiltration. The following day samples were manually embedded in paraffin blocks, orientated to permit sagittal sectioning to the long axis of the DP.

3.4.5 Sectioning

Parasagittal 10µm sections were cut on a Leica RM 2245 microtome (Milton Keynes, UK). To minimise friction and tissue scarring from any residual bone mineral,

particularly across the enthesis, the block was cut in a tendon to bone direction and moistened with a wet paper towel every 2-3 sections. Sections were floated onto standard glass slides (Thermo Scientific, Cramlington, UK) and left to dry in a 37°C oven overnight before storing at room temperature until staining.

A particular sectioning method was devised to sample the central (mid-sagittal) portion of the enthesis (i.e. halfway across the medial-lateral/radio-ulnar enthesis width), assumed to provide the most representative and generalisable enthesis sections. This was based on the morphometric investigations in *Chapter 2* that found a vertically symmetrical trapezoidal FDP insertion shape. Initial optimisation trials with FPL-DP samples noted that 5-8 sections could be mounted onto a glass slide. By cutting a ribbon of 10 sections with the current samples, 5-8 of the best sections were mounted, discarding the remainder. 8 slides per sample were taken, assumed to cover various potential stains and investigations. This amounted to a total width of 800µm (8 slides, sampling 10 x 10µm sections). From *Chapter 2* morphometric data, mean base width of the FDP attachment for any finger of either gender was known. By starting the µm width counter on the microtome as soon as a parasagittal section moved from bone alone to the tendon-bone enthesis, 800µm across the mid-sagittal plane of the enthesis could be sectioned. For example, *Chapter 2* data showed that the average width of a male index finger was 9036µm (see **Table 2.5**). The mid-sagittal point thus lay at 4518µm, and an 800µm region centred on this was 4118-4918µm. Section collection thus began at a width of 4118µm.

3.4.6 Staining

Sections were dewaxed in 100% xylene (Fisher Scientific) and rehydrated through an ethanol series from 100% to 70% (Fisher Scientific) into water. Full sets of sections, containing one slide for each of the 48 fingers, were stained in hematoxylin and eosin (H+E) (*Section 3.4.6.1*) for overview, toluidine blue (*Section 3.4.6.2*) for focus on (fibro)cartilage, and Van Gieson's (*Section 3.4.6.3*) and Masson's trichrome (*Section 3.4.6.4*) for focus on collagen. As standard after staining, sections were dehydrated back through the 70-100% ethanol series, cleared in 100% xylene and mounted using dibutylphthalate polystyrene xylene (DPX) (Sigma-Aldrich) and glass coverslips (VWR). After a minimum of 72 hours drying at room temperature, high resolution

images of whole sections were acquired using a Nanozoomer XR slide scanner (Hamamatsu, Welwyn Garden City, UK) for qualitative and quantitative analysis.

3.4.6.1 Hematoxylin and Eosin

Sections required 20 minutes total staining in Shandon Harris hematoxylin (Thermo Scientific), in sequences of 3-5 minute staining and review under a Leica DMi1 light microscope to check nuclear staining, followed by 60 seconds in Shandon 0.1% water-based eosin-Y (Thermo Scientific). Sections were briefly rinsed with de-ionised water after both stains.

3.4.6.2 Toluidine Blue

Sections were stained for a total of 2.5–3 minutes in 0.1% toluidine blue (Sigma-Aldrich) in deionised water, with successive 30-90 second staining and light microscope review, then briefly rinsed in de-ionised water.

3.4.6.3 Van Gieson's

50% Van Gieson's solution (Sigma-Aldrich) in deionised water stained sections for a total of 2-3 minutes with consecutive 1 minute staining and light microscope review. Promptly after staining sections were immersed in 70% ethanol followed by 95% ethanol (Fisher Scientific) before dehydrating fully to 100% ethanol and clearing in 100% xylene as standard.

3.4.6.4 Masson's Trichrome

Sections for modified Masson's trichrome staining followed the protocol from the staining kit manufacturer (Sigma-Aldrich), except using 30 minute hematoxylin staining rather than the suggested 5 minutes (explained in *Section 3.6.4.2*). After dewaxing and rehydrating through the ethanol series as standard, sections were immersed in Bouin's solution (Sigma-Aldrich) overnight at room temperature as a mordant, then washed in running tap water for 30 minutes the following day. Sections were then sequentially immersed in working Weigert's iron hematoxylin [solution A + solution B (Sigma-Aldrich)] (30 minutes), Biebrich scarlet-acid fuchsin (5 minutes), working phosphotungstic / phosphomolybdic acid (5 minutes), aniline blue (5 minutes) and 1% acetic acid (Fisher Scientific) (2 minutes). Sections were briefly rinsed in de-ionised water after the hematoxylin, scarlet-acid fuchsin and acetic acid steps.

3.4.7 Tendon Fibre Angle Measurements

The set of sections stained with toluidine blue was used to quantitatively assess the angle of tendon fibres (collagen fibre bundles) at the FDP-DP enthesis. For each single slide (representing 1 of the 48 fingers), 1 of the 5-8 mounted sections on the scanned digital image was chosen for analysis. Selection was designated by random number generation, from 1 to the total number of sections available on the slide, counting from top to bottom of the slide, using an online 'true random number service' (www.random.org). 1 slide was found to contain crumpled sections that would not allow a representative assessment of tendon fibre angles, and was excluded from analysis. Sample size therefore totalled 47 FDP-DP entheses.

Measurement of the angle of tendon fibres was adapted from a method employed by Beaulieu *et al* (2015; 2016) using ImageJ software (National Institutes of Health, Bethesda, USA), defining the angle between a line parallel with the fibres and a line of best fit of the tidemark. **Figure 3.2** illustrates and explains the measurement technique. To trace the tidemark, the proximal point (beginning) of the tendon enthesis tidemark was located, and the software's segmented line tool then used to plot points along the tidemark at approximately 25-50µm regular intervals. The proximal-distal length of the enthesis was set using the mean value of the FDP insertion footprint height for the corresponding finger and gender (*Chapter 2* data, see **Table 2.4**), with the tidemark traced for this length to its endpoint. The line of best fit of the tidemark was generated by fitting a first order polynomial curve to the points. Where a duplicated tidemark was visualised (see **Figure 3.6**), the tidemark most proximal on the tendon was followed.

To investigate and describe both the fibre insertion angle and the typical curving of fibres in their passage across the enthesis, 2 measurements were assessed: 1) angle of fibres intersecting the tidemark, and 2) angle of approaching fibres – a broader evaluation of the direction of inbound fibres over a 20% enthesis distance. For each section, both measurements were assessed at 5 distance measurement points along the enthesis from proximal to distal: 20%, 40%, 50%, 60% and 80%, in order to compare values or enhance the accuracy of an accumulated average angle. Subtracting the angle of approaching fibres from the angle of tidemark intersection provided an estimate of the change in angle of the fibres.

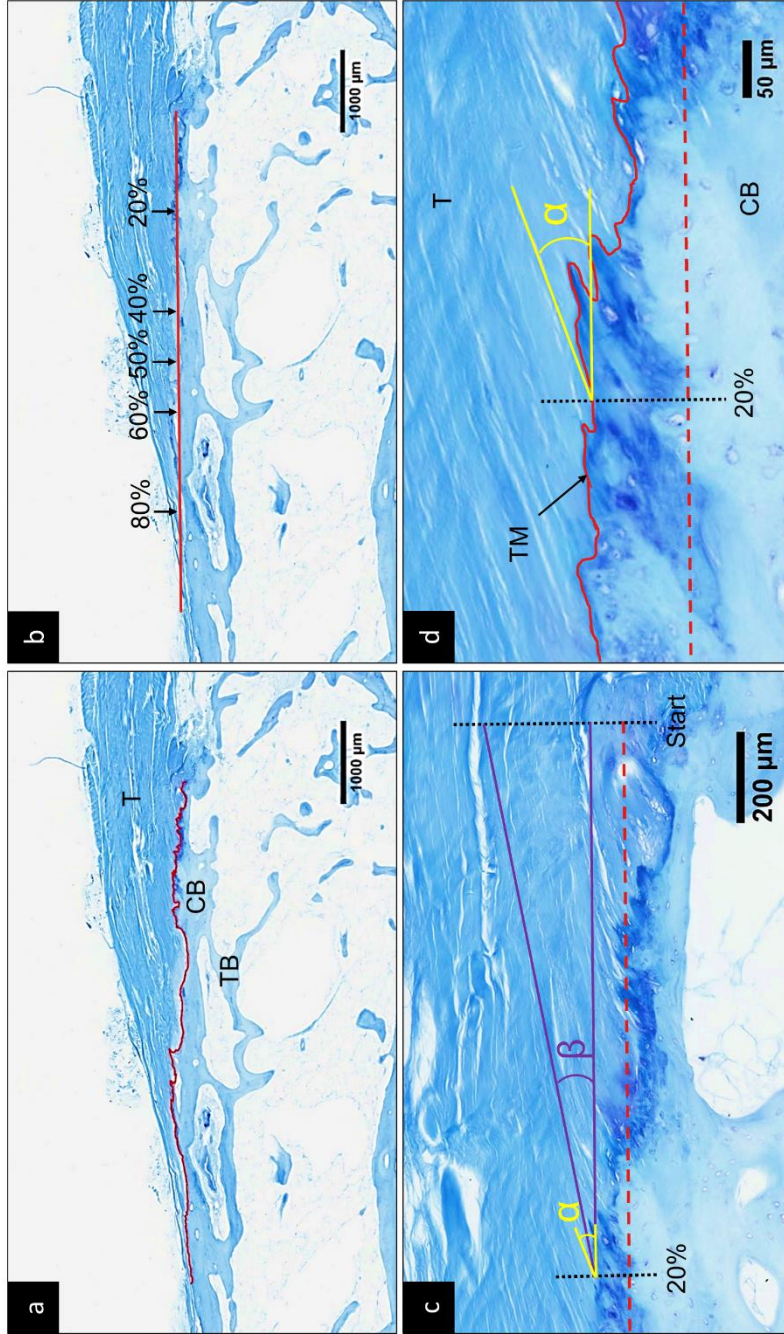


Figure 3.2 | Tendon Fibre Angle Measurement Methodology

a) The tidemark (red line) is traced along the length of the FDP enthesis, from proximal (right) (base of FDP tendon insertion) to distal (left) (apex of insertion). **b)** A line of best fit of the tidemark (red line) is produced, marking the points at 20%, 40%, 50%, 60% and 80% along the enthesis. **c)** Example measurements of angle of tidemark intersection fibres (α , yellow) and angle of approaching fibres (β , purple) at 20% along the enthesis. The location of 20% along the tidemark is found on a perpendicular line (black dotted line) from 20% along the line of best fit of the tidemark (red broken line). The angle of tidemark intersection (α) measures the angle of directly intersecting fibres; the angle of approach (θ) measures a line parallel to the average angle of fibres approaching over a preceding 20% distance of the enthesis. Angles are measured against a line parallel to the line of best fit of the tidemark (red broken line). **d)** Magnified view to highlight the angle of tidemark (TM) intersection (α) at this 20% region of the enthesis. Micrographs of the mid-sagittal section of an FDP enthesis (female right middle finger), toluidine blue. CB = cortical bone; T = tendon; TB = trabecular bone; TM = tidemark.

3.4.7.1 Inter-Observer Reliability

The tendon fibre angle measurement methodology was assessed for reliability by comparing the measurements made by the 1st (primary) observer with the results of a 2nd observer. The 2nd observer, different to the 2nd observers in *Chapter 2*, was trained in the methodology by the 1st observer, and completed the same full set of measurements on the same single selected scanned section on a different workstation. Both observers traced the tidemark over the same pre-determined enthesis length, however judgement of the beginning of the tendon enthesis and the outline of the tidemark was determined independently. Agreement and reliability between the 2 observers was ascertained by the intraclass correlation coefficient (ICC) of single measures of absolute agreement, and by Cronbach's alpha, using SPSS version 24 (IBM, Armonk, USA).

3.4.8 Data Analysis

Quantitative angle measurement data was handled and graphed in the same way, and with the same software, as per *Chapter 2* (see *Section 2.4.7*). Similarly, linear mixed effects models were employed in SPSS version 24 (IBM) to account for the non-independence of fingers measured from the same cadaveric specimen, and for multiple distance points (20%, 40%, 50%, 60% and 80%) measured along the same enthesis, generating estimated marginal means (**Tables 3.1a** and **3.1b**). Various models again tested the pre-selected factors of finger, gender and side, and compared sizing categories and distance measurements, with multiple pairwise comparisons using an alpha level of 0.05 and Bonferroni post-hoc correction. No further corrections were made for running multiple models. Unless otherwise stated, data in the chapter is presented as estimated marginal means \pm standard error of the mean (\pm SEM), with graphical error bars also indicating \pm SEM, and the level of any statistical significance highlighted as * $p < 0.05$, ** $p < 0.01$, *** $p < 0.001$.

Table 3.1a | Build and Application of Linear Mixed Effects Model Series (1)

Continued overleaf as **Table 3.1b**. See **Table 3.1b** for details.

Linear Mixed Effects Models					
Factor Analysis	Effect of Factor		Application		
	Fixed	Random	EM Means; SEM	Tables	Figures
Model 1					
Genders (Combined Fingers) Fingers (Combined Genders)	Gender Finger	Specimen	All (Collective) Male (All) Female (All) Index (All) Middle (All) Ring (All) Little (All)	3.2 3.4	3.7a,b 3.8a,b 3.9a,b 3.10a,b 3.11a, b 3.12a, b
Model 2					
Individual Fingers	Individual Finger	Specimen	Male Index Male Middle Male Ring Male Little Female Index Female Middle Female Ring Female Little	3.2 3.4	3.7c 3.8c 3.9c 3.10c 3.11c 3.12c
Model 3					
Size Categories	Size Category	Specimen	Large Medium Small	3.2 3.4	3.7d 3.8d 3.9d 3.10d 3.11d 3.12d
Model 4					
All Distance (Combined Genders & Fingers)	Finger Gender Side Distance	Specimen	All 20% All 40% All 50% All 60% All 80%	3.3 3.5	3.13a
Model 5a					
Male Distance (Combined Fingers)	Finger Side Distance	Specimen	Male 20% Male 40% Male 50% Male 60% Male 80%	3.3 3.5	3.13b
Model 5b					
Female Distance (Combined Fingers)	Finger Side Distance	Specimen	Female 20% Female 40% Female 50% Female 60% Female 80%	3.3 3.5	3.13b
Model 6a					
Index Distance (Combined Genders)	Gender Side Distance	Specimen	Index 20% Index 40% Index 50% Index 60% Index 80%	3.3 3.5	3.13c
Model 6b					
Middle Distance (Combined Genders)	Gender Side Distance	Specimen	Middle 20% Middle 40% Middle 50% Middle 60% Middle 80%	3.3 3.5	3.13c
Model 6c					
Ring Distance (Combined Genders)	Gender Side Distance	Specimen	Ring 20% Ring 40% Ring 50% Ring 60% Ring 80%	3.3 3.5	3.13c
Model 6d					
Little Distance (Combined Genders)	Gender Side Distance	Specimen	Little 20% Little 40% Little 50% Little 60% Little 80%	3.3 3.5	3.13c

Table 3.1b | Build and Application of Linear Mixed Effects Model Series (2)

Continued from **Table 3.1a**. Multiple explorative SPSS linear mixed effects models were utilised to adjust for the non-independence relationship of individual fingers measured from the same specimen. *Specimen* (identifier) was therefore always a random effect in the model series. Fixed factors included *gender*, *finger*, *individual finger* (gender specified), *size category* (gender and finger specified) and *distance* along the enthesis. *Side* was excluded as a fixed factor from *models 1, 2 and 3* for model simplification, but was included where the effect of side was specifically investigated (*models 7a, 7b, 8a, 8b, 8c and 8d*). *Side* was also included where distance measurements along the enthesis were compared (*models 4, 5a, 5b, 6a, 6b, 6c and 6d*), as this was a determining factor in the grouping of repeated distance measurement points along the same enthesis (on left or right side of the same finger grouping). Statistical output generated estimated marginal (*EM*) means and standard error of estimated marginal means (*SEM*), used as the reported means and for multiple pairwise comparisons in figures and tables throughout the chapter. Factors are tested as main effects, and a type III sum of squares model is applied to fixed effects. Models assume normal data distributions, which were checked graphically as Q-Q normal probability plots of observed versus expected residual values from each model.

Linear Mixed Effects Models					
Factor Analysis	Effect of Factor		Application		
	Fixed	Random	EM Means; SEM	Tables	Figures
Model 7a					
Male Side (Combined Fingers)	Finger Side	Specimen	Male Left Male Right	3.6	/
Model 7b					
Female Side (Combined Fingers)	Finger Side	Specimen	Female Left Female Right	3.6	/
Model 8a					
Index Side (Combined Genders)	Gender Side	Specimen	Index Left Index Right	3.6	/
Model 8b					
Middle Side (Combined Genders)	Gender Side	Specimen	Middle Left Middle Right	3.6	/
Model 8c					
Ring Side (Combined Genders)	Gender Side	Specimen	Ring Left Ring Right	3.6	/
Model 8d					
Little Side (Combined Genders)	Gender Side	Specimen	Little Left Little Right	3.6	/

3.5 Results

3.5.1 Qualitative Analysis

3.5.1.1 Enthesis Classification

The FDP enthesis was fibrocartilaginous. A fibrocartilage transition zone between the FDP tendon and DP bone was apparent in all 47 samples examined. **Figure 3.3** highlights the defining histological features. H+E and toluidine blue stains proved more valuable than Van Gieson's and Masson's trichrome (**Figure 3.4**) for both qualitative description and quantitative tendon fibre angle measurements.

3.5.1.2 General Findings

The FDP tendon contained dense collagen fibre bundles with intervening elongated fibroblasts (see **Figure 3.3b**), often aggregated into rows. The tendon fibres ran over the base of the flexor surface of the DP roughly parallel to the long axis of the bone, before beginning a sloping descent, at a point approximately perpendicular to the base of the insertion area, to their bony attachment (see **Figure 3.2a,b** and **3.3a**).

Tendon fibres reached the tidemark either directly or through an area of uncalcified fibrocartilage. Uncalcified fibrocartilage contained a variable number of fibrochondrocytes, typically ordered in rows which were most obvious where they were less numerous (see **Figure 3.3b**). Staining was generally most intense around fibrochondrocytes, noticeable with H+E (**Figure 3.3**) and especially toluidine blue (**Figure 3.5**), demonstrating a high level of pericellular glycosaminoglycans (GAGs).

The enthesis tidemark commenced as a continuation of the tidemark in the volar plate tissue (see **Figure 3.2c**), indicating that the FDP tendon and volar plate merge microscopically at their insertion. The enthesis tidemark was present either between uncalcified and calcified fibrocartilage zones, or between tendon and calcified fibrocartilage when there was no uncalcified fibrocartilage (see **Figure 3.5d**). The tidemark merged with the tendon-bone junction in fibrous regions without any fibrocartilage. It followed a grossly smooth and gently curved line. Magnified, it displayed rougher, tighter undulations; however the underlying tendon-bone junction was more irregular (see **Figure 3.3b**).

A calcified fibrocartilage zone existed with or without an adjacent uncalcified fibrocartilage zone. Fibrochondrocytes here were more hypertrophic and less numerous compared to those in uncalcified fibrocartilage, and displayed variable pericellular metachromasia (see **Figure 3.3b** and **3.5b**). Tendon fibres could be discerned traversing both fibrocartilage zones, embedded within a more homogenous cartilage matrix stain not seen in the tendon, before they attached to cortical bone. Tendon fibres did not generally deviate as they crossed through calcified fibrocartilage, maintaining the same angle at the tidemark as at the tendon-bone junction.

Cortical bone was thin around the whole DP perimeter, but particularly so at the enthesis. The cortical bone profile at the enthesis was either flat to the DP flexor surface (e.g. see **Figure 3.2**) or convex and drawn up into the tendon region (e.g. see **Figure 3.3a** and **3.5a**). Where the profile was convex, the peak was usually biased proximally, towards the insertion base, which appeared to coincide with the area of greatest fibrocartilage.

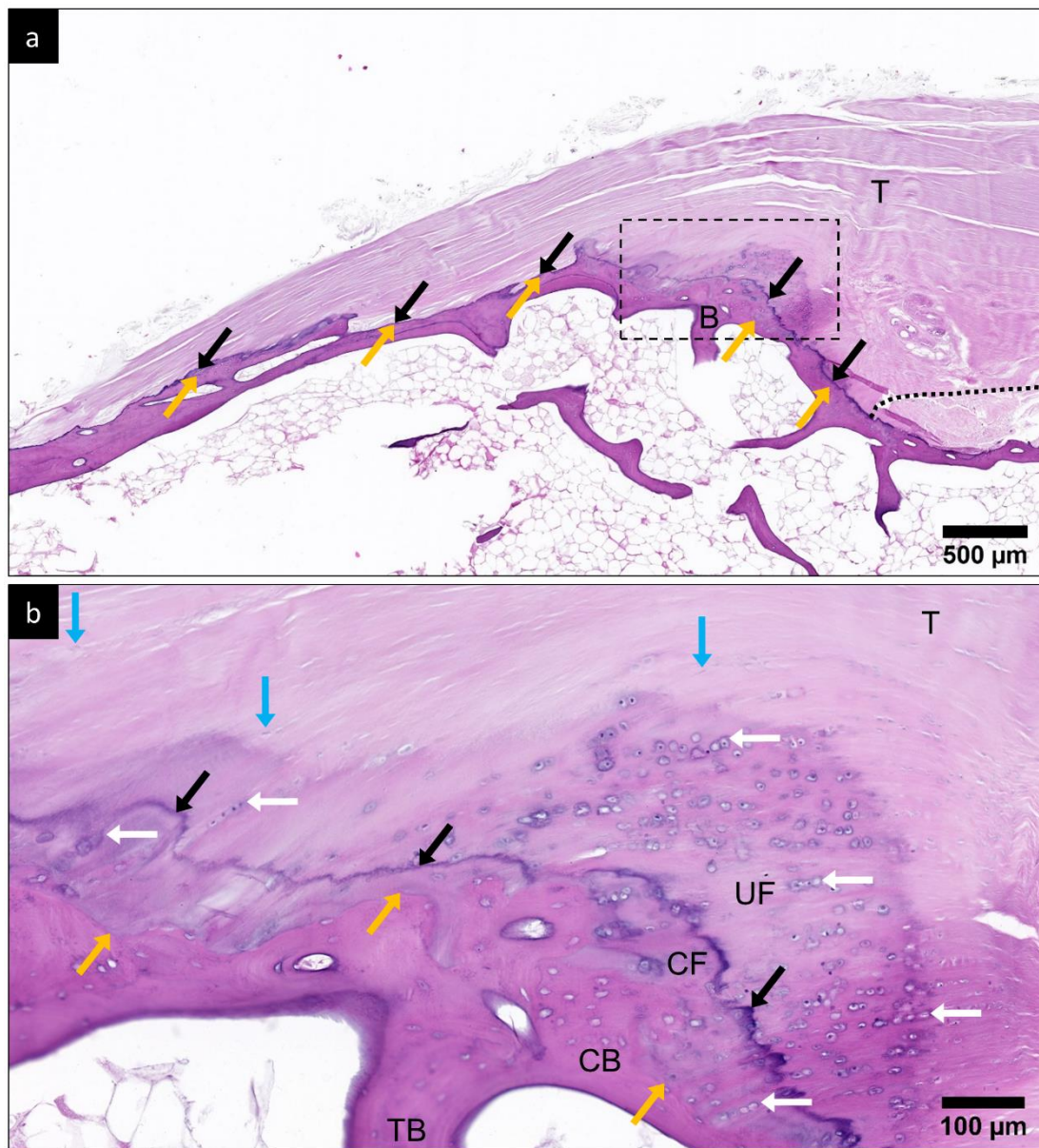


Figure 3.3 | Histology of the FDP Enthesis (1)

a) The FDP tendon (*T*) attaches to the DP bone (*B*) as a fibrocartilagenous enthesis, signified by areas of intervening fibrocartilage. Fibrocartilage predominates in the more proximal enthesis region, nearer the distal interphalangeal joint (to *right* of image), demonstrated by a thicker layer of calcified fibrocartilage between the separated tidemark (*black arrows*) and tendon-bone junction (*gold arrows*). Elsewhere, the tidemark and tendon-bone junction approximate each other, indicating fibrous enthesis regions. The dorsal surface of the tendon is highlighted by a *dotted black line*, with remaining volar plate tissue beneath. Box indicates (*b*). Micrograph of a typical mid-sagittal section of an FDP enthesis (female right middle finger), H+E. **b)** Magnified box view of the enthesis, demonstrating the 4 zones of the fibrocartilagenous enthesis: tendon (*T*), uncalcified fibrocartilage (*UF*), calcified fibrocartilage (*CF*) and bone. The cortical bone (*CB*) is as thin as the trabecular bone (*TB*). The calcified fibrocartilage lies between the tidemark (*black arrows*) and the tendon-bone junction (*gold arrows*). Fibrochondrocytes (*white arrows*), rounded and lying in lacunae within cartilage matrix, indicate the cartilagenous areas and generally align in rows. They are more numerous in the uncalcified fibrocartilage (*UF*) zone. Elongated fibroblasts (*blue arrows*, not deeply stained) lie between the tendon collagen fibre bundles, which are continuous through the fibrocartilage areas to attach to the cortical bone. H+E.

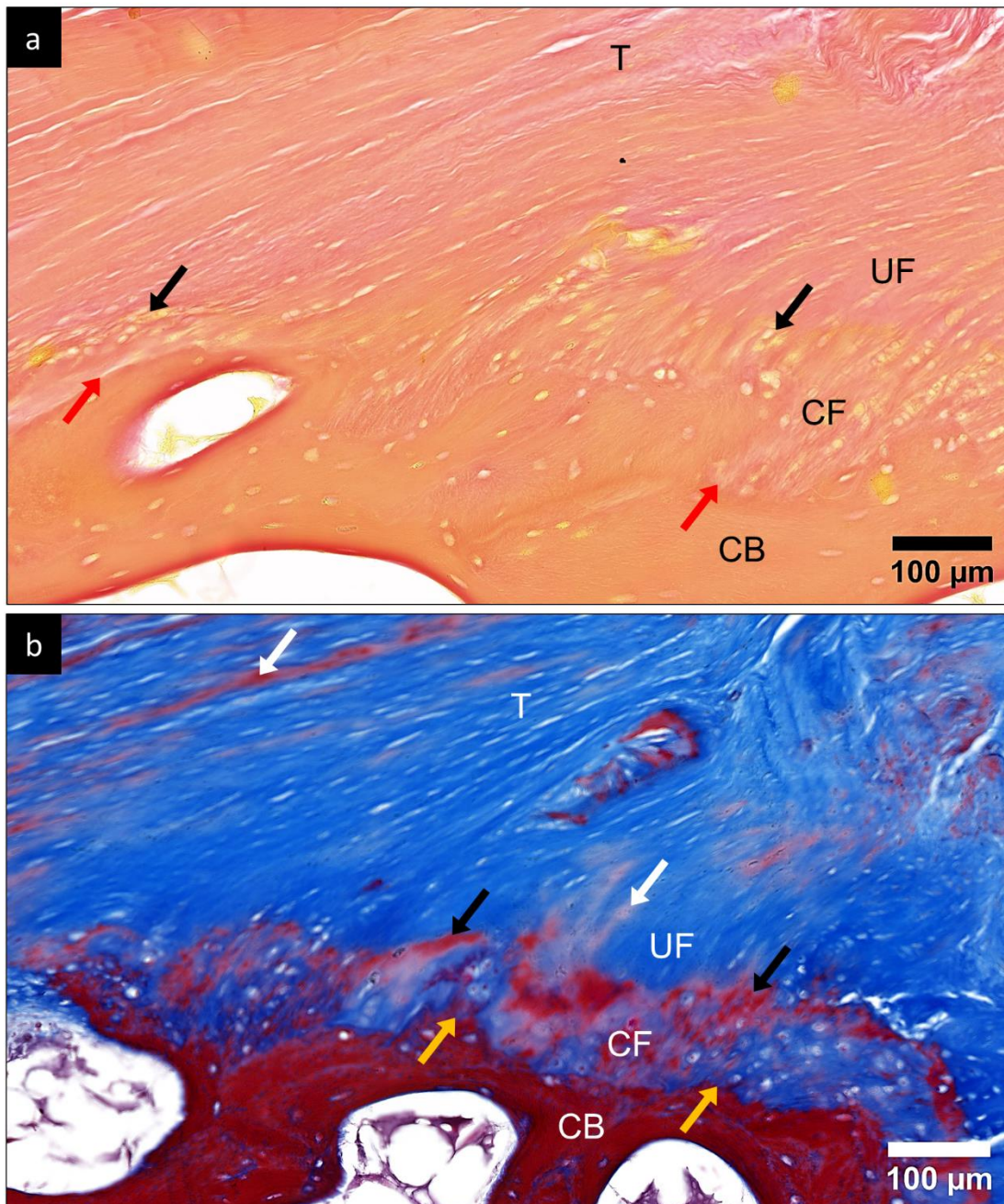


Figure 3.4 | Histology of the FDP Enthesis (2)

Van Gieson's (a) and Masson's trichrome (b) stains of fibrocartilaginous regions of the FDP enthesis. The 4 tissue zones are present: tendon (T), uncalcified fibrocartilage (UF), calcified fibrocartilage (CF) and bone (cortical bone – CB). Both stains visualised the tendon and bone elements, but were less effective than H+E or toluidine blue for qualitative and quantitative analysis of the enthesis. With Van Gieson's stain, (a) (red/orange: collagen; yellow: remaining connective tissue), both the tendon-bone junction (red arrows) and tidemark (black arrows) were difficult to discern, and cell nuclei were not stained. With Masson's trichrome, (b) [blue: collagen; deep red: cytoplasm; black (understained): nuclei], the tidemark was often difficult to differentiate from streaky staining in the tendon (white arrows), and the tendon-bone junction (gold arrows) could be obscured by variable patchy staining in the calcified fibrocartilage zone. Cell nuclei were generally weakly stained, and, as with Van Gieson's, identification of fibrochondrocytes relied on the presence of circular lacunae. Magnified typical mid-sagittal section micrographs of similar regions of the same FDP enthesis (male left ring finger).

3.5.1.3 Regional Variation

The structure and composition of the enthesis varied along its length, demonstrated and described in **Figure 3.5**. In particular, fibrocartilage zones were not present throughout the entire length of the enthesis. Many areas contained no fibrocartilage at all, indicating localised fibrous attachment, with others only demonstrating calcified fibrocartilage. Fibrocartilage, especially uncalcified fibrocartilage, predominated in the proximal enthesis region. Regional variation in the angle of tendon fibres was also apparent, quantitatively reported in *Section 3.5.2*. The alignment of fibrochondrocytes in the uncalcified fibrocartilage zone in the more proximal enthesis region was often curved, indicating the bending of tendon fibres through this zone as they neared the tidemark and cortical bone.

3.5.1.4 Histopathology

The FDP enthesis samples displayed a number of microscopic pathological features, some of which were pertinent to measuring the angle of the tendon fibres (see *Sections 3.4.7 and 3.5.2.1*) (**Figure 3.6**). Focal areas of cortical bone loss were a common feature, with tendon fibres entering into bone marrow spaces, deviating to attach to the nearest cortical bone edge, or degenerating. Degenerated fibres were also noted around contained micro-avulsions (<200µm) at the tendon-bone junction, often amongst disorganised repair tissue. A double or even triple tidemark, generally considered pathological (Lane and Bullough, 1980; Binks *et al*, 2014), was also occasionally apparent, especially in the proximal enthesis region.

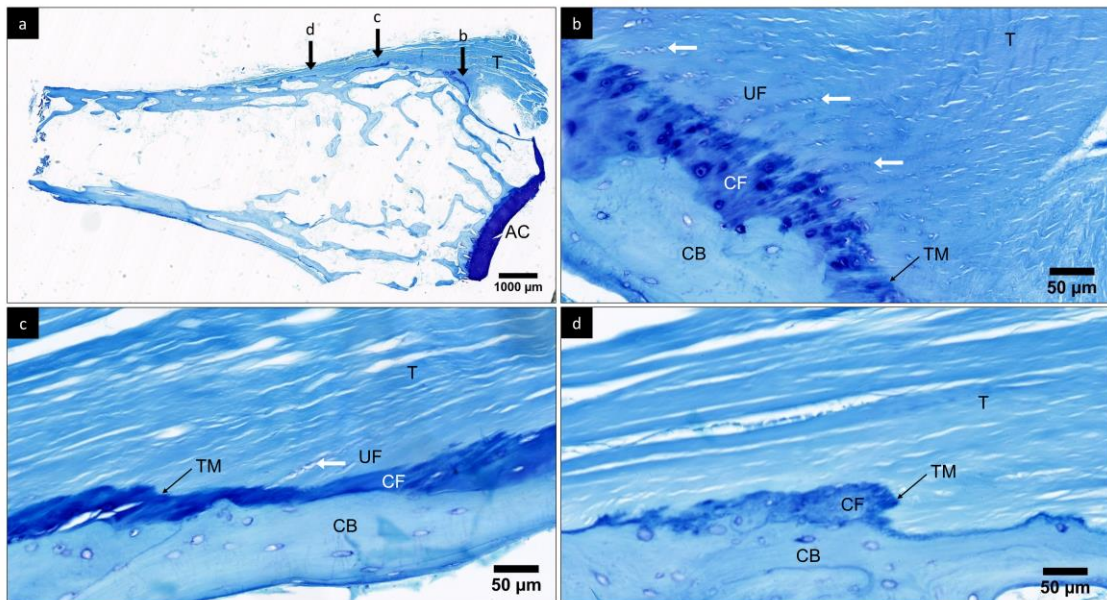


Figure 3.5 | Comparison of Proximal, Middle and Distal Regions of the FDP Enthesis

a) Entire section of the FDP-DP tendon-bone sample. The FDP tendon (*T*) attaches to the flexor surface of the DP. The proximal end of the DP (*right*) is covered by deeply stained DIPJ articular cartilage (*AC*). The dorsal aspect of the DP (*bottom*) is removed due to physical testing for the end point of decalcification. *b*, *c* and *d* indicate proximal, middle and distal regions of the enthesis, respectively, corresponding to the proceeding panels. Note the presence of a convexity in the bone at the tendon-bone interface, inclined towards the proximal region – this was not an uncommon feature. **b)** Proximal enthesis region. The 4 zones of a fibrocartilaginous enthesis are apparent. The approaching tendon fibres undergo a considerable change in angle in reaching the tidemark (*TM*) and cortical bone (*CB*). The majority of the angle change occurs in the uncalcified fibrocartilage (*UF*) zone, indicated by the curved alignment of fibrochondrocytes (*white arrows*). The deeper blue staining around the fibrochondrocytes represents typical pericellular metachromasia. **c)** Middle enthesis region. A calcified fibrocartilage (*CF*) zone is present, although less thick than in the proximal region, with a layer of uncalcified fibrocartilage (*UF*) demonstrated by the limited but perceptible presence of fibrochondrocytes (*white arrow*). Compared to the proximal enthesis region, the approaching tendon fibres are generally less acute to the horizontal, and there is less angle change between the approaching fibres and tidemark intersection fibres. **d)** Distal enthesis region. Areas of calcified fibrocartilage (*CF*) are sporadic and are interspersed between fibrous enthesis regions which lack any fibrocartilage. The absence of fibrochondrocytes proximal to the calcified fibrocartilage indicates no uncalcified fibrocartilage zone. Tendon fibres approach the tidemark (*TM*) more acutely than the middle enthesis region. Micrographs of a typical mid-sagittal section of an FDP enthesis (male left ring finger), toluidine blue. *AC* = articular cartilage; *CB* = cortical bone; *CF* = calcified fibrocartilage; *T* = tendon; *TM* = tidemark; *UF* = uncalcified fibrocartilage.

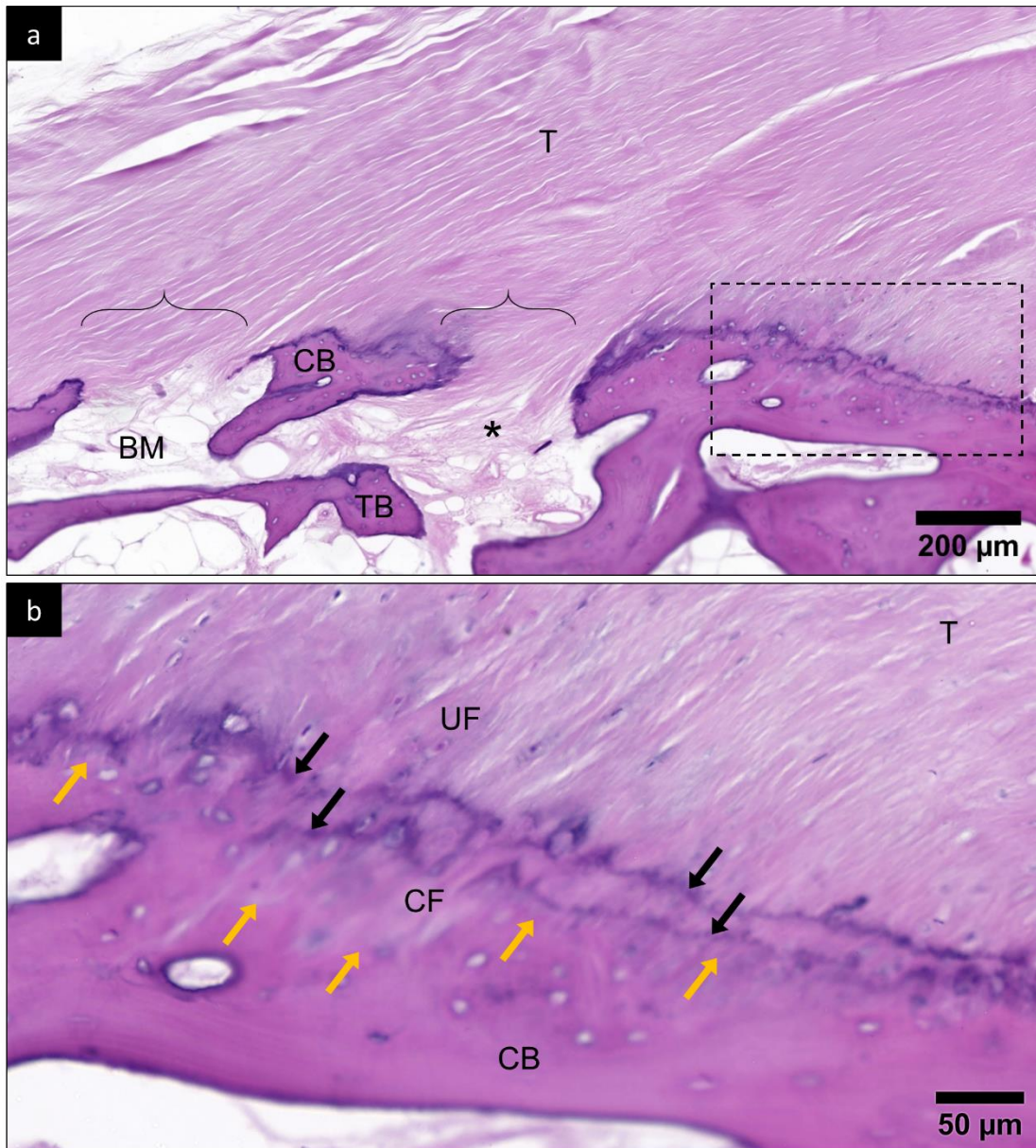


Figure 3.6 | FDP Enthesis Histopathology

a) Areas of cortical bone loss (*brackets*), exposing the tendon to the bone marrow. In some regions the tendon fibres extend down into the marrow space to blend with the bone marrow tissue (*). Box indicates (b). Micrograph of middle(*left*)-proximal(*right*) region of mid-sagittal section of an FDP enthesis (female right little finger), H+E. **b)** Magnified box view, showing a duplicated tidemark (*black arrows*) between the uncalcified fibrocartilage zone and tendon-bone junction (*gold arrows*). H+E. BM = bone marrow; CB = cortical bone; CF = calcified fibrocartilage; T = tendon; TB = trabecular bone; UF = uncalcified fibrocartilage.

3.5.2 Tendon Fibre Angle Measurements

3.5.2.1 Tidemark Intersection Fibres

The tidemark intersection tendon fibre angles could be measured in 71.9% of all 235 measurement points (169/235). Angle measurements could not be accurately or reliably recorded in the remaining 28.1% either due to a measurement point coinciding with an area of cortical bone loss (see **Figure 3.6**), or, at the tidemark, haphazard degenerated fibres or poor fibre definition. Most measurements were taken at the 60% entheses distance point (76.6%; 36/47), followed by 20% (74.5%; 35/47), 80% (72.3%; 34/47), 50% (70.2%; 33/47), with the least measurements taken at the 40% distance (66.0%; 31/47).

Table 3.2 details the tidemark intersection angles broken down across gender and fingers. Also tabulated are the values for size category groupings as determined in *Chapter 2, Section 2.5.5*. Values are separately graphed and compared between gender, finger and size category for each distance point measured along the entheses in **Figures 3.7** (20%), **3.8** (40%), **3.9** (50%), **3.10** (60%), **3.11** (80%) and **3.12** (average of all distances measured).

Overall, mean tidemark intersection angles were similar across all distances, ranging from $27.69 \pm 1.51^\circ$ (80%) to $33.05 \pm 1.47^\circ$ (40%), and averaging $30.05 \pm 0.72^\circ$, for combined gender and finger means (**Table 3.2**). Significant angle differences when comparing fingers, genders and size categories at each distance were scarce. For the average angle across all distances measured (**Figure 3.12**), the only slight significant difference was between males and females ($p < 0.05$), with a small angle discrepancy of 4.55° ; different fingers and size categories had very similar angles.

At the 20% distance (**Figure 3.7**), the most proximal measurement point, no comparisons were significant. Mean angles ranged from $26.80 \pm 6.63^\circ$ (female little finger) to $43.60 \pm 5.95^\circ$ (female index, the largest mean angle of all distances), with a combined mean of $31.97 \pm 3.09^\circ$ (**Table 3.2**). Female finger mean angles appeared to evenly decrease from index across to little finger, although the standard errors indicated this was not a dependable pattern.

At 40% (**Figure 3.8**), males and females had a significant angle difference of 6.56° ($p < 0.05$), with no other significant differences or trends of note. Mean angles ranged from $27.01 \pm 3.20^\circ$ (male little finger) to $39.43 \pm 5.55^\circ$ (female middle) (**Table 3.2**).

At 50% (**Figure 3.9**), representing the midpoint of the enthesis, all mean angles were alike and no significant differences existed. The combined mean was $29.67 \pm 1.45^\circ$. Mean angles ranged from $26.44 \pm 4.97^\circ$ (male middle finger) to $34.66 \pm 6.09^\circ$ (female little), (**Table 3.2**) the narrowest range (8.22°) of all distances points measured.

The widest range of values (17.07°) was at the 60% distance (**Figure 3.10**), ranging from $25.10 \pm 2.79^\circ$ (male ring finger) to $42.17 \pm 3.60^\circ$ (female little) (**Table 3.2**). The sizeable female little finger mean angle imparted a significant difference over 4/7 other fingers ($p < 0.05$ compared to male index, middle and ring, and female middle). This also dictated that the little finger (combined genders) mean angle was greater than all other fingers, significantly so compared to the middle ($p < 0.05$), that the small size category was significantly different to both other size categories ($p < 0.01$ medium; $p < 0.001$ large), and that females were significantly greater than males ($p < 0.05$). The combined mean angle was however similar to the other distances, at $28.89 \pm 1.08^\circ$.

At 80% (**Figure 3.11**), the most distal measurement point, no comparisons were significant. Mean angles ranged from $22.42 \pm 4.02^\circ$ (male index finger, the smallest mean angle of all distances) to $32.95 \pm 3.60^\circ$ (female index) (**Table 3.2**).

Table 3.2 | Tidemark Intersection Angle Measurements

Collated measurement means of the FDP tendon fibre angle intersecting the tidemark at distances of 20%, 40%, 50%, 60% and 80% along the enthesis. 'Average' is the calculated mean from measurements made at all 5 distances. 'All' represents mean of combined genders, fingers, or both. Size categories refer to the regrouping of data as performed in Chapter 2 (see Section 2.5.5). EM mean (\pm SEM). Values are plotted in Figures 3.7, 3.8, 3.9, 3.10, 3.11 and 3.12.

		Angle of Tidemark Fibres (°)																	
		20%			40%			50%			60%			80%			Average		
Fingers		Male	Female	All	Male	Female	All	Male	Female	All	Male	Female	All	Male	Female	All	Male	Female	All
		Index	28.08 (5.15)	43.60 (5.95)	34.53 (3.96)	26.97 (3.20)	36.14 (3.20)	31.56 (2.17)	29.08 (2.74)	28.70 (3.85)	29.27 (4.30)	28.49 (3.12)	25.25 (3.12)	28.49 (3.12)	26.87 (2.27)	22.42 (4.02)	32.95 (3.60)	28.04 (2.65)	26.77 (1.85)
Middle	29.08 (5.42)	36.67 (4.95)	32.96 (3.72)	34.56 (4.53)	39.43 (5.55)	37.16 (3.37)	28.05 (3.11)	26.44 (4.97)	29.55 (4.30)	25.45 (2.79)	25.58 (2.79)	25.45 (2.79)	25.51 (2.03)	30.39 (4.02)	30.38 (3.29)	29.97 (2.52)	27.98 (2.03)	31.37 (1.85)	29.62 (1.35)
Ring	27.61 (5.79)	31.65 (4.95)	29.23 (3.82)	30.99 (3.92)	36.83 (4.53)	33.96 (2.85)	30.63 (2.59)	30.07 (3.85)	31.18 (3.85)	31.61 (2.79)	25.10 (2.79)	31.61 (2.79)	28.35 (2.03)	26.14 (3.60)	28.56 (3.29)	27.27 (2.39)	28.42 (1.85)	31.51 (1.85)	29.96 (1.30)
Little	30.32 (4.95)	26.80 (6.63)	31.16 (3.97)	27.01 (3.20)	28.20 (7.84)	29.52 (3.02)	30.93 (3.16)	28.75 (3.85)	34.66 (6.09)	42.17 (3.60)	29.34 (2.79)	42.17 (3.60)	34.81 (2.29)	22.95 (8.05)	27.67 (4.65)	25.46 (4.03)	28.07 (1.85)	32.44 (2.03)	30.26 (1.35)
All	28.77 (4.36)	35.18 (4.42)	31.97 (3.09)	29.77 (1.77)	36.33 (2.31)	33.05 (1.47)	29.67 (1.45)	28.54 (1.96)	30.80 (2.16)	31.50 (1.57)	26.27 (1.48)	31.50 (1.57)	28.89 (1.08)	25.62 (2.26)	29.75 (1.83)	27.69 (1.51)	27.78 (1.01)	32.33 (1.01)	30.05 (0.72)
Size Category		Large	Medium	Small	Large	Medium	Small	Large	Medium	Small	Large	Medium	Small	Large	Medium	Small	Large	Medium	Small
		30.28 (3.87)	33.45 (3.34)	24.87 (6.29)	30.35 (2.44)	33.26 (2.10)	27.39 (8.33)	34.66 (5.62)	28.70 (2.20)	29.72 (1.87)	28.73 (1.37)	25.32 (1.60)	28.73 (1.37)	42.17 (3.46)	26.30 (2.18)	30.08 (1.85)	27.67 (4.54)	28.14 (1.29)	31.00 (1.07)

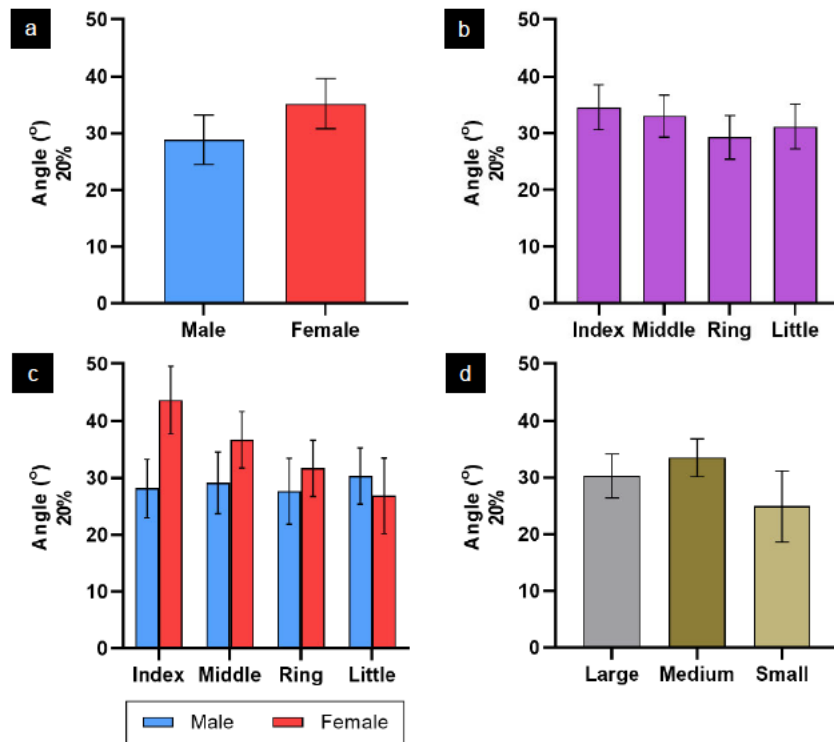


Figure 3.7 | Angle of Tidemark Fibres at 20% Enthesis Distance

a) Gender comparison, all fingers combined. **b)** Finger comparison, genders combined. **c)** Separated fingers and gender comparison. **d)** Size category groupings. No clear trend or significant differences are apparent. EM mean \pm SEM. See **Table 3.2**.

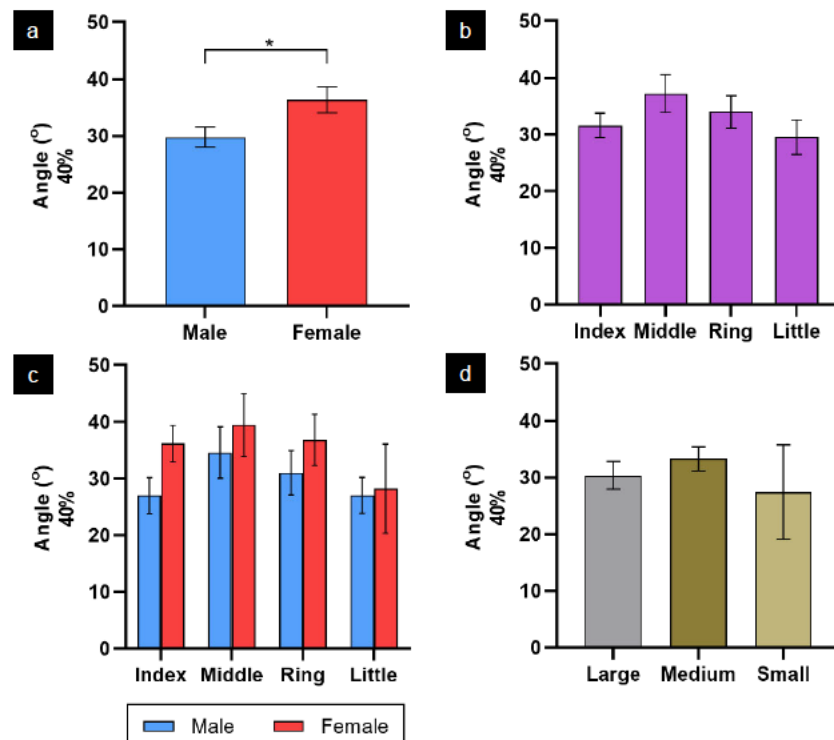


Figure 3.8 | Angle of Tidemark Fibres at 40% Enthesis Distance

Male and female comparison, all fingers combined, is significant ($p=0.031$) **(a)**. No clear trends or significant differences are apparent for fingers with genders combined **(b)**, separated fingers and gender **(c)**, or size category groupings **(d)**. EM mean \pm SEM. * $p<0.05$. See **Table 3.2**.

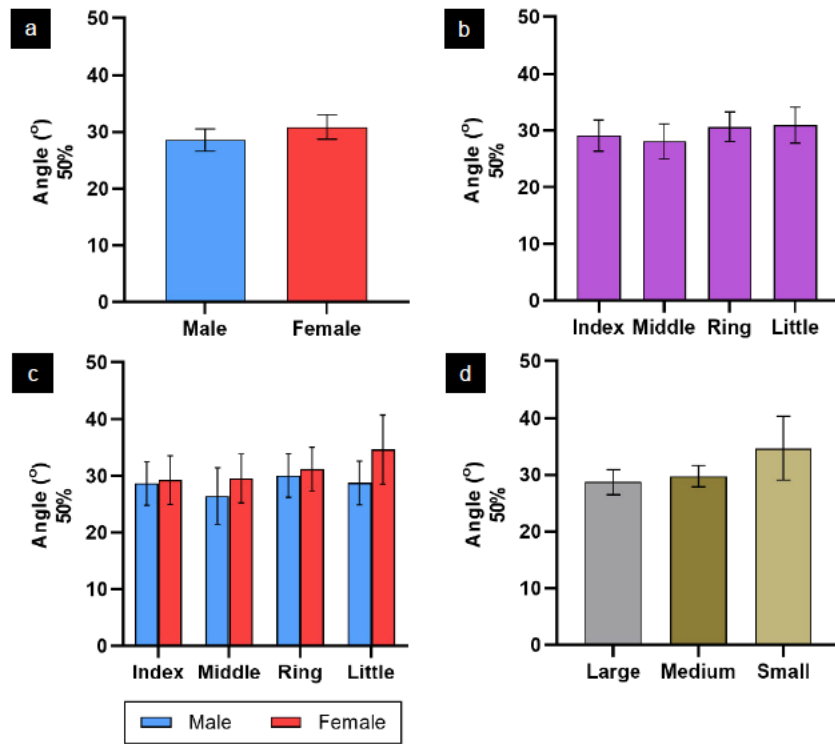


Figure 3.9 | Angle of Tidemark Fibres at 50% Enthesis Distance

Mean values are similar and no significant differences exist between genders with all fingers combined (a), fingers with genders combined (b), separated fingers and genders (c), or size category groupings (d). EM mean \pm SEM. See Table 3.2.

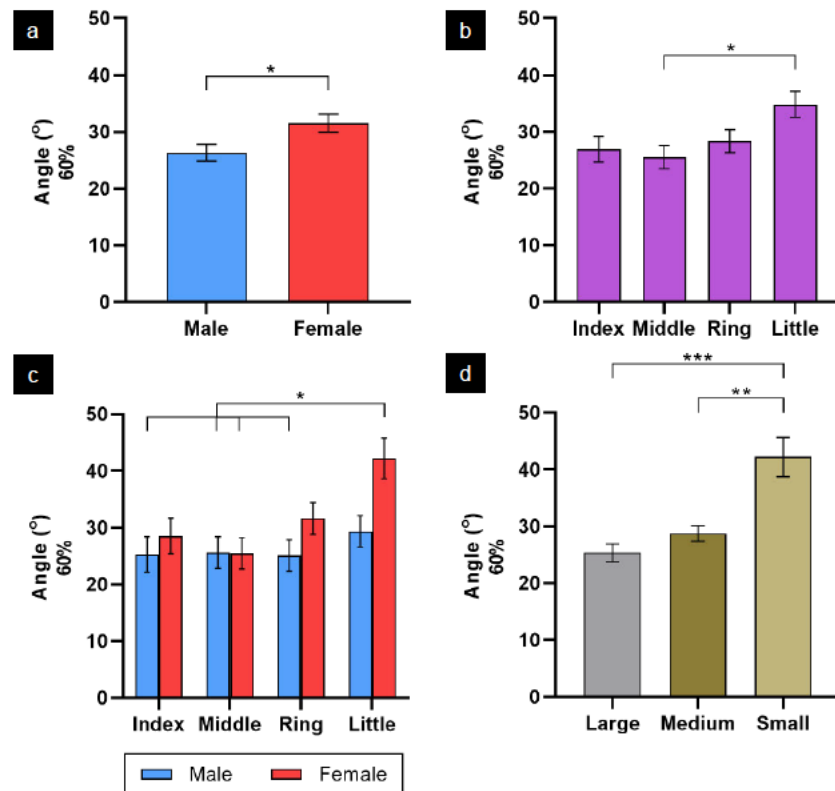


Figure 3.10 | Angle of Tidemark Fibres at 60% Enthesis Distance

a) Male versus female comparison, all fingers combined, is significantly different ($p=0.021$). b) Finger comparison, genders combined. The little finger angle is significantly greater than the middle finger ($p=0.029$). c) Separated finger and gender comparison, showing the female little finger angle is significantly greater than other male and female fingers. d) The small size category angle is significantly greater than both other categories. EM mean \pm SEM. * $p<0.05$, ** $p<0.01$, *** $p<0.001$. See Table 3.2.

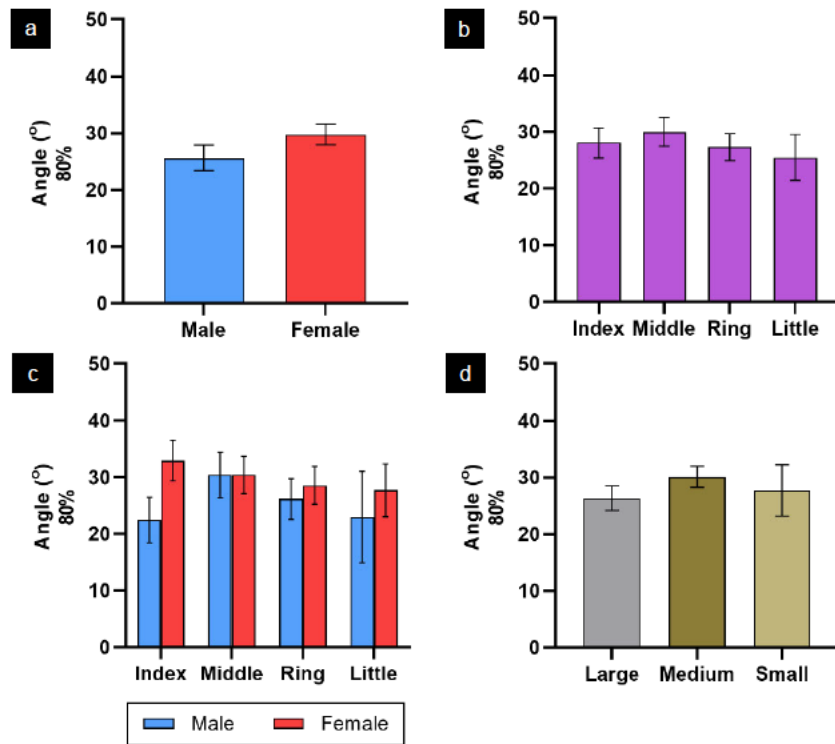


Figure 3.11 | Angle of Tidemark Fibres at 80% Enthesis Distance

No significant differences exist between genders with all fingers combined (a), fingers with genders combined (b), separated fingers and genders (c), or size category groupings (d). EM mean ± SEM. See Table 3.2.

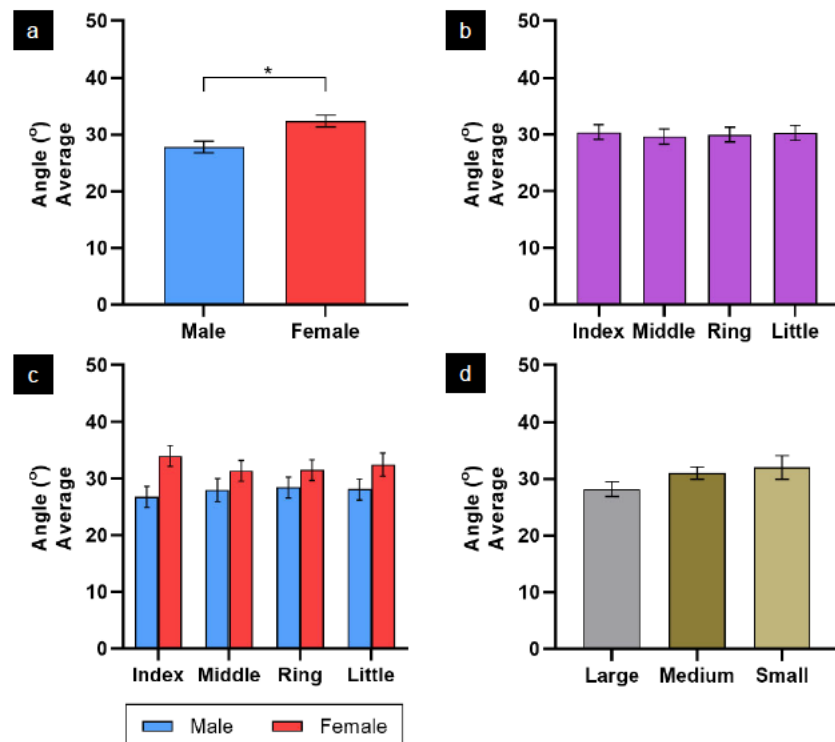


Figure 3.12 | Angle of Tidemark Fibres Averaged Across All Enthesis Distances

Male and female comparison, all fingers combined, is significantly different ($p=0.033$) (a). No significant differences exist between fingers with genders combined (b), separated fingers and genders (c), or size category groupings (d). EM mean ± SEM. * $p<0.05$. See Table 3.2.

3.5.2.1.1 Effect of Enthesis Distance

The tidemark intersection angle did not vary significantly across the different distance points measured along the enthesis (**Table 3.3**). Females, ranging from $29.75 \pm 1.83^\circ$ (80%) to $36.33 \pm 2.31^\circ$ (40%), and middle fingers, ranging from $25.51 \pm 2.03^\circ$ (60%) to $37.16 \pm 3.37^\circ$ (40%) (see **Table 3.2**) were the most variable gender and finger groups, but did not reach a significant threshold.

Table 3.3 | Tidemark Intersection Fibres Enthesis Distance Comparison

Multiple comparisons analysis between angle measurements made at the 20%, 40%, 50%, 60%, and 80% enthesis distance points for tidemark intersection tendon fibres. No distance point is significantly different to another within *genders* (combined fingers), *fingers* (combined genders) or overall combined gender and finger mean ('All'). Parentheses indicate p value. 'ns' = non-significant.

Tidemark Fibres Distance Comparison						
Gender		Finger				All
Male	Female	Index	Middle	Ring	Little	
ns (0.432)	ns (0.125)	ns (0.163)	ns (0.109)	ns (0.312)	ns (0.417)	ns (0.083)

3.5.2.2 Approaching Fibres

A greater proportion of approaching tendon fibre angles could be measured compared to tidemark intersection fibres, at 83.4% (196/235 measurement points). The ability to take an accurate and reliable measurement decreased in a proximal direction, with 87.2% of measurements recorded at the 80% and 60% distance points (41/47), 83.0% at 50% distance (39/47), 80.9% at 40% (38/47) and 78.7% at 20% (37/47). Approaching fibre angle could not be reliably judged where fibres had degenerated or become fragmented from sectioning.

Table 3.4 shows the mean angles of approaching fibres, broken down for gender, finger and size category grouping for each measurement distance along the enthesis. Approaching fibre angles were primarily of interest in influencing the size of angle change between them and the tidemark intersection fibres (see *Section 3.5.2.3*).

The overall combined mean angle of approaching fibres was $15.20 \pm 0.97^\circ$, averaged across all enthesis distance measurement points (**Table 3.4**). However, regional variation was noticeable between the distance points. Mean angles were smallest (most acute) at the 20% distance point, the most proximal region measured, with a combined mean of $11.27 \pm 2.16^\circ$, ranging from $4.87 \pm 4.48^\circ$ (male ring finger, the

smallest mean angle of any distance) to $14.21 \pm 3.34^\circ$ (male index). They were then next smallest at the most distal region measured, at 80% distance, with a combined mean of $13.99 \pm 1.09^\circ$, ranging from $12.45 \pm 2.44^\circ$ (male index finger) to $16.27 \pm 2.10^\circ$ (female ring). The approaching fibres were least acute across the central enthesis region, at the 40%, 50% and 60% distance points, showing similar combined mean angles of $16.92 \pm 1.43^\circ$, $17.42 \pm 0.92^\circ$ and $16.36 \pm 0.93^\circ$, respectively. Approaching fibre angles at the 50% distance point were greatest on average, ranging from $11.89 \pm 2.80^\circ$ (male middle finger) to $21.05 \pm 2.48^\circ$ (female little finger), with a range of $13.61 \pm 2.63^\circ$ (male little finger) to $21.52 \pm 3.04^\circ$ (female ring, the largest mean angle of any distance) at 40% distance, and $11.06 \pm 1.85^\circ$ (male middle finger) to $20.01 \pm 1.85^\circ$ (female little) at 60%. The majority of size category groupings showed similar mean angles for each size at each distance point, with a $<3^\circ$ range of mean angles for the average of all distances. Larger ranges were seen at the 50% (5.91°) and 60% distance (8.52°), principally because of the considerable mean angles in the small size category ($20.91 \pm 2.28^\circ$ at 50%, $21.22^\circ \pm 1.94$ at 60%).

Table 3.4 | Approaching Angle Measurements

Collated measurement means of the FDP tendon approaching fibre angle at distances of 20%, 40%, 50%, 60% and 80% along the enthesis. 'Average' is the calculated mean from measurements made at all 5 distances. 'All' represents mean of combined genders, fingers, or both. Size categories match the regrouping of data as performed in Chapter 2 (see Section 2.5.5). EM mean (\pm SEM).

		Angle of Approaching Fibres (°)																	
		20%			40%			50%			60%			80%			Average		
Fingers		Male	Female	All	Male	Female	All	Male	Female	All	Male	Female	All	Male	Female	All	Male	Female	All
		Index	14.21 (3.34)	13.85 (4.01)	14.52 (2.60)	16.56 (2.63)	18.35 (2.63)	17.48 (1.79)	15.52 (2.06)	19.60 (2.22)	17.56 (1.44)	16.96 (1.85)	14.48 (1.85)	14.48 (1.85)	15.71 (1.33)	12.45 (2.44)	13.25 (2.24)	12.85 (1.63)	14.93 (1.73)
Middle	9.86 (3.66)	10.65 (3.34)	10.13 (2.53)	14.85 (2.97)	17.57 (2.78)	16.08 (1.96)	11.89 (2.80)	18.79 (2.22)	15.82 (1.67)	16.84 (1.85)	11.06 (1.85)	11.06 (1.85)	13.92 (1.33)	15.45 (2.44)	13.61 (2.10)	14.30 (1.57)	12.08 (1.82)	15.10 (1.73)	13.64 (1.24)
Ring	4.87 (4.48)	11.06 (3.34)	9.03 (2.67)	14.31 (2.97)	21.52 (3.04)	17.86 (2.06)	15.68 (2.06)	17.59 (2.22)	16.73 (1.44)	14.92 (1.85)	16.22 (1.85)	16.22 (1.85)	15.57 (1.33)	13.86 (2.24)	16.27 (2.10)	15.18 (1.52)	14.65 (1.73)	15.66 (1.73)	15.16 (1.21)
Little	10.02 (3.34)	12.90 (3.66)	11.41 (2.53)	13.61 (2.63)	19.63 (3.23)	16.29 (1.96)	18.06 (2.22)	21.05 (2.48)	19.56 (1.58)	20.01 (1.85)	20.30 (1.74)	20.30 (1.85)	20.25 (1.38)	13.92 (2.24)	13.41 (2.10)	13.62 (1.52)	14.88 (1.73)	17.31 (1.73)	16.10 (1.21)
All	10.21 (3.07)	12.34 (3.06)	11.27 (2.16)	14.90 (2.01)	18.95 (2.05)	16.92 (1.43)	15.55 (1.30)	19.28 (1.30)	17.42 (0.92)	17.17 (1.32)	15.56 (1.31)	15.56 (1.32)	16.36 (0.93)	13.86 (1.57)	14.12 (1.51)	13.99 (1.09)	14.16 (1.38)	16.23 (1.37)	15.20 (0.97)
Size Category		Large	Medium	Small	Large	Medium	Small	Large	Medium	Small	Large	Medium	Small	Large	Medium	Small	Large	Medium	Small
		11.71 (2.47)	10.80 (2.07)	12.33 (3.25)	17.08 (2.06)	16.65 (1.78)	17.98 (3.10)	15.00 (1.29)	18.48 (1.10)	20.91 (2.28)	12.70 (1.48)	17.92 (1.28)	21.22 (1.94)	14.01 (1.49)	14.29 (1.20)	13.32 (1.93)	14.28 (1.20)	15.48 (1.04)	17.03 (1.54)

3.5.2.3 Angle Change

The difference between the angle of approaching fibres and angle of tidemark intersection fibres generated a value for change in angle that was generally similar across genders and fingers, but different across enthesis distance measurement points. **Table 3.5** displays the angle change values for genders and fingers, and **Figure 3.13** graphs and summarises the pattern of comparisons between distance points.

The most consistent result was that the mean angle change at the 20% distance point was always greater than that at all other distances, with a combined mean of $21.05 \pm 1.47^\circ$, ranging from $18.69 \pm 1.69^\circ$ (males) to $24.18 \pm 2.44^\circ$ (females) (**Table 3.5**). It was the only distance point to register significant angle change differences compared to other distances. Mean angle change then appeared to decrease distally, from the 40% distance, with a combined mean of $16.51 \pm 1.56^\circ$ [range $14.10 \pm 2.64^\circ$ (index fingers) to $22.50 \pm 4.18^\circ$ (middle fingers)], to the 50%, 60% and 80% distances. The distal 3 distances provided a cluster of similar ranges [$11.85 \pm 2.55^\circ$ to $13.59 \pm 2.55^\circ$ (50%), $9.95 \pm 1.60^\circ$ to $13.54 \pm 2.39^\circ$ (60%), $10.86 \pm 4.00^\circ$ to $15.89 \pm 2.23^\circ$ (80%)], with a less predictable pattern of comparative mean values within gender and finger groups. Overall, the combined mean angle change at the 80% distance of $13.71 \pm 1.49^\circ$ was slightly greater than that at the 50% ($12.64 \pm 1.50^\circ$) and 60% ($11.84 \pm 1.44^\circ$) distances, but never significantly so.

Table 3.5 | Angle Change between Approaching and Tidemark Fibres

Collated means of FDP tendon fibre change in angle between approaching and tidemark intersection fibres, at distances of 20%, 40%, 50%, 60% and 80% along the enthesis. 'All' represents mean of combined genders and fingers. EM mean (\pm SEM). See Figure 3.13 for plots and significant difference levels.

Angle Change (°)							
	Gender		Finger				All
	Male	Female	Index	Middle	Ring	Little	
20%	18.69 (1.69)	24.18 (2.44)	23.39 (3.25)	22.79 (3.00)	20.26 (2.80)	18.79 (2.86)	21.05 (1.47)
40%	14.56 (1.60)	19.04 (2.90)	14.10 (2.64)	22.50 (4.18)	17.82 (2.94)	14.98 (3.13)	16.51 (1.56)
50%	13.32 (1.64)	11.85 (2.55)	12.51 (3.05)	11.97 (3.56)	13.59 (2.55)	12.41 (3.00)	12.64 (1.50)
60%	9.95 (1.60)	13.54 (2.39)	10.39 (3.25)	11.53 (2.99)	13.24 (2.54)	12.50 (2.76)	11.84 (1.44)
80%	11.21 (1.88)	15.89 (2.23)	14.57 (3.05)	15.88 (2.98)	12.23 (2.45)	10.86 (4.00)	13.71 (1.49)

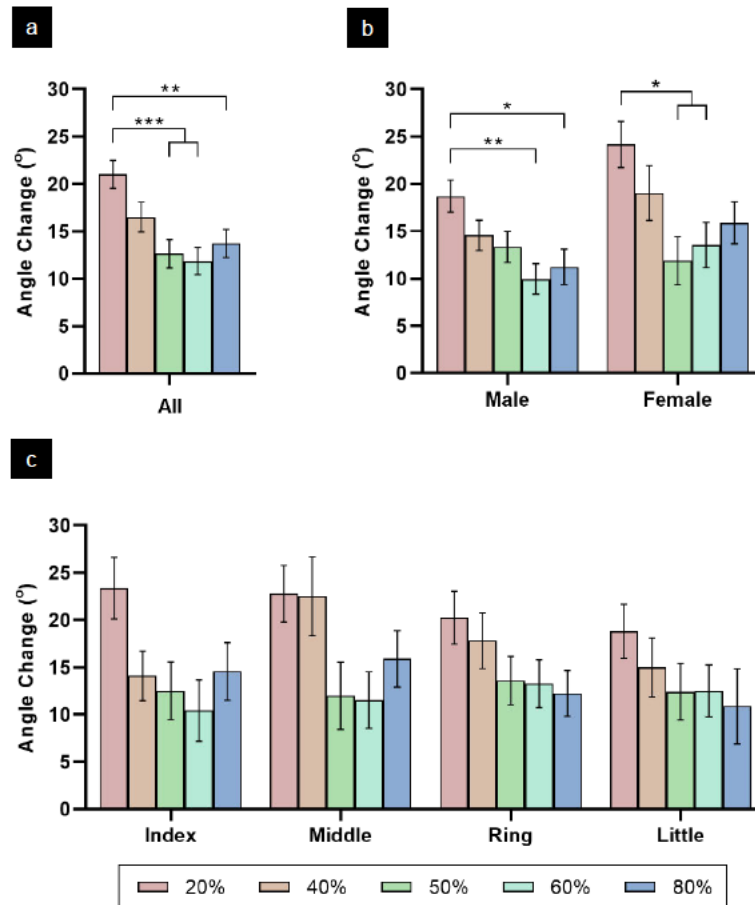


Figure 3.13 | Angle Change between Approaching and Tidemark Fibres

Graphical representation of comparison of angle change between approaching and tidemark FDP tendon fibres at each enthesis distance measurement point, for all combined data (a), genders (combined fingers) (b) and fingers (combined gender) (c). The typical pattern of angle change magnitude is 20%>40%>50%>60% distance point, as seen for all combined data, males, index, middle and ring fingers. Angle change at 50% and 60% is generally similar, and one or both distance points have angle changes significantly different from the 20% distance for all combined data and both genders. The angle change at 80% is comparatively more variable, being both more and less sizeable than the 50% and 60% distances, depending on category. It is always smaller than the 20% and 40% distances, significantly smaller than the 20% distance in all combined data and males. EM mean \pm SEM. *p<0.05, **p<0.01, ***p<0.001.

3.5.2.4 Effect of Side

For all tendon fibre angle measurements, data was split into left and right side values and compared to check if side exerted a significant effect. **Table 3.6** summarises the results, showing that the overall influence of a particular side on mean angle measurements was low.

Table 3.6 | Influence of Side on Tendon Fibre Angle Measurements

Statistical results from left versus right comparisons at all distance measurement points along the entheses for tidemark intersection and approaching fibres, within gender (combined fingers) and finger (combined genders), using a series of linear mixed effects models (see **Table 3.1b** – *models 7a, 7b, 8a, 8b, 8c, 8d*). Side influence is low. Where significant differences are present, parentheses indicate mean angle difference between left and right means. All mean differences are <8°, with the majority of significance approximating 5°. Analysis for tidemark intersection angle comparisons on the middle finger at 40% and the little finger at 80% could not be run as the number of observations made was ≤ the number of model parameters. ‘Sig’ = significant difference; ‘ns’ = non-significant; ‘n/a’ = not applicable. *p<0.05.

Left vs Right Comparison						
	Gender		Finger			
	Male	Female	Index	Middle	Ring	Little
Tidemark						
20%	ns	ns	ns	ns	Sig* (7.65°)	ns
40%	ns	ns	ns	n/a	ns	ns
50%	ns	ns	ns	ns	ns	ns
60%	Sig* (5.48°)	ns	ns	ns	ns	ns
80%	ns	ns	ns	ns	ns	n/a
Average	Sig* (4.28°)	ns	ns	ns	ns	ns
Approaching						
20%	ns	ns	ns	ns	ns	Sig* (5.48°)
40%	ns	Sig* (4.86°)	ns	ns	ns	ns
50%	ns	ns	ns	ns	ns	ns
60%	ns	ns	ns	ns	ns	ns
80%	Sig* (4.55°)	ns	ns	ns	ns	ns
Average	ns	ns	ns	ns	ns	ns

3.5.2.5 Inter-Observer Reliability

Reliability statistics, with interpretation scales, comparing the agreement of 2 observers undertaking all tendon fibre angle measurements are displayed in **Table 3.7**, for collective measurement groupings, and **Table 3.8**, for more individual measurements.

Overall reliability for all measurements made was 'excellent', with an intraclass correlation coefficient (ICC) of 0.907 and Cronbach's alpha of 0.953. The reliability of both tidemark intersection and approaching fibre measurements was 'good', with tidemark fibres (ICC 0.820) more reliable than approaching fibres (ICC 0.796). Measurements made at each distance along the enthesis showed either 'excellent' or 'good' reliability, ranging from an ICC of 0.939 (20% distance) to 0.862 (40% distance), and there was no clear differentiation between reliability of more proximal or distal distances.

For tidemark intersection measurements specifically, reliability was predominantly 'good', being 'moderate' at the 40% distance (ICC 0.709) only. The majority of approaching fibre measurements also had 'good' reliability, with a high 'moderate' result at the 50% (ICC 0.740) and 80% (ICC 0.732) distances.

Table 3.7 | Inter-Observer Reliability of Collective Tendon Fibre Angle Measurements

SPSS reliability statistics (95% confidence intervals) comparing 2 observers. *Raw measurements* are the total number of measurements taken within the collective variable group. *Measurement sets per variable* represents the number of distinct subset variables measured within the collective variable group (i.e. both tidemark and approaching fibre measurements for a specific distance along the entheses, and all 5 distances along the entheses for tidemark or approaching fibre measurements). Subset variables are broken down in Table 3.8. *Excluded measurements* are the number of measurements that could not be compared due to one or both observer(s) being unable to record an angle. A 2-way mixed effects model for the *intraclass correlation coefficient* (ICC) is employed; observers are not randomly selected and each observer measures each variable. The ICC stated is for absolute agreement (comparing exact measurements) of single measures [reliability of a single observer's reported measurements (i.e. the 1st observer's measurements)]. *Cronbach's alpha* approximates the ICC of average measures (reliability of both observers' measurements averaged together). ICC interpretation (Koo and Li, 2016): <0.5 poor; 0.5-0.75 moderate; 0.75-0.9 good; >0.9 excellent reliability. Cronbach's alpha interpretation (Portney and Watkins, 2000): ≥0.70 acceptable. Full SPSS statistical output is provided in *Appendix 3.1*.

		Reliability Statistics						
	All	Tidemark	Approaching	Distance Along Enthesis				
				20%	40%	50%	60%	80%
<i>Raw Measurements</i>	470	235	235	94	94	94	94	94
<i>Measurement Sets per Variable</i>	10	5	5	2	2	2	2	2
<i>Excluded Measurements</i>	126 [26.8%]	78 [33.2%]	48 [20.4%]	26 [27.7%]	29 [30.9%]	27 [28.7]	21 [22.3%]	23 [24.5%]
<i>Intraclass Correlation Coefficient</i>	0.907 (0.886-0.925)	0.820 (0.753-0.869)	0.796 (0.736-0.843)	0.939 (0.899-0.963)	0.862 (0.783-0.913)	0.864 (0.788-0.914)	0.923 (0.880-0.951)	0.926 (0.885-0.954)
<i>Cronbach's Alpha</i>	0.953	0.907	0.886	0.970	0.927	0.926	0.960	0.962

Table 3.8 | Inter-Observer Reliability of Individual Tendon Fibre Angle Measurements
 SPSS reliability statistics (95% confidence intervals) comparing 2 observers. Collective variable groups from Table 3.7 are broken down to show reliability of each distance along the enthesis for either tidemark or approaching fibres. See Table 3.7 for details and interpretation. Full SPSS statistical output is provided in Appendix 3.2.

	Reliability Statistics									
	Tidemark					Approaching				
	20%	40%	50%	60%	80%	20%	40%	50%	60%	80%
<i>Raw Measurements</i>	47	47	47	47	47	47	47	47	47	47
<i>Measurement Sets per Variable</i>	1	1	1	1	1	1	1	1	1	1
<i>Excluded Measurements</i>	15 [31.9%]	18 [38.3%]	17 [36.2%]	14 [28.8%]	14 [28.8%]	11 [23.4%]	11 [23.4%]	10 [21.3%]	7 [14.9%]	9 [19.1%]
Intraclass Correlation Coefficient	0.870 (0.725-0.938)	0.709 (0.467-0.852)	0.758 (0.554-0.876)	0.872 (0.756-0.935)	0.871 (0.753-0.935)	0.757 (0.575-0.868)	0.783 (0.612-0.883)	0.740 (0.546-0.857)	0.811 (0.670-0.896)	0.732 (0.541-0.852)
Cronbach's Alpha	0.940	0.826	0.867	0.935	0.935	0.861	0.885	0.859	0.894	0.842

3.6 Discussion

3.6.1 The FDP Enthesis

The FDP entheses can be classified as fibrocartilaginous since a fibrocartilage layer was consistently identified on tissue sections. This was principally detected by the presence of fibrochondrocytes, including their pericellular metachromasia on toluidine blue staining, and an elevated tidemark, indicating calcification extending into the tendon as the zone of calcified fibrocartilage. This classification was expected since the FDP inserts onto the base of the DP near the DIPJ, and the attachment to bony epiphyses and apophyses is characteristic of fibrocartilaginous entheses (Biermann, 1957; Knese and Biermann, 1958; Benjamin, Evans and Copp, 1986; Apostolakos *et al*, 2014).

Regions of genuine fibrocartilage in the transition from tendon to bone were however the minority of the insertion overall. The greater proportion lacked distinguishable fibrocartilage and was assumed to form a fibrous insertion. In their general survey of human tendon insertion histology, Benjamin, Evans and Copp (1986) noted that areas devoid of cartilage, such as found exclusively in the deltoid and pronator teres, consisted of tendon collagen fibres inserting at acute angles to the bone. Aligning with their observation, an acute angle of insertion was found across the majority of the FDP insertion (further discussed in *Section 3.6.2.2*) signifying that the majority of the insertion was fibrous. It should therefore be recognised that although the FDP insertion is classified and described as a fibrocartilaginous entheses, the average angle of fibre insertion onto the bone across the whole entheses is (perhaps counterintuitively) acute.

The greatest quantity of fibrocartilage was observed in the proximal half of the entheses, towards the DIPJ. This was also an expected finding, guided by previous descriptions that fibrocartilage is most apparent in the portion of the tendon nearest the joint it crosses (Benjamin, Evans and Copp, 1986; Frowen and Benjamin, 1996). Although volar plate tissue of the DIPJ capsule was grossly excised during original dissection of the sample, the elevated tidemark at the proximal commencement of the

FDP enthesis was found as a continuation of the tidemark of the volar plate, a fibrocartilaginous structure, evidently fused with the FDP at their insertion.

Both the uncalcified and calcified fibrocartilage layers appear to relate to forces generated at the enthesis interface. Uncalcified cartilage in particular protects against compression forces (Benjamin and Ralphs, 1998; 2004; Benjamin *et al*, 2006). Benjamin and Ralphs (1998) describe the degree of fibrocartilaginous differentiation relative to the distance from the bony surface against which the tendon is compressed, i.e. the closer to the bony surface, the greater the uncalcified fibrocartilage as an adaptation to compression. The deepest fibres of the FDP insertion are the most proximal fibres, becoming compressed by the more superficial fibres (fibres eventually inserting more distally) during movement of the DIPJ, especially in extension. These deep proximal fibres are also likely to undergo the greatest change in angle during DIPJ movement, as the presence of uncalcified fibrocartilage here also mitigates against the shear force of an abrupt insertional angle change by promoting gradual fibre bending (Evans, Benjamin and Pemberton, 1990; Benjamin *et al*, 1991; Benjamin and Ralphs, 1995; 1998; Benjamin *et al*, 2002).

Calcified fibrocartilage is suggested to relate to the degree of tendon loading on the bone (Evans, Benjamin and Pemberton, 1991; Benjamin *et al*, 1991; Gao and Messner, 1996; Benjamin and Ralphs, 1998). This layer was more variably distributed along the enthesis compared to the uncalcified fibrocartilage, often being present in all 3 proximal, middle and distal regions, however it appeared to be most evident in the proximal region. This perhaps suggests that greater force at the enthesis is transmitted through these proximal/deeper tendon fibres, although the thickness/area of the calcified fibrocartilage was not quantified to substantiate any potential correlations.

An unexpected feature present in some, but not all, FDP entheses was a convex bone profile (see **Figure 3.3a** and **3.5a**), instead of a flat interface. The cortical shell of the DP appeared drawn up into the tendon, with both the convex elevation as a whole and the peak of the elevation usually inclined proximally. This was not noticed in the gross morphological assessments of the FDP-DP interface made in *Chapter 2*. The cortical bone throughout the DP in mid-sagittal section was remarkably thin, although this agreed with previous descriptions (Benjamin *et al*, 2002; Benjamin *et al*, 2007).

The reason for thin bone has been suggested as a contribution to the overall enthesis function of stress dissipation, by allowing slight deformation of the bony shell under tendon load (Benjamin *et al*, 2002; Benjamin *et al*, 2007). The frequent convex bone profiles observed here may substantiate this idea, where deformation has now become obvious and permanent. Since the tissue originated from donors of latter age (mean 79.3), the bony convexity may be a manifestation of the cumulative lifetime effect of tendon pull, in addition to the recognised thinning of cortical bone with age (Benjamin *et al*, 2006) (age-related changes are further discussed in *Section 3.6.4.1*). Furthermore, it appeared that the convexity coincided with the greatest region of fibrocartilage. It would be interesting to investigate whether a correlation exists between thickness of calcified fibrocartilage and peak bone convexity, to further corroborate the association between extent of calcified fibrocartilage and force through the tendon at the enthesis.

3.6.2 Tendon Fibre Insertion Angle

3.6.2.1 Methodology Rationale

The principal reason for undertaking a quantitative histological analysis of the enthesis was to investigate pertinent features that could be translated to the tendon-bone *in vitro* model design. The angle of tendon fibre insertion at the enthesis influences shear and compression (see *Section 1.4.4*), forces particularly associated with a fibrocartilaginous enthesis, and thus insertion angle was both a biomechanically important and feasible design feature for an anatomically relevant model. Change in fibre angle, especially, at the insertion appears related to the presence and magnitude of enthesis fibrocartilage (Evans, Benjamin and Pemberton, 1990; Benjamin *et al*, 1991; Benjamin and Ralphs, 1995; 1998), and so this was also investigated to further characterise the FDP enthesis.

Analysis of tendon fibre angle was based on a published method by Beaulieu *et al* (2015; 2016), who used toluidine blue histology sections to measure a gross single angle of ligamentous insertion against a line of best fit of the tidemark. The current methodology used in this chapter adapted this technique to measure multiple focal angles to amass a more detailed appreciation of the tendon insertion. Since the angle of tendon fibres appeared to differ the closer the fibres were to the bone, a distinction between approaching fibres and inserting fibres was made in the current method.

These fibres were measured at 5 enthesis distance points to explore if the angles changed both along the enthesis length as well as between approaching and inserting fibres. More advanced techniques to assess the tendon collagen fibre insertions were considered, such as electron microscopy, to visualise individual fibres, and polarised light microscopy (PLM), for semi-quantitative orientation analysis through measurement of fibre birefringence. However, these techniques focus on a highly specific region, whereas histological analysis allowed a better overall assessment of the insertion, more suited to a macroscopically relevant tendon-bone model, and was more readily available for the collection of a larger data set.

The tidemark was the key reference point in the histological methodology. This was selected as the point of 'fibre insertion' rather than the tendon-bone junction (the location of true anatomical insertion) for a number of reasons. The tidemark is used as the reference for similarly measuring inserting angles on histology images in published methodologies, both by Beaulieu *et al* (2015; 2016), and Chandrasekaran *et al* (2017), who also specifically examined the digital flexor tendon-bone insertion in pigs. The tendon-bone junction and the tidemark have similar general profiles, and in stained sections the tidemark was often more apparent and easier to trace than the tendon-bone junction. Fibres could be visualised intersecting (traversing) the tidemark, thus the angle was easier to appreciate than at the tendon-bone junction where no fibres were visible 'emerging below' this junction line. Fibres also maintained their angle from the tidemark to the tendon-bone junction, appearing generally linear in sagittal section, and so the angle corresponded at the tidemark and tendon-bone junction. This was expected due to the mineralised fibrocartilage matrix holding the fibres rigid in the calcified fibrocartilage zone. Denoting the angle of tidemark intersection as the reference for the angle of 'insertion' was also based on the classical description of the tidemark representing the mineralisation line, and the mechanical boundary between soft and hard tissues, such as in the preparation of the dry skeleton (see *Section 1.4.4.2.3*). Overall therefore, referencing angle measurements to the tidemark was considered the best representative of the soft-hard tissue interface for a tendon-bone *in vitro* model.

Generating a line of best fit of the tidemark from multiple mapped points also followed the published method of Beaulieu *et al* (2015; 2016). This technique created a single reference line against which to measure angles on the same enthesis, and provided

standardisation for comparison of different entheses. This best represented entheses with flat bone profiles, as was anticipated at the FDP enthesis. However, in addition to flat profiles, many of the current samples displayed an area of bony convexity, particularly towards the proximal enthesis end. This had a minor impact on the gradient of the line of best fit, but primarily influenced the rationale to record multiple measurements along the enthesis length. In areas of bony convexity, the line of best fit of the tidemark and the 'true' tangent of the tidemark could lie at dissimilar gradients, and vary with a positive or negative inclination depending on whether the comparison was made on the upslope or downslope of the convexity. It is unclear how much the convexity affected the angle of intersection of the 'true' tidemark (further discussed in *Section 3.6.2.2*), however it is likely that measurements recorded on a bony upslope undersized representative angles, and those on a downslope oversized representative angles. By taking multiple measurements along the enthesis, recordings were liable to be taken on both upslopes and downslopes of any convexities, controlling for an undulating bony profile. Measuring angles against the 'true' tidemark tangent at every measurement point was considered, however it was difficult to consistently judge the tidemark tangent, whereas the single best fit line was definitive. Most relevantly, the basic design for the *in vitro* model was planned as a flat tendon-bone interface, and the line of best fit was the optimum method to represent the average angle against a flat tendon-bone interface profile.

The selection of toluidine blue as the stain for angle measurement analysis again followed the Beaulieu *et al* (2015; 2016) method. Toluidine blue is useful for cartilage staining since as well as general background staining, the GAGs in the cartilage proteoglycans produces a violet/purple colour shift distinguishable from the regular blue, 'metachromasia', (Sridharan and Shankar, 2012) which aided identification of fibrochondrocytes with an abundant pericellular cartilage matrix. Calcified fibrocartilage was particularly well stained compared to H+E, Van Gieson's and Masson's trichrome. Consequently, this provided the most reliable indication of the both the tidemark, as the upper limit of the calcified fibrocartilage zone, and the tendon-bone junction, as the lower limit, whilst still allowing visualisation of the tendon fibres running in the zone and hence the angle of tidemark intersection. Toluidine blue was generally less adept at isolating the tidemark, particularly compared to H+E (see **Figure 3.3**). Multiple tidemarks could therefore rarely be identified with toluidine blue. However, if a multiple tidemark existed (see **Figure 3.6b**), the tidemark of interest was

the most proximal on the tendon, still represented by the well-defined upper border of the calcified fibrocartilage with toluidine blue. Overall, toluidine blue was judged to provide the greatest overall information for both the angle measurement method and qualitative description.

The main modification to the Beaulieu *et al* (2015; 2016) method was assessing multiple angles on the same enthesis section. Focusing on fibres at the tidemark was considered the optimum location to evaluate the angle of inserting fibres, as recently described. The measurement of approaching tendon fibres was more similar to their method, requiring judgement of an average angle from a wide region of fibres. This was a particularly subjective measurement, perhaps reflecting a slightly less reliable agreement in angles on inter-observer analysis (ICC 0.796) compared to tidemark intersection angles (ICC 0.820), although both still reflected 'good' reliability of the measurement methodology. Evaluating the approaching fibre angle over a preceding 20% enthesis distance was deemed long enough to appreciate the change in angle compared to angle at the tidemark, but short enough to capture fibres fixed in position that reflected the native angle (further discussed in *Section 3.6.4.2*).

Examining multiple measurement points along the length of the enthesis brought a number of benefits. It allowed comparison and greater appreciation of the angle differences along the enthesis length (see *Sections 3.5.2.1.1* and *3.5.2.3*), similarly using 5 comparative measurement points as per Thomopoulos (2006) and Chandrasekaran *et al* (2017) in their insertional fibre orientation studies. As previously described, multiple measurement points also controlled for undulation of the bone (tidemark) profile when reporting an average angle across the whole enthesis length. Primarily however, it maximised opportunities to generate measurement data in samples with multiple areas of pathology, such as cortical bone loss (see *Section 3.5.1.4*), which precluded recording an angle measurement. This improved the validity of the analysis, further discussed in *Section 3.6.2.5*. 5 distance measurement points were selected to provide a representative spread across the enthesis length. 4 points were equally distributed across the enthesis at 20% distances (20%, 40%, 60%, 80%). The 50% point was also examined to ensure that the data set included values for the midpoint of the enthesis length, which would be important when considering a potential single interface angle for an *in vitro* model. The whole data set (measurements at 20%, 40%, 50%, 60% and 80%) was therefore weighted to the

central area of the enthesis, however this was also considered advantageous for generating an average single angle, as the central area was thought to contain the most representative angles.

In the current method, the length of the enthesis, and hence tidemark, was determined by measurement data from *Chapter 2* of the height of the FDP insertion footprint, rather than judgement on the section scan image itself. On sagittal section the length of the FDP enthesis (the FDP footprint height dimension in *Chapter 2*) was difficult to discern. The proximal FDP enthesis tidemark blended with that of the remaining volar plate tissue, although the 2 structures were relatively simple to differentiate. Judging the distal end of the tidemark was particularly problematic due to microscopic connective tissue layers on the tendon that were not grossly visible in the dissections performed in *Chapter 2*. Whether these layers inserted into bone and formed part of the tendon at the enthesis was not clear. Using pre-determined gender- and finger-matched FDP footprint height data overcame this issue, provided a standardised length of measurement for sample comparison, and also combined investigations from macroscopic (*Chapter 2*) and microscopic (current chapter) investigations that are mutual to the design of the *in vitro* model. The pre-determined lengths also aided inter-observer comparisons (see *Section 3.6.2.5*) as the 2 observers were more likely to examine the same precise distance point, and hence test the reliability of the angle measurement technique, rather than measuring an angle at slightly different distance points.

3.6.2.2 Tidemark Intersection Fibres

Data collected on the angle of tidemark intersection was explored in depth as this measurement was considered the most important to the design of an anatomically relevant *in vitro* model. As per *Chapter 2*, the influence of gender, finger and side, as specific factors of interest, was explored; however it is again acknowledged that greater emphasis on analysing variation in the total dataset, rather than testing pre-selected factors, could have provided a useful alternate approach. Since a model design guide based on 3 size categories (large, medium and small) was established in *Chapter 2* (see *Section 2.6.4*), finger and gender data was likewise re-categorised here to assess whether the different size categories also had a significant effect on value differences. Furthermore, data was analysed to investigate whether the angle differed at varying points along the proximal-distal length of the enthesis.

Unlike data in *Chapter 2*, there was no clear pattern of influence amongst genders, fingers or size categories. When considering the average angle across all 5 entheses distances measured (**Figure 3.12**) the only categorical significant difference was gender, comparing females (mean of $32.33 \pm 1.01^\circ$) and males ($27.78 \pm 1.01^\circ$) (**Table 3.2**). This significance pattern was found in only 2/5 of the distance points measured (40% and 60%), and since this average angle difference was $<5^\circ$, the discrepancy seems of limited importance. A significance difference between fingers was only demonstrated at the 60% entheses distance (**Figure 3.10b**), where the little finger angle was significantly greater than the middle finger, including a noticeably greater mean value (but not significant) compared to the index and ring fingers. When separating the fingers across genders, the female little finger was revealed to have the greatest angle (**Figure 3.10c**), which also led to rare significant differences between size categories (**Figure 3.10d**), since the female little finger is the only finger in the 'small' category. The reason for this particular finger at 60% distance having a mean angle of roughly 10° greater than all other fingers is unclear, and is likely to be an anomaly in the data. The 60% distance point itself is unlikely to have had a particular effect, since all other fingers, when broken down by finger and gender, are of an approximately similar value. This is reinforced by finding no significant differences when comparing the distance measurement points across gender and finger groups (**Table 3.3**). A particular side also did not impart an important influence on the tidemark intersection angle (**Table 3.6**).

The overall finding that the angle of tidemark intersection remained approximately the same across finger, gender, size category and side groupings was not unexpected. The size discrepancies between fingers apparent on gross observation that predicted much of the morphometric data relationships in *Chapter 2* are unlikely to affect how fibres of a particular FDP tendon are microscopically positioned at the entheses tidemark. The proximal-distal longitudinal axes of the FDP tendon, held down by the fibrous flexor sheath, and the DP bone, in neutral resting position at the DIPJ joint, are grossly the same in all fingers. Factors that might affect the long-term relationship between the longitudinal FDP tendon and DP axes, such as chronic joint, tendon or entheses pathology, are unlikely to have a predilection for a particular finger across a population as they are inherently systemic.

Although no significant angle differences between distance measurement points along the enthesis for tidemark intersection fibres were found (**Table 3.3**), it should be recognised that angles were measured against a line of best fit of the tidemark, not the 'true' tidemark tangent at the particular measurement point. In reference to the 'true' tidemark tangent, general observation of fibres intersecting the tidemark in the proximal region was much more perpendicular (see **Figure 3.5b**), compared to those in the middle (see **Figure 3.5c**) or distal regions (see **Figure 3.5d**). Whether the presence of the bony convexity in the proximal region precipitated this more perpendicular angle, or whether the same angle at the tidemark existed when the bone profile was flat, is uncertain. The presence of the plug of fibrocartilage in the proximal region, characteristic of where fibres cross the tidemark at approximately perpendicular angles (Benjamin, Evans and Copp, 1986), probably suggests that the same angle was already present. Even so, the bony convexity is likely to be pathological, or at least a feature developed in the life of the cadaveric donors, so any acquired associated angle differences would not represent the normal physiological state. Hence this was a prime reason for collecting multiple measurements along the enthesis, where the average angle across all the distance points measured is more representative than specific angles at certain distance points.

The mean combined tidemark intersection angle across all genders, fingers and different distance measurement points was $30.05 \pm 0.72^\circ$, with mean angles ranging from $22.42 \pm 4.02^\circ$ to $43.60 \pm 5.95^\circ$ (**Table 3.2**). As previously described, this result reflects an average angle across the whole length of the enthesis, measured against a line of best fit of the tidemark. Additionally, some angle measurements may have been slightly undersized if a convex bone profile existed in the proximal enthesis region, marginally tilting the gradient of the line of best fit of the tidemark against which angles were measured. Even so, 30.05° is in contrast to the classical description of fibrocartilaginous fibres generally crossing the tidemark at right angles (Redler *et al*, 1975; Benjamin *et al*, 2002). Where the fibrocartilaginous transition was most obvious, in the proximal enthesis region, many fibres did appear to have a near perpendicular angle to the 'true' tidemark tangent. However, the average result of 30.05° reflects that a large proportion of the FDP is fibrous, associated with much more acute insertion angles (Benjamin, Evans and Copp, 1986).

The current study measures collagen fibre bundles visible on light microscopy scans, which, although adapted from a published technique (see *Section 3.6.2.1*), cannot be compared to any known study of similar methodology that focuses on fibre bundles intersecting the tidemark. A much more detailed investigation of the tendon collagen fibres, such as with electron microscopy or PLM, would give insight into the highly magnified true fibre attachment angle onto bone. At this level of magnification, fibres may lie at a less acute angle. However, in aid of an overall design for a whole multi tissue *in vitro* replica model, the present level of magnification and investigation was both microscopically insightful but still practical. The finding of an average shallow angle with the current methodology may in fact be a contributing factor to the frequency of FDP avulsions, since a less perpendicular angle of insertion increases the possibility of stress singularities at the interface (Lu and Thomopoulos, 2013).

3.6.2.3 Approaching Fibres

The angle of approaching tendon fibres was principally a subsidiary measurement to the tidemark intersection fibres, as an attempt to quantify the amount of angle change between the 2 sets of measurements (see *Section 3.6.2.4*). The approaching fibre angle was planned to be of less direct relevance to the *in vitro* model design, so hypothesis testing of the influence of gender, finger and size category was not explored with inferential statistics for each measurement distance along the enthesis. However, the mean angles were still collated for each of these groupings as per the tidemark intersection fibres (**Table 3.4**) for reference.

Mean angles within gender, finger and size categories were generally similar. For the average of all distances measured along the enthesis, the mean angle difference between the maximum and minimum of the range was limited to 2.07° (gender), 2.46° (fingers) and 2.75° (size categories) (**Table 3.4**). A particular side also did not substantially impact mean angles (**Table 3.6**). As reasoned for the tidemark intersection fibres in *Section 3.6.2.2*, these findings of similarity were not unexpected.

Along the length of the enthesis, angles did appear to vary, although the range was not vastly extensive, from the most acute mean angle of $11.27 \pm 2.16^\circ$ (at the 20% distance measurement point) to the widest mean angle of $17.42 \pm 0.92^\circ$ (at 50%) (**Table 3.4**). The finding that the most acute approaching fibre angles were at the peripheral measurement points (20% and 80%), with the widest centrally (40%, 50%

and 60%), may be explained by the macroscopic distal flattening of the FDP tendon as it came to insert on the DP (i.e. in sagittal section, the proximal-distal length of the enthesis was greater than the flexor-dorsal depth of the tendon). The most distally inserting fibres (i.e. measured at the 80% distance) had an extended distance to travel to insert and therefore approached the insertion at a shallow angle. The most proximal fibres (i.e. measured at the 20% distance) had the most abrupt angle of descent to their insertion, however as the measurement was taken over a 20% preceding length of the enthesis, a large proportion of these fibres were still running nearly parallel with the long axis of the tendon, and had yet to start their abrupt descent into the insertion. The fibres included in this area of measurement interest could therefore widely vary between more flat or steep angles, reflected in the largest standard error of the combined mean for this 20% distance measurement point (2.16°), compared to the others (1.43° , 40%; 0.92° , 50%; 0.93° , 60%; 1.09° , 80%) (**Table 3.4**). For the centrally inserting fibres (i.e. measured at the 40%, 50% and 60% distance), the fibres were already descending more uniformly to their attachment point in the area of measurement interest, and were therefore of the widest comparative angles.

3.6.2.4 Angle Change

Investigation of the change in angle of fibres from their approach to their insertion provided interesting supplementary data to the qualitative description of the FDP enthesis (*Section 3.5.1*). The general pattern was for the greatest angle change proximally, progressively decreasing distally (**Table 3.5, Figure 3.13**). This matched with the general observation of a greater presence of fibrocartilage in the proximal region of the enthesis, although the area or thickness of the fibrocartilage was not quantified. In particular, uncalcified fibrocartilage appeared much more prominent in proximal region (see **Figure 3.5b**) where the change in angle was greatest. This supports the classical analogy of uncalcified fibrocartilage protecting fibres in the same way as a rubber grommet of a plug, allowing a supported gradual bending of fibres/wires into the insertion/plug (Schneider, 1956; Benjamin and Ralphs, 1998; Benjamin *et al*, 2002). The proximal fibres would otherwise be particularly susceptible to damage from shear forces from a large change in angle over a short distance. Future work to quantify the thickness of the uncalcified fibrocartilage at the same distance measurement points as the angle change readings would help to confirm these suspected observations, however for this project these investigations were considered less relevant to an initial *in vitro* model design.

Although the angle change measurements at the 20% and 40% enthesis distance points were consistently the points of largest angle change, they were still potentially undersized. The common presence of a proximal convexity in the enthesis bone profile, as described in *Sections 3.6.2.1* and *3.6.2.2*, necessitated that these proximal points were often measured where fibres were approaching and inserting into an upslope of bone. If the measurement point lay on a flat bone profile, when compared to a line of best fit of the tidemark, the approaching fibres would have a similar angle but the inserting fibres would have a greater angle, thus the angle change would be increased.

The angle change registered at the most distal measurement point, 80%, often did not follow the general pattern of being the smallest, although it was always smaller than the most proximal measurement points. Although the reason for variability is not entirely clear, this is partially described by the distal flattening in sagittal section of the FDP as it inserts, as described in *Section 3.6.2.3*. Since the approaching fibre measurements at this 80% point were generally shallower compared to the central measurement points, but angle of tidemark intersection angle was similar between all measurement points, this could make the angle change greater in the distal region compared to the central region. Uncalcified fibrocartilage was however limited in both central and distal regions on general overview observations. Despite a wider range of angle change measurements at the 80% measurement point, the values are not large, and the associated shear forces are perhaps not likely to demand a guided uncalcified fibrocartilage transition.

3.6.2.5 Validity and Reliability

The angle measurement data gathered in this chapter aimed to be valid primarily to guide the design of an anatomically relevant *in vitro* model. The measurement methodology was devised with this in mind, and the issues pertinent to the validity of the method itself are previously discussed in *Section 3.6.2.1*, such as measuring fibre angle at the tidemark rather than tendon-bone junction, and controlling for a bony convexity at the tendon-bone interface. The method explicitly describes angle relative to a line of best fit of the entire tidemark, rather than relative to the 'true' tidemark tangent at each particular distance measurement point. Although this could be considered misleading for specific measurement points, a single best fit line was a

deliberate choice to be most valid to represent a single straight interface, as would be replicated in the basic tendon-bone interface for the *in vitro* model.

Angle measurements were a subjective assessment, thus validation of the methodology with a 2nd observer was a crucial process. Absolute agreement of measurements was scrutinised, as the strictest model of the intraclass correlation coefficient (ICC). The overall reliability of the method was 'excellent', where even for the lowest ICC for a specific category of measurements, the tidemark intersection fibres at 40% distance, the agreement was a high 'moderate' (**Table 3.7** and **3.8**). The slightly higher ICC for tidemark intersection fibres (0.907) over approaching fibres (0.886) reflects that tidemark intersection angles were more defined, whereas the approaching fibres required a judgement of average angle of fibres that often had a range of angles. Despite this, reliability of the approaching fibre methodology between the 2 observers remained in the upper range of 'good'. When taking the measurements, the proximal 20% distance measurement point seemed to require the greatest degree of judgement over approaching or tidemark intersection angles, due to the greatest range of angles, however this was not manifested by a lower ICC at 20%. In fact, the 20% distance measurement point had the highest level of agreement of any distance when both tidemark intersection and approaching fibres were amalgamated (ICC 0.970), demonstrating that the methodology was still robust when having to judge a single average angle from a range.

Early attempts to measure angles were performed at 3 distance measurement points rather than 5, however this was regarded as too few to provide an overall representation of angles along the enthesis and an accurate mean. Due to a number of pathological features (see *Section 3.5.1.4*), particularly areas of cortical bone loss, many measurement points fell in areas where a reliable angle was problematic to record. Therefore if any doubt existed, the measurement was excluded. By increasing the measurement points to 5 rather than 3, more data could then be recorded, with a confidence that the measurements were reliable. Even so, a considerable proportion of measurements could not be recorded: 28.1% of tidemark intersection fibres and 16.6% of approaching fibres. Samples with less or no pathological features (further discussed in *Section 3.6.4.1*), would have provided a more valid set of measurements. For tidemark intersection angle data, most relevant to *in vitro* model design, over 25% of potential data was unrecordable. Fortunately, for both tidemark intersection and

approaching fibre data, the spread of immeasurable data points for different distances along the enthesis was relatively similar and did not heavily skew to a particular distance, ranging from 23.4% (60% distance point) to 34.0% (40% distance) for tidemark intersection and 12.8% (80% and 60% distance) to 21.3% (20% distance) for approaching fibres. Comparing mean values at the different distance points was therefore still felt to be reliable.

3.6.3 Tendon-Bone Interface Model Design

Histological investigation of the FDP enthesis revealed a number of characteristics that could potentially be incorporated into the design of a replica *in vitro* enthesis model; for example a fibrocartilagenous transition, greater fibrocartilage in the proximal insertion region, and a general decrease in the change in angle between approaching and tidemark fibres distally along the enthesis. Such specific findings might form the theoretical blueprint for an advanced replica model, such as a triphasic tendon-fibrocartilage-bone design, using nanoscaffolds to control tendon fibre angle and mechanical stimulation to replicate tendon fibre movement at the enthesis. However the key findings to inform the initial, feasible enhancing features for a specific FDP-DP *in vitro* model for this project were the angle of tidemark intersection results, which would determine the angle at which tendon and bone components would interface.

When pre-planning the interface design of the model before commencing work in this chapter, 2 competing principles were contemplated. Since the long axis of the FDP tendon and DP bone are approximately parallel at rest, it was clear that tendon fibres needed to incline at an angle to insert into the bone. However, fibrocartilagenous enthesis tendon fibres are suggested to insert at a roughly perpendicular angle (Redler *et al*, 1975; Benjamin *et al*, 2002), and a fibrocartilagenous FDP enthesis was anticipated. An initial design idea was therefore a simple tissue transition in series from tendon analogue to bone anchor, with a straight perpendicular interface, and to let the pliability of the tendon component produce a natural angle of inclination during movement. Yet the opportunity was taken to evaluate the inserting fibres histologically in more detail, and indeed such a design would have oversimplified the angle at the interface. The FDP enthesis had a considerable fibrous insertion component, and with it many fibres inserting at a shallow angle.

The design for the interface between tendon and bone elements for the *in vitro* model was based on a straight bone anchor surface into which the tendon analogue would insert. The use of the line of best fit of the tidemark as a single straight reference line was therefore an important feature of the methodology. The angle that the tendon fibres crossed this line, the angle of tidemark intersection, could then be explored in the same way as per *Chapter 2* data, assessing the influence of finger, gender, side and the novel size category designs previously established.

The angle of tidemark intersection was revealed to be similar, whether evaluated by finger, gender, side or size category (see *Section 3.5.2.1*). A single average angle was therefore thought the most appropriate selection for each of the 'large', 'medium' and 'small' model design sizes (see *Chapter 2*, **Table 2.17**). The overall mean angle for all genders and fingers, averaged across all distances measured along the enthesis, was $30.05 \pm 0.72^\circ$ (**Table 3.2**). The mean angle at the 50% distance measurement point, the centre of the enthesis and considered to represent the most regular and reliable fibre insertions, was similarly $29.67 \pm 1.45^\circ$. These values both rounded to 30° , as the nearest whole degree. Notably, although these mean values were determined as estimated marginal means, calculated from statistical models due to the nature of the data, raw means were within 0.03° for the overall mean (30.08°) and 0.05° for the 50% distance mean (29.62°), also both rounding to 30° . For the design of an anatomically-based, single angle of interface between tendon analogue and bone anchor for the *in vitro* model, this was now set at 30° for all model sizes.

3.6.4 General Limitations

3.6.4.1 Sample

Investigation of human tissue was fundamental to the project concept of designing an anatomically and clinically relevant tendon-bone model. Although images of living human anatomy were considered for analysis of tendon fibre angles, such as ultrasound or MRI, cadaveric tissue allowed a much more versatile range of investigations through histology and microscopic examination. The availability of human cadaveric tissue was limited, and inferring means, patterns and differences in the sample data to the population come with a number of caveats. *Chapter 2*, *Section 2.6.5.1* discusses these general caveats, also directly relevant to the use of human cadaveric tissue in this chapter. Notably, reasonable sample size was considered in

relation to the same published work as cited in that section; the same statistical models were used to maximise sample number from pseudoreplicated finger data; sample source should be explicitly acknowledged as a regional Scottish population; and other unknown variables about the donors, such as handedness, may have influenced the observations.

The age range of the sample (73-91; mean 79.3) was very likely associated with the number of histopathological changes observed. Villotte and Knüsel (2013) noted that from the 6th decade onwards, the fibrocartilaginous enthesis is targeted by degeneration processes, including microtears, microdamage, disturbance of collagen fibres and cell columns, bony resorption, increased calcified fibrocartilage thickness and fibrocartilage vascularisation. Microtears and microdamage were certainly apparent in the present work, as was bone resorption with thin, or frank loss, of cortical bone in a number of regions. Discontinuity of the cortical shell is common in later age, with Benjamin *et al* (2007) noting similar small cortical holes (100–400 µm wide), in 90% of 60 cadavers with a mean age 84 (range 49-101). Interestingly they also found rare large holes (>1mm wide) in the FDP insertion, not observed here. The form of the tidemark may also disclose pathology, such as poor definition (Shaw and Benjamin, 2007) and particularly duplication, associated with osteoarthritis (Lane and Bullough, 1980; Binks *et al*, 2014), both features noted in the present sample. A further feature observed here was the common partial convexity in the enthesis bone profile. This may well have resulted from a cumulative lifetime of stress at the FDP enthesis and buckling of the cortical bone shell in line with the tension force. All these histopathological findings affected the design of the measurement methodology (see *Section 3.6.2.1* and *3.6.2.5*), however measurements in such affected regions were excluded if any abnormality impacted on the angle of the fibres. Yet it is not possible to assume that these findings are not present in a younger sample population. With a greater level and intensity of activity, microdamage and remodelling may also exist, potentially to a higher degree. Even so, the results determined in this chapter should be recognised to derive from a particular sample of latter age donors.

3.6.4.2 Sample Preparation

Preparation of the histological samples entailed some minor limitations in both the qualitative and quantitative assessment. Human cadaveric tissue was fresh but had undergone a freeze-thaw cycle necessary for storage and use, which may have

affected staining and tissue detail. Poor or abnormal visualisation of tidemark or tendon fibres may have slightly impacted on angle measurements, however no apparent loss of differentiation between enthesis zones or major tissue disruption, such as from ice crystal damage, was apparent. Lack of tissue detail was more likely the result of the decalcification process in the acidic solution. Such was this explicit hazard that trials were run with FPL samples before FDP samples to discover the minimum decalcification time necessary to allow smooth microtome tissue sectioning. Despite this, cellular staining was deficient in the majority of sections. Nuclear staining with hematoxylin was performed for 4x the suggested time length for H+E samples, and 6x for Masson's trichrome, attempting to compensate for the many ensuing counterstains and washes, with regular microscope review during the staining process. However, an ideal level of nuclear visualisation was very rarely achieved. Thus cells were identified more by morphology than stain, in particular by lacunae for fibrochondrocytes, and thus slender fibroblasts, packed between collagen fibres, were difficult to identify. Preferably, harder blades specialised for cutting mineralised tissue should be used where available, which may allow a reduction, or perhaps even avoidance, of decalcification.

Tissue dissection to isolate the FDP-DP tendon-bone sample necessarily disturbed the surrounding tissue envelope. Dissection beneath the FDP tendon near the insertion, for example to free the sample from the volar plate, required elevating the FDP tendon about its insertion and moving it through an excessive, non-physiological, range of motion (see *Chapter 2, Figure 2.1*). Despite only brief manoeuvring, inserting tendon fibres may have been bent out of position, although this is very unlikely to have affected the deep fibres at the tidemark which influenced the *in vitro* model design. Furthermore, although the FDP was returned to its natural position for the remaining dissection steps, its position in relation to the DP was not fixed once the sample was isolated and no supporting tissues were in place, before being placed in formalin. In assessing a single macroscopic ligament insertion angle, Beaulieu *et al* (2015; 2016) fixed their samples in formalin in a custom-built fixation device to maintain a natural angle of attachment. Samples in this project were free-floating in formalin without support, which may have fixed the tendon fibres in non-physiological angles. The current samples were much smaller than the comparative study, which used human knee ligament and bone tissue, and gravity was thought to have a minimal effect on relative tissue positions. No macroscopic abnormalities were perceptible. Even if

some tendon fibre angles were mal-positioned, these would most likely be the most proximal FDP fibres near where the tendon was cut in preparing the sample. The angle measurement methodology was designed to measure much deeper fibres, even for the approaching fibre measurement.

3.6.4.3 Tissue Analysis

As with any body region, the enthesis is a 3D structure. Although histology was selected as the most practical and informative investigation technique, only 2D information was possible. To manage this limitation, the methodology was designed to collect the most representative samples of the enthesis. Since Milz *et al* (2002) showed in 3D reconstructions of the human Achilles tendon insertion that the most complex arrangements of the fibrocartilaginous enthesis layers were located centrally, and Thomopoulos *et al* (2006) demonstrated by PLM that collagen fibres were more organised centrally, the mid-sagittal plane was assumed to be the optimal sample plane. As the FDP insertion footprint was previously found to be a vertically symmetrical trapezoid with its near triangular apex tapering distally (see *Chapter 2*), the mid-sagittal plane also provided the greatest amount of tissue in section, to observe for patterns and variations. A deliberate numerical sampling technique using the microtome counter was therefore designed to obtain mid-sagittal sections. Sections were also collected in a parasagittal plane, midway between the lateral edge of the enthesis and the mid-sagittal plane, with the intention to compare with the mid-sagittal tissue, however these sections were not analysed. Including these in the measurement data set would have improved inferences about the entire 3D enthesis. Indeed, if a large variety of parasagittal sections were analysed, a 3D computer reconstruction may have been possible, such as achieved by Dai *et al* (2015) with ACL histology sections at 50µm intervals. Time limitations dictated that only mid-sagittal sections were analysed, and, similarly, only 1 section per finger, where ideally multiple sections per finger would have enhanced the data set. The data analysis was however deemed to be more powerful through having a single section from a larger sample of the population rather than more sections from a smaller population sample.

3.7 Summary of Findings

Histological appraisal of the human FDP has revealed a fibrocartilaginous enthesis, with a considerable element of fibrous insertion. Enthsis fibrocartilage predominated

in the proximal enthesis region, coinciding with the region of greatest angle change as tendon fibres neared their bony insertion. The angle of tendon fibres at the enthesis tidemark averaged 30°, with little variation between genders, fingers, side, size categories and distance along the enthesis, and this will inform the angle of interface between tendon analogue and bone anchor components for all size categories of the *in vitro* FDP-DP model.

CHAPTER 4

ASSESSMENT OF TENDON AND BONE COMPONENTS FOR IN VITRO MODEL DEVELOPMENT

4.1 Chapter Overview

This chapter commences and explores the *in vitro* tissue engineering of the 3-dimensional (3D) tendon-bone model. Cell and tissue culture experiments are performed on each of the essential components of the co-culture model – cells, tendon analogue and bone anchor – to determine their optimal individual contribution to a representative and anatomically-relevant model. Results of the studies guide the selection of materials and culture methods for the culminating co-culture designs in *Chapter 5*.

4.2 Introduction

Tissue engineering ultimately aims to generate replica 3D tissues to replace damaged or diseased native tissues, providing hope for therapeutic advancements in all areas of medicine. It is especially applicable to the musculoskeletal system and the orthopaedic sciences, where form and function are well characterised and a wealth of research aims to progress particularly limited surgical treatments. Within the field of hand surgery and digital flexor tendon reconstruction, tissue engineering has recently focused on the use of decellularised flexor tendon allograft as a pre-formed scaffold (Drake, Tilt and DeGeorge, 2013; Galvez *et al*, 2014; Samora and Klinefelter, 2016), enabling production of reseeded human flexor tendon (Pridgen *et al*, 2011; Raghavan *et al* 2012) and *in vivo* reconstruction in animal models (Kryger *et al*, 2007; Thorfinn *et al*, 2012). This principle has been extended to flexor zone I injuries, decellularising a tendon-bone composite graft consisting of the flexor digitorum profundus (FDP) and attached portion of the distal phalanx (DP) in human cadavers (Bronstein *et al*, 2013; Fox *et al*, 2013), although yet without clinical trials. The tendon-bone composite graft recognises the importance of an intact soft-hard tissue interface, obviating the need to restore the transition between 2 tissues of different structural and mechanical properties. A similar multi-tissue stratified construct is the engineering focus of the current project, but without the need for precious human donor tissue and decellularisation processes.

The basis for the *in vitro* project work is the established 35mm well fibroblast-seeded fibrin hydrogel construct, formed between suture or brushite anchors (**Figure 4.1**).

Silk suture is a standard anchoring material, providing adherence points and an intervening basal tension, between which soft tissue analogues may form, from either cellular monolayers self-organising into a cylinder (Calve *et al*, 2004; Hairfield-Stein *et al*, 2007) or cell-seeded 3D scaffolds. Fibrin is a versatile natural polymer of high biocompatibility and degradability with great potential as a cell-seeded scaffold (Ahmed, Dare and Hincke, 2008) and has been used with this suture anchor system to create constructs of skeletal muscle (Huang *et al*, 2005; Huang, Dennis and Baar, 2006), smooth muscle (Hecker *et al*, 2005), cardiac muscle (Huang, Khait and Birla, 2007) and tendon (Kapacee *et al*, 2008; Bayer *et al*, 2010). Introducing a second tissue creates a more advanced construct by including a tissue interface, such as tendon anchors in muscle constructs (Dennis and Kosnik, 2000; Larkin *et al*, 06). Assembling the more demanding hard-soft tissue interface, by using a 'bone' anchor in the fibrin gel construct system, was first established by Paxton *et al* (2009) and Paxton, Grover and Baar (2010). Brushite, a bioresorbable calcium phosphate salt and excellent bone substitute material due to its similar structural and biological properties (Paxton *et al*, 2010), was used as the bone anchor material to create the hard-soft tissue interface in a whole bone-ligament-bone construct (Paxton, Grover and Baar, 2010) (**Figure 4.1b**). The current project adapts and develops this bone-ligament-bone construct in 3 ways: 1) creating a tendon construct with single bone anchor and single soft anchorage point (suture); 2) shaping and scaling the tendon and bone components to anatomically match the FDP and DP; and 3) seeding osteoblasts onto the bone anchor to establish a co-culture system with the fibroblast-seeded fibrin gel.

This chapter encompasses a number of *in vitro* studies on the cellular, tendon and bone elements of the model. Cell work focused on obtaining representative cells from a single species; tendon work on manipulating the morphology of the developing cell-seeded fibrin; and bone work on achieving successful cell seeding. The majority of the studies were observational, exploring cell and tissue behaviour over time and the effects of different additional factors, to gain a deeper knowledge of the culture system. Early study designs were therefore generally qualitative, with later studies quantitative as relevant parameters were identified and measured. As experience and understanding of basic model development increased, the components were engineered to try and improve their physiological and morphological relevance to an FDP-DP tendon-bone model, for example with different culture media or fibrin gel

additives. Further developed studies introduced more of a hypothesis testing design, with consideration of study power and inferential statistics. Nevertheless, nearly all of the studies were broad ranging and exploratory, acting as an assortment of pilot studies to determine the optimal *in vitro* materials and methods for use with the model design criteria established in *Chapters 2 and 3*, to trial in final anatomically relevant co-culture designs in *Chapter 5*.

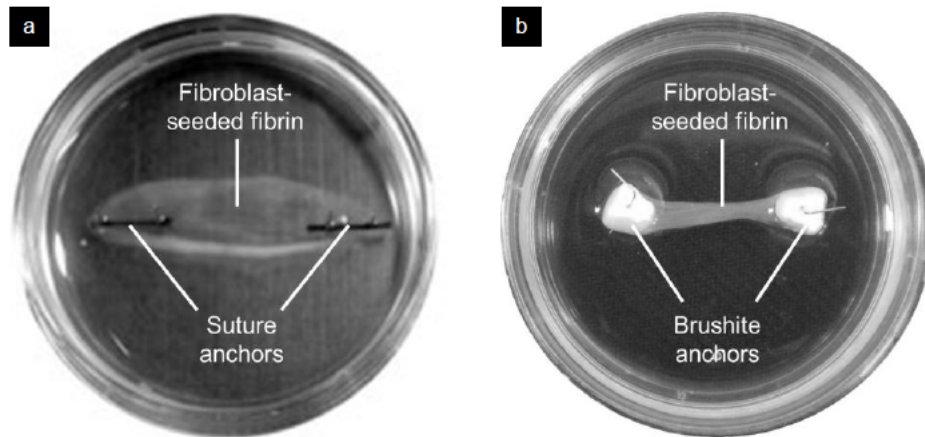


Figure 4.1 | Established Fibroblast-Seeded Fibrin Gel Soft Tissue Constructs
Plan view of established soft tissue suture anchor construct [(a), image adapted from Paxton, Grover and Baar, 2010] and brushite anchor construct [(b), image adapted from Paxton *et al*, 2012a] in 35mm wells. The fibrin hydrogel scaffold seeded with fibroblasts forms the soft tissue element in both constructs. Sutures act solely as an anchor point for the gel whereas brushite also acts as a bone component, generating a bone-ligament-bone construct with 2 soft-hard tissue interfaces.

4.3 Aim and Objectives

The aim of the chapter was to experimentally explore, develop and enhance the individual components of an *in vitro* tendon-bone co-culture model, as both general engineered tendon and bone tissues and specific anatomical representations of the FDP and DP.

The objectives were to optimise:

- 1) Cell choice and culture media;
- 2) Tendon analogue morphology and culture;
- 3) Bone anchor seeding and culture.

4.4 Materials and Methods

4.4.1 Cell and Tissue Culture

4.4.1.1 Sterility

All cell and tissue construct culture work was performed in a class II laminar flow biological safety cabinet, with preceding decontamination of surfaces and non-sterile equipment with 70% industrial methylated spirit (IMS) (Genta Medical, York, UK) in de-ionised water. PBS (phosphate buffered saline), distilled water, and additional glassware, plasticware and dissection instruments were autoclaved (Astell Scientific, Sidcup, UK) at 115°C for 30 minutes before use. Culture media were prepared and maintained sterile. Culture media additives and reagents that could not be prepared sterile were ultimately sterile filtered through a 0.2µm syringe filter (Sartorius Stedim Biotech, Goettingen, Germany) in the laminar flow cabinet before use.

4.4.1.2 Phosphate Buffered Saline

PBS was prepared as a 1x concentration of 0.01M phosphate buffer, 0.0027M potassium chloride and 0.137M sodium chloride (Sigma-Aldrich, Merck Life Science, Gillingham, UK), and was without calcium. PBS was used sterile for cell culture, isolations and reagent preparation.

4.4.1.3 Culture Media

4.4.1.3.1 S-DMEM

Supplemented Dulbecco's modified eagles medium (S-DMEM) was the standard general cell culture medium, consisting of Dulbecco's modified eagles medium (DMEM) (Sigma-Aldrich) with addition of 10% fetal bovine serum (FBS) (Labtech, Heathfield, UK), 2% L-glutamine (Gibco, Thermo Fisher Scientific, Cramlington, UK), 2.4% 4-(2-hydroxyethyl)-1-piperazineethanesulfonic acid (HEPES) buffer and 1% penicillin/streptomycin (Gibco).

4.4.1.3.2 RODM

Rat osteoblast differentiation medium (RODM) was acquired from Cell Applications, Inc (San Diego, USA). Although the precise ingredients were commercially withheld,

the medium was stated to be fully supplemented to promote osteoblast differentiation in culture, and to allow mineralisation of differentiated osteoblast extracellular matrix.

4.4.1.3.3 50:50 Medium

A 50%:50% combination of S-DMEM and RODM (50:50 medium) was freshly mixed from pre-made S-DMEM and RODM on the day of use.

4.4.1.3.4 Ascorbic Acid and Proline

250µM ascorbic acid (AA) and 50µM proline (P) often supplemented S-DMEM. AA was prepared as a 250mM stock, by dissolving 362mg of L-ascorbic acid 2-phosphate sesquimagnesium salt hydrate powder (Sigma-Aldrich) in 5ml pre-warmed 37°C PBS. P was prepared as a 50mM stock, by dissolving 576mg L-proline powder (Sigma-Aldrich) in 10ml PBS. Both reagent stocks were sterilised through a 0.2µm syringe filter, stored at 4°C, and on each day of use freshly added S-DMEM.

4.4.1.3.5 Media Changes

Medium used in cell and tissue construct cultures was changed every 2-3 days unless stated.

4.4.1.4 Culture Methods

4.4.1.4.1 General

Cells were expanded in T25cm³, T75cm³ or T175cm³ vented cell culture-treated polystyrene flasks (Greiner Bio-One Cellstar, Fisher Scientific), and cells and tissue constructs were cultured in cell culture-treated 6-well plates (Greiner Bio-One Cellstar) unless stated. Cells and tissue constructs were kept in a 37°C, 5% CO₂ incubator (Panasonic, Bracknell, UK) when not in use, and solutions used for culture were pre-warmed to 37°C in a digital water bath (Grant, Fisher Scientific) unless stated.

4.4.1.4.2 Sub-Culture

Cells were expanded until approximately 80% confluent in flasks, then either used for experiments or sub-cultured (passaged). Cell detachment from plastic was achieved by 1-3ml of TrypLE Express (Gibco) for 3-5 minutes with 37°C, 5% CO₂ incubation, after initial removal of culture medium and washing of the cell layer with PBS. Dissociated cells were then re-suspended in fresh culture medium, either to be

counted in preparation for experiments, or moved to a fresh flask for further expansion (as such undergoing 1 passage).

4.4.1.4.3 Cell Counting

Cell counting was performed using a haemocytometer counting chamber (Hawksley, Lancing, UK). A sample of evenly mixed cell suspension from a known total volume was transferred into the counting chamber to obtain a 1mm² count. An average 1mm² count was acquired from 5 x 1mm² grid areas viewed under a Leica DMI1 light microscope (Milton Keynes, UK), repeated on a 2nd grid of 5 x 1mm² areas and further averaged, then multiplied by 10⁴ to estimate the number of cells per ml.

Desired cell concentrations were prepared by counting cells, centrifuging the cell suspension at 1000rpm for 3 minutes using a tabletop centrifuge (Heraeus, Cambridge, UK), removing the supernatant from the cell pellet with an aspirator pump, and evenly re-suspending cells in a calculated volume of fresh culture medium.

4.4.1.5 Cell Storage

Expanded cells in culture not intended for imminent experimental use were cryopreserved in their exponential growth phase (70-80% confluent) for future use. Dissociated cells were counted and centrifuged at 1000rpm for 3minutes, the supernatant aspirated and the cell pellet re-suspended in 4°C pre-chilled freezing medium [10% dimethyl sulfoxide (DMSO) (Sigma-Aldrich) in DMEM] at 1 million cells/ml. 1ml cell suspension in cryopreservation vials (Cryo.s, Greiner Bio-One, Stonehouse, UK) were held in a Mr Frosty isopropanol freezing container (Thermo Scientific, Cramlington, UK) at -80°C overnight, until transfer to liquid nitrogen storage at -196°C.

4.4.1.6 Cell Thawing

Cryopreservation vials were retrieved from liquid nitrogen storage, transferred in dry ice and rapidly thawed in a 37°C water bath. The 1ml cell suspension was pipetted into 9ml culture medium and centrifuged at 1000rpm for 3minutes. The supernatant was aspirated from the cell pellet, the cells re-suspended in fresh culture medium, transferred to a T75cm³ culture flask and incubated at 37°C, 5% CO₂. Cells were always passaged once after thawing before experimentation.

4.4.1.7 Imaging and Photography

Cell cultures and histology sections were studied with a Leica DMI1 light microscope and digital images captured with a fitted Leica MC170 HD microscope camera. Overview photographs of cellular monolayers and tissue constructs were taken with a Canon IXUS 275 HS digital camera (Tokyo, Japan), mounted on a retort stand and clamp. Sterile cultures were photographed in the laminar flow cabinet with a black fabric background, culture plate lids removed and culture medium in place, unless stated.

4.4.2 Cells

4.4.2.1 Procurement, Isolation and Expansion

4.4.2.1.1 General Rat Dissection

Primary cell cultures of rat tendon fibroblasts (RTFs), bone marrow-derived mesenchymal stem cells (BMSCs) and osteoblasts (RObs) were isolated concurrently on separate occasions from 3 freshly euthanised female Sprague-Dawley rats, aged 14, 15, and 16 weeks old, obtained from the local animal facilities at The University of Edinburgh.

Animals were pinned on benchtop cork boards and the skin was sprayed with 70% IMS. Sterile dissection instruments (Fine Science Tools, Cambridge, UK), number 15 disposable scalpels (Swann-Morton, Sheffield, UK) and x3 loupe magnification (UK Loupes, Bristol, UK) were used throughout dissection and cleaning of tendons and bones. A circumferential skin incision was made around the top of each hind limb, and a fresh scalpel used to deglove and remove the hind limb skin down to the feet. The femoral heads were dislocated from their acetabula and the hind limbs were detached by incising through the hip joint musculature and ligaments. RTFs (*Section 4.4.2.1.2*), BMSCs (*Section 4.4.2.1.3*) and RObs (*Section 4.4.2.1.4*) were then isolated by further dissection of the hind limbs.

4.4.2.1.2 Rat Tendon Fibroblasts

RTFs were sourced from the full length of both Achilles tendons by collagenase digestion. Excised tendons were immediately placed in 5% antibiotic-antimycotic solution (ABAM) (Gibco) in PBS until transfer to a sterile laminar flow cabinet for further work. They were then carefully scraped clean with a fresh scalpel and residual

connective tissue cleared away. Any remaining debris was removed with 4 washes of PBS using manual hydraulic pressure from a 10ml syringe and 21 gauge needle. Tendons were then placed in 20ml 0.1% collagenase type II solution (Gibco) in DMEM and incubated overnight at 37°C, 5% CO₂. After 15 hours, when the tendons were frayed but not fragmented, the solution was vigorously manually shaken, producing mild tendon disintegration. Using a 10ml serological pipette, the tendons were held down to the bottom of the collagenase tube and pipetted up and down in order to release the cells. The solution was then passed through a 100µm cell strainer (Falcon, Fisher Scientific) and centrifuged at 1250rpm for 5 minutes. Although a pellet was not obvious, the supernatant was aspirated to leave ≈0.5ml, which was re-suspended in 20ml FBS to deactivate the collagenase. This suspension was further centrifuged at 1250rpm for 2 minutes, the supernatant again aspirated to leave ≈0.5ml, which was finally re-suspended in 15ml S-DMEM and transferred to a T75cm³ flask for culture of the isolated cells at 37°C, 5% CO₂. Both supernatants were also processed as above into T25cm³ culture to maximise cell capture.

4.4.2.1.3 Rat Bone Marrow-Derived Mesenchymal Stem Cells

Rat BMSCs were isolated by direct plastic adherence. Continuing the general rat dissection (*Section 4.4.2.1.1*), bilateral femurs and tibias were excised after gross removal of surrounding soft tissues, collected in 5% ABAM in PBS and transferred to a sterile laminar flow cabinet. The bones were then meticulously scraped clean of remaining soft tissue with a fresh blade and repeatedly washed with PBS. The epiphyses were removed from the bones and the marrow cavities thoroughly washed out with PBS under hydraulic pressure using a 10ml syringe and 21 gauge needle. The 40ml of washed-through marrow in PBS was collected in a 150mm dish and the marrow cells dissociated by drawing the solution up and down through a 21 gauge needle. The suspension was then transferred into a centrifuge tube, centrifuged at 1000rpm for 5 minutes, the supernatant aspirated, and the cell pellet washed and re-suspended in 20ml PBS. After a further centrifuge (1000rpm for 5 minutes) and supernatant aspiration step, the pellet was re-suspended in 25ml S-DMEM and transferred to a T175cm³ flask for culture at 37°C, 5% CO₂. After 3 days, S-DMEM was removed and the substantial population of non-adherent haematopoietic cells cleared away with 2x PBS washes, before S-DMEM was replenished and culture of the attached BMSCs continued. The PBS wash step was also repeated on day 6 to remove any remaining non-adherent cells. A further T75cm³ flask was processed as

above from a PBS wash-out of the 150mm dish after transfer of the cell suspension, to capture any remaining cells.

4.4.2.1.4 Rat Osteoblasts

Isolation of RObs followed a published protocol (Bakker and Klein-Nulend, 2012) for long bone explant culture, using the same bilateral femurs and tibias as for the BMSC isolation (see *Section 4.4.2.1.3*). After removal of the epiphyses and flushing of the marrow cavities to obtain the BMSCs, the marrow cavities were meticulously cleaned with needle tip scraping and further multiple flushes of PBS with a 21 gauge needle and syringe. The clean diaphyses were then cut into 1-2mm² pieces using bone cutting scissors, and further washed with PBS. The bony pieces were placed into a 0.2% collagenase type II solution to remove any remaining soft tissue; the solution was warmed in a 37°C water bath for 2 hours, with manual inversion of the solution every 5 minutes and vigorous shaking every 30 minutes. After aspiration of the collagenase supernatant the bone pieces were rinsed and shaken 3x in S-DMEM, allowing the FBS component to deactivate the collagenase. 20-30 pieces were then equally distributed to each of 4x T25cm³ flasks containing 5ml S-DMEM. Pieces were spread evenly over the bottom of the flask by swirling, and left to incubate at 37°C, 5% CO₂, undisturbed for 3 days before standard S-DMEM exchanges commenced. Bone pieces were removed on first passage of the cells when areas of patchy confluence from explanted cells was reached.

4.4.2.1.5 Differentiated Rat Osteoblasts

Differentiated rat osteoblasts (dRObs) were pre-prepared and cryopreserved by previous laboratory members in passage 4-6 before the start of the project. These rat osteoblasts were acquired from Cell Applications, Inc (San Diego, USA), as a cryovial of 1st passage cells obtained from normal healthy adult rat bone (secondary cell culture). The vial was thawed and placed into culture with S-DMEM according to provider protocols. Cells were cultured at full confluency for up to 14 days for 4-5 passages, where a progression in cell phenotype from a large, rounded morphology to smaller, rounded cells with faster proliferation was observed, when cells were considered differentiated.

4.4.2.1.6 Chick Tendon Fibroblasts

Before isolation of RTFs, early tendon analogue work employed primary cultures of chick tendon fibroblasts (CTFs), pre-prepared and cryopreserved by previous lab members before project commencement. CTFs were isolated from hind limb tendons dissected from 13.5 day old chick embryos. Tendons were collected in 5% ABAM in PBS, transferred to the sterile laminar flow cabinet, washed 3x with PBS and isolated by collagenase digestion. Collagenase digestion and subsequent isolation steps then proceeded as per RTFs (see *Section 4.4.2.1.2*), except using a 1.5 hour collagenase digestion.

4.4.2.2 Mineralisation Testing

Cultures of RTFs, BMSCs, RObs and dRObs underwent testing with alizarin red in various culture media for the ability to produce a mineralised extracellular matrix (ECM) within 25 days of culture. This allowed qualitative observation of cell behaviour in extended cultures, and aimed to establish the optimum cell type and culture medium for use in a co-culture of fibroblasts and osteoblasts. The effect of culture media on cellular phenotype was observed, in particular whether: 1) RTFs transdifferentiated towards an osteoblast phenotype in RODM, 2) BMSCs differentiated into functional osteoblasts in RODM, 3) RObs and dRObs required RODM over S-DMEM for mineralising ability, and 4) whether 50:50 medium maintained both fibroblast and osteoblast phenotypes.

4.4.2.2.1 S-DMEM

3 sets of RTFs (from each rat cell isolation as biological repeats, all in passage 2, 'P₂'), and 1 set each of BMSCs (P₃), RObs (P₂) and dRObs (P₆) were tested in S-DMEM. All cells were seeded in duplicate at 100,000 cells per well in 4 x standard treated 6-well plates in 2ml S-DMEM and incubated at 37°C, 5% CO₂, with S-DMEM replacement every 2-3 days. When 100% confluence was approximately reached, encountered for all cell types by day 4, cells of 1 plate from each cell type were fixed in 1ml 4% formaldehyde (Sigma Aldrich) per well for 1 hour at 4°C, after preceding removal of S-DMEM and 2x PBS washes. The 4% formaldehyde was then aspirated, the cells again washed 2x in PBS and then left in 2ml PBS at 4°C until staining. Remaining plates continued to be cultured, with 1 plate from each cell type similarly fixed at weekly intervals (days 11, 18, 25).

4.4.2.2.2 RODM

RTFs, BMSCs, RObs and dRObs were set up for testing in RODM in the same passages as per S-DMEM testing (see *Section 4.4.2.2.1*). The exception was dRObs, in P₇, seeded at 50,000 cells per well, since preliminary investigation of dRObs seeded at 100,000 cells produced over-confluence and a fragile cell layer with excessive ECM that began to disintegrate before completion of the experiment. All cells were seeded in 2ml S-DMEM, but after 24 hours S-DMEM was exchanged for 2ml RODM, and RODM culture then sustained. Plates were fixed as per S-DMEM testing, at the same day 4, 11, 18 and 25 time points.

4.4.2.2.3 50:50 Medium

RTFs (P₅) and dRObs (P₇) were also tested in 50:50 medium. Both cell types were seeded at 100,000 cells per well and set up in the same way as for S-DMEM testing (see *Section 4.4.2.2.1*), but with S-DMEM exchanged for 2ml 50:50 medium after 24 hours, and 50:50 medium culture then sustained. Plates were fixed as per S-DMEM testing and at the same time points.

4.4.2.2.4 Alizarin Red Staining

Fixed plates were stained in batches with alizarin red (Millipore, Merck Life Science, Gillingham, UK), pre-filtered through a 0.2µm syringe filter for sediment removal, to positively stain any extracellular calcium bright red. Fixed plates were retrieved from 4°C storage, PBS was aspirated and wells each washed with 1ml distilled water. 1ml of alizarin red was then added to each well, and plates incubated in the dark at room temperature for 45 minutes. The alizarin red was then aspirated and excess stain carefully washed away with 4x 1ml washes of distilled water. Digital images of the cell layer and wells were captured directly after staining.

4.4.3 Tendon Analogue

4.4.3.1 Fibrin Hydrogel Reagents

Fibrin hydrogel was the cellular scaffold for the tendon analogue component in all model development constructs. Insoluble fibrin was formed through the action of thrombin on soluble fibrinogen, with addition of the fibrinolysis inhibitors aminohexanoic acid and aprotinin. A 'thrombin mix' solution of S-DMEM containing 10U/ml thrombin (*Section 4.4.3.1.1*), 2µl/ml aminohexanoic acid (200mM) (*Section*

4.4.3.1.2) and 2µl/ml aprotinin (10mg/ml) (*Section 4.4.3.1.3*) was initially prepared, to which fibrinogen (20mg/ml) (*Section 4.4.3.1.4*) was added in the ratio 1 part fibrinogen to 2.5 parts thrombin mix. The fibrin gel was then polymerised at 37°C for 1 hour before fibroblast seeding.

4.4.3.1.1 Thrombin

Thrombin was prepared as a 200U/ml stock solution. A 1000U vial of powdered bovine thrombin (Merck, Darmstadt, Germany) was dissolved in a 0.2µm syringe filtered 5ml solution of 0.1% bovine serum albumin (Sigma-Aldrich) in F-12K nutrient mixture (Kaighn's modification) medium (Gibco), stored at -20°C and thawed at room temperature before use.

4.4.3.1.2 Aminohexanoic Acid

Aminohexanoic acid stock was prepared as a 200mM 10ml solution. 0.262g of 6-aminohexanoic acid powder (Sigma-Aldrich) was dissolved in 10ml PBS, the solution then sterilised through a 0.2µm syringe filter, and stored at 4°C until use.

4.4.3.1.3 Aprotinin

A 1% stock solution (10mg/ml) of aprotinin was prepared by dissolving a 10mg vial of aprotinin powder (Sigma-Aldrich) in 1ml PBS, pre-warmed in a 37°C water bath. The solution was transferred to an open 35mm dish and sterilised by UV (ultraviolet) light in the laminar flow cabinet for 20 minutes. 50µl aliquots were stored at -20°C and thawed at room temperature before use.

4.4.3.1.4 Fibrinogen

Fibrinogen was prepared as a 2% stock solution (20mg/ml). 1g of bovine plasma fibrinogen powder (Sigma-Aldrich) was dissolved in 50ml F-12K nutrient mixture (Kaighn's modification) medium, using a 37°C water bath with manual inversions every 15-30 minutes for 4-6 hours. The dissolved solution was sterilised by 0.22µm bottle-top vacuum filtration (Corning Life Sciences, Amsterdam, Netherlands), and stored in 15ml aliquots at -20°C until room temperature thawing for use.

4.4.3.2 Basic Suture-Suture Constructs

4.4.3.2.1 General Method

The tendon analogue was formed by seeded fibroblast contraction of the fibrin hydrogel scaffold between 2 anchor points. Basic tendon constructs were made with 2 silk sutures as anchors set 12mm apart in a 35mm well, as part of a 6-well plate, summarised in **Figure 4.2**.

The base of wells of a 6-well plate were coated with 1.5ml Sylgard 184 silicone elastomer, prepared as 9 parts base agent to 1 part curing agent by mass as provided in the kit (Dow Corning, Wiesbaden, Germany), and left to polymerise at either room temperature for a minimum of 7 days or 50°C in an oven overnight. 2 x 5mm lengths of number 1 silk suture (Ethicon, Bridgewater, USA) were set down flat onto the Sylgard 12mm apart, end to end in series, held in place by Austerlitz minutens stainless steel insect pins (Fine Science Tools) at the suture ends. Sutures were cut to length using a plastic millimetre slide rule and sharp dissecting scissors (Fine Science Tools), and the 12mm separating distance judged by pinning sutures at each end of a 12mm line visible through the bottom of the well, all conducted under x3 loupe magnification (UKloupes, Bristol, UK). The wells, plate and lid were sterilised by thorough spraying with 70% IMS in the laminar flow cabinet, leaving to soak for 20-30 minutes, then vacuum aspirating the IMS and air drying for a minimum of 20 minutes before use. 500µl of 'thrombin mix' (see *Section 4.4.3.1*) was added dropwise to each well, making sure to fully attach to the suture anchors, and agitated to cover the whole well surface. 200µl of fibrinogen was subsequently added dropwise throughout the well surface and the fibrin gel left to polymerise at 37°C for 1 hour. Fibroblasts (RTFs or CTFs) were seeded onto the fibrin gel in droplets at a density of 100,000 cells in 1ml S-DMEM per well. Plates were then incubated at 37°C, 5% CO₂, with a minimum cell attachment time considered 4 hours, and further culture continued with 2ml S-DMEM exchange every 2-3 days. The first culture medium exchange took place on day 3, when any gel remaining adhered to the well rim was encouraged to contract away by gently sweeping between the rim and gel with a micropipette tip.

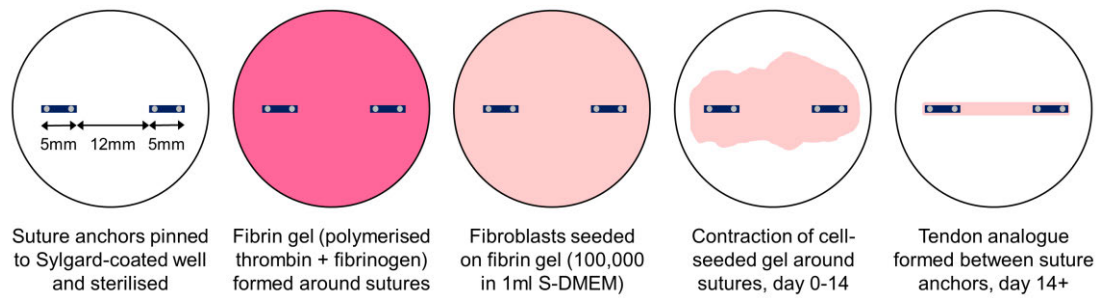


Figure 4.2 | Method of Tendon Analogue Formation in Basic Suture-Suture Constructs

Schematic methodology diagram, plan view of 35mm wells.

4.4.3.2 Investigations

For early handling experience and general qualitative descriptive morphology of formation and maturation over time, multiple constructs were variously set up with P₃ and P₇ CTFs and P₅ RTFs, photographed in overview twice weekly in cultures of up to 35 days.

Extended cultures were performed to compare morphology at earlier and later time points, on constructs grown using P₅ CTFs and cultured in S-DMEM, with supplementation of AA (250µM) and P (50µM) into S-DMEM from week 3 onwards. Histology was performed on 2 constructs after 4 weeks of culture and 2 constructs after 8 weeks (see *Section 4.4.3.4*).

4.4.3.3 Multi-Strand Suture-Suture Constructs

Multi-strand suture-suture constructs were made by combining multiple pre-formed single-strand basic suture-suture constructs. 40 single basic suture-suture constructs, formed with P₅ CTFs in S-DMEM as per *Section 4.4.3.2.1*, were cultured for 21 days and then combined to form 8 double parallel constructs and 8 triple parallel constructs. Single constructs, containing the tendon analogue and both suture ends, were transferred by removing the insect pins and transferring to the well of another single construct using forceps. The construct was then re-pinned directly in parallel with the occupying construct, aiming for contact between tendon analogue strands along their entire long edge, with slight overlap preferable to gapping. Double or triple constructs were formed by transfer of 1 or 2 constructs, respectively, into another occupied well with S-DMEM remaining in place. After combining the constructs, S-DMEM was replaced with 4ml S-DMEM supplemented with AA (250µM) and P (50µM), maintained for the remaining culture. Formation and maturation was studied by overview photography twice per week, and histology (*Section 4.4.3.4*) was performed

on 4 double and 4 triple constructs at both 1 week and 5 weeks of culture after combination of single pre-formed constructs (therefore totalling 4 and 8 weeks from the set up of the single constructs, respectively).

4.4.3.4 Histology

Both single-strand (*Section 4.4.3.2.2*) and multi-strand (*Section 4.4.3.3*) suture-suture constructs underwent histology. Constructs were fixed in 3-4ml 4% formaldehyde for 1 hour at 4°C, then washed and held in PBS at 4°C until histology processing.

4.4.3.4.1 Paraffin Wax Embedding and Sectioning

Constructs underwent paraffin wax processing as per *Chapter 3, Section 3.4.4*. 8µm sections were cut in the transverse and coronal plane on a Leica RM 2245 microtome, and multiple sections floated onto standard glass slides (Thermo Scientific), left to dry in a 37°C oven overnight and stored at room temperature until staining.

4.4.3.4.2 Staining

Construct sections were stained with hematoxylin and eosin (H+E) for general overview and modified Masson's trichrome for a qualitative focus on collagen production. Sections were dewaxed, rehydrated, and dehydrated and mounted after staining as per *Chapter 3, Section 3.4.6*.

Sections for H+E underwent 2 minutes of staining in Shandon Harris hematoxylin (Thermo Fisher Scientific) and 90 seconds in Shandon eosin-Y (Thermo Fisher Scientific). Modified Masson's trichrome staining was performed as per *Chapter 3, Section 3.4.6.4* except for 5 minutes staining in working Weigert's iron hematoxylin.

4.4.3.5 Suture Manipulation Experiments

The length and orientation of the suture anchors in basic single-strand suture-suture constructs were varied to observe the consequence on developing shape morphology of the tendon analogue. These experiments were the first step in investigating larger, vertically positioned anchors and their effect on gel width at regular intervening distances between the anchor points, as a prelude to the 'anatomical suture experiments' (*Section 4.4.3.6*) based on native tendon morphometrics.

Fibroblast-seeded fibrin constructs using 100,000 P₃ RTFs per 35mm well were set up and cultured as per basic suture-suture constructs (see *Section 4.4.3.2.1*), with the same 12mm distance between suture anchors, but with sutures pinned in vertical/vertical (*Section 4.4.3.5.1*) or vertical/horizontal (*Section 4.4.3.5.2*) arrangements. Triplicate technical repeats of each size of vertical/vertical or vertical/horizontal construct were set up and cultured for 35 days. Overview digital photographs were taken every 2-4 days to qualitatively observe macroscopic shape and to quantitate widths of the tendon analogue (fibrin gel) using ImageJ software (National Institutes of Health, Bethesda, USA), as subsequently described.

4.4.3.5.1 Vertical/Vertical

Vertical/vertical constructs consisted of parallel, symmetrical vertical silk sutures of either 10mm, 5mm or 2mm (**Figure 4.3a**). Width measurements of the fibrin gel of the developing tendon analogue were taken at the mid-point of each left and right suture and at quartered distance points between the sutures, namely at 25% (3mm), 50% (6mm) and 75% (9mm) of the distance from the left suture to the right suture (**Figure 4.3b**), to aid descriptive analysis of the shape of the tendon analogue. The analysis focused on whether the fibrin gel widths at the distance measurement points between the sutures contracted to more, or less than, or equal to, the gel width at the level of the sutures (as a single suture gel width average from both left and right sutures). Such contraction patterns would respectively describe a more round, 'H' shaped, or rectangular tendon analogue shape. It was hypothesised that larger sized constructs would produce more of an 'H' shape as gel contraction continued over time between and around the larger sutures, whereas the smaller constructs would remain rectangular or more round.

4.4.3.5.2 Vertical/Horizontal

Vertical/horizontal constructs consisted of vertical 10mm, 5mm, or 2mm sutures set perpendicular to a horizontal 5mm suture (**Figure 4.3c**). Fibrin gel width measurements were correspondingly taken as for vertical/vertical constructs (see *Section 4.4.3.5.1*), noting that the 25%, 50% and 75% distance measurement points were determined by the length between the mid-point of the vertical suture and left edge (inward facing) of the horizontal suture (**Figure 4.3d**). Gel width at the horizontal suture was measured at the mid-point of the suture.

Descriptive analysis of shape focused on whether the developing tendon analogue maintained a triangular shape, with base at the vertical suture and apex at the horizontal suture, or whether gel contraction between the sutures continued to produce a more sideways 'T' shape (with crossbar as the vertical suture). The analysis considered that where the gel width of the distance measurement points between the sutures was equal or less than the width of the gel at the horizontal suture, a near 'T' shape was described. The constructs with larger vertical sutures were hypothesised to produce a proportionally greater 'T' shape, from anticipated continued gel contraction around the vertical suture over time.

4.4.3.5.3 Suture Gel Contraction

It was also investigated whether the fibrin gel at the upper and lower edges of the suture anchor contracted to the same size as the suture itself, using the digital photograph measurements of the vertical/vertical constructs. As well as the gel width measurement taken at the mid-point of each vertical suture (as shown in **Figure 4.3b**), gel width was also measured at the left and right edges of each suture, giving a mean gel width at the suture calculated from left edge, mid-point and right edge measurements. Similarly, a mean width of the suture itself was averaged from left edge, mid-point and right edge width measurements of the suture, and this was compared to the gel width. Both left and right sutures in each vertical/vertical construct were individually added into the data pool from the 3 repeats for each size of construct, providing an n of 6 for each 10mm, 5mm and 2mm suture.

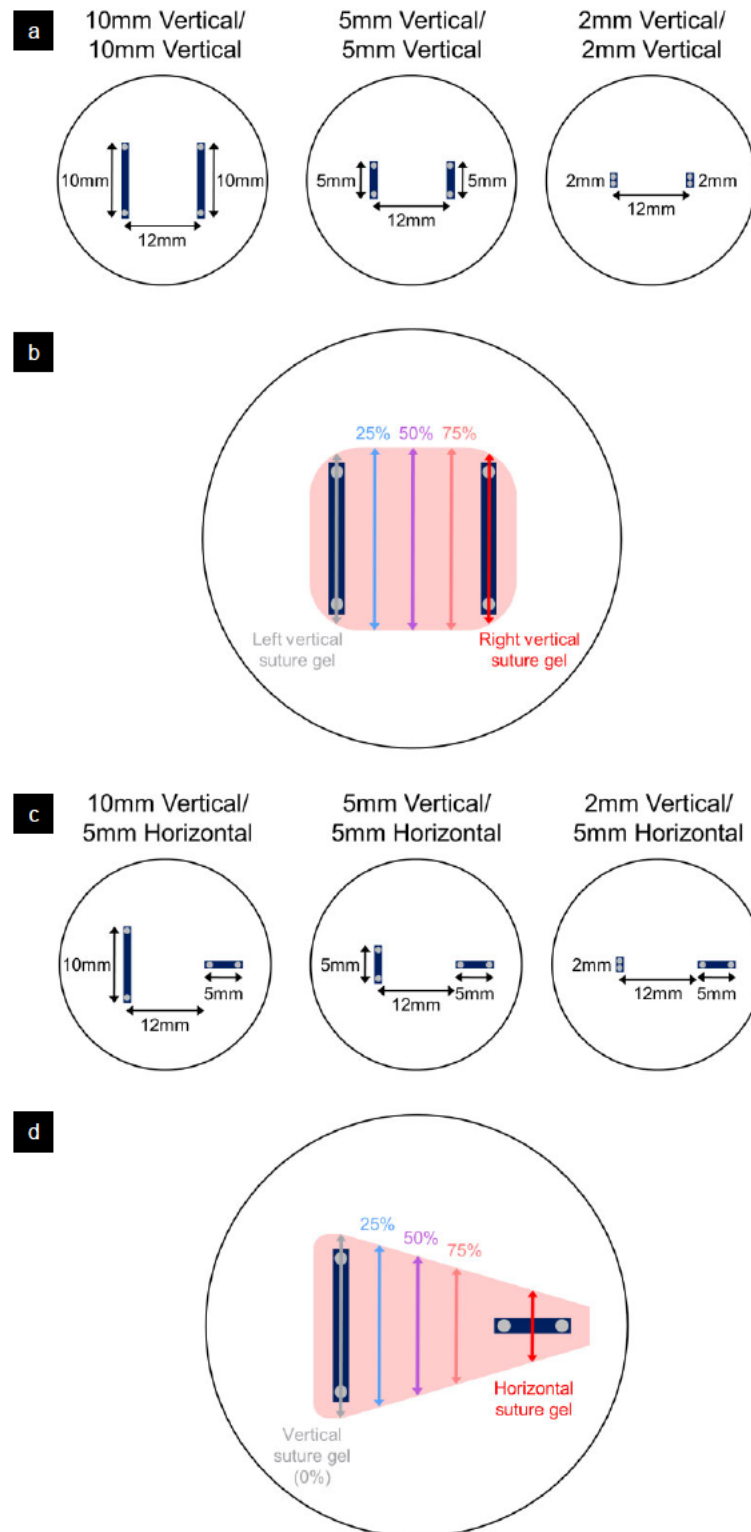


Figure 4.3 | Set Up and Measurement Methodology for Suture Manipulation Experiments

Suture set up for the 3 vertical/vertical suture constructs **(a)** and positions of distance measurement points of gel width in the forming tendon analogue **(b)**. Distance measurement points are illustrated using an enlarged example 10mm construct, with colours of measurement points matching graphed data point results (see **Figure 4.15**). Vertical/horizontal suture constructs are likewise depicted for suture set up **(c)** and distance measurement points **(d)** with an example 10mm/5mm construct and similar colour matching of measurement points to graphed results (see **Figure 4.17**). Plan views of 35mm wells.

4.4.3.6 Anatomical Suture Experiments

Single strand vertical/vertical tendon analogue constructs were subsequently set up using suture anchor sizes (widths) based on the human flexor digitorum profundus (FDP) tendon width data from *Chapter 2*. The left suture was that of the mean width of the base of the FDP insertion onto the bone, 8.58mm (see *Chapter 2*, **Table 2.5**), and the right suture was that of the mean width of the FDP tendon at 12mm distance from its insertion base, 4.69mm (see *Chapter 2*, **Table 2.12**), positioned in parallel with central opposite alignment.

Fibroblast-seeded fibrin gel constructs in 35mm wells with a 12mm gap between sutures were set up as per the vertical/vertical constructs in the suture manipulation experiments (see *Section 4.4.3.5*). 8 different culture variables, as detailed in the following *Sections 4.4.3.6.1* and *4.4.3.6.2*, were investigated. Each culture variable was set up using 3 different sets of RTFs, isolated from 3 different rats (see *Section 4.4.2.1*) as biological replicates, all in P₃. Each separate RTF-seeded construct was prepared with 3 technical repeats, giving 9 constructs per culture variable. 2 constructs for each variable were also set up without cells and maintained under the same culture conditions, including media changes, as controls.

Constructs underwent overview photography and width measurements of the gel every 7 days, commencing at day 7, over 56 days of culture. Width measurements were assessed using Image J as per vertical/vertical constructs (see *Section 4.4.3.5.1* and **Figure 4.3b**), measuring the distance points between the sutures at 0% (mid-point of the 8.58mm left suture), 25%, 50%, 75% and 100% (mid-point of the 4.69mm right suture). Such measurements could thus be related to the measurements of corresponding mean width of the human FDP tendon; at 3mm (25% distance of the 12mm gap between sutures), 6mm (50%), 9mm (75%) and 12mm (100%) from the base of its bony insertion (see *Chapter 2*, **Table 2.12**).

4.4.3.6.1 Standard Volume Gel

4 culture variables were applied to the standard (single) volume fibrin gel set up, using 500µl thrombin mix and 200µl fibrinogen for fibrin formation per 35mm well, as per the standard general method (*Section 4.4.3.2.1*), with standard cell seeding at 100,000 cells in 1ml S-DMEM per well. Culture variables were:

- 1) 'S-DMEM': Standard S-DMEM culture medium throughout.

- 2) '+AA+P': Supplementation of S-DMEM with 250µM ascorbic acid (AA) and 50µM proline (P), introduced at the first medium change on day 3 and continued thereafter.
- 3) 'RODM': S-DMEM changed to RODM at the first medium change on day 3 and continued thereafter.
- 4) 'Mid-point Pins': 2 extra insect pins, as used to secure the sutures, were pinned midway (at 6mm) between the sutures to act as extra anchorage points for the contracting gel, in S-DMEM culture throughout. The pins were separated by a vertical distance of 6.05mm [that of the mean FDP tendon width at 6mm (see *Chapter 2*, **Table 2.12**), parallel and in central alignment to the sutures. Distances were judged with a flexible millimetre paper ruler under x3 loupe magnification.

4.4.3.6.2 Double Volume Gel

4 further culture variables were applied to double the standard volume fibrin gel setup, using 1000µl thrombin mix and 400µl fibrinogen for fibrin formation per 35mm well. Culture variables were:

- 1) 'Double Gel': Standard S-DMEM culture medium throughout.
- 2) 'Double Gel/+AA+P': Supplementation of S-DMEM with 250µM AA and 50µM P, introduced at the first medium change on day 3 and continued thereafter.
- 3) 'Double Gel/Double Cells': Double the standard number of cells seeded in 1ml S-DMEM to 200,000 cells (density ratio of cells to fibrin now remains the same as standard volume gel set ups). Standard S-DMEM culture medium throughout.
- 4) 'Double Gel/Double Cells/+AA+P': As per 'double gel/double cells' but with supplementation of S-DMEM with 250µM AA and 50µM P, introduced at the first medium change on day 3 and continued thereafter.

4.4.3.6.3 Hypotheses

Culture variables were investigated for their effect on gel contraction compared to standard culture in S-DMEM, and their proximity to corresponding human FDP tendon widths. Addition of AA+P to S-DMEM was expected to produce greater contraction over time compared to S-DMEM alone, both in standard volume gel and double volume gel cultures, with and without doubling cell seeding number. Culture in RODM

was also expected to produce greater contraction due to its ascorbate content. Addition of mid-point pins was expected to increase the gel width at the 50% anchorage point, and also provide a consequential increased width at the 25% and 75% points. Double gel volume was expected to increase gel width, but doubling both gel volume and cell seeding number was not. Double cell seeding number, whether with the addition of AA+P to S-DMEM or not, was expected to produce greater contraction than standard cell seeding number, as compared in double volume gels. These effects on fibrin gel width were expected to occur predominantly at the measurement points between the sutures (25%, 50% and 75% points) rather than at the suture anchors themselves (0% and 100% points).

4.4.3.6.4 Optical Coherence Tomography

As an adjunct to the 2D width analyses, optical coherence tomography (OCT) was performed to obtain cross sectional 2D images and 3D reconstructions of the constructs by sub-surface, full depth, imaging. Since 2D overview photography suggested a greater density of gel at the construct peripheries, OCT images would help confirm this observation and provide greater appreciation of the overall morphology and formation of the constructs for each culture variable. Scanning was conducted on 1 construct from each culture variable group after fixation on day 77 of culture. Constructs were fixed in 3-4ml 4% formaldehyde for 1 hour at 4°C, then washed and held in PBS at 4°C until the day of scanning.

OCT was performed using a TEL220C1 Spectral Domain OCT System (Thorlabs, Ely, UK) at Heriot-Watt University, Edinburgh. The system comprised a high resolution Telesto TEL220 base unit and OCTG-1300 scanner of 170nm bandwidth centred at 1300nm. Images were taken at 5µm axial (depth) resolution and 8µm lateral resolution, with a single point A-scan line rate of 28kHz. B-scan 2D cross-sectional images of at least 15mm² scanned area per construct were obtained from multiple A-scans, and 3D volume images were reconstructed from multiple B-scans moving orthogonally through the length of the construct. Image data, including stills from an integrated video camera, were acquired from the integrated ThorImageOCT software package.

4.4.4 Bone Anchor

Experimental bone anchors employed during the project were phosphate mineral based ceramic materials, either brushite (*Section 4.4.4.1*) or Reprobone® (*Section 4.4.4.2*). Brushite, castable and microporous, was the principle (acellular) bone anchor scaffold used in the design of the original bone-ligament-bone construct (Paxton, Grover and Baar, 2010) (see **Figure 4.1b**), and was therefore the main material studied towards development of a seeded bone anchor for the co-culture model. Reprobone, a commercially produced macroporous material, was investigated initially as an alternate scaffold, but, not being castable into custom shapes, was not assessed further in comparison with brushite.

4.4.4.1 Brushite

4.4.4.1.1 β -Tricalcium Phosphate

A stock of CAPTAL® β -tricalcium phosphate (TCP) crystalline powder, used in the formation of brushite, was acquired from Plasma Biotal (Buxton, UK). β -TCP had a theoretical calcium to phosphate molar ratio of 1:5, with a phase purity and crystallinity of >95% and average particle size of 15-30 μ m.

4.4.4.1.2 Cement Formation

The basis for brushite cement formation was combining β -TCP with orthophosphoric acid (OA). Pre-optimisations of the concentration of OA, β -TCP:OA powder:liquid ratio mix and use of cement-setting retardants had been previously investigated and standardised by the supervisor (Paxton *et al*, 2010) and former laboratory members. Cements were accordingly made by mixing β -TCP with a solution of 3.5M 85% pure OA (Sigma-Aldrich), containing 200mM citric acid (Sigma-Aldrich) and 200mM sodium pyrophosphate (Sigma-Aldrich) as retardants, at a powder:liquid ratio of 3.5g/ml. Mixing was performed on a vibrating plate (Jintai R&D, China) as a further retardant. The resulting cement was microporous with 45% porosity (Paxton *et al*, 2010).

4.4.4.1.3 Cement Casting

Brushite cement was cast into a specific shape by reverse molding. The unique designs for various experiments are specified in separate subsequent sections, however the standard process for manufacture of the brushite bone anchors by

reverse molding is described here. The desired shape was composed and integrated into a multi-shape casting tray as a computer-aided design (CAD) file in Tinkercad software (Autodesk, San Rafael, USA). The casting tray was 3D printed in Acrylonitrile Butadiene Styrene (ABS), a strong and lightweight thermoplastic, using a ThermoJet solid object printer (3D Systems, Valencia, USA) at facilities at Edinburgh College of Art, The University of Edinburgh. The mold for the brushite cement was created by filling the casting tray with Kemsil silicone (Associated Dental Products, Swindon, UK), setting within 10 minutes at room temperature, and removing the mold. Brushite cement paste was formed (see *Section 4.4.4.1.2*) and immediately spread and packed into the negative shapes of the mold with a spatula. The cement completely set within 30-60 seconds at room temperature, after which time the specific brushite shapes were removed from the mold for use. Brushite was mixed and cast on the day of sterilisation.

4.4.4.1.4 Sterilisation

Brushite bone anchors required sterilisation before tissue culture experimentation. After casting, the anchors were transferred to the sterile laminar flow cabinet and thoroughly sprayed with 70% IMS, leaving them to soak for 20-30 minutes submerged in a dish of 70% IMS. The 70% IMS was then vacuum aspirated from the dish and anchors, and the anchors left to air dry at room temperature for 20-30 minutes. The anchors were then used directly for experimentation or kept in a sterile container overnight for use the next day.

4.4.4.2 Reprobone

Reprobone[®] material was provided by Ceramisys (Sheffield, UK), as pre-manufactured, sterile, cubed ($\approx 3 \times 3 \times 3 \text{mm}$) or cuboidal ($\approx 3.5 \times 3.5 \times 6 \text{mm}$) blocks. Reprobone is a synthetic, resorbable clinical bone graft substitute made from 60% hydroxyapatite (HA) and 40% β -TCP, at 80% porosity with pore sizes of 200-800 μm (macroporous), affording a composition and structure approximating that of trabecular bone.

4.4.4.3 Basic Tendon-Bone Constructs

Reprobone blocks were used for an initial trial of a basic bone anchor-suture anchor tendon-bone construct, to observe the development and attachment of a tendon analogue to a bone anchor. A 6-well plate of 6 single basic constructs was set up as

per *Section 4.4.3.2.1* except with Reprobone blocks (3 cubes and 3 cuboids) replacing one of the suture anchors. Bone anchors were wedged in place on the Sylgard-coated wells, by 4 surrounding insect pins positioned centrally at each edge, 12mm from the remaining suture anchor. Formulation of the fibrin gel, cell seeding and culture was performed as per *Section 4.4.3.2.1*, seeding P₅ CTFs. Constructs were cultured in S-DMEM for 12 weeks, with serial overview photography every few days. At 5 weeks and 12 weeks, the cuboid blocks were lifted from the well floor with forceps to verify tendon-bone attachment, with and without gentle axial tension from the forceps, and to observe the arrangement of the attachment.

4.4.4.4 Brushite Acid Washout Trials

Brushite tendon-bone constructs had been previously observed to acidify culture medium, with an adverse effect on tendon-bone attachment (reported ahead in *Chapter 5, Section 5.5.2.1.1*). It was therefore investigated if the acid in the brushite could be washed out before cell culture commenced, and if so, how many washes were required. S-DMEM was used for washes, being the standard culture medium, and because the DMEM formulation contained phenol red, a colorimetric pH indicator that transitions from yellow to red along a working range of pH 6.4 to 8.2 (Morgan *et al*, 2019).

Trapezoidal brushite bone anchors in 'large', 'medium' and 'small' sizes were made to the specifications of the bone anchor design guide in **Table 2.17** (*Chapter 2*). The fabrication specifics for these anchors is described in *Section 5.4.1.1* and **Figure 5.1** (*Chapter 5*), but in short, the bone anchors were cast from fresh brushite cement filling the negative shapes in Kemsil silicone molds made from specifically designed multi-shape casting trays. The anchors were then sterilised as per *Section 4.4.4.1.4*.

Single 'large', 'medium', and 'small' brushite bone anchors were placed in triplicate into wells of a 12-well plate. 1ml S-DMEM was added to these experimental wells, making sure to fully submerge the anchor, and also added to triplicate control wells in the same plate containing no anchor. After 10 minutes (1st 'wash'), any colour change of the S-DMEM in the experimental wells compared to the control wells was noted by gross observation, the plate photographed against a white paper towel background, and the S-DMEM vacuum aspirated from the wells and anchors. The anchors were then transferred to a fresh 12-well plate, in the same arrangement, and left to air dry

for 30 minutes. Following drying, 1ml of S-DMEM was again added to the experimental wells and control wells. After 10 minutes (2nd 'wash'), the process of colour change observation, photography, S-DMEM aspiration, plate transfer and 30 minutes air drying was repeated. The procedure was continued until the S-DMEM in all experimental wells was observed to not undergo a colour change compared to the controls in the 10 minute period.

The trial was repeated with different brushite anchors from the same batch on the same day, with some modifications to test validity: 1) different, freshly made S-DMEM, 2) no 30 minute air drying time between washes, 3) further washes after no colour change between experimental and control wells, and 4) repeat photography of a final wash plate after 7 hours left at room temperature in the laminar flow cabinet.

4.4.4.5 Osteoblast Seeding Trial

The proliferation of dRObs seeded on a brushite scaffold and cultured over a 1 week period was investigated using the CyQUANT cell proliferation assay kit (Invitrogen, Thermo Fisher Scientific), a fluorescence-based nucleic acid cell proliferation assay.

4.4.4.5.1 Preparations

Trial brushite scaffolds were manufactured as discs, as a perceived optimum shape to receive drops of cell suspension, of 4.6mm diameter by 2mm height. A 20 disc casting tray was designed, 3D printed and used to create a Kemsil silicone mold. Brushite cement was formed and spread into the negative shapes of the mold, casting the discs, which were then sterilised as per *Section 4.4.4.1.4*.

Some discs were used to plan the optimum volume of suspension for cell seeding. 100µl, 50µl, 20µl and 10µl of tap water were pipetted in drops onto the discs to observe for spillage and disc coverage. 100µl and 50µl spilled over the disc edge, whilst 10µl seemed too small a volume to reach the peripheries of the disc. 20µl was optimum, as pipetting 2-3 separate drops of the volume and pausing for a few seconds for absorption allowed good coverage of the whole disc without spillage.

4.4.4.5.2 Acid Washouts

The brushite scaffolds required washout of acid before cell seeding (see *Section 4.4.4.4*), serving also to pre-soak the material in culture medium for improved cell

attachment. Washes took place in 24-well, flat bottomed, non-tissue culture treated plates (Falcon, Fisher Scientific), to avoid the potential for the hydrophilic treatment applied to treated plates transferring onto the bottom surface of scaffolds.

12 brushite discs were placed singly into wells of the top row of the 24-well plates and 1ml S-DMEM added to each well to submerge the discs. After 10 minutes, S-DMEM was aspirated from the well and disc, and the discs transferred to a fresh well (row below in plates) for another 10 minute wash in S-DMEM. 5 washes of S-DMEM were performed, as per the results of the acid washout trials (see *Section 4.5.3.2*). After the 5^h wash, S-DMEM was aspirated, and the discs transferred to fresh wells to dry at room temperature for 1 hour before cell seeding.

4.4.4.5.3 Cell Seeding

After drying, the discs were transferred to 3x fresh experimental 24-well plates, set up identically for testing at day (D) 0, 2 and 7. Flat bottomed, non-tissue culture treated plates were again used to prevent seeded cells potentially migrating towards a treated well base by chemotaxis. 3 discs per plate were seeded with 10,000 P₁₀ dROBs in 20µl by carefully pipetting the cell suspension onto the top of the disc in 2-3 drops, pausing for absorption between drops, and ensuring no direct spillage of suspension over the disc edge. As positive controls, 20µl of 10,000 cells was also plated out in sextuplicate into wells of 3x flat bottomed, tissue culture treated 24-well plates for D0, 2 and 7. All plates were then incubated at 37°C, 5% CO₂ for 5 hours for cell attachment.

4.4.4.5.4 Cell Collection and Freezing

After 5 hours incubation, cells in the D0 plate were prepared for the CyQUANT assay. Each disc was lifted out of its well with forceps, rinsed with 750µl PBS into the same well, and directly transferred into a 1.5ml reaction tube (Greiner Bio-One, Fisher Scientific) ('Tube A' – *attached seeded cells*). The 750µl of PBS rinse was collected into a 2nd 1.5ml reaction tube, added to which was a further 750µl PBS rinse to maximise cell collection ('Tube B' – *unattached seeded cells*). To detach cells adhered to the discs, 250µl of TrypLE Express was added to Tube A, submerging the disc, following which the tube was incubated at 37°C, 5% CO₂ for 10 minutes and then briefly flicked and tapped on the worktop. With fresh forceps each disc was then lifted out of its tube and rinsed with 1000µl of PBS into the same tube to collect the dissociated cells, and the disc discarded. For the D0 positive control plate, 250µl of

TrypLE Express was also added to each well, the plate incubated for 10 minutes at 37°C, 5% CO₂ and then tapped to dissociate cells, and the 250µl cell suspension added to a 3rd 1.5ml reaction tube ('Tube C' – *plastic-adhered positive control cells*). Wells were rinsed with 1000µl of PBS to collect any residual cells and added to the same tube.

Tubes A, B and C were then micro-centrifuged (Eppendorf, Stevenage, UK) at 2000rpm for 5 minutes, and the supernatant aspirated to leave ≈25µl (as a cell pellet was not often apparent). A PBS wash step was performed to wash away/dilute the phenol red in the S-DMEM that might affect fluorescence readings: 900µl of PBS was added to each tube, micro-centrifuged again at the same settings and the supernatant aspirated to leave ≈25µl. Tubes were then frozen and stored at -80°C until assaying.

D2 and D7 plates, instead of undergoing cell collection and freezing, underwent culture medium addition after the 5 hour cell seeding incubation. Each disc was moved into a new empty well in the same plate (so only attached cells from the initial seeding would be captured in future cell collections), 1ml S-DMEM added to each disc well, and plates incubated at 37°C, 5% CO₂.

On day 2, D2 plates underwent the same cell collection and freezing protocol as D0 plates, with the exception that Tube B contained 1ml of S-DMEM (as the culture medium addition) and a 500µl rinse of PBS (instead of 750µl, beyond the capacity of the reaction tube). D7 plates underwent 1ml S-DMEM exchanges on this day, and at day 5. On day 7, D7 plates underwent the same cell collection and freezing protocol as D2 plates.

4.4.4.5.5 Assaying

All tubes were assayed with 5x concentration of CyQUANT dye, due to its extended linear detection range for predicted cell numbers, from pre-performed standard curves (see *Section 4.4.4.5.6*). The CyQUANT dye fluoresces green when bound to the nucleic acids released from lysed cells and, as per manufacturer instructions, the dye and cell-lysis buffer (both from the Invitrogen kit) were pre-mixed into one working solution. The 5x dye concentration was thus prepared by an 80 fold dilution of the provided 400x concentrated dye in a 1x concentration of cell-lysis buffer, itself diluted from the provided 20x concentration in nuclease-free water (Omega Bio-tek, Norcross,

USA). To prevent photodegradation of the dye, the working solution was prepared fresh and held in a centrifuge tube wrapped in tin foil, and the assay was conducted on the benchtop without overhead lights.

Frozen tubes were serially defrosted and assayed at room temperature in batches to prevent thawed tube contents from degrading. 200µl of the dye/cell-lysis buffer was added to each defrosted cell suspension, mixed by pipetting up and down in the tube, and the entire contents transferred into a well of a flat-bottomed, black chimney, 96-well plate (Greiner Bio-One, Cellstar). A number of tubes were prepared for the plate whilst allowing the optimum 2-5 minute incubation period at room temperature, then fluorescence was read using a GloMax[®] Explorer microplate reader (Promega, Southampton, UK) with excitation at 475nm and emission detection at 500-550nm.

4.4.4.5.6 Standard Curves

Standard curve experiments of known cell numbers were performed before assaying the osteoblast seeding trial collections to ascertain the optimum concentration of CyQUANT dye to achieve a linear cell number vs fluorescence relationship to translate to a predicted range of cell numbers in the seeding trial.

A dilution series of 50, 100, 500, 1000, 5000, 10,000, 25,000 and 50,000 P₉ dRObs in S-DMEM was prepared in quadruplicate in 1.5ml reaction tubes. The cells were collected and frozen as per *Section 4.4.4.5.4*: all tubes were micro-centrifuged at 2000rpm for 5 minutes, the supernatant aspirated leaving ≈25µl, cells washed with 900µl of PBS, and a 2nd micro-centrifuge step and supernatant aspiration leaving ≈25µl for -80°C freezing. These tubes were assayed with CyQUANT as per *Section 4.4.4.5.5*, in the first instance with a 1x concentration of dye, prepared by a 400 fold dilution of the dye in a 1x concentration of cell-lysis buffer. 200µl of the dye/cell-lysis buffer without cells was also plated in quadruplicate and measured in the same way. The standard curve was repeated with the same dilution series using P₈ dRObs, but assayed with 5x dye concentration, as per *Section 4.4.4.5.5*. Resultant standard curves are graphed in *Appendix 4*.

4.4.5 Data Analysis

Quantitative tendon analogue and bone anchor data was recorded and tabulated in Excel 2016 (Microsoft, Redmond, USA) and graphed in GraphPad Prism version 8 (GraphPad Software Inc, San Diego, USA). All descriptive and inferential statistics were performed in GraphPad Prism version 8.

To analyse the anatomical suture constructs (*Section 4.4.3.6*) linear mixed effects models were employed in GraphPad Prism version 8 to account for the non-independence of the same constructs undergoing repeated measures over time. A single design was used for all comparisons, where the main effect of the culture variable (fixed factor) on mean values was tested in a type III sum of squares model including time (fixed factor) and construct measured (random factor); sphericity was not assumed and a Geisser-Greenhouse correction was therefore applied (**Figures 4.21 to 4.25**, and *Appendix 5*).

When analysing osteoblast seeding trial data (*Section 4.4.4.5*), a 2-tailed paired t-test was used for seeding efficiency to compare attached and unattached cells (**Figure 4.31**) and a 1-way analysis of variance (ANOVA) for proliferation on both the brushite scaffold and plastic compared between different days (**Figure 4.32**).

The appropriate normality of data was confirmed through Shapiro-Wilk tests. An alpha level of 0.05 was set, and a Bonferroni post-hoc correction applied to multiple pairwise comparisons for mixed effects and ANOVA models. Unless otherwise stated, data in the chapter is presented as mean \pm standard error of the mean (\pm SEM), with graphical error bars also indicating \pm SEM, and the level of any statistical significance highlighted as * $p < 0.05$, ** $p < 0.01$, *** $p < 0.001$.

4.5 Results

4.5.1 Cells

4.5.1.1 Isolation and Phenotype

4.5.1.1.1 Rat Tendon Fibroblasts

Cells from Achilles tendon collagenase digestion were first observed in isolation on day 2 of primary culture, and confidently seen in small colonies on day 5 (**Figure 4.4**). After adherence, cells soon displayed a classical spindle-shaped morphology and colonies proliferated exponentially until confluence. In established 2D sub-culture, RTFs maintained a large, spindle-shaped morphology and proliferated rapidly. All isolations behaved similarly, although RTFs from the 3rd rat appeared, by observation, to proliferate at a slower rate.

4.5.1.1.2 Rat Bone Marrow-Derived Mesenchymal Stem Cells

Plastic-adhered cells from bone marrow isolations were observed as disparate single cells on day 3 of primary culture, with small colonies noted on day 6 of varying morphology from more rounded to spindle-shaped cell groups (**Figure 4.4**). Colonies proliferated at a moderate rate initially, with the rate appearing to increase with time, where the majority of cells were of haphazard morphology with multiple processes and a large nucleus. Once established in higher cell densities, BMSCs were mostly spindle-shaped, and, compared to RTFs, appeared of similar size with a similar proliferation rate. All isolations behaved alike.

4.5.1.1.3 Rat Osteoblasts

Cells first emerged as explant cultures from bone pieces on day 6, with small colonies in all flasks at day 8 (**Figure 4.4**). Cells were primarily large, rounded/polygonal cells with substantial cytoplasm, although some patches were more spindle-shaped. Most ROb cell explants developed from the smallest bone pieces and microscopic fragments. Disparate cell colonies grew slowly with small confluent areas around bone pieces at day 13-15 as colonies coalesced. After sub-culture, RObs grew more evenly but still appeared slow to proliferate. When cells then became fully confluent they developed a smaller polygonal shape with a higher nuclear-cytoplasmic ratio that together produced a cobblestone appearance (see **Figure 4.6 and 4.7**). With further

sub-culture of these smaller confluent cells, RObs grew much quicker than in the initial primary and early passage cultures, similar to the rate of RTFs and BMSCs.

Unlike the RTF and BMSC primary cell isolations, ROb explant culture was only successful on the 1st of the 3 occasions. In the 2nd isolation attempt, 1 small explant colony of 4 cells was noted on day 8, but this did not proliferate and receded after a further week of culture. No cells were observed on the 3rd attempt.

4.5.1.1.4 Differentiated Rat Osteoblasts

dRObs, from a separate cell line of rat osteoblasts (see *Section 4.4.2.1.5*), had a relatable phenotype to sub-cultured RObs (see *Section 4.5.1.1.3*), but to a further extent. They similarly appeared rounded/polygonal in 2D culture but were noticeably smaller, with an apparent faster proliferation rate (**Figure 4.5**). At confluence they also displayed characteristics distinct from isolated primary RObs, forming multi-layered nodules of cells and ECM, further described in *Section 4.5.1.2.1*.

4.5.1.1.5 Chick Tendon Fibroblasts

CTFs had a similar morphological and behavioural phenotype to RTFs, appearing more spindle-shaped and smaller overall.

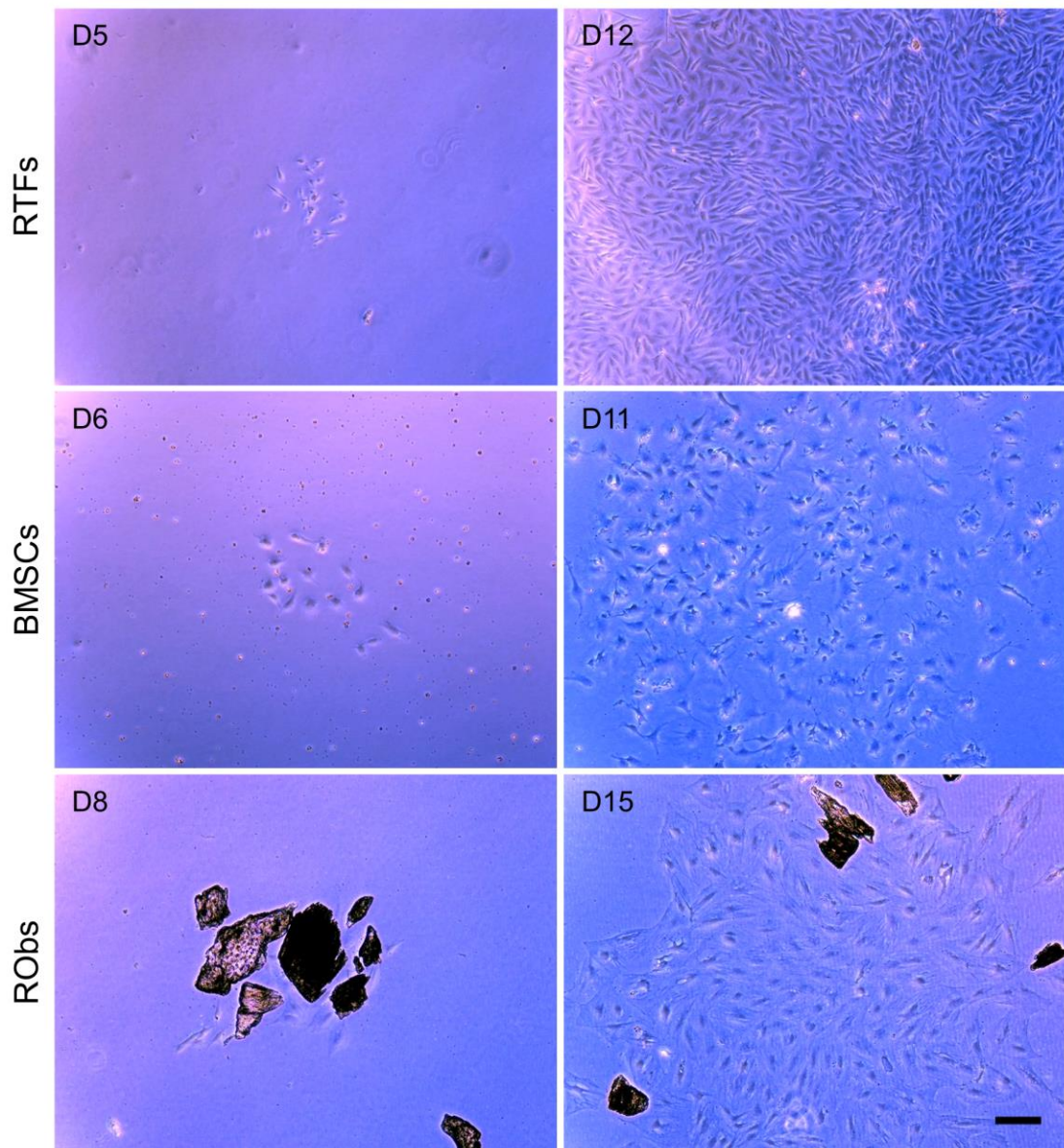


Figure 4.4 | Primary Rat Cell Isolation Cultures and Proliferation

Light micrographs of early (*left panels*) and later (*right panels*) time points of primary isolation cultures of rat tendon fibroblasts (*RTFs*), bone marrow-derived mesenchymal stem cells (*BMSCs*) and osteoblasts (*RObs*) from the same animal. *RTFs* in colony were first seen adhering to culture plastic on day (D)5 of culture, though yet to develop full spindle-shaped morphology. Once established, proliferation was rapid and full confluence was reached by D12. *BMSCs* were first confidently seen at D6 as groups of rounded or spindle-shaped cells, with large cell colonies of mostly haphazard morphology noted by D11. *RObs* first emerged from bone pieces at D6-8, proliferating slowly. By D15, colonies of large rounded/polygonal cells with extensive cytoplasm were forming around and between bone chips, merging together. Scale bar 200 μ m throughout.

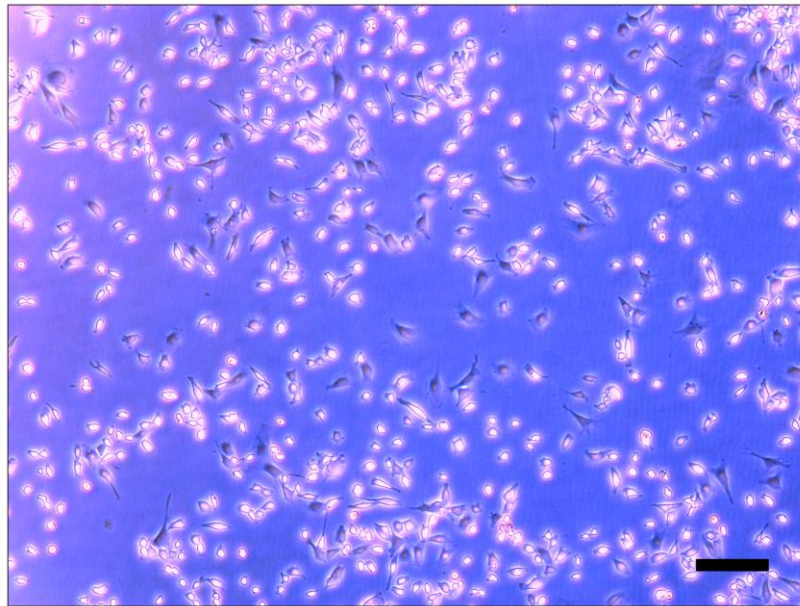


Figure 4.5 | Differentiated Rat Osteoblasts in Early Culture

Light micrograph of differentiated rat osteoblasts (dROBs) at P₆, previously sub-cultured multiple times at full confluence from a separate rat osteoblast cell line, on day 1 in culture. In approximately the first 48 hours of culture, the majority of dROb cell bodies remain highly refractile, possibly still undergoing full anchorage, but are not free floating. The cells are generally polygonal with a high nuclear-cytoplasmic ratio; cell processes are more notable here due to the low cell density. dROBs are conspicuously smaller than ROBs. Scale bar 200µm.

4.5.1.2 Mineralisation Testing

Mineralisation tests were performed in duplicate (technical repeats), and RTFs were also performed with 2 further biological repeats. All results described below represent the qualitative general findings observed in all repeats.

4.5.1.2.1 S-DMEM

No cell types showed evidence of a mineralised ECM when cultured in S-DMEM for 25 days (**Figure 4.6**). All cell types reached 100% confluence by day 4, with the greatest cell density observable in dROb cultures. After day 4, RTFs continued to proliferate gradually as they packed together, and appeared to have produced patchy areas of unmineralised ECM by day 18, which were more obvious and coalesced by day 25. In contrast, BMSCs and ROBs, behaving similarly, were able to pack together with a seemingly greater cell density, often with a whorled appearance, but no distinct ECM was perceived on light microscopy. BMSCs and ROBs were discernible by their cell morphology until they reached 100% confluence, after which both cultures were

not perceptibly different. dRObs rapidly developed many patches of high density polygonal cells, forming a niche of multi-layered cells in different focal planes, already more opaque and clearly observable by day 4. These regions became more dense and numerous by day 11, developing into macroscopic nodules of apparent ECM and cells by day 18, and continued to amass into a trabecular-like network by day 25.

4.5.1.2.2 RODM

dRObs were the only cell type to produce a mineralised ECM when cultured in RODM (**Figure 4.7**). dROb morphology, proliferation and production of nodular ECM forming a trabecular pattern was similar to when cultured in S-DMEM, but with added mineralisation of the ECM nodules by day 18, and further ECM expansion and mineralisation beyond the nodules by day 25. RTFs did not appear to radically change phenotype or transdifferentiate in RODM, but there were some added observations, as follows. Compared to S-DMEM culture, RTFs appeared to proliferate to a higher density and by day 18 more areas of patchy ECM seemed present. By day 25 the cell layer was certainly more fragile, potentially signalling a difference in the amount or quality of the ECM, and in some cultures the ECM appeared nodular. RTF ECM however remained unmineralised. Neither BMSC nor ROb cultures produced a mineralised ECM. BMSC and ROb behaviour appeared very similar in RODM culture compared to S-DMEM, with no obvious ECM observable, and no apparent BMSC differentiation or ROb progression towards a more dROb phenotype.

4.5.1.2.3 50:50 Medium

In 50:50 medium, dRObs still produced a mineralised ECM, although mineralisation occurred at a later stage (day 25) (**Figure 4.8**) compared to RODM culture (day 18) (**Figure 4.7**). dROb behaviour and trabecular-like nodular ECM production was similar to S-DMEM and RODM culture. RTFs appeared to produce a more nodular ECM than in S-DMEM culture, more similar to RODM culture, but the cell layer remained intact and was less contracted than in RODM culture. RTFs did not show an obvious change in morphology and their culture did not display any mineral.

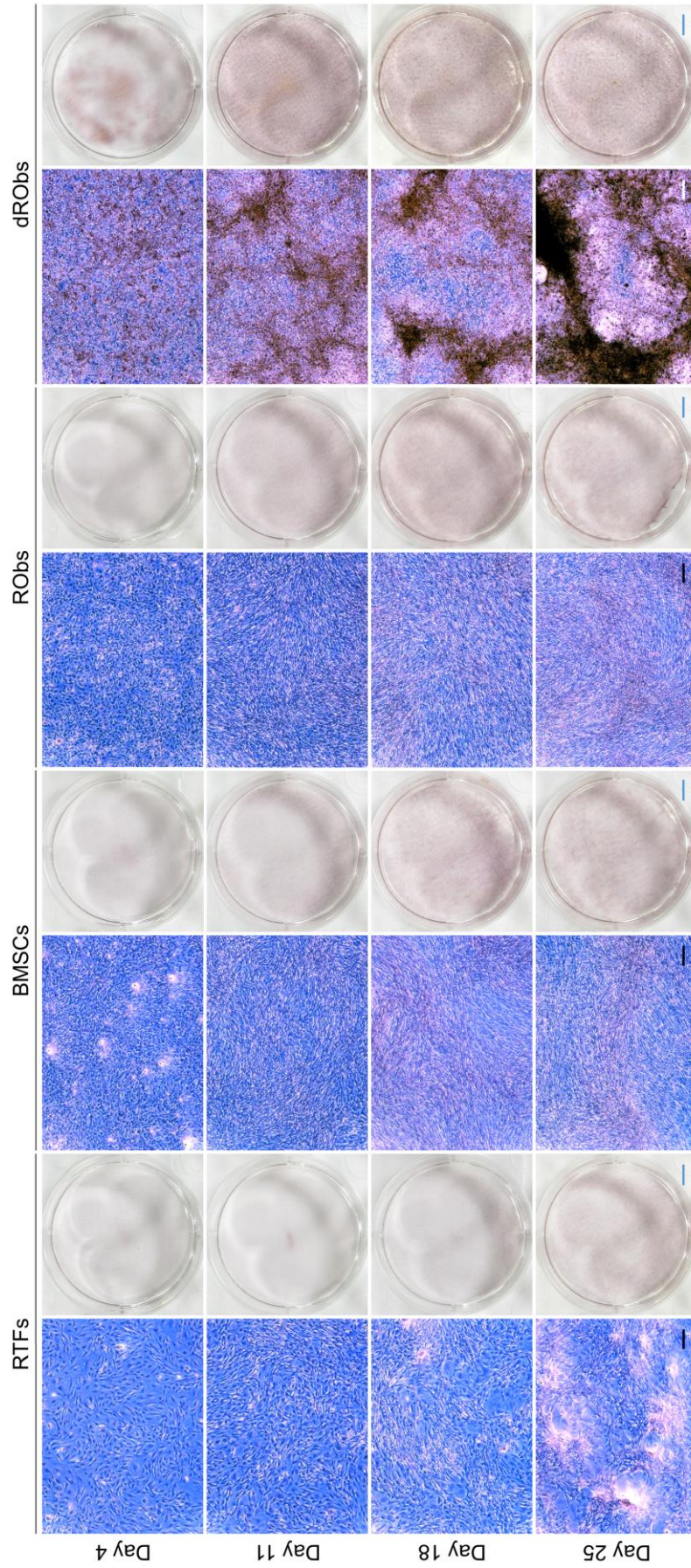


Figure 4.6 | Mineralisation Testing of RTF, BMSC, ROB and dROB Cultures in S-DMEM

Representative light micrographs (*left panels*) and 35mm culture wells (*right panels*) for each cell type grown in standard S-DMEM culture medium, fixed and stained with alizarin red at various time points. No cell type at any time point shows positive red staining, indicating that no calcium is present. All cell types have reached 100% confluence by day 4. dROBs progressively assemble a web-like trabecular pattern of nodular ECM (*dark condensed areas*), whilst RTFs appear to produce a patchy ECM at later time points (*whiter condensed areas*, day 18 and 25). BMSCs and ROBs show no discernible ECM. The cobblestone pattern of confluent ROBs is evident at day 4, becoming less obvious with time as cells compress together. Scale bar 200µm for all micrographs (*black/white*) and 5mm for all wells (*blue*).

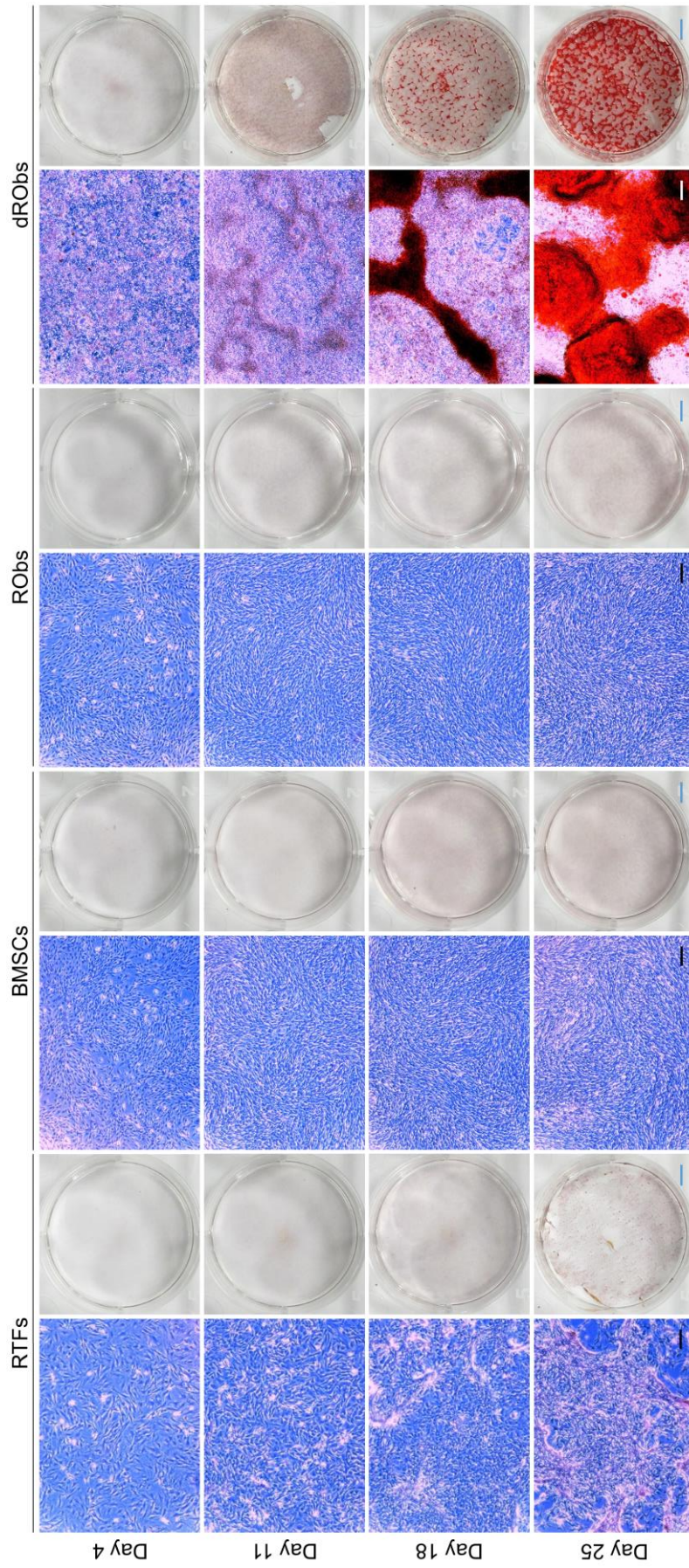


Figure 4.7 | Mineralisation Testing of RTF, BMSC, ROb and dROb Cultures in RODM

Representative light micrographs (*left panels*) and 35mm culture wells (*right panels*) for each cell type grown in rat osteoblast differentiation medium (RODM), fixed and stained with alizarin red at various time points. All cell types have reached 100% confluence by day 4. Only dROBs show positive red staining for calcium, from mineralisation of the expanding web of nodular ECM from day 18 onwards. RTFs appear to produce a patchy, occasionally slightly nodular, unmineralised ECM (*whiter condensed areas*) most noticeably by day 18, and by day 25 contraction of the cell layer with ECM has begun to fragment the monolayer. BMSCs and ROBs show no discernible ECM. The cobblestone pattern of confluent ROBs is again evident, particularly at day 4 before cellular overcrowding. Scale bar 200µm for all micrographs (*black/white*) and 5mm for all wells (*blue*).

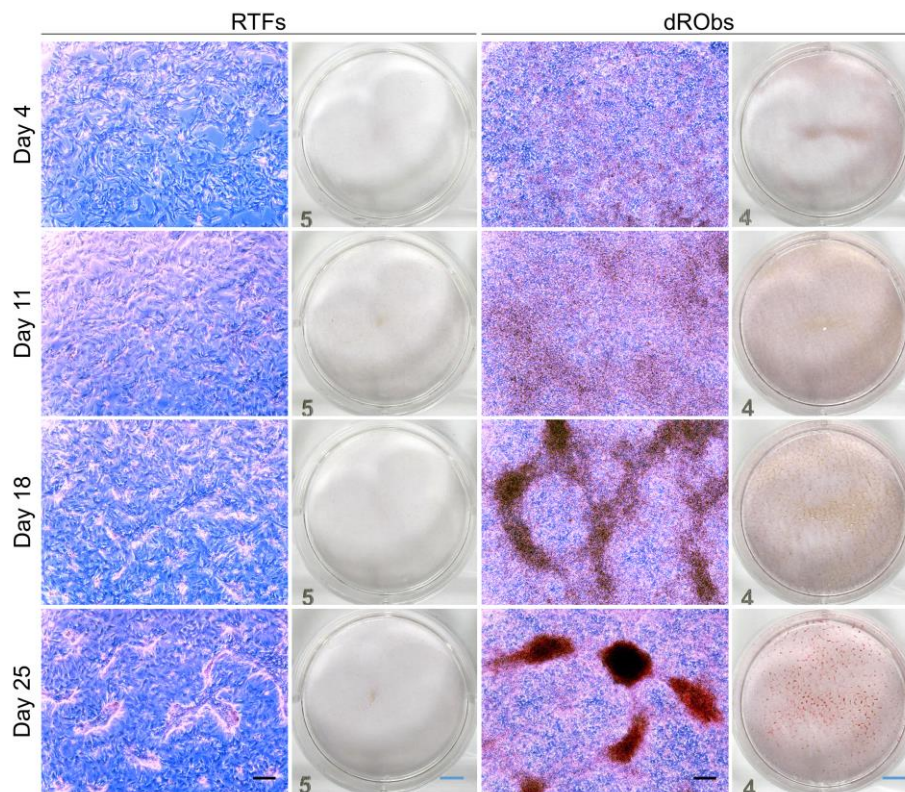


Figure 4.8 | Mineralisation Testing of RTF and dROb Cultures in 50:50 Medium
 Representative light micrographs (*left panels*) and 35mm culture wells (*right panels*) for RTFs and dRObs grown in 50:50 S-DMEM:RODM medium, fixed and stained with alizarin red at various time points. dRObs have started to mineralise their trabecular-like ECM by day 25, shown by areas of faint positive red stain for calcium. RTFs show focal nodular areas of unmineralised ECM by day 18 (*thickened areas*) and the cell monolayer has retained full integrity by day 25. Scale bar 200µm for all micrographs (*black*) and 5mm for all wells (*blue*).

4.5.2 Tendon Analogue

4.5.2.1 Basic Suture-Suture Constructs

The general overview of the formation of the tendon analogue between 2 suture anchors in series is displayed in **Figure 4.9**. The fibroblast-seeded fibrin gel rapidly contracted from the well rim towards and around the suture anchors within the first few days. The vast proportion of contraction occurred within the first week, and by 7 days the shape of the fibrin gel in overview had conformed to the position of the anchors, stretched between them. From day 7-14, the gel noticeably condensed down further between the anchors, becoming slimmer and denser. From day 14-28 macroscopic changes were minimal, although a subtle progression in slimming and density continued. By day 28, the gel continued to be present around all edges of the suture anchors, with the region of gel attached to the inward facing (opposing) edge often tending to be least dense. The general smoothness and uniformity of the shape of the tendon analogue was primarily affected by the regularity of contraction within the first week: where more fibrin gel converged around one particular anchor or regions contracted at different rates, the resulting tendon analogue was often less symmetrical.

Histology of a single-stranded tendon analogue (**Figure 4.10**) showed that inward folding of the fibrin gel was the principle process in its formation through contraction. The folds became tighter and more elaborate with maturity, as the tendon analogue cross section progressed from elliptical to more circular. Cells seeded initially on top of the gel were shown to have migrated throughout the structure, and with time cell numbers comparatively increased and there were regions of cellular alignment in parallel in the direction of tension between the suture anchors. These areas of linear organisation were also where cellular deposition of collagen was most evident in the fibrin (**Figure 4.11**). The amount of stained collagen throughout the structure increased with time but was still low after 8 weeks. A particular histological feature was the presence of a surrounding cellular capsular layer (**Figure 4.10** and **4.11**), present at both the 4 and 8 week investigation time points. H+E and Masson's trichrome stains showed that this layer was external to the fibrin and particularly cell dense, and by 8 weeks it was also a focus of collagen deposition (**Figure 4.11**).

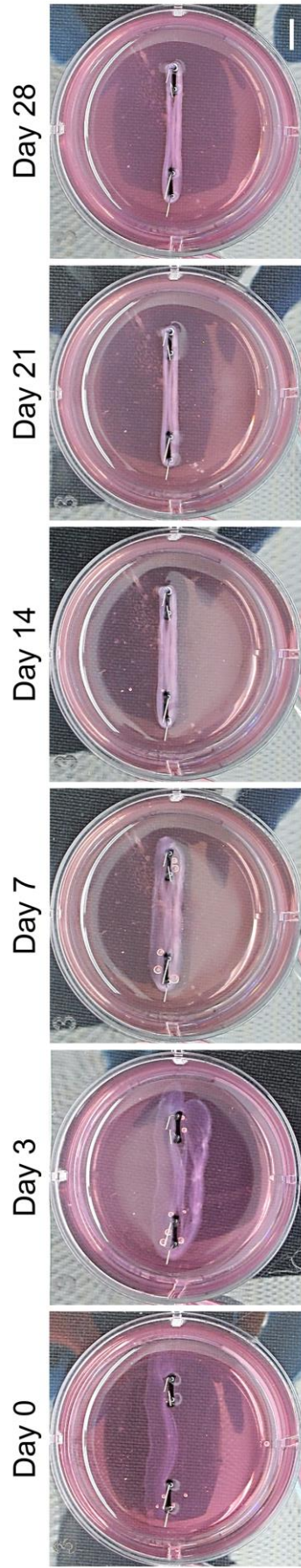


Figure 4.9 | Tendon Analogue Formation in the Basic Suture-Suture Construct

Overview photographs of RTF tendon analogue formation and maturation between basic suture anchors in series over time in 35mm wells, cultured in S-DMEM. The majority of fibroblast-seeded fibrin gel contraction occurs within 7 days, with maturation and further compaction of the tendon analogue from day 7-14 onwards. Although the fibrinogen and thrombin components are spread over the entire well base in preparing the construct, during polymerisation on day 0 the fibrin gel may already have drawn away from the well rim in some areas even before the cells are seeded, as seen here in the 'contracted' upper portion of the gel in the day 0 photograph. Scale bar 5mm throughout.

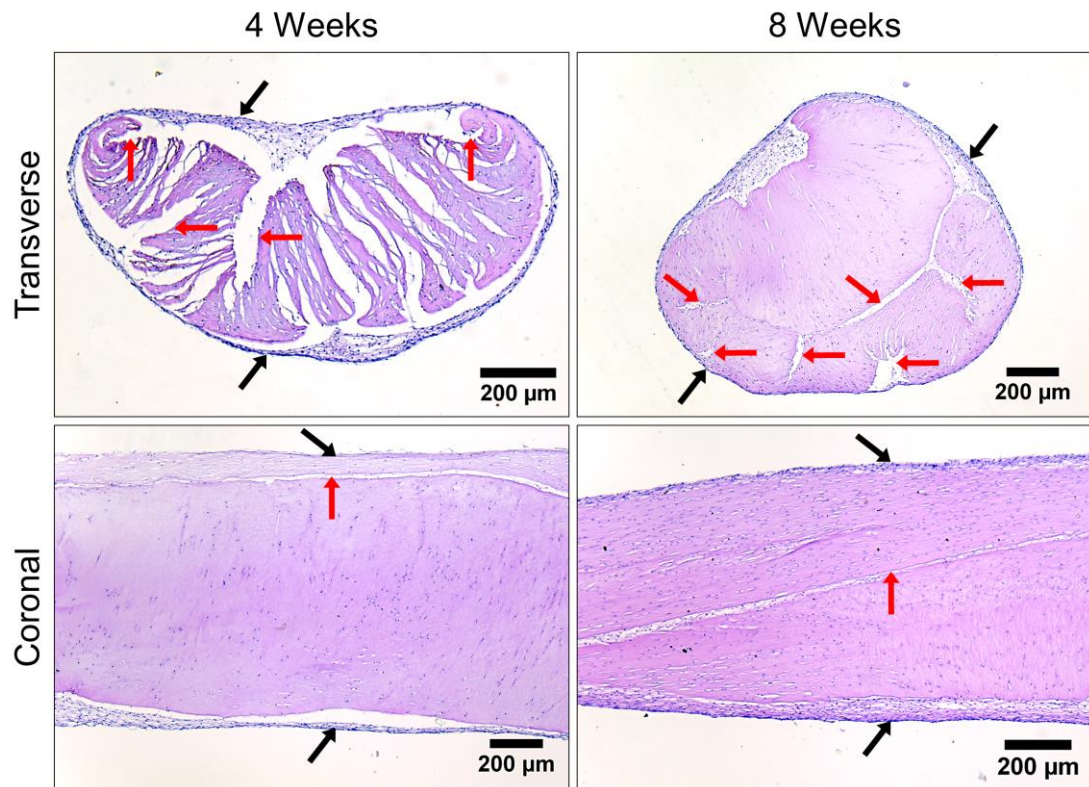


Figure 4.10 | Histology of the Basic Single-Strand Tendon Analogue (1)

Representative histology micrographs of a single tendon analogue at 4 weeks (*left panels*) and 8 weeks culture (*right panels*) in mid-transverse (*upper panels*) and mid-coronal section (*lower panels*) showing morphological progression. Folds in the fibrin gel (*red arrows*) become more convoluted and deeper with time. Cells have seeded throughout the fibrin gel, although a marked cellular capsular layer (*black arrows*) is conspicuous at the periphery. At 4 weeks, the fibrin gel is flatter, wider and less folded and compact. At 8 weeks, the fibrin is folded in on itself and condensed into a more circular cross-section within the surrounding capsular layer. The structure also appears more cellular at 8 weeks, with cells more aligned in the direction of tension between the anchors (*to right and left of coronal panels*). H+E.

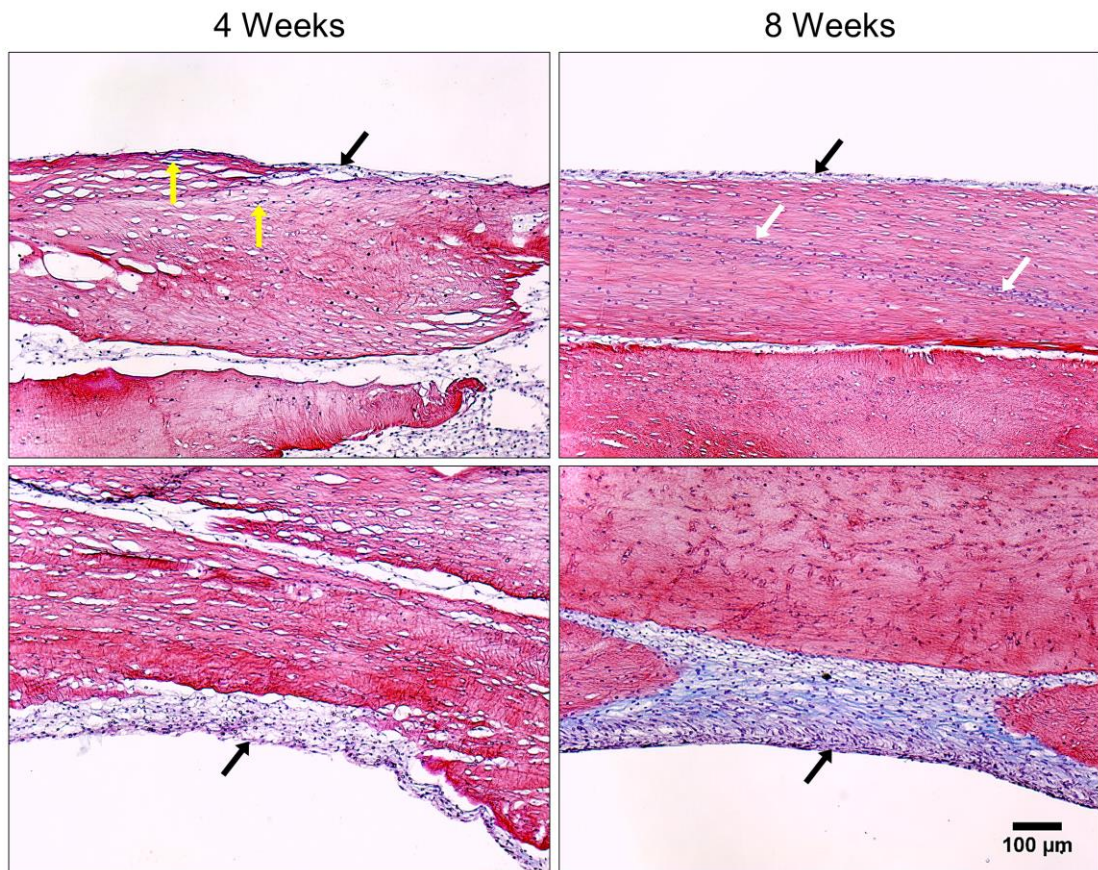


Figure 4.11 | Histology of the Basic Single-Strand Tendon Analogue (2)

Representative mid-coronal section histology micrographs of a single tendon analogue at 4 weeks (*left panels*) and 8 weeks culture (*right panels*) comparing collagen production (*blue stain*) and tissue organisation in 2 similar regions (*upper or lower panels*). At 4 weeks, the overall structure of the tendon analogue is less condensed, and the cells are less arranged. Collagen production is limited to small pericellular areas (*yellow arrows*). At 8 weeks, the tissue is more compact. Cells are more organised along the line of tension between anchors (*to right and left of all panels*), where production of parallel bands of collagen is evident (*white arrows*). The ever-present highly cellular capsular layer (*black arrows*) appears to be a region of particular collagen production with time (*lower panels*). Modified Masson's trichrome stain (deep red: cytoplasm; blue: collagen; black: nuclei). Scale bar 100 μ m all panels.

4.5.2.2 Multi-Strand Suture-Suture Constructs

Macroscopic overview of the development of double- and triple-stranded suture-suture tendon analogue constructs is depicted in **Figure 4.12**. The separate strands appeared to grossly fuse together with time. By day 15 of combined culture the transparencies between separate strands, indicating their division, was progressively difficult to discern, and at final observation on day 35 the constructs appeared as single units. Histology however revealed that the individual strands remained separate (**Figure 4.13**). The interface between individual strands narrowed to the point where no cellular capsular layer was interpositioned between the strands at 5 weeks of combined culture, however the separate tendon analogue strands had not fused together. This resembled the interfacial arrangement of folds of the same strand against (within) itself. The overall cross-sectional shape of the double-stranded tendon analogue was roughly biconcave (**Figure 4.13**), flatter at 1 week and bulkier at 5 weeks, representing the continuing compression of folds of fibrin gel in each maturing individual single-stranded tendon analogue. Histological findings were the same for triple-stranded constructs as for double-stranded, including the result of no strand fusion, except that the cross-sectional shape of triple-strands had 2 concavities on each upper and lower surface.

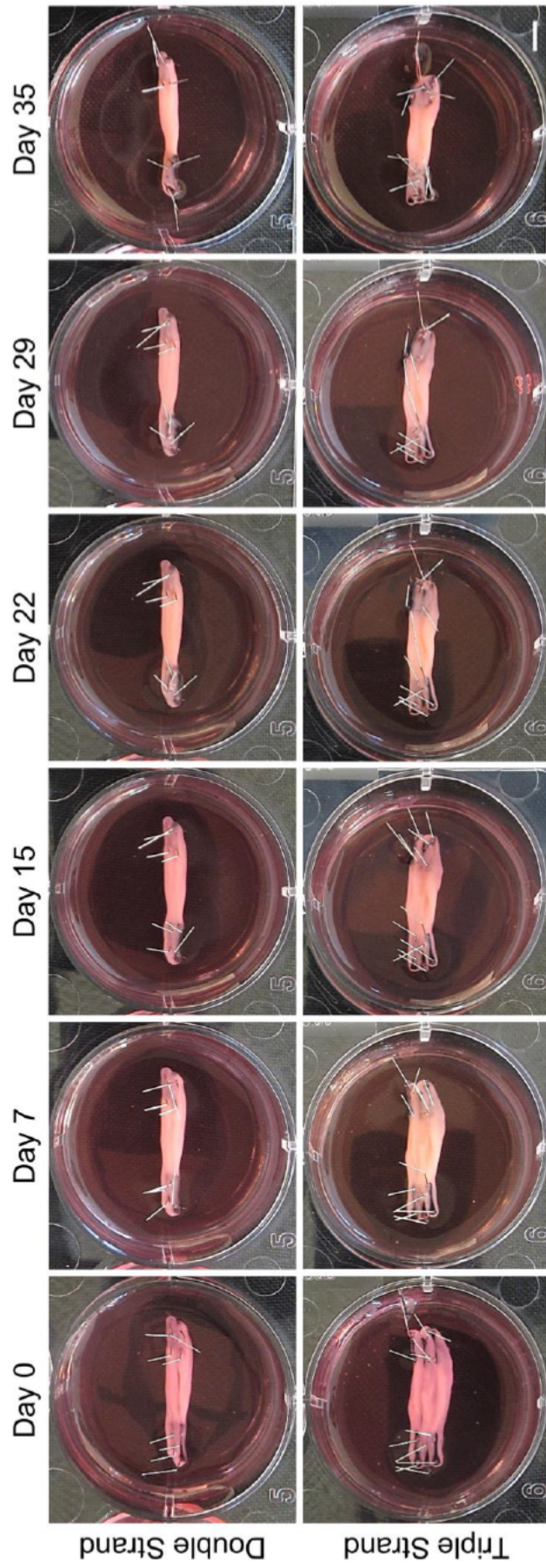


Figure 4.12 | Multi-Strand Tendon Analogue Constructs

Overview photographs of maturation of double (*upper panels*) and triple (*lower panels*) parallel multi-strand tendon analogue constructs over time in 35mm wells. On combination of single constructs on day 0 (after 3 weeks of single construct culture) the individual strands are apparent by transparencies between them, but by day 35 they are not grossly distinguishable. The strands appear to progressively integrate together as they mature. Scale bar 5mm throughout.

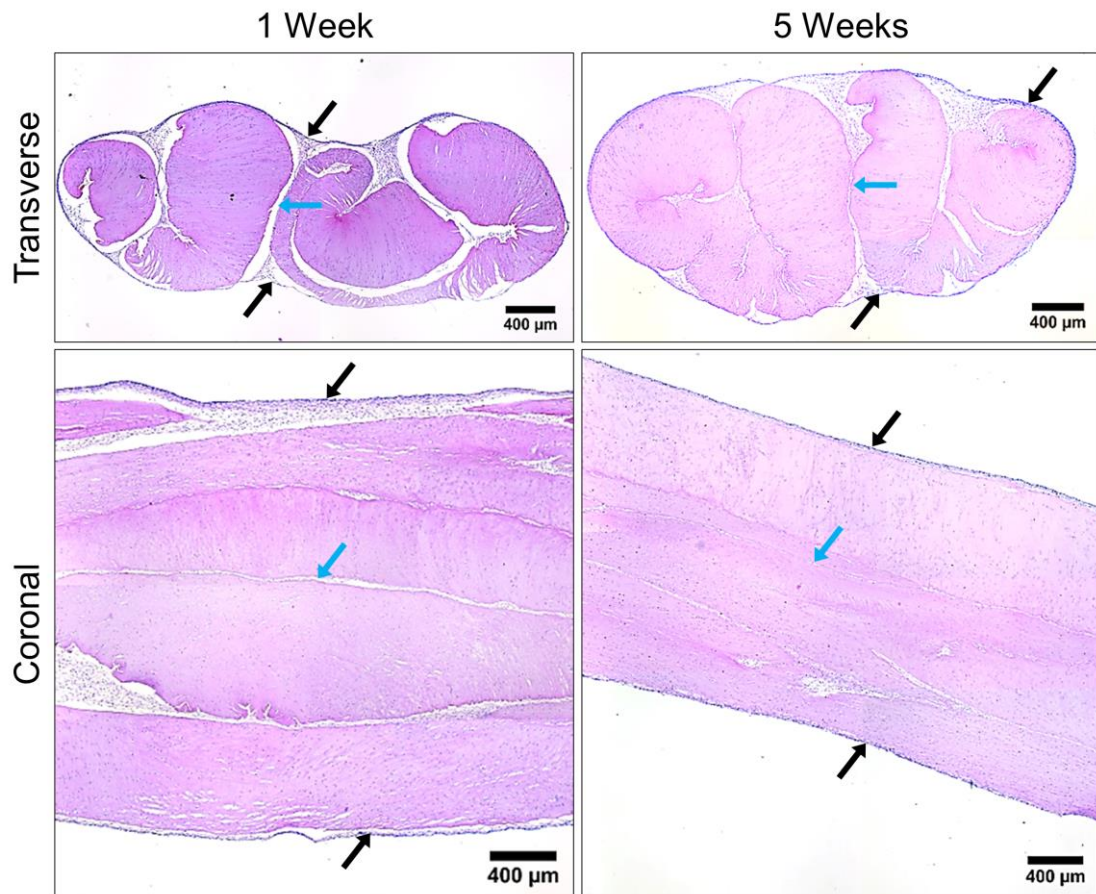


Figure 4.13 | Histology of the Double Multi-Strand Tendon Analogue

Representative histology micrographs of a double stranded tendon analogue at 1 week (*left panels*) and 5 weeks culture (*right panels*) after combination of pre-formed single strand tendon analogues, in mid-transverse (*upper panels*) and mid-coronal section (*lower panels*), showing morphological progression. By 1 week, the capsular cell layer (*black arrows*) has encompassed both strands as a single structure, although at the interface of the 2 strands (*blue arrows*) the capsular layer remains. At 5 weeks, the whole double tendon analogue structure is more rounded, compact and less flat, as the single strands fold tighter both into themselves and against each other. The interface between the 2 strands (*blue arrows*) is almost obliterated in some areas by 5 weeks, and barely perceptible in coronal section, and although the capsular cell layer may not be continuous at the interface, the 2 strands have not merged together. H+E.

4.5.2.3 Suture Manipulation Experiments

4.5.2.3.1 Vertical/Vertical

The development of tendon analogues between opposing parallel vertical sutures is depicted in **Figure 4.14** and graphed in **Figure 4.15**, highlighting general trends. Early formation was similar to basic suture-suture constructs (see *Section 4.5.2.1*), with most fibrin gel contraction occurring in the first 3 days and a roughly predictable rounded rectangle shape stretched between the suture anchors by day 7 (**Figure 4.14**).

At day 0, the relative mean width of the gel at all 3 of the 25%, 50% and 75% distance measurement points (relative to the width of the gel averaged at both sutures) was similar in all constructs, ranging between $103.58 \pm 1.12\%$ (75% point, 10mm construct) and $106.87 \pm 1.00\%$ (50% point, 2mm construct) (**Figure 4.15**). The relative widths all increased by day 3 [ranging from mean widths of 105.06% (75% point, 5mm construct) to $118.39 \pm 7.33\%$ (25% point, 2mm construct)], apart from a small decrease at the 75% measurement in the 5mm construct (**Figure 4.15b**), and then followed a generally decreasing trend over the remaining time (**Figure 4.15**).

Bowing of the tendon analogues between the sutures to a more 'H' shape was represented by a relative mean width of $<100\%$ of the width of the gel at the sutures, highlighted in graphed results (**Figure 4.15**). All 3 distance measurement points were $<100\%$ by day 7 in the 5mm construct (**Figure 4.15b**) and by day 14 and 21 in the 10mm (**Figure 4.15a**) and 2mm (**Figure 4.15c**) constructs, respectively. The 50% measurement point (mid-point between sutures) for both the 10mm and 2mm constructs was however $<100\%$ by day 10.

In the 10mm construct (**Figure 4.15a**), relative widths for all measurement points decreased until around day 21, where they then appeared to plateau and the tendon analogue shape did not clearly contract further (**Figure 4.14**). The 50% measurement registered the lowest relative mean width, to a minimum of $89.27 \pm 2.28\%$ at day 35, indicating that the bowing was greatest in the middle of the tendon analogue. The 25% measurement was consistently slightly less wide than the 75% measurement from day 10 onwards, reaching minimums of $93.04 \pm 2.98\%$ at day 28 and $95.65 \pm 0.31\%$ at day 35, respectively. From day 14 onwards, all 3 measurements generated small standard errors of the mean (error bars), showing that the shape of the tendon analogue from this point on was particularly consistent between the technical repeats.

In the 5mm construct (**Figure 4.15b**), after a large decrease in relative width from day 3-7 for all measurement points (25%: 14.39% decrease in relative width; 50%: 29.42%; 75%: 20.82%), there was a general gradual decrease in relative widths until day 35, with the greatest rate of decrease in the 25% measurement and least in the 75%. The 50% measurement point maintained the lowest relative width from day 14 onwards, reaching a minimum of 72.70% at day 35, the lowest relative width of all constructs, producing the greatest proportional macroscopic mid-point bowing (**Figure 4.14**). The

75% and 25% measurements reached similar, but larger, minimums on day 35, of 79.24% and 79.99%, respectively.

In the 2mm construct (**Figure 4.15c**), all 3 measurement points generally continued to decline in width from days 3-35, at a faster and steadier rate than the 5mm construct. The 50% measurement generally maintained the lowest relative width from day 7 onwards, finishing at a minimum of $75.10 \pm 13.20\%$ on day 35, followed by the 75% measurement (minimum of $81.17 \pm 9.95\%$ on day 28) and then the 25% measurement (minimum of $88.83 \pm 8.06\%$ on day 35). The relative widths of the 75% and 25% measurement points appeared to plateau from day 21 onwards as the 50% point continued to decrease, further pronouncing the macroscopic mid-point bowing (**Figure 4.14**).

In summary, all constructs showed minor mid-point bowing by day 10, which then generally increased with time, more so in smaller constructs. Bowing was greatest at the mid-point (50%) rather than the 25% or 75% points. All constructs therefore developed beyond a rectangular or more round shape, contracting to a slight 'H' shape, which was proportionally greatest in the 5mm and 2mm constructs. The 10mm construct was the least proportionally 'H' shaped, in contrast to hypothesised results.

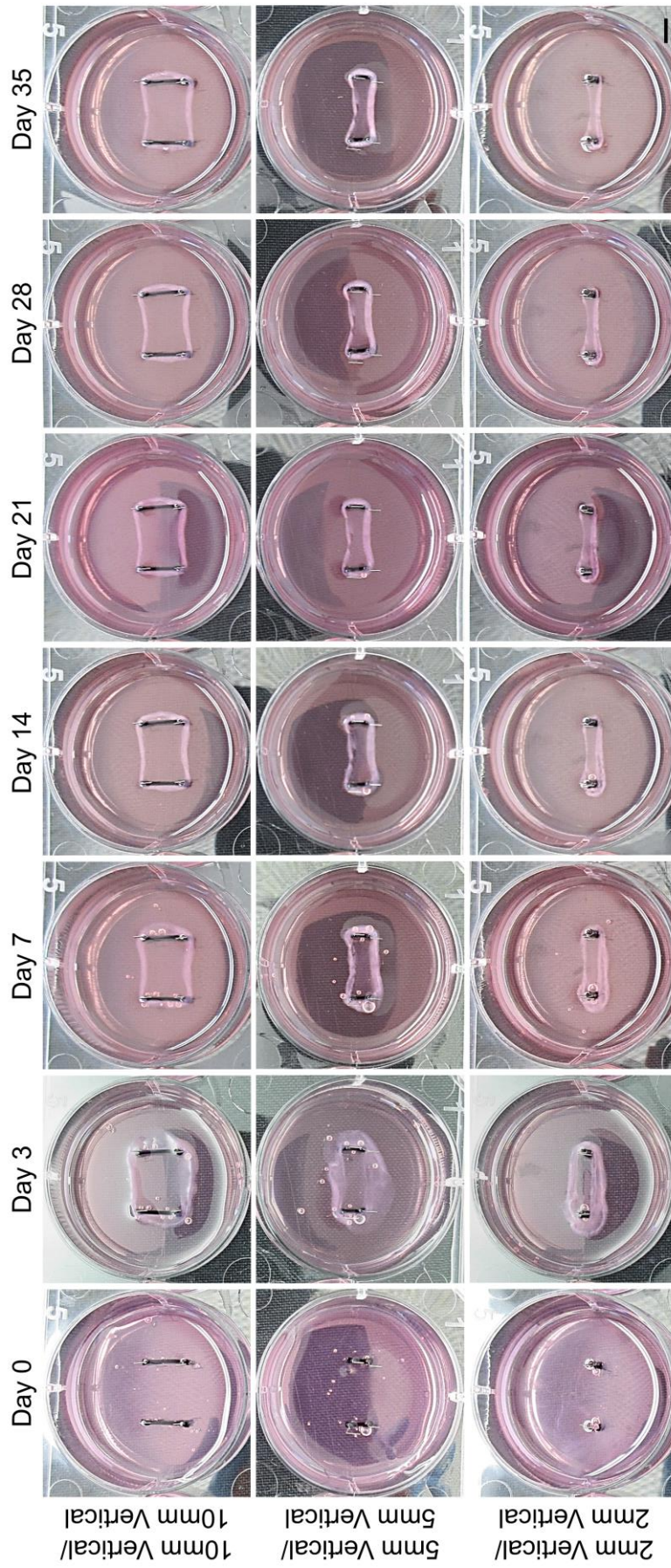


Figure 4.14 | Formation of Vertical/Vertical Suture Tendon Analogue Constructs

Overview photographs of representative 10mm (*upper panels*), 5mm (*middle panels*) and 2mm (*lower panels*) vertical/vertical suture tendon analogue constructs forming over time in 35mm well culture. Fibrin gel fills the entire well base at day 0, contracting considerably around the sutures by day 3, and achieving a relatively well-formed shape as dictated by the suture anchors by day 7. After day 7 the tendon analogue matures, with the greatest continued macroscopic modification of shape in the smaller constructs (2mm and 5mm) than the 10mm construct. All tendon analogues appear to be centrally bowed by days 7-14. Scale bar 5mm throughout. See **Figure 4.15** for graphical representations.

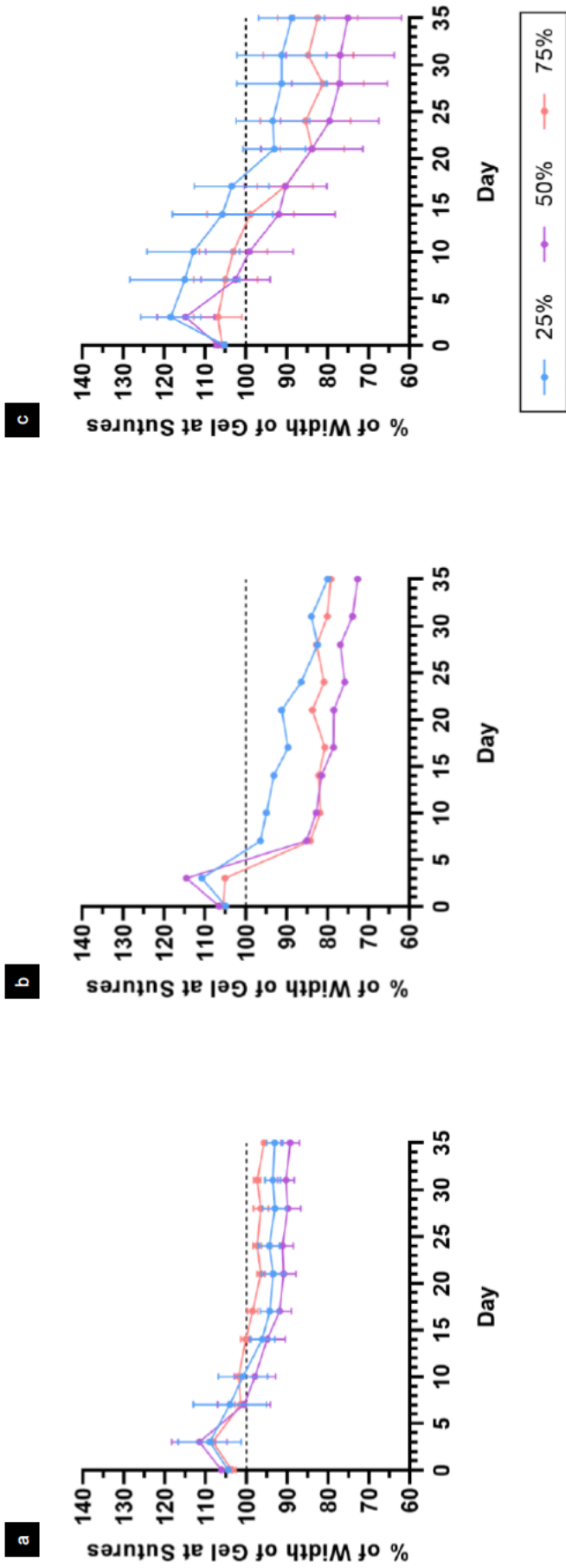


Figure 4.15 | Gel Width in the Formation of Vertical/Vertical Suture Tendon Analogue Constructs

Fibrin gel width measured at 25%, 50% and 75% distance points between sutures in 10mm (a), 5mm (b) and 2mm (c) vertical/vertical suture constructs. Gel width is presented relative to the suture gel width, as the percentage of the gel at both sutures, with 100% marked with a broken line. After a general increase in relative gel width from days 0-3, there is a subsequent continued decrease in all constructs as contraction is dictated by suture anchor size. The range of decrease in relative gel width is smallest with the largest suture anchors (10mm, a), and largest, similarly, with the 5mm (b) and 2mm (c) suture anchors, albeit with differing rates of decreasing relative width over time. The 50% distance is generally the smallest relative width of the distances measured, and by day 10 the gel width at this measurement point is smaller than at the sutures (<100% relative suture width) in all constructs, indicating central bowing of the tendon analogue. Mean \pm SEM. No error bars are shown for the 5mm construct as only 1 of 3 constructs maintained complete fibrin gel integrity throughout formation and was analysed. See Figure 4.14 for overview photographic representations.

4.5.2.3.2 Vertical/Horizontal

Tendon analogue development between perpendicular vertical/horizontal sutures is depicted in **Figure 4.16** and graphed in **Figure 4.17**. As per the vertical/vertical suture constructs, the general contracted shape of the gel, as directed by suture size and orientation, had formed by day 7, with only incremental shape changes thereafter. By day 7 the general macroscopic shape was a roughly rounded triangle, with a base (gel at vertical suture) wider than apex (gel at horizontal suture), although in the 2/5mm construct the base was only very marginally wider than the apex (**Figure 4.16**).

All construct gels began contraction from a similar mean width relative to the horizontal suture at day 0, ranging from $110.52 \pm 0.94\%$ (75% point, 2/5mm construct) to $113.58 \pm 0.72\%$ (50% point, 10/5mm construct) (**Figure 4.17**). Each construct then developed differently in relation to the horizontal gel width, whether maintaining the triangular shape or bowing to a 'T' shape.

In the 10/5mm construct (**Figure 4.17a**), the mean width at each of the 25%, 50% and 75% distance measurement points, also including that of the vertical suture itself (0%), increased with a roughly logarithmic-shaped curve relative to the width at the horizontal suture. At each time point values were always $0\% > 25\% > 50\% > 75\%$, and all measured points remained $>100\%$ of the horizontal suture width. The differences in relative mean widths between each of the measurement points also remained of similar proportional value as time progressed, describing a triangular shape without obvious bowing of its sides between the sutures (**Figure 4.16**).

In the 5/5mm construct (**Figure 4.17b**), the relative mean width at each of the 25%, 50% and 75% distance measurement points increased from day 0-3, after which the 75% and 50% points decreased to $<100\%$ width of the horizontal suture gel by day 14 and 17, respectively. From these days forward, the 50% point remained roughly equal to the 100% relative width, whilst the 75% point continued $<100\%$, to a minimum of $87.57 \pm 4.32\%$ on day 21. These $\leq 100\%$ measurements relative to the horizontal suture gel described a more 'T' shape of the tendon analogue, seen in overview from day 14 onwards (**Figure 4.16**). However, the gel did not contract tightly around the vertical suture ('crossbar' of the sideways 'T'), as the width at the 25% point remained $>100\%$ width of the horizontal suture gel throughout, maintaining a similar value from day 3 onwards (**Figure 4.17b**).

In the 2/5mm construct (**Figure 4.17c**), the relative mean width of each of the 3 main distance measurement points generally gradually decreased with time, directly from day 0 for the 25% and 50% points, and from day 3 for the 75% point. The 25% and 50% points decreased to <100% width of the horizontal suture gel by day 7, reaching minimum mean relative widths of $85.84 \pm 10.96\%$ and $66.36 \pm 7.42\%$ (the lowest relative width of all constructs), respectively, both at day 28. The 75% point reached <100% by day 10, to a minimum of $88.05 \pm 4.67\%$ on day 31. The minimum mean widths for each of the 25%, 50% and 75% points were all lowest in this construct, showing that it developed the greatest proportional 'T' shape. Yet since the gel width at the 2mm vertical suture (0% distance) only reached a maximum mean value of $136.87 \pm 13.08\%$, at day 35, clearly much less than in the constructs with larger vertical sutures ($210.94 \pm 28.51\%$, 5/5mm construct; $377.85 \pm 54.50\%$, 10/5mm construct), the 'T' shape was less obvious in overview (**Figure 4.16**).

In summary, the 10/5mm construct remained triangular whilst the gel between the sutures bowed to a more 'T' shape in the 5/5mm and 2/5mm construct, proportionally greatest in the 2/5mm construct. The smaller the vertical suture the greater the proportional T shape, which was the opposite of hypothesised results.

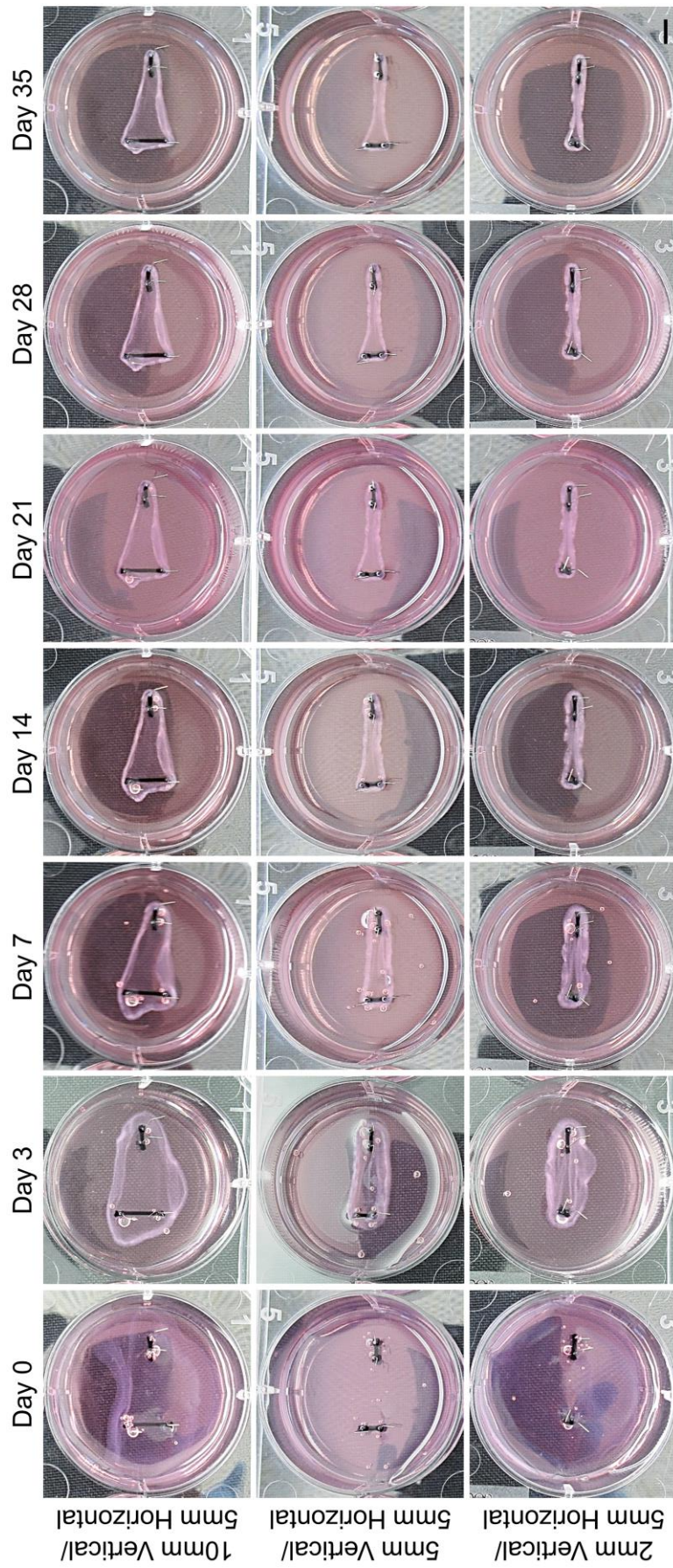


Figure 4.16 | Formation of Vertical/Horizontal Suture Tendon Analogue Constructs

Overview photographs of representative 10/5mm (upper panels), 5/5mm (middle panels) and 2/5mm (lower panels) vertical/horizontal suture tendon analogue constructs forming over time in 35mm well culture. By day 7 the fibrin gel in all constructs has contracted to a rounded triangular shape, with a base width determined by the vertical suture size. After day 14 the progressive bowing of gel between the sutures in 2/5mm and 5/5mm constructs becomes more obvious, whilst the 10/5mm construct remains triangular. Scale bar 5mm throughout. See **Figure 4.17** for graphical representations.

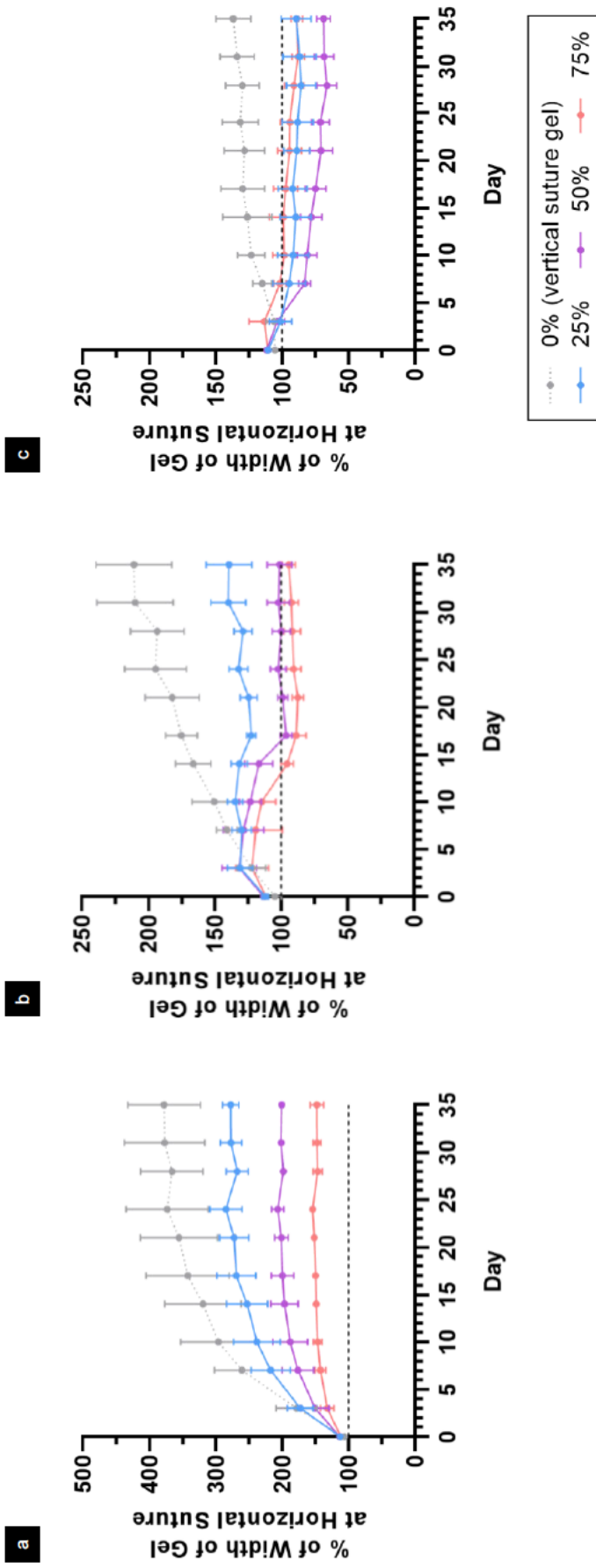


Figure 4.17 | Gel Width in the Formation of Vertical/Horizontal Suture Tendon Analogue Constructs

Fibrin gel width measured at 25%, 50% and 75% distance points from the 10mm, 5mm and 2mm vertical suture in 10/5mm (a), 5/5mm (b) and 2/5mm (c) vertical/horizontal suture constructs, respectively, including the reference point of the gel width at the vertical suture (0%). Gel width is presented relative to the horizontal suture gel width, with 100% of this width marked with a broken line. For all 3 constructs, the 3 main distance measurement points (25%, 50%, 75%) reach fairly stable relative widths from day 17 onwards, however their relationship to the gel width at the horizontal suture varies in each construct. Gel width in the 10/5mm construct (a), for all distance measurement points, is always >100% of the horizontal gel; in the 5/5mm construct (b), the 50% and 75% points decrease to <100%; and in the 2/5mm construct (c), all 3 of the 25%, 50% and 75% points decrease to <100%. Mean \pm SEM. See Figure 4.16 for overview photographic representations.

4.5.2.3.3 Suture Gel Contraction

The fibrin gel of the developing tendon analogue did not contract fully to the same width as that of the suture anchor within 35 days for any of 10mm, 5mm or 2mm vertical sutures. **Figure 4.18** shows graphically that by far the greatest fibrin gel contraction occurred from day 0-3, then from day 3-7, following which there was a gradual decline in gel width with time, although this always remained greater than the width of the suture.

Table 4.1 enumerates the width differences between gel and suture. At day 35, the fibrin gel was still $0.43 \pm 0.03\text{mm}$ wider than the 10mm suture, $0.52 \pm 0.19\text{mm}$ wider than the 5mm suture and $1.27 \pm 0.17\text{mm}$ wider than the 2mm suture. These were the minimum width differences for 10mm and 5mm sutures, although the minimum for the 2mm suture was $1.23 \pm 0.20\text{mm}$, on day 31; however, the overarching trend was a decreasing difference with time. For all time points, the larger the suture size the less the width difference between gel and suture ($10\text{mm} < 5\text{mm} < 2\text{mm}$), except for day 3 in early contraction where the width difference for the 5mm suture was greater than the 2mm suture.

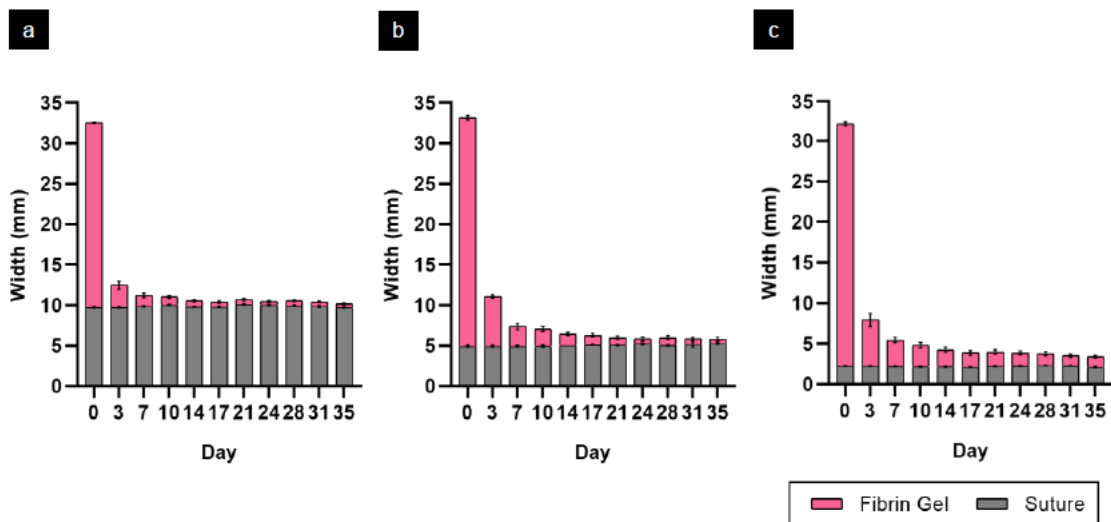


Figure 4.18 | Width Comparison of Gel at Suture and Suture Itself

Stacked bar charts showing the measured width of fibrin gel in line with the suture compared to the width of the suture itself, at progressive time points for vertical/vertical tendon analogue constructs using 10mm (a), 5mm (b) and 2mm (c) sutures. The gel decreases width with time but does not reach the width of the suture. Mean \pm SEM. Values of width differences between the gel and suture are shown in **Table 4.1**.

Table 4.1 | Width Difference between Gel at Suture and Suture Itself

Table of collated calculated measurements at progressive time points. 'Suture Size' refers to size (width) of sutures used in vertical/vertical suture tendon analogue constructs. Mean (\pm SEM). See **Figure 4.18**.

		Width Difference (mm)										
Day		0	3	7	10	14	17	21	24	28	31	35
Suture Size												
10mm		22.77 (0.09)	2.70 (0.44)	1.35 (0.22)	1.00 (0.15)	0.73 (0.13)	0.59 (0.09)	0.61 (0.08)	0.47 (0.08)	0.62 (0.10)	0.55 (0.08)	0.43 (0.03)
5mm		28.22 (0.40)	6.14 (0.06)	2.45 (0.31)	2.13 (0.18)	1.43 (0.19)	1.16 (0.27)	0.89 (0.16)	0.60 (0.16)	0.93 (0.20)	0.67 (0.15)	0.52 (0.19)
2mm		30.02 (0.23)	5.69 (0.78)	3.24 (0.32)	2.64 (0.31)	2.09 (0.34)	1.73 (0.32)	1.74 (0.29)	1.58 (0.22)	1.45 (0.25)	1.23 (0.20)	1.27 (0.17)

4.5.2.4 Anatomical Suture Experiments

4.5.2.4.1 Standard Volume Gel

Overview photographs of developing standard volume gel anatomical suture-suture tendon analogue constructs are displayed in **Figure 4.19**. Graphical representations of fibrin gel contraction over time for all culture variables (including double volume gel variables) are shown at each distance measurement point in **Figures 4.21a** (0% distance, left suture), **4.22a** (25%), **4.23a** (50%), **4.24a** (75%) and **4.25a** (100%, right suture), with standard volume gel culture variables isolated for clarity in *Appendix 5*. OCT images of standard volume gel constructs are included in **Figure 4.26**.

Of the 9 constructs set up for each culture variable, 3 from each 'S-DMEM' and '+AA+P' cultures and 2 from each 'RODM' and 'mid-point pins' cultures were excluded from gel width analysis. Exclusion was due to failure of integrity of the fibrin gel between or around suture anchors which was deemed to have affected gel width within the 56 day analysis period. Failure between anchors often resulted from foci of poor gel attachment to suture anchors. Examples are displayed in *Appendix 6*. Construct n numbers analysed were therefore 6 for 'S-DMEM' and '+AA+P' cultures and 7 for 'RODM' and 'mid-point pins' cultures.

Overview photographs (**Figure 4.19**) showed that the tendon analogue for all constructs had taken general shape by day 7, and that the fibrin gel had contracted well around the sutures by day 14. The general morphology appeared to undergo no further clear macroscopic morphological change after days 21-28. The extra mid-point pin anchors evidently restricted gel contraction, with the gel region between the

sutures appearing of greater width than the 'S-DMEM', '+AA+P' and 'RODM' cultures. Mild-minimal central bowing was apparent in 'S-DMEM', '+AA+P' and 'RODM' cultures, distinct from around day 14-21 onwards. The 'RODM' tendon analogue developed regions of opacity after a few weeks, with an opaque precipitate also gathering in the well bottom by day 14. Addition of alizarin red to this precipitate layer at the conclusion of culture (day 77) positively stained for calcium mineral, although the tendon analogue itself had already been removed and was not tested.

Mean gel widths at the 0% distance measurement point (at the mid-point of the left suture) (**Figure 4.21a**, *Appendix 5a*) were similar between culture variables, with no standard volume gel culture variable significantly different to 'S-DMEM'. The greatest decrease in recorded mean width was between day 7 and 14 for all standard gel volume variables, then from day 14-21, as was generally common for all distance measurement points. Mean gel width generally plateaued after day 21, apart from '+AA+P' culture which decreased further to day 28, at which point it was the only culture variable to approximate the corresponding human FDP tendon width at the base of its bony insertion (8.58mm, also the suture size), continuing close to this value over subsequent weeks. Mean gel width in other culture variables remained around 0.5mm wider from day 21 onwards, at \approx 9mm.

At 25% distance between sutures (**Figure 4.22a**, *Appendix 5b*), 'S-DMEM' and '+AA+P' cultures were similar, reaching a plateau in mean gel width close to the corresponding human FDP tendon width (7.16mm) around day 28. 'Mid-point pins' culture was significantly wider than 'S-DMEM' culture ($p < 0.01$), similarly plateauing at day 28 but approximately 1-1.5mm wider than 'S-DMEM' and '+AA+P' cultures. Gel width contracted more steadily with 'RODM' culture, appearing to plateau later at day 42, and remained at a greater width than 'S-DMEM' culture at all measured time points, but was not significantly different overall.

At the 50% distance point (**Figure 4.23a**, *Appendix 5c*), the pattern was very alike to the 25% distance. 'Mid-point pins' culture was the only variable significantly wider than 'S-DMEM' culture ($p < 0.001$), remaining around 2mm wider from day 14 onwards. 'S-DMEM' and '+AA+P' cultures were similar, although mean gel width with '+AA+P' was greater at early (day 7) time points and less at later time points (day 35 onwards), but the overall difference was non-significant. '+AA+P' culture contracted the gel to a

mean width of $5.50 \pm 0.13\text{mm}$ by day 56, 0.55mm less than the corresponding human FDP tendon width (6.05mm). Mean gel width in 'S-DMEM' culture plateaued at the approximate FDP tendon width from day 21-28, whilst 'RODM' cultures plateaued at a similar width on day 42, as per the 25% distance. OCT images at the 50% distance point (**Figure 4.26**) revealed the cross-sectional morphology of the standard volume gel constructs, clearly showing bunching and folding of the gel at the peripheries with a thin central region, as suggested by 2D overview photography. Inward folding/rolling of the peripheral gel was particularly striking in the '+AA+P' tendon analogue, in contrast to the 'mid-point pins' tendon analogue which was relatively even throughout cross-section, maintained by the additional pin anchors.

The general comparative pattern between the standard volume gel culture variables persisted into the 75% distance measurement point (**Figure 4.24a**, *Appendix 5d*). 'Mid-point pins' culture was again the only variable significantly wider than 'S-DMEM' ($p < 0.01$), maintaining a mean gel width approximately 1-1.5mm greater than 'S-DMEM' culture from day 21 onwards. Each culture variable reached a plateau in mean gel width at day 28, apart from 'RODM', again at day 42. 'RODM' culture reached a similar mean width at plateau to 'S-DMEM', which was around 0.5mm greater than the corresponding FDP tendon width of 5.08mm. '+AA+P' culture was the only culture variable to produce a mean gel contraction to the approximate width of the corresponding FDP tendon width, from day 28 onwards.

At 100% distance (mid-point of the right suture) (**Figure 4.25a**, *Appendix 5e*) the pattern of gel contraction over time across standard volume gel culture variables was similar to at 0%. No culture variables were significantly different to 'S-DMEM'. However, gel width in '+AA+P' culture was notably smaller than other cultures from day 21 onwards, from where its mean gel width continued at a similar width to the corresponding FDP tendon (4.69mm, also the suture size) without fully reaching it (minimum $4.73 \pm 0.14\text{mm}$, day 56). Plateauing of mean gel width generally occurred between day 21 and 28, although 'RODM' culture appeared to plateau later, reaching a minimum width at day 42 ($5.13 \pm 0.21\text{mm}$).

4.5.2.4.2 Double Volume Gel

Overview photographs of developing double volume gel anatomical suture-suture tendon analogue constructs are displayed in **Figure 4.20**. Graphical representations

of fibrin gel contraction over time for double volume gel culture variables are shown with all culture variables and compared to 'S-DMEM' in **Figures 4.21a** (0% distance, left suture), **4.22a** (25%), **4.23a** (50%), **4.24a** (75%) and **4.25a** (100%, right suture), and are shown in isolation and compared to the standard double volume gel culture (i.e. 'double gel', cultured in S-DMEM) at the same distance measurement points in **Figures 4.21b, 4.22b, 4.23b, 4.24b** and **4.25b**. OCT images of double volume gel constructs are included in **Figure 4.26** and are the focus of **Figure 4.27**.

Tendon analogues in all double volume gel constructs were more robust than in standard volume gel constructs. There were no integrity failures in the developing fibrin gel, and all constructs set up were included in analysis (n=9 for each culture variable).

Overview photographs (**Figure 4.20**) demonstrated that the general formation and maturation of double volume gel constructs was similar to standard volume gel constructs (**Figure 4.19**), taking shape by day 7 and maintaining a very similar macroscopic morphology from day 21-28 onwards. Their increased robustness compared to standard volume gel counterparts was evident in their denser, more opaque appearance. 'Double gel/+AA+P', 'double gel/double cells' and 'double gel/double cells/+AA+P' cultures showed relatively similar gel contraction in general overview, with mild-minimal central bowing between sutures, compared to the less contracted 'double gel' culture, which maintained straighter sides to the tendon analogue shape.

At the 0% distance measurement point (mid-point of the left suture) (**Figure 4.21**), mean gel width in 'double gel' and 'double gel/+AA+P' cultures was significantly wider than 'S-DMEM' culture ($p < 0.01$ and $p < 0.001$, respectively) (**Figure 4.21a**). However, all culture variables, including standard volume gel variables, showed a tight range in mean gel widths, particularly from day 14 onwards where the range from widest ('double gel') to smallest ('+AA+P') at each time point was always $< 1.00\text{mm}$. Comparing the double volume gels in isolation (**Figure 4.21b**), 'double gel/double cells' and 'double gel/double cells/+AA+P' cultures were significantly more contracted than 'double gel' culture ($p < 0.001$ and $p < 0.01$, respectively), whilst the 'double gel/+AA+P' culture maintained similar mean gel widths to 'double gel' throughout. All double volume gels appeared to plateau around day 28, although each variable

reached its lowest mean gel width on the final day of analysis. No variables reached the corresponding FDP tendon width of 8.58mm (also the suture size), the closest being 'double gel/double cells' culture on day 56, at 8.84 ± 0.09 mm.

Gel width data was more spread at the 25% distance point (**Figure 4.22**). All double volume gel variables were significantly wider than 'S-DMEM' culture ('double gel', $p < 0.001$; 'double gel/+AA+P', $p < 0.001$; 'double gel/double cells', $p < 0.05$; 'double gel/double cells/+AA+P', $p < 0.05$), although notably those with double cell number were more contracted and less significantly different from 'S-DMEM' (**Figure 4.22a**). Compared to 'double gel' culture (**Figure 4.22b**), all other double volume gel variables were significantly narrower (all $p < 0.001$), with 'double gel/double cells' and 'double gel/double cells/+AA+P' being the narrowest and registering very similar mean gel widths at all time points. Although the majority of contraction had occurred in all double volume gels by day 28, mean gel width continued to incrementally fall with subsequent time points, with all minimum values reached on day 56. No variables reached the corresponding FDP tendon width of 7.16mm, with 'double gel/double cells' and 'double gel/double cells/+AA+P' closest, ≈ 0.5 mm wider on day 56.

Midway between the sutures at the 50% distance (**Figure 4.23**), the individual and comparative patterns in mean gel widths were very similar to the 25% distance. All double volume gel variables were significantly wider than 'S-DMEM' culture ('double gel', $p < 0.001$; 'double gel/+AA+P', $p < 0.001$; 'double gel/double cells', $p < 0.01$; 'double gel/double cell/+AA+P', $p < 0.05$), although 'double gel/double cells/+AA+P' was within 0.40mm of 'S-DMEM' culture by day 56 (**Figure 4.23a**). Compared to 'double gel' culture (**Figure 4.23b**), all other double volume gel variables were again significantly narrower (all $p < 0.001$). 'Double gel/double cells/+AA+P' culture was the narrowest at all time points, however remained just wider than the corresponding FDP tendon width of 6.05mm, at 6.31 ± 0.27 mm on day 56. Mean gel width continued to decrease with time for each variable, although the difference in mean widths between day 28 and 56 was always < 0.65 mm.

Patterns were similar at the 75% distance (**Figure 4.24**), although the main difference was that 'double gel/double cells/+AA+P' culture was not significantly different to 'S-DMEM' (**Figure 4.24a**). The other double volume gel variables remained significantly wider than 'S-DMEM' ('double gel', $p < 0.001$; 'double gel/+AA+P', $p < 0.001$; 'double

gel/double cells', $p < 0.01$). As with 25% and 50% distances, all other double volume gel variables were significantly narrower compared to 'double gel' culture (all $p < 0.001$) (**Figure 4.24b**). 'Double gel/double cells/+AA+P' culture was again clearly the narrowest at all time points, but not reaching the corresponding FDP tendon width of 5.08mm, closet at 5.35 ± 0.24 mm on day 56. Each variable showed a continuous decreasing pattern in mean gel width over all time points in the same manner as at the 25% and 50% distances.

At the 100% distance (mid-point of the right suture) (**Figure 4.25**), mean gel widths for all culture variables, including standard gel volume variables, were spread over a tighter range at all time points (**Figure 4.25a**), as at 0% distance, compared to the distance measurement points between the sutures. In contrast to the 0% distance however, only 'double gel' culture was significantly wider than 'S-DMEM' ($p < 0.01$) and the data range from day 14 onwards between widest mean gel width ('double gel') and narrowest ('+AA+P') was slightly greater, from 1.57mm at day 14 to 1.08mm at day 56. Compared to 'double gel' culture (**Figure 4.25b**), all other double volume gel variables were significantly narrower, at various levels of significance, from most significantly different ('double gel/double cells/+AA+P', $p < 0.001$) to least ('double gel/double cells', $p < 0.05$). As at 0% distance, the mean gel width of each variable appeared to plateau more from day 28 onwards, however each variable's minimum mean gel width was registered on the final day of analysis, day 56. 'Double gel/double cells/+AA+P' culture again gave the most contracted gel, at a minimum of 4.90 ± 0.16 mm on day 56, but still not contracted to the corresponding FDP width (also right suture) of 4.69mm.

OCT images showed the increased thickness (depth) of double volume gel constructs in cross-section at the 50% distance, in comparison to standard volume gel constructs (**Figure 4.26**). However, the central region of double volume gel constructs could still show non-uniform thickness, even becoming as thin as standard volume gel counterparts in focal areas (see 'double gel' variable, **Figure 4.26**). Folding and bunching of the peripheral gel regions was similar to standard volume gel constructs, but of greater 2D area, and similarly those constructs in media supplemented with AA+P appeared to demonstrate a greater degree of folding, as opposed to bunching, at their peripheries. Multiple slices through the same tendon analogue construct ('double gel/double cells/+AA+P', **Figure 4.27**) showed that the extent of peripheral

folding increased from 25% to 50% to 75% distance through the construct, suggesting an increase in folded area the nearer to the smaller suture anchor. In accordance, while the central region remained of relatively similar thickness, the width of the gel generally decreased towards the smaller suture anchor, leaving a greater area (volume) of gel for folding/bunching at the periphery if equivalent contraction occurred throughout the construct.

4.5.2.4.3 Summary of Effect of Culture Variables

Supplementation of S-DMEM with AA+P: In standard volume gels, '+AA+P' cultures were more contracted at every time point from day 14 onwards than 'S-DMEM' cultures (except for day 14 at 50% distance), but never significantly so overall. Notably however, '+AA+P' cultures were always less contracted than 'S-DMEM' cultures on day 7. In double volume gels with regular cell number, 'double gel/+AA+P' cultures were more contracted at every time point than 'double gel' cultures (except for day 14 at 0% distance), significantly so overall at all distances except 0%. In double volume gels with double cell number, 'double gel/double cells/+AA+P' cultures were always more contracted than 'double gel/double cells' cultures at every time point at 50%, 75% and 100% distances, but were very similar at 0% and 25% distances. 'Double gel/double cells/+AA+P' was the double volume gel variable most similar to 'S-DMEM' culture, not significantly different at 0%, 75% and 100% distances.

Culture in RODM: 'RODM' cultures were never significantly different to 'S-DMEM' cultures. At the position of the sutures, at 0% and 100% distances, both cultures were very similar at all time points. Between the sutures, at 25%, 50% and 75%, 'RODM' cultures were notably less contracted than 'S-DMEM' cultures from day 7-35, but then reached a plateau at a similar width as 'S-DMEM' from day 42 onwards.

Addition of extra pin anchors between sutures: 'Mid-point pins' cultures were significantly less contracted than 'S-DMEM' cultures between sutures (at 25%, 50% and 75% distance), but not significantly different at the position of the sutures (at 0% and 100% distance). 'Mid-point pins' cultures were wider most significantly at the 50% distance where the pins were placed, ($p < 0.001$), compared to the 25% and 75% distance (both $p < 0.01$). Despite placing the pins at an intervening width of 6.05mm, that of the corresponding FDP tendon width, mean gel width plateaued at 1.58-1.81mm wider from day 28 onwards.

Doubling gel volume: 'Double gel' cultures were always significantly wider than 'S-DMEM' cultures, more so between sutures (25%, 50%, 75% distances, $p < 0.001$) than at the suture position (0% and 100% distances, $p < 0.01$). Mean gel width for 'double gel' cultures was always the least contracted variable at all time points for all distances (apart from day 14 at 0% distance).

Doubling cell number: 'Double gel/double cell' cultures were significantly more contracted than 'double gel' cultures at all distances. Compared to 'S-DMEM' cultures, 'double gel/double cell' cultures were still significantly wider at the 25%, 50% and 75% distance points, but always less significantly different than 'double gel' cultures.

Acellular control cultures did not display contraction of the fibrin gel (*Appendix 7*).



Figure 4.19 | Maturation of Standard Volume Gel Anatomical Suture-Suture Constructs

Overview photographs of representative standard volume gel anatomical suture-suture tendon analogue constructs cultured with 'S-DMEM', '+AA+P', 'RODM' and 'Mid-point Pins' variables contracting over time in 35mm wells. By day 7 the majority of fibrin gel contraction has already occurred, after which follows maturation with only finer changes in contraction. Macroscopic changes are difficult to identify after day 21-28. The gel region between the sutures contracts less in 'Mid-point Pins' cultures than in 'S-DMEM', '+AA+P' and 'RODM'. 'RODM' cultures show a layer of mineral precipitate on the well bottom, breaking up by day 35. Scale bar 5mm throughout. See **Figures 4.21a, 4.22a, 4.23a, 4.24a, 4.25a** and **Appendix 5** for graphical representations.



Figure 4.20 | Maturation of Double Volume Gel Anatomical Suture-Suture Constructs

Overview photographs of representative double volume gel anatomical suture-suture tendon analogue constructs contracting over time in 35mm wells. Constructs are cultured with S-DMEM and 100,000 cells unless the addition of +AA+P and double cell number is stated, giving the culture variables 'Double Gel', 'Double Gel/+AA+P', 'Double Gel//Double Cells' and 'Double Gel//Double Cells/+AA+P'. Formation and maturation before and after day 7, respectively, and lack of macroscopic morphological changes after day 21-28 for all culture variables are similar to standard volume gels, but the tendon analogues are thicker and less translucent (compare with **Figure 4.19**). The gel region between the sutures for the standard 'Double Gel' culture variable is noticeably the least contracted over time. Scale bar 5mm throughout. See **Figures 4.21, 4.22, 4.23, 4.24, and 4.25** for graphical representations.

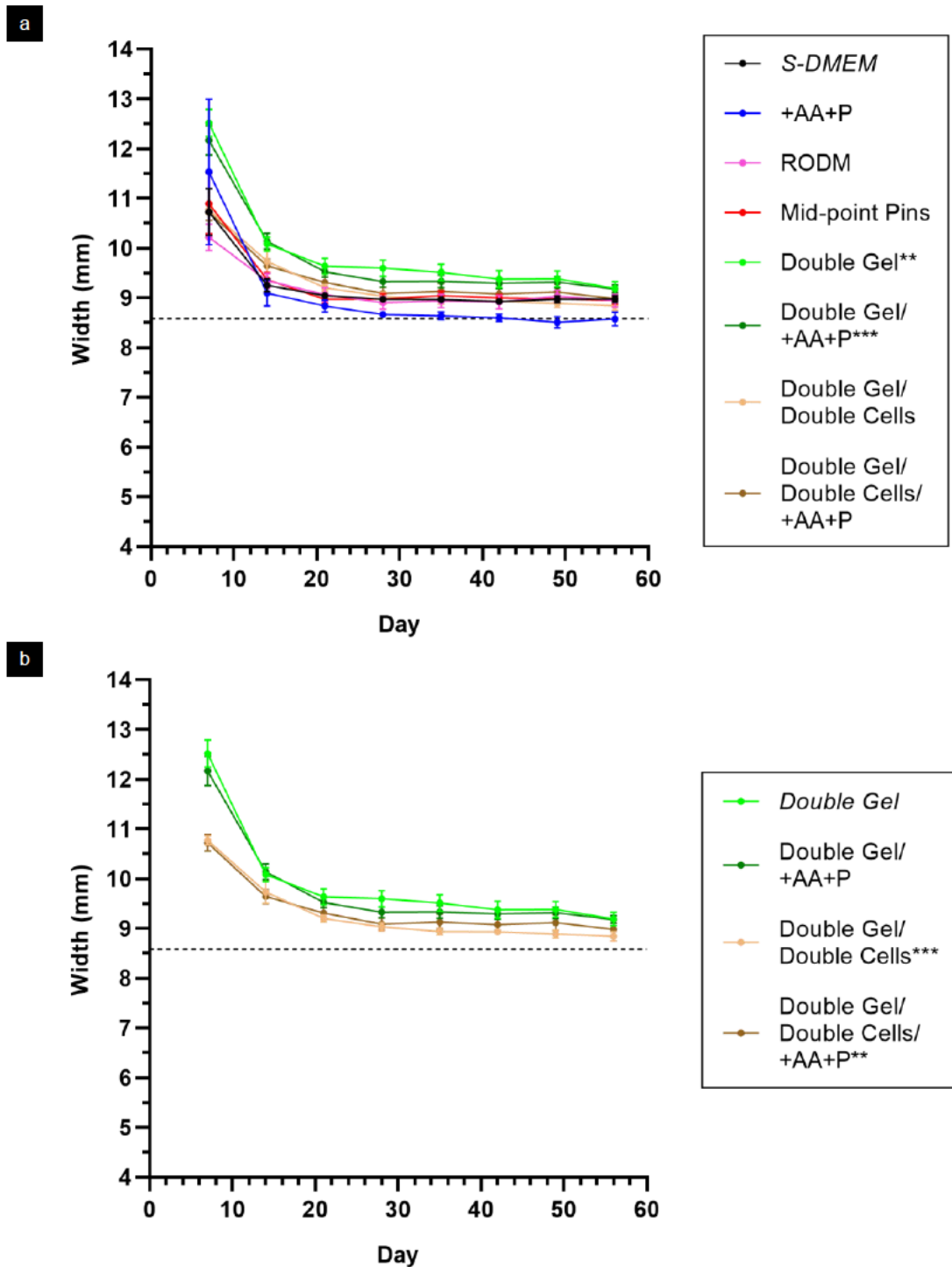


Figure 4.21 | Gel Width at 0% Distance in Anatomical Suture-Suture Constructs

Influence of multiple fibroblast-seeded fibrin gel culture variables on gel width at the 0% distance measurement point (left suture) in anatomical suture-suture tendon analogue constructs over time. **a)** Comparison of all culture variables to 'S-DMEM'; **b)** isolated comparison of all double volume gel culture variables to standard 'Double Gel' culture. Broken line shows mean human FDP tendon width at the corresponding base of the FDP insertion, of 8.58mm (left suture size). The 'Double Gel' and 'Double Gel/+AA+P' variables are significantly different to 'S-DMEM', and only '+AA+P' culture contracts the gel to the suture size (corresponding width of the FDP insertion base) (a). 'Double Gel/Double Cells' and 'Double Gel/Double Cells/+AA+P' variables are significantly different to standard 'Double Gel' culture (b). Isolated comparison of standard volume gel culture variables ('+AA+P', 'RODM' and 'Mid-point Pins') to 'S-DMEM' is separately graphed in Appendix 5a. Mean \pm SEM. ** $p < 0.01$, *** $p < 0.001$.

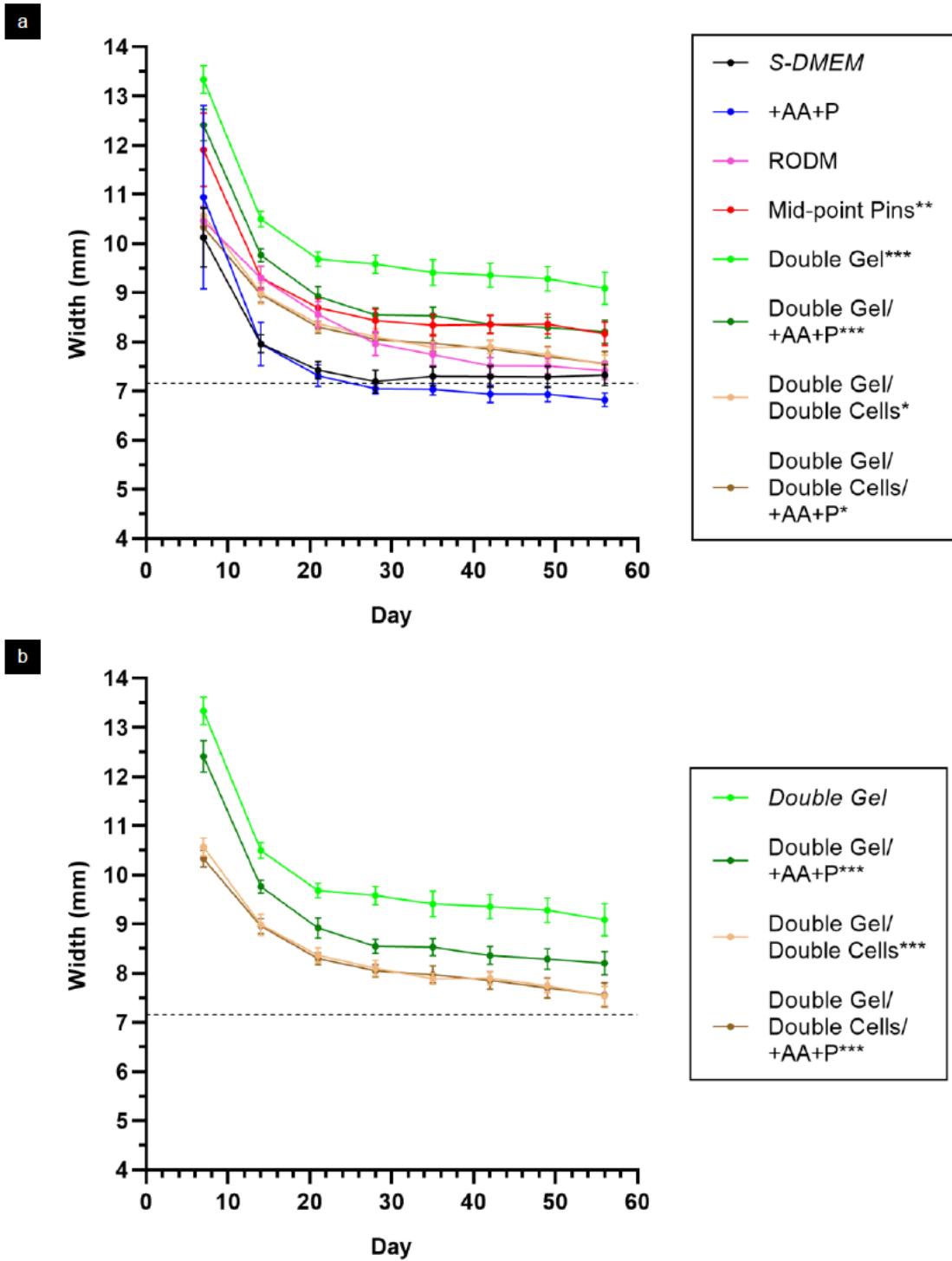


Figure 4.22 | Gel Width at 25% Distance in Anatomical Suture-Suture Constructs

See **Figure 4.21** for outline. 25% distance measurement point between sutures. Broken line shows mean human FDP tendon width at corresponding 3mm from FDP insertion, of 7.16mm. All culture variables except for '+AA+P' and 'RODM' are significantly different to ' S -DMEM', and only '+AA+P' culture contracts the gel mean to and beyond the corresponding human FDP width (a). All double gel culture variables are significantly different to standard 'Double Gel' culture (b). Isolated standard volume gel comparisons are separately graphed in *Appendix 5b*. Mean \pm SEM. * $p < 0.05$, ** $p < 0.01$, *** $p < 0.001$.

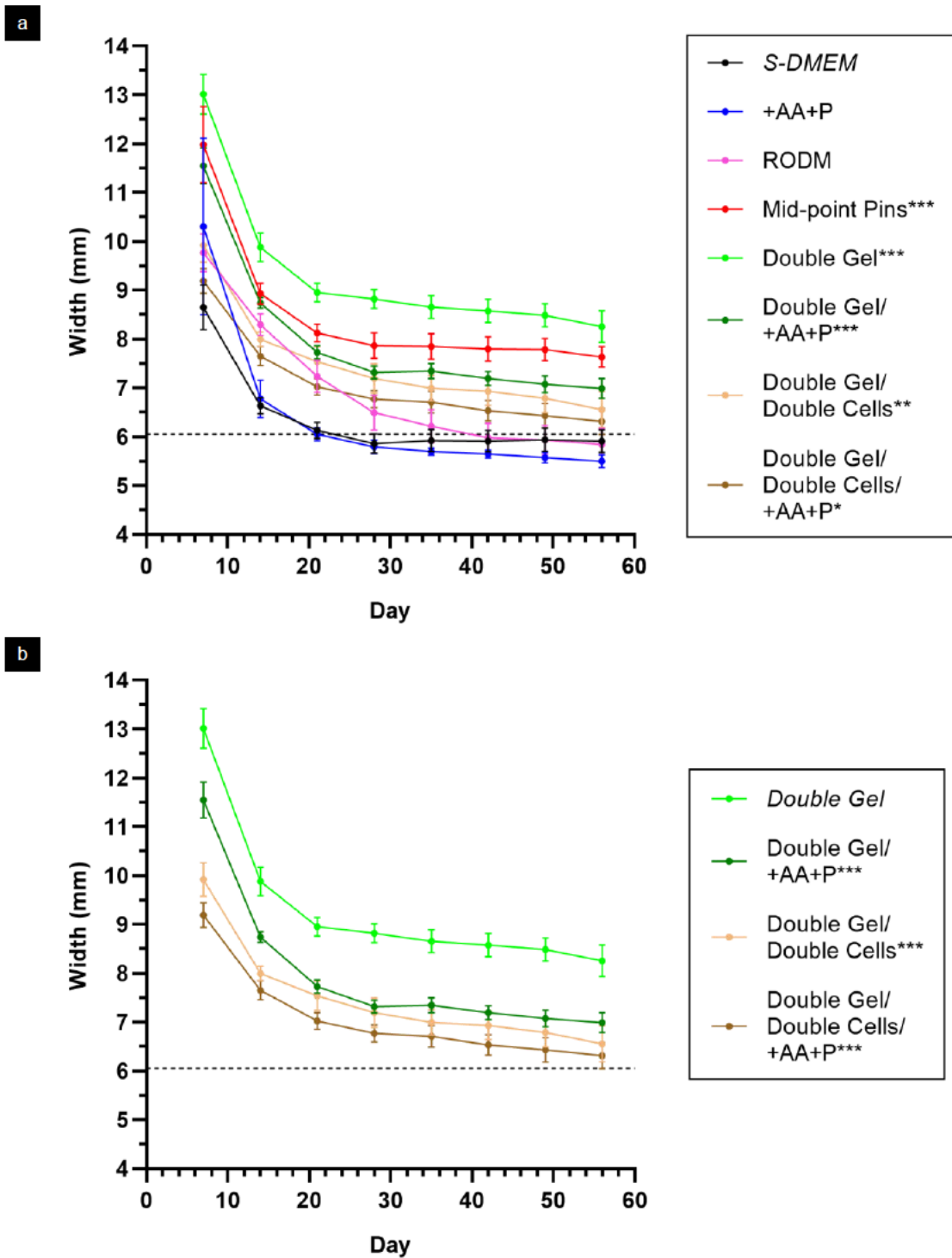


Figure 4.23 | Gel Width at 50% Distance in Anatomical Suture-Suture Constructs

See **Figure 4.21** for outline. 50% distance measurement point between sutures. Broken line shows mean human FDP tendon width at corresponding 6mm from FDP insertion, of 6.05mm. All culture variables except for '+AA+P' and 'RODM' are significantly different to '*S-DMEM*', with the '*S-DMEM*', '+AA+P' and 'RODM' cultures contracting the gel to and beyond the corresponding human FDP width (a). All double gel culture variables are significantly different to standard '*Double Gel*' culture (b). Isolated standard volume gel comparisons are separately graphed in *Appendix 5c*. Mean \pm SEM. * $p < 0.05$, ** $p < 0.01$, *** $p < 0.001$.

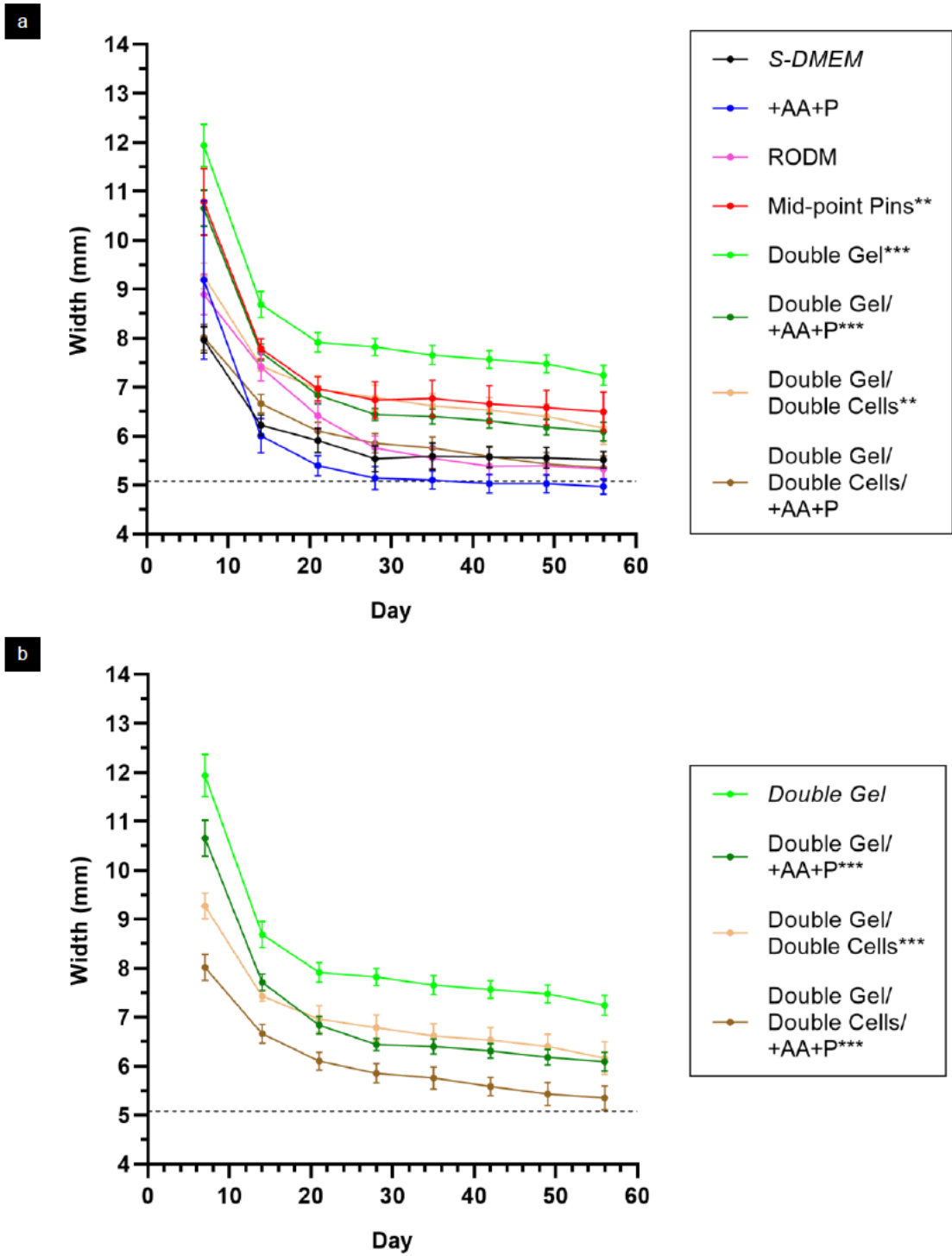


Figure 4.24 | Gel Width at 75% Distance in Anatomical Suture-Suture Constructs

See **Figure 4.21** for outline. 75% distance measurement point between sutures. Broken line shows mean human FDP tendon width at corresponding 9mm from FDP insertion, of 5.08mm. '+AA+P', 'RODM' and 'Double Gel/Double Cells/+AA+P' are the culture variables not significantly different to '*S-DMEM*', and only '+AA+P' culture contracts the gel to and beyond the corresponding human FDP width (a). All double gel culture variables are significantly different to standard '*Double Gel*' culture (b). Isolated standard volume gel comparisons are separately graphed in *Appendix 5d*. Mean \pm SEM. ** $p < 0.01$, *** $p < 0.001$

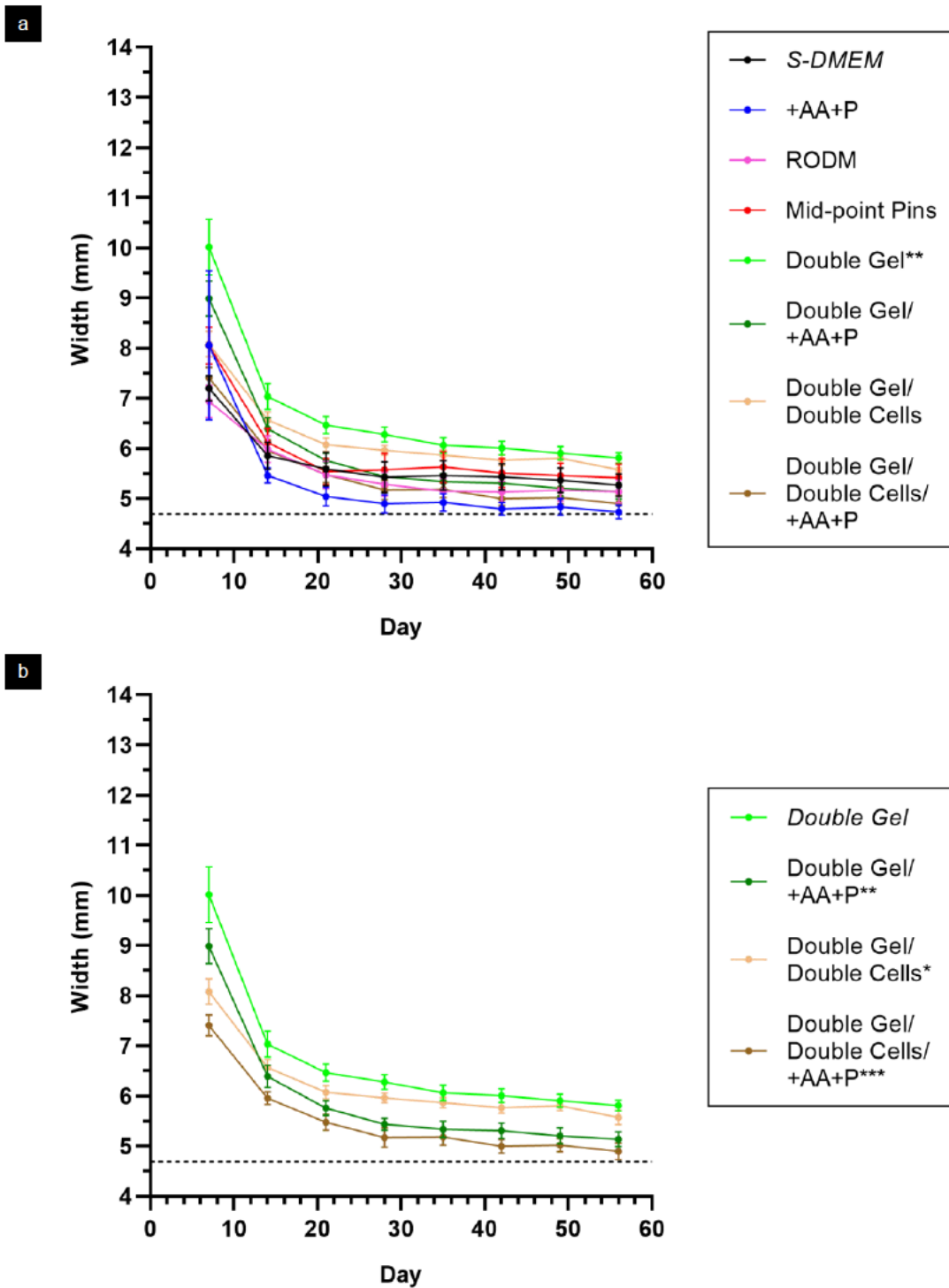


Figure 4.25 | Gel Width at 100% Distance in Anatomical Suture-Suture Constructs

See **Figure 4.21** for outline. 100% distance measurement point (right suture). Broken line shows mean human FDP tendon width at corresponding 12mm from FDP insertion, of 4.69mm (right suture size). 'Double Gel' is the only culture variable significantly different to 'S-DMEM', and no cultures contract the gel to a mean width of the corresponding human FDP width (suture size) (a). All double gel culture variables are significantly different to standard 'Double Gel' culture (b). Isolated standard volume gel comparisons are separately graphed in *Appendix 5e*. Mean \pm SEM. * $p < 0.05$, ** $p < 0.01$, *** $p < 0.001$.

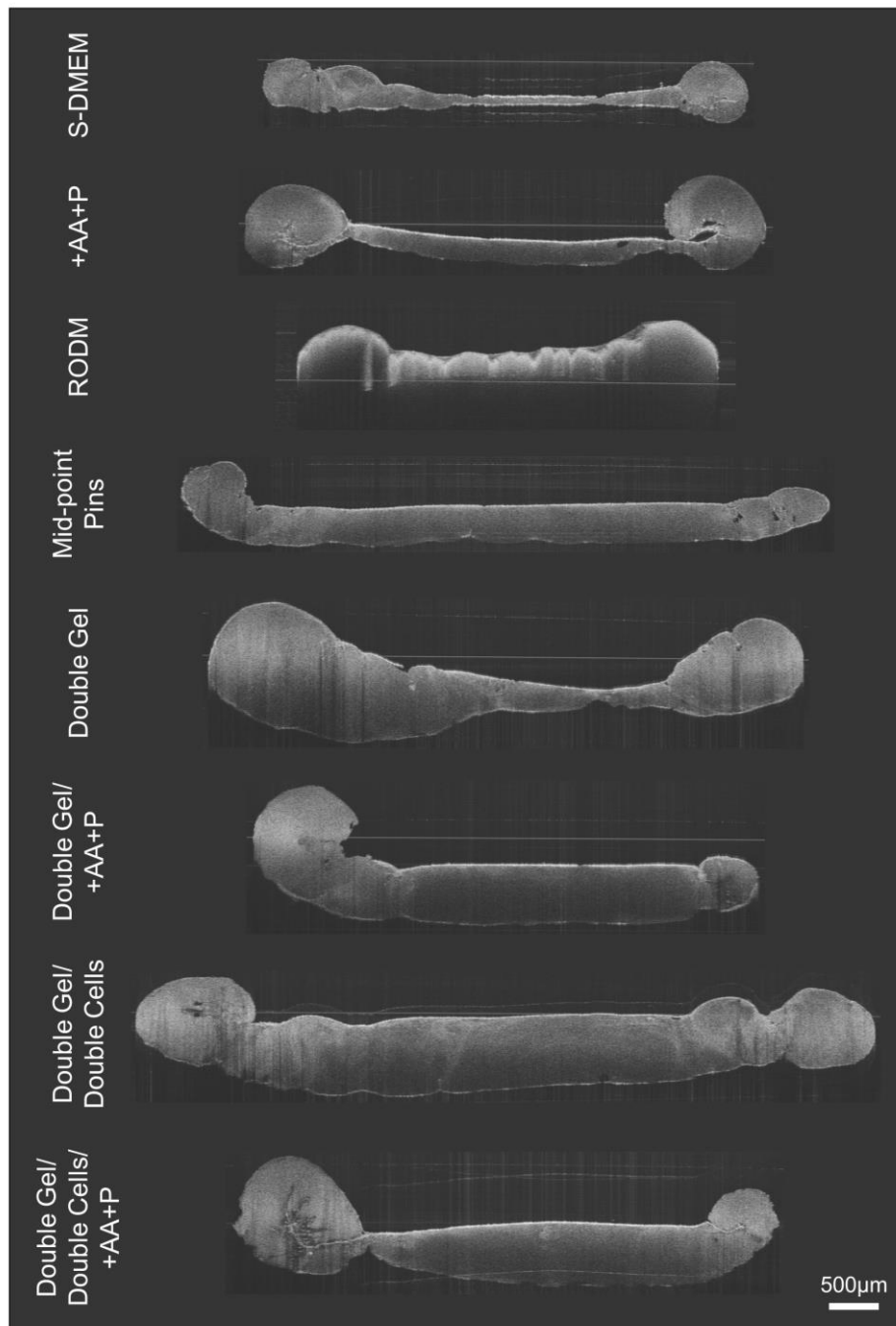


Figure 4.26 | OCT Images at 50% Distance through Anatomical Suture Constructs

2D cross-sectional OCT scan images midway between sutures (50% distance) for all culture variables in anatomical suture tendon analogue constructs, obtained from constructs fixed on day 77. The 'Mid-point Pins' scan was taken just beyond 50% distance to avoid interference from the positioned pins. Tendon analogue formation has occurred by folding or bunching of fibrin gel at the peripheries, with the central gel region remaining generally flat. The central region in the standard volume gels ('S-DMEM', '+AA+P', 'RODM' and 'Mid-point Pins') is particularly thin, although it is thicker for the 'Mid-point Pins' culture where the pin anchors have prevented excessive peripheral gel folding/bunching. Constructs with addition of AA and P to culture media ('+AA+P', 'Double Gel/+AA+P' and 'Double Gel/Double Cells/+AA+P') appear to have a more folded peripheral gel appearance, whereas those in S-DMEM alone ('S-DMEM', 'Mid-point Pins', 'Double Gel', 'Double Gel/Double Cells') show a comparatively more bunched appearance at gel peripheries. The 'RODM' tendon analogue appears hyperdense, most likely due to precipitants from the RODM, causing light attenuation and consequently the lower half is shadowed. Scale bar 500µm throughout.

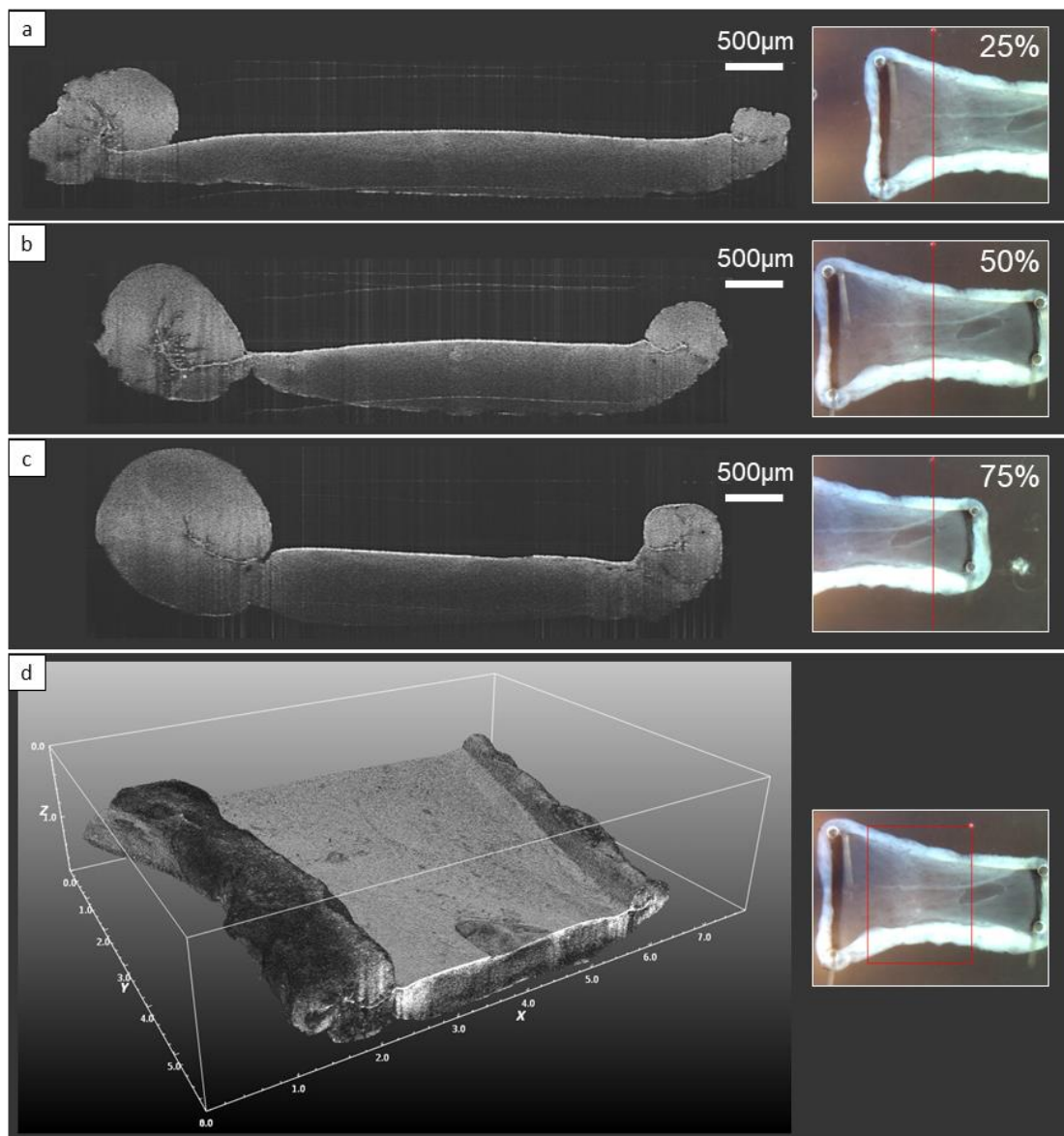


Figure 4.27 | OCT Images through a ‘Double Gel/Double Cells/+AA+P’ Anatomical Suture Construct
 Multiple OCT scan images through a single anatomical suture-tendon analogue construct, showing 2D cross-sections at 25% (a), 50% (b) and 75% (c) distances between sutures and a 3D volumetric segment (d). Inset images (right) show the corresponding region of cross-sectional slice (red line) or area segment (red box) on the construct (equal scale all panels). The closer the fibrin gel to the smaller suture anchor, the greater the 2D area of peripheral folded gel (a, b, c). The 3D reconstruction (d) shows the comparatively flat profile of the central region, with an elliptical area of deficiency in the gel crossed by the right edge of the area segment (red box, inset image) only a discontinuity of the cortical layer. Scale bar 500µm for 2D cross-sectional images, surrounding box in 3D image shows millimetre scale.

4.5.3 Bone Anchor

4.5.3.1 Basic Tendon-Bone Constructs

The bone block acted as a successful anchor to the fibrin gel, and gel contraction and maturation proceeded similarly over time as per a basic suture-suture construct (see Section 4.5.2.1). The majority of gel contraction occurred within the 1st week, with slow maturation of the tendon analogue continuing to the full 12 weeks of culture (Figure 4.28). The tendon analogue attached around all sides of the base of the bone anchor, representative of the fibrin gel contracting from the well edge and enclosing around the bone anchorage point (Figure 4.28). The tendon-bone attachment was maintained on lifting the bone anchor and gently stressing the attachment at weeks 5 and 12 of culture (Figure 4.29). Approximately equal gentle axial tension was applied during both time points, however no assessment of (difference in) strength to failure was made.

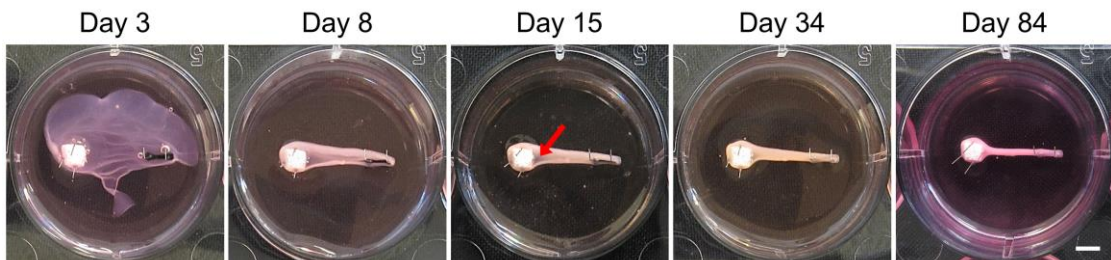


Figure 4.28 | Basic Tendon-Bone Construct Formation

Overview photographs of a basic tendon-bone construct forming by fibrin gel contraction around a cubed Reprobone bone anchor (*left*) and suture anchor (*right*) in a 35mm well, over 12 weeks (84 days) of culture in S-DMEM. Fibrin gel initially fills the whole well, already considerably contracted by day 3, and by day 8 the majority of contraction has occurred. Gel contraction becomes progressively tighter around the bone anchor and suture anchor with time. As the fibrin contracts, the greatest gel density lies at its peripheries, with a thinner, more translucent, area at the leading edge of the bone anchor (see day 15, *red arrow*); this progressively fills in as the tendon analogue matures. Scale bar 5mm throughout.

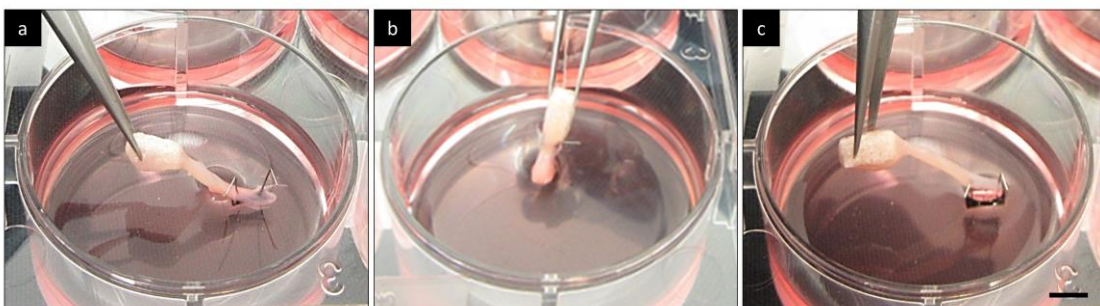


Figure 4.29 | Attachment of Basic Tendon-Bone Construct at 12 Weeks

Oblique overview photographs of a tendon analogue attaching to a cuboidal Reprobone bone anchor at 12 weeks (day 84) of culture in S-DMEM in a 35mm well. The bone anchor is picked up with forceps to demonstrate attachment around its base, showing the lateral surface (**a**), inferior surface (**b**) and superior surface (rotated 90° to face camera) of the bone anchor (**c**). The tendon analogue attaches to each bone anchor surface around its base but not onto the inferior surface itself. Scale bar 5mm throughout.

4.5.3.2 Brushite Acid Washout Trials

Brushite bone anchors ceased to acidify their culture medium on their 5th wash (**Figure 4.30**). S-DMEM acidity was most obvious in the 1st wash of S-DMEM, turning the S-DMEM yellow. pH change in the 2nd, 3rd and 4th washes was progressively less, with a more subtle orange-red colour change. By the 4^h wash, some wells appeared the same colour as controls, but only by the 5th wash were all experimental wells judged to be the same colour as controls. Size of anchor did not make an obvious difference to the culture medium acidity. These results were found for both the air drying trial (**Figure 4.30a**) and non-air drying repeat (**Figure 4.30b**).

6^h and 7th washes beyond a 5th wash, undertaken in the non-air drying repeat (**Figure 4.30b**), produced the same colour of S-DMEM in all wells as the 5th wash, demonstrating that these had no additional effect on pH. After 7 hours in the 7th S-DMEM wash, the colour still remained the same between experimental and control wells, suggesting that no further acid had been released by the brushite. However, in all wells the S-DMEM was bright pink, indicating an increase in alkalinity in the culture medium with or without brushite.

A further observation from both trials was that the anchors effervesced in the early period of the 10 minute S-DMEM wash in the 1st and 2nd washes. This was obvious in the 1st wash, with very slight effervescence in the 2nd wash, but was not apparent in the 3rd or following washes. With progressive washes it was also noticed that the slight remaining material sediment in the anchor wells after they had been transferred to a fresh plate became progressively less with each wash, and much reduced after the 3rd and following washes.

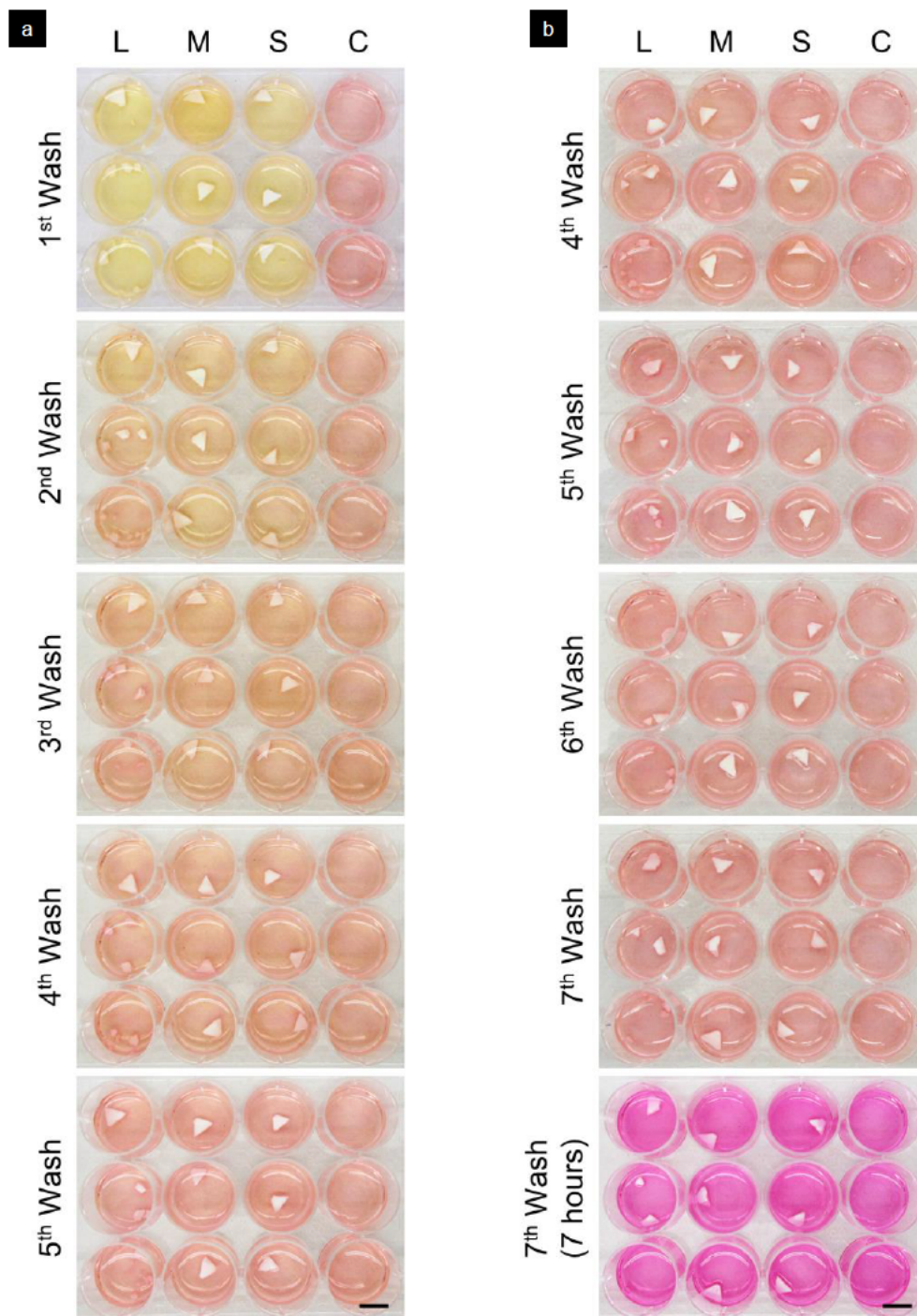


Figure 4.30 | Brushite Acid Washout Trials

Overview photographs comparing triplicate column repeats of 'large' (L), 'medium' (M) and 'small' (S) brushite anchors against *control* (C) wells of no anchors in 12 well plates (22mm diameter wells) after various 10 minute (unless stated) washes of S-DMEM. Some large anchors have broken up but still retain the same amount of material. S-DMEM phenol red colorimetric pH approximations: yellow, pH<6.8; orange-red, 6.8-8.2; bright pink, >8.2. **a)** Trial with drying between washes, 1st to 5th wash. After the 1st wash, brushite anchors clearly acidify the S-DMEM. With further washes the pH colour change is progressively more subtle, until the 5th wash where no difference between all experimental and control wells is seen. Scale bar 10mm all panels. **b)** Repeat trial without drying between washes, 4th to 7th wash. The 4th wash still displays subtle pH colour change in some experimental wells, not apparent on further washes. After 7 hours in the 7th S-DMEM wash, all wells are more alkaline but there is no difference between experimental and control wells. Scale bar 10mm all panels.

4.5.3.3 Osteoblast Seeding Trial

dRObs attached and proliferated on the brushite scaffold discs over a 7 day period.

4.5.3.3.1 Seeding Efficiency

Of the 10,000 dRObs seeded, a mean of ≈ 1300 cells (1314 ± 305) was measured attached to the scaffold after 5 hours, yielding a total seeding efficiency of 13%. A similar mean of ≈ 1500 cells (1535 ± 128) was measured unattached, suggesting 46% of recorded cells were able to attach, however ≈ 7200 cells (72%) were unaccounted for (**Figure 4.31**). dRObs displayed approximately 6x better attachment to the treated culture plastic of the positive controls, with ≈ 8200 cells (8244 ± 361) attached after 5 hours on day 0 (**Figure 4.32b**), compared to the scaffold.

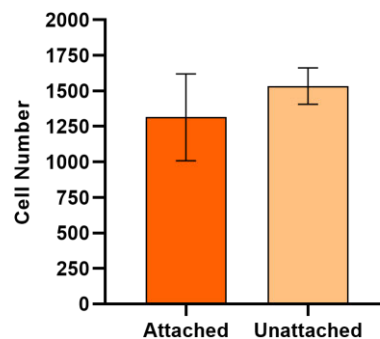


Figure 4.31 | Osteoblast Seeding Efficiency on Brushite Scaffold

Comparison of number of dRObs attached to the brushite scaffold with those unattached (recovered from the seeding well) after seeding on day 0. Cell numbers are comparatively similar and not significantly different. Mean \pm SEM.

4.5.3.3.2 Proliferation

From day 0 to day 2, numbers of dRObs attached to the brushite scaffold disc were similar, proliferating slightly from a mean of approximately 1300 (1314 ± 305) to 1400 (1418 ± 248), respectively. At day 7, dRObs had proliferated more considerably to ≈ 4000 cells (3944 ± 1404), although this was not a significant increase (**Figure 4.32a**). On the treated culture plastic of the positive controls, dRObs doubled from approximately 8200 (8244 ± 361) to 16,200 ($16,246 \pm 1582$) ($p < 0.01$) after 2 days of culture. At day 7, they had significantly proliferated to $\approx 106,200$ cells ($106,213 \pm 1762$) ($p < 0.001$) (**Figure 4.32b**), 27x more numerous than on the scaffold at the same time point.

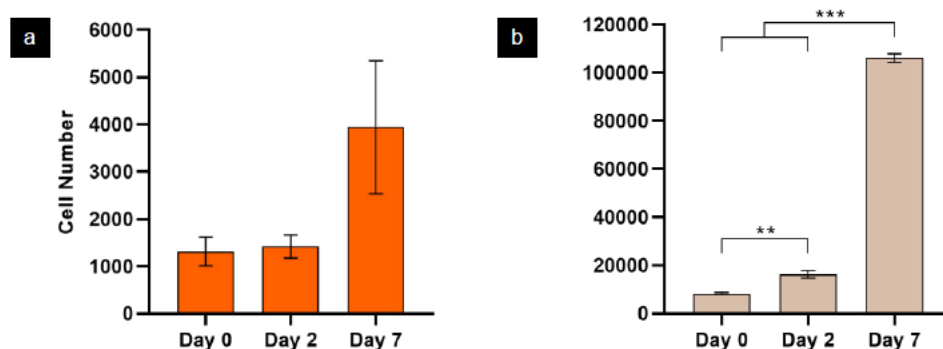


Figure 4.32 | Osteoblast Proliferation on Brushite Scaffold and Plastic

Comparison of dROb cell numbers seeded on brushite scaffold **(a)** and treated culture plastic **(b)** and cultured over 7 days in S-DMEM. The initial number of attached cells on the scaffold is much lower than that on plastic, however both groups show a comparable pattern of increase in cells with time. From day 0 to day 2, the increase in cells is minimal on the scaffold (non-significant), but significant on plastic. From day 2 to day 7, there is an approximately 3 fold increase on the scaffold and 6-7 fold increase on plastic, although this is only significant for plastic. Mean \pm SEM. **p<0.01, ***p<0.001.

4.6 Discussion

4.6.1 Cells

4.6.1.1 Mineralising Ability and Effect of Culture Medium

Different cell types were cultured in S-DMEM or RODM, or a 50:50 combination of both media, to observe their cellular phenotypic effects. S-DMEM (ingredients listed in Section 4.4.1.3.1) was the basal culture medium and did not include AA as standard. RODM, as a medium made available to encourage osteoblast differentiation, was presumed to contain AA and glucocorticoid (e.g. dexamethasone), as the key supplements of an osteogenic medium, and a phosphate solution [either organic, such as β -glycerophosphate (GP), or inorganic], which allows cell-mediated *in vitro* mineralisation (Gartland *et al*, 2012). It is acknowledged however that the results and their subsequent discussion are based on a medium of unknown true formulation, in ingredients or their concentration. RODM was provided with the commercially acquired rat osteoblasts and was readily available pre-manufactured, but ideally a mineralising media with known deliberate ingredients would be made in house and the concentration of supplements tested and optimised.

4.6.1.1.1 Rat Tendon Fibroblasts

RTFs never produced a mineralised ECM in any tested media in the current experiments, showing that they did not transdifferentiate into osteoblasts in RODM culture. In both S-DMEM and RODM cultures, they were spindle-shaped cells that appeared to produce regions of ECM within 2 weeks of confluence (day 18) on light microscopy. However, in later culture periods (day 18 and 25) there were observable differences, suggesting that sustained RODM culture was causing some phenotypic drift. In RODM, cells appeared more tightly packed, with greater areas of more discretely observable ECM, and fragmentation of the cell layer occurred. This was likely due to the AA in RODM. AA increases the synthesis and secretion of collagen, by functioning as a co-factor in the hydroxylation of lysine and proline residues to collagen (Gallagher, Gundle and Beresford, 1996) and increasing procollagen messenger ribonucleic acid (RNA) gene transcription and stability (Prockop and Kivirikko, 1984). It also increases cellular proliferation, for example in fibroblasts (Lima *et al*, 2009), MSCs (Fujisawa *et al*, 2018) and osteoblasts (Gartland *et al*, 2012), and increases total non-collagenous protein synthesis (Gallagher, Gundle and Beresford, 1996). The cells were therefore probably producing an ECM of increased collagenous (and non-collagenous) matrix in the RODM, noticeable as more nodular areas in culture, generating contraction of a monolayer of increased stiffness and leading to the regions of fragmentation. Whether this represented enhanced function of fibroblasts or a true drift towards an osteoblast phenotype is not discernible by observation alone. In either case, culture in 50:50 medium appeared to reduce the progressive characteristics noted in RODM, and although the ECM did appear more nodular than in S-DMEM culture, the degree of ECM production/composition that might cause monolayer fragmentation did not occur.

4.6.1.1.2 Rat Bone Marrow-Derived Mesenchymal Stem Cells

BMSCs were isolated to especially explore if they could develop functional osteoblast characteristics for use in the tendon-bone model, as well as to potentially provide a future source of differentiated fibroblasts or chondrocytes. It was thought that the constituents of RODM would confer an osteoblastic ability to mineralise ECM upon the BMSCs, but this did not occur within the 25 day experiments. A basal culture medium with the addition of AA and phosphate, with or without glucocorticoid, can induce osteoblast differentiation in MSCs, for example in human (Jaiswal *et al*, 1997; Tare *et al*, 2012) or rat (Maniatopoulos, Sodek and Melcher, 1988), even after

maintenance of primary cultures in basal medium without AA for an initial 1-2 weeks. If AA and phosphate were ingredients in RODM, the current BMSCs may not have undergone osteoblast differentiation due a number of potential reasons. The limit of 25 experimental days may not have allowed sufficient time for differentiation, which may require several weeks (Vater, Kasten and Stiehler, 2011). Primary and early sub-cultures were not immediately cultured in AA, potentially precluding mineralising capability or indeed an ability to generate ECM at all, as seen in osteoblast primary cultures (further discussed in *Section 4.6.1.1.3*). Many osteogenic differentiation protocols also include additional vitamin D3 and factors such as transforming growth factor(TGF)- β and bone morphogenetic proteins (BMPs) (Vater, Kasten and Stiehler, 2011), which may not have been present in RODM. Despite not conferring a mineralising ability, BMSCs did however display a morphology and behaviour very similar to RObs. This suggests possible development down a 'pre-osteoblast' lineage (see *Section 4.6.1.1.3*), yet is unlikely since this observable phenotype was also seen in S-DMEM as well as RODM cultures. Although BMSCs were only tested in a single biological set of cells, following these results they were not explored further for use in the tendon-bone model.

4.6.1.1.3 Rat Osteoblasts

RObs, from the single successful explant culture, did not produce a mineralised ECM in either S-DMEM or RODM cultures, or appear to generate any ECM visible on light microscopy altogether. In RODM culture this was highly unexpected, as RODM was stated to promote osteoblast differentiation and matrix mineralisation, which indeed did occur in dRObs cultured in RODM (*Section 4.6.1.1.4*). Bone explant cultures consist of osteogenic lineage cells of all stages of differentiation and maturation (Gartland *et al*, 2012), and cultures may have been dominated by particularly proliferative pre-osteoblasts. Such cells have yet to develop full osteoblast phenotype, and may explain the observed similarity to BMSC cultures if the BMSCs were likewise partially differentiated. Yet the current primary ROb cultures did display osteoblast characteristics of a rounded/polygonal morphology and a cobblestone appearance at early confluence, different to BMSCs, and isolates were from an adult, rather than neonate, where cells are more liable to be mature, less proliferative and more differentiated. A further reason for lack of mineralisation may be that, despite the current cells being in a relatively early 2nd passage, osteoblasts are known to lose their osteoblastic phenotype on repeated culture (Gartland *et al*, 2012), with foetal rat

calvarial osteoblasts even reportedly losing mineralising ability on or after their 3rd population doubling (Moskalewski, Boonekamp and Scherft, 1983). The most pertinent issue however appears to be the lack of AA, necessary for osteogenic differentiation of primary osteoblast isolates (Orriss *et al*, 2014), in extended early culture. Early investigators also came upon lack of mineralising ability in primary bone isolates for this reason (Ashton *et al*, 1985). AA is required continuously in primary culture to provide cells with the capability to mineralise their ECM, and even if AA is first added to secondary sub-cultures for extended periods, the cells will not mineralise or secrete significant matrix (Gallagher, Gundle and Beresford, 1996; Gartland *et al*, 2012). The current cells were grown in primary culture for 15 days, then in 1st passage for 33 days, both in S-DMEM alone, before cryopreservation. It seems therefore that RObs, whether pre-osteoblasts or originally mature osteoblasts, were in a state incapable of secreting or mineralising ECM even if cultured in RODM. RObs were therefore not used as the osteoblast source for further experiments in developing the tendon-bone co-culture model.

4.6.1.1.4 Differentiated Rat Osteoblasts

dRObs were derived from a commercially acquired line of healthy rat bone isolates, which appeared of differing phenotype in the acquired 1st passage (larger morphology, slower proliferation) to those cells considered 'differentiated' (dRObs) after 4-5 passages. Testing whether these dRObs had not transdifferentiated towards a more fibroblastic phenotype and were still osteoblasts capable of mineralising was a principle reason for conducting the set of mineralising experiments. dRObs were duly confirmed as differentiated and active osteoblasts, showing ECM secretion and mineralising abilities, and were therefore used as the osteoblast source for the tendon-bone co-culture model.

dRObs produced macroscopically visible 3D nodular aggregates of cells, raised into different focal planes by secreted ECM, in both S-DMEM and RODM. Although the nodules were not analysed in depth, their formation matched descriptions of the characteristic collagenous ECM formed in differentiated osteoblast cultures (Bellows *et al*, 1986; Maniatopoulos, Sodek and Melcher, 1988; Gallagher, Gundle and Beresford, 1996; Mechiche Alami *et al*, 2016). In particular, the nodules coalesced into a web-like trabecular pattern, characteristic of rat osteoblast cultures (Orriss *et al*, 2014). ECM nodules do not form without a medium containing AA (Bellows *et al*, 1986;

Gartland *et al* 2012), however the current cells still formed ECM nodules when cultured in S-DMEM without AA. This suggests that the original commercially acquired isolates were primary cultured in a medium containing AA, potentiating an ECM secreting and mineralising ability despite the lack of AA in subsequent sub-culture media, highlighting its importance in primary culture. As expected, dRObs only mineralised the ECM in RODM and 50:50 medium culture, due to the presumed phosphate ingredient in RODM that is essential to mineralisation (Bellows *et al*, 1986; Maniatopoulos, Sodek and Melcher, 1988; Gallagher, Gundle and Beresford, 1996; Gartland *et al*, 2012; Orriss *et al*, 2014). Analysis of such mineralised nodules have shown their histological and immunochemical similarity to *in vivo* woven bone, containing surface osteoblast-like cells and osteocyte-like cells buried deeper within a mineralised matrix of predominantly type I collagen (Bellows *et al*, 1986; Maniatopoulos, Sodek and Melcher, 1988; Beresford, Graves and Smoothy, 1993; Mechiche Alami *et al*, 2016).

4.6.1.2 Selection for Co-Culture

The ultimate goal of the project was to design an *in vitro* 3D tendon-bone model with co-culture of fibroblasts and osteoblasts. The mineralisation experiments were designed to select the most suitable fibroblasts, osteoblasts and culture medium for co-culture from the cells and media formulations reasonably available. A single species co-culture was important for observations of cellular interaction in cells of the same species, and to maintain translational proximity to an eventual human co-culture model as an immunocompatible implant. Rat cell populations were therefore isolated and acquired, as cells easily obtainable and well characterised for literature comparison. In addition, since a compartmentalised bioreactor design of different culture media was beyond the scope of the project, an important feature for a single compartment co-culture design was a medium choice to optimally maintain both fibroblasts and osteoblasts simultaneously.

RTFs and dRObs were suitable and representative fibroblast and osteoblast populations, due to the observed phenotype in their respective supporting media (S-DMEM or RODM) as described in *Section 4.6.1.1*. Although certain changes in cell behaviour were perceived when one cell type was cultured in medium supportive of the other, culture of either cell type in a 50:50 mix of both media was encouraging for single compartment co-culture. The increased proliferation and ECM production of

RTFs in RODM was lessened in 50:50 medium, and dRObs, not able to mineralise ECM in S-DMEM, achieved mineralisation in 50:50 medium, although a week later than in RODM. Avoidance of fibroblast osteogenic drift and osteoblast loss of mineralising ability are key lines of inquiry in the development of novel co-culture systems (Wang *et al*, 2007; Cooper *et al*, 2014; Calejo *et al*, 2018). These studies were able to induce fibroblast ECM mineralisation with medium containing AA, β -GP, \pm dexamethasone, not seen in the current mineralisation experiments with RTFs in RODM, or 50:50 medium. Concentration of β -GP was particularly crucial to their optimum co-culture medium, where 1-3mM β -GP maintained osteoblast mineralisation but limited fibroblast mineralisation (Wang *et al*, 2007; Cooper *et al*, 2014). This is notably similar to the 2mM optimal β -GP concentration for culturing bone-forming rat osteoblasts (Orriss *et al*, 2014), although comparison cannot be made with the current dROb cultures as the concentration of β -GP in RODM is unknown. Where detailed control of mineralising medium supplements is beyond the scope of investigation and only basal medium (S-DMEM) and mineralising medium (RODM) are available, the current results agree with Calejo *et al* (2018) in selecting a 50:50 media mix as the optimal co-culture medium.

4.6.1.3 Limitations

4.6.1.3.1 Isolations and Cell Type

Rat cells were isolated to create populations of same species primary cells, ultimately for co-culture of different cell types. However the cells were not characterised in depth, for example in the expression of cell-specific markers, and assumptions of cell type were based on isolation protocols, and observed *in vitro* morphology and behaviour, where some crossover in cell type may exist.

RTFs were recognised confidently by their conspicuous spindle-shaped morphology and rapid proliferation. All cells in RTF cultures appeared similar, within and between biological replicates, and also were comparable to CTFs used in early stages of the project. Their proliferation characteristics and apparent deposition of ECM after confluence was as expected. BMSCs were less confidently distinguished. Early cultures in particular contained a variety of morphologies, where separate colonies of narrow spindle shaped or larger rounded/polygonal cells were common, although morphological heterogeneity can be typical of BMSC cultures (Javazon, Beggs and Flake, 2004). The present isolation technique relied on the selective physical property

of plastic adherence of BMSCs, however macrophages, endothelial cells, lymphocytes and smooth muscle cells are also known to adhere and contaminate early BMSC cultures (Javazon, Beggs and Flake, 2004). BMSCs underwent mineralisation testing in P₃, and the repeated expansion and culture in basal S-DMEM would probably have not supported the propagation of these contaminating cells over BMSCs. Fibroblast contamination seems less likely, as, although most BMSC populations appeared fibroblastoid in morphology, particularly at high densities, collagenase was not used in the isolation technique and BMSCs did not produce obvious ECM as per RTFs. The lack of BMSC differentiation to mineralising cells in RODM was nonetheless unexpected, but this does appear to be explained by the lack of AA in primary culture medium or other subsequent differentiating factors, as discussed in *Section 4.6.1.1.2*.

Since RObs did not produce mineralised ECM in RODM, there was concern that a different cell type was isolated. Non-osteoblastic cells such as osteoclasts and particularly periosteal fibroblasts, which may overgrow the primary osteoblast cultures, can be preferentially isolated (Bakker and Klein-Nulend, 2012). Although ROb cultures had morphological similarities to RTFs in high densities, care was taken to remove all soft tissue from the extracted bones with sharp dissection and collagenase, and cells were seen to grow out from bone pieces with a generally rounded/polygonal morphology. Bone is a difficult tissue from which to extract cells, due to the heterogeneity of cell types, complex structure and mineralised ECM (Gartland *et al*, 2012) and indeed only 1 of 3 osteoblast isolation attempts was successful. In the unsuccessful attempts, no other cell types were cultured, suggesting the technique did not support fibroblast extraction anyway. The most likely reason for unsuccessful attempts may have been disturbing the cultures and bone pieces too early, undertaking a first medium change on day 3, as was customary for other cells, which was not specifically stated in the followed protocol (Bakker and Klein-Nulend, 2012). Other protocols highlight the importance of not dislodging the explants and leaving the cultures undisturbed for 7 days, changing medium initially on day 7 and 14 only (Gallagher, Gundle and Beresford, 1996; Gartland *et al*, 2012). Since the same technique proved successful in the 1st attempt, it may be that the FBS, different in the 1st attempt to the other 2 attempts, was superior in supporting osteoblast isolation. Different FBS batches are known to have considerable variation in stimulation and

survival of primary bone cells (Bakker and Klein-Nulend, 2012), and a few explant cells were even seen in the 2nd attempt, but died off before proliferation.

The exact phenotype of dRObs was not clear, however, as a population able to mineralise their ECM, they were satisfactorily verified as mature osteoblasts. Their progression from the larger, less proliferative cells acquired commercially in 1st passage to smaller, more proliferative cells and with more refractile cell bodies in 4th or 5th passage is not typically described in the literature. It may be that the cells acquired some fibroblastic characteristics with sustained culture in the non-osteogenic S-DMEM, although retained an ability to secrete ECM and mineralise from their commercially performed primary culture. In future, a more revealing phenotype profile could be evaluated with quantified expression of fibroblastic and osteoblastic markers.

4.6.1.3.2 Applicability and Validity

The age of the rats from which RTFs, BMSCs and RObs were isolated was 14-16 weeks, representative of the young adult stage (Sengupta, 2013). These ages were selected based on the adult osteoblast explant protocol (Bakker and Klein-Nulend, 2012), and to balance the physiological differences of younger, more proliferative, active cells, such as in neonates, with the more differentiated but less active cells of adulthood (Gartland *et al*, 2012). It was important to use mature cells with adult characteristics, particularly where a translational model was most applicable to an adult human population, so young adults were chosen in anticipation of retaining reasonable proliferative potential. The use of mature mineralised bone over neonatal bone may have however made osteoblasts especially difficult to extract, potentially contributing to failure of explant culture in 2 of the 3 attempts. Furthermore, in using cells from a narrow age range of rats, results and cellular characteristics are restricted to this age group or level of maturity, although descriptions and differences in the rat cell population was not under investigation.

Use of primary cell lines was also an important feature. Cells were isolated, or acquired in the case of dRObs, to retain representative, close *in vivo* characteristics. Cells were investigated in as early a passage as reasonably possible (RTFs P₂ and P₅; BMSCs P₃; RObs P₂) although ideally investigations would have occurred in P₁, negating cell senescence and possible loss of phenotype, as may have been

encountered in RObs (see *Section 4.6.1.1.3*). dRObs were investigated in P₆ and P₇, when indeed their phenotype had somewhat altered ('differentiated'), however their increased proliferation rate was beneficial for experimental preparations.

Consideration was always given to features that could best develop a tendon-bone model with translational human potential. Human cells would have been ideal, however their acquisition was beyond project timings. Rats were the best available source as a common mammalian model system, however potential cell physiology differences between rat and human are acknowledged. Attempts were made to isolate both functional fibroblasts and osteoblasts from the same animal, and as multiple biological repeats, to preferably study individual-specific co-culture cellular responses. A single animal system would provide corresponding study for the potential of a patient requiring a tendon-bone model graft with their own, non-immunogenic, cells. Isolated RObs were unfortunately unsatisfactory for use as mature osteoblasts, so a single species different animal approach was progressed (isolated RTFs and acquired dRObs). Better still, isolation of MSCs capable of fibroblast and osteoblast differentiation would be most satisfactory to develop a single cell source non-immunogenic translational human model. BMSCs were isolated, but appeared to lack osteoblast differentiation potential in the current culture conditions, so were not explored further. However, MSCs may in fact represent the best clinically-applicable cell type to explore in future model development.

4.6.2 Tendon Analogue

4.6.2.1 Formation and Maturation

4.6.2.1.1 Single-Strand

The basis for generation of a tendon analogue was contraction of a flat 3D layer of fibrin hydrogel scaffold seeded with fibroblasts around 2 suture anchor points. Gel contraction was cell mediated, since control constructs, set up during the anatomical suture experiments without cells but maintained under the same culture conditions as seeded constructs, did not contract (*Appendix 7*). Occasional fibrin gels were noted to be 'contracted' before cell seeding, after retrieval from 37°C polymerisation (see **Figure 4.9**), which, although of uncertain true cause, appeared to be due to a combination of slight mechanical vibration from the incubator and nearby refrigeration units and the highly hydrophobic nature of the underlying Sylgard. Sylgard's

hydrophobicity was a crucial property to prevent cell and gel attachment and provide a low friction surface for unhindered contraction, and indeed in these cases the pre-seeded gel appeared to have 'slipped' and folded over, without losing volume. In contrast, fibroblast mediated contraction occurs from the traction force produced as cells degrade the fibrin and start to replace it with a thin filamentous matrix and subsequent collagen fibrils that crosslink together (Huang, Khait and Birla, 2007; Kapacee *et al*, 2008; Paxton *et al*, 2012a).

Gel contraction was apparent within 24 hours, with the vast majority occurring within 7 days. Contraction proceeded from the peripheries towards the centre of the well, revealed by histology to be a structural result of peripheral folding and compaction, and described by Huang, Khait and Birla (2007) as a process of delamination from the underlying culture surface. Radial contraction was directed into a linear form by the suture anchors, without which the gel would have compressed into a central circular mass (Hecker *et al*, 2005). The first few days of contraction, when the gel peripheries lay at a distance from the imposing tension force between the anchors, were therefore often uneven, which if substantially irregular could residually distort the morphological uniformity of the mature construct. After 7 days the general shape of the tendon analogue was formed along the tension line between the sutures, and as contraction reduced in subsequent weeks, gel opacity increased, seemingly a result of the progressively more dense and elaborate folding as shown in histology transverse sections. These observations agreed with the monitoring of near identically formed fibroblast-seeded fibrin constructs by Paxton *et al* (2012a), describing the stages of development as early (day 0-7), maturation (day 7-35) and late maturation (day 35 onwards), also noting that the enhancing opacity was indicative of increased matrix deposition.

Fibrin provided a supportive 3D cellular environment, with histology showing proliferating cells spread throughout the gel. With time the cells appeared to align in parallel between the sutures, also described by Hecker *et al* (2005), Bayer *et al* (2010) and Paxton *et al* (2012a) as a result of the mechanical tension force provided by the suture anchors. Modified Masson's trichrome staining showed that these cells were the focus of collagen production, itself likewise in parallel linear bands, suggesting that these cells were the most stimulated and functional and were beginning to organise the scaffold into the histological structure of fibrous tissue. Indeed the

importance of maintaining mechanical tension on cellular function has been illustrated by the disorganised collagen produced after constructs are severed at their midpoint, as performed by Kapacee *et al*, 2008. Nevertheless, even at 8 weeks, staining for collagen was limited. Cells characteristically replace the fibrin with their own ECM, and similar constructs have shown near complete fibrin degradation in 1-4 weeks (Huang *et al*, 2005; Huang, Khait and Birla, 2007; Kapacee *et al*, 2008). It may be that more collagen was present but that staining was poor; or that the intense red cytoplasmic stain of the modified Masson's stain masked the weaker blue collagenous stain, since the densely cellular construct peripheries, external to the fibrin, showed much clearer blue staining. Yet collagenous blue staining was abundant with the same staining technique in the previously investigated human tendon samples (see *Chapter 3, Figure 3.4b*). Paxton, Grover and Baar (2010) however note that fibrin is only degraded and replaced by collagen when AA and P is added to maintenance culture media, so the paucity of collagen in the present constructs may most likely be the result of an initial 3 weeks of culture without AA and P.

A particular histological characteristic was the aggregation of cells on the surface of the fibrin, forming a capsular layer, also noted by Huang *et al* (2005) and Paxton *et al* (2012a). This may have been due to the droplet seeding technique, rather than cell embedding during formation of the gel, and although histology showed that cells migrated throughout the fibrin, a preponderance remained lining the surface. These cells also appeared to be a hub of collagen production on modified Masson's trichrome staining as development proceeded. Bayer *et al* (2010) similarly distinguished a cortical surrounding of collagen type I using immunohistochemistry in their constructs. The enhanced ECM production of these cells may have been a result of increased cellular density and interactions, and/or better access to nutrients and more proficient waste elimination due to their surface position.

4.6.2.1.2 Multi-Strand

Multi-strand constructs were investigated for the potential to create a mechanically superior tendon analogue of multiple macroscopic bundles, similar to 3^o collagen fibre bundles in the hierarchical structure of tendon (*Chapter 1, Figure 1.2*). Of particular interest was whether the separate strands merged into a single unit, which was revealed by histology to have not occurred by 5 weeks of culture (after 3 weeks of preceding single strand culture). The cellular capsular layers from each strand did

rapidly integrate by week 1, and this bridging area between the separate strands was a focal area of cellular proliferation and potentially of fibrin degradation. However, although the fibrin from the separate strands did directly interface as the structure became more compact at later time points, it did not appear to have fused. This appearance was potentially because of the overall limited fibrin degradation seen, as previously discussed, leaving the separate folds of fibrin in their similar individual forms. It would have been interesting to compare the process of multi-strand fibrin degradation with constructs cultured earlier in media more encouraging of collagen production, such as with growth factors along with AA and P, to establish if and how separate strands might merge. Further work would have also particularly focused on mechanical testing, as the principle tissue engineering reason to progress development of these multi-strand tendon analogues is if they are stronger than the sum of individually-tested single strands.

Morphologically, through the basic single-strand suture-suture method, the flat layer of fibroblast-seeded fibrin gel latterly matured into a tight cylindrical structure (see **Figure 4.10**). As noted by Paxton *et al* (2012a), this is not an ideal individual morphological replicate for tendon or ligament. The distal FDP tendon is a biconcave bean shape in transverse section, seemingly composed of 2 distinct large fibre bundles either side of a median sulcus on flexor and dorsal sides (see *Chapter 1, Section 1.2.3.2*). The double strand construct was therefore also an investigation of morphological interest, as a potentially enhanced native morphological match. The double strand tendon analogue was biconcave in transverse section throughout its combined culture of single strands, but, likewise to single strands, transitioned from an overall flatter shape at earlier time points to become subsequently more rounded. Thus morphological matching to the distal FDP appeared to be more optimal after 1 week of combined culture rather than 5 weeks (**Figure 4.13**), presumably principally due to the preceding 3 weeks of single strand culture, although at 5 weeks this was still a better shape than a basic single strand suture-suture tendon analogue. The double strand construct was not investigated further in favour of increasing the gel volume in a single strand, primarily because of the time involved in first culturing single strands before combination. Nonetheless, an improved tendon analogue may have been formed by earlier combination of single strands, for example after 7 days once the general linear form has been established, followed by longer double strand culture.

This may have potentially balanced the earlier flatter biconcave morphology with more time for fibrin degradation and potential merging of the 2 strands.

4.6.2.2 Suture Anchor Manipulation

The tight cylindrical morphology of the mature basic suture-suture tendon analogue was not well matched to the distal FDP, not only in cross-section but also in the size and shape of its proximal and distal ends. The proximal end should be of similar size to the native tendon where potential graft-to-native tenorrhaphy might occur, and the distal end is that of the bone interface where attachment area and position affects biomechanics. Beyond further exploration of the double stranded construct, the best way to achieve an equivalent native morphology appeared to be using the size and position of the construct anchors to manipulate the shape of the contracting fibrin gel. The suture manipulation experiments were therefore primarily observational studies to explore how the gel contracted around vertically placed suture anchors, and, since analysis of human FDP tendon width (*Chapter 2*) showed that the bone insertion end and the end 12mm proximal were of different sizes, how it contracted around differently sized opposing sutures. As 5mm sutures were used for the basic (horizontally placed) suture-suture tendon analogues, this 5mm size, as well as larger (10mm) and smaller (2mm) sizes, were investigated. In addition to primarily observing the shape of the contracting gel, particularly between the anchors, 4 width measurements were taken across the 12mm construct, as analogous to the measurements of the human FDP tendon at its insertion (*Chapter 2*), to add a quantitative interpretation.

A degree of continued gel contraction was expected in the region between the anchors, gradually driving the linear rectangular shape of vertical/vertical tendon analogue constructs towards an 'H' shape and the triangular shape of vertical/horizontal constructs towards a sideways 'T' shape. Yet to what degree of contraction was difficult to predict. Since the contracting gel was previously shown to tend towards a thin cylindrical morphology, greater relative gel contraction between sutures was expected in constructs with larger anchors (i.e. with a 10mm vertical suture), producing more distinct 'H' and 'T' shapes, than constructs with smaller anchors. Continued gel contraction did continue between the sutures in all constructs, but not to a large degree, with mid-point widths (50% distance measurement point) remaining at $\approx 75\text{-}90\%$ of gel width at the sutures in vertical/vertical constructs.

Comparative quantitative results between different sized constructs in fact suggested the opposite to original hypotheses, with the smaller constructs of 2mm or 5mm vertical sutures producing greater 'H' and 'T' shapes. It appears that, for the volume of gel used, the vertical 10mm suture in either vertical/vertical or vertical/horizontal constructs was able to maintain enough outward tension in the gel between the sutures to minimise substantial contraction to an 'H' or 'T' shape. For constructs with 2mm or 5mm vertical sutures, the gel between the sutures was perhaps comparatively less taut and cell mediated contraction could continue to overcome the tension force, demonstrating an interplay between mechanical (tension) and biological (cell based contraction) factors. The smaller anchors were less well able to maintain linear margins to the contracting gel shape.

Measurement of gel width in line with the sutures notably showed that the gel did not contract to the width of the suture itself. This was illustrative of the means of gel contraction, by compaction and folding of the gel peripheries towards the centre of the well. The gel peripheries bunched up and attached against the suture anchor, as also shown histologically by Paxton *et al* (2012a) at a cement anchor. Smaller anchors displayed a greater difference in width between the gel and suture itself because there was a greater distance for the gel to contract from periphery to anchor, and thus a greater volume of compacted/folded gel lying against the suture. Even for 5-10mm vertical anchor sizes, as a similar size range to the native human tendon widths at bony insertion and 12mm proximal, although the difference between gel width and suture width progressively declined there was still an approximate width difference of 0.5mm by 35 days of culture.

Overall, the suture manipulation studies demonstrated that although some bowing of contracting gel does occur between anchors, larger anchors used in this system can generate enough outward gel tension to maintain a relatively defined linear shape in the maturation phase of development. However, due to the general folding/compaction process of contraction and variability across replicates, achieving a precise gel width is challenging, even at the anchor position itself.

4.6.2.3 Effect of Culture Variables

Culture variables were tested in constructs containing suture anchor sizes directed by human FDP tendon widths at its bony insertion and 12mm proximal to the insertion.

The general development of the tendon analogues cultured with any of the variables was similar to that of basic suture-suture constructs and suture manipulation experiments, with basic shape formation in 7-14 days and maturation thereafter. Macroscopic effects on gel contraction by the culture variables were subtle, but quantitative statistical analyses demonstrated that different variables did yield significant effects. The results highlighted that culture media, additional anchors, fibrin gel volume and cell number can all be employed advantageously to tissue engineer a predictable and morphologically relevant tendon analogue.

4.6.2.3.1 Culture Medium

Addition of AA and P to standard S-DMEM in general produced greater gel contraction than S-DMEM alone, agreeing with expectations. The effect was most apparent in double volume gels with regular cell number, where 'double gel/+AA+P' cultures were significantly more contracted than 'double gel' cultures over all distance measurement points between the suture anchors, so under these conditions the null hypothesis of no effect can be rejected. The greater contraction effect of additional AA and P was also evidenced by smaller mean gel widths in standard volume gels from day 14 onwards, and in double volume gels with double cell number, although they were either respectively of non-significance or not statistically compared.

AA and P are promoters of collagen synthesis. AA, as previously described, is an essential co-factor for prolyl-4-hydroxylase and is required in the hydroxylation of lysine and P for collagen fibril assembly (Gallagher, Gundle and Beresford, 1996; Paxton *et al*, 2012a); as such, P forms a substantial amino acid component of the collagen protein. The more collagen fibrils produced, the more they crosslink together and the greater the gel contraction. AA and P additionally appear to increase cell proliferation and affect matrix metalloproteinase (MMP) activity, likely intensifying fibrin degradation and reducing gel volume, whilst AA may also initiate a level of transdifferentiation in fibroblasts towards a more contractile myofibroblastic phenotype (Paxton *et al*, 2012a). The environment of fibrin, collagen and fibroblasts is similar to that of wounds, where supplementation of AA thus predictably accelerates contraction in animal wound models (Cabbabe and Korock, 1986; Jagetia *et al*, 2007).

The chosen concentrations of supplementing AA and P were standard in the laboratory, allowing direct comparison to the supervisor's similar previous work

[Paxton *et al* (2012a)], which also described the increased contraction effect of AA and P in fibroblast-seeded fibrin constructs using smaller anchors. This work highlighted that additional AA and P accelerated gel contraction only in the maturation phase of tendon analogue development, also agreeing that at early time points contraction was slower with AA and P. In the present study, '+AA+P' cultures were initially less contracted than 'S-DMEM' cultures at day 7 in standard volume gels, but not in double volume gels. Why addition of AA and P initially appears to have less of a contraction effect than basal medium alone, but not when gel volume is doubled, is unclear. Even if perhaps AA and P caused an initial slower decrease in scaffold size due to earlier immature (less contractile) ECM deposition before substantial fibrin degradation, this effect would have been expected whatever the gel volume, so the results may reflect the variability of contraction in early stage formation. Paxton *et al* (2012a) also used OCT to observe the 3D cross section of the contracting gel in their small anchor constructs, noting that addition of AA and P folded the gel into thin cylinders, rather than the broad and flat shape without AA and P. In the present studies, OCT images suggested that the contracting gel peripheries were more tightly folded over with AA and P, rather than bunched up without AA and P, which may similarly reflect the increased folding effect of additional AA and P when the contracting peripheries are restricted due to wider anchors.

Since AA was a presumed component of RODM (Gartland *et al*, 2012), it was also expected that gel contraction would be greater with RODM than S-DMEM, however there was no clear evidence to support this. In the regions between the sutures, 'RODM' cultures were in fact less contracted than 'S-DMEM' cultures until day 35-42, after which both were similar until the day 56 experimental end point. If AA was indeed an RODM ingredient, it may have been at lower concentrations than the AA used for the '+AA+P' culture variable (250µm) and so exerted less or no contraction effect. Yet in 2D fibroblast culture in RODM there appeared to be increased cell proliferation and collagenous matrix production, although this was inferred by general observation rather measurement (see *Section 4.6.1.1.1*). The other probable ingredients, including glucocorticoid and phosphate solution, may have added the diminished contraction effect, by affecting cellular function or ECM properties. A phenotypic drift of fibroblasts towards osteoblasts may have resulted in the production of a less contractile ECM. The 'RODM' tendon analogues were also noted to appear more opaque and brittle than other cultures. Alizarin red testing of the RODM precipitate

remaining in the well of 'RODM' constructs after tendon analogue removal stained positively for mineral (see *Section 4.5.2.4.1*), suggesting that mineral may also have precipitated in the 3D constructs [despite calcium not being present in 2D fibroblast cultures with RODM, (see *Section 4.5.1.2.2*)]. This may have hardened the contracting gel, also producing the light attenuation noted on OCT (**Figure 4.26**). The hardened gel may have resisted contraction in early weeks, slowing contraction rate, but not prevented the plateau in contraction being reached, as per 'S-DMEM' cultures, around day 42. The potential varying effects of RODM on RTFs may be representative of altered cellular behaviour in 2D and 3D environments.

4.6.2.3.2 Additional Anchor Points

2 additional anchor pins were placed at the mid-point between the suture anchors, at a width of 6.05mm, corresponding to the native human FDP width at its mid-point (6mm proximal to bony insertion) between FDP bony insertion (0mm) and 12mm proximal. These mid-point pins significantly increased the gel width at the 3 measurements points between the sutures (25%, 50% and 75% points), most significantly at the 50% point, compared to S-DMEM culture without mid-point pins, confirming the hypothesis of their effect on gel contraction. This demonstrated that pin anchors can successfully be utilised to manipulate the width of contracting gel. As the gel width at the 50% measurement point, where the mid-point pins were placed, was approximately 1.5-1.8mm wider from day 28 onwards, this indicated that the folding/compacting peripheries of the gel had gathered against the pin and were prevented from further inwards contraction. If a precise gel width was required using this additional pin anchor technique, pins would need to be placed more narrowly together than the intended gel width, requiring consideration of both gel volume and the ideal time to harvest the model.

4.6.2.3.3 Fibrin Gel Volume

Doubling the volume of fibrin gel was trialled since standard volume gels produced thin (depth dimension) tendon analogues when cultured with wide anchors, not well morphologically matched to the distal FDP tendon, and also resulted in occasional gel fragmentation during formation. Doubling gel volume was however hypothesised to also increase gel width, specifically when compared to standard (single) volume gels when both cultured in S-DMEM. This was, not unsurprisingly, confirmed, by 'double gel' cultures being significantly less contracted than 'S-DMEM' cultures at all

measurement points. All double volume gel culture variables did nevertheless appear more robust and anatomically-relevant than standard volume gel culture variables, and none fragmented during formation. Compensation for the inevitably increased width from doubling gel volume was attempted by changes to other variables to increase contraction towards the ideal human tendon width, either with AA and P (as discussed in *Section 4.6.2.3.1*) or increased cell number (next discussed).

4.6.2.3.4 Cell Number

The effect of doubling cell seeding number, examined in gels of double volume, was confirmed to increase gel contraction, as hypothesised, as 'double gel/double cell' cultures were significantly more contracted than 'double gel' cultures at all distance measurement points. 'Double gel/double cell' cultures represented the same fibrin gel:cell ratio (i.e. density) as standard 'S-DMEM' cultures, whilst 'double gel' cultures represent a halved ratio, so a more accurate description is that halving cell density significantly decreased gel contraction. Hecker *et al* (2005) also showed that their fibroblast-seeded fibrin constructs contracted faster with 100,000 cells rather than 50,000 cells, therefore a greater number of fibroblasts presumably degrades fibrin faster and produces a greater quantity of contractile ECM. Doubling cell number in the double volume gel did not contract the double volume gel to the level of 'S-DMEM' (a standard volume gel), as 'double gel/double cell' cultures were still significantly wider at measurement points between the anchors compared to 'S-DMEM' cultures. This suggests that doubling gel volume has a greater gel expansion effect than the contraction effect of doubling cell number. Also, although not compared statistically, it is not clear whether the contraction effect of doubling cell number produces more contraction than adding AA and P. These variables appear relatively similar in effect, with a slight tendency for greater contraction with double cell number, since mean gel widths for 'double gel/double cell' cultures are less at every time point than 'double gel/+AA+P' at 0%, 25% and 50% measurements, whilst 'double gel/+AA+P' cultures are mainly less at 75% and 100% measurement points.

4.6.2.4 Optimum Set Up for Co-Culture Construct

The anatomical suture experiments, with suture anchors representative of human FDP tendon width, were used to analyse potential culture specifics for an optimum tendon analogue morphology by the proximity of their contracting fibrin gel to ideal human widths at various measurement points. Within 56 culture days, these widths

were only reached in standard volume gel cultures, in '+AA+P' cultures (all distance measurement points except 12mm) and also 'RODM' and 'S-DMEM' cultures at the 6mm point, where gel contraction was greatest. No double volume gel culture variables contracted to the ideal human width. However, double volume gels were sturdier and more morphologically relevant, making them better candidates for the final co-culture model. With addition of AA and P and doubling cell number, 'double gel/double cells/+AA+P' cultures contracted the double volume gel closest to ideal human width, and were not significantly different to 'S-DMEM' cultures at the 0%, 75% and 100% measurement points.

Time to construct harvest, for example for potential graft use, was also an important consideration. By 4 weeks in most cultures, the majority of gel contraction had occurred and gel width then plateaued, suggesting that ECM production and contraction was balanced with residual scaffold volume. Double volume gel culture variables did appear to still be contracting, minimally, from week 4 onwards at measurement points between the sutures (25%, 50% and 75% points), but over the following 4 weeks only contracted by a further maximum of ≈ 0.5 mm.

The size of anchors also clearly influenced tendon analogue morphology. At either suture anchor (0% and 100% distance measurement points) only '+AA+P' cultures reached the intended width, at the 0% point. Additional pin anchors were able to influence contracting gel width, but, as with the main suture anchors, the gel contracted against the side of the anchors and was therefore always of greater than intended width. Addition of mid-point pins at an ideal width actually made the developing gel less morphologically accurate than without extra anchor pins at all.

Overall, the most relevant tendon analogue morphology seems to be a balance of greater gel volume with culture variables that can contract the gel to the greatest extent, whilst providing anchorage points of a matching, or just less than ideal, size. A contracted tendon analogue is well formed at 2 weeks, but for added maturation the time to harvest seems optimal at 4 weeks. A 4 week culture of 'double gel/double cells/+AA+P' therefore seems the most ideal for the final model, although the culture medium may need further consideration for support of osteoblasts in the co-culture model.

4.6.2.5 Limitations

The method of fibroblast-seeded contraction of fibrin hydrogel to form a tendon analogue was reliable but the precise morphology (width/volume/folding pattern) resulting from the gel contraction was quite variable, particularly in the early stages of development. Contraction variability could potentially be compounded if areas of the gel had adhered to the well base, creating additional lines of stress and interfering with contraction and ECM formation (Kapacee *et al*, 2008). Gels were released from any adherence to the well rim on day 3 of experiments, but no further intervention followed thereafter, to encourage as natural a contraction as possible. Such sizeable natural variation in contraction would be best countered by multiple replicates. Most tendon analogue studies were akin to pilot studies, aiming to gain a broad range of observational trends on tendon analogue formation rather than comprehensively studying one area, and as such most studies contained limited replicates. Constructs were vulnerable to infection or failure of gel integrity over long investigative time courses, for example reducing initial triplicate repeats of the suture manipulation experiments (*Section 4.5.2.3*) over 35 days to an n of 1 for the 5mm vertical/vertical construct. Histology of single- and multi-strand basic constructs were performed on an n of 2-4, with qualitative assessment of representative mid-axis sections, and did not involve a specific sample section selection technique or quantification, so subjectivity bias was potentially prevalent. Extending such results to 'population' traits is cautioned, although they are representative of the samples obtained. The last set of tendon analogue experiments, the anatomical suture experiments (*Section 4.5.2.4*), however aimed to test hypotheses and select the materials to take forward into the summative co-culture model. These were designed with an n of 9 over technical and biological repeats and can therefore be viewed with the most certainty of reliable findings.

Most analyses of the developing tendon analogue were of gel width, as a representation of contraction and morphology. Measurement of width as a gel contraction guide was a published method (Paxton *et al*, 2012a), could be related to human FDP measurements and was easily achievable and available, but is acknowledged as a 2D parameter to assess developing 3D morphology. The nature of gel contraction by folding and bunching of the gel peripheries, whilst the central area of wide anchored constructs remains relatively flat, makes this caveat particularly pertinent. Although gel contraction was variable in the formation stage (days 0-7), with

subsequent maturation it was more stable and width was therefore judged as a reasonable method for comparison between constructs, particularly after a week of formation. 3D assessment of form would however have been more representative. 3D form is essential at the tendon insertion onto the bone, for example in the relationship of attached surface area to biomechanical performance, or at the proximal tendon analogue end, which as a graft may potentially be sutured to native tendon and require 3D matching of apposed surfaces. Furthermore, a significant experimental focus was on doubling gel volume to create a more anatomically relevant tendon analogue, however this was only assessed in 2D, and still more gel would likely have been required to match 3D morphology. OCT was performed at another institution on mature constructs and gave fantastic insight into the 3D structure and process of gel contraction. Had this been more readily available, 3D assessment over time may have been possible, although achieving cross sectional images over multiple specific regions repeated over time, attained in 2D by ImageJ measurements, would have been much more variable with OCT. With some constructs it was also difficult to achieve an image of the entire depth of the tendon analogue, which would have prevented comparable assessments. Nevertheless, OCT provided excellent 3D visualisation and further work would incorporate its use further, as an increasingly important evaluation of the dynamic changes in engineered tissues (Liang, Graf and Boppart, 2009).

The basis for gel contraction, and therefore the effects of culture variables tested, was fibrin degradation and replacement with collagenous ECM. An improved or more complete picture of the effect of culture variables on 3D cellular function could have been an increased focus on collagen. Collagen was assessed, but only by qualitative interpretation of modified Masson's trichrome staining on histology. A method could be devised to quantify collagen staining through assessment of stained areas with ImageJ software of images of sections systemically acquired in a number of constructs, potentially with selective immunohistochemistry for greater accuracy. Alternatively, constructs could be processed for collagen content with assays or specific expression of collagen genes with quantitative polymerase chain reaction (qPCR). These may have particularly aided the investigation of culture media, already limited by the unknown true ingredients and concentrations in RODM. An important set of investigations in association with collagen assessment would have been mechanical strength testing of the tendon analogues. It may be expected that greater

collagen presence would increase ultimate tensile strength, and testing and confirming such a hypothesis would increase support for the use of culture media driving greater fibroblast derived collagen production.

Lastly, it should be noted that although the human FDP tendon width guide measurements, calculated in *Chapter 2* through digital software, were given to 0.01mm, the resulting construct set ups were less accurate. The size of the suture anchors, the 12mm distance between sutures, and the ideal intervening width and mid-point placement of the extra mid-point pins anchors were all prepared with a millimetre slide rule. Although accuracy was enhanced by judging the scale under x3 magnification, these measurements were likely to be to the nearest quarter millimetre rather than 0.01mm. Measurements of the gel widths themselves were however still accurate to 0.01mm through the ImageJ software measuring technique.

4.6.3 Bone Anchor

4.6.3.1 Tendon Analogue Attachment

The basic tendon-bone construct was a proof of concept study that confirmed that a ceramic scaffold of bone substitute material could act as an anchor point for an *in vitro* tendon-bone model. The tendon analogue formed in the same way as a suture-suture construct and, similarly, the fibrin gel attached around all sides of the bone anchor base. Light microscopy showed continuous gel attachment around the base sides, even at the leading bone anchor edge facing the suture anchor, where in early weeks the gel was thinner due to contraction concentrating the gel peripherally.

Although not robustly tested, the tendon-bone attachment was strong enough to withstand gentle axial tension at 5 and 12 weeks of culture. However, if strength to failure was assessed, the recorded failure force would likely be a small fraction of that of *in vivo* tendon-bone attachment. This highlights the importance of formal future mechanical testing, of not only the tendon analogues (as discussed in the previous section), but also of the engineered tendon-bone interface, providing quantifiable baseline attachment strength values and future comparative data when testing new experimental variables. Viewing the interface at higher magnification was also planned but not ultimately performed due to time, and may have revealed collagenous bony ingrowth, such as is seen with Sharpey's fibres in the fibrous enthesis, providing

the attachment strength. On electron microscopy of similar fibroblast-seeded fibrin constructs, Paxton, Grover and Baar (2010) noted areas of both fibrin gel invagination into their cement anchors and reciprocal calcium phosphate crystals in the attaching fibrin gel, possibly even signifying the development of a graded soft-hard interface.

The tendon-bone attachment of the basic construct demonstrated that, even at 84 culture days, the fibrin gel attachment remained around all edges of the anchor and did not rearrange under tension to form a single attachment area at the leading edge opposite the suture. This provides a challenge in developing an anatomically relevant FDP insertion model, where a defined insertion area on a single surface of bone anchor is required. Accordingly, the gel would need to be guided onto a specific attachment point, and this key design feature is addressed in *Chapter 5*. Such a design would also reveal whether the strength of the maintained gel-bone anchor attachment, briefly tested here, was primarily a result of gel encasement around the anchor, or gel-anchor integration at the interface. Furthermore, this design challenge suggested that a custom castable bone anchor material was required, rather than a block of material onto which to guide the gel attachment. The commercially acquired Reprobone was only provided in blocks, so for the remainder of the project the focus of bone anchor development switched to brushite, readily available and castable into any shape from a paste.

4.6.3.2 Brushite Acid Washout

Brushite blocks, formed from mixing β -TCP and OA, were seen to noticeably liberate acid on addition of S-DMEM. The acid washout trials were qualitative observational studies, utilising the phenol red indicator in DMEM rather than a calibrated pH meter, so specific pH was not quantified. However, on initial addition of S-DMEM to the brushite, acidification was rapid and yellow discolouration, indicating a pH below 6.8, occurred within a few minutes with all blocks trialled. The prompt and vivid colour change suggested that the pH could in fact be well below 6.8. Such a change in environment is likely to have a significant effect on the physiology of any adhered cells and on the material properties of an attached soft tissue scaffold in a tendon-bone model, and is an important issue to mitigate in model development.

The S-DMEM washes appeared to have an immediate and beneficial effect on liberating and subsequently clearing the acid. The S-DMEM colour change was by far

greatest with the 1st wash, moderately evident with the 2nd wash, then only very subtle with the 3rd and 4th washes. The same pattern was notable with both effervescence, presumably a release of a hydrogen compound gas, and the slight sediment residue left behind after moving the blocks to a new well after each wash, indicating the lessening extent of chemical reaction between the brushite and S-DMEM. By the 5th wash, no colour change, effervescence or excess residue was apparent on gross observation, suggesting no substantial chemical reaction within that 10 minute wash period. A pH meter would have confirmed with more accuracy when the S-DMEM had stopped acidifying, however continued 6th and 7th washes remained identical to the 5th wash on gross observation.

The 1ml of wash and 10 minute timeframe seemed to be sufficient quantities for effective acid washout with the current size of brushite blocks. There were no obvious experimental differences between the different block sizes, suggesting that 10 minutes was adequate for full dispersal of the S-DMEM through the internal porous structure of even the largest blocks, accomplishing acid liberation over all the 3D structure. This was also endorsed by the lack of obvious differences between larger blocks that had fragmented, exposing a more accessible surface area to the S-DMEM, and those that had maintained original shape, and also the lack of colour difference compared to controls even after 7 hours of the 7th wash.

The results were replicated over 2 trials and without obvious differences between the triplicate blocks tested in each size. Use of a fresh S-DMEM preparation and removal of the drying period between washes in the 2nd trial appeared to have no influence. The technique of 5x10 minute S-DMEM washouts, without a requirement to dry blocks between washes, therefore appeared reliable for the current block sizes and could be utilised in the future preparation of brushite bone anchors for cell seeding and integration into the co-culture tendon-bone model.

4.6.3.3 Osteoblast Seeding

4.6.3.3.1 Methodology Rationale

The methodology for the osteoblast seeding trial had no pre-optimised protocol and was developed solely from literature review. Each step was carefully considered to best achieve the representative number of cells attached to the ceramic brushite scaffold. The first key question was choice of quantification method and assay. Many

methods to assess cell proliferation exist, most commonly haemocytometer cell counting, metabolic assays such as 3-(4,5-dimethylthiazol-2-yl)-2,5-diphenyl tetrazolium bromide (MTT), and quantification of deoxyribonucleic acid (DNA) content using fluorophores such as CyQUANT or PicoGreen. Assessment of DNA content is regarded as the most accurate method, particularly as metabolic activity greatly varies with cellular density and therefore metabolic assays are inappropriate to assess cell number in high density 2D and 3D cultures (Ng, Leong and Hutmacher, 2005; Quent *et al*, 2010). CyQUANT, measuring both DNA and RNA, was therefore selected as the assay most representative of proliferation and most familiar to the laboratory group. This specific assay choice then required planning of the appropriate cell extraction technique, handling of factors affecting fluorescence, and cell seeding number, as subsequently discussed.

Quantifying nucleic acids requires their extraction into solution by cell lysis. Cell lysis is usually accomplished by enzymes (e.g. proteinase K), chemicals (e.g. surfactants such as triton X-100) or physical means (e.g. snap freezing, sonication) (Piccinini, Sadr and Martin, 2010), often in combination. Where scaffolds are natural polymers, the scaffold itself is commonly solubilised during enzymatic digestion along with the cell contents; however with ceramic scaffolds methods are particularly variable and can also involve additional crushing (Liu *et al*, 2008), scissor maceration (Jones *et al*, 2010) and scraping cells from the scaffold (Kotobuki *et al*, 2006). CyQUANT also employs a single working solution of combined cell lysis buffer and fluorescent dye, so the nucleic acids should be in a homogenised solution rather than on a solid 3D scaffold for measurement of fluorescence. Furthermore, nucleic acids are known to electrostatically bind to ceramics, underestimating their quantification (Piccinini, Sadr and Martin, 2010). These issues prompted the use of trypsin in the present method, to first detach cells from the scaffold into a cellular suspension before addition of the combined cell lysis buffer and fluorescent dye, which theoretically was an effective method although not one obviously reported in the literature.

CyQUANT manufacturer's instructions specifically state that phenol red in culture medium may interfere with the fluorescence of the dye. Since the scaffolds were cell-seeded and cultured in S-DMEM, containing phenol red, an extra PBS wash step was included as standard in the methodology to wash away/dilute the phenol red in the sample before cell freezing. Extra samples without the PBS wash step were prepared

for comparison while performing standard curves, and were clearly observed to have a red tint in the final measurement solutions, recording considerably greater fluorescence readings compared to those without the wash step for preparations ≤ 1000 cells. A second concern regarding altered fluorescence was whether dissolved brushite would have an effect. This was another reason why trypsin was used to detach cells from the brushite scaffold before cell lysis, and also why the reaction tubes containing the trypsinised cell scaffolds were flicked/tapped to release the cells, maintaining scaffold structure, rather than the more disruptive technique of vortexing.

Seeding scaffolds with 10,000 cells was decided by scaffold shape and size, commonly used seeding numbers, CyQUANT cell detection range and prediction of cell proliferation over the 7 day time course. Cylindrical discs are a frequently used scaffold shape to assess cell adherence and proliferation, and appeared to accommodate drops of cell suspension well for even seeding (see *Section 4.4.4.5.1*). A number of studies using similarly sized scaffold discs to study cell proliferation were consulted, their scaffold volume gauged and the equivalent cell seeding number calculated for the present brushite scaffold volume. Approximate equivalent cell seeding numbers, if used for the present brushite discs, were 20,000 (Wu, Lin and Qin, 2015), 50,000 (Chen *et al*, 2007), 120,000 (Yan *et al*, 2015), 150,000 (Thibault *et al*, 2010) and 200,000 (Materna *et al*, 2008). Yet the standard CyQUANT linear cell detection range is 50 to 50,000 cells (Jones *et al*, 2001) and, although a reasonable proportion of cells were expected to fall through the scaffold and not seed, those seeded were anticipated to proliferate considerably. Seeding at 10,000 cells was therefore considered reasonable to allow a good proportion of cells to seed and then proliferate over 7 days, but not beyond the CyQUANT linear detection range of 50,000 cells.

4.6.3.3.2 Seeding

The number of cells measured after seeding was roughly equal between those attached (46%) and those unattached (54%). Although more cells were expected to attach than not, this showed that the present developed method using trypsin was indeed able to register nucleic acids from cells originally attached to the scaffold. Reasons for why approximately half of the cells remained unattached may be explained by issues with either seeding methodology, attachment time or handling technique, as discussed separately in the following paragraphs.

Cells were seeded with a static droplet seeding method, where a proportion of cells naturally falls through the porous scaffold by gravity before being able to attach. Specific steps in the experimental method aimed to mitigate against this effect. The acid washouts served as pre-soaking in culture medium to allow FBS proteins to coat the scaffold, promoting cellular adhesion and preventing cells in suspension sliding off the ceramic; non-tissue culture treated plates were used to avoid cell chemotaxis towards a preferential attachment surface on the well base; and cells were dropped slowly onto the scaffolds without forced pressure. Yet a different seeding method altogether may have increased cell attachment, for example using a dynamic procedure (e.g. centrifugal seeding), which can result in seeding densities of 65-90% (Tan, Ren and Kuijer, 2012).

The 5 hour incubation period between cell seeding and collection for assaying may not have been long enough for full cell attachment, so that a proportion of cells that would have later attached were rinsed away and counted as unattached. Standard practice in our laboratory group is a minimum of 4 hours for cell attachment to cell culture-treated plastic, and the CyQUANT manufacturer's instructions suggest 0.5-8 hours depending on cell type and other experimental parameters. Brushite was not expected to promote cell attachment as well as cell culture treated plastic, so an increased attachment time was employed. However similar studies seeding on ceramic based/incorporated scaffolds appeared to in fact favour a shorter attachment time of 2-3 hours (Du, Furukawa and Ushida, 2008; Materna *et al*, 2008; Jones *et al*, 2010; Chen *et al*, 2015; Yan *et al*, 2015). 5 hours in the present study should have therefore been adequate, whilst still short enough to avoid the risk of cell proliferation.

The methodology demanded lifting the scaffold out of its seeding well with forceps for PBS rinsing to remove unattached cells and transfer to a reaction tube for trypsinisation. Mechanical disruption from the forceps may have dislodged attached cells which were then read as unattached, although this is a more minor explanatory point due to the overall limited surface area of the gripping forceps.

Despite 46% of recorded cells attaching, the more pertinent issue is that this represents only 13% of the originally seeded cells. This was particularly unexpected and, although a single cause is not clear, may be explained by a combination of different factors. Beyond procedural limitations, such as limiting the rinses of scaffolds

and wells for cell collection to the reaction tube volume of 1.5ml, the foremost factors for apparent cell loss could be material interaction issues, low cell numbers, and nucleic acid degradation, as subsequently discussed.

The main issue may be the known reversible electrochemical bond that occurs between ceramic material and nucleic acids, often overlooked in cell proliferation studies. This effect underestimates DNA retrieval by 90% at low DNA concentrations (low cell number), and even at high DNA stock concentrations (320mg/ml) there is still 10% underestimation (Piccinini, Sadr and Martin, 2010). Since cell numbers used in the current study were relatively low (further discussed later in this section), DNA retrieval and derived cell number conversions are likely to have been considerably lowered. This phenomenon is reversible with a phosphate buffer (Piccinini, Sadr and Martin, 2010), but whether or not the CyQUANT cell lysis buffer contains phosphate is unknown. If it does, this explanation would be ruled out, however future cell proliferation studies on ceramics should ensure phosphate is included in cell lysis solutions. A further material interaction issue may be that 10 minute exposure to trypsin may not have been enough time for effective cell detachment from the 3D scaffold. TrypLE Express dissociates dRObs from cell culture-treated plastic in 3-5 minutes, but even over an extended 10 minutes may not have diffused well enough through a 3D scaffold to fully dissociate centrally located cells, which would then be lost when the scaffold is discarded. Centrally located cells may also have evaded washout into the trypsinised solution, due to their protected position, even if they were fully detached. Furthermore, enzymes in trypsin are most active at pH 8 (Gilbert, Sellaro and Badylak, 2006) so any residual acid on the scaffold surface may have reduced its dissociative activity.

Seeding 10,000 cells was relatively low compared to other similar studies (see *Section 4.6.3.3.1*), but was primarily based on the CyQUANT linear detection range of 50 to 50,000 cells with 1x dye concentration. Yet when performing standard curves of cell number up to 50,000 cells, 1x dye concentration did not produce a linear fluorescence-cell number relationship, whereas 5x dye concentration did (*Appendix 4*) and so was used for experiments. However, since the trial produced unexpectedly low cell numbers, such as around 1000 recorded here for seeding, at these quantities both dye concentrations produced a linear fluorescence-cell number relationship, but the 5x concentration represented around 250 less cells than the 1x dye concentration

for the same fluorescence value (*Appendix 4a*). The issue of low cell numbers therefore not only underestimated nucleic acid retrieval due to the ceramic material reaction, but also underestimated cell number based on the fluorescence of the nucleic acid that was retrieved due to use of the 5x concentration of dye.

Serum contains nucleases with the ability to degrade nucleic acids (von Köckritz-Blickwede, Chow and Nizet, 2009; Hahn *et al*, 2014; Bruno and Sivils, 2016), therefore precluding their fluorophore binding and fluorescence measurement. FBS was constituent in S-DMEM used throughout cell seeding and culture, but nucleic acids were only deliberately released during addition of the CyQUANT cell lysis buffer/dye solution to the defrosted cell pellet. The cell pellet was prepared during micro-centrifuge steps and removal of S-DMEM supernatant, also including a further PBS wash step and supernatant removal, so even where $\approx 25\mu\text{l}$ of supernatant remained with the pellet, contact between nucleic acids and FBS nucleases would be minimal. However, cell death during seeding and/or cell culture may have led to early cell lysis and exposure of nucleic acids to S-DMEM over longer time periods, for example 5 hours during cell seeding or indeed over 7 days for the final assay time point. Cell seeding may have been the occasion of greatest cell death, since cells were seeded in only $20\mu\text{l}$ of S-DMEM, and the subsequent 5 hour incubation at 37°C may have evaporated enough medium to leave some cells unviable. From this point forward serum nucleases could then start degrading any released nucleic acids and cell number measurements would decrease.

4.6.3.3 Proliferation

dROBs were shown to proliferate on the brushite scaffold by approximately 3 fold over a 7 day period, with the majority of the increase occurring between day 2 and 7. A similar increasing proliferation pattern was exhibited on the cell culture treated plastic, demonstrating that brushite was likewise a material that could support cell adherence and proliferation. The much greater cell numbers and significant differences across time points for the treated culture plastic was due to an increased seeding number, a material optimised for adherence, and very similar replicates. The measured cell number seeded on the treated culture plastic of 8244, although similar to the 10,000 intended for seeding, was an almost 20% reduction and may indicate that under-seeding was another reason for unexpectedly low cell numbers across the experiment. The cells' preference for the treated culture plastic was anticipated and evident in their

exponential increase and narrow standard error ranges, suggesting a similarity amongst replicates of healthy proliferation. This was in contrast to the wider error ranges for brushite, where cell behaviour thus appeared more variable, however the material still supported an increasing cell population overall.

4.6.3.3.4 Integration into Co-Culture Construct

In the development of the bone anchor component for the tendon-bone model, brushite was a material demonstrated to allow rapid casting into any shape and to support dROb proliferation. Furthermore, as a bone substitute it is osteoconductive, of relatively high compressive strength, and can be biologically resorbed (Paxton *et al*, 2010). It was therefore taken forward into the final designs for 3D co-culture with the fibroblast-seeded fibrin tendon analogue. The present data showed that seeding at 10,000 cells on a brushite disc of 2mm height and 4.6mm diameter, after removal of acid with 5x S-DMEM washes, produced proliferating dRObs by day 7. These successful criteria for cell number:scaffold volume ratio, acid washout, and time period for proliferation would thus also provide the principles for setting up the osteoblast-seeded bone anchor before integration into co-culture with the fibroblast-seeded fibrin.

4.6.3.3.5 Limitations

Although the methodology was carefully considered, the osteoblast seeding trial results were only based on triplicate technical repeats performed on a single occasion, due to time constraints. The trial should therefore be viewed more as a preliminary, rather than definitive, experiment and although reasonable results were achieved, their interpretation should be cautioned.

The study lacks power due to the low number of replicates. This is a principle reason why cell proliferation on brushite was non-significant, despite a 3 fold increase between day 0 and day 7. Although cell behaviour on brushite was likely quite variable, more so than on treated culture plastic for example, further repeats, both technical and biological with dRObs from a different rat, would have provided a more definitive answer to whether the increase in cell number was significant. dRObs were employed in their 10th passage, and cell senescence may have affected their brushite adherence, proliferation or viability, despite both young and old cell cultures having been shown to produce near identical standard curves with CyQUANT when grown on plastic

(Jones *et al*, 2001). Even so, ideally younger cells would have also been trialled, and if no differences were shown between young and old cells, result could have been combined for increased study power.

As a newly developed methodology, various steps would ideally be optimised before running definitive experiments. Although the theoretical steps were deliberately devised through literature review, actual performance of the steps exposed unforeseen technical difficulties or additional potential variables. Many of the sources of unexpected results or variability have been previously discussed in *Section 4.6.3.3.2*, and an optimised method would address these issues. For example, trials of greater cell seeding number, a cell lysis buffer containing phosphate, greater volume of scaffold washes for cell collection, an active seeding technique and reduced incubation time for seeding may identify areas that could increase the validity and reliability of results. The use of trypsin to detach cells from ceramic was particularly unfamiliar, in both technique and timing, along with a possible effect on fluorescence readings from variably fragmented scaffolds through flicking/tapping the reaction tubes to release the trypsinised cells. Future trials might focus on a technique to fully solubilise the scaffold whilst also lysing the cells, and then separately perform the nucleic acid dye binding step.

Once more familiarity is gained with the technique, greater exploration of key issues in the development of a cell seeded bone anchor could be addressed. Within the remit of this project, different scaffold materials and cells could be investigated, for example fibroblast and osteoblast proliferation and MSC differentiation on different ceramics, particularly comparing the microporous structure of brushite with macroporous materials more similar to trabecular bone. Further beyond, developing and assessing a cell-embedded bone anchor material to match the cell-embedded fibrin of the tendon analogue, rather than having cells adhere in 2D onto the surfaces of a porous structure, would progress towards a truly 3D co-culture model.

4.7 Summary of Findings

RTFs and dRObs were characterised as the most suitable single species fibroblast and osteoblast cell choices for use in the tendon-bone co-culture model, with 50:50 medium optimum to maintain dROb ECM mineralising ability whilst retaining RTF

phenotype. Fibroblast-seeded fibrin gel formed a tendon analogue by cell-mediated contraction around suture anchors, establishing an overall morphology in approximately 7 days as directed by suture size and orientation, with subsequent maturation and collagen deposition. Fibrin gel contraction increased with greater cell number and addition of AA and P to S-DMEM, and decreased with greater gel volume, although with the overriding benefit of a more robust tendon analogue. Brushite cement provided a castable bone substitute scaffold, but required 5x10 minute rinses with S-DMEM to washout its constituent acid. dRObs attached onto brushite with a static droplet seeding efficiency of 13%, proliferating over 7 days.

CHAPTER 5

INTEGRATED ANATOMICAL MODEL DESIGN AND TENDON-BONE CULTURES

5.1 Chapter Overview

This chapter combines data from *Chapters 2, 3 and 4*, culminating in the production of the 3-dimensional (3D) tissue engineered tendon-bone model. A bespoke anatomical culture zone of various clinically relevant sizes is designed, molded and utilised *in vitro* to guide tendon analogue culture and bone anchor attachment. The development and established morphology of tendon fibroblast monoculture constructs and added bone osteoblast co-culture constructs are qualitatively assessed as the completion of the project work.

5.2 Introduction

Chapter 2 investigated the morphometrics of the human distal flexor digitorum profundus (FDP) tendon, distal phalanx (DP) and the FDP insertion footprint, establishing the optimal dimensions to tissue engineer an anatomically matched tendon analogue inserting onto a bone anchor. Clinical relevance was enhanced by dividing the dimensions into 3 main size groupings, 'large', 'medium' and 'small', as well as an overall 'universal' average size, resulting in the model design guide (**Table 2.17, Chapter 2**). *Chapter 3* examined the angle of bony attachment of human FDP tendon collagen fibres, finding an average of 30°. *Chapter 4* explored *in vitro* culture components, suggesting that a tendon analogue of double volume fibrin gel seeded with double cell number of rat tendon fibroblasts (RTFs), attaching to a brushite bone anchor seeded with differentiated rat osteoblasts (dRObs), cultured in 50:50 medium, would deliver the optimal tendon-bone construct. This chapter references and integrates these previous results in the design of a culture zone to direct the anatomically and clinically relevant dimensions and attachment angle, and subsequently progress tendon-bone monoculture trials towards an ultimate co-culture construct.

The anatomical modelling of interfacial tissue engineering constructs is lacking and not explored in the literature, requiring a novel design technique. Although casting of individual components, such as bone scaffolds, is common, using this approach to derive a whole multi-tissue stratified design is scarce. The silicone impression system employed in this chapter develops the standard use of Sylgard as a culture well

coating, which creates a hydrophobic, smooth and transparent culture base suitable for fibrin hydrogel contraction, pinning of suture anchors and examination by microscopy, by exploiting its potential for molding in 3D. Just as 3D printed casting trays can reverse mold multiple sizes and shapes of bone anchors using silicone (Paxton *et al*, 2010), a bespoke culture zone could be molded around specially designed 3D prints to any size and shape using Sylgard. In this way, the 2 key design considerations of generating a single surface bone anchor attachment and a 30° interface between tendon analogue and bone anchor could be realised.

The chapter completes the project by producing tendon-bone co-culture constructs using the anatomical model design. 3 sizes of constructs are produced for the final co-cultures to demonstrate the future potential to apply the basic model system design with clinical utility as a graft for injury across any finger or gender. The development of preparatory monocultures, with only the tendon analogue component seeded with cells, and final co-cultures, with both tendon analogue and bone anchor components seeded, is qualitatively assessed through serial overview photography and observation.

5.3 Aim and Objectives

The aim of this chapter was to integrate the morphometric and *in vitro* culture findings from previous chapters into the production of an anatomically and clinically relevant FDP-DP tendon-bone tissue engineered model.

The objectives were to:

- 1) Design and create a bespoke anatomical culture zone;
- 2) Employ the culture zone to achieve a tendon-bone co-culture construct.

5.4 Materials and Methods

5.4.1 Model Design and Production

The model design elements were based on the specific dimensions in **Table 2.17** (*Chapter 2*), aiming to create a single surface bone anchor attachment and tendon-bone interface of 30°. Modelling of size and shape relied upon carefully devised 3D printed molds and surrounding silicone impressions, either in Sylgard 184 silicone elastomer (Dow Corning, Wiesbaden, Germany) or Kemsil silicone (Associated Dental Products, Swindon, UK). 3D prints were designed in Tinkercad software (Autodesk, San Rafael, USA), printed in Acrylonitrile Butadiene Styrene (ABS) through a ThermoJet solid object printer (3D Systems, Valencia, USA), at facilities at Edinburgh College of Art, The University of Edinburgh.

5.4.1.1 Bone Anchor

Brushite was cast into 3D trapezoidal bone anchor blocks by a process of reverse molding (**Figure 5.1**), described in *Section 4.4.4.1.3* (*Chapter 4*). The 3D printed casting tray consisted of 6 identical shapes, matching the dimensions of the resultant bone anchors. Dimensions of bone anchor height, base width and apex width, and therefore the shapes in the casting tray, were determined by the specific size guide of **Table 2.17** (*Chapter 2*), with a common depth of 2.00mm for all sizes.

5.4.1.2 Culture Zone

5.4.1.2.1 'Fish Shape' Mold

A 'fish shape' 3D mold design was established as the optimum shape to create the bespoke culture zone in surrounding Sylgard in a 35mm diameter culture well. A 'tail' section, varying in size depending on the model size, allowed presentation of the bone anchor from below, at a fixed 30° angle, to a horizontal culture surface for tendon analogue development provided by the 'body', common to all models (**Figure 5.2**).

5.4.1.2.2 Lattice Frame Mold

For ease of simultaneous preparation of all wells in a 6-well plate, 6 fish shape designs were incorporated into a 3D printed lattice suspension frame (**Figure 5.3**). The frame

was able to sit unsupported on a lid-less 6-well plate, suspending each fish shape centrally within each well, whilst providing strength to the overall mold structure.

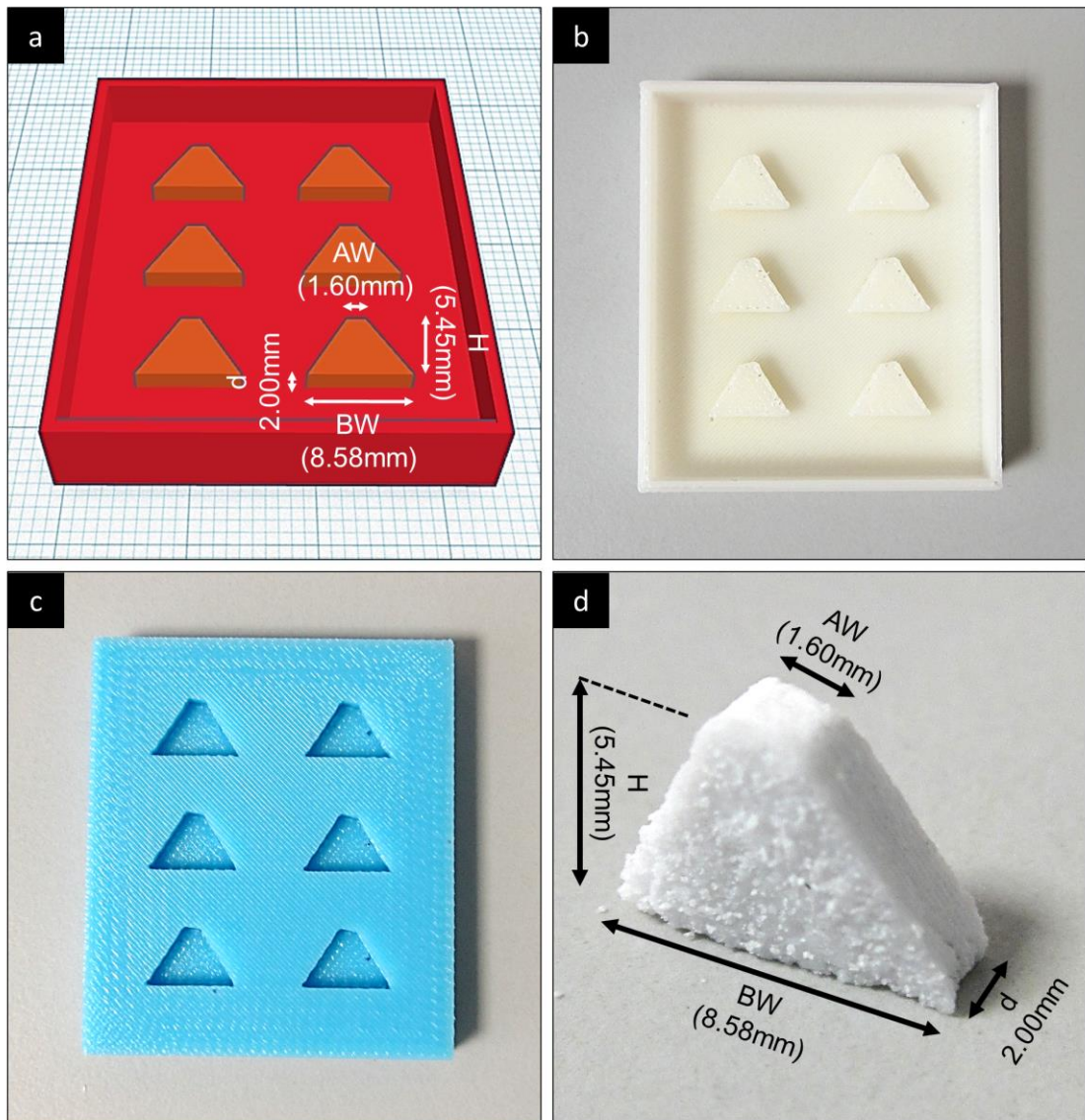


Figure 5.1 | Bone Anchor Production

Manufacture of an anatomical brushite bone anchor block by reverse molding. The ‘universal’ size is shown; specific ‘universal’ size dimensions are in parentheses, common dimensions are not. **a)** Tinkercad software design of casting tray for 6 bone anchors, superior oblique view; entire tray dimensions – length 40mm, width 35mm, depth 8mm. The projecting trapezoidal shapes represent the dimensions of the desired bone anchor. For ‘large’, ‘medium’ and ‘small’ bone anchor (model) sizes, the trapezoidal shape designs are modified: ‘large’ – height (H) 6.36mm, base width (BW) 9.30mm, apex width (AW) 1.66mm; ‘medium’ – H 5.05mm, BW 8.30mm, AW 1.56mm; ‘small’ – H 4.33mm, BW 7.57mm, AW 1.65mm. Depth (d) remains 2.00mm for all sizes, as do the whole tray dimensions. **b)** ABS 3D print of (a), superior view. **c)** Kemsil silicone mold from (b), superior view. **d)** Cast brushite bone anchor block formed from a single trapezoidal impression from (c), superior-lateral oblique view. H , BW , AW and d are the same dimensions as the projecting trapezoidal shapes in the Tinkercad tray design in (a). Note the roughened surfaces of the brushite block.

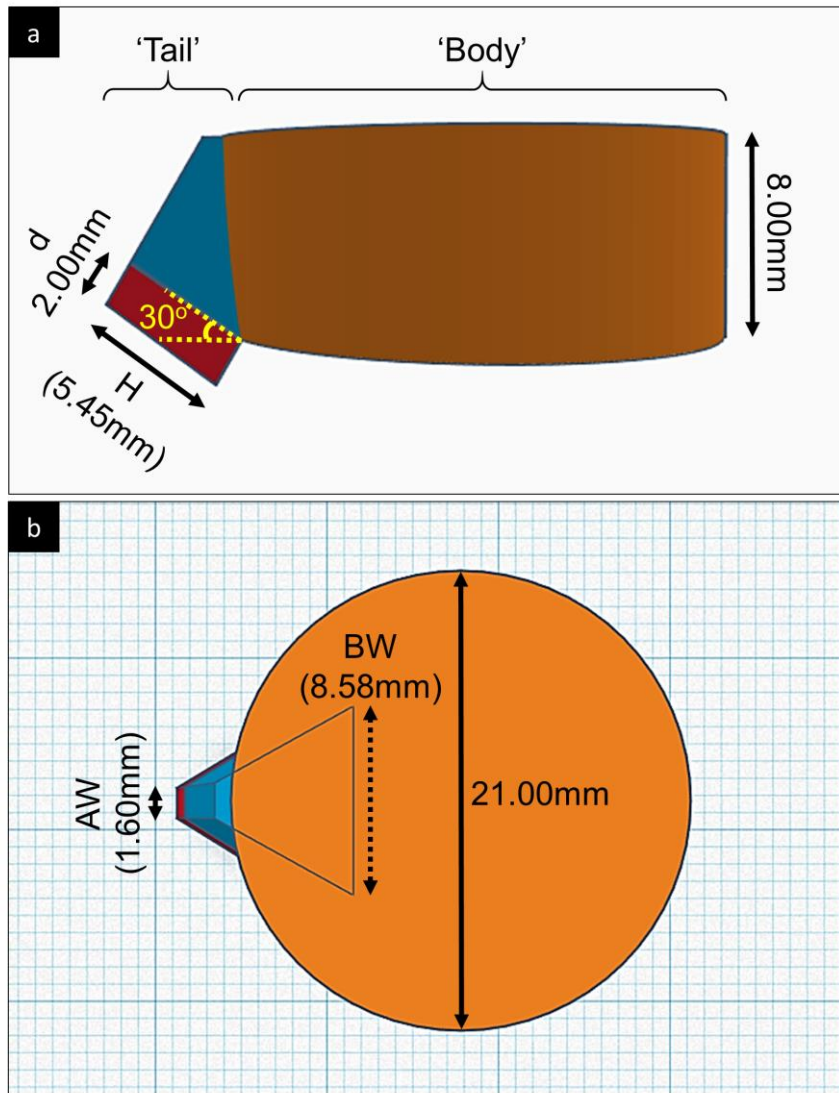


Figure 5.2 | 'Fish Shape' Culture Zone Mold Design

Tinkercad design specifications for the 'fish shape' mold, to create an impression in Sylgard and direct attachment of the developing tendon analogue onto a single surface of the bone anchor at 30°. The 'universal' size is depicted; specific 'universal' dimensions are in parentheses, common dimensions are not. **a)** Lateral view of component elements of design (superior and inferior surfaces appear rounded in 3D). The 'tail', composed of *blue* and *red* blocks, provides space for insertion and housing, respectively, of the bone anchor. The 'body', composed of a cylindrical *orange* block, provides space for the developing tendon analogue. The *red* block mimics the trapezoidal bone anchor size and shape, set at 30° to the horizontal inferior surface of the *orange* block, positioned at the point where its 2 forward-facing bottom corners both intersect the curved edge of the *orange* block. The height (H) of the *red* block (bone anchor) is specific to the size of model required, whilst depth (d) is common to all sizes. The *blue* block continues the 3D shape of the *red* block to the level of the superior surface of the *orange* block to create the space necessary to insert the bone anchor. The common 8.00mm depth of the *orange* block was designed large enough to contain a volume of contracting fibrin gel and culture medium without extending above the height of a standard 35mm diameter well. **b)** Superior view of component elements. The common 21.00mm diameter of the *orange* block ("body") provides the new sizeable culture space for the tendon analogue, fitting comfortably within a standard 35mm diameter well, whilst allowing enough space for the additional 'tail' components of all specific model size. The apex width (AW) and superimposed base width (BW) of the *red/blue* blocks are determined by the specific model size required.

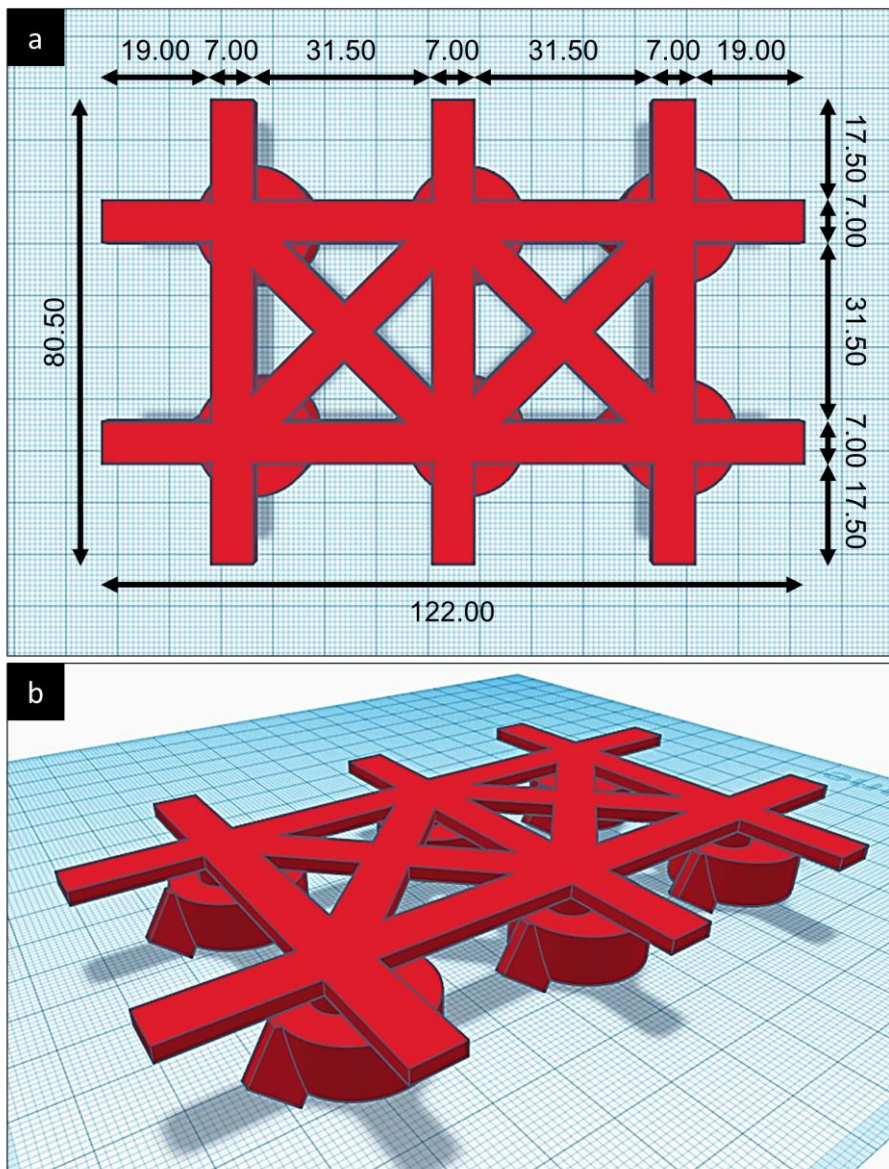


Figure 5.3 | Lattice Mold Design

Superior **(a)** and superior-lateral oblique **(b)** view of Tinkercad design for the lattice mold. Lattice frame dimensions were calculated so as to allow 6 'fish shapes' to each be held centrally within the wells of a standard 6-well plate, whatever the model size (fish shape) required. Fish shapes ('universal' size shown) are suspended centrally by 7.00mm (diameter) x 4.00mm (depth) cylinders at the intersection of the horizontal and vertical bars of the lattice. Lattice frame depth 2.00mm. All units in millimetres.

5.4.1.2.3 Preparation and Set Up

See **Figure 5.4**. The lattice frame mold was placed on a 6-well plate (**Figure 5.4a**), with the fish shapes located in the wells away from the well rim (**Figure 5.4b**). Sylgard was filled around the fish shapes to the level of the superior surface of the 'body' (**Figure 5.4b**), requiring approximately 9ml for each well, and cured at either room temperature for a minimum of 7 days or 50°C in an oven overnight. For positional security the frame was temporarily fixed to the plate with adhesive tape during Sylgard filling and curing. The entire mold was then removed to leave the impression (**Figure 5.4c**), requiring gentle freeing of each fish shape mold from the Sylgard with a stainless steel micro spatula followed by removal of the frame with pliers.

The suture anchor was prepared by cutting number 1 silk suture (Ethicon, Bridgewater, USA) with sharp dissecting scissors (Fine Science Tools, Cambridge, UK) to the same width as the ideal tendon width of a particular model size in the model design guide based on human data in **Table 2.17** (*Chapter 2*). The suture was secured flat onto the Sylgard with stainless steel insect pins (Fine Science Tools) at the suture ends, vertical, parallel and central to the point where the fish shape 'body' impression becomes the 'tail' (i.e. the nearest bone anchor edge when in position), at a 12mm distance (**Figure 5.4d-f**). Suture and construct distances were judged under guidance of a millimetre slide rule and x3 loupe magnification (UKloupes, Bristol, UK). Plates and lids were then sterilised with 70% industrial methylated spirit (IMS) in the laminar flow cabinet as described in *Section 4.4.3.2.1* (*Chapter 4*), taking care that all areas of the new internal culture zone were sterilised. Bone anchors were separately sterilised as per *Section 4.4.4.1.4* (*Chapter 4*). A sterile bone anchor, seeded with osteoblasts for co-culture or acellular for monoculture of tendon analogue fibroblasts only, was positioned into the base of the 'tail' impression of the culture zone (**Figure 5.4d-f**) with a stainless steel micro spatula with angled end under x3 loupe magnification in the laminar flow cabinet.

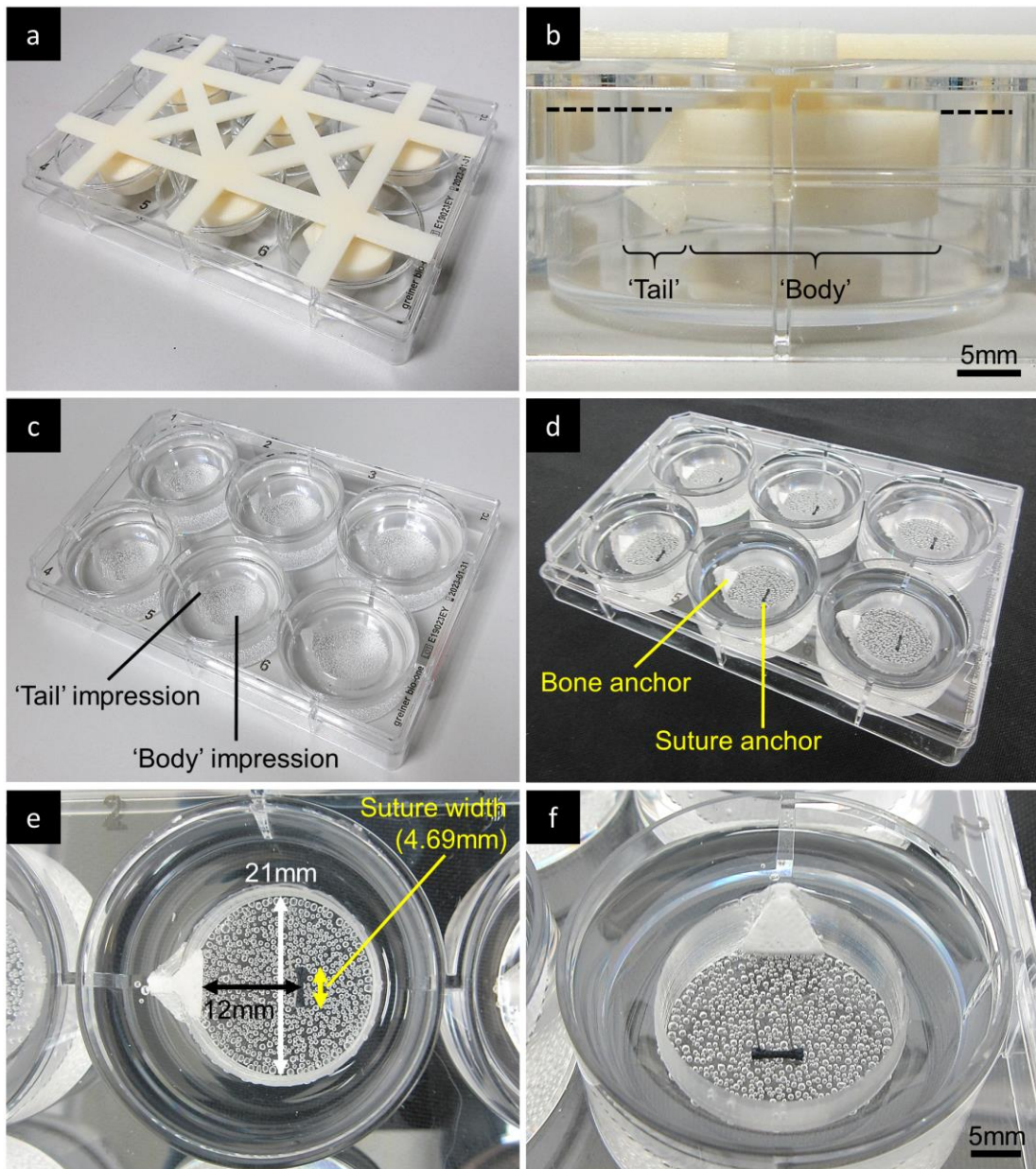


Figure 5.4 | Culture Zone Production and Set Up

a) Lattice mold in place on a standard lid-less 35mm well diameter 6-well plate. ‘Universal’ size shown and subsequently followed. **b)** Magnified side view of a single 35mm well of the 6-well plate, showing the ‘fish shape’ suspended centrally in the well, above the well base. Sylgard is then filled around the fish shape up to the *broken line*, level with the superior surface of the fish shape. **c)** Fish shape impressions produced in the cured Sylgard after removal of the lattice mold, creating the bespoke internal culture zones. **d)** Sterilised wells set up with bone anchors and pinned sutures in position. **e)** Plan view of a single 35mm well, displaying the newly created internal culture zone with 21mm diameter ‘body’. The bone anchor, pre-seeded with osteoblasts for co-culture, or acellular for monoculture, is located at the base of the ‘tail’ of the culture zone. The suture is positioned 12mm from the nearest edge of the bone anchor, secured with vertical pins onto the Sylgard. Suture width is determined by the size of the model, shown here as 4.69mm for the ‘universal’ size: ‘large’ – 5.38mm; ‘medium’ – 4.39mm; ‘small’ – 3.68mm. Air bubbles in the Sylgard formed beneath the mold during curing are evident, however these lie just below the surface of the internal culture zone base. The culture zone base is flat but roughened by the texture of the inferior surface of the 3D printed material, whilst the culture zone sides are smooth. **f)** Superior oblique view of (e), showing the full face of the bone anchor, ready for addition of the fibrin and fibroblasts.

5.4.2 Construct Cultures

5.4.2.1 Culture Methods

Cell and tissue culture methods, including sterility, cell preparation, construct culture and photography, were conducted as described in *Section 4.4.1 (Chapter 4)*, unless stated. Preparation, use and exchange of supplemented Dulbecco's modified eagles medium (S-DMEM), S-DMEM supplemented with 250µM ascorbic acid (AA) and 50µM proline (P) (molarities unchanged throughout), and rat osteoblast differentiation medium (RODM) in 50%:50% combination with S-DMEM (50:50 medium) was as per *Section 4.4.1.3 (Chapter 4)*, with medium exchanges of 1ml volume. As standard, cells were seeded in S-DMEM and exchanged to a particular medium for continued culture at the first medium change on day 3. The source of RTFs and dROBs is described in *Section 4.4.2 (Chapter 4)*.

All tendon-bone construct cultures were performed in the bespoke 3D culture zones of each well of a 6-well plate, using brushite bone anchors and suture anchors, prepared and set-up as described in *Section 5.4.1*. Fibrin gel preparation, fibroblast seeding and continued culture was performed as per basic suture-suture constructs (*Section 4.4.3.2.1, Chapter 4*), unless stated. Particular care was taken to ensure formation of fibrin over the bone anchor, with directed agitation of the thrombin mix and delivery of the fibrinogen into the 'tail' of the culture zone impression. At the completion of the culture period, selected constructs were photographed with gentle axial tension on the tendon analogue with forceps, and also after freeing from the Sylgard with a disposable scalpel (Swann-Morton, Sheffield, UK).

5.4.2.2 Monoculture Constructs

Initial trials of the tendon-bone model design were monocultures, consisting of fibroblast-seeded fibrin tendon analogue cultures with acellular bone anchors. All monocultures continued for 14 days with gross overview photography every 2-3 days.

5.4.2.2.1 Without Brushite Acid Washout

The 1st monoculture constructs were set up in the 'universal' size in 6 wells of the same 6-well plate. Bone anchors were sterile but did not undergo preceding acid washout. Standard (single) volume fibrin gel (500µl of thrombin mix with 200µl of fibrinogen) was polymerised at 37°C for 2 hours, since after the standard 1 hour the

thrombin appeared semi-solid. P₅ RTFs (from the 1st RTF isolation) were seeded on the fibrin with standard cell number (100,000 cells in 1ml S-DMEM per well) and the constructs then continually cultured in S-DMEM ('S-DMEM' culture).

A 2nd monoculture trial, also using the 'universal' size, was performed to investigate a number of the promising culture variables tested in the 'anatomical suture experiments' in *Section 4.4.3.6 (Chapter 4)*, namely '+AA+P' and 'double gel/double cells/+AA+P'. In the same 6-well plate, 3 constructs were set up with standard volume fibrin gel and standard cell number, and 3 constructs with double volume fibrin gel (1000µl thrombin mix with 400µl fibrinogen) and double cell number (200,000 cells per well), cultured in S-DMEM supplemented with AA and P ('+AA+P' and 'double gel/double cells/+AA+P' cultures, respectively). For seeding, P₅ RTFs (from the 2nd RTF isolation) were prepared in a cell concentration of 200,000 cells/ml S-DMEM, adding 0.5ml/well to '+AA+P' cultures (with additional 0.5ml/well S-DMEM top up) and 1ml/well to 'double gel/double cells/+AA+P' cultures. This technique was followed for constructs of both standard and double cell number in the remaining constructs of the chapter.

5.4.2.2.2 With Brushite Acid Washout

A 3rd monoculture trial was conducted with additional acid washout of the brushite bone anchors before their positioning into the 'tail' of the culture zone. 'Medium' size bone anchors and culture models were used, with further investigation of culture variables from the 'anatomical suture experiments' (*Section 4.4.3.6, Chapter 4*).

12 sterile 'medium' bone anchors underwent acid washout with 5 washes of S-DMEM as per *Section 4.4.4.5.2 (Chapter 4)*, then were inset into all 12 wells of 2x 6-well plates, with approximately 1 hour drying time at room temperature between the last wash and formation of overlying fibrin. Each plate was set up with duplicates of 3 culture variables, using P₅ RTFs (1st isolation), with each plate cultured in either S-DMEM or S-DMEM supplemented with AA and P. In the S-DMEM plate, duplicates of standard volume gel and standard cell number ('S-DMEM' cultures), double volume gel and standard cell number ('double gel') and double volume gel and double cell number ('double gel/double cells') were set up. In the plate supplemented with AA and P, the same 3 sets of duplicates were set up, respectively forming '+AA+P', 'double gel/+AA+P' and 'double gel/double cells/+AA+P' cultures.

5.4.2.3 Co-Culture Constructs

Tendon-bone co-culture constructs were prepared similarly to the monocultures, including the brushite acid washout step. However, co-culture constructs investigated all 3 of the 'large', 'medium' and 'small' model sizes, used RTFs isolated from all 3 rat isolations (biological repeats), extended culture time to 28 days, and included the key addition of osteoblasts seeded on the bone anchor.

5.4.2.3.1 Osteoblast Bone Anchor Seeding

Osteoblast seeding on 'large', 'medium' and 'small' brushite bone anchors was based on the successful seeding of 10,000 dROBs in 20µl S-DMEM onto brushite discs, as per *Section 4.4.4.5.3 (Chapter 4)*, proliferating over 7 days. Since the trapezoidal bone anchor scaffolds were different volumes to the discs, and to each other, scaling was required to maintain the ratio of both cell density and volume of cell seeding solution on the scaffold (**Table 5.1**).

Table 5.1 | Bone Anchor Scaling for Osteoblast Seeding

Calculations to maintain the scaffold cell seeding density and cell solution volume from discs to trapezoidal bone anchors. *2D area* for discs was calculated by πr^2 , where disc diameter was 4.6mm. *2D area* for trapezoidal bone anchors was calculated using the dimensions of the model design guide in **Table 2.17 (Chapter 2)**, splitting the trapezoid into component elements of a central rectangle and 2 outer triangles. *3D volume* was calculated by *2D area x depth*.

Bone Anchor Scaling				
	Disc	Bone Anchors		
		Large	Medium	Small
Shape				
2D Area (mm²)	16.62	34.85	24.90	19.96
Depth (mm)	2.00	2.00	2.00	2.00
3D Volume (mm³)	33.24	69.71	49.79	39.92
Scale	x1.00	x2.10	x1.50	x1.20
Seeding				
Cells	10,000	21,000	15,000	12,000
Solution Volume (µl)	20	42	30	24

After bone anchor production and sterilisation, 6 anchors each of 'large', 'medium' and 'small' size underwent the brushite acid washout steps as per *Section 4.4.4.5.2*

(Chapter 4). S-DMEM colour changes surrounding the bone anchors were compared to a control of anchor-free S-DMEM, and despite the increased volume of the trapezoidal bone anchors compared to discs, 5x 10minute S-DMEM washes remained sufficient to prevent further S-DMEM colour change. Following the S-DMEM washes, the bone anchors were air dried for 1 hour at room temperature before cell seeding. A 500,000 cell/ml seeding solution of P₇ dRObs in S-DMEM was prepared and seeded onto each bone anchor in flat bottomed, non-tissue culture treated 24-well plates as per Section 4.4.4.5.3 (Chapter 4), pipetting the required volume of cell seeding solution onto each 'large' (21,000 cells), 'medium' (15,000 cells) and 'small' (12,000 cells) bone anchor as per **Table 5.1**. After 5 hours of incubation at 37°C, 5% CO₂ for cell attachment, the bone anchors were moved into fresh wells of the same plates, 1ml S-DMEM added (submerging the anchors), and then returned to 37°C, 5% CO₂ incubation for continued culture. Osteoblast-seeded bone anchors were cultured for 7 days, with exchange of 1ml S-DMEM every 2-3 days.

5.4.2.3.2 Co-Culture Integration

After 7 days of osteoblast culture on the bone anchors, the S-DMEM was aspirated and the 6 bone anchors of each 'large', 'medium' and 'small' size were inset into the 'tails' of 6 culture zones in a 6-well plate each of reciprocal 'large', 'medium' and 'small' size (**Figure 5.4d-f**). The tendon analogue component of all wells was set up with double volume fibrin gel and double cell number, with 2 groups of triplicates in each plate (model) size cultured in either S-DMEM supplemented with AA and P ('double gel/double cells/+AA+P') or 50:50 medium ('double gel/double cells/50:50'). Each construct of a triplicate was a biological replicate of P₅ RTFs from each of the 3 rat isolations. Cultures were maintained for 28 days with overview photography every 3-7 days.

5.5 Results

5.5.1 Culture Zone

Sylgard cured as intended around the 'fish shape' mold to create a transparent, 3D culture zone within a 35mm diameter well. The lattice frame allowed simultaneous 6-well preparation and adequately positioned fish shapes in all wells without contact

with interior well surfaces. Sylgard molded closely to the fish shape, and the 'tail' impression provided a tight fit for the angled bone anchor and ensured single surface attachment by the tendon analogue onto the 'presenting' surface, with no fibrin gel present in the tail area on or around unintended bone anchor surfaces. The 21mm diameter 'body' impression provided enough space for tendon analogue formation and maturation between the bone and suture anchors, and the freshly polymerised fibrin gel on day 0 appeared to cover the entire presenting surface of the bone anchor, as was essential. However, the markedly reduced volume, compared to a 35mm diameter well, necessitated media exchanges of 1ml and cell concentrations for seeding prepared at 200,000 cells/ml S-DMEM, rather than the standard 2ml media exchanges and 100,000 cells/ml for seeding, as only just over 1ml of volume remained after the fibrin gel had been added.

Air bubbles were trapped under the surface of the fish shape mold during Sylgard curing (**Figure 5.4e**), usually <1mm diameter but occasionally coalesced into larger bubbles of >5mm. Although these lay below the flat culture surface and did not cause undulation, freeing of the fish shape molds from the Sylgard did occasionally penetrate into larger bubbles through the thin flat culture surface, rendering the well unsuitable for culture.

ABS printed molds were faithful to the Tinkercad designs, but lacked perfect finish on edges and surfaces. Resolution was not refined to the 0.01mm accuracy of designs, but this did not drastically affect the Sylgard impression and the key feature of single surface bone anchor attachment was retained. The upper and lower surfaces of the ABS prints, although not side surfaces, were slightly textured, translating to a fine notching on the horizontal culture zone surface. This did not seem to grossly impinge on fibrin gel contraction, not requiring any procedures to release the gel from the under surface, but it was notably less smooth than the unroughened side wall of the well.

5.5.2 Construct Cultures

5.5.2.1 Monoculture Constructs

5.5.2.1.1 Without Brushite Acid Washout

The main feature of the initial 2 monoculture trials was yellowing of the culture medium, signifying acidification due to the colorimetric phenol red pH indicator within the S-DMEM.

In the 1st monoculture trial (**Figure 5.5**), culturing standard volume gel and standard cell number constructs in S-DMEM, the thrombin mix over the brushite bone anchor began to turn markedly yellow soon after its addition into the culture zone. After an hour of fibrin polymerisation, all fibrin gel constituents were yellowed to some degree, most heavily so, and the fibrin correspondingly appeared semi-solid. A further hour of 37°C incubation to encourage polymerisation resulted in an increase in, but not complete, solidification. Furthermore, after fibrin polymerisation, a curved area of thin, translucent gel was present, like a 'halo', at the bone anchor interface, suggesting gel attachment was poor or even absent (**Figure 5.5a**). Over the ensuing culture period, the majority of the gel contracted as expected, forming the general morphology of the tendon analogue by day 3-5, with minor continued contraction over the following days until the trial conclusion at 14 days. The tendon analogue extended in roughly rectangular morphology between suture anchor and bone anchor, but only attached to the bone anchor by 2 slips either side of a curved absence of gel (**Figure 5.5b** and **5.5c**). The tendon analogue was thin, and, once removed from the culture zone without tension on the suture anchor, contracted to a vastly reduced width (**Figure 5.5d**). Notably, the thrombin mix and culture medium of 1 of the 6 tendon analogues was much less yellow than all others at day 0 and beyond, and this tendon analogue never developed the halo of thin gel at the bone interface (**Figure 5.5b**).

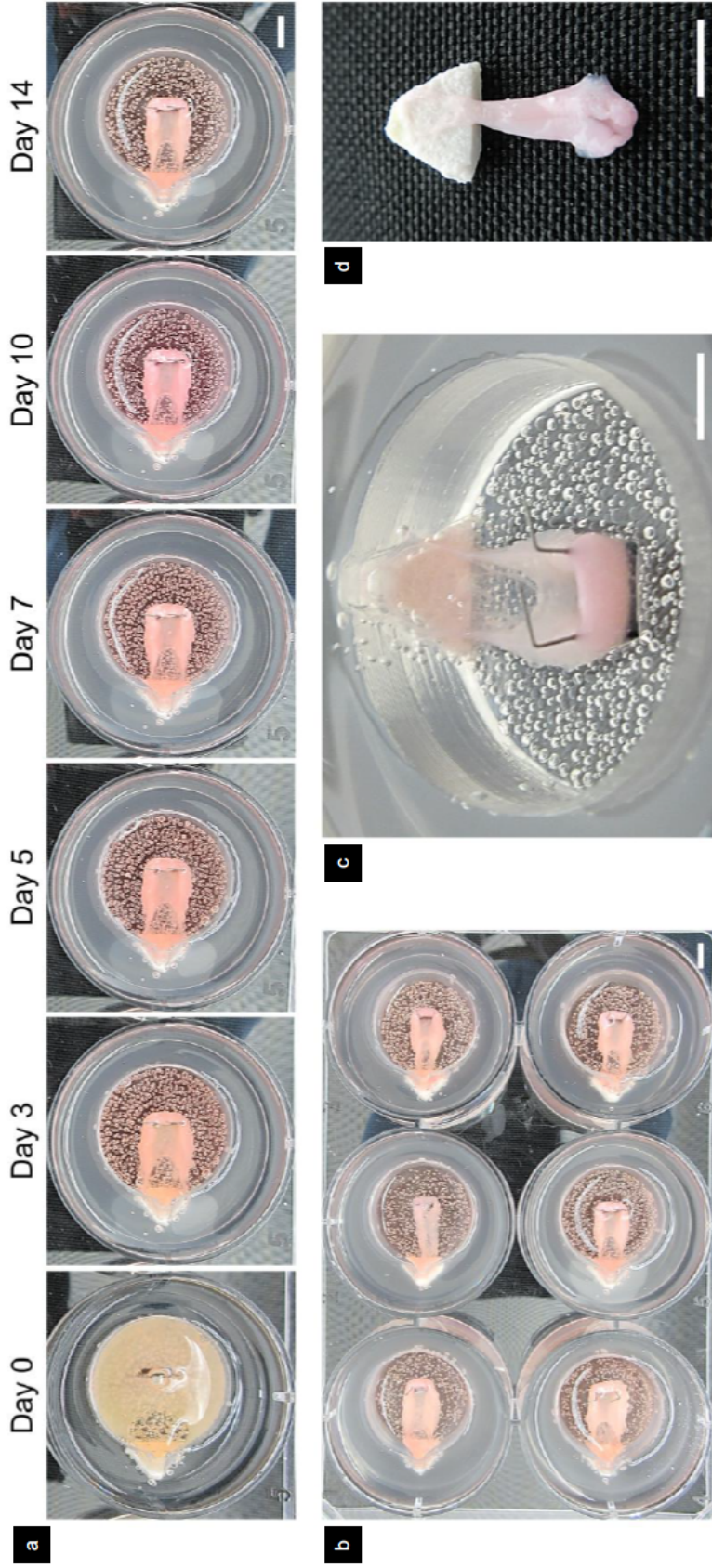


Figure 5.5 | Tendon-Bone Monocultures without Acid Washout in S-DMEM

a) Overview photographs of a representative monoculture construct (1st trial) of standard gel volume and standard cell number developing over time in S-DMEM. Constructs develop in the 2.1mm diameter 'body' area of the bespoke culture zone within a 35mm diameter well. The day 0 photograph was taken after cell seeding and 2 hours of previous fibrin polymerisation, revealing the acidity of the S-DMEM through yellowing of the constituent phenol red pH indicator; on all other days photographs were taken after a change of medium. A curved translucent 'halo' of fibrin gel, ranging from thin to absent gel, is present at the bone anchor interface from day 0 onwards. b) Overview photograph of all 6 constructs in a 6-well plate of 35mm wells on day 14, showing range of tendon analogue morphologies. 5 of 6 tendon analogues demonstrate the 'halo' of fibrin gel at the bone anchor interface, not obviously apparent in the *upper middle* construct. c) Superior oblique view of construct from (a) lying within the 2.1mm diameter culture zone on day 14 without media, demonstrating the lack of fibrin gel centrally at the interface. d) Isolated construct from (a) and (c) removed from culture on day 14. The tendon analogue contracts considerably once tension is lost after removing the pins holding the suture anchor in position. The attachment interface consists of 2 thin slips of tendon analogue over a minimal region of the bone anchor presenting surface. Scale bars 5mm.

In the 2nd monoculture trial (**Figure 5.6**), the yellowing (acidification) of the thrombin mix and culture medium was similar, although the fibrin gel seemed marginally more solid after the standard 1 hour of polymerisation before cell seeding. The halo of translucent gel at the bone interface was present in both the '+AA+P' and 'double gel/double cells/+AA+P' cultures, but less obvious in 'double gel/double cells/+AA+P' cultures. At day 2, 2 of the 'double gel/double cells/+AA+P' tendon analogues had detached from their bone anchor, and by day 3 all 3 tendon analogues had detached. All '+AA+P' tendon analogues were still attached by day 7 and were contracted between the suture and bone anchors despite the lack of gel at the interface. By day 10, however, 2 of the '+AA+P' tendon analogues had detached from their bone anchor, with the 3rd remaining attached on day 14 by approximately half the width of the base of the bone anchor.

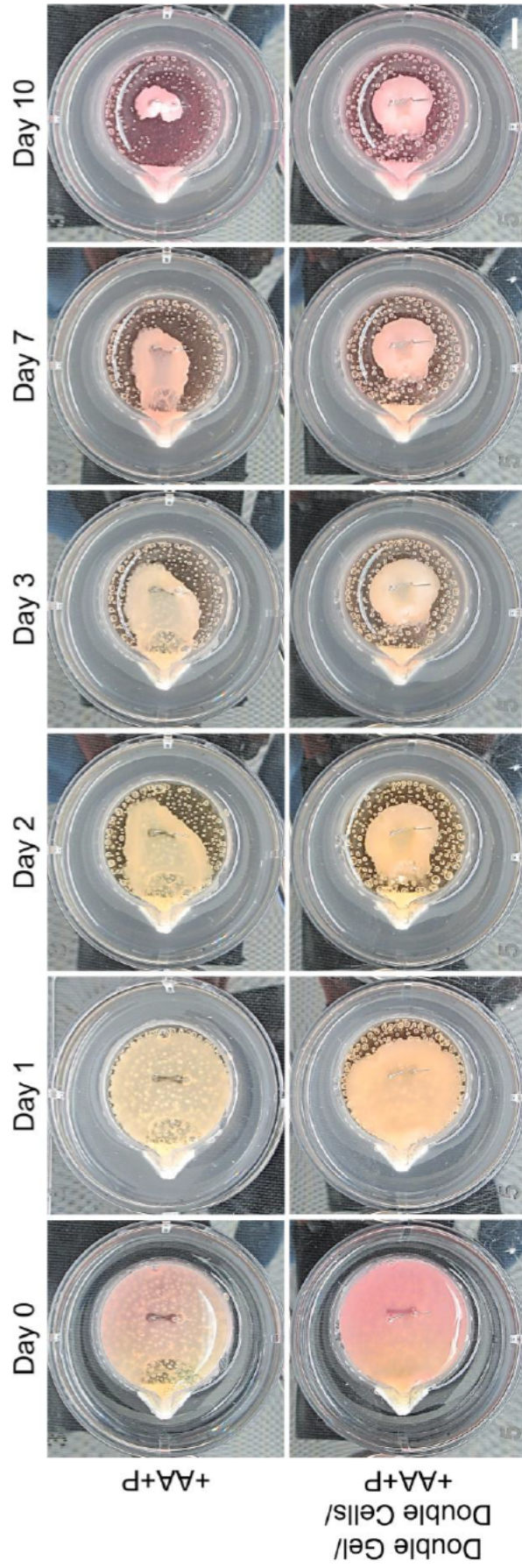


Figure 5.6 | Tendon-Bone Monocolture without Acid Washout in S-DMEM with AA and P
 Overview photographs of representative '+AA+P' and 'Double Gel/Double Cells/+AA+P' monocolture constructs (2nd trial) in 35mm wells developing over time. The day 0 photograph was taken after cell seeding and 1 hour of previous fibrin polymerisation, showing the acidity (yellow of the phenol red pH indicator) focused over the bone anchor. Day 3, 7 and 10 photographs were taken before medium changes, and show the progressive decrease in acidity (yellowing) of the medium as medium changes occur over the culture period (phenol red pH approximations: yellow, pH<6.8; orange-red, 6.8-8.2; bright pink, >8.2). The 'halo' of curved fibrin gel translucency at the bone anchor interface is evident in both cultures from day 0 onwards. The gel has fully contracted away from the bone anchor by day 10 in the '+AA+P' culture, and by day 2-3 in the 'Double Gel/Double Cells/+AA+P' culture, forming a ball around the suture anchor. Scale bar 5mm all panels.

5.5.2.1.2 With Brushite Acid Washout

The 3rd monoculture trials, which included the brushite acid washout steps, did not display acidic yellow media or the curved halos of translucent gel at the bone interface, and the fibrin was fully solid after 1 hour of polymerisation. All tendon analogues remained attached to the bone anchor at the conclusion of the trial on day 14.

Both the monocultures cultured in S-DMEM (**Figure 5.7**) and S-DMEM supplemented with AA and P (**Figures 5.8** and **5.9**) revealed commonalities in tendon analogue development. The standard volume gel cultures ('S-DMEM' and '+AA+P') contracted the most and produced the thinnest (of depth) tendon analogues. The double volume gel with double cell number cultures ('double gel/double cells' and 'double gel/double cells/+AA+P') were more contracted than double volume gel with standard cell number cultures ('double gel' and 'double gel/+AA+P'), but less than the standard volume gel cultures. The general morphology of the tendon analogue formed by approximately day 5, after which those tendon analogues supplemented with AA and P (**Figures 5.8** and **5.9**) appeared to continue contracting more than those cultured in S-DMEM alone (**Figure 5.7**).

By day 14, the most anatomically relevant construct was the 'double gel/double cells/+AA+P' culture, where the peripheral edges of the fibrin gel formed a relatively rectangular tendon analogue with attachment to the bone anchor (**Figure 5.9**). In all constructs, however, the bulk of the gel was in the half to two-thirds of the tendon analogue towards the suture anchor side, as the gel peripheries folded/bunched in contraction towards the suture anchor, whilst remaining attached to the bone anchor. Despite the fibrin gel on formation at day 0 being of a depth to seemingly cover the entire presenting surface of the bone anchor, tendon analogue attachment on day 14 was only to the lower aspect of the bone anchor (**Figure 5.9**).

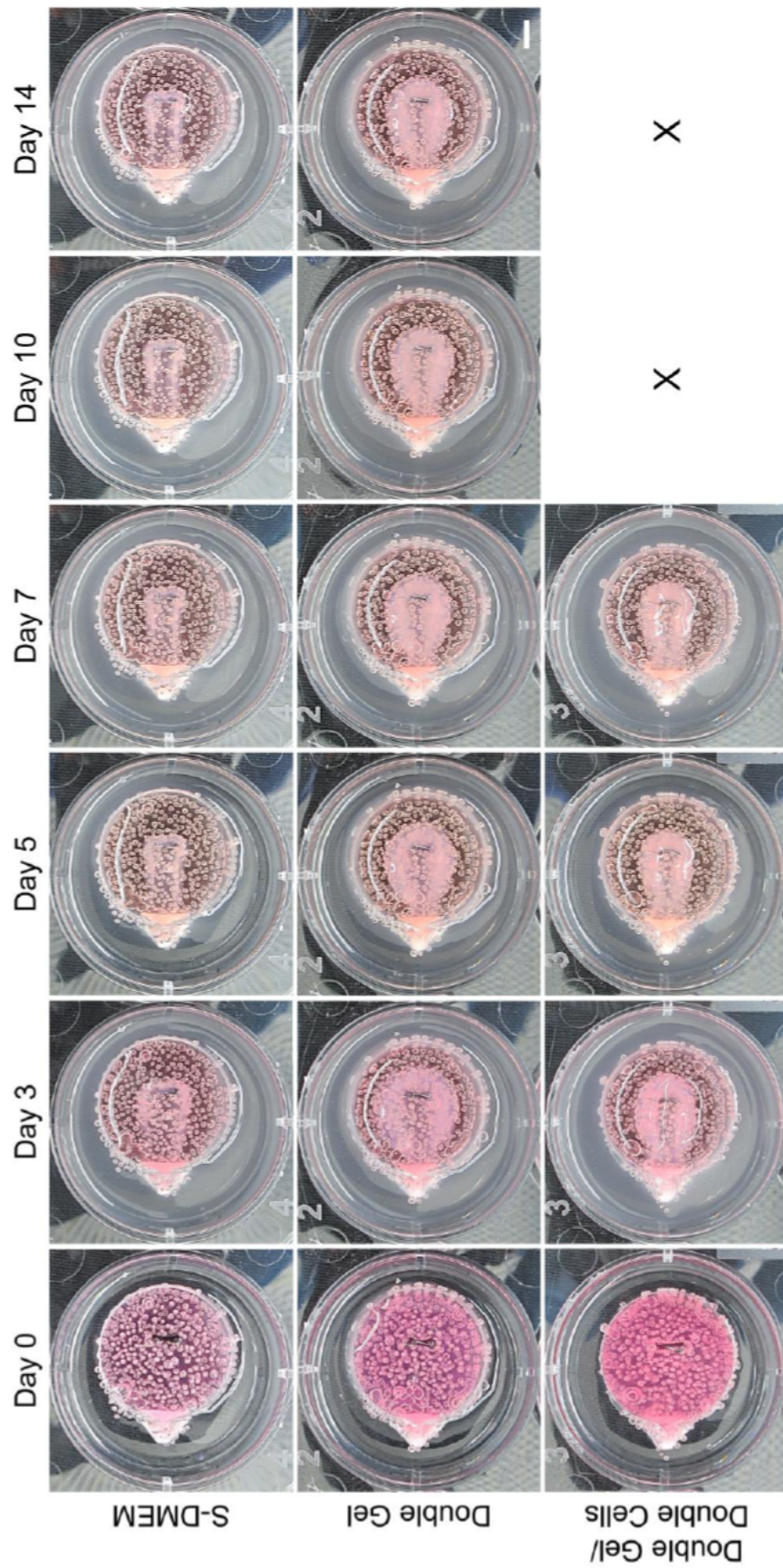


Figure 5.7 | Tendon-Bone Monocultures with Acid Washout in S-DMEM

Overview photographs of representative 'S-DMEM', 'Double Gel', and 'Double Gel/Double Cells' monoculture constructs (3rd trial) in 35mm wells developing over time. The tendon analogues of double volume gel ('Double Gel' and 'Double Gel/Double Cells') are notably thicker, wider and less translucent than the standard volume gel 'S-DMEM' culture. 'Double Gel/Double Cells' tendon analogue cultures are more contracted than 'Double Gel' cultures at comparable time points. The majority of gel contraction in the formation of tendon analogues for all culture variables occurs by day 5. 'Double Gel/Double Cells' cultures were discarded after day 7 due to bacterial contamination. Scale bar ('Double Gel' day 14) 5mm all panels.

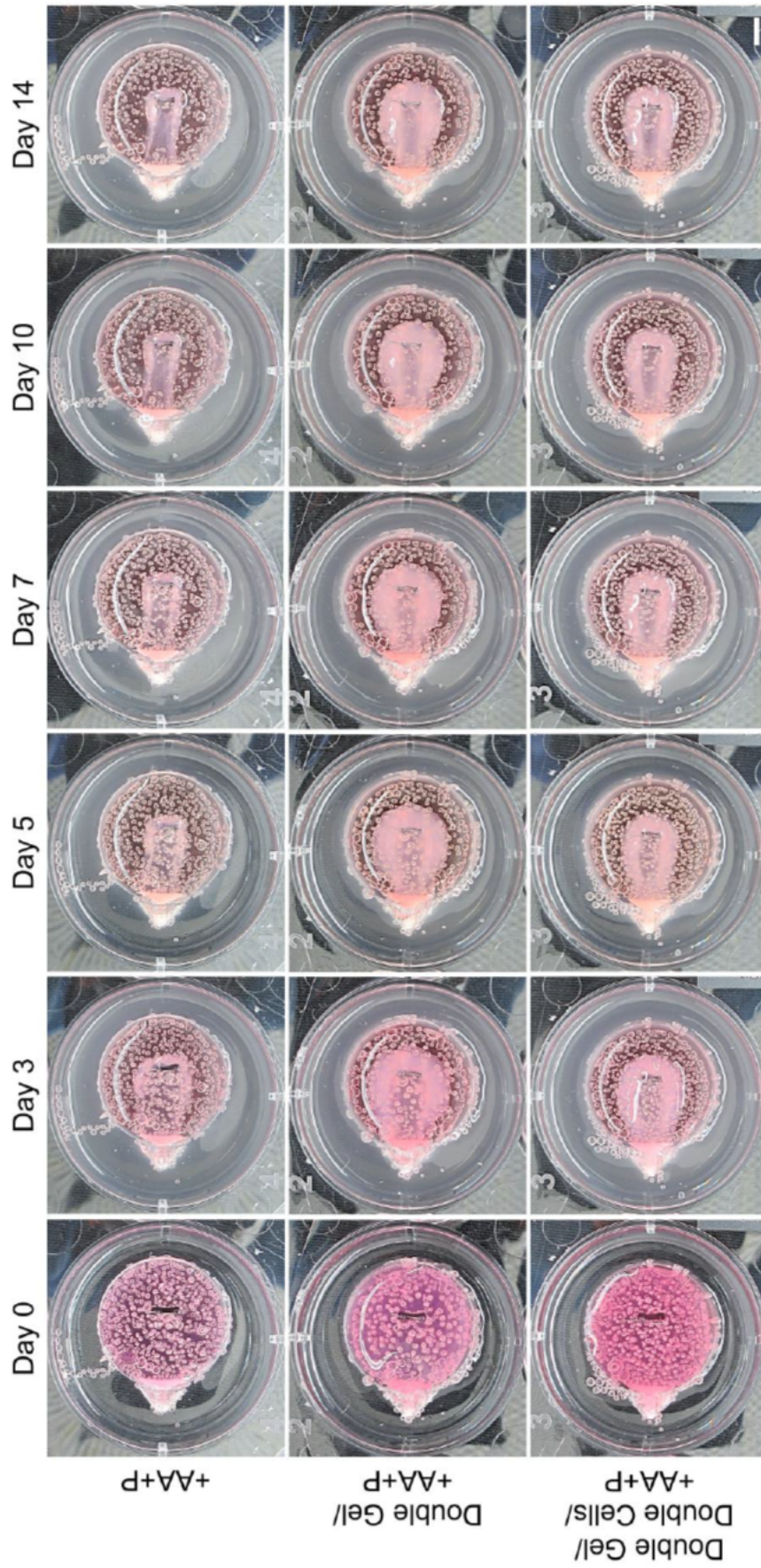


Figure 5.8 | Tendon-Bone Monocultures with Acid Washout in S-DMEM with AA and P (1)
 Overview photographs of representative '+AA+P', 'Double Gel/+AA+P' and 'Double Gel/Double Cells/+AA+P' monoculture constructs (3rd trial) in 35mm wells developing over time. General observations are similar to Figure 5.7. For all culture variables, although tendon analogue formation has generally occurred by day 5, contraction then gradually continues such that by day 14 the tendon analogues appear more contracted than culture variables in S-DMEM alone (compare Figure 5.7). Scale bar 5mm all panels.

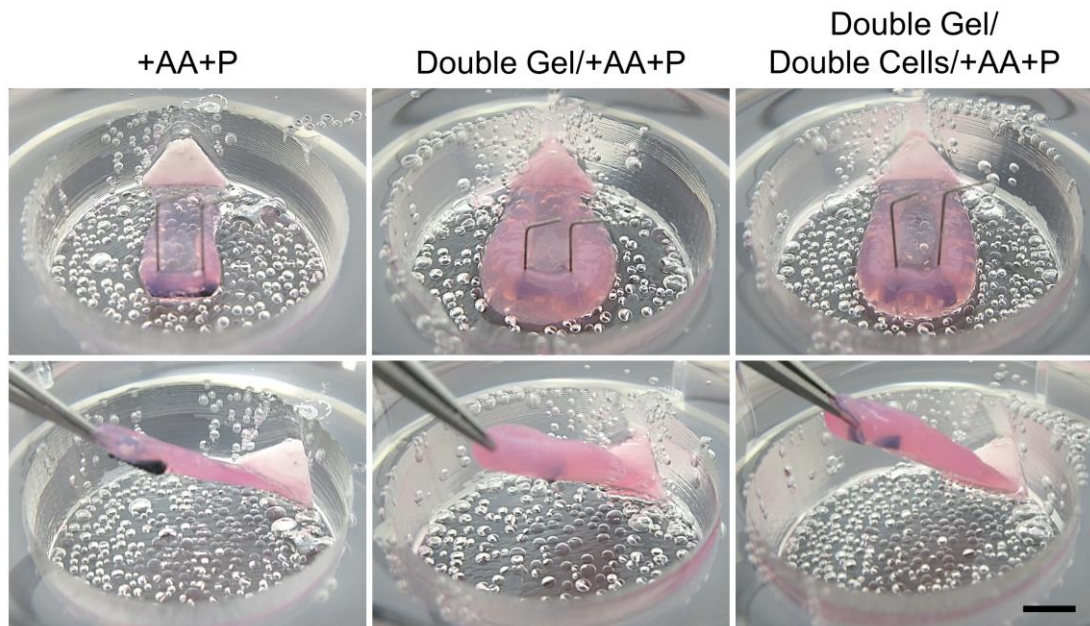


Figure 5.9 | Tendon-Bone Monocultures with Acid Washout in S-DMEM with AA and P (2)
 Superior oblique (*upper panels*) and superior-lateral oblique (*lower panels*) photographs of the '+AA+P', 'Double Gel/+AA+P' and 'Double Gel/Double Cells/+AA+P' monoculture constructs from **Figure 5.8** on day 14 without culture medium. Noticeable is the extent of rolling/folding at the peripheries of the fibrin gel in the contraction and formation of the tendon analogues; the comparative thinness of the standard volume gel '+AA+P' culture; and the increased contraction of 'Double Gel/Double Cells/+AA+P' culture over 'Double Gel/+AA+P'. Gentle axial tension on the tendon analogues (*lower panels*) highlights that the tendon-bone attachment occurs on the lower aspect of the bone anchor presenting surface, with the single volume gel '+AA+P' seemingly attaching over the smallest area and on the lowest aspect, compared to the other double volume gel constructs. Scale bar 5mm all panels.

5.5.2.2 Co-Culture Constructs

Cultures incorporating osteoblast seeded bone anchors were also capable of forming tendon-bone constructs. The general tendon analogue morphology between suture and bone anchor again formed within the first week. Those constructs cultured in S-DMEM supplemented with AA and P (**Figure 5.10**) did not demonstrate a clear morphological progression after day 7, and by day 28 the tendon analogue remained largely flat (**Figure 5.11**), rather than being noticeably rolled up at the peripheries had significant contraction occurred. In comparison, the 50:50 medium constructs continued to contract after day 7 to a greater extent (**Figure 5.12**), and by day 28 the fibrin gel width over the whole distance of these tendon analogues was much more similar to the dictating widths of the suture and bone anchors (**Figure 5.13**). The fibrin gel was not however tightly contracted around the suture anchor by day 28, with most tendon analogues appearing of wider (S-DMEM with AA and P constructs) or approximately equal (50:50 medium constructs) width at the suture anchor compared

to the bone anchor, despite the suture anchor always being of smaller width than the bone anchor. Overall gel contraction appeared greatest in 'small' sized models, followed by 'medium' and then 'large', as expected by the corresponding increase in size of the suture and bone anchors dictating gel width.

The tendon-bone constructs could be successfully extracted from the Sylgard culture zones with maintenance of the interface (**Figure 5.14**). Closer observation revealed that, although the fibrin gel was attached, the attachment did not encompass the entire intended trapezoidal presenting surface of the bone anchor, remaining attached only to the lower third, with a width less than that of the base of the attachment surface. The removal of tension from the pinned suture anchor during extraction caused a narrowing of gel at the distal end of the tendon analogue near the bone anchor, highlighting that the greater volume of gel, resisting relaxation, lay at the proximal area nearer the suture anchor. This more proximal gel did not contract in the same fashion as the more distal gel on removal of tension, retaining its width.

2 of the constructs cultured in 50:50 medium, 1 'large' and 1 'medium' construct, failed at the tendon-bone interface during culture. The 'medium' tendon analogue had detached from the bone anchor on examination at day 21, whilst the large tendon analogue had detached on day 28. In both constructs, a reduced attachment was first noted on day 17, along with mild yellowing (acidification) of the culture medium in the same wells. Increasing detachment and deeper yellowing of the medium occurred over time until full detachment. Macroscopic contamination was not clearly evident, and the fibrin gel remained solid, although the construct and medium was not visualised microscopically due to the raised culture zone now being at a plane beyond focus for standard light microscopy. Despite both tendon analogue detachments occurring in RTFs from the 3rd isolation, there was no obvious trend between RTFs from different isolations and differences in gel contraction throughout the co-cultures seemed only within the limits of natural variation.

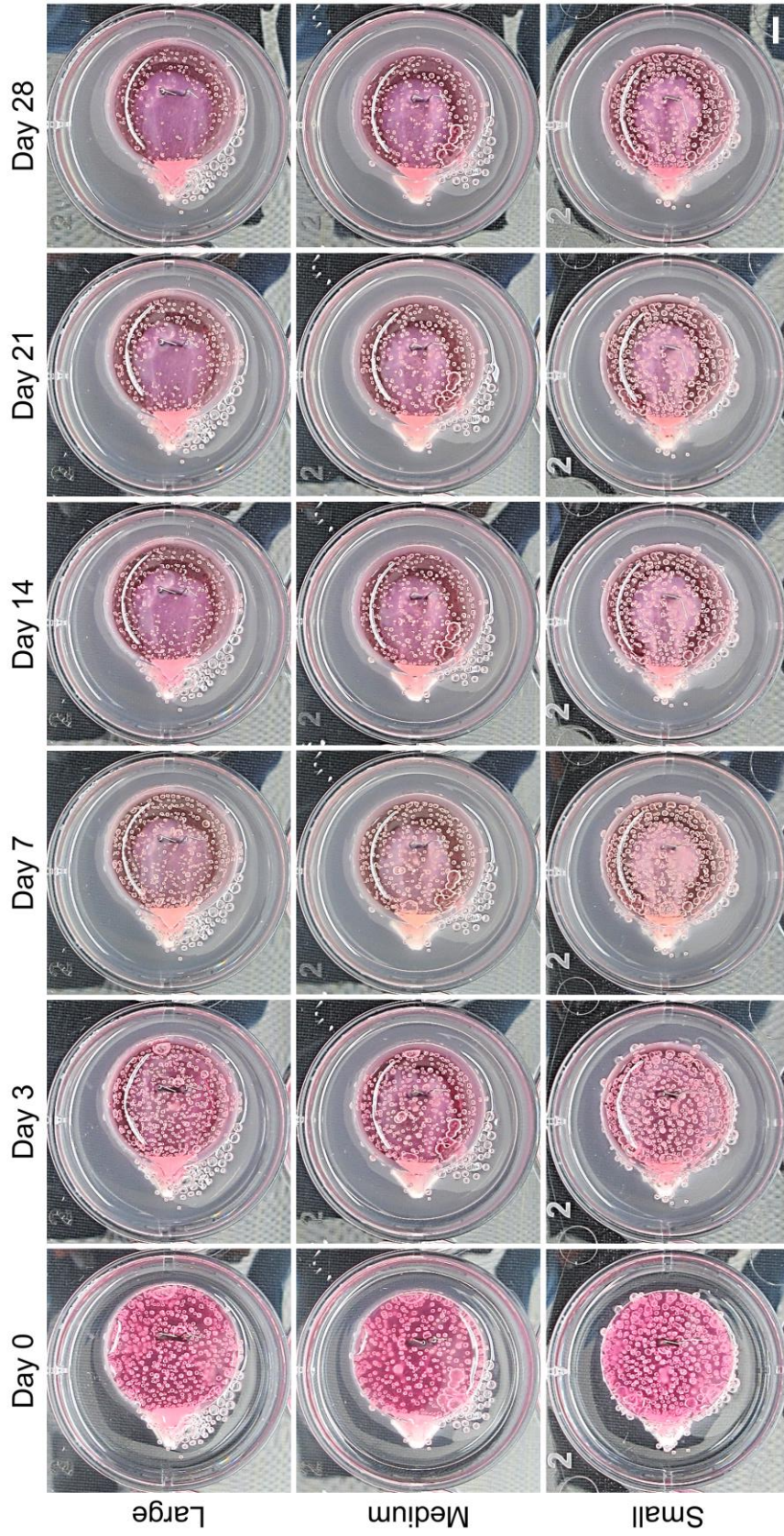


Figure 5.10 | Tendon-Bone Co-Cultures in S-DMEM with AA and P (1)
 Overview photographs of representative 'large', 'medium' and 'small' co-culture constructs of double volume gel and double cell number, cultured in S-DMEM with AA and P ('double gel/double cells/+AA+P') in 35mm wells, developing over time. All construct sizes behave similarly: contraction is variable at day 3, general tendon analogue morphology is formed by day 7, and continuing development is represented by only minimal further contraction in subsequent weeks up to day 28. Scale bar 5mm all panels.

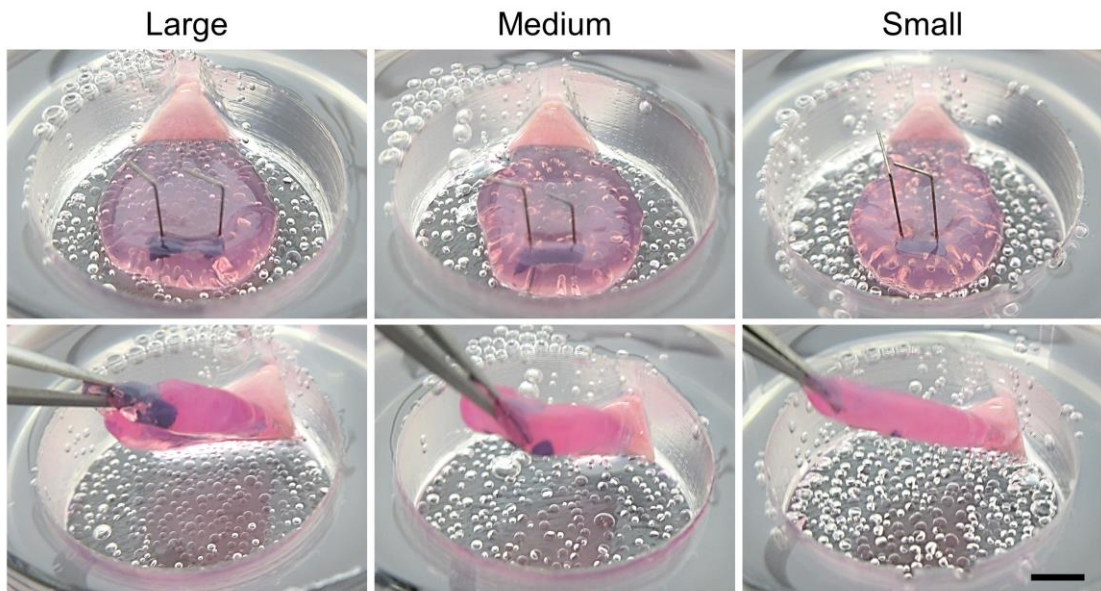


Figure 5.11 | Tendon-Bone Co-Cultures in S-DMEM with AA and P (2)

Superior oblique (*upper panels*) and superior-lateral oblique (*lower panels*) photographs of the 'large', 'medium' and 'small' 'double gel/double cells/+AA+P' co-culture constructs from **Figure 5.10** on day 28 without culture medium. All tendon analogues have yet to contract fully between the suture and bone anchors, maintaining a relatively flat profile (rather than rolled peripheries and thinner central region as per **Figure 5.9**) and curved, rather than straight, peripheral edges between the anchors. The *lower panels* demonstrate the focus of tendon-bone attachment over the lower half of the bone anchor presenting surface. Scale bar 5mm all panels.

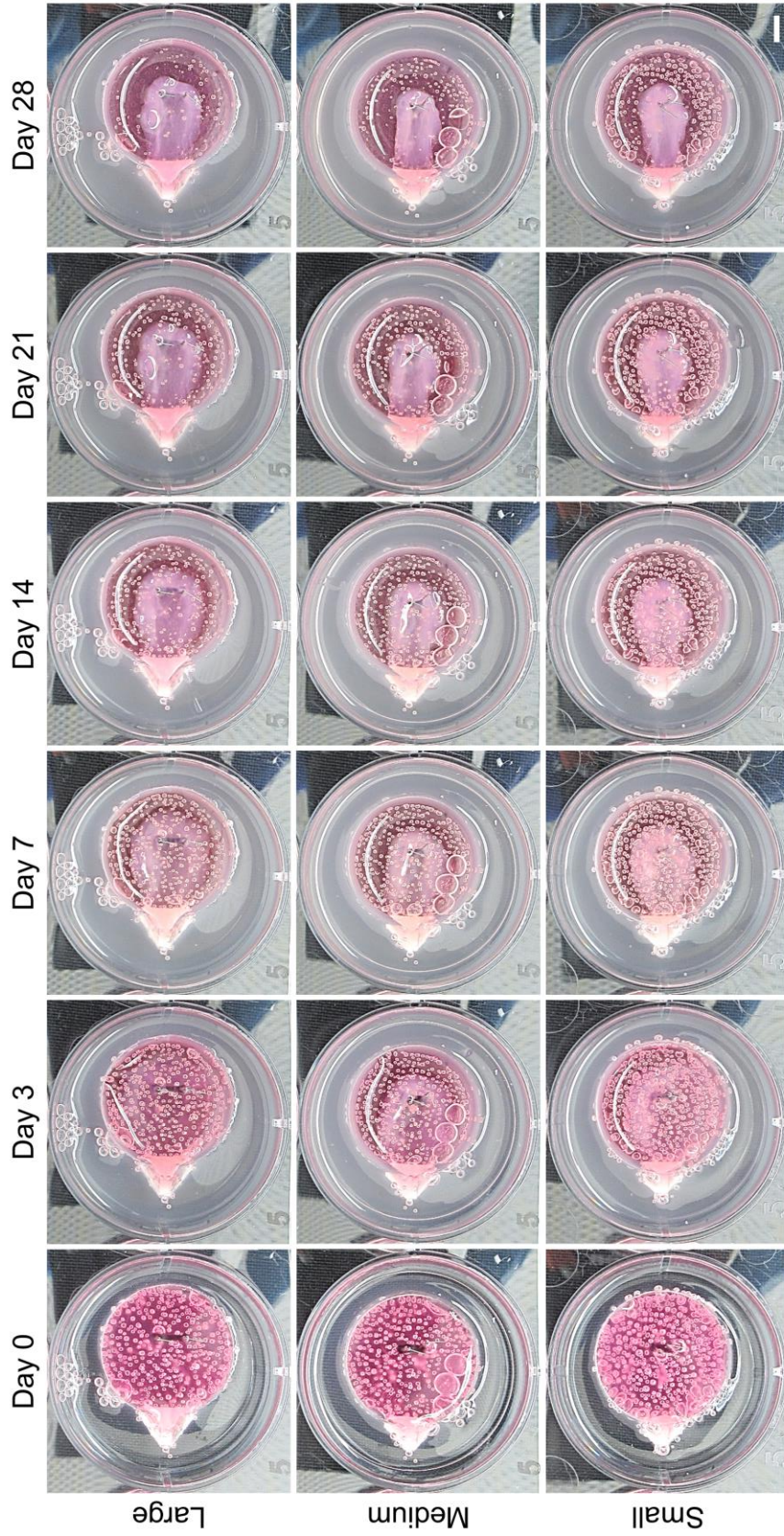


Figure 5.12 | Tendon-Bone Co-Cultures in 50:50 Medium (1)

Overview photographs of representative 'large', 'medium' and 'small' co-culture constructs of double volume gel and double cell number, cultured in 50:50 medium ('double gel/double cells/50:50') in 35mm wells, developing over time. Although general formation of the tendon analogue has occurred by day 7, further continued contraction of the developing tendon analogue in all sizes is more obvious than similar co-cultures in S-DMEM with AA and P (compare Figure 5.10). Scale bar 5mm all panels.

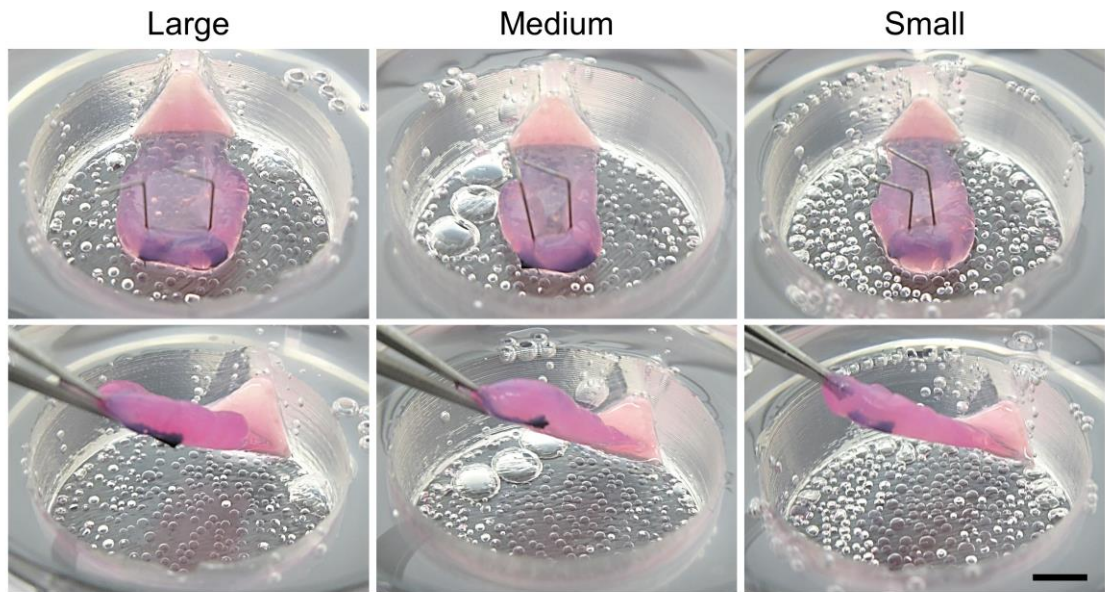


Figure 5.13 | Tendon-Bone Co-Cultures in 50:50 Medium (2)

Superior oblique (*upper panels*) and superior-lateral oblique (*lower panels*) photographs of the 'large', 'medium' and 'small' 'double gel/double cells/50:50' co-culture constructs from **Figure 5.12** on day 28 without medium. The *upper panels* demonstrate the greater contraction of the tendon analogue in all construct sizes as compared to similar 'double gel/double cells/+AA+P' co-cultures, forming a straighter, more rectangular morphology between suture and bone anchor (compare **Figure 5.11**). The lower panels again demonstrate tendon-bone attachment on the lower aspect of the bone anchor presenting surface, appearing even lower than 'double gel/double cells/+AA+P' co-cultures (compare **Figure 5.11**). Scale bar 5mm all panels.



Figure 5.14 | Isolated Tendon-Bone Co-Culture Constructs

'Small' (*left*), 'medium' (*middle*) and 'large' (*right*) 'double gel/double cells/50:50' tendon-bone co-culture constructs removed from culture on day 28, representing the culmination of an anatomically and clinically relevant tissue engineered FDP-DP tendon-bone model. Slight contraction of the tendon analogue has occurred, particularly at its 'neck' just proximal to bone insertion, due to removal of the tension from the pinned suture anchor; however the double volume of gel limits contraction much more than a construct of standard volume gel (compare **Figure 5.5d**). The brushite bone anchor is softer than at the start of culture, but retains attachment of the tendon analogue, albeit on the lower third of the desired attachment surface.

5.6 Discussion

5.6.1 Culture Zone

5.6.1.1 Anatomical Design

The 'fish shape' culture zone was designed to direct the anatomical assembly of the *in vitro* model components. The 'tail' region provided a key advancement from the previously established brushite bone anchor with fibrin gel construct system (Paxton, Grover and Baar, 2010), regulating a single surface attachment where previously gel attached all around the base of the bone anchor. The tail also presented the bone anchor at a 30° angle to the tendon analogue, aiming to induce tension lines in the contracting fibrin gel between the anchors to slope at 30° at the bone anchor attachment and encourage developing collagen fibres to follow correspondingly.

Macroscopically, the culture zone and resulting set up of the tendon-bone constructs successfully integrated the intended elements of the anatomical design. The tendon analogue did not appear to attach to any bone anchor surface other than the presenting surface, although this was not microscopically examined. As further discussed in *Section 5.6.2.3*, the key finding at the interface was that the tendon analogue did not attach over the entire presenting surface of the bone anchor, but contracted to a smaller area. Future design modifications might consider working on a principle of post-culture sculpting of the anatomical interface, by culturing a tendon analogue attachment over a greater than intended single surface area on the bone anchor, then physically shaping the attachment area after culture by sharp dissection to the optimum anatomical shape. This optimum shape could be imprinted on the bone anchor, visible through the translucent tendon analogue at the attachment area, as a stencil to guide post-culture shaping. The 30° attachment angle was also not examined in detail, and ideally the angle at which the bone anchor was presented in culture would have been checked with measurements of side view photographs and the insertion angle of collagen fibres or tension lines in the gel quantified histologically, as per *Chapter 3*. Since the tendon-bone construct removed from culture is not fixed macroscopically at this 30° interface angle, histology would further reveal the impact of 30° interface culture and if the anticipated benefits existed, for example compared to 0° or 90° interface culture.

5.6.1.2 3D Printing and Molding

ABS afforded low cost production of relatively strong 3D printed molds. Its main drawback was textured printed surfaces, preventing a smooth culture surface impression in the Sylgard. This was in contrast to smooth culture surfaces when Sylgard was used in wells without molds, and provided a confounding factor when comparing fibrin gel contraction in tendon-bone constructs in this chapter with the anatomical suture-suture constructs of *Chapter 4 (Section 4.5.2.4)*. Although Sylgard is hydrophobic and should allow natural contraction, a textured surface could provide physical points of focal gel-surface attachment and obstruct contraction. No snagging of the gel was macroscopically evident during construct cultures, however this may have been present microscopically and caused a slowing of contraction. Other members of the laboratory group have attempted to wrap similar ABS-printed molds in flexible laboratory film, creating a smoother Sylgard impression. However, this increased the dimensions of the impression so that fibrin gel could infiltrate around the bone anchor in the tail region, attaching to multiple bone anchor surfaces. This technique was therefore not employed, but could be explored further so that only the inferior surface of the body of the fish shape mold (producing the tendon analogue culture surface) is wrapped. Otherwise, utilising printers and materials capable of producing molds of entirely smooth surfaces should be used with future designs.

The curing of Sylgard tightly around the fish shape molds was welcomed in the creation of accurate impressions, but this also made the molds difficult to remove. The lack of flexibility in the ABS material meant that the removal procedure required particular care and technical experience, as breakages in the mold, especially at the junction between the fish shape and suspending lattice frame, were common during early removal attempts. A material with moderately high flexibility, maintaining position against the curing Sylgard but able to bend on removal after curing, would be a greater attribute than increased strength against breakage. Flexible filaments, thermoplastic elastomers of combined hard plastic and rubber, are printing materials possessing these properties and should be explored for future designs.

Air bubble entrapment was not an issue when curing Sylgard without printed molds, as the bubbles rose to the surface and usually escaped within ≈ 15 minutes when unobstructed. However, with the multi-surfaced and angled components of the fish shape molds, the bubbles were prevented from release and, although not directly

impacting upon cultures, prevented adequate preparation of some wells if the bubbles against the culture surface were breached. Minimising air entrapment during mixing in preparation of the Sylgard was challenging, and future degassing techniques may be best employed at the curing stage. After pouring, the 6-well plate could be first placed in a vacuum to draw out the air bubbles, for example for 30 minutes (Nguyen *et al*, 2014), before heat curing. Using a flexible printed mold material might also allow attempts to clear the bubbles manually. During early curing an instrument could be inserted beneath the fish shape to sweep away the bubbles, made much easier if the fish shape was able to bend to one side and then reliably return to its original position.

With general overall success of the design of the culture zone, future preparations might consider 3D printing the entire culture zone itself, for example as a 35mm diameter well insert. This negates the issues surrounding Sylgard use, but still requires a material of accurate and smooth surface finish. Sylgard possesses many useful properties for tissue culture, including hydrophobicity, transparency, and the ability to be surface sterilised, and a printed material for culture use would also ideally demand these qualities.

5.6.2 Construct Cultures

5.6.2.1 Brushite Acid Leaching

Monocultures without brushite acid washout were the first cultures in the project to use a brushite bone anchor combined with fibrin gel tendon analogue culture. 3 unexpected but important findings were quickly apparent: addition of thrombin mix or culture medium alone to the brushite – 1) liberated acid into solution, 2) impaired polymerisation of fibrin, and 3) created a deficiency in fibrin at the tendon-bone interface. These phenomena were not noticeably reported on review of the literature using the fibrin gel system with brushite. Whilst the 1st monoculture trials produced the ‘halo’ of fibrin deficiency at the tendon-bone interface, the 2nd monoculture trials confirmed the major issue, with tendon analogues fully detaching from their bone anchors by day 2. Pre-culture washout of brushite acid was therefore investigated (*Chapter 4, Section 4.5.3.2*) and the washout procedure mandated before any subsequent cultures with brushite.

Brushite was formed from a combination of orthophosphoric acid (OA) with β -tricalcium phosphate (TCP), using a high 3.5 molarity of OA, previously shown to increase the attachment time of a fibrin gel soft tissue analogue (Paxton *et al*, 2010). Citric acid was also employed as a retardant during the cement formation process. The liberation of acid into solution should therefore not be surprising, and its effects may be remarkable in this project due to the larger volumes of brushite anchors used (e.g. 'universal' size anchor $\approx 5 \times 9 \times 2$ mm) compared to anchors of 3-4mm dimensions in similar fibrin gel-brushite constructs (Paxton *et al*, 2010; Paxton, Grover and Baar, 2010; Paxton *et al*, 2012). The explanation for 1 of the 6 identically sized brushite anchors in the 1st monoculture trial releasing noticeably less acid is not immediately obvious. In the formation of the cement, that particular portion of paste may have accumulated more acid; or more likely, during the sterilisation with 70% IMS before culture, it may have been subjected to a comparatively greater volume of IMS and had more acid washed out. Either way, the tendon analogue forming against this anchor did not seemingly suffer the fibrin deficiency of the other tendon analogues.

As well as affecting cell physiology, pH has a considerable effect on fibrin formation and structure (Kurniawan *et al*, 2017; Weisel and Litvinov, 2017). *In vitro* studies of blood coagulation have previously shown that fibrin polymerisation time doubles at a pH of 6.4 and polymerisation is virtually absent at pH 5.4 (Green *et al*, 1978). The rapid and obvious conversion of the S-DMEM in the thrombin mix to a yellow colour when added to brushite suggested that the phenol red's working limit low of pH 6.4 (Morgan *et al*, 2019) had at least been achieved, and the pH was potentially even lower. Towards an acidic extreme of pH, thrombin would denature and reduce the conversion of soluble fibrinogen to insoluble fibrin, explaining the general increase in polymerisation time seen and the focal lack of polymerisation alongside the brushite anchor where the acid was most concentrated. It was therefore crucial to reduce the brushite acid content for suitable formation of the tendon analogue and its bone anchor attachment.

5.6.2.2 Contraction and Morphology

Although fibrin gel contraction was not quantified by width measurements for definitive comparison between constructs, as per *Chapter 4*, the morphology of all developing tendon analogues was serially observed and recorded photographically. The perceived trends observed amongst the varying constructs are subsequently

discussed with reference to general contraction, gel volume and cell number, and culture media, and also ahead in *Section 5.6.2.4* for co-cultures.

5.6.2.2.1 General Contraction

Tendon-bone constructs cultured in the bespoke culture zone displayed similar early stage development to anatomical suture-suture constructs (*Section 4.5.2.4, Chapter 4*), forming their general shape, as dictated by the anchor sizes, within the first week. Most tendon-bone constructs appeared to contract to their general shape by day 5, rather than approximately day 7 for anatomical suture-suture constructs, likely due to the more confined culture well body of 21mm diameter rather than 35mm.

Contraction proceeded from the culture zone 'body' rim towards the centre of the well, whilst the gel formed over the bone anchor in the 'tail' of the well anchored to the bone anchor presenting surface. As the gel gathered around the suture anchor, there was a bias of gel volume in the proximal tendon analogue end towards the suture anchor over the distal end towards the bone anchor. Ideally the gel volume should be similar over the full length of the tendon analogue, and this might be addressed in future developments by altering the shape of the culture zone 'body'. For example, a more elliptical shape might be employed; the rim could be tighter to the suture anchor, preventing excessive gel gathering behind the suture anchor, but wider more centrally, encouraging greater bulk over the length of the tendon analogue.

Over the 2 week monocultures and 4 week co-cultures, the gel never contracted fully to the width of suture anchor, as had previously been noted in *Chapter 4 (Section 4.5.2.3.3)*. Although the suture provided attachment for the gel, the pins appeared to have greater influence over the 3D tendon analogue morphology, as they restrained the contracting peripheral gel folds from meeting centrally. Where the aim is to generate a biconcave engineered tendon analogous to the 3D human morphology, the pins could in future be placed close together rather than at the ends of the suture, still providing 2 point fixation, but allowing the bulky folds of fibrin to meet centrally. With the gel folds contracted more centrally, the suture itself may be better able to define the intended width.

A notable finding in this chapter was the gel contraction (relaxation) that occurred after removal of the construct from culture. This emphasised the tension generated by the

anchors, crucial for organised collagen fibre alignment in the tendon analogue (Kapacee *et al*, 2008; Bayer *et al*, 2010). The contraction was particularly striking in tendon analogues with a standard volume of gel, where contraction appeared to occur in both length and width directions. Doubling the volume of gel reduced this post-culture contraction effect, although contraction was still conspicuous in areas of the double volume gel tendon analogues where less gel had aggregated (i.e. at the 'neck' before bone anchor attachment). To negate this effect, there should be a balance of present tension during culture of the tendon analogue without an undue stretch on completion of development that would lead to considerable recoil on removal of the construct from culture, for which starting gel volume is likely to be a key factor.

5.6.2.2.2 Gel Volume and Cell Number

Trends in regard to tendon analogue fibrin gel volume and cell number for tendon-bone constructs in this chapter were similar compared to the anatomical suture-suture constructs in *Chapter 4*: tendon analogues with standard volume gel contracted more than those with double volume gel, and those with higher cell number contracted more than those lower cell number. Although standard volume tendon analogues contracted into a more optimal rectangular, rather than rounded, shape between suture and bone anchor, they were insubstantial and mismatched in volume compared to the human FDP. The tendon analogues of double volume gel were more robust, but still lacked the 3D bulk to match the human FDP and attach over the full intended surface of the bone anchor. Future trials with this bespoke culture well design might therefore employ triple or quadruple volumes of gel. Cell number was an important factor in tendon analogue morphological development, and a scaling of gel volume should be matched by a scaling of cell number, in order to retain the same cell density per volume of gel. Constructs of double gel volume and standard cell number equated to half the cell density per volume of gel, producing inferior contraction and morphological development compared to constructs of double gel volume and double cell number. Where future trials use triple or quadruple gel volume, a cell number of 300,000 or 400,000 cells, respectively, should be added in the first instance. Greater volumes of gel may also require an increase in the volume of the culture zone body to allow enough space for culture media, which should not be problematic since extra space was available in the surrounding 35mm diameter well.

5.6.2.2.3 Culture Media

Chapter 4 established that the addition of 250µM AA and 50µM P to S-DMEM increased gel contraction after the initial formation stage of the tendon analogue, and produced the most morphologically relevant tendon analogue in cultures of double volume gel and double cell number in suture-suture constructs. The initial tendon-bone monoculture trials in the current chapter were affected by brushite acid leaching, however it was noticeable that comparable standard volume constructs cultured with AA and P (2nd monoculture trial) resulted in interface detachment of 2 of 3 tendon analogues by day 10, whilst all 6 constructs cultured in S-DMEM alone (1st monoculture trial) had not detached by day 14. This suggested that detachment may also be a manifestation of the increased contraction forces in constructs cultured with AA and P. In the 3rd monoculture trials, unaffected by acid and culturing tendon-bone constructs both with and without AA and P supplementation, comparative differences were difficult to perceive over the 14 day culture period. The constructs cultured with AA and P supplementation did appear more contracted at day 14 over day 5, whilst those in S-DMEM alone appeared very similar at the 2 time points, suggesting continued contraction with AA and P, as would be expected. Width quantification as per *Chapter 4* would however be needed to confirm the small contraction margins. As per the anatomical suture-suture constructs of *Chapter 4*, the ‘double gel/double cells/+AA+P’ monoculture constructs were the most morphologically relevant at the completion of the 3rd monoculture trials at day 14. The final co-culture trials therefore included this set up, in addition to culturing constructs in 50:50 medium as the most suitable medium for co-culture of osteoblasts and fibroblasts, and these constructs are discussed separately in *Section 5.6.2.4*.

5.6.2.3 Tendon-Bone Interface Attachment

Chapter 2 showed that the native human FDP-DP attachment footprint was trapezoidal. The *in vitro* bone anchors represented this entire attachment shape, with the aim of the culture zone design to direct the developing tendon analogue onto the whole of this surface. Despite the fibrin gel initially appearing to fully cover the bone anchor presenting surface on day 0 after polymerisation, axial tension on the tendon analogue at the conclusion of successful constructs (3rd trial of monocultures, and co-cultures) demonstrated that the attachment was concentrated on the lower third of the presenting surface only. This was a consistent finding, although the remaining

attachment area was not analysed in detail in order to establish its precise size and shape or predictability in reduction from the original attachment area.

The reduced attachment was potentially due to a combination of contraction, gravity and gel volume factors. Contraction forces away from the bone anchor seemingly drew the gel down onto the lower aspect of the presenting surface, enhanced by gravity on a sloping surface. The most important factor however was likely to be gel volume, as a bulkier tendon analogue, initially attaching over a greater area, seemed better able to resist contraction and gravity. Standard volume gel cultures appeared to attach over a lesser area and lower down on the presenting surface compared to double volume gel cultures. Both tendon analogue morphology, as previously discussed in *Section 5.6.2.2.2*, and the interface attachment should be enhanced with greater gel volume in future trials.

After establishing the pre-culture brushite acid washout steps, the tendon-bone interface remained intact in 100% of monocultures at 2 weeks (3rd trial, n = 12/12) and 89% of co-cultures at 4 weeks (n = 16/18). This interface, and the provision of tension as a counterpoint anchor to the suture during gel contraction, relied on the inherent attachment between the fibroblast-seeded fibrin and brushite (osteoblast-seeded in co-cultures). Unlike similar fibrin-based soft tissue models contracting around sutures (Huang *et al*, 2005; Huang, Dennis and Baar, 2006; Huang, Khait and Birla, 2007; Kapacee *et al*, 2008; Bayer *et al*, 2010) or brushite anchors (Paxton, Grover and Baar, 2010; Paxton *et al*, 2012), the attachment was not bolstered by the additional restraint and increased surface area of attachment behind the anchor. Brushite is known to augment tendon-bone integration *in vivo* (Wen *et al*, 2009) and the physical attachment in the *in vitro* constructs was likely based on ingrowth of the fibrin and potential collagen fibres into the brushite, as demonstrated by Paxton, Grover and Baar (2010) through electron microscopy of their brushite-fibrin constructs. Although the current bone anchor presenting surface is macroscopically straight, the brushite is porous and any ingrowth of the tendon analogue creates a microscopic interface region of mixed soft and hard tissue, much like the fibrocartilaginous enthesis. To further increase the inherent attachment between tendon analogue and bone anchor, additional physical modification could be made to the bone anchor presenting surface. This surface could be designed either to recreate the multi-directional, irregular, 'jigsaw-like' interdigitation at the bone-calcified fibrocartilage junction in the

fibrocartilaginous enthesis, or to balance the known positive effects of surface area against the negative effects of stress concentration on attachment duration and strength (Paxton *et al*, 2010), for example with smooth micro-undulations. Such designs would also increase the 'enthesis' region of mixed soft and hard tissue. Engineering ceramics to these custom, high resolution specifications might be accomplished with techniques such as 3D powder printing (Gbureck *et al*, 2008), selective laser sintering (Wilson *et al*, 2004), or stereolithography (Levy *et al*, 1997; Chu *et al*, 2002).

5.6.2.4 Co-Cultures

The co-culture constructs represented the culmination of the tissue engineered FDP-DP model, integrating anatomical design and clinically relevant sizes into 3D soft-hard tissue co-culture. All model sizes could be successfully cultured, and no particular size appeared better or worse in generating anatomical tendon analogue morphology or bone anchor attachment, likewise noted across the 3 RTFs from separate isolations.

A distinction between monocultures and co-cultures was not observable macroscopically, as tendon analogue formation and continued development was similar in both culture types. Through observation alone, the seeding of osteoblasts onto the bone anchor did not appear to clearly enhance or reduce the attachment area at the interface. It should be acknowledged, however, that the interface was not studied in detail, due to time limitations at the end of the project, for investigation not only of the surface area of attachment but also the microscopic environment. Function, interaction and migration of interface cells, and their matrix environment, was not investigated, but would be expected to differ between co-cultures and monocultures, even if macroscopic overview observation was similar. Such studies are integral to interface tissue engineering, and now that this co-culture model system has been established these key questions about cellular behaviour and microenvironment can be addressed.

One dissimilarity noted between co-cultures and monocultures was that 2 co-culture constructs detached at the interface, not seen in monocultures with brushite acid washout. Since the detachments occurred at days 21 and 28, and the monocultures, as briefer preliminary studies, only ran until day 14, detachment may have also ensued in monocultures if similar time periods were reached. However, full

detachment in the co-cultures was preceded by acidification of the culture medium, suggesting a change in environment or cell physiology, often as a result of contamination, although this was not confirmed. Seeding and 7 day culture of osteoblasts on the bone anchor introduces additional techniques and culture time that can result in contamination, as a drawback of co-culture preparation. Yet if preceding osteoblast culture was the source of contamination, its effects would probably have arisen before day 17 of the co-culture (when the first abnormal signs were noted), and so the detachments most likely represent an issue not specific to co-culture. The osteoblast seeding and 7 day culture period followed the method that achieved proliferating osteoblasts as demonstrated in *Chapter 4 (Section 4.5.3.3)*. Further optimisation would likely increase seeding density and reduce culture time before integration into the co-culture, which may have positive cellular effects on the interface attachment whilst lessening contamination risk through reduced time and interventions.

Work in *Chapter 4* previously established that the 'double gel/double cells/+AA+P' culture set up produced the most anatomically relevant tendon analogue, whilst 50:50 medium was the most appropriate medium for fibroblast and osteoblast co-culture. Both 'double gel/double cells/+AA+P' and 'double gel/double cells/50:50' culture variables were trialled in the final co-cultures, and, surprisingly, 'double gel/double cells/50:50' constructs produced the more contracted and morphologically relevant tendon analogues. 'Double gel/double cells/+AA+P' constructs did not appear to undergo any great contraction after day 7, in contrast to the 'double gel/double cells/+AA+P' anatomical suture constructs in *Chapter 4 (Section 4.5.2.4.2)*. 50:50 medium was not investigated in the anatomical suture constructs of *Chapter 4*, although (100%) RODM was, and was found to contract fibrin gel noticeably less than cultures in S-DMEM or S-DMEM supplemented with AA and P. It is not clear why these findings were seemingly reversed in the co-culture constructs, as they are unlikely to be the result of the added osteoblast-seeded bone anchor. Since cell viability was not checked, unseen contamination may have reduced cell function in the 'double gel/double cells/+AA+P' cultures. Nevertheless, it was encouraging that 'double gel/double cells/50:50' cultures produced morphologically relevant tendon analogues as well as providing the most suitable co-culture medium, and this set up should form the basis for future work on the model.

5.6.2.5 Limitations

The main limitation to the results and trends described for the constructs in this chapter is the lack of quantification and statistical analysis to substantiate similarities and differences. Subjective observation alone was used for assessment. Had further time been available, gel contraction would have been assessed as per *Chapter 4*, with 2nd observer validation, permitting greater confidence in describing results and implications. In describing relevance and relationships to human morphology, constructs would ideally have undergone histological assessment of the angle of fibre insertion, as per *Chapter 3*, and also the analysis of the tendon-bone insertion footprint, as per *Chapter 2*. Furthermore, as discussed in the previous section, detailed investigation of the interface biological microenvironment would be a crucial line of enquiry, as well as mechanical interface properties. As the project time concluded, these assessments remain as the basis for future work.

Further specific limitations in this chapter have been discussed elsewhere, such as the textured surfaces and resolution of the ABS prints (*Section 5.6.1.2*). More general limitations pertinent to the construct cultures performed in this chapter have already been discussed in *Chapter 4*, including greater replicates to overcome the natural variation in gel contraction (and potential for contaminations) (*Section 4.6.2.5*), accuracy of suture anchor size and distances measured in the construct set up (*Section 4.6.2.5*), unknown true RODM ingredients (*Section 4.6.1.1*) and the need for biological replicates of osteoblasts (*Section 4.6.3.3.5*).

5.7 Summary of Findings

The human morphometric data from *Chapters 2* and *3* could be translated into the anatomical design of an *in vitro* FDP-DP tendon-bone co-culture model by creating a bespoke culture zone using a 3D printed mold and surrounding silicone impression. Single surface attachment of the tendon analogue onto the bone anchor was achieved, but the area of attachment after fibrin gel contraction was considerably less than intended. Brushite scaffolds in culture acidified their medium and impaired fibrin formation, and acid washout was essential for maintenance of the tendon-bone interface. Tendon analogues formed from higher volumes of gel and higher cell number were the most comparable to human morphology, and better resisted

contraction on removal from culture. Co-culture constructs appeared macroscopically similar to monoculture constructs, and 50:50 medium was suitable for morphological development of co-culture constructs.

CHAPTER 6

GENERAL DISCUSSION

6.1 Chapter Overview

This final chapter reviews the main findings of the project, addressing the global aim and objectives, and discusses the implications for continued research. Avenues of future work with the novel 3-dimensional (3D) model, as a completed design or for improvement of particular design features, are suggested. The chapter concludes by highlighting the position and value of the work within the wider research landscape.

6.2 Review of Results

The aim of the project was to tissue engineer an *in vitro* tendon-bone model applicable to the treatment of flexor digitorum profundus (FDP) insertion injury at the distal phalanx (DP). The central focus was model design, with the essential feature of investigating and reproducing the native human anatomy to enhance translation towards a future clinical product.

After introducing the fundamental themes of the project in *Chapter 1*, *Chapter 2* examined the macroscopic morphology of the FDP insertion, distal FDP tendon and DP bone. The principal findings were:

- A trapezoidal tendon-bone interface footprint;
- An FDP insertion footprint of 20-25% DP flexor surface area, centred 25-30% distally along the DP;
- A distal FDP tendon arranged as 2 major fibre bundles, flaring out at insertion;
- Limited depth of DP bone at the FDP insertion, narrower at the distal point than proximal point of insertion;
- Morphometric data clustering across factors of finger and gender type into 3 size categories.

Chapter 3 examined the histology of the FDP insertion, primarily finding:

- A fibrocartilaginous enthesis;
- FDP fibres inserting across the tidemark at 30°;
- Greatest angle change in fibres nearing their insertion in the proximal enthesis region, where fibrocartilage predominated.

Chapter 4 began *in vitro* development, assessing individual cellular, tendon and bone components for optimal design of an anatomically-matched, stratified co-culture model. The main findings were:

- Rat tendon fibroblasts (RTFs) and differentiated rat osteoblasts (dROBs) as the most suitable and representative fibroblast and osteoblast cell populations;
- 50:50 medium as the most appropriate co-culture medium;
- Tendon analogue formation by contraction of RTF-seeded fibrin hydrogel around anchor points;
- Establishment of general tendon analogue morphology in approximately 7 days, shaped by the size and position of the anchors, with little width change in anatomically-sized tendon constructs after 4 weeks;
- An increase in fibrin gel contraction with greater RTF cell numbers or addition of ascorbic acid (AA) and proline (P) to basal medium, and a decrease in contraction with greater gel volume;
- Contracted fibrin gel always remaining wider than the width of the suture anchor;
- Limited tendon analogue collagen staining, even in extended 8 week cultures;
- Brushite as a bone anchor scaffold capable of custom casting, allowing dROB seeding and subsequent proliferation over 7 days.

Chapter 5 integrated the morphometric and tissue culture findings from the previous data chapters to produce the final FDP-DP tissue engineered co-culture model. The major design and *in vitro* findings were:

- The production of a novel culture well through a 3D printed mold and silicone impression system;
- Leaching of acid from brushite bone anchors, affecting fibrin formation;
- Achievement of single surface bone anchor attachment;
- Interface attachment of less than intended area;
- Improved tendon analogue morphology with greater fibrin gel volume and RTF numbers.

The ultimate production of a novel, anatomically relevant FDP-DP co-culture model satisfied the overall project aim. As project work progressed, each data chapter addressed the 4 original objectives: through evaluation of the morphology (*Chapter 2*) and histology (*Chapter 3*) of the native human FDP-DP insertion, then developing the

pre-established stratified soft-hard tissue culture model (*Chapter 4*) towards an anatomical design and co-culture (*Chapter 5*).

Anatomical assessments strove to establish the most useful macroscopic and microscopic culture design parameters. In doing so, reliability-tested methods of analysing the tendon insertion footprint and angle of tendon fibre insertion were developed, which can be applied to any other enthesis in the body. Evaluation of the anatomical data also established 3 different model sizes for improved clinical relevance and utility. The transition from pure analysis to synthesis of the *in vitro* model demonstrates how tissue engineering represents a new, contemporary phase of anatomical research (Mironov and Markwald, 2001).

6.3 Implications, Applications and Future Work

The basis of this project was to demonstrate the concept of human anatomy-informed tissue engineering. It was therefore of broad scope, ranging from first principles to novel culture model production, and encompassed gross anatomy, histology, clinical application, cell sourcing and culture, tissue engineering of tendon, bone and the intervening interface, and engineering design. As such, each area was investigated to a certain level, but most results demanded prompt application elsewhere in the project rather than continued deeper exploration. The anatomical (*Chapter 2*) and histological (*Chapter 3*) results were directly applied to the tissue engineering work, fulfilling the overall project concept, and ultimately a culture model was produced. One theme of future work is investigation of this model as a completed design. Another theme is the deeper exploration of the many avenues opened throughout the project, in particular addressing the results of culture trials (*Chapters 4 and 5*). With the anatomical requirements established, greater optimisation of *in vitro* materials, methods and design will enhance the potential for clinical translation of the model.

This project has launched the development of an *ex vivo* FDP-DP replicate. The ultimate aim is for future use as an *in vivo* graft, yet many complex issues would need consideration before clinical use, such as immunocompatibility and maintenance of structural integrity in an inflammatory surgical environment. Further development and investigation of the *ex vivo* model is first required, for example to realise the optimal anatomical design and acquire native tendon-bone fixation strength. The following

sections suggest themes for the most pertinent initial developments and investigations, in the context of the tendon analogue, bone anchor, tendon-bone interface, and cells.

6.3.1 Tendon Analogue

The engineered tendon has not yet matched the native human FDP tendon morphology in 2D width, cross section or 3D volume using existing methods. Foremost future trials using the current model would test increasing volumes of fibrin gel and fibroblast numbers, aiming for a more substantial tendon analogue whilst still retaining good contraction. If greater gel volume overall does not improve the preponderance for gel to gather around the suture anchor, the culture zone may need to be redesigned. A possible modification could involve a shorter but wider elliptical shape rather than a circle, with minimal distance ($\leq 2\text{mm}$) behind the suture anchor but greater width between the 2 anchors to encourage more gel bulk to gather along the whole length of the tendon analogue. Since the gel does not contract to the width of the suture anchor, seemingly impaired by the anchoring pins, early future trials would also secure the suture anchor by 2 pins placed centrally in the suture, rather than at either end. This aims to allow the contracting rolls of peripheral gel between the suture anchor and bone anchor to meet centrally at the pins, encouraging the biconcave morphology of the native distal FDP, with greater potential for the gel width to match the directing suture width. The distal FDP arrangement of 2 distinct side-by-side gross fibre bundles suggests that the double-stranded tendon analogue construct could provide an excellent morphological match. However, since the double-strand technique requires separate single-strand cultures before incorporation together, and the FDP-DP model requires bone anchor attachment, incorporation of 2 single-strand cultures with bone anchors would also demand fixing the 2 bone anchors together. This would be a major drawback to model production, however if double-stranded tendon analogues were demonstrated to be of increased strength over an equal volume of combined single strands, then this may be a challenge worth investigating.

3D bioprinting provides the ideal opportunity to produce optimal tendon analogue morphology, and would overcome the current reliance on contraction and manipulating factors. A fibroblast encapsulated hydrogel, such as fibrin or collagen, could be employed as a bioink and printed in a desired shape as a single strand or

parallel double strand onto an osteoblast seeded bone block, forming a construct for immediate investigation or for further co-culture. Printing would also allow precise positioning of the hydrogel onto the bone block, ensuring single surface connection and a specific interface shape. Once such a print is achieved, culture trials would be required to assess the level of further fibroblast mediated hydrogel contraction, particularly of fibrin, which may alter the morphology of the tendon analogue and area of tendon-bone attachment, as encountered in this project.

Fibrin remained the major component of the current cultured tendon analogues, providing only limited strength, and which *in vivo* would be degraded. Increasing the collagen content of tendon analogues will be essential for improving structural integrity and strength, and should be investigated and incorporated into the model. AA and P, as promoters of collagen synthesis (Gallagher, Gundle and Beresford, 1996; Paxton *et al*, 2012a), were used at a single standard concentration in the project, and higher concentrations could be explored. Growth factors which increase fibroblast extracellular matrix (ECM) deposition, such as basic fibroblast growth factor (bFGF) and platelet-derived growth factor (PDGF) (Thomopoulos *et al*, 2005), could also be incorporated into the culture medium. Additionally, mechanical stimulation of collagen production might be employed, most optimal in fibroblast-seeded fibrin constructs as short, intermittent stretch loads using a bioreactor (Paxton *et al*, 2012b). This highlights the utility of a bioreactor in the next stage of investigations, where both mechanical strength testing and further enthesis maturation can be addressed.

6.3.2 Bone Anchor

Brushite was the only material to be trialled as an anatomically-shaped bone anchor and undergo osteoblast seeding for co-cultures. Although a good bone scaffold candidate, being osteoconductive and of relatively high compressive strength and biological resorption capability (Paxton *et al*, 2010), its propensity for acid leaching interfered with fibrin formation and potentially with cell attachment and proliferation. Furthermore, the microporous nature of brushite at 45% porosity is not ideally matched to the approximately 80% macroporous trabecular bone found *in vivo* (Yang and Temenoff, 2009), since 3D bone cell proliferation and function is favoured by large pore sizes of 100µm order magnitude (Armitage and Oyen, 2015). Other materials of greater porosity should therefore be compared to brushite over a range

of investigations, including cell seeding and proliferation, tendon analogue interface formation and longevity, and testing of both inherent material mechanical properties as well as interface attachment strength. Reprobone is an excellent initial candidate, but ideal future materials might also include freeze casted porous bioactive glass or nanofibrous polymer scaffolds with incorporated mineral. In the current model design, a material of customisable shape is ultimately required to realise the desired anatomical dimensions, being the main reason why Reprobone was not explored further in the project, but tangential work could first compare similarly sized blocks of any design as a bone anchor in fibroblast-seeded fibrin gel co-culture.

The bone anchor was designed primarily to model an *in vitro* FDP-DP interface, but its clinical application as part of a composite graft, requiring fixation of the engineered bone to native bone at the traumatised/pathological insertion, was also considered. The 2mm bone anchor depth was based on native bone depth measurements, aiming to balance a perceived adequate depth of platform for tendon attachment with adequate depth of remaining native bone for fixation. For graft use with the current model, the native DP would need to be prepared with a reciprocally-shaped bone 'trough' to seat the anchor, which may not require extensive preparation if the cortical bony shell has already avulsed with the tendon. However, fixing the 2mm deep bone anchor to native bone would be technically demanding, as 2mm is unlikely to hold screws unless driven across the attachment from the tendon to bone side, disrupting the engineered interface. Such technical assessments could indeed be tested in a cadaveric model. With such small amounts of engineered and native bone to place metalwork, a biocompatible bone adhesive with suitable bond strength for osteosynthesis would be ideal, but, although an area of promising developments, no product is currently in clinical use (Böker *et al*, 2019). Until a suitable bone adhesive is found, future work might consider designing the bone anchor as the fixation device itself, such as a screw, barb or flange. Although more advanced designs, results from this project have revealed the ideal positioning of the tendon attachment on the DP and the depth of native bone available at the interface, providing a basis for further clinically relevant testing.

6.3.3 Tendon-Bone Interface

The ideal engineered tendon-bone attachment would match both FDP-DP interface anatomy and mechanical strength. To improve the anatomical attachment area achieved in the current constructs, early future work would investigate a greater volume of fibrin gel and 3D bioprinting (discussed in *Section 6.3.1*) before considering modifications to the culture zone, such as engineering a larger attachment area and subsequently sculpting the ideal trapezoidal interface shape (discussed in *Section 5.6.1.1, Chapter 5*). The mechanical strength of the current model is unknown and fundamental future work should establish the ultimate tensile strength of these constructs before comparing those with future modifications aiming to increase attachment strength. To match native demands, the engineered interface needs to withstand from 20N (active FDP flexion) to 118N (fingertip pinch) (Schuind *et al*, 1992), and although the current model necessitates single surface bone anchor attachment, it is encouraging that constructs of fibrin and brushite have previously achieved an interface ultimate tensile strength in the same order of magnitude as embryonic ligaments (Paxton, Grover and Baar, 2010).

Augmentation of the engineered tendon-bone attachment will be vital to advance interface strength towards the ideal native levels, particularly with single surface tendon-bone attachment. As well as improving the topography of the hard-soft tissue interface (discussed in *Section 5.6.2.3, Chapter 5*), biological and chemical modifications should be explored. Bioactive molecules targeting cell adhesion can be added to ceramics to enhance their biological properties (Poli *et al*, 2019). Although ceramics can adsorb pro-adhesive proteins from serum (Hennessy *et al*, 2008), incorporation of additional ligands can improve cell adhesion, particularly with osteogenic cells (LeBaron and Athanasiou, 2000; Paxton *et al*, 2009; Poli *et al*, 2019) and could be particularly investigated for promotion of fibroblast adhesion in the attachment of the tendon analogue. The current model is biphasic, focusing on tendon-bone attachment as 2 tissue types, however a key line of subsequent enquiry is generation of the native fibrocartilaginous interface to improve the mechanical properties and reduce the stress focus across the soft-hard tissue junction. Chemical cellular stimulation with growth factors might be investigated, with bone morphogenetic protein (BMP)-2 an excellent starting candidate due to its ability to increase both fibrocartilage formation and mechanical strength at the healing tendon-

bone interface (Hashimoto *et al*, 2007; Kim *et al*, 2007; Chen *et al*, 2011). Growth factors can be incorporated into brushite cements for gradual release (Le Nihouannen 2008; Hofmann, 2009), and similar incorporation of BMP-2, potentially concentrated at the tendon attachment surface, could be trialled for fibrocartilage conversion in cells around the interface and effects on mechanical properties.

6.3.4 Cells

Establishing the model as a future 3D tool for investigating enthesis generation was an important purpose of the work. The model uses a stratified, rather than gradient, approach, most suited to distinct cell populations and the potential for cell-mediated metaplasia through heterotypic interactions at the interface. Examination of the co-culture interface would have formed the next stage of investigation in the current project if time. As well as electron microscopy to view the interconnection of the tendon analogue and bone anchor, the biological microenvironment requires examination. The key question is whether a replicate of the native fibrocartilaginous enthesis can be achieved, with principle analysis being of cellular function and the surrounding matrix. Such work could investigate interface expression of fibrocartilage markers, for example collagen type II and aggrecan with immunohistochemistry or gene expression measurement, or presence of glycosaminoglycans (GAGs) using a specific detection assay.

The current model was established with rat cells, and the natural progression towards a translational model is the use of human cells. Human fibroblasts and osteoblasts could be isolated from discarded surgical tendon/ligament and bone tissue, respectively, at operation with patient consent. Isolation methods would learn from the findings of isolation techniques in this project, for example using an osteoblast culture medium containing AA from the outset and avoiding disturbing bone explant cultures for at least 7 days after plating. The human cells could also follow the same characterisation experiments as performed in this project to test functionality and optimum co-culture medium choice, and then undergo investigations of interface strength and potential fibrocartilage formation as recently discussed. As a biphasic model, fibroblasts and osteoblasts would form the basis for initial future investigations, however further work on enthesis generation may consider seeding of either differentiated chondrocytes or mesenchymal stem cells (MSCs) inter-positioned at the

interface, aiming for chondrogenesis of MSCs through intercellular signals and paracrine factors. A single source of human MSCs for the whole model would be optimal for clinical use, but would rely on much preliminary work to establish osteogenic and tenogenic differentiation in the bone anchor and tendon analogue component, respectively, before consideration of the interface.

6.4 Conclusion

This thesis presents a journey from descriptive anatomy to novel *in vitro* culture design and production, standing to emphasise the role of anatomy and anatomists in tissue engineering. Tissue engineering provides an important prospect for therapeutic advances, and establishing the anatomical basis for the culture model in this project, as an example for any body region, endeavours to expedite its clinical translation. FDP avulsion injury not only brings significant individual disability but wider social and economic impact, and current treatments remain sub-optimal. Further work is required to advance the current FDP-DP model towards an implantable composite graft, but results from these anatomical investigations and *in vitro* culture trials are hoped to contribute to improved treatment, lessened impact, and better quality of life for patients with FDP avulsion injury.

Bibliography

- Abdul Azeem M, Marwan Y, Esmaeel A. Avulsion Injuries of the Flexor Digitorum Profundus Tendon: An Unclassified Pattern of Injury. *Hand Surg*. 2015; 20(2):319-321.
- Abrego MO, Shamrock AG. *Jersey Finger*. StatPearls [Internet]. Treasure Island, FL: StatPearls Publishing, 2019.
- Ahmed TA, Dare EV, Hincke M. Fibrin: a versatile scaffold for tissue engineering applications. *Tissue Eng Part B Rev*. 2008; 14(2):199-215.
- Al-Dubaiban WI, Al-Abdulkarim AO, Arafah MM, Al-Qattan MM. Flexor tendon-to-volar plate repair: an experimental study and 3 case reports. *J Hand Surg Am*. 2014; 39(11):2222-2227.
- Alghamdi NH, Killian M, Aitha B, Pohlig RT, Grävare Silbernagel K. Quantifying the Dimensions of Achilles Tendon Insertional Area Using Ultrasound Imaging A Validity and Reliability Study. *Muscles Ligaments Tendons J*. 2019; 9(4):544-551.
- Al-Qattan MM. Type 5 avulsion of the insertion of the flexor digitorum profundus tendon. *J Hand Surg Br*. 2001; 26(5):427-431.
- Al-Qattan MM, Al-Turaiki TM, Al-Zahrani AY, Al-Harbi MS, Al-Kahtani FS. A new technique of flexor profundus repair in the distal part of zone I: inclusion of the palmar plate. *J Hand Surg Eur Vol*. 2010; 35(6):459-463.
- Al-Qattan MM. Suturing of the flexor digitorum profundus tendon to the entire volar plate in distal zone I injuries. *J Plast Surg Hand Surg*. 2016a; 50(2):119-124.
- Al-Qattan MM. Use of the Volar Plate of the Distal Interphalangeal Joint as a Distally Based Flap in Flexor Tendon Surgery. *J Hand Surg Am*. 2016b; 41(2):287-290.
- Alsaykhan HM. *Design, development, and assessment of novel 3-dimensional co-culture systems to model musculoskeletal interfaces*. (Ph.D. Thesis). Edinburgh: University of Edinburgh, 2019.
- Amini AR, Laurencin CT, Nukavarapu SP. Bone tissue engineering: recent advances and challenges. *Crit Rev Biomed Eng*. 2012; 40(5):363-408.
- Angeline ME, Rodeo SA. Biologics in the management of rotator cuff surgery. *Clin Sports Med*. 2012; 31(4):645-663.
- Angermann P, Lohmann M. Injuries to the hand and wrist. A study of 50, 272 injuries. *J Hand Surg Br*. 1993; 18(5):642-644.
- Antoni D, Burckel H, Josset E, Noel G. Three-dimensional cell culture: a breakthrough in vivo. *Int J Mol Sci*. 2015; 16(3):5517-5527.
- Apostolakos J, Durant TJ, Dwyer CR, Russell RP, Weinreb JH, Alaei F, Beitzel K, McCarthy MB, Cote MP, Mazzocca AD. The enthesis: a review of the tendon-to-bone insertion. *Muscles Ligaments Tendons J*. 2014; 4(3):333-342.
- Armitage OE, Oyen ML. Hard-soft tissue interface engineering. *Adv Exp Med Biol*. 2015; 881:187-204.
- Ashton BA, Abdullah F, Cave J, Williamson M, Sykes BC, Couch M, Poser JW. Characterization of cells with high alkaline phosphatase activity derived from human

- bone and marrow: preliminary assessment of their osteogenicity. *Bone*. 1985; 6(5):313-319.
- Azeem MA, Marwan Y, Morshidy AE, Esmaeel A, Zakaria Y. A new classification scheme for closed avulsion injuries of the flexor digitorum profundus tendon. *J Hand Surg Asian Pac Vol*. 2017; 22(1):46-52.
- Bachoura A, Ferikes AJ, Lubahn JD. A review of mallet finger and jersey finger injuries in the athlete. *Curr Rev Musculoskelet Med*. 2017; 10(1):1-9.
- Baker BM, Nathan AS, Gee AO, Mauck RL. The influence of an aligned nanofibrous topography on human mesenchymal stem cell fibrochondrogenesis. *Biomaterials*. 2010; 31(24):6190-6200.
- Bakker AD, Klein-Nulend J. Osteoblast isolation from murine calvaria and long bones. In Helfrich MH, Ralston SH (Eds) *Bone research protocols. Methods in molecular biology (methods and protocols)*, vol 816. Totowa, NJ: Humana Press, 2012, pp 19-29.
- Bayer ML, Yeung CY, Kadler KE, Qvortrup K, Baar K, Svensson RB, Magnusson SP, Krogsgaard M, Koch M, Kjaer M. The initiation of embryonic-like collagen fibrillogenesis by adult human tendon fibroblasts when cultured under tension. *Biomaterials*. 2010; 31(18):4889-4897.
- Beaulieu ML, Carey GE, Schlecht SH, Wojtys EM, Ashton-Miller JA. Quantitative comparison of the microscopic anatomy of the human ACL femoral and tibial entheses. *J Orthop Res*. 2015; 33(12):1811-1817.
- Beaulieu ML, Carey GE, Schlecht SH, Wojtys EM, Ashton-Miller JA. On the heterogeneity of the femoral enthesis of the human ACL: microscopic anatomy and clinical implications. *J Exp Orthop*. 2016; 3(1):14.
- Bedi A, Fox AJ, Kovacevic D, Deng XH, Warren RF, Rodeo SA. Doxycycline-mediated inhibition of matrix metalloproteinases improves healing after rotator cuff repair. *Am J Sports Med*. 2010; 38(2):308-317.
- Bellows CG, Aubin JE, Heersche JN, Antosz ME. Mineralized bone nodules formed in vitro from enzymatically released rat calvaria cell populations. *Calcif Tissue Int*. 1986; 38(3):143-154.
- Benjamin M, Evans EJ, Copp L. The histology of tendon attachments to bone in man. *J Anat*. 1986; 149:89-100.
- Benjamin M, Evans EJ, Rao RD, Findlay JA, Pemberton DJ. Quantitative differences in the histology of the attachment zones of the meniscal horns in the knee joint of man. *J Anat*. 1991; 177:127-134.
- Benjamin M, Ralphs JR. Functional and developmental anatomy of tendons and ligaments. In Gordon SL, Blair SJ, Fine LJ (Eds) *Repetitive motion disorders of the upper extremity*. Rosemont, IL: American Academy of Orthopaedic Surgeons, 1995, pp 185-203.
- Benjamin M, Ralphs JR. Fibrocartilage in tendons and ligaments — an adaptation to compressive load. *J Anat*. 1998; 193(Pt 4): 481–494.
- Benjamin M, McGonagle D. The anatomical basis for disease localisation in seronegative spondyloarthropathy at entheses and related sites. *J Anat*. 2001; 199(Pt 5):503-526.
- Benjamin M, Kumai T, Milz S, Boszczyk BM, Boszczyk AA, Ralphs JR. The skeletal attachment of tendons—tendon "entheses". *Comp Biochem Physiol A Mol Integr Physiol*. 2002; 133(4):931-945.

- Benjamin M, Ralphs JR. Biology of fibrocartilage cells. *Int Rev Cytol.* 2004; 233:1-45.
- Benjamin M, Redman S, Milz S, Büttner A, Amin A, Moriggl B, Brenner E, Emery P, McGonagle D, Bydder G. Adipose tissue at entheses: the rheumatological implications of its distribution. A potential site of pain and stress dissipation? *Ann Rheum Dis.* 2004a; 63(12):1549-1555.
- Benjamin M, Moriggl B, Brenner E, Emery P, McGonagle D, Redman S. The "enthesis organ" concept: why enthesopathies may not present as focal insertional disorders. *Arthritis Rheum.* 2004b; 50(10):3306-3313.
- Benjamin M, Toumi H, Ralphs JR, Bydder G, Best TM, Milz S. Where tendons and ligaments meet bone: attachment sites ('entheses') in relation to exercise and/or mechanical load. *J Anat.* 2006; 208(4):471-490.
- Benjamin M, McGonagle D. Histopathologic changes at "synovio-entheseal complexes" suggesting a novel mechanism for synovitis in osteoarthritis and spondylarthritis. *Arthritis Rheum.* 2007; 56(11):3601-3609.
- Benjamin M, Toumi H, Suzuki D, Redman S, Emery P, McGonagle D. Microdamage and altered vascularity at the enthesis-bone interface provides an anatomic explanation for bone involvement in the HLA-B27-associated spondylarthritides and allied disorders. *Arthritis Rheum.* 2007; 56(1):224-233.
- Benjamin M, McGonagle D. Enteses: tendon and ligament attachment sites. *Scand J Med Sci Sports.* 2009; 19(4):520-527.
- Beresford JN, Graves SE, Smoothy CA. Formation of mineralized nodules by bone derived cells in vitro: a model of bone formation? *Am J Med Genet.* 1993; 45(2):163-178.
- Bessa PC, Casal M, Reis RL. Bone morphogenetic proteins in tissue engineering: the road from laboratory to clinic, part II (BMP delivery). *J Tissue Eng Regen Med.* 2008; 2(2-3):81-96.
- Bicho D, Pina S, Oliveira JM, Reis RL. In vitro mimetic models for the bone-cartilage interface regeneration. *Adv Exp Med Biol.* 2018; 1059:373-394.
- Biermann H. Die knochenbildung im bereich periostaler-diaphysärer sehnen- und bandansätze. *Z Zellforsch.* 1957; 46:635-671.
- Biewener AA, Fazzalari NL, Konieczynski DD, Baudinette RV. Adaptive changes in trabecular architecture in relation to functional strain patterns and disuse. *Bone.* 1996; 19(1):1-8.
- Binks DA, Bergin D, Freemont AJ, Hodgson RJ, Yonenaga T, McGonagle D, Radjenovic A. Potential role of the posterior cruciate ligament synovio-entheseal complex in joint effusion in early osteoarthritis: a magnetic resonance imaging and histological evaluation of cadaveric tissue and data from the Osteoarthritis Initiative. *Osteoarthritis Cartilage.* 2014; 22(9):1310-1317.
- Bland YS, Ashhurst DE. Fetal and postnatal development of the patella, patellar tendon and suprapatella in the rabbit; changes in the distribution of the fibrillar collagens. *J Anat.* 1997; 190(Pt 3):327-342.
- Blitz E, Viukov S, Sharir A, Shwartz Y, Galloway JL, Pryce BA, Johnson RL, Tabin CJ, Schweitzer R, Zelzer E. Bone ridge patterning during musculoskeletal assembly is mediated through SCX regulation of bmp4 at the tendon-skeleton junction. *Dev Cell.* 2009; 17(6):861-873.

- Blitz E, Sharir A, Akiyama H, Zelzer E. Tendon-bone attachment unit is formed modularly by a distinct pool of Scx- and Sox9-positive progenitors. *Development*. 2013; 140(13):2680-2690.
- Bois AJ, Johnston G, Classen D. Spontaneous flexor tendon ruptures of the hand: case series and review of the literature. *J Hand Surg Am*. 2007; 32(7):1061-1071.
- Böker KO, Richter K, Jäckle K, Taheri S, Grunwald I, Borcharding K, von Byern J, Hartwig A, Wildemann B, Schilling AF, Lehmann W. Current state of bone adhesives-necessities and hurdles. *Materials (Basel)*. 2019; 12(23):3975.
- Bond S, Rust P, Boland M. The accommodation of bone anchors within the distal phalanx for repair of flexor digitorum profundus avulsions. *J Hand Surg Am*. 2019; 44(11):986.e1-986.e6.
- Boyer MI, Gelberman RH, Burns ME, Dinopoulos H, Hofem R, Silva MJ. Intrasynovial flexor tendon repair. An experimental study comparing low and high levels of in vivo force during rehabilitation in canines. *J Bone Joint Surg Am*. 2001; 83(6):891-899.
- Boyer MI, Harwood F, Ditsios K, Amiel D, Gelberman RH, Silva MJ. Two-portal repair of canine flexor tendon insertion site injuries: histologic and immunohistochemical characterization of healing during the early postoperative period. *J Hand Surg Am*. 2003; 28(3):469-474.
- Boyer MI. Flexor tendon biology. *Hand Clin*. 2005; 21(2):159-66.
- Boyes JH, Wilson JN, Smith JW. Flexor-tendon ruptures in the forearm and hand. *J Bone Joint Surg Am*. 1960; 42-A: 637-646.
- Boys AJ, McCorry MC, Rodeo S, Bonassar LJ, Estroff LA. Next generation tissue engineering of orthopaedic soft tissue-to-bone interfaces. *MRS Commun*. 2017; 7(3):289-308.
- Brar R, Owen JR, Melikian R, Gaston RG, Wayne JS, Isaacs JE. Reattachment of flexor digitorum profundus avulsion: biomechanical performance of 3 techniques. *J Hand Surg Am*. 2014; 39(11):2214-2219.
- Braun B, Bogle A, Wiesler E. Morphometric analysis of distal interphalangeal joint and implications for arthrodesis with a headless compression screw. *J Surg Orthop Adv*. 2015; 24(1):5-11.
- Bright DS, Urbaniak JS. Direct measurements of flexor tendon tension during active and passive digit motion and its application to flexor tendon surgery. *Orthop Trans*. 1977; 1:4-5 (abstr).
- Bronstein JA, Woon CY, Farnebo S, Behn AW, Schmitt T, Pham H, Castillo AB, Chang J. Physicochemical decellularization of composite flexor tendon-bone interface grafts. *Plast Reconstr Surg*. 2013; 132(1):94-102.
- Brooks PM. The burden of musculoskeletal disease—a global perspective. *Clin Rheumatol*. 2006; 25(6):778-781.
- Bruno JG, Sivils JC. Studies of DNA aptamer oligonucleotide and picogreen fluorescence interactions in buffer and serum. *J Fluoresc*. 2016; 26(4):1479-1487.
- Brustein M, Pellegrini J, Choueka J, Heminger H, Mass D. Bone suture anchors versus the pullout button for repair of distal profundus tendon injuries: a comparison of strength in human cadaveric hands. *J Hand Surg Am*. 2001; 26(3):489-96.
- Buller LT, Best MJ, Baraga MG, Kaplan LD. Trends in anterior cruciate ligament reconstruction in the united states. *Orthop J Sports Med*. 2014; 3(1):2325967114563664.

- Bunnell S. *Surgery of the hand*, 2nd ed. Philadelphia, PA: JB Lippincott, 1948, pp 381-466.
- Burkhart SS. The deadman theory of suture anchors: observations along a south Texas fence line. *Arthroscopy*. 1995; 11(1):119-123.
- Butler DL, Juncosa-Melvin N, Boivin GP, Galloway MT, Shearn JT, Gooch C, Awad H. Functional tissue engineering for tendon repair: a multidisciplinary strategy using mesenchymal stem cells, bioscaffolds, and mechanical stimulation. *J Orthop Res*. 2008; 26(1):1-9.
- Bynum DK Jr, Gilbert JA. Avulsion of the flexor digitorum profundus: anatomic and biomechanical considerations. *J Hand Surg Am*. 1988; 13(2):222-227.
- Cabbabe EB, Korock SW. Wound healing in vitamin C-deficient and nondeficient guinea pigs: a pilot study. *Ann Plast Surg*. 1986; 17(4):330-334.
- Calejo I, Costa-Almeida R, Gonçalves AI, Berdecka D, Reis RL, Gomes ME. Bi-directional modulation of cellular interactions in an in vitro co-culture model of tendon-to-bone interface. *Cell Prolif*. 2018; 51(6):e12493.
- Calejo I, Costa-Almeida R, Gomes ME. Cellular complexity at the interface: challenges in entheses tissue engineering. *Adv Exp Med Biol*. 2019; 1144:71-90.
- Calve S, Dennis RG, Kosnik PE 2nd, Baar K, Grosh K, Arruda EM. Engineering of functional tendon. *Tissue Eng*. 2004; 10(5-6):755-761.
- Chan BP, Leong KW. Scaffolding in tissue engineering: general approaches and tissue-specific considerations. *Eur Spine J*. 2008; 17(Suppl 4):467-479.
- Chandrasekaran S, Pankow M, Peters K, Huang HS. Composition and structure of porcine digital flexor tendon-bone insertion tissues. *J Biomed Mater Res A*. 2017; 105(11):3050-3058.
- Chang CB, Seong SC, Kim TK. Preoperative magnetic resonance assessment of patellar tendon dimensions for graft selection in anterior cruciate ligament reconstruction. *Am J Sports Med*. 2009; 37(2):376-382.
- Chen CH, Chang CH, Wang KC, Su CI, Liu HT, Yu CM, Wong CB, Wang IC, Whu SW, Liu HW. Enhancement of rotator cuff tendon-bone healing with injectable periosteum progenitor cells-BMP-2 hydrogel in vivo. *Knee Surg Sports Traumatol Arthrosc*. 2011; 19(9):1597-1607.
- Chen M, Le DQ, Kjems J, Bünger C, Lysdahl H. Improvement of distribution and osteogenic differentiation of human mesenchymal stem cells by hyaluronic acid and β -tricalcium phosphate-coated polymeric scaffold in vitro. *Biores Open Access*. 2015; 4(1):363-373.
- Chen X, Macica C, Nasiri A, Judex S, Broadus AE. Mechanical regulation of PTHrP expression in entheses. *Bone*. 2007; 41(5):752-759.
- Chepla KJ, Goitz RJ, Fowler JR. Anatomy of the flexor digitorum profundus insertion. *J Hand Surg Am*. 2015; 40(2):240-244.
- Cheriyian T, Neuhaus V, Mudgal CS. Bony avulsion injury of flexor digitorum profundus -- description of a new subtype. *J Hand Surg Eur Vol*. 2013; 38(1):91-92.
- Choueka J, Heminger H, Mass DP. Cyclical testing of zone II flexor tendon repairs. *J Hand Surg Am*. 2000; 25(6):1127-34.
- Chu JY, Chen T, Awad HA, Elfar J, Hammert WC. Comparison of an all-inside suture technique with traditional pull-out suture and suture anchor repair techniques for flexor digitorum profundus attachment to bone. *J Hand Surg Am*. 2013; 38(6):1084-1090.

- Chu TM, Orton DG, Hollister SJ, Feinberg SE, Halloran JW. Mechanical and in vivo performance of hydroxyapatite implants with controlled architectures. *Biomaterials*. 2002; 23(5):1283-1293.
- Clayton RA, Court-Brown CM. The epidemiology of musculoskeletal tendinous and ligamentous injuries. *Injury*. 2008; 39(12):1338-1344.
- Cook JL, Purdam CR. Is tendon pathology a continuum? A pathology model to explain the clinical presentation of load-induced tendinopathy. *Br J Sports Med*. 2009; 43(6):409-416.
- Cooper JO, Bumgardner JD, Cole JA, Smith RA, Haggard WO. Co-cultured tissue-specific scaffolds for tendon/bone interface engineering. *J Tissue Eng*. 2014; 5:2041731414542294.
- Cooper RR, Misol S. Tendon and ligament insertion. A light and electron microscopic study. *J Bone Joint Surg Am*. 1970; 52(1):1-20.
- Corry IS, Webb JM, Clingeffer AJ, Pinczewski LA. Arthroscopic reconstruction of the anterior cruciate ligament. A comparison of patellar tendon autograft and four-strand hamstring tendon autograft. *Am J Sports Med*. 1999; 27(4):444-454.
- Dai C, Guo L, Yang L, Wu Y, Gou J, Li B. Regional fibrocartilage variations in human anterior cruciate ligament tibial insertion: a histological three-dimensional reconstruction. *Connect Tissue Res*. 2015; 56(1):18-24.
- Darowish M, Brenneman R, Bigger J. Dimensional analysis of the distal phalanx with consideration of distal interphalangeal joint arthrodesis using a headless compression screw. *Hand (N Y)*. 2015; 10(1):100-104.
- de Jong JP, Nguyen JT, Sonnema AJ, Nguyen EC, Amadio PC, Moran SL. The incidence of acute traumatic tendon injuries in the hand and wrist: a 10-year population-based study. *Clin Orthop Surg*. 2014; 6(2):196-202.
- Demirag B, Sarisozen B, Ozer O, Kaplan T, Ozturk C. Enhancement of tendon-bone healing of anterior cruciate ligament grafts by blockage of matrix metalloproteinases. *J Bone Joint Surg Am*. 2005; 87(11):2401-2410.
- Demoor M, Ollitrault D, Gomez-Leduc T, Bouyoucef M, Hervieu M, Fabre H, Lafont J, Denoix JM, Audigié F, Mallein-Gerin F, Legendre F, Galera P. Cartilage tissue engineering: molecular control of chondrocyte differentiation for proper cartilage matrix reconstruction. *Biochim Biophys Acta*. 2014; 1840(8):2414-2440.
- Dennis RG, Kosnik PE 2nd. Excitability and isometric contractile properties of mammalian skeletal muscle constructs engineered in vitro. *In Vitro Cell Dev Biol Anim*. 2000; 36(5):327-335.
- de Putter CE, Selles RW, Polinder S, Panneman MJ, Hovius SE, van Beeck EF. Economic impact of hand and wrist injuries: health-care costs and productivity costs in a population-based study. *J Bone Joint Surg Am*. 2012; 94(9):e56.
- Derwin KA, Galatz LM, Ratcliffe A, Thomopoulos S. Enthesis repair: challenges and opportunities for effective tendon-to-bone healing. *J Bone Joint Surg Am*. 2018; 100(16):e109(1-7).
- Dias JJ, Garcia-Elias M. Hand injury costs. *Injury*. 2006; 37(11): 1071-1077.
- Dickerson DA, Misk TN, Van Sickle DC, Breur GJ, Nauman EA. In vitro and in vivo evaluation of orthopedic interface repair using a tissue scaffold with a continuous hard tissue-soft tissue transition. *J Orthop Surg Res*. 2013; 8:18

- Ditsios K, Boyer MI, Kusano N, Gelberman RH, Silva MJ. Bone loss following tendon laceration, repair and passive mobilization. *J Orthop Res*. 2003a; 21(6):990-996.
- Ditsios K, Leversedge FJ, Gelberman RH, Silva MJ, Boyer MI. Neovascularization of the flexor digitorum profundus tendon after avulsion injury: an in vivo canine study. *J Hand Surg Am*. 2003b; 28(2):231-236.
- Dolgo-Saburoff B. Über ursprung und insertion der skelettmuskeln. *Anatomischer Anzeiger*. 1929; 68:80-87.
- Dörfl J. Vessels in the region of tendinous insertions. I. Chondroapophyseal insertion. *Folia Morphol*. 1969a; 17(1):74-78.
- Dörfl J. Vessels in the region of tendinous insertions. II. Diaphysoperiosteal insertion. *Folia Morphol*. 1969b; 17(1):79-82.
- Doschak MR, Zernicke RF. Structure, function and adaptation of bone-tendon and bone-ligament complexes. *J Musculoskelet Neuronal Interact*. 2005; 5(1):35-40.
- Drake DB, Tilt AC, DeGeorge BR. Acellular flexor tendon allografts: a new horizon for tendon reconstruction. *J Hand Surg Am*. 2013; 38(12):2491-2495.
- Du D, Furukawa K, Ushida T. Oscillatory perfusion seeding and culturing of osteoblast-like cells on porous beta-tricalcium phosphate scaffolds. *J Biomed Mater Res A*. 2008; 86(3):796-803.
- Eglseder WA, Russell JM. Type IV flexor digitorum profundus avulsion. *J Hand Surg Am*. 1990; 15(5):735-739.
- Engler AJ, Sen S, Sweeney HL, Discher DE. Matrix elasticity directs stem cell lineage specification. *Cell*. 2006; 126(4):677-689.
- Evans EJ, Benjamin M, Pemberton DJ. Fibrocartilage in the attachment zones of the quadriceps tendon and patellar ligament of man. *J Anat*. 1990; 171:155-162.
- Fedorczyk JM. Tennis elbow: blending basic science with clinical practice. *J Hand Ther*. 2006; 19(2):146-153.
- Felder JJ, Guseila LM, Saranathan A, Shary TJ, Lippitt SB, Elias JJ. Mechanical properties of the flexor digitorum profundus tendon attachment. *J Hand Microsurg*. 2013; 5(2):54-57.
- Font Tellado S, Balmayor ER, Van Griensven M. Strategies to engineer tendon/ligament-to-bone interface: Biomaterials, cells and growth factors. *Adv Drug Deliv Rev*. 2015; 94:126-140.
- Font Tellado S, Bonani W, Balmayor ER, Foehr P, Motta A, Migliaresi C, van Griensven M. Fabrication and characterization of biphasic silk fibroin scaffolds for tendon/ligament-to-bone tissue engineering. *Tissue Eng Part A*. 2017; 23(15-16):859-872.
- Fox PM, Farnebo S, Lindsey D, Chang J, Schmitt T, Chang J. Decellularized human tendon-bone grafts for composite flexor tendon reconstruction: a cadaveric model of initial mechanical properties. *J Hand Surg Am*. 2013; 38(12):2323-2328.
- François RJ, Braun J, Khan MA. Entheses and enthesitis: a histopathologic review and relevance to spondyloarthritides. *Curr Opin Rheumatol*. 2001; 13(4):255-264.
- Franko OI, Winters TM, Tirrell TF, Hentzen ER, Lieber RL. Moment arms of the human digital flexors. *J Biomech*. 2011; 44(10):1987-1990.
- Freilich AM. Evaluation and treatment of jersey finger and pulley injuries in athletes. *Clin Sports Med*. 2015; 34(1):151-166.

- Frowen P, Benjamin M. Variations in the quality of uncalcified fibrocartilage at the insertions of the extrinsic calf muscles in the foot. *J Anat.* 1995; 186(Pt 2):417-421.
- Fu Q, Saiz E, Rahaman MN, Tomsia AP. Bioactive glass scaffolds for bone tissue engineering: state of the art and future perspectives. *Mater Sci Eng C Mater Biol Appl.* 2011; 31(7):1245-1256.
- Fujisawa K, Hara K, Takami T, Okada S, Matsumoto T, Yamamoto N, Sakaida I. Evaluation of the effects of ascorbic acid on metabolism of human mesenchymal stem cells. *Stem Cell Res Ther.* 2018; 9:93.
- Fukuta S, Oyama M, Kavalkovich K, Fu FH, Niyibizi C. Identification of types II, IX and X collagens at the insertion site of the bovine achilles tendon. *Matrix Biol.* 1998; 17(1):65-73.
- Galanis N, Savvidis M, Tsifountoudis I, Gkouvas G, Alafropatis I, Kirkos J, Kellis E. Correlation between semitendinosus and gracilis tendon cross-sectional area determined using ultrasound, magnetic resonance imaging and intraoperative tendon measurements. *J Electromyogr Kinesiol.* 2016; 26:44-51.
- Galatz LM, Ball CM, Teefey SA, Middleton WD, Yamaguchi K. The outcome and repair integrity of completely arthroscopically repaired large and massive rotator cuff tears. *J Bone Joint Surg Am.* 2004; 86(2):219-224.
- Galatz LM, Rothermich SY, Zaegel M, Silva MJ, Havlioglu N, Thomopoulos S. Delayed repair of tendon to bone injuries leads to decreased biomechanical properties and bone loss. *J Orthop Res.* 2005; 23(6):1441-1447.
- Galatz LM, Sandell LJ, Rothermich SY, Das R, Mastny A, Havlioglu N, Silva MJ, Thomopoulos S. Characteristics of the rat supraspinatus tendon during tendon-to-bone healing after acute injury. *J Orthop Res.* 2006; 24(3):541-550.
- Galatz L, Rothermich S, Vanderploeg K, Petersen B, Sandell L, Thomopoulos S. Development of the the supraspinatus tendon-to-bone insertion: localized expression of extracellular matrix and growth factor genes. *J Orthop Res.* 2007; 25(12):1621-1628.
- Gallagher JA, Gundle R, Beresford JN. Isolation and culture of bone-forming cells (osteoblasts) from human bone. In Jones GE (Ed) *Human cell culture protocols. Methods in molecular medicine*, vol 2. Totowa, NJ: Humana Press, 1996, pp 233-262.
- Galvez MG, Crowe C, Farnebo S, Chang J. Tissue engineering in flexor tendon surgery: current state and future advances. *J Hand Surg Eur Vol.* 2014; 39(1):71-78.
- Gao J, Messner K. Quantitative comparison of soft tissue-bone interface at chondral ligament insertions in the rabbit knee joint. *J Anat.* 1996; 188(Pt 2):367-373.
- Gao J, Räsänen T, Persliden J, Messner K. The morphology of ligament insertions after failure at low strain velocity: an evaluation of ligament entheses in the rabbit knee. *J Anat.* 1996a; 189(Pt 1):127-133.
- Gao J, Messner K, Ralphs JR, Benjamin M. An immunohistochemical study of entheses development in the medial collateral ligament of the rat knee joint. *Anat Embryol.* 1996b; 194(4):399-406.
- Gartland A, Rumney RMH, Dillon JP, Gallagher JA. Isolation and culture of human osteoblasts. In Mitry R, Hughes R (Eds) *Human cell culture protocols. Methods in molecular biology (methods and protocols)*, vol 806. Totowa, NJ: Humana Press, 2012, pp 337-355.

- Gbureck U, Hölzel T, Biermann I, Barralet JE, Grover LM. Preparation of tricalcium phosphate/calcium pyrophosphate structures via rapid prototyping. *J Mater Sci Mater Med.* 2008; 19(4):1559-1563.
- Ge Z, Goh JC, Lee EH. Selection of cell source for ligament tissue engineering. *Cell Transplant.* 2005; 14(8):573-583.
- Gelberman R, Goldberg V, An KN, Banes A. Tendon. In: Woo SL-Y, Buckwalter JA (Eds) *Injury and repair of the musculoskeletal soft tissues.* Park Ridge, IL: American Academy of Orthopaedic Surgeons, 1988, pp 5–44.
- Gelberman RH, Boyer MI, Brodt MD, Winters SC, Silva MJ. The effect of gap formation at the repair site on the strength and excursion of intrasynovial flexor tendons. An experimental study on the early stages of tendon-healing in dogs. *J Bone Joint Surg Am.* 1999; 81(7):975-982.
- Genin GM, Kent A, Birman V, Wopenka B, Pasteris JD, Marquez PJ, Thomopoulos S. Functional grading of mineral and collagen in the attachment of tendon to bone. *Biophys J.* 2009; 97(4):976-985.
- Gerber C, Schneeberger AG, Perren SM, Nyffeler RW. Experimental rotator cuff repair. A preliminary study. *J Bone Joint Surg Am.* 1999; 81(9):1281-1290.
- Giannikas D, Athanaselis E, Matzaroglou C, Saridis A, Tyllianakis M. An unusual complication of Mitek suture anchor use in primary treatment of flexor digitorum profundus tendon laceration: a case report. *Cases J.* 2009; 2:9319.
- Gilbert TW, Sellaro TL, Badylak SF. Decellularization of tissues and organs. *Biomaterials.* 2006; 27(19):3675-3678.
- Gillig JD, Smith MD, Hutton WC, Jarrett CD. The effect of flexor digitorum profundus tendon shortening on jersey finger surgical repair: a cadaveric biomechanical study. *J Hand Surg Eur Vol.* 2015; 40(7):729-734.
- Goers L, Freemont P, Polizzi KM. Co-culture systems and technologies: taking synthetic biology to the next level. *J R Soc Interface.* 2014; 11(96):20140065.
- Goislard de Monsabert B, Rossi J, Berton E, Vigouroux L. Quantification of hand and forearm muscle forces during a maximal power grip task. *Med Sci Sports Exerc.* 2012; 44(10):1906-1916.
- Goldman SM, Barabino GA. Spatial engineering of osteochondral tissue constructs through microfluidically directed differentiation of mesenchymal stem cells. *Biores Open Access.* 2016; 5(1):109-117.
- Goodman HJ, Choueka J. Biomechanics of the flexor tendons. *Hand Clin.* 2005; 21(2):129-149.
- Grant I, Pandya A, Mahaffey PJ. The re-attachment of tendon and ligament avulsions. *J Hand Surg Br.* 2002; 27(4):337-341.
- Green FW Jr, Kaplan MM, Curtis LE, Levine PH. Effect of acid and pepsin on blood coagulation and platelet aggregation. A possible contributor to prolonged gastroduodenal mucosal hemorrhage. *Gastroenterology.* 1978; 74(1):38-43.
- Guinard D, Montanier F, Thomas D, Corcella D, Moutet F. The Mantero flexor tendon repair in zone 1. *J Hand Surg Br.* 1999; 24(2):148-151.
- Gulotta LV, Kovacevic D, Ehteshami JR, Dagher E, Packer JD, Rodeo SA. Application of bone marrow-derived mesenchymal stem cells in a rotator cuff repair model. *Am J Sports Med.* 2009; 37(11):2126-2133.

- Gunter GS. Traumatic avulsion of the insertion of flexor digitorum profundus. *Aust N Z J Surg.* 1960; 30:1-9.
- Hahn J, Wickham SF, Shih WM, Perrault SD. Addressing the instability of DNA nanostructures in tissue culture. *ACS Nano.* 2014; 8(9):8765-8775.
- Hairfield-Stein M, England C, Paek HJ, Gilbraith KB, Dennis R, Boland E, Kosnik P. Development of self-assembled, tissue-engineered ligament from bone marrow stromal cells. *Tissue Eng.* 2007; 13(4):703-710.
- Halát G, Negrin L, Koch T, Erhart J, Platzer P, Hajdu S, Streicher J. Biomechanical characteristics of suture anchor implants for flexor digitorum profundus repair. *J Hand Surg Am.* 2014; 39(2):256-261.
- Halát G, Negrin L, Erhart J, Ristl R, Hajdu S, Platzer P. Treatment options and outcome after bony avulsion of the flexor digitorum profundus tendon: a review of 29 cases. *Arch Orthop Trauma Surg.* 2017; 137(2):285-292.
- Halát G, Negrin LL, Unger E, Koch T, Streicher J, Erhart J, Platzer P, Hajdu S. Introduction of a new repair technique in bony avulsion of the FDP tendon: A biomechanical study. *Sci Rep.* 2018; 8(1):9906.
- Harryman DT 2nd, Mack LA, Wang KY, Jackins SE, Richardson ML, Matsen FA 3rd. Repairs of the rotator cuff. Correlation of functional results with integrity of the cuff. *J Bone Joint Surg Am.* 1991; 73(7):982-989.
- Hashimoto Y, Yoshida G, Toyoda H, Takaoka K. Generation of tendon-to-bone interface “entheses” with use of recombinant BMP-2 in a rabbit model. *J Orthop Res.* 2007; 25(11):1415-1424.
- Hayes A, Easton K, Devanaboyina PT, Wu JP, Kirk TB, Lloyd D. A review of methods to measure tendon dimensions. *J Orthop Surg Res.* 2019; 14(1):18.
- He P, Ng KS, Toh SL, Goh JC. In vitro ligament-bone interface regeneration using a trilineage coculture system on a hybrid silk scaffold. *Biomacromolecules.* 2012; 13(9):2692-2703.
- Hecker L, Baar K, Dennis RG, Bitar KN. Development of a three-dimensional physiological model of the internal anal sphincter bioengineered in vitro from isolated smooth muscle cells. *Am J Physiol Gastrointest Liver Physiol.* 2005; 289(2):G188-196.
- Hems T, Tillmann B. Tendon entheses of the human masticatory muscles. *Anat Embryol.* 2000; 202(3):201-208.
- Hennessy KM, Clem WC, Phipps MC, Sawyer AA, Shaikh FM, Bellis SL. The effect of RGD peptides on osseointegration of hydroxyapatite biomaterials. *Biomaterials.* 2008; 29(21):3075-3083.
- Hewett TE, Ford KR, Hoogenboom BJ, Myer GD. Understanding and preventing acl injuries: current biomechanical and epidemiologic considerations - update 2010. *N Am J Sports Phys Ther.* 2010; 5(4):234-251.
- Hofmann MP, Mohammed AR, Perrie Y, Gbureck U, Barralet JE. High-strength resorbable brushite bone cement with controlled drug-releasing capabilities. *Acta Biomater.* 2009; 5(1):43-49.
- Huang YC, Dennis RG, Larkin L, Baar K. Rapid formation of functional muscle in vitro using fibrin gels. *J Appl Physiol.* 2005; 98(2):706-713.

- Huang YC, Dennis RG, Baar K. Cultured slow vs. fast skeletal muscle cells differ in physiology and responsiveness to stimulation. *Am J Physiol Cell Physiol*. 2006; 291(1):C11-17.
- Huang YC, Khait L, Birla RK. Contractile three-dimensional bioengineered heart muscle for myocardial regeneration. *J Biomed Mater Res A*. 2007; 80(3):719-731.
- Hume MC, Gellman H, McKellop H, Brumfield RH Jr. Functional range of motion of the joints of the hand. *J Hand Surg Am*. 1990; 15(2):240-243.
- Huq S, George S, Boyce DE. Zone 1 flexor tendon injuries: a review of the current treatment options for acute injuries. *J Plast Reconstr Aesthet Surg*. 2013; 66(8):1023-1031.
- Im GI, Shin YW, Lee KB. Do adipose tissue-derived mesenchymal stem cells have the same osteogenic and chondrogenic potential as bone marrow-derived cells? *Osteoarthritis Cartilage*. 2005; 13(10):845-853.
- Imbriglia JE, Goldstein SA. Intratendinous ruptures of the flexor digitorum profundus tendon of the small finger. *J Hand Surg Am*. 1987; 12(6):985-991.
- Inoue N, Zakai AN, Thomas DB, Boykin AM, McFarland EG, Chao EYS. Quantitative analysis of trabecular orientation at the canine patellar tendon insertion site. *Trans Orthop Res Soc*. 1998; 23:555.
- Jagetia GC, Rajanikant GK, Mallikarjun Rao KV. Ascorbic acid increases healing of excision wounds of mice whole body exposed to different doses of gamma-radiation. *Burns*. 2007; 33(4):484-494.
- Jain DK, Kakarala G, Compson J, Singh R. Do the dimensions of the distal phalanges allow suture anchor fixation of the flexor digitorum profundus? A cadaver study. *J Hand Surg Eur Vol*. 2011; 36(8):698-700.
- Jain NB, Higgins LD, Losina E, Collins J, Blazar PE, Katz JN. Epidemiology of musculoskeletal upper extremity ambulatory surgery in the United States. *BMC Musculoskelet Disord*. 2014; 15:4.
- Jaiswal N, Haynesworth SE, Caplan AI, Bruder SP. Osteogenic differentiation of purified, culture-expanded human mesenchymal stem cells in vitro. *J Cell Biochem*. 1997; 64(2):295-312.
- James R, Kumbar SG, Laurencin CT, Balian G, Chhabra AB. Tendon tissue engineering: adipose-derived stem cell and GDF-5 mediated regeneration using electrospun matrix systems. *Biomed Mater*. 2011; 6(2):025011.
- Javazon EH, Beggs KJ, Flake AW. Mesenchymal stem cells: paradoxes of passaging. *Exp Hematol*. 2004; 32:414-425.
- Jiang J, Nicoll SB, Lu HH. Co-culture of osteoblasts and chondrocytes modulates cellular differentiation in vitro. *Biochem Biophys Res Commun*. 2005; 338(2):762-770.
- Jones GL, Walton R, Czernuszka J, Griffiths SL, El Haj AJ, Cartmell SH. Primary human osteoblast culture on 3D porous collagen-hydroxyapatite scaffolds. *J Biomed Mater Res A*. 2010; 94(4):1244-1250.
- Jones LJ, Gray M, Yue ST, Haugland RP, Singer VL. Sensitive determination of cell number using the CyQUANT cell proliferation assay. *J Immunol Methods*. 2001; 254(1-2):85-98.
- Jones RA, Reich CD, Dissanayake KN, Kristmundsdottir F, Findlater GS, Ribchester RR, Simmen MW, Gillingwater TH. NMJ-morph reveals principal components of synaptic

- morphology influencing structure-function relationships at the neuromuscular junction. *Open Biol.* 2016; 6(12).
- Kakinoki R. Secondary reconstructive options in failed fingertip and nail bed injuries. In: Duncan SFM (Ed) *Reoperative hand surgery*. New York, NY: Springer, 2012, pp 329-358.
- Kang N, Marsh D, Dewar D. The morbidity of the button-over-nail technique for zone 1 flexor tendon repairs. Should we still be using this technique? *J Hand Surg Eur Vol.* 2008; 33(5):566-570.
- Kannus P. Structure of the tendon connective tissue. *Scand J Med Sci Sports.* 2000; 10(6):312-320.
- Kapacee Z, Richardson SH, Lu Y, Starborg T, Holmes DF, Baar K, Kadler KE. Tension is required for fibripositor formation. *Matrix Biol.* 2008; 27(4):371-375.
- Kapickis M. New "loop" suture for FDP zone I injuries. *Tech Hand Up Extrem Surg.* 2009; 13(3):141-144.
- Kearney EM, Farrell E, Prendergast PJ, Campbell VA. Tensile strain as a regulator of mesenchymal stem cell osteogenesis. *Ann Biomed Eng.* 2010; 38(5):1767-1779.
- Keaveny TM, Morgan EF, Niebur GL, Yeh OC. Biomechanics of trabecular bone. *Annu Rev Biomed Eng.* 2001; 3:307-333.
- Kelsey JL, Praemer A, Nelson LM, Felberg A, Rice DP. *Upper extremity disorders: Frequency, impact and cost*, 1st ed. New York, NY: Churchill Livingstone, 1997.
- Killian ML, Cavinatto L, Galatz LM, Thomopoulos S. The role of mechanobiology in tendon healing. *J Shoulder Elbow Surg.* 2012; 21(2):228-237.
- Kim HJ, Kang SW, Lim HC, Han SB, Lee JS, Prasad L, Kim YJ, Kim BS, Park JH. The role of transforming growth factor-beta and bone morphogenetic protein with fibrin glue in healing of bone-tendon junction injury. *Connect Tissue Res.* 2007; 48(6):309-315.
- Kim HM, Galatz LM, Patel N, Das R, Thomopoulos S. Recovery potential after postnatal shoulder paralysis. An animal model of neonatal brachial plexus palsy. *J Bone Joint Surg Am.* 2009; 91(4):879-891.
- Kinney MA, Hookway TA, Wang Y, McDevitt TC. Engineering three-dimensional stem cell morphogenesis for the development of tissue models and scalable regenerative therapeutics. *Ann Biomed Eng.* 2014; 42(2):352-367.
- Knese K-H, Biermann H. Die knochenbildung an sehnen- und bandansätzen ursprünglich im bereich chondraler apophysen. *Z Zellforsch.* 1958; 49:142- 187.
- Koo TK, Li MY. A guideline of selecting and reporting intraclass correlation coefficients for reliability research. *J Chiropr Med.* 2016; 15(2):155-163.
- Kotobuki N, Kawagoe D, Nomura D, Katou Y, Muraki K, Fujimori H, Goto S, Ioku K, Ohgushi H. Observation and quantitative analysis of rat bone marrow stromal cells cultured in vitro on newly formed transparent beta-tricalcium phosphate. *J Mater Sci Mater Med.* 2006; 17(1):33-41.
- Kryger GS, Chong AK, Costa M, Pham H, Bates SJ, Chang J. A comparison of tenocytes and mesenchymal stem cells for use in flexor tendon tissue engineering. *J Hand Surg Am.* 2007; 32(5):597-605.
- Kubota H, Aoki M, Pruitt DL, Manske PR. Mechanical properties of various circumferential tendon suture techniques. *J Hand Surg Br.* 1996; 21(4):474-480.

- Kumai T, Takakura Y, Rufai A, Milz S, Benjamin M. The functional anatomy of the human anterior talofibular ligament in relation to ankle sprains. *J Anat.* 2002; 200(5):457-465.
- Kuntz LA, Rossetti L, Kunold E, Schmitt A, von Eisenhart-Rothe R, Bausch AR, Burgkart RH. Biomarkers for tissue engineering of the tendon-bone interface. *PLoS One.* 2018; 13(1):e0189668.
- Kurniawan NA, van Kempen THS, Sonneveld S, Rosalina TT, Vos BE, Jansen KA, Peters GWM, van de Vosse FN, Koenderink GH. Buffers strongly modulate fibrin self-assembly into fibrous networks. *Langmuir.* 2017; 33(25):6342-6352.
- Kursa K, Lattanza L, Diao E, Rempel D. In vivo flexor tendon forces increase with finger and wrist flexion during active finger flexion and extension. *J Orthop Res.* 2006; 24(4):763-769.
- Lam TC, Shrive NG, Frank CB. Variations in rupture site and surface strains at failure in the maturing rabbit medial collateral ligament. *J Biomech Eng.* 1995; 117(4):455-461.
- Lane LB, Bullough PG. Age-related changes in the thickness of the calcified zone and the number of tidemarks in adult human articular cartilage. *J Bone Joint Surg Br.* 1980; 62(3):372-375.
- Langer R, Vacanti JP. Tissue engineering. *Science.* 1993; 260(5110):920-926.
- Larkin LM, Calve S, Kostrominova TY, Arruda EM. Structure and functional evaluation of tendon-skeletal muscle constructs engineered in vitro. *Tissue Eng.* 2006; 12(11):3149-3158.
- Latendresse K, Dona E, Scougall PJ, Schreuder FB, Puchert E, Walsh WR. Cyclic testing of pullout sutures and micro-mitek suture anchors in flexor digitorum profundus tendon distal fixation. *J Hand Surg Am.* 2005; 30(3):471-478.
- Latenser S, Keller H, Leupin O, Rausch M, Graf-Hausner U, Rimann M. A novel microplate 3D bioprinting platform for the engineering of muscle and tendon tissues. *SLAS Technol.* 2018; 23(6):599-613.
- LeBaron RG, Athanasiou KA. Extracellular matrix cell adhesion peptides: functional applications in orthopedic materials. *Tissue Eng.* 2000; 6(2):85-103.
- Leddy JP, Packer JW. Avulsion of the profundus tendon insertion in athletes. *J Hand Surg Am.* 1977; 2(1):66-69.
- Leddy JP. Avulsions of the flexor digitorum profundus. *Hand Clin.* 1985; 1(1):77-83.
- Lee SK, Fajardo M, Kardashian G, Klein J, Tsai P, Christoforou D. Repair of flexor digitorum profundus to distal phalanx: a biomechanical evaluation of four techniques. *J Hand Surg Am.* 2011; 36(10):1604-1609.
- Le Nihouannen D, Hacking SA, Gbureck U, Komarova SV, Barralet JE. The use of RANKL-coated brushite cement to stimulate bone remodelling. *Biomaterials.* 2008; 29(22):3253-3259.
- Leversedge FJ, Ditsios K, Goldfarb CA, Silva MJ, Gelberman RH, Boyer MI. Vascular anatomy of the human flexor digitorum profundus tendon insertion. *J Hand Surg Am.* 2002; 27(5):806-812.
- Levy RA, Chu TM, Halloran JW, Feinberg SE, Hollister S. CT-generated porous hydroxyapatite orbital floor prosthesis as a prototype bioimplant. *AJNR Am J Neuroradiol.* 1997; 18(8):1522-1525.

- Liang X, Graf BW, Boppart SA. Imaging engineered tissues using structural and functional optical coherence tomography. *J Biophotonics*. 2009; 2(11):643-655.
- Liao HT, Chen CT. Osteogenic potential: comparison between bone marrow and adipose-derived mesenchymal stem cells. *World J Stem Cells*. 2014; 6(3):288-295.
- Lima CC, Pereira AP, Silva JR, Oliveira LS, Resck MC, Grechi CO, Bernardes MT, Olímpio FM, Santos AM, Incerpi EK, Garcia JA. Ascorbic acid for healing of skin wounds in rats. *Braz J Biol*. 2009; 69(4):1195-1201.
- Lin TW, Cardenas L, Soslowsky LJ. Biomechanics of tendon injury and repair. *J Biomech*. 2004; 37(6):865-877.
- Liu C-F, Breidenbach A, Aschbacher-Smith L, Butler D, Wylie C. A role for hedgehog signaling in the differentiation of the insertion site of the patellar tendon in the mouse. *PLoS One*. 2013; 8(6):e65411.
- Liu Q, Cen L, Yin S, Chen L, Liu G, Chang J, Cui L. A comparative study of proliferation and osteogenic differentiation of adipose-derived stem cells on akermanite and beta-TCP ceramics. *Biomaterials*. 2008; 29(36):4792-4799.
- Liu SH, Panossian V, al-Shaikh R, Tomin E, Shepherd E, Finerman GA, Lane JM. Morphology and matrix composition during early tendon to bone healing. *Clin Orthop Relat Res*. 1997; 339:253-260.
- Liu W, Lipner J, Xie J, Manning CN, Thomopoulos S, Xia Y. Nanofiber scaffolds with gradients in mineral content for spatial control of osteogenesis. *ACS Appl Mater Interfaces*. 2014; 6(4):2842-2849.
- Longati P, Jia X, Eimer J, Wagman A, Witt MR, Rehnmark S, Verbeke C, Toftgård R, Löhr M, Heuchel RL. 3D pancreatic carcinoma spheroids induce a matrix-rich, chemoresistant phenotype offering a better model for drug testing. *BMC Cancer*. 2013; 13:95.
- Lu HH, Thomopoulos S. Functional attachment of soft tissues to bone: development, healing, and tissue engineering. *Annu Rev Biomed Eng*. 2013; 15:201-226.
- Lu H, Chen C, Xie S, Tang Y, Qu J. Tendon healing in bone tunnel after human anterior cruciate ligament reconstruction: A systematic review of histological results. *J Knee Surg*. 2019; 32(5):454-462.
- Lunn PG, Lamb DW. "Rugby finger"--avulsion of profundus of ring finger. *J Hand Surg Br*. 1984; 9(1):69-71.
- Ma J, Goble K, Smietana M, Kostrominova T, Larkin L, Arruda EM. Morphological and functional characteristics of three-dimensional engineered bone-ligament-bone constructs following implantation. *J Biomech Eng*. 2009; 131(10):101017.
- Ma J, Smietana MJ, Kostrominova TY, Wojtys EM, Larkin LM, Arruda EM. Three-dimensional engineered bone-ligament-bone constructs for anterior cruciate ligament replacement. *Tissue Eng Part A*. 2012; 18(1-2):103-116.
- Mahalingam VD, Behbahani-Nejad N, Ronan EA, Olsen TJ, Smietana MJ, Wojtys EM, Wellik DM, Arruda EM, Larkin LM. Fresh versus frozen engineered bone-ligament-bone grafts for sheep anterior cruciate ligament repair. *Tissue Eng Part C Methods*. 2015; 21(6):548-556.
- Malafaya PB, Reis RL. Bilayered chitosan-based scaffolds for osteochondral tissue engineering: influence of hydroxyapatite on in vitro cytotoxicity and dynamic

- bioactivity studies in a specific double-chamber bioreactor. *Acta Biomater.* 2009; 5(2):644-660.
- Malerich MM, Baird RA, McMaster W, Erickson JM. Permissible limits of flexor digitorum profundus tendon advancement--an anatomic study. *J Hand Surg Am.* 1987; 12(1):30-33.
- Maniatopoulos C, Sodek J, Melcher AH. Bone formation in vitro by stromal cells obtained from bone marrow of young adult rats. *Cell Tissue Res.* 1988; 254(2):317-330.
- Manske PR, Lesker PA. Avulsion of the ring finger flexor digitorum profundus tendon: an experimental study. *Hand.* 1978; 10(1):52-55.
- Manske PR, Lesker PA. Nutrient pathways of flexor tendons in primates. *J Hand Surg Am.* 1982; 7(5):436-444.
- Manske PR, Lesker PA. Palmar aponeurosis pulley. *J Hand Surg Am.* 1983; 8(3):259-263.
- Manske PR, Lesker PA. Flexor tendon nutrition. *Hand Clin.* 1985; 1(1):13-24.
- Marco RA, Sharkey NA, Smith TS, Zissimos AG. Pathomechanics of closed rupture of the flexor tendon pulleys in rock climbers. *J Bone Joint Surg Am.* 1998; 80(7):1012-1019.
- Martini FH, Timmons MJ, Tallitsch RB. *Human anatomy*, 8th ed. Boston, MA: Pearson, 2015.
- Mason ML, Shearon CG. The process of tendon repair: an experimental study of tendon suture and tendon graft. *Archives of Surgery.* 1932; 25(4):615-692.
- Materna T, Rolf HJ, Napp J, Schulz J, Gelinsky M, Schliephake H. In vitro characterization of three-dimensional scaffolds seeded with human bone marrow stromal cells for tissue engineered growth of bone: mission impossible? A methodological approach. *Clin Oral Implants Res.* 2008; 19(4):379-386.
- Matsuzaki H, Zaegel MA, Gelberman RH, Silva MJ. Effect of suture material and bone quality on the mechanical properties of zone I flexor tendon-bone reattachment with bone anchors. *J Hand Surg Am.* 2008; 33(5):709-717.
- Matyas JR, Bodie D, Andersen M, Frank CB. The developmental morphology of a "periosteal" ligament insertion: growth and maturation of the tibial insertion of the rabbit medial collateral ligament. *J Orthop Res.* 1990; 8(3):412-424.
- McCallister WV, Ambrose HC, Katolik LI, Trumble TE. Comparison of pullout button versus suture anchor for zone I flexor tendon repair. *J Hand Surg Am.* 2006; 31(2):246-251.
- McGonagle D, Benjamin M. Enthesopathies. In Hochberg MC, Silman AJ, Smolen JS, Weinblatt ME, Weisman MH (Eds) *Rheumatology*, 6th ed. Philadelphia, PA: Elsevier, 2015, pp 1014-1020.
- McMaster PE. Tendon and muscle ruptures. Clinical and experimental studies on the causes and location of subcutaneous ruptures. *J Bone Joint Surg.* 1933; 15(3):705-722.
- McNeilly CM, Banes AJ, Benjamin M, Ralphs JR. Tendon cells in vivo form a three dimensional network of cell processes linked by gap junctions. *J Anat.* 1996; (Pt 3):593-600.
- Mechiche Alami S, Gangloff SC, Laurent-Maquin D, Wang Y, Kerdjoudj H. Concise review: in vitro formation of bone-like nodules sheds light on the application of stem cells for bone regeneration. *Stem Cells Transl Med.* 2016; 5(11):1587-1593.
- Merrell G, Hastings H. Dislocations and ligament injuries of the digits. In Wolfe SW, Hotchkiss RN, Pederson WC, Kozin SH, Cohen MS (Eds) *Green's operative hand surgery*, 7th ed. Philadelphia, PA: Elsevier, 2017, pp 278-317.

- Millar NL, Murrell GA, McInnes IB. Inflammatory mechanisms in tendinopathy - towards translation. *Nat Rev Rheumatol*. 2017; 13(2):110-122.
- Milz S, Rufai A, Buettner A, Putz R, Ralphs JR, Benjamin M. Three-dimensional reconstructions of the Achilles tendon insertion in man. *J Anat*. 2002; 200(2): 145–152.
- Milz S, Benjamin M, Putz R. Molecular parameters indicating adaptation to mechanical stress in fibrous connective tissue. *Adv Anat Embryol Cell Biol*. 2005; 178:1-71.
- Mintalucci D, Lutsky KF, Matzon JL, Rivlin M, Niver G, Beredjikian PK. Distal interphalangeal joint bony dimensions related to headless compression screw sizes. *J Hand Surg Am*. 2014; 39(6):1068-1074. e1.
- Mironov V, Markwald RR. Anatomy of tissue engineering. *Anat Rec*. 2001; 263(4):335.
- Moffat KL, Sun WH, Pena PE, Chahine NO, Doty SB, Ateshian GA, Hung CT, Lu HH. Characterization of the structure-function relationship at the ligament-to-bone interface. *Proc Natl Acad Sci U S A*. 2008; 105(23):7947-7952.
- Moiemen NS, Elliot D. Primary flexor tendon repair in zone 1. *J Hand Surg Br*. 2000; 25(1):78-84.
- Moore KL, Agur AMR. *Essential clinical anatomy*, 2nd ed. Baltimore, MD: Lippincott, Williams & Wilkins, 2002.
- Morgan A, Babu D, Reiz B, Whittal R, Suh LYK, Siraki AG. Caution for the routine use of phenol red – It is more than just a pH indicator. *Chem Biol Interact*. 2019; 310:108739.
- Mosher CZ, Spalazzi JP, Lu HH. Stratified scaffold design for engineering composite tissues. *Methods*. 2015; 84:99-102.
- Moskalewski S, Boonekamp PM, Scherft JP. Bone formation by isolated calvarial osteoblasts in syngeneic and allogeneic transplants: Light microscopic observations. *Am. J Anat*. 1983; 167(2):249-263.
- Murphy BA, Mass DP. Zone I flexor tendon injuries. *Hand Clin*. 2005; 21(2):167-171.
- Narang A, Gupta S, Kanojia RK, Sinha S. An unusual pattern of flexor digitorum profundus avulsion injury with a large extra-articular bony fragment. *J Orthop Case Rep*. 2019; 9(3):65-67.
- Nayak BP, Goh JC, Toh SL, Satpathy GR. In vitro study of stem cell communication via gap junctions for fibrocartilage regeneration at entheses. *Regen Med*. 2010; 5(2):221-229.
- Newsham-West R, Nicholson H, Walton M, Milburn P. Long-term morphology of a healing bone-tendon interface: a histological observation in the sheep model. *J Anat*. 2007; 210(3):318-327.
- Ng KW, Leong DT, Hutmacher DW. The challenge to measure cell proliferation in two and three dimensions. *Tissue Eng*. 2005; 11(1-2): 182–191.
- Nguyen L, Hang M, Wang W, Tian Y, Wang L, McCarthy TJ, Chen W. Simple and improved approaches to long-lasting, hydrophilic silicones derived from commercially available precursors. *ACS Appl Mater Interfaces*. 2014; 6(24):22876-22883.
- Nho JH, Lee SW, Nam MA, Kim BS, Jung KJ. Repair technique using a combination of suture anchor and miniscrew in flexor digitorum profundus bony avulsion fracture with bone fragment in zone 1. *J Hand Surg Asian Pac Vol*. 2018; 23(3):430-436.

- Noguchi M, Kitaura T, Ikoma K, Kusaka Y. A method of in-vitro measurement of the cross-sectional area of soft tissues, using ultrasonography. *J Orthop Sci.* 2002; 7(2):247-251.
- O'Connell, Garcia J, Amir J. 3D bioprinting: new directions in articular cartilage tissue engineering. *ACS Biomater Sci Eng.* 2017; 3(11):2657–2668.
- Ootes D, Lambers KT, Ring DC. The epidemiology of upper extremity injuries presenting to the emergency department in the United States. *Hand (N Y).* 2012; 7(1):18-22.
- Orriss IR, Hajjawi MO, Huesa C, MacRae VE, Arnett TR. Optimisation of the differing conditions required for bone formation in vitro by primary osteoblasts from mice and rats. *Int J Mol Med.* 2014; 34(5):1201-1208.
- Palesy PD. Tendon and ligament insertions — a possible source of musculoskeletal pain. *Cranio.* 1997; 15(3):194-202.
- Park JS, Yang HJ, Woo DG, Yang HN, Na K, Park KH. Chondrogenic differentiation of mesenchymal stem cells embedded in a scaffold by long-term release of TGF-beta 3 complexed with chondroitin sulfate. *J Biomed Mater Res A.* 2010; 92(2):806-816.
- Park SH, Choi YJ, Moon SW, Lee BH, Shim JH, Cho DW, Wang JH. Three-dimensional bioprinted scaffold sleeves with mesenchymal stem cells for enhancement of tendon-to-bone healing in anterior cruciate ligament reconstruction using soft-tissue tendon graft. *Arthroscopy.* 2018; 34(1):166-179.
- Patel S, Caldwell JM, Doty SB, Levine WN, Rodeo S, Soslowky LJ, Thomopoulos S, Lu HH. Integrating soft and hard tissues via interface tissue engineering. *J Orthop Res.* 2018; 36(4):1069-1077.
- Paxton JZ, Donnelly K, Keatch RP, Baar K. Engineering the bone-ligament interface using polyethylene glycol diacrylate incorporated with hydroxyapatite. *Tissue Eng Part A.* 2009; 15(6):1201-1209.
- Paxton JZ, Donnelly K, Keatch RP, Baar K, Grover LM. Factors affecting the longevity and strength in an in vitro model of the bone-ligament interface. *Ann Biomed Eng.* 2010; 38(6):2155-2166.
- Paxton JZ, Grover LM, Baar K. Engineering an in vitro model of a functional ligament from bone to bone. *Tissue Eng Part A.* 2010; 16(11):3515-3525.
- Paxton, JZ, Baar K, Grover LM. Current progress in enthesis repair: strategies for interfacial tissue engineering. *Orthopedic Muscul Sys.* 2012; S1:003.
- Paxton JZ, Wudebwe UN, Wang A, Woods D, Grover LM. Monitoring sinew contraction during formation of tissue-engineered fibrin-based ligament constructs. *Tissue Eng Part A.* 2012a; 18(15-16):1596-1607.
- Paxton JZ, Hagerty P, Andrick JJ, Baar K. Optimizing an intermittent stretch paradigm using ERK1/2 phosphorylation results in increased collagen synthesis in engineered ligaments. *Tissue Eng Part A.* 2012b; 18(3-4):277-284.
- Phillips JE, Burns KL, Le Doux JM, Guldborg RE, García AJ. Engineering graded tissue interfaces. *Proc Natl Acad Sci U S A.* 2008; 105(34):12170-12175.
- Piccinini E, Sadr N, Martin I. Ceramic materials lead to underestimated DNA quantifications: a method for reliable measurements. *Eur Cell Mater.* 2010; 20:38-44.
- Polfer EM, Sabino JM, Katz RD. Zone I Flexor digitorum profundus repair: A surgical technique. *J Hand Surg Am.* 2019; 44(2):164.e1-164.e5.

- Poli E, Magnaudeix A, Damia C, Lalloué F, Chaleix V, Champion E, Sol V. Advanced protocol to functionalize CaP bioceramic surface with peptide sequences and effect on murine pre-osteoblast cells proliferation. *Bioorg Med Chem Lett*. 2019; 29(9):1069-1073.
- Polinder S, Iordens GI, Panneman MJ, Eygendaal D, Patka P, Den Hartog D, Van Lieshout EM. Trends in incidence and costs of injuries to the shoulder, arm and wrist in The Netherlands between 1986 and 2008. *BMC Public Health*. 2013; 13:531.
- Portney LG, Watkins MP. *Foundations of clinical research: applications to practice*, 2nd ed. Upper Saddle River, NJ: Prentice Hall, 2000.
- Pridgen BC, Woon CY, Kim M, Thorfinn J, Lindsey D, Pham H, Chang J. Flexor tendon tissue engineering: acellularization of human flexor tendons with preservation of biomechanical properties and biocompatibility. *Tissue Eng Part C Methods*. 2011; 17(8):819-828.
- Prockop DJ, Kivirikko KI. Heritable diseases of collagen. *N Engl J Med*. 1984; 311(6):376-386.
- Putnam JG, Adamany D. Biomechanical comparison of flexor digitorum profundus avulsion repair. *J Wrist Surg*. 2019; 8(4):312-316.
- Qiu Y, Lei J, Koob TJ, Temenoff JS. Cyclic tension promotes fibroblastic differentiation of human MSCs cultured on collagen-fibre scaffolds. *J Tissue Eng Regen Med*. 2016; 10(12):989-999.
- Quent VM, Loessner D, Friis T, Reichert JC, Hutmacher DW. Discrepancies between metabolic activity and DNA content as tool to assess cell proliferation in cancer research. *J Cell Mol Med*. 2010; 14(4):1003-1013.
- Raghavan SS, Woon CY, Kraus A, Megerle K, Pham H, Chang J. Optimization of human tendon tissue engineering: synergistic effects of growth factors for use in tendon scaffold repopulation. *Plast Reconstr Surg*. 2012; 129(2):479-489.
- Ralphs JR, Benjamin M, Thornett A. Cell and matrix biology of the suprapatella in the rat: a structural and immunocytochemical study of fibrocartilage in a tendon subject to compression. *Anat Rec*. 1991; 231(2):167-177.
- Rawson S, Cartmell S, Wong J. Suture techniques for tendon repair; a comparative review. *Muscles Ligaments Tendons J*. 2013; 3(3):220-228.
- Redler I, Mow VC, Zimny ML, Mansell J. The ultrastructure and biomechanical significance of the tidemark of articular cartilage. *Clin Orthop Relat Res*. 1975; 112:357-362.
- Reef TC. Avulsion of the flexor digitorum profundus: An athletic injury. *Am J Sports Med*. 1977; 5(6):281-285.
- Rehak DC, Sotereanos DG, Bowman MW, Herndon JH. The mitek bone anchor: application to the hand, wrist and elbow. *J Hand Surg Am*. 1994; 19(5):853-860.
- Ricchetti ET, Aurora A, Iannotti JP, Derwin KA. Scaffold devices for rotator cuff repair. *J Shoulder Elbow Surg*. 2012; 21(2):251-265.
- Robins PR, Dobyns JH. Avulsion of the insertion of the flexor digitorum profundus tendon associated with fracture of the distal phalanx: A brief review. *AAOS*. 1974: 151–156.
- Robinson LS, Sarkies M, Brown T, O'Brien L. Direct, indirect and intangible costs of acute hand and wrist injuries: A systematic review. *Injury*. 2016; 47(12):2614-2626.

- Rodeo SA, Arnoczky SP, Torzilli PA, Hidaka C, Warren RF. Tendon-healing in a bone tunnel. A biomechanical and histological study in the dog. *J Bone Joint Surg Am.* 1993; 75(12):1795-1803.
- Rosberg HE, Carlsson KS, Dahlin LB. Prospective study of patients with injuries to the hand and forearm: costs, function, and general health. *Scand J Plast Reconstr Surg Hand Surg.* 2005; 39(6):360-369.
- Rossetti L, Kuntz LA, Kunold E, Schock J, Müller KW, Grabmayr H, Stolberg-Stolberg J, Pfeiffer F, Sieber SA, Burgkart R, Bausch AR. The microstructure and micromechanics of the tendon-bone insertion. *Nat Mater.* 2017; 16(6):664-670.
- Rothrauff BB, Tuan RS. Cellular therapy in bone-tendon interface regeneration. *Organogenesis.* 2014; 10(1):13-28.
- Rozmaryn LM. The collateral ligament of the digits of the hand: anatomy, physiology, biomechanics, injury, and treatment. *J Hand Surg Am.* 2017; 42(11):904-915.
- Ruchelsman DE, Christoforou D, Wasserman B, Lee SK, Rettig ME. Avulsion injuries of the flexor digitorum profundus tendon. *J Am Acad Orthop Surg.* 2011; 19(3):152-162.
- Rufai A, Ralphs JR, Benjamin M. Ultrastructure of fibrocartilages at the insertion of the rat Achilles tendon. *J Anat.* 1996; 189(Pt 1):185-191.
- Salehi-Nik N, Amoabediny G, Pouran B, Tabesh H, Shokrgozar MA, Haghighipour N, Khatibi N, Anisi F, Mottaghy K, Zandieh-Doulabi B. Engineering parameters in bioreactor's design: a critical aspect in tissue engineering. *Biomed Res Int.* 2013; 2013:762132.
- Samavedi S, Guelcher SA, Goldstein AS, Whittington AR. Response of bone marrow stromal cells to graded co-electrospun scaffolds and its implications for engineering the ligament-bone interface. *Biomaterials.* 2012; 33(31):7727-7735.
- Samora JB, Klinefelter RD. Flexor tendon reconstruction. *J Am Acad Orthop Surg.* 2016; 24(1):28-36.
- Samson D, Gupta M. The effect of distal phalanx bony dimensions in suture anchor fixations of tendon avulsion. *J Hand Surg Asian Pac Vol.* 2018; 23(3):347-350.
- Sasaki N, Ishibashi Y, Tsuda E, Yamamoto Y, Maeda S, Mizukami H, Toh S, Yagihashi S, Tonosaki Y. The femoral insertion of the anterior cruciate ligament: discrepancy between macroscopic and histological observations. *Arthroscopy.* 2012; 28(8):1135-1146.
- Sasaki Y, Nomura S. An unusual role of the vinculum after complete laceration of the flexor tendons. *J Hand Surg Br.* 1987; 12(1):105-108.
- Schlecht SH. Understanding entheses: bridging the gap between clinical and anthropological perspectives. *Anat Rec.* 2012; 295:1239-1251.
- Schneider H. Zur Struktur der Sehnenansatzzonen. *Z Anat Entwicklung.* 1956; 119: 421-456.
- Schreuder FB, Scougall PJ, Puchert E, Vizesi F, Walsh WR. The effect of mitek anchor insertion angle to attachment of FDP avulsion injuries. *J Hand Surg Br.* 2006; 31(3):292-295.
- Schuind F, Garcia-Elias M, Cooney WP 3rd, An KN. Flexor tendon forces: in vivo measurements. *J Hand Surg Am.* 1992; 17(2):291-298.
- Schultz RO, Drake DB, Morgan RF. A new technique for the treatment of flexor digitorum profundus tendon avulsion. *Ann Plast Surg.* 1999; 42(1):46-48.

- Schwartz AG, Pasteris JD, Genin GM, Daulton TL, Thomopoulos S. Mineral distributions at the developing tendon enthesis. *PLoS One*. 2012; 7(11): e48630.
- Schwartz AG, Lipner JH, Pasteris JD, Genin GM, Thomopoulos S. Muscle loading is necessary for the formation of a functional tendon enthesis. *Bone*. 2013; 55(1): 44-51.
- Schwartz AG, Long F, Thomopoulos S. Enthesis fibrocartilage cells originate from a population of Hedgehog-responsive cells modulated by the loading environment. *Development*. 2015; 142(1):196-206.
- Seiler JG. Flexor tendon injury. In Wolfe SW, Hotchkiss RN, Pederson WC, Kozin SH, Cohen MS (Eds) *Green's operative hand surgery*, 7th ed. Philadelphia, PA: Elsevier, 2017, pp 183-230.
- Sengupta P. The laboratory rat: relating its age with human's. *Int J Prev Med*. 2013; 4(6): 624-630.
- Shaieb MD, Singer DI. Tensile strengths of various suture techniques. *J Hand Surg Br*. 1997; 22(6):764-767.
- Shapiro LM, Kamal RN. Evaluation and treatment of flexor tendon and pulley injuries in athletes. *Clin Sports Med*. 2020; 39(2):279-297.
- Sharma P, Maffulli N. Tendon injury and tendinopathy: healing and repair. *J Bone Joint Surg Am*. 2005; 87(1):187-202.
- Shaw HM, Benjamin M. Structure-function relationships of entheses in relation to mechanical load and exercise. *Scand J Med Sci Sports*. 2007; 17(4):303-315.
- Shaw HM, Santer RM, Watson AH, Benjamin M. Adipose tissue at entheses: the innervation and cell composition of the retromalleolar fat pad associated with the rat Achilles tendon. *J Anat*. 2007; 211(4):436-443.
- Shinohara Y, Kumai T, Higashiyama I, Hayashi K, Matsuda T, Tanaka Y, Takakura Y. Histological and molecular characterization of the femoral attachment of the human ligamentum capitis femoris. *Scand J Med Sci Sports*. 2014;24(4):e245-253.
- Silfverskiöld KL, Andersson CH. Two new methods of tendon repair: an in vitro evaluation of tensile strength and gap formation. *J Hand Surg Am*. 1993; 18(1):58-65.
- Silva M, Hollstien SB, Brodt MD, Boyer MI, Tetro AM, Gelberman RH. Flexor digitorum profundus tendon-to-bone repair: an ex vivo biomechanical analysis of 3 pullout suture techniques. *J Hand Surg Am*. 1998; 23(1):120-126.
- Silva MJ, Hollstien SB, Fayazi AH, Adler P, Gelberman RH, Boyer MI. The effects of multiple-strand suture techniques on the tensile properties of repair of the flexor digitorum profundus tendon to bone. *J Bone Joint Surg Am*. 1998; 80(10):1507-1514.
- Silva MJ, Boyer MI, Ditsios K, Burns ME, Harwood FL, Amiel D, Gelberman RH. The insertion site of the canine flexor digitorum profundus tendon heals slowly following injury and suture repair. *J Orthop Res*. 2002; 20(3):447-53.
- Silva MJ, Thomopoulos S, Kusano N, Zaegel MA, Harwood FL, Matsuzaki H, Havlioglu N, Dovan TT, Amiel D, Gelberman RH. Early healing of flexor tendon insertion site injuries: Tunnel repair is mechanically and histologically inferior to surface repair in a canine model. *J Orthop Res*. 2006; 24(5):990-1000.
- Sinnatamby CS. *Last's anatomy: regional and applied*, 12th ed. Edinburgh: Churchill Livingstone, 2011.
- Skoff HD, Hecker AT, Hayes WC, Sebell-Sklar R, Straughn N. Bone suture anchors in hand surgery. *J Hand Surg Br*. 1995; 20(2):245-248.

- Smith JH Jr. Avulsion of a profundus tendon with simultaneous intraarticular fracture of the distal phalanx--case report. *J Hand Surg Am.* 1981; 6(6):600-601.
- Smith L, Xia Y, Galatz LM, Genin GM, Thomopoulos S. Tissue-engineering strategies for the tendon/ligament-to-bone insertion. *Connect Tissue Res.* 2012; 53(2):95-105.
- Song JH, Lee JY, Chung YG, Park IJ. Distal interphalangeal joint arthrodesis with a headless compression screw: morphometric and functional analyses. *Arch Orthop Trauma Surg.* 2012; 132(5):663-669.
- Sood MK, Elliot D. A new technique of attachment of flexor tendons to the distal phalanx without a button tie-over. *J Hand Surg Br.* 1996; 21(5):629-632.
- Spalazzi JP, Doty SB, Moffat KL, Levine WN, Lu HH. Development of controlled matrix heterogeneity on a triphasic scaffold for orthopedic interface tissue engineering. *Tissue Eng.* 2006; 12(12):3497-3508.
- Spalazzi JP, Dagher E, Doty SB, Guo XE, Rodeo SA, Lu HH. In vivo evaluation of a multiphased scaffold designed for orthopaedic interface tissue engineering and soft tissue-to-bone integration. *J Biomed Mater Res A.* 2008; 86(1):1-12.
- Sridharan G, Shankar AA. Toluidine blue: a review of its chemistry and clinical utility. *J Oral Maxillofac Pathol.* 2012; 16(2):251-255.
- Stamos BD, Leddy JP. Closed flexor tendon disruption in athletes. *Hand Clin.* 2000; 16(3):359-365.
- Stewart DA, Smitham PJ, Gianoutsos MP, Walsh WR. Biomechanical influence of the vincula tendinum on digital motion after isolated flexor tendon injury: a cadaveric study. *J Hand Surg Am.* 2007; 32(8):1190-1194.
- Strickland JW. Development of flexor tendon surgery: twenty-five years of progress. *J Hand Surg Am.* 2000; 25(2):214-235.
- Sugimoto Y, Takimoto A, Akiyama H, Kist R, Scherer G, Nakamura T, Hiraki Y, Shukunami C. *Scx*⁺/*Sox9*⁺ progenitors contribute to the establishment of the junction between cartilage and tendon/ligament. *Development.* 2013; 140(11):2280-2288.
- Sundararaj SK, Cieply RD, Gupta G, Milbrandt TA, Puleo DA. Treatment of growth plate injury using IGF-I-loaded PLGA scaffolds. *J Tissue Eng Regen Med.* 2015; 9(12):E202-9.
- Suresh S. Graded materials for resistance to contact deformation and damage. *Science.* 2001; 292(5526):2447-2451.
- Takahashi I, Nuckolls GH, Takahashi K, Tanaka O, Semba I, Dashner R, Shum L, Slavkin HC. Compressive force promotes *sox9*, type II collagen and aggrecan and inhibits IL-1beta expression resulting in chondrogenesis in mouse embryonic limb bud mesenchymal cells. *J Cell Sci.* 1998; 111(Pt 14):2067-2076.
- Tan L, Ren Y, Kuijer R. A 1-min method for homogenous cell seeding in porous scaffolds. *J Biomater Appl.* 2012; 26(7):877-889.
- Tare RS, Mitchell PD, Kanczler J, Oreffo ROC. Isolation, differentiation, and characterisation of skeletal stem cells from human bone marrow in vitro and in vivo. In Helfrich M, Ralston S (Eds) *Bone research protocols. Methods in molecular biology (methods and protocols)*, vol 816. Totowa, NJ: Humana Press, 2012, pp 83-99.

- Tempelaere C, Brun M, Doursounian L, Feron JM. Traumatic avulsion of the flexor digitorum profundus tendon. Jersey finger, a 29 cases report. *Hand Surg Rehabil.* 2017; 36(5):368-372.
- Teo TC, Dionyssiou D, Armenio A, Ng D, Skillman J. Anatomical repair of zone 1 flexor tendon injuries. *Plast Reconstr Surg.* 2009; 123(2):617-622.
- Thibault RA, Scott Baggett L, Mikos AG, Kasper FK. Osteogenic differentiation of mesenchymal stem cells on pregenerated extracellular matrix scaffolds in the absence of osteogenic cell culture supplements. *Tissue Eng Part A.* 2010; 16(2):431-440.
- Thomopoulos S, Williams GR, Gimbel JA, Favata M, Soslowsky LJ. Variation of biomechanical, structural, and compositional properties along the tendon to bone insertion site. *J Orthop Res.* 2003; 21(3):413-419.
- Thomopoulos S, Williams GR, Soslowsky LJ. Tendon to bone healing: differences in biomechanical, structural, and compositional properties due to a range of activity levels. *J Biomech Eng.* 2003; 125(1):106-113.
- Thomopoulos S, Harwood FL, Silva MJ, Amiel D, Gelberman RH. Effect of several growth factors on canine flexor tendon fibroblast proliferation and collagen synthesis in vitro. *J Hand Surg Am.* 2005; 30(3):441-447.
- Thomopoulos S, Marquez JP, Weinberger B, Birman V, Genin GM. Collagen fiber orientation at the tendon to bone insertion and its influence on stress concentrations. *J Biomech.* 2006; 39(10):1842-1851.
- Thomopoulos S, Kim HM, Rothermich SY, Biederstadt C, Das R, Galatz LM. Decreased muscle loading delays maturation of the tendon enthesis during postnatal development. *J Orthop Res.* 2007; 25(9):1154-1163.
- Thomopoulos S, Zampiakos E, Das R, Kim HM, Silva MJ, Havlioglu N, Gelberman RH. Use of a magnesium-based bone adhesive for flexor tendon-to-bone healing. *J Hand Surg Am.* 2009; 34(6):1066-1073.
- Thomopoulos S, Genin GM, Galatz LM. The development and morphogenesis of the tendon-to-bone insertion What development can teach us about healing. *J Musculoskelet Neuronal Interact.* 2010; 10(1): 35-45.
- Thomopoulos S, Das R, Birman V, Smith L, Ku K, Elson EL, Pryse KM, Marquez JP, Genin GM. Fibrocartilage tissue engineering: the role of the stress environment on cell morphology and matrix expression. *Tissue Eng Part A.* 2011; 17(7-8):1039-1053.
- Thorfinn J, Angelidis IK, Gigliello L, Pham HM, Lindsey D, Chang J. Bioreactor optimization of tissue engineered rabbit flexor tendons in vivo. *J Hand Surg Eur Vol.* 2012; 37(2):109-114.
- Thorpe CT, Screen HR. Tendon structure and composition. *Adv Exp Med Biol.* 2016; 920:3-10.
- Tiong WH, O'Sullivan ST. Extrusion of bone anchor suture following flexor digitorum profundus tendon avulsion injury repair. *J Plast Reconstr Aesthet Surg.* 2011; 64(9):1242-1244.
- Toumi H, Higashiyama I, Suzuki D, Kumai T, Bydder G, McGonagle D, Emery P, Fairclough J, Benjamin M. Regional variations in human patellar trabecular architecture and the structure of the proximal patellar tendon enthesis. *J Anat.* 2006; 208(1):47-57.

- Toumi H, Larguech G, Filaire E, Pinti A, Lespessailles E. Regional variations in human patellar trabecular architecture and the structure of the quadriceps enthesis: a cadaveric study. *J Anat.* 2012; 220(6):632-637.
- Toumi H, Best TM, Mazor M, Coursier R, Pinti A, Lespessailles E. Association between individual quadriceps muscle volume/enthesis and patello femoral joint cartilage morphology. *Arthritis Res Ther.* 2014; 16(1):R1.
- Toumi H, Larguech G, Cherief M, Batakis A, Hambli R, Jennane R, Best TM, Lespessailles E. Implications of the calf musculature and Achilles tendon architectures for understanding the site of injury. *J Biomech.* 2016; 49(7):1180-1185.
- Tripathi AK, Mee SN, Martin DL, Katsarma E. The "transverse intraosseous loop technique" (TILT) to re-insert flexor tendons in zone 1. *J Hand Surg Eur Vol.* 2009; 34(1):85-89.
- Tuttle HG, Olvey SP, Stern PJ. Tendon avulsion injuries of the distal phalanx. *Clin Orthop Relat Res.* 2006; 445:157-168.
- Uhthoff HK, Seki M, Backman DS, Trudel G, Himori K, Sano H. Tensile strength of the supraspinatus after reimplantation into a bony trough: an experimental study in rabbits. *J Shoulder Elbow Surg.* 2002; 11(5):504-509.
- Vadodaria S, Ponniah A, McFetrich J, Preston C, Page, R. A technique for re-insertion following flexor tendon injuries in zone I using Mitek bone anchors. *Eur J Plast Surg.* 2007; 29:263-266.
- Vater C, Kasten P, Stiehler S. Culture media for the differentiation of mesenchymal stromal cells. *Acta Biomater.* 2011; 7(2):463-477.
- Verdan CE. Primary repair of flexor tendons. *J Bone Joint Surg Am.* 1960; 42:647-657.
- Verdan CE. Half a century of flexor-tendon surgery: Current status and changing philosophies. *J Bone Joint Surg Am.* 1972; 54(3):472-491.
- Vigouroux L, Quaine F, Labarre-Vila A, Moutet F. Estimation of finger muscle tendon tensions and pulley forces during specific sport-climbing grip techniques. *J Biomech.* 2006; 39(14):2583-2592.
- Villotte S, Knüsel CJ. Understanding enthesal changes: definition and life course changes. *Int J Osteoarchaeol.* 2013; 23:135-146.
- von Köckritz-Blickwede M, Chow OA, Nizet V. Fetal calf serum contains heat-stable nucleases that degrade neutrophil extracellular traps. *Blood.* 2009; 114(25):5245-5246.
- Wade PJ, Wetherell RG, Amis AA. Flexor tendon repair: significant gain in strength from the Halstead peripheral suture technique. *J Hand Surg.* 1989; 14B:232-235.
- Waggett AD, Ralphs JR, Kwan AP, Woodnutt D, Benjamin M. Characterization of collagens and proteoglycans at the insertion of the human Achilles tendon. *Matrix Biol.* 1998; 16(8):457-470.
- Wagner CJ. Delayed advancement in the repair of lacerated flexor profundus tendons. *J Bone Joint Surg Am.* 1958; 40-A(6):1241-1244.
- Wang IE, Shan J, Choi R, Oh S, Kepler CK, Chen FH, Lu HH. Role of osteoblast-fibroblast interactions in the formation of the ligament-to-bone interface. *J Orthop Res.* 2007; 25(12):1609-1620.
- Wang X, Wenk E, Zhang X, Meinel L, Vunjak-Novakovic G, Kaplan DL. Growth factor gradients via microsphere delivery in biopolymer scaffolds for osteochondral tissue engineering. *J Control Release.* 2009; 134(2):81-90.

- Warwick R, Williams PL. *Gray's anatomy*, 35th ed. Edinburgh: Longman, 1973.
- Weisel JW, Litvinov RI. Fibrin formation, structure and properties. *Subcell Biochem.* 2017; 82:405-456.
- Wen CY, Qin L, Lee KM, Chan KM. The use of brushite calcium phosphate cement for enhancement of bone-tendon integration in an anterior cruciate ligament reconstruction rabbit model. *J Biomed Mater Res B Appl Biomater.* 2009; 89(2):466-474.
- Wilkinson JL. The insertions of the flexores pollicis longus et digitorum profundus. *J Anat.* 1953; 87(1):75-88.
- Wilson CE, de Bruijn JD, van Blitterswijk CA, Verbout AJ, Dhert WJ. Design and fabrication of standardized hydroxyapatite scaffolds with a defined macro-architecture by rapid prototyping for bone-tissue-engineering research. *J Biomed Mater Res A.* 2004; 68(1):123-132.
- Woo SL-Y, Maynard J, Butler D, Lyon R, Torzilli P, Akeson W, Cooper R, Oakes B. Ligament, tendon, and joint capsule insertions to bone. In Woo SL-Y, Buckwalter JA (Eds) *Injury and repair of the musculoskeletal soft tissues*. Park Ridge, IL: American Academy of Orthopaedic Surgeons, 1988, pp 133–166.
- Wopenka B, Kent A, Pasteris JD, Yoon Y, Thomopoulos S. The tendon-to-bone transition of the rotator cuff: A preliminary raman spectroscopic study documenting the gradual mineralization across the insertion in rat tissue samples. *Appl Spectrosc.* 2008; 62(12):1285-1294.
- Wu L, Lin L, Qin YX. Enhancement of cell ingrowth, proliferation, and early differentiation in a three-dimensional silicon carbide scaffold using low-intensity pulsed ultrasound. *Tissue Eng Part A.* 2015; 21(1-2):53-61.
- Wyrsh B, Dawson J, Aufranc S, Weikert D, Milek M. Distal interphalangeal joint arthrodesis comparing tension-band wire and Herbert screw: a biomechanical and dimensional analysis. *J Hand Surg Am.* 1996; 21(3):438-443.
- Yan LP, Oliveira JM, Oliveira AL, Reis RL. In vitro evaluation of the biological performance of macro/micro-porous silk fibroin and silk-nano calcium phosphate scaffolds. *J Biomed Mater Res B Appl Biomater.* 2015; 103(4):888-898.
- Yang PJ, Temenoff JS. Engineering orthopedic tissue interfaces. *Tissue Eng Part B Rev.* 2009; 15(2):127-141.
- Yasumoto M, Deie M, Sunagawa T, Adachi N, Kobayashi K, Ochi M. Predictive value of preoperative 3-dimensional computer tomography measurement of semitendinosus tendon harvested for anterior cruciate ligament reconstruction. *Arthroscopy.* 2006; 22(3):259-264.
- Yilgor C, Yilgor Huri P, Huri G. Tissue engineering strategies in ligament regeneration. *Stem Cells Int.* 2012; 2012:374676.
- Yoon JH, Halper J. Tendon proteoglycans: biochemistry and function. *J Musculoskelet Neuronal Interact.* 2005; 5(1):22-34.
- Young B, O'Dowd G, Woodford P. *Wheater's functional histology: a text and colour atlas*, 6th ed. Philadelphia, PA: Elsevier, 2014, pp 180-196.
- Zajac FE. How musculotendon architecture and joint geometry affect the capacity of muscles to move and exert force on objects: a review with application to arm and forearm tendon transfer design. *J Hand Surg Am.* 1992; 17(5):799-804.

- Zelzer E, Blitz E, Killian ML, Thomopoulos S. Tendon-to-bone attachment: from development to maturity. *Birth Defects Res C Embryo Today*. 2014; 102(1):101-112.
- Zhang X, Shao X, Zhang K. Pull-out wire traction for the treatment of avulsion of the flexor digitorum profundus from its insertion. *J Hand Surg Eur Vol*. 2014; 39(6):667-669.
- Zhao J, Zhang P, Qin L, Pan XH. Hypoxia is essential for bone-tendon junction healing: the molecular biological evidence. *Int Orthop*. 2011; 35(6):925-928.
- Zhao F, Hu X, Zhang J, Shi W, Ren B, Huang H, Ao Y. A more flattened bone tunnel has a positive effect on tendon-bone healing in the early period after ACL reconstruction. *Knee Surg Sports Traumatol Arthrosc*. 2019; 27(11):3543-3551.
- Zhu Y, Liu T, Song K, Fan X, Ma X, Cui Z. Adipose-derived stem cell: a better stem cell than BMSC. *Cell Biochem Funct*. 2008; 26(6):664-675.

Appendices

1	Inter-Observer Reliability Statistics for FDP Insertion Morphology Measurement Methodologies (<i>Chapter 2</i>)	363
2	Raw Means for Component Design Guide for Tissue Engineered Model (<i>Chapter 2</i>).....	365
3	Inter-Observer Reliability Statistics for FDP Tendon Fibre Angle Measurement Methodologies (<i>Chapter 3</i>)	366
4	Standard Curves of dROb Cell Number for CyQUANT Fluorescence Assay (<i>Chapter 4</i>).....	368
5	Gel Width in Standard Volume Gel Anatomical Suture Constructs (<i>Chapter 4</i>)	369
6	Unsuccessful Anatomical Suture Construct Examples (<i>Chapter 4</i>).....	370
7	Acellular Anatomical Suture Construct Controls (<i>Chapter 4</i>)	371
8	Oral and Poster Presentations	372

Reliability Statistics											
	All	FDP Footprint			Distal Phalanx			Distance from DIPJ			
		Surface Area	Height	Base Width	Apex Width	Internal Angles	Surface Area	Height	Base Width	FDP Base	FDP Centroid
Raw Measurements											
Measurement Sets per Variable	1081	47	94	47	47	376	47	94	47	188	94
	23	1	2	1	1	8	1	2	1	4	2
Absolute Agreement											
Single Measures (ICC)	0.997 (0.996-0.997)	0.971 (0.947-0.984)	0.807 (0.722-0.868)	0.846 (0.733-0.913)	0.398 (0.042-0.645)	0.992 (0.990-0.993)	0.933 (0.879-0.963)	0.929 (0.895-0.952)	0.728 (0.561-0.838)	0.877 (0.834-0.909)	0.977 (0.966-0.985)
Average Measures (ICC)	0.998 (0.998-0.999)	0.985 (0.973-0.992)	0.893 (0.838-0.929)	0.917 (0.846-0.954)	0.569 (0.080-0.784)	0.996 (0.995-0.997)	0.965 (0.936-0.981)	0.963 (0.945-0.976)	0.842 (0.718-0.912)	0.935 (0.909-0.953)	0.989 (0.983-0.992)
Cronbach's Alpha	0.998	0.986	0.897	0.923	0.671	0.996	0.968	0.963	0.843	0.938	0.989
Consistency											
Single Measures (ICC)	0.997 (0.996-0.997)	0.972 (0.950-0.984)	0.812 (0.730-0.871)	0.856 (0.756-0.917)	0.505 (0.258-0.691)	0.992 (0.990-0.993)	0.937 (0.890-0.965)	0.929 (0.894-0.952)	0.729 (0.561-0.840)	0.884 (0.848-0.912)	0.977 (0.966-0.985)
Average Measures (ICC)	0.998 (0.998-0.999)	0.986 (0.974-0.992)	0.897 (0.844-0.931)	0.923 (0.861-0.957)	0.671 (0.410-0.817)	0.996 (0.995-0.997)	0.968 (0.942-0.982)	0.963 (0.944-0.975)	0.843 (0.719-0.913)	0.938 (0.918-0.954)	0.989 (0.983-0.992)
Cronbach's Alpha	0.998	0.986	0.897	0.923	0.671	0.996	0.968	0.963	0.843	0.938	0.989

Appendix 1.1 | Inter-Observer Reliability of FDP Footprint and Distal Phalanx Measurements

See Table 2.11. Full SPSS reliability statistics output (95% confidence intervals) comparing 2 observers using a 2-way mixed effects model for the intraclass correlation coefficient (ICC). *Absolute agreement* compares exact measurements; *consistency* assesses for a linear correlation relationship ignoring systematic observer errors. *Single measures* assesses reliability of a single observer's reported measurement; *average measures* assesses reliability of both observers' measurements averaged together.

Reliability Statistics					
	All	Distance from FDP Insertion Base			
		3mm	6mm	9mm	12mm
<i>Raw Measurements</i>	256	64	64	64	64
<i>Measurement Sets per Variable</i>	4	1	1	1	1
Absolute Agreement					
Single Measures (ICC)	0.938 (0.917-0.953)	0.910 (0.852-0.945)	0.916 (0.863-0.948)	0.919 (0.868-0.950)	0.849 (0.760-0.906)
Average Measures (ICC)	0.968 (0.957-0.976)	0.953 (0.920-0.972)	0.956 (0.926-0.973)	0.958 (0.929-0.974)	0.918 (0.864-0.951)
Cronbach's Alpha	0.970	0.955	0.958	0.959	0.922
Consistency					
Single Measures (ICC)	0.941 (0.925-0.954)	0.915 (0.863-0.947)	0.919 (0.870-0.950)	0.922 (0.875-0.952)	0.855 (0.772-0.909)
Average Measures (ICC)	0.970 (0.961-0.976)	0.955 (0.927-0.973)	0.958 (0.931-0.974)	0.959 (0.933-0.975)	0.922 (0.871-0.952)
Cronbach's Alpha	0.970	0.955	0.958	0.959	0.922

Appendix 1.2 | Inter-Observer Reliability of Tendon Width Measurements

See **Table 2.13** and *Appendix 1.1*. Full SPSS reliability statistics output (95% confidence intervals) comparing 2 observers using a 2-way mixed effects model for the intraclass correlation coefficient (ICC).

Model Design Guide (mm) (<i>Raw Means</i>)					
	Bone Anchor				Tendon Width at 12mm
	Height	Base Width	Apex Width	Depth	
Large	6.57 (0.17)	9.41 (0.28)	1.65 (0.16)	2.00	5.33 (0.15)
Medium	5.00 (0.13)	8.24 (0.19)	1.56 (0.14)	2.00	4.42 (0.08)
Small	4.23 (0.17)	7.46 (0.36)	1.66 (0.19)	2.00	3.75 (0.13)
Universal	5.43 (0.15)	8.57 (0.17)	1.60 (0.09)	2.00	4.79 (0.11)

Appendix 2 | Raw Means for Component Design Guide for Tissue Engineered Model

Raw mean values (\pm SEM) for **Table 2.17**, provided for comparison. See **Table 2.17** legend for details. Raw mean values are all within a difference of 0.11mm of estimated marginal means except for 'large' bone anchor height (0.21mm difference), demonstrating the small but statistically necessary correction made for non-independence of samples. Such minor adjustments are of limited practical concern for the scale of surgical application and tissue engineering modelling.

Reliability Statistics								
	All	Tidemark	Approaching	Distance Along Enthesis				
				20%	40%	50%	60%	80%
Raw Measurements	470	235	235	94	94	94	94	94
Measurement Sets per Variable	10	5	5	2	2	2	2	2
Excluded Measurements	126 [26.8%]	78 [33.2%]	48 [20.4%]	26 [27.7%]	29 [30.9%]	27 [28.7]	21 [22.3%]	23 [24.5%]
Absolute Agreement								
Single Measures (ICC)	0.907 (0.886-0.925)	0.820 (0.753-0.869)	0.796 (0.736-0.843)	0.939 (0.899-0.963)	0.862 (0.783-0.913)	0.864 (0.788-0.914)	0.923 (0.880-0.951)	0.926 (0.885-0.954)
Average Measures (ICC)	0.952 (0.940-0.961)	0.901 (0.859-0.930)	0.886 (0.848-0.915)	0.968 (0.947-0.981)	0.926 (0.878-0.955)	0.927 (0.881-0.955)	0.960 (0.936-0.975)	0.962 (0.939-0.976)
Cronbach's Alpha	0.953	0.907	0.886	0.970	0.927	0.926	0.960	0.962
Consistency								
Single Measures (ICC)	0.909 (0.889-0.926)	0.829 (0.773-0.872)	0.795 (0.735-0.842)	0.943 (0.908-0.964)	0.863 (0.785-0.914)	0.862 (0.785-0.913)	0.923 (0.880-0.951)	0.928 (0.886-0.954)
Average Measures (ICC)	0.953 (0.941-0.962)	0.907 (0.872-0.932)	0.886 (0.847-0.914)	0.970 (0.952-0.982)	0.927 (0.880-0.955)	0.926 (0.880-0.955)	0.960 (0.936-0.975)	0.962 (0.940-0.977)
Cronbach's Alpha	0.953	0.907	0.886	0.970	0.927	0.926	0.960	0.962

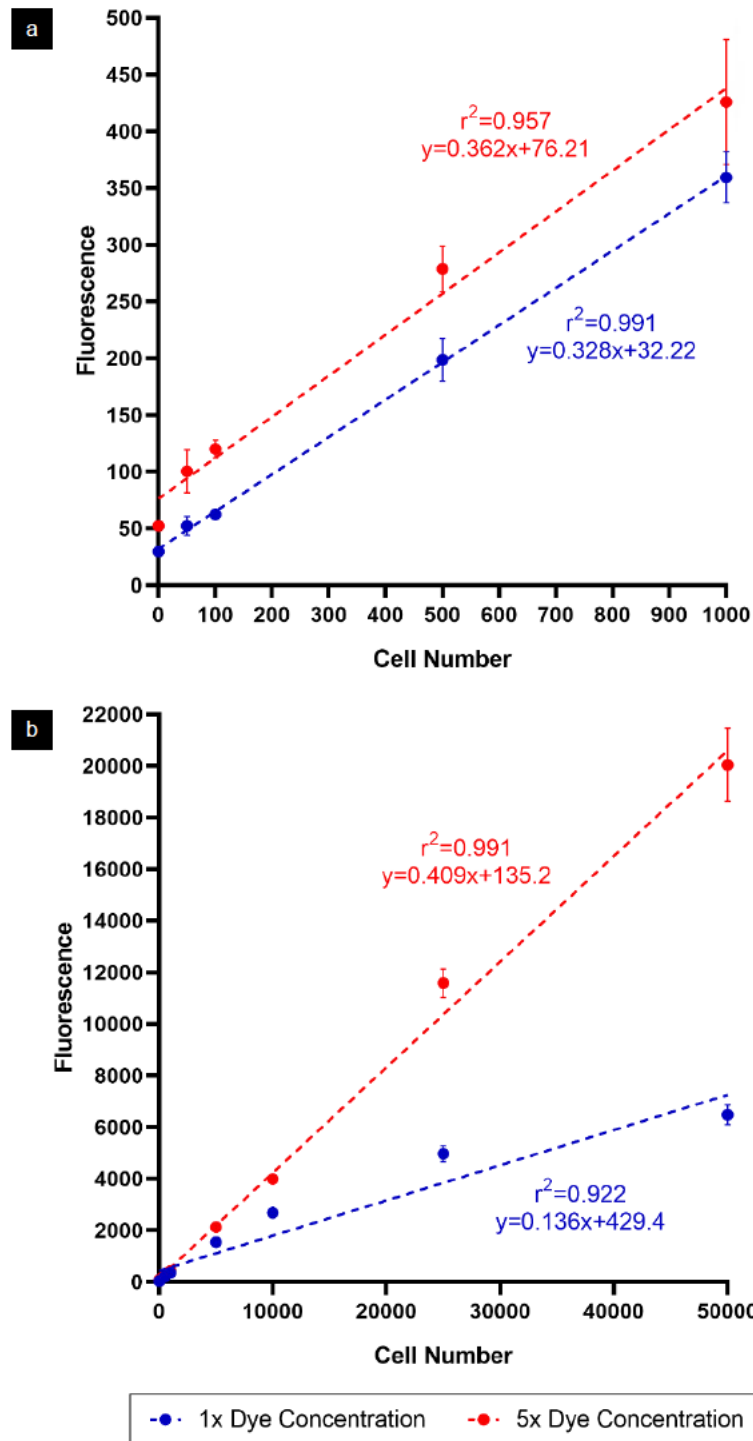
Appendix 3.1 | Inter-Observer Reliability of Collective Tendon Fibre Angle Measurements

See Table 3.7. Full SPSS reliability statistics output (95% confidence intervals) comparing 2 observers using a 2-way mixed effects model for the intraclass correlation coefficient (ICC). *Absolute agreement* compares exact measurements; *consistency* assesses for a linear correlation relationship ignoring systematic observer errors. *Single measures* assesses reliability of a single observer's reported measurement; *average measures* assesses reliability of both observers' measurements averaged together.

Reliability Statistics										
	Tidemark					Approaching				
	20%	40%	50%	60%	80%	20%	40%	50%	60%	80%
Raw Measurements	47	47	47	47	47	47	47	47	47	47
Measurement Sets per Variable	1	1	1	1	1	1	1	1	1	1
Excluded Measurements	15 [31.9%]	18 [38.3%]	17 [36.2%]	14 [28.8%]	14 [28.8%]	11 [23.4%]	11 [23.4%]	10 [21.3%]	7 [14.9%]	9 [19.1%]
Absolute Agreement										
Single Measures (ICC)	0.870 (0.725-0.938)	0.709 (0.467-0.852)	0.758 (0.554-0.876)	0.872 (0.756-0.935)	0.871 (0.753-0.935)	0.757 (0.575-0.868)	0.783 (0.612-0.883)	0.740 (0.546-0.857)	0.811 (0.670-0.896)	0.732 (0.541-0.852)
Average Measures (ICC)	0.930 (0.841-0.968)	0.829 (0.637-0.920)	0.862 (0.713-0.934)	0.932 (0.861-0.966)	0.931 (0.859-0.966)	0.862 (0.730-0.929)	0.878 (0.759-0.938)	0.850 (0.707-0.923)	0.896 (0.803-0.945)	0.846 (0.702-0.920)
Cronbach's Alpha	0.940	0.826	0.867	0.935	0.935	0.861	0.885	0.859	0.894	0.842
Consistency										
Single Measures (ICC)	0.887 (0.781-0.943)	0.704 (0.459-0.849)	0.766 (0.564-0.881)	0.878 (0.768-0.938)	0.878 (0.768-0.938)	0.755 (0.571-0.867)	0.793 (0.631-0.889)	0.753 (0.571-0.865)	0.808 (0.665-0.893)	0.728 (0.535-0.849)
Average Measures (ICC)	0.940 (0.877-0.971)	0.826 (0.629-0.918)	0.867 (0.721-0.937)	0.935 (0.869-0.968)	0.935 (0.869-0.968)	0.861 (0.727-0.929)	0.885 (0.774-0.941)	0.859 (0.727-0.928)	0.894 (0.799-0.944)	0.842 (0.697-0.918)
Cronbach's Alpha	0.940	0.826	0.867	0.935	0.935	0.861	0.885	0.859	0.894	0.842

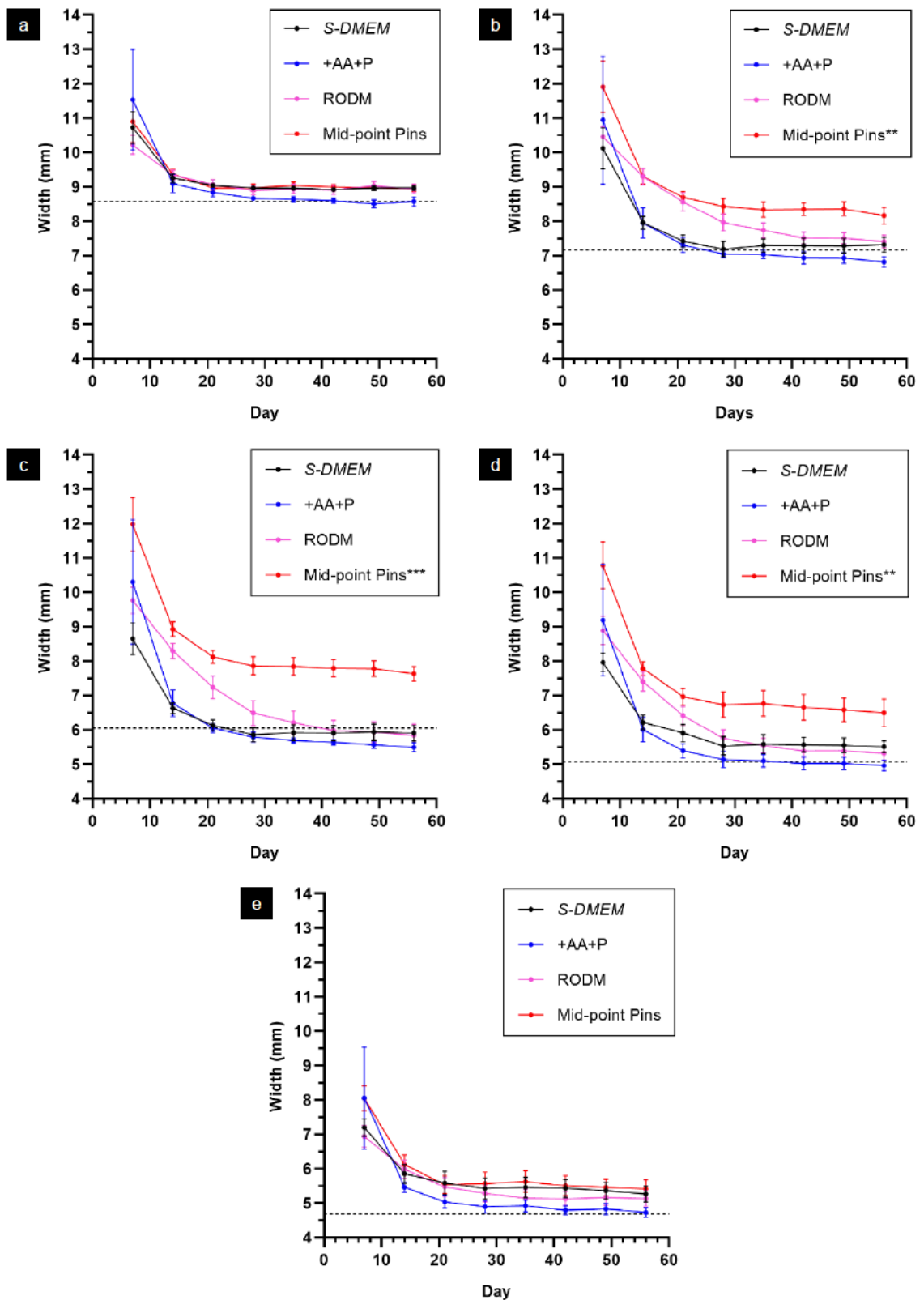
Appendix 3.2 | Inter-Observer Reliability of Individual Tendon Fibre Angle Measurements

See Table 3.8 and Appendix 3.1. Full SPSS reliability statistics output (95% confidence intervals) comparing 2 observers using a 2-way mixed effects model for the intraclass correlation coefficient (ICC).



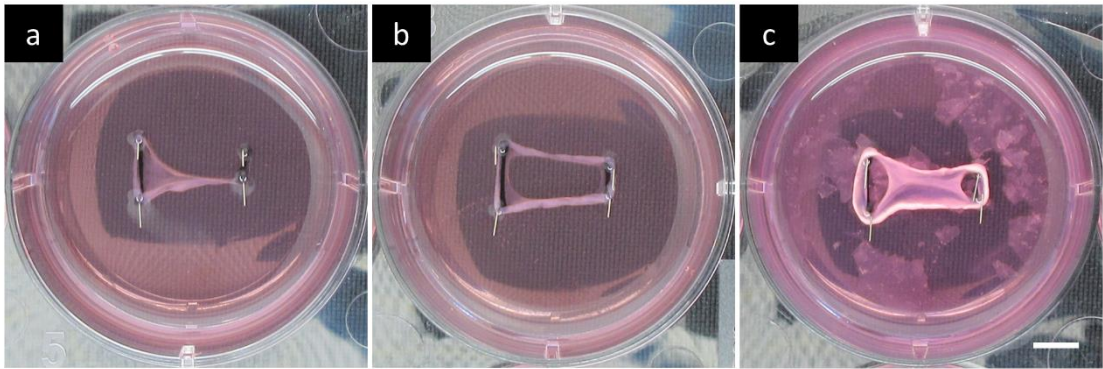
Appendix 4 | Standard Curves of dROB Cell Number for CyQUANT Fluorescence Assay

Fluorescence quantitation of known numbers of dROBs at lower (a) and higher (b) cell numbers in same dilution series comparing 1x (blue) and 5x (red) concentration of CyQUANT dye. 5x dye concentration provides the most valid linear assay range for 50 to 50,000 cells and was therefore used for experimental assays. 1x concentration gives a linear range up to 1000 cells, although registering up to ≈250 more cells than 5x concentration for a given fluorescence (a), but appears non-linear thereafter (b). Fluorescence measured with a microplate reader with excitation/emission detection at 475/500-550nm. Mean ± SEM, with broken line of best fit. See Section 4.4.4.5.6 for details.



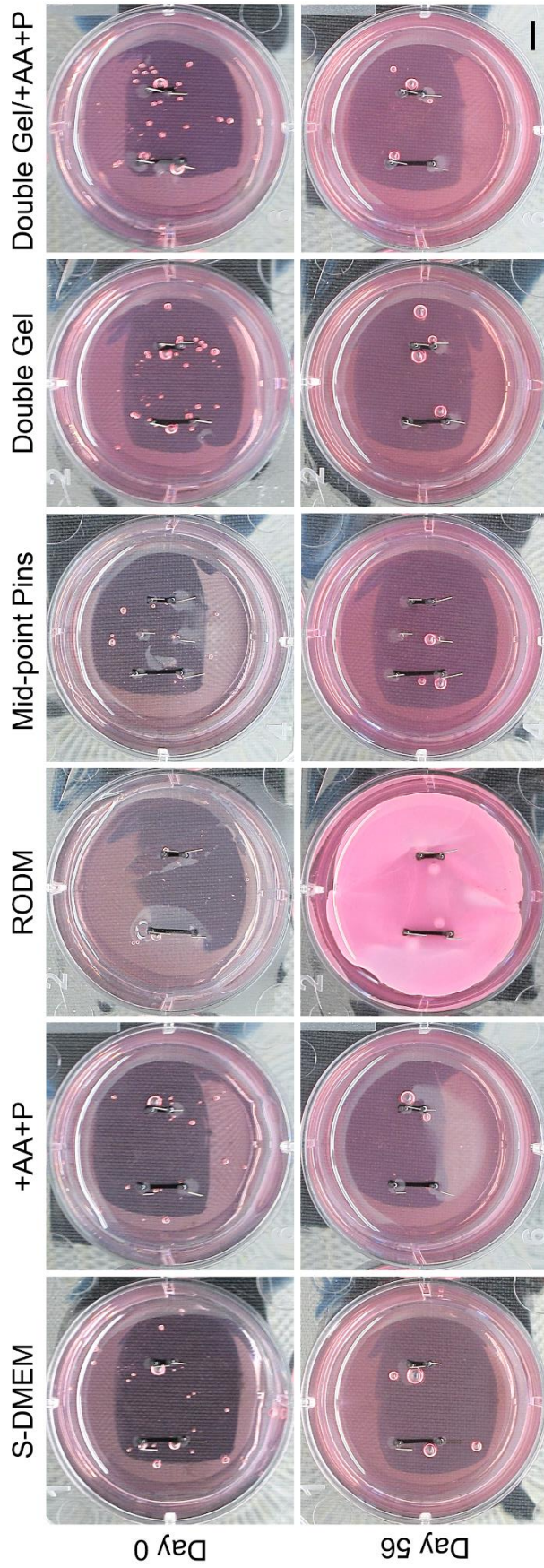
Appendix 5 | Gel Width in Standard Volume Gel Anatomical Suture Constructs

Influence of multiple culture variables on standard volume fibroblast-seeded fibrin gel width in anatomical suture constructs, compared to standard *S-DMEM* culture. **a)** 0% distance measurement point (left suture); see **Figure 4.21a**. **b)** 25% distance measurement point; see **Figure 4.22a**. **c)** 50% distance measurement point; see **Figure 4.23a**. **d)** 75% distance measurement point; see **Figure 4.24a**. **e)** 100% distance measurement point (right suture); see **Figure 4.25a**. Mean \pm SEM. ** $p < 0.01$, *** $p < 0.001$.



Appendix 6 | Unsuccessful Anatomical Suture Construct Examples

Examples of failed integrity of the fibrin gel forming the tendon analogue in anatomical suture constructs at day 56 of culture (see *Section 4.5.2.4.1*). Such constructs were excluded from gel width analyses. **a)** Failure of retained attachment to a suture anchor ('+AA+P' culture). **b)** Failure of the central gel region ('S-DMEM' culture). **c)** Substantial failure at the suture attachment region ('RODM' culture). Scale bar 5mm throughout.



Appendix 7 | Acellular Anatomical Suture Construct Controls

Comparison of day 0 and day 56 acellular fibrin gel constructs in anatomical suture experiments (see Section 4.5.2.4.3). Day 0 photographs taken following polymerisation of the fibrin gel. Control constructs underwent all media changes as per experimental constructs. Control constructs are not contracted over time, demonstrating that gel contraction is cell mediated. The opacity of the *RODM* culture after 56 days is likely due to the mineralising components of the *RODM* precipitating out over time. Scale bar 5mm throughout.

Presentations					
Date	Authors	Title	Conference	Location	Prize
Oral					
9 th -11 th August 2019	<u>Mortimer JW</u> , Alsaykhan HM, Rust PA, Paxton JZ	Applied anatomical considerations for the surgical repair of human flexor digitorum profundus avulsions	19 th Congress of the International Federation of Associations of Anatomists (IFAA)	London, UK	/
11 th -13 th June 2019	<u>Mortimer JW</u> , Macia M, Vonk NP, Rust PA, Paxton JZ	Investigations of human tendon width for the anatomical design of an <i>in vitro</i> flexor digitorum profundus enthesis model	Tissue & Cell Engineering Society – UK Society for Biomaterials (TCES-UKSB) Joint Conference	Nottingham, UK	UKSB oral presentation prize, runner-up
9 th -10 th November 2017	<u>Mortimer JW</u> , Paxton JZ, Rust PA	Characterising the anatomy of the flexor digitorum profundus insertion to guide avulsion repair	British Society for Surgery of the Hand (BSSH) Autumn Scientific Meeting	Edinburgh, UK	/
Poster					
11 th -15 th December 2020	<u>Mortimer JW</u> , <u>Loukopoulou C</u> , Vonk NP, Fassoula V, Macia M, Rust PA, Paxton JZ	Using human tendon morphology to guide <i>in vitro</i> model development	11 th World Biomaterials Congress	Virtual	/
23 th -24 th November 2020	<u>Loukopoulou C</u> , <u>Mortimer JW</u> , Rust PA, Vorstius JB, Paxton JZ	Modelling enthesis development <i>in vitro</i> to produce anatomically and clinically relevant bone-tendon constructs for flexor tendon repair	UK-Poland Bioinspired Materials Conference	Virtual	Best poster presentation
9 th -11 th August 2019	<u>Mortimer JW</u> , Macia M, Vadibeler S, Vonk NP, Graute M, Rust PA, Paxton JZ	Anatomical design of a tissue engineered <i>in vitro</i> model of the human flexor digitorum profundus enthesis	19 th Congress of the International Federation of Associations of Anatomists (IFAA)	London, UK	Cave young investigator poster prize
11 th -13 th June 2019	<u>Mortimer JW</u> , Vadibeler S, Macia M, Graute M, Rust PA, Paxton JZ	Designing an angled interface for an <i>in vitro</i> flexor digitorum profundus enthesis model through human histological investigation	Tissue & Cell Engineering Society – UK Society for Biomaterials (TCES-UKSB) Joint Conference	Nottingham, UK	/
4 th December 2018	<u>Mortimer JW</u> , Rust PA, Paxton JZ	Designing an anatomically and clinically relevant bone anchor for tissue engineering the enthesis at the human flexor digitorum profundus insertion	Edinburgh Musculoskeletal Group Regional Winter Research Symposium	Edinburgh, UK	Best poster and flash talk presentation
8 th -12 th July 2018	<u>Mortimer JW</u> , Rust PA, Paxton JZ	Designing an anatomically and clinically relevant bone anchor for tissue engineering the enthesis at the human flexor digitorum profundus insertion	8 th World Congress of Biomechanics	Dublin, Ireland	/
11 th -12 th April 2018	<u>Mortimer JW</u> , Alsaykhan HM, Rust PA, Paxton JZ	Designing clinically-relevant tissue-engineered models of the tendon-bone interface	Tendon UK: Emerging Themes in Translational Tendon Science	Oxford, UK	/
27 th April 2017	<u>Mortimer JW</u> , Rust PA, Paxton JZ	Bone anchor design for a clinically relevant <i>in vitro</i> model to investigate flexor tendon to bone repair	Edinburgh Musculoskeletal Group Regional Meeting	Edinburgh, UK	/

Appendix 8 | Oral and Poster Presentations

Table of project related presentations. Presenter underlined.